Tyco Laboratories, Inc.
Bear Hill
Waltham, Massachusetts 02154

STUDY OF THE GENERAL MECHANISM OF STRESS CORROSION OF ALUMINUM ALLOYS AND DEVELOPMENT OF TECHNIQUES FOR ITS DETECTION

by

S. B. Brummer
R. O. Bell
F. H. Cocks
A. Cordellos

Covering Period

1 June 1966 to 1 June 1969

Final Report
Contract No. NAS 8-20297

Control No.
BCN 1-6-54-01079 (1F)

September 1969

PREPARED FOR

NATIONAL AERONAUTICS AND SPACE ADMINISTRATION
G. C. MRSHALL SPACE FLIGHT CENTER
HUNTSVILLE, ALABAMA 35812

Tyco Laboratories, Inc.
Bear Hill
Waltham, Massachusetts 02154

STUDY OF THE GENERAL MECHANISM OF STRESS CORROSION OF ALUMINUM ALLOYS AND DEVELOPMENT OF TECHNIQUES FOR ITS DETECTION

by

S. B. Brummer
R. O. Bell
F. H. Cocks
A. Cordellos

Covering Period

1 June 1966 to 1 June 1969

Final Report

Contract No. NAS 8-20297

Control No.
BCN 1-6-54-01079 (1F)

September 1969

Prepared for

National Aeronautics and Space Administration
G. C. Marshall Space Flight Center
Huntsville, Alabama 35812

This report was prepared by Tyco Laboratories, Inc., under Contract No. NAS 8-20297, "Study of the General Mechanism of Stress Corrosion of Aluminum Alloys and Development of Techniques for Its Detection," for the George C. Marshall Space Flight Center of the National Aeronautics and Space Administration. The work was administered under the technical direction of the Aeronautics Laboratory, Materials Division of the George C. Marshall Space Flight Center, with Mr. D. B. Franklin acting as project manager.

ABSTRACT

The objectives of this investigation have been to examine the mechanism of the stress corrosion cracking (SCC) of Al alloys (phase I), and to study the feasibility of using instrumental methods to detect stress corrosion cracking on fabricated Al alloy parts (phase II).

The mechanism of SCC of high strength Al alloys has been investigated using electrochemical, mechanical, and electron microscopic techniques. Corrosion and stress corrosion experiments have been carried out in 1M NaCl buffered to pH 4.7, usually at 30 °C, using the commercial alloys 7075 and 2219 and also relevant pure materials. Correlations have been made between susceptibility to SCC and the following properties of the particular alloys:

1. Metallurgical condition
2. Mechanical properties (macroscopic and local)
3. Corrodibility (macroscopic and local)
4. Ambient conditions in the corrodent
5. Surface treatment.

The results of these studies are summarized in the following paragraphs.

Although the importance of metallurgical treatment on the susceptibility of Al alloys to stress corrosion is well known, the underlying reasons for this sensitivity are not completely understood. This relationship has been explored for both pure and commercial alloys using electron microscopy and mechanical tests.

True stress-true strain curves were obtained for the alloys 2219-T851 and -T37, and 7075-T6(51) and -T73. Measurements were made at two different strain rates to determine the activation volume for dislocation movement. It was concluded that for 7075-T6, dislocations are more highly entangled in the highly susceptible short transverse direction than in the rolling direction. For 7075-T73 (nonsusceptible) and for both tempers of 2219, the dislocations were relatively unentangled. The results for 7075 are consistent with our stress corrosion data in suggesting that it is primarily

the mechanical properties of this material, as a function of heat treatment, which determine its sensitivity to stress corrosion. However, the role of dislocation movements for 2219 is much less important. Thus, the effect of the stress level on the SCC failure time of 7075 is much larger than 2219.

With pure alloys, electron microscopy has been used to study their age hardening process and to examine the mode of mechanical deformation and of corrosive attack.

The microscopic features of the age hardening of Al-4Cu and Al-7.5Zn-2.4Mg have been studied. Precipitation begins in the grain boundaries. Both the precipitate free zone (PFZ) and the precipitate particles grow with increasing aging time and temperature. The particles never link up, as required for the Dix theory for Al-Zn-Mg, and the PFZ is always continuous for aged Al-4Cu, irrespective of the aging time. This indicates that whatever the role of age hardening in promoting SCC susceptibility in this alloy, it does not provide a continuous anodic path.

Deformation of foils in the electron microscope indicates that age hardened Al-Zn-Mg tends to cleave along grain boundaries, whereas age hardened Al-Cu tears across the grains. These results support the above conclusions on these alloy systems, based on the deformation of the commercial alloys. The conclusions may be expanded: for Al-Zn-Mg (7075), it is the local, grain boundary mechanical properties which are critically important. For Al-4Cu, preferential corrosive intergranular attack occurs in all tempers, susceptible and nonsusceptible. This attack proceeds by dissolution of the Cu-depleted zone parallel with the boundary; the $CuAl_2$ particles are left behind. In Al-7.5Zn-2.4Mg, the particles of $MgZn_2$ are attacked first, but since they are never continuously linked, no specific grain boundary attack is evident. These results show that in neither case can the Dix theory of stress corrosion be applied.

Corrosion of foils of Al-7.5Zn-2.4Mg, heat treated and strained to produce planar arrays of dislocations, have shown that such substructural features are preferred sites for dissolution.

The corrosion of Al, Al-Cu, $CuAl_2$, Al-Zn-Mg, and $MgZn_2$ has been studied in pH 4.7 solutions of Cl^- and SO_4^{2-}. The polarization phenomena for the alloys and the mode of attack on them have been characterized.

In the Al-Cu system, the corrodibility is determined both by the composition and by the heat treatment. The effect of Cu in general is to make dissolution harder. However, 2219-T37 is much less generally corrodible than 2219-T851 in Cl^- solutions, although their compositions are identical. The nonsusceptible -T851 temper showed only general attack, but the stress corrosion susceptible -T37 temper experienced intergranular attack. Similar effects were found for pure Al-4Cu alloys: the heavily overaged material was more corrodible than less precipitated tempers. All Al-Cu materials corrode more easily in Cl^- than in SO_4^{2-}, in line with their ease of stress corrodibility. All of these observations support the Dix theory of stress corrosion in these alloys.

For the pure ternary (Al-7.5Zn-2.4Mg) the ease of corrosion in Cl^- solutions decreases as we proceed from the solutionized to the maximum susceptibility to the overaged tempers. In all three forms, the dissolution occurs much more readily than that of 7075. In addition, in the overaged condition, a secondary passivation effect is observed at about –680 mV versus NHE. In SO_4^{2-} solutions, the overaged form of the pure ternary is much more readily attacked than the solutionized form, and both are more readily attacked than 7075 or pure Al. It is shown that the differences between the pure ternary and 7075 result from the presence of Cu in the latter. An explanation of the effects of aging and of Cu on the corrosion of the pure ternary is presented. This involves the effects of incorporation of Mg and/or Zn and/or Cu in Cl^- and SO_4^{2-} formed Al_2O_3 films.

In this alloy system, there are no significant differences in macroscopic mode of attack with temper, i.e., there is no evidence for preferential intergranular attack in stress corrosion susceptible tempers. Also, the ease of corrodibility of $MgZn_2$ is similar in Cl^- and SO_4^{2-}, although SCC of the alloys occurs much more readily in the former. The Dix theory of SCC does not then appear applicable to this alloy system.

The stress corrosion of 7075, 2219, and appropriate pure alloys in pH 4.7 Cl^- and SO_4^{2-} solutions has been studied under galvanostatic forced corrosion conditions at 30 °C. The failure time in stress corrosion is strongly influenced by mass transport in solution. This must be controlled by appropriate stirring conditions. Low currents are somewhat more efficient in causing stress corrosion than large currents. It is suggested that the galvanostatic method of testing could be used as an accelerated and reproducible stress corrosion test.

The mode of failure is quite different for Al-Zn-Mg and Al-Cu. For Al-Zn-Mg, failure is catastrophic. That is, the load decreases only slightly with time during constant strain stress corrosion and then suddenly drops to zero as a single crack propagates across the specimen. For Al-Cu, the load falls in a stepwise manner during test. Experiments with large grained Al-4Cu show that this is due to the periodical advancement of a single crack from grain boundary intersection to grain boundary intersection. The necessity for continuous loading throughout this periodic failure process shows that the process is not a periodic electrochemical mechanical (PEM) phenomenon; rather, it is a periodic electrochemical-mechanical, mechanical (PEMM) phenomenon.

Although stress must be continuously applied for failure in 2219, most of the attack on 7075 does not require the presence of stress. These phenomena were investigated by exploring the effects of pure corrosion on subsequent stress corrosion life. Such experiments led to the definition of a precorrosion susceptibility index (PSI):

$$\text{PSI} = \frac{-\text{d (time to failure after precorrosion)}}{\text{d (time of precorrosion)}}$$

Where the PSI is 0, as in 2219-T37, precorrosion has no effect on subsequent stress corrosion. Where the PSI is 1, as it is initially for 7075-T6(51), the failure process occurs equally efficiently in the absence as in the presence of stress.

These experiments yield the following information on the failure of Al-Zn-Mg:

1. More than 80% of the normal time to failure has nothing to do with "stress corrosion," but is a pure corrosion effect (the "precorrosion" effect). A true stress corrosion process only accounts for 20% of the normal life in normal stress corrosion tests. Conclusions on the stress corrosion mechanism of 7075, based on normal times to failure, are not likely then to be generally valid.

2. Two stages are involved in crack propagation. The first is the longest and is purely electrochemical. The second involves the combined effects of chemical and stress factors. The precorrosion effect results from mechanical destruction of the grain boundary structure by working of the surface (e. g. , by machining). It has important implications for the protection of finished structures of Al and Ti alloys.

3. The effect of temperature on SCC life depends strongly on surface preparation because of the precorrosion effect. For electro-polished samples, the time to failure decreases with increasing temperature, while for as machined samples, the reverse is true. These effects result from the changing morphology of attack on surface deformed layers with increasing temperature.

4. Overaging of 7075-T6 leads to enhanced "stress corrosion" life. In fact, it turns out that all of this improvement results from improvement in precorrosion susceptibility, and that the pure stress corrosion life is shorter for overaged alloys. A new heat treatment procedure is suggested which retains the strength of 7075-T6, but improves its overall stress corrosion resistance by two orders of magnitude.

Localization of deformation in Al-Zn-Mg alloys has been investigated by studying current transients during straining. For 7075, correlations in the elastic deformation region suggest that localization of deformation is strongly correlated with susceptibility to SCC. For pure Al-Zn-Mg, however, the opposite is true and more SCC susceptible tempers do not exhibit such localized deformation.

The second phase of the program involved the study of the feasibility of detecting incipient stress corrosion damage in Al alloy parts in a nondestructive manner. A survey of testing techniques pertinent to surface damage was carried out. Of the techniques available, ultrasonic surface (Rayleigh) waves and surface conductivity (eddy currents) appeared to be most promising.

A feasibility study for crack detection on 7075 was performed with eddy currents at 6 MHz. They proved to be very sensitive to surface finishes with scratch depths as shallow as 0.3 μ. However, the threshold of detection of single grooves on a smooth surface was as deep as 10 μ. It was also demonstrated that eddy currents are sensitive to surface curvature. Various SCC conditions produced increases in apparent resistivity ranging from 10 to 120%. The results demonstrated the feasibility of eddy currents to detect SCC. A principal disadvantage of the eddy current technique is the small area that can be sampled (~1/8-in.-diameter circle) with each measurement. This vitiates its practical usefulness.

Ultrasonic measurements were performed mainly at 4 MHz using a $BaTiO_3$ probe. The SCC investigation was performed with U-bend specimens of 7075 and 2219. Before the SCC studies began, the effect of surface finish on the wave attenuation and general galvanic corrosion (GGC) were investigated. It was found that the surface finish has a small effect on the attenuation compared to that produced by SCC. Also, the damage produced by GGC is small compared to that of SCC.

An investigation of the effect of simulated defects on Rayleigh wave propagation was carried out. It was shown that if the dimension of a defect is of the order of a few tenths of a wavelength, reflections are readily visible with an effective increase in attenuation. Defects located deeper than 1 wavelength below the surface are not detectable. The resolution between closely spaced reflectors is ~1.5 mm.

Detectability of SCC on 7075-T651 and 2219-T37 is largely affected by the conditions of testing. In particular, release of the stress allows the cracks to close and makes their detection less easy. For example in 7075, with SCC carried out at 90% of the yield stress, surface attenuation is about

five times higher in the stressed as unstressed testing condition. Test of practical configurations in the substantially loaded state is therefore recommended. However, even in the unloaded state, SCC can be readily detected and distinguished from GGC and other surface markings.

Most of the SCC experiments were carried out galvanostatically at pH 4.7. Under these conditions, SCC produced at 60 and 90% of the 0.2% offset yield strength can be detected ultrasonically on 7075 after approximately a 0.2 C/cm^2 incubation period at 90 and 60% of the yield strength. This corresponds to less than 10% of the total life of the specimen. In 2219 under similar conditions there is little if any incubation period for the detection of cracking. This ultrasonic threshold is determined by the reflections from grain boundaries.

After the onset of SCC, the attenuation increases approximately linearly with further stress corrosion for 2219 and 7075, in both the stressed and unstressed conditions at both the 60 and 90% stress levels. The increase in attenuation for 2219 is not as smooth as for 7075. This is related to the more periodic nature of crack propagation in 2219.

Even after the stress has been released, the ultrasonic attenuation and reflectivity from cracks are substantially greater for SCC after a given amount of corrosion than for GGC samples.

For SCC produced at low stresses, e.g., at 30% of the yield stress, the ultrasonic attenuation is much less than that of samples corroded at high stress and, in the unloaded testing state, it is difficult to differentiate ultrasonically between the 30% SCC and GGC samples, at least by simple attenuation measurements.

A study was made of the detectability of SCC caused under other ambient conditions. The ultrasonic properties of samples corroded between 1.5 and 0.55 mA/cm^2 are in very good agreement when plotted as a function of total charge passed. At a pH of 2.1, the slope of the increase in attenuation expressed in db/cm with increasing corrosion is approximately 50% larger than for pH 4.7. The ultrasonic attenuation in 7075 U-bends is less in a basic solution (pH = 11.8) than in more acidic solutions (pH = 4.7 and 2.1). The ratios of slope of the increase in attenuation expressed in db/cm with increasing corrosion are 2:1.2:1 for pH's of 2.1, 4.7, and 11.8, respectively.

The precorrosion studies of phase I of this program suggest that the incipient damage detected by nondestructive testing (NDT) is not that which finally leads to failure. Therefore, an investigation of the effect of precorrosion on subsequent crack propagation was carried out. Precorrosion was found to be very effective in establishing surface conditions where stress corrosion can occur. The conclusions drawn from this investigation are similar to those of the mechanism study. Here, in the NDT part, it was shown that if the precorrosion exposure is equal to or smaller than 70% of the total exposure, the total damage is equal to the damage produced by conventional SCC at the same exposure. For precorrosion exposure, the total damage is smaller than for conventional SCC, and it decreases with increasing precorrosion exposure.

Application of GGC after the stress applied during an SCC test is relaxed indicated that such subsequent GGC produces additional damage at a rate only equal to conventional GGC. This shows that SCC does not set up the surface for localized further attack.

Water trapped in corrosion cracks causes an apparent decrease in their depth (as indicated by surface waves) by acting as a coupling medium between the two sides of the crack. Since this decreases the detectability of the cracks, careful cleaning of the surface is necessary to remove this water.

The reflectivity from SCC cracks is anisotropic with the largest reflection coefficient in a direction parallel to the stress (i. e. , perpendicular to the cracking). GGC also exhibits some anisotropy, due to grain orientation in the sample. The strong anisotropy of SCC reflections allows their ready distinguishability from other kinds of surface damage, e. g. , GGC.

The conclusion is that Rayleigh waves are suitable for SCC detection on fabricated parts. Correspondingly, an investigation of techniques for detecting SCC in practical conditions was carried out.

One such possibility involves introducing a reflector with a reproducible reflection coefficient, such as a brass plate, onto the surface. Then the attenuation, which depends critically on the amount of SCC, may be measured.

Since Rayleigh waves are not extremely sensitive to surface finish, it appears that this technique of measuring surface attenuation is very promising for routine detection of SCC damage.

Studies have also been made of single pass measurements of ultrasonic Rayleigh wave attenuation involving the use of a second (receiving) transducer. Such transducers can be coupled to the surface with a reproducibility of approximately 1 db ($\pm \frac{1}{2}$ db), allowing accurate correlation of attenuation with SCC damage.

Instrumental design parameters have been explored experimentally and theoretically: the probability of detecting a crack when only a fraction of the surface is examined has been considered for various conditions. Problems associated with the relative length of the crack compared with the width of the ultrasonic beam, and the angle between the crack and beam, have been analyzed and a technique for an optimal examination of the surface is proposed.

Work to explore the detection of SCC at higher frequencies, i. e., with greater sensitivity, was carried out. Surface wave transducers with flint glass prisms were used. These can be operated at their 4-MHz fundamental and at their first two overtones: 12 to 20 MHz. No significant advantage in detection ability was found.

Various modes of ready transducer attachment to the surface were explored. Rubber sheets attached to the foot of normal surface wave transducers do couple the acoustic waves to the sample but, with the configurations we have used, the additional loss over a cement bond is a minimum of 5 db.

The behavior of rubber cement transducer couplings versus time for different laboratory conditions was investigated. It was found that when the rubber cement bond dries without being disturbed (without handling), it reaches a value of about 14 db at approximately 20 hr, after which no further change in coupling occurs. If the sample is tested while the bond is drying, this value ($\sim$ 14 db) is reached after approximately 3 hr. During intermittent tests in which the U-bend is both corroded and at rest for successive time intervals, the terminal value, due to the combined losses of drying of the rubber cement bond and handling, is about 21 db.

Reproducible bonding to the surface is the most critical problem for practical situations. As an alternative to cement bonds, a liquid filled transducer was studied. The longitudinal velocity of acoustic waves in liquids is such that they could make good media for launching Rayleigh waves onto Al, and a possible configuration using an enclosed liquid probe is discussed. The constructed transducer was made of copper, at an angle of 47 degrees with the horizontal, and was filled with distilled water. It successfully launched surface waves.

Using the SCC and precorrosion data, a method is proposed for determining the amount of SCC damage on a fabricated part of 7075 with a minimum of knowledge of its prior treatment. This method involves slight stressing of the corroded part to a small fraction of the stress used in the SCC test.

Table of Contents

Table of Contents (Cont.)

Table of Contents (Cont.)

Table of Contents (Cont.)

List of Illustrations

List of Illustrations (Cont.)

List of Illustrations (Cont.)

List of Illustrations (Cont.)

List of Illustrations (Cont.)

List of Illustrations (Cont.)

List of Illustrations (Cont.)

List of Illustrations (Cont.)

List of Illustrations (Cont.)

List of Illustrations (Cont.)

List of Illustrations (Cont.)

List of Illustrations (Cont.)

List of Tables

I. INTRODUCTION

The aims of this research program have been: (1) to investigate the mechanism of stress corrosion cracking (SCC) of Al alloys, and (2) to examine nondestructive testing (NDT) techniques for detecting SCC in fabricated parts.

For phase I (the mechanism study), we have concentrated on the commercial alloy systems 7075 and 2219, with ancillary work on pure alloys and phases. The approach has been to investigate in detail the physical and structural metallurgy of the materials and also their corrosion characteristics. These results are presented in Sections II and III of this report.

For phase II (the use of NDT to detect SCC), studies have been made with eddy currents and ultrasonic surface (Rayleigh) waves. Experiments have been made on 7075-T6 and 2219-T37. Results are presented in Section IV and Appendix A.

II. METALLURGICAL CHARACTERIZATION OF ALUMINUM ALLOYS

A. General

The metallurgical characterization of both high purity and commercial Al alloys has been undertaken to provide metallurgical information which can be correlated with the results of stress corrosion tests.

Although the importance of metallurgical treatment and condition on the susceptibility of Al alloys is well known, the underlying reasons for this sensitivity are not yet completely understood. For commercial materials, the aim has been to correlate susceptibility with the dislocation structure determined from the mechanical tests. For the high purity materials, we have attempted to correlate corrosive attack and mode of mechanical deformation with specific structures developed during aging.

B. Mechanical Tests

True stress-true strain curves were obtained for 2219-T851 and -T37, as well as for 7075-T6(51) and -T73. All mechanical tests have been made on standard tensile specimens cut from a 1.5-in.-thick plate. The dimensions of these specimens are given in Fig. 1. Specimens have been taken in both the short transverse and in the rolling directions. Two different strain rates, 4.4×10^{-3} and 4.4×10^{-2} min^{-1}, were used. In order to ensure high accuracy in the determination of strain, an extensometer was used, rather than the cross-head position alone. The extensometer was calibrated using a micrometer to give an extension magnification of 500 to 1. The load was measured to ±0.5%. Gauge diameters were measured to ±0.0001 in., gauge lengths to ±0.003 in.

True plastic strain and the true stress were calculated from the equations:

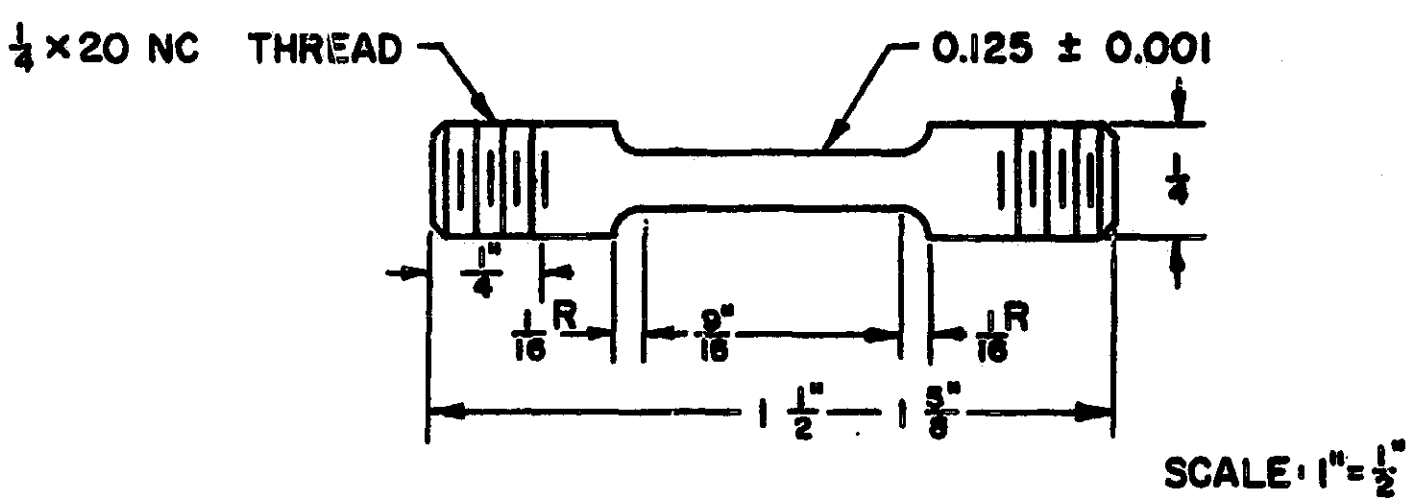

Fig. 1. Dimensions of specimens used for tensile tests

$$\epsilon_T = \int_{\ell_0}^{\ell} \frac{d\ell}{\ell}$$

$$\sigma_T = \frac{L}{A_0} \frac{\ell}{\ell_0}$$

where ϵ_T = true plastic strain

σ_T = true stress

ℓ_0 = original gauge length

ℓ = instantaneous gauge length minus elastic extension

A_0 = original cross-sectional area

L = instantaneous load

The change in specimen dimension occurring during elastic extension was corrected, assuming a Poisson's ratio of 0. 33.

Both short transverse and rolling direction specimens were tested. In addition, in the case of the rolling direction, specimens cut from both the center and the surface of the plate were examined.

The results of these experiments (Figs. 2 and 3) show true stress-true strain curves for 7075-T6(51), 7075-T73, 2219-T851, and 2219-T37 short transverse specimens, as well as for 7075-T6(51), 2219-T851, and 2219-T37 rolling direction specimens. In each case, these materials were tested at two different strain rates. From these data, noting the change in flow stress with change in strain rate, and remembering that for 7075 strain aging can occur, two conclusions can be drawn.

First, for 7075-T6(51), dislocations are more highly entangled in the short transverse than in the rolling direction. Second, for the -T73 temper of 7075 and for both tempers of 2219, the dislocations were found to be relatively unentangled.

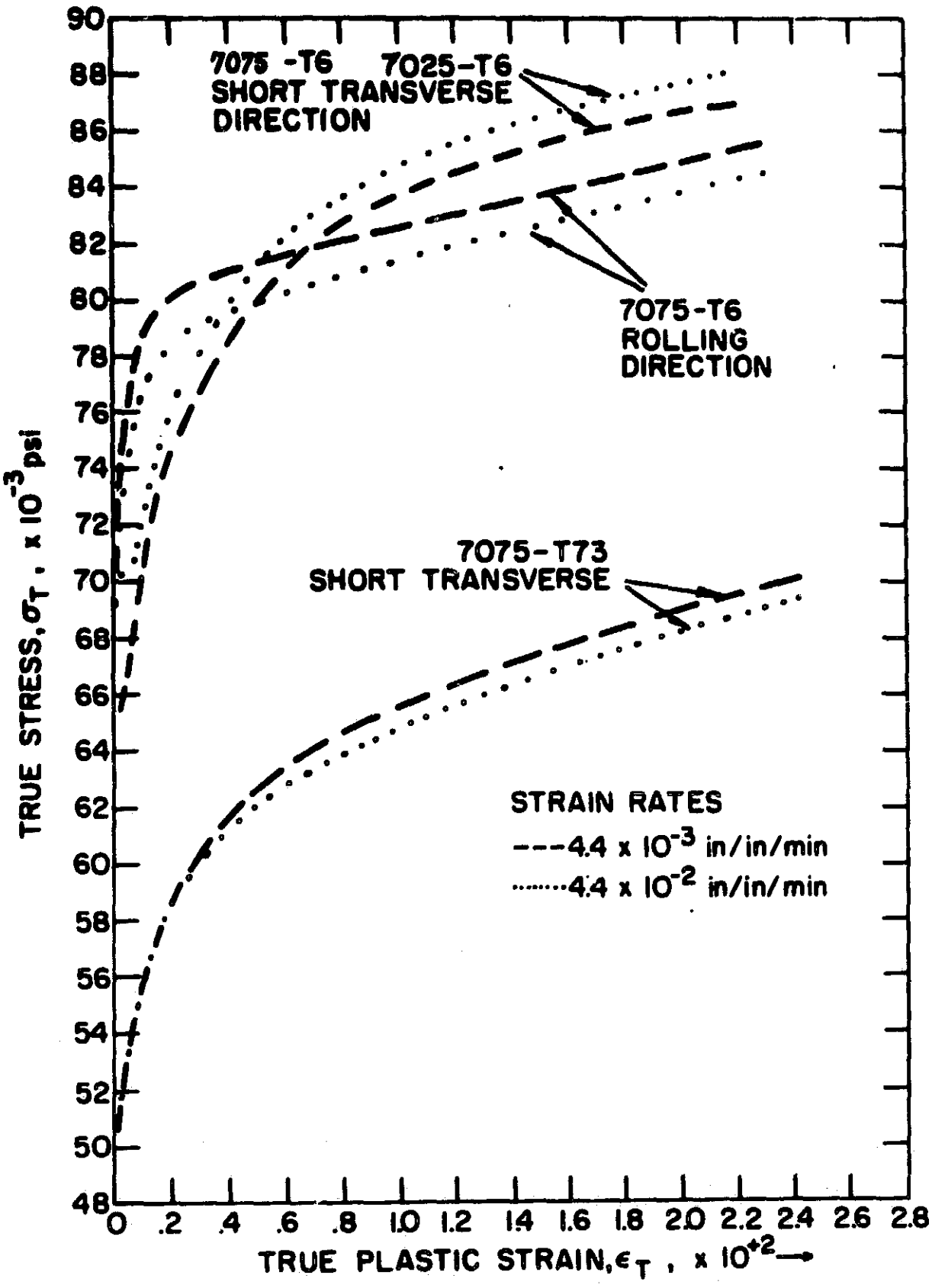

Fig. 2. True stress - true plastic strain curves for 7075-T6 and 7075-T73

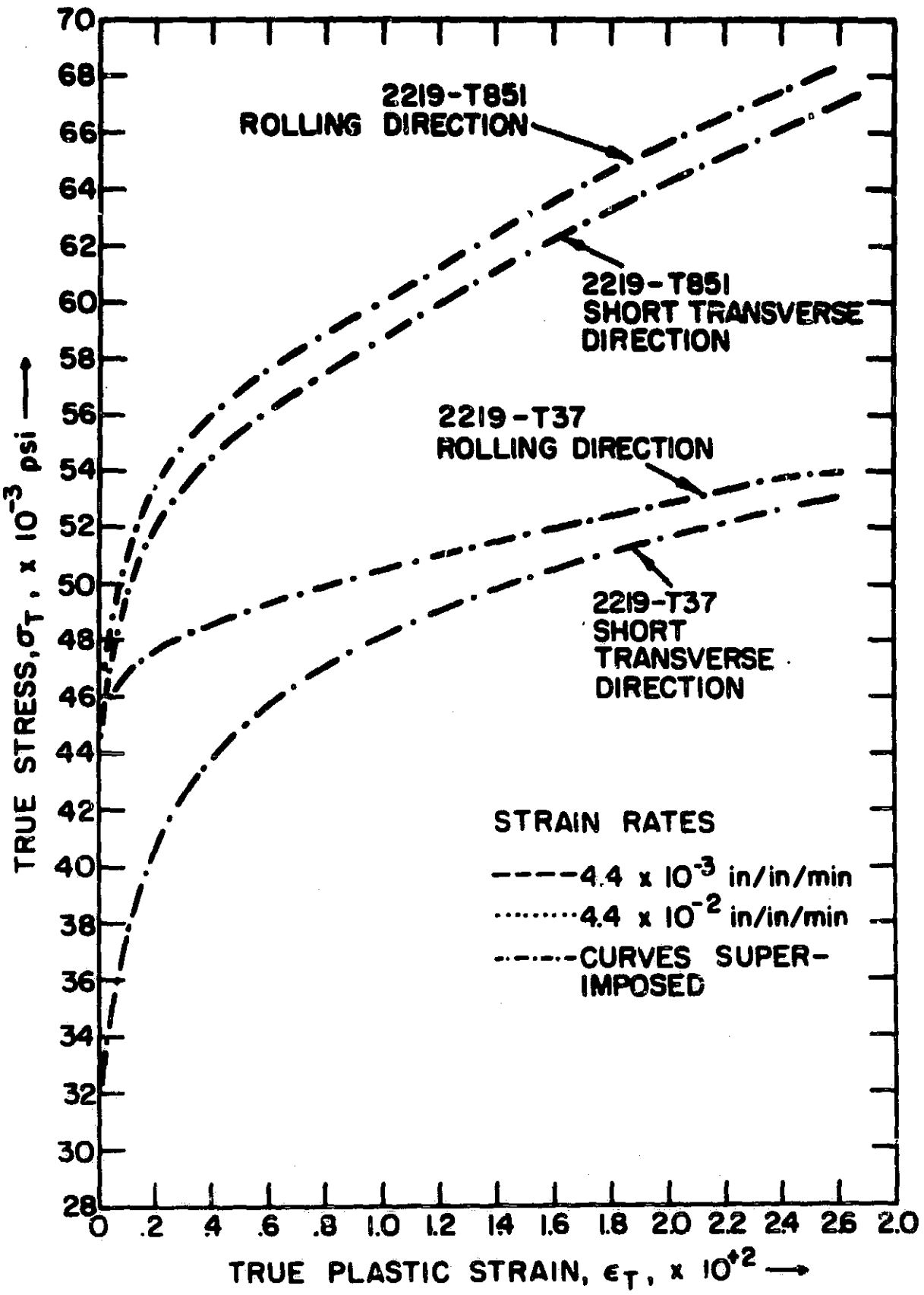

Fig. 3. True stress - true plastic strain curves for 2219-T851 and 2219-T37

The results for 7075 are in agreement with the known relative susceptibilities of the rolling and the short transverse directions. For 2219, these results would indicate that the mechanical state of this alloy is not as relevant to stress corrosion as it is for 7075. This conclusion is in agreement with results discussed in part C of this section which show that the high purity analogue of 7075 tends to crack along grain boundaries even in the absence of a corroding medium, hence indicating the strong role played by purely mechanical considerations. The high purity analogue of 2219, on the other hand, shows no tendency towards such intergranular failure.

C. Localization of Deformation of Pure Alloys

Deformation experiments in the mechanical stage of the microscope have illustrated the great difference in behavior between the ternary and the binary alloys. Fig. 4 shows what happens when aged specimens of both alloys are strained in vacuum. As can be seen, the Al-Zn-Mg has begun to fracture along grain boundaries. The Al-Cu, on the other hand, does not rupture along these boundaries, but tears transgranularly.

These results indicate that the grain boundary cleavage energy of Al-Mg-Zn is substantially lower than Al-4Cu, even without the presence of a corrosive environment. As will be shown later, this difference plays an important role in the failure mode of these alloys under stress corrosion conditions.

D. Nature of Cracking of Al-Zn-Mg

Because of the importance of the mechanical properties of Al-Zn-Mg in determining its SCC susceptibility, a scanning electron microscopic study was carried out to examine features on the fracture surfaces of cracking specimens.

For these experiments, Al-7.5Zn-2.4Mg was aged (to bring it into the region of susceptibility) in three stages. These treatments were:

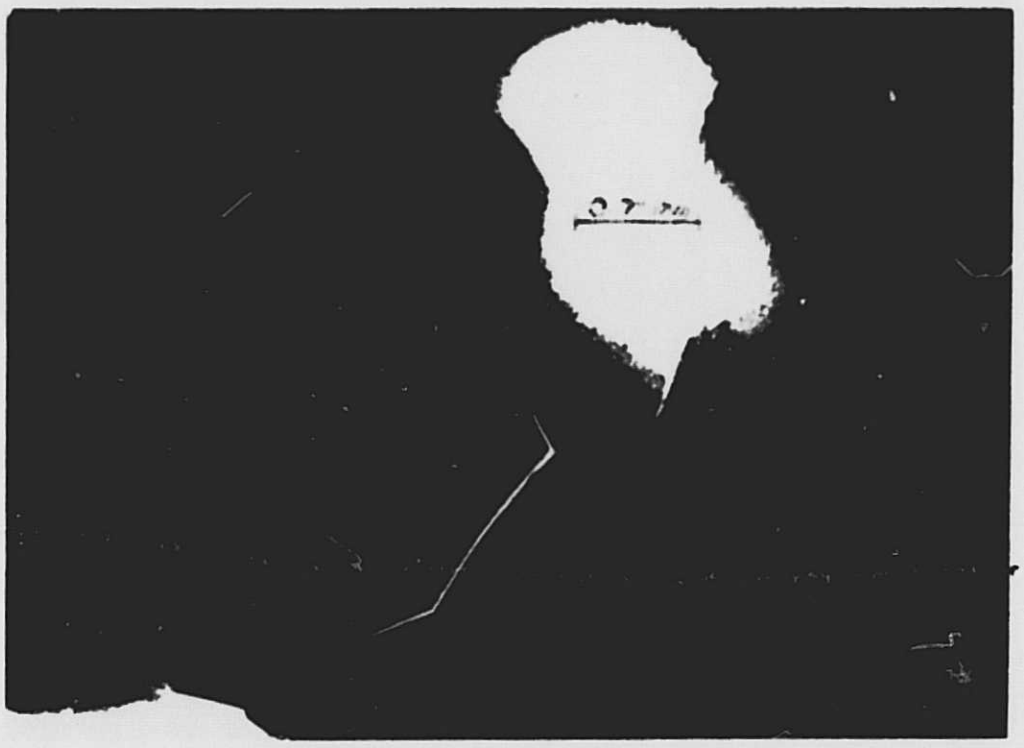

(a) Al-7.5 Zn - 2.4 Mg

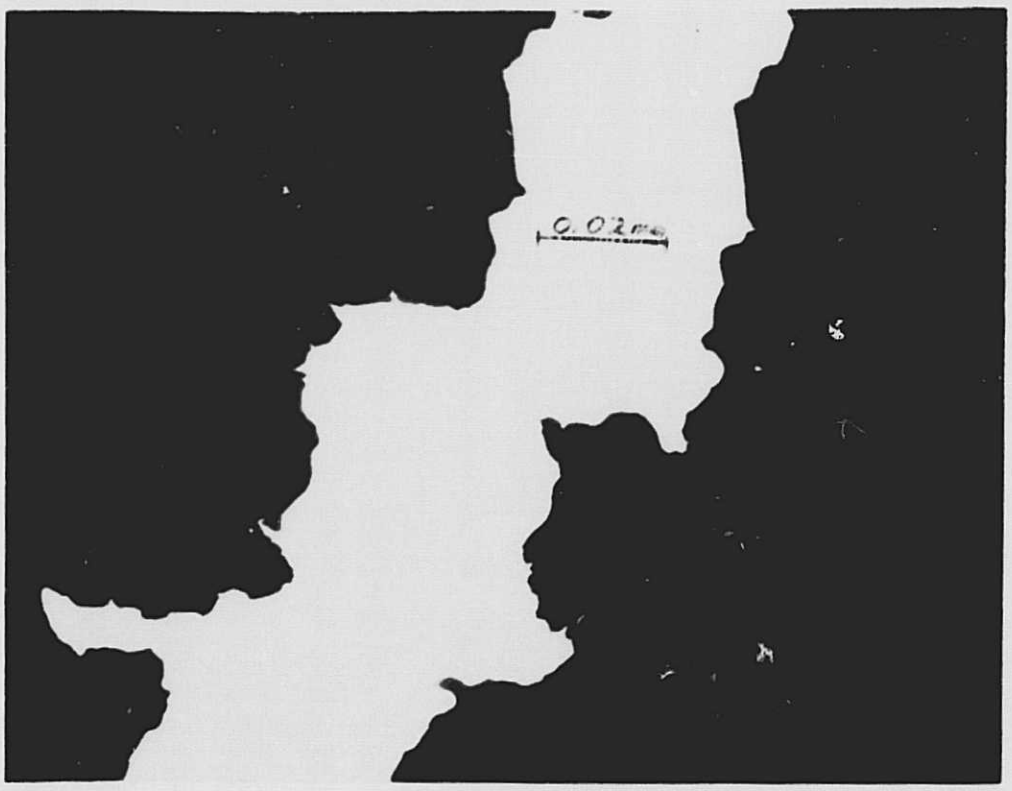

(b) Al-4 Cu

Fig. 4. Deformation of aged foils in vacuum

(1) heating for 24 hr at 100 °C, (2) heating for 72 hr at 100 °C, and (3) heating for 16 hr at 150 °C. In all cases, the specimens were first put in the solutionized condition by heating at 480 °C for 6 hr and were then water quenched. In this study, photographs were obtained which show the change in marking form and type which occurred on going from treatment (1) to (2) to (3) (Fig. 5a, b, and c, respectively).

In condition (2) in which the alloy is most susceptible to SCC, the striations were observed to be coarser than in either condition (1) or (3). This finding is in agreement with the theories of Holl[1] and of Speidel[2] that maximum susceptibility should be associated with the appearance of planar arrays of dislocations.

These planar arrays would be expected to produce coarse striations on the fracture surface. This is because they represent points of stress concentration when stress is applied to the sample, and hence would perturb the advance of the crack front, i.e., at a dislocation pileup. The crack would advance faster because of the higher stress concentration. Similarly, between pileups, advance would be slower. These sudden changes in crack velocity would cause a concomitant change in plastic relaxation at the crack tip which would in turn lead to markings on the fracture surface.

E. Aging of Aluminum Alloys

The importance of the aging characteristics of Al alloys on their stress corrosion susceptibility has long been known. More recently,[3] the specific importance of the precipitate free zone (PFZ) has been shown for the case of Al-Zn-Mg alloys. We have examined foils of both Al-4Cu and Al-7.5Zn-2.4Mg to determine the characteristics of the PFZ in these alloys.

Typical results for the case of Al-4Cu in the solutionized condition are shown in Fig. 6. As expected, no precipitates are visible either along the boundary or within the body of the grains. Fig. 7 shows a similar grain boundary after 3 hr at 200 °C. In this case, both precipitates and a PFZ

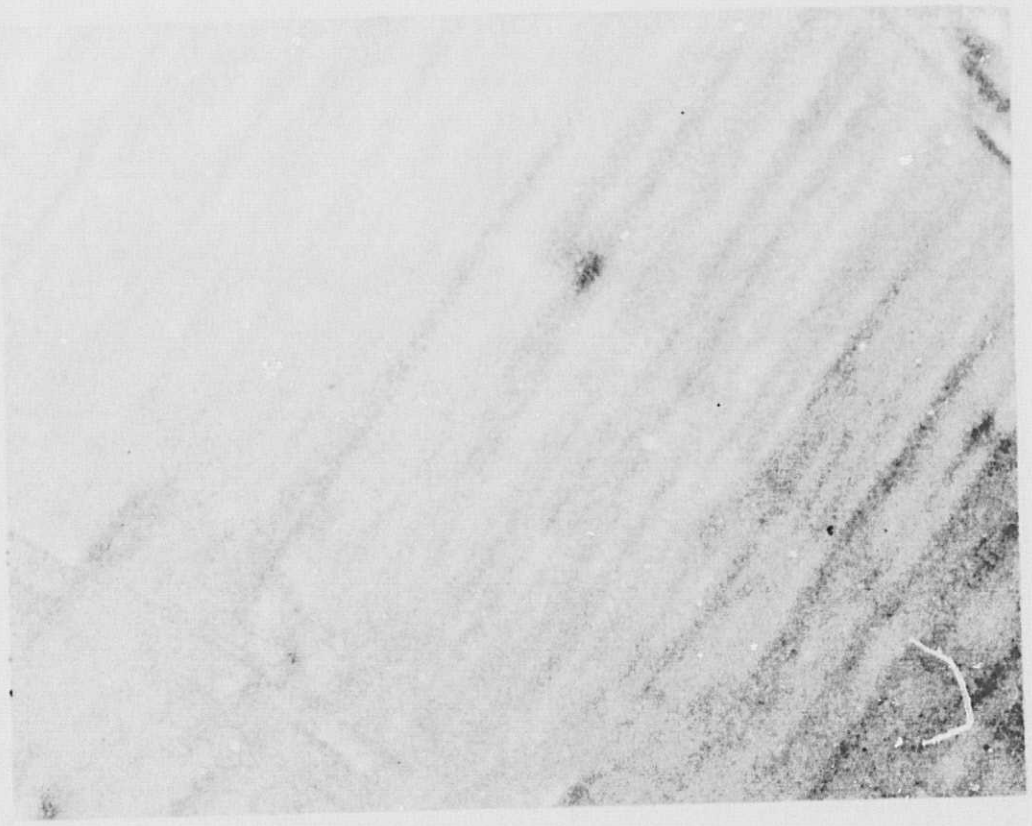

(a) Aged 24 hr at 100 °C

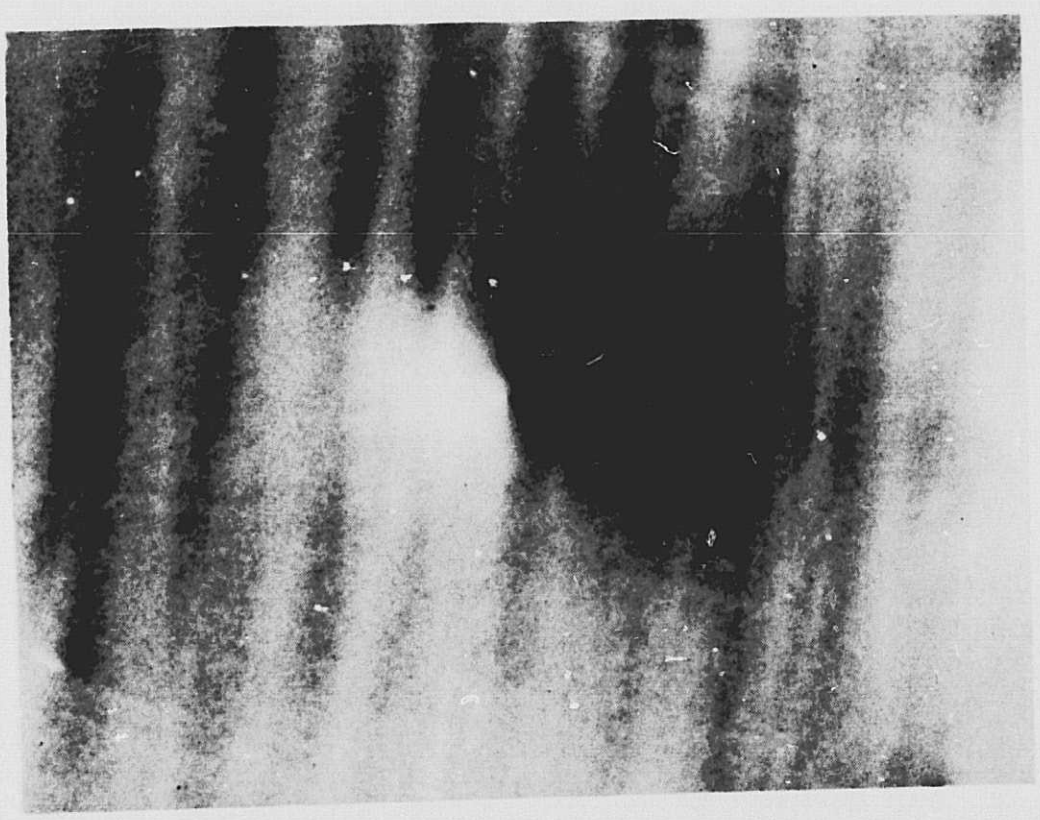

(b) Aged 72 hr at 100 °C

Fig. 5. Fracture surfaces of Al-7.5Zn-2.4Mg (1600X)

(c) Aged 16 hr at 150 °C

Fig. 5 Fracture surfaces of Al-7.5Zn-2.4Mg (1600X) (Cont.)

Fig. 6. Grain boundary in Al-4 Cu when alloy is in solutionized condition (37,000X)

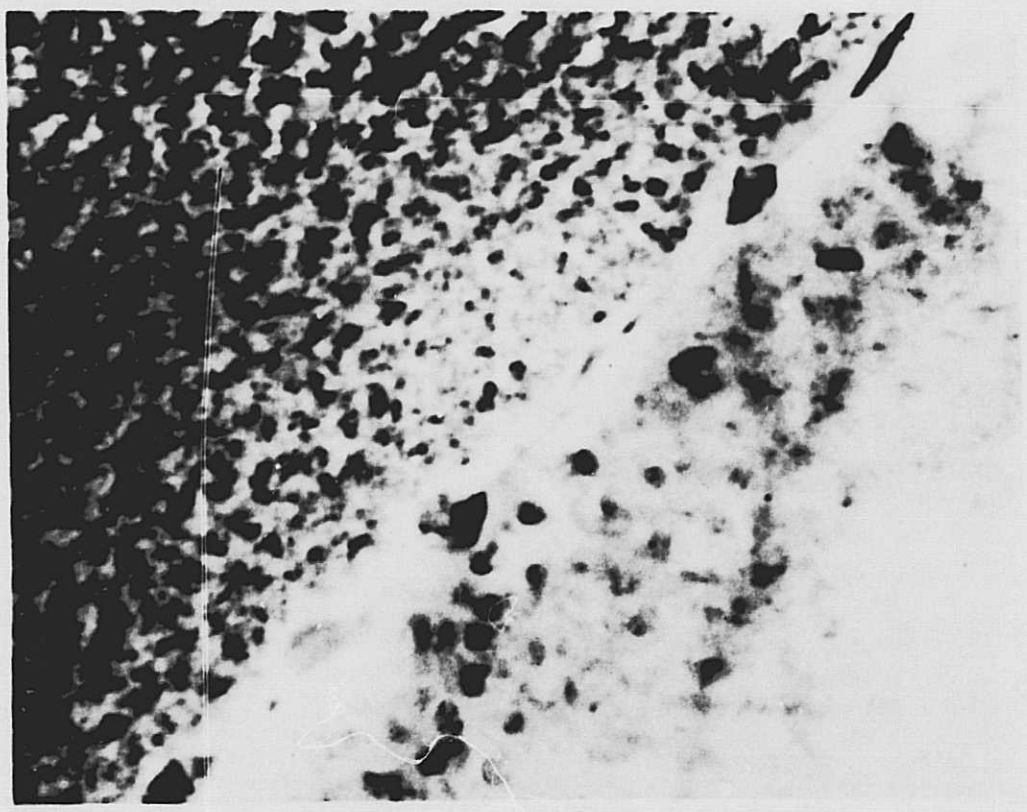

Fig. 7. Grain boundary in Al-4 Cu after alloy has been aged 3 hr at 200 °C (37000X)

are visible. Similarly, Fig. 8 shows a boundary in Al-4Cu after 20 hr at 200 °C. Here, both the precipitate particles and the PFZ have grown in size.

Fig. 9 shows a similar result for the Al-7.5Zn-2.4Mg alloy heated for 89 hr at 100 °C. Again, a PFZ is clearly visible.

In summary, the longer the aging time and the higher the aging temperature, the larger are both the grain boundary precipitates and the wider is the PFZ. However, even for relatively short times at low temperatures, precipitate particles and a PFZ appear. Also, in every case, the formation of particles at the boundaries precedes that in the grain interiors. This result is to be expected, since the grain boundary is a low nucleation energy site. Lastly, in no case are the grain boundary precipitates continuous. In every case they occur at discrete particles. The PFZ, however, is always continuous, even at very early stages of the hardening process.

F. Summary

Many of the results summarized in this section will be drawn upon in the discussion of our stress corrosion results and discussed further there. An important conclusion which is appropriate here is the large difference in mechanical behavior between Al-Zn-Mg-(Cu) and 7075 on the one hand, and Al-4Cu and 2219 on the other. The former alloys show strong correlation of mechanical properties with SCC susceptibility, the latter show none. The former alloys show ready intergranular cleavage, and this is probably the prime reason for their very great susceptibility to failure by intergranular SCC.

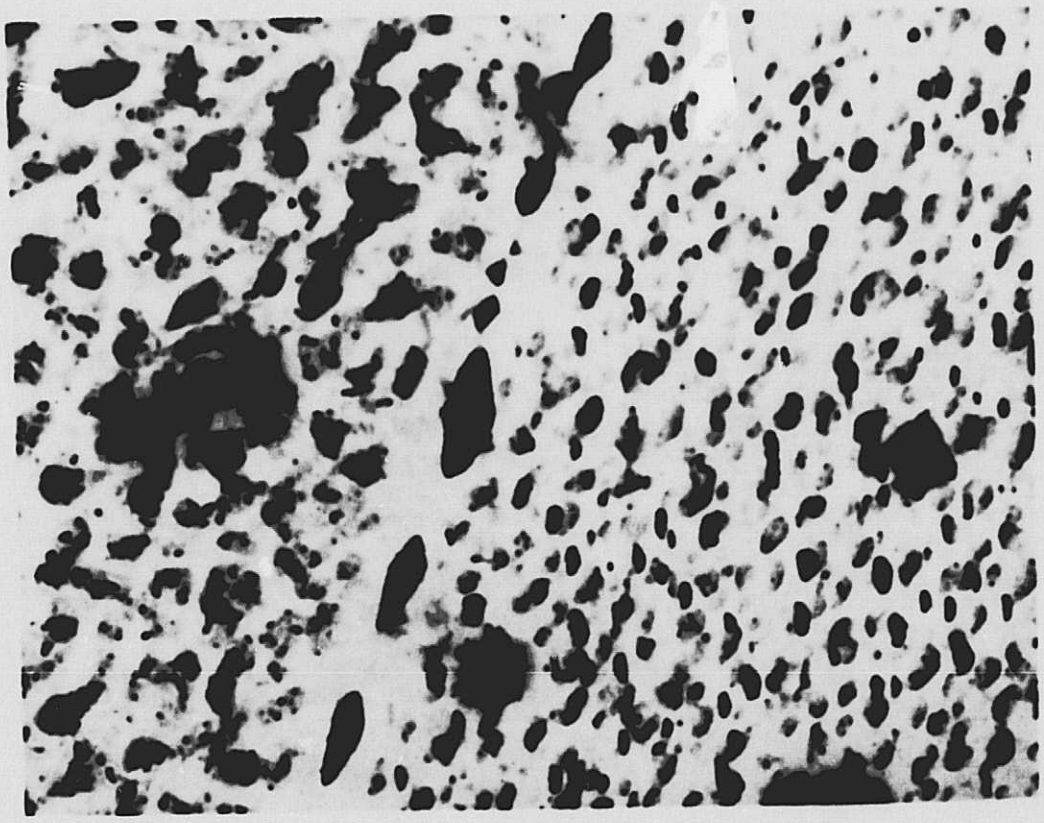

Fig. 8. Grain boundary in Al-4 Cu after alloy has been aged 20 hr at 200 °C (37000X)

Fig. 9. Grain boundary in Al-7.5 Zn-2.4 Mg after alloy has been aged 89 hr at 100 °C (10000X)

III. CORROSION AND STRESS CORROSION OF ALUMINUM ALLOYS

A. Introduction

The main purpose of the corrosion portion of the overall investigation of SCC in high strength Al alloys has been to characterize the electrochemical and corrosion behavior of all the materials involved in the systems of interest. This is considered to be of prime importance, because stress corrosion is not a purely mechanical process but one which involves a complex interaction between mechanical and electrochemical factors. The initial stage, that involving formation of the critical crevice or notch from which the ultimate crack results, may be purely electrochemical. Indeed, as will appear, this is the case for 7075-T6. However, even when stress is required in the crack initiation phase, as in 2219-T37, the role of corrosion is essential and must be understood.

In marked contrast to the abundance of stress corrosion data on these systems in the literature, there is a very meager amount of reliable electrochemical data. It has, therefore, been deemed necessary to obtain these required data on all the components of the two systems of interest under well defined conditions. This has involved a variety of techniques: polarization curve determinations via the potentiostatic method, weight loss studies, and galvanostatic anodizations. These have been carried out at constant temperature (30 °C), in an oxygen free environment (hydrogen atmosphere), using high purity reagents.

B. Polarization Curves

The bulk of the work has involved determining the polarization behavior of the materials in both 1M NaCl and 1M Na_2SO_4 using the potentiostatic method. In most cases, the cathodic as well as anodic polarization behavior has been characterized. Such measurements are complicated in the case of alloys, because invariably one of the components is more active than the others. The preferential removal of this component simultaneously alters the composition of the material being investigated. This is the case in all of the materials studied, with the

exception of the pure metals and the intermetallic phase, $MgZn_2$. In the latter, both Mg and Zn are very active and dissolve in the same ratio as present in the compound.

In spite of difficulties associated with preferential removal of more active species from the alloy materials and hydrogen evolution during anodic polarization, reproducible data were obtainable. In all cases, polarization measurements commenced at the open circuit potential, and the applied potential adjusted in suitable increments: 10 mV for anodic determinations in Cl^-, 200 mV for anodic measurements in SO_4^{2-}, and 100 mV for cathodic measurements in Cl^- and SO_4^{2-}. The open circuit potentials for these materials are included in Table I. The currents, especially in Cl^-, were somewhat time dependent, but measurements were recorded within 2 min after each increment in potential when most current levels were nearly steady

The polarization data are summarized in Figs. 10 through 13. The anodic curves for the Al-Cu system in pH 4.7 Cl^- are presented in Fig. 11; those for the Al-Zn-Mg system are shown in Fig. 10. The anodic curves obtained in pH 4.7 SO_4^{2-} for both systems are given in Fig. 12, and cathodic polarization curves for both systems in both media are shown in Fig. 13.

It can be seen from Fig. 11 that Al and Cu define the potential limits of the system (Al being the most active component and Cu the most noble). It is readily apparent that the position of the anodic curve for a given material is not related in a simple way to the quantity of Cu present. The metallurgical state of the material seems to be of prime importance. This is easily seen by considering the relative positions of the -T851 and -T37 tempers of 2219 in Fig. 11. Although they contain nearly identical amounts of Cu, the overaged -T851 is displaced approximately 100 mV more negative towards pure Al itself, whereas the -T37 temper lies very close to the curve for $CuAl_2$. A similar trend can be seen in the curves for the pure binary alloy in the same figure. The overaged pure alloy curve is almost superimposed on that for pure Al, whereas that for the solutionized material occupies a position close to the $CuAl_2$ curve.

Table I. Open Circuit Potentials in pH 4.7 1.0M NaCl

Material	Open Circuit Potential Versus NHE, mV
$MgZn_2$	–865 ± 5
Al	–680 ± 25
Pure ternary (PT)	
Solutionized, PT (S)	–741 ± 1
Maximum susceptibility, PT (MS)	–729 ± 3
Overaged, PT (OA)	–722 ± 15
7075-T651	–570 ± 30
7075-T73	–528 ± 10
Ternary without copper (T)	
Solutionized, T (S)	–760
Overaged, T (OA)	–645
Ternary with copper (T + Cu)	
Solutionized, T + Cu (S)	–586
Overaged, T + Cu (OA)	–528
2219-T851	–485 ± 5
2219-T37	–410 ± 20
Pure Al-4Cu alloy	
Solutionized	–440 ± 40
Maximum susceptibility	–492 ± 2
Overaged	–512 ± 12
$CuAl_2$	–395 ± 8

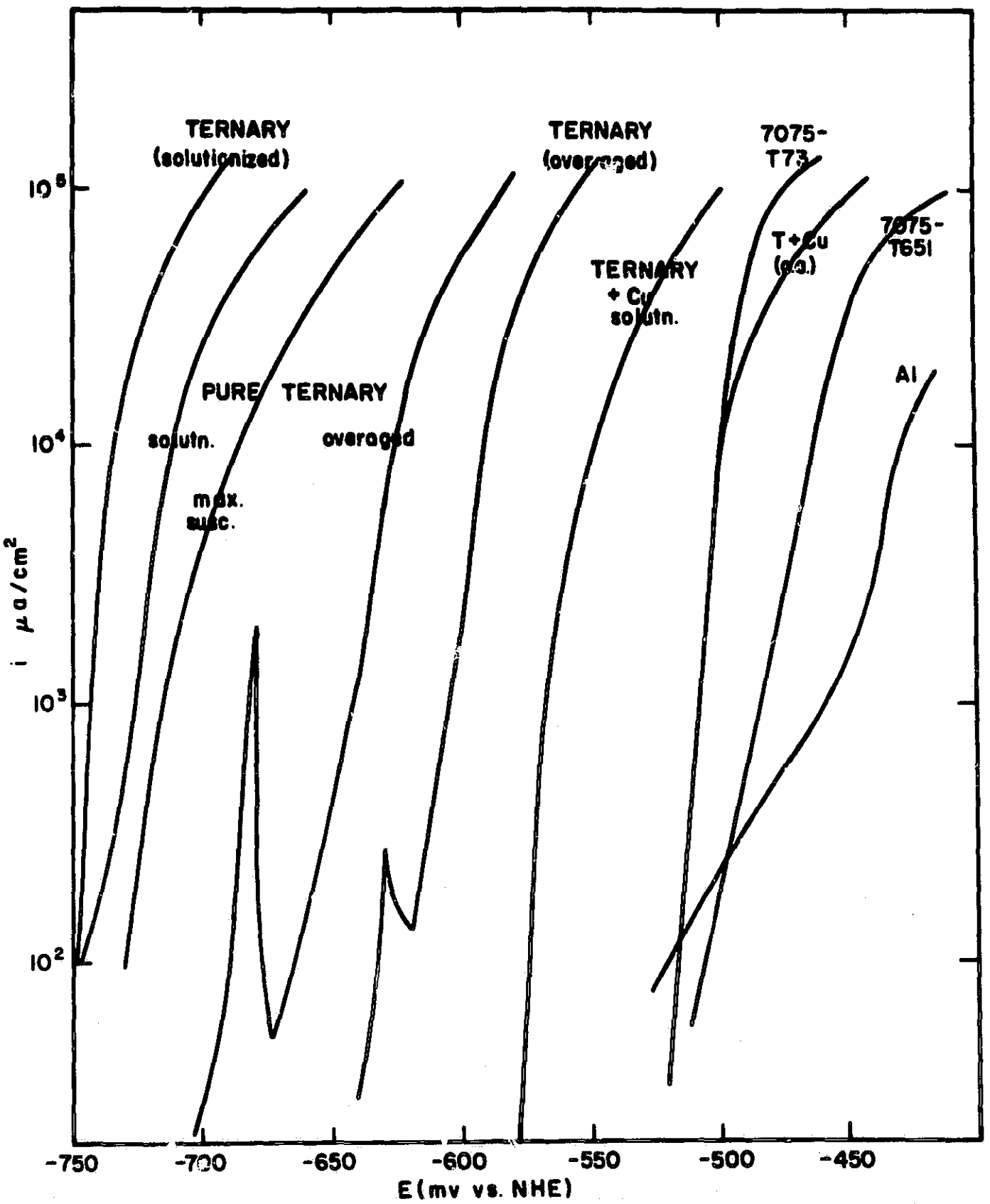

Fig. 10. Anodic current-voltage curves for ternary system in 1.0M NaCl, pH = 4.7

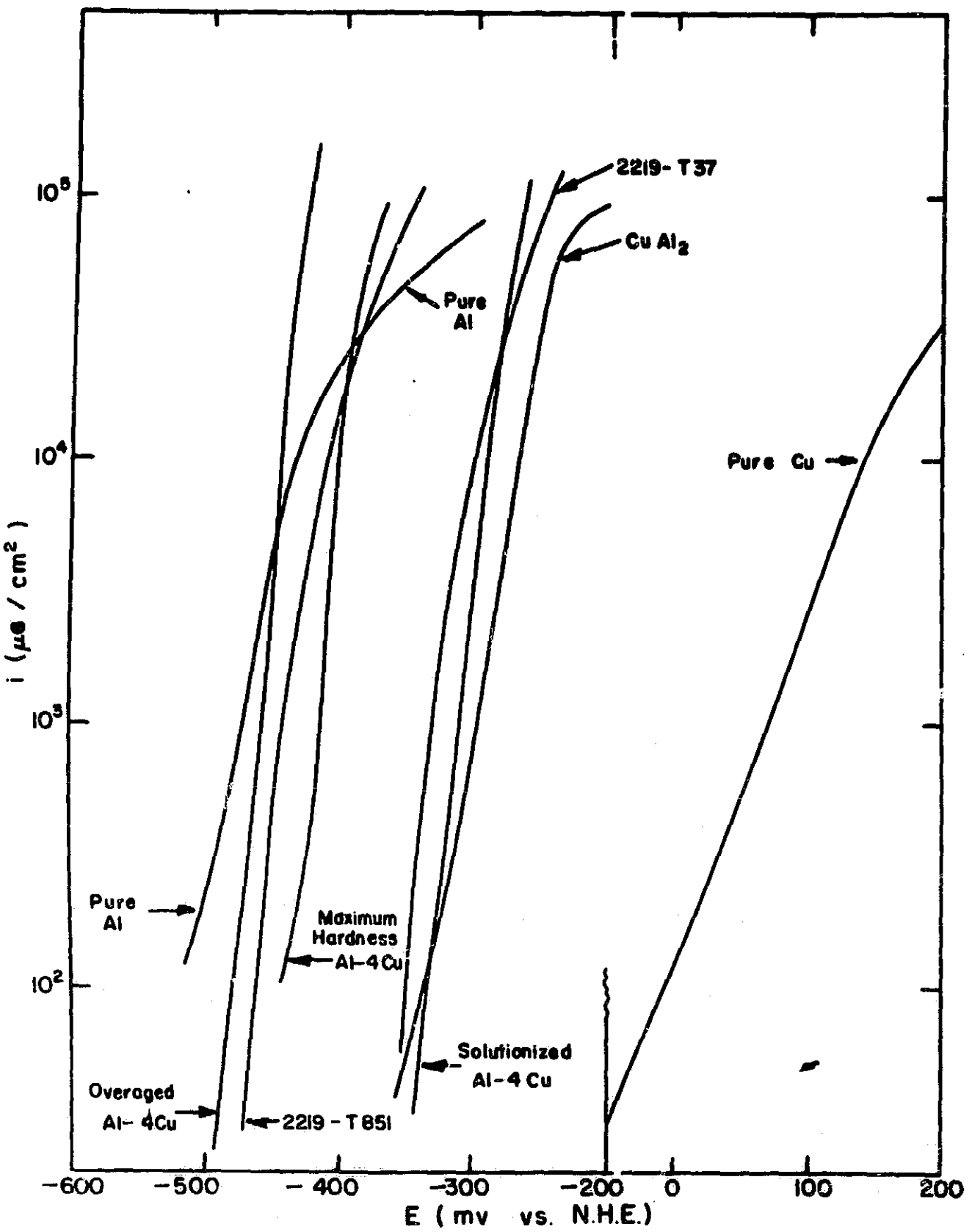

Fig. 11. Anodic polarization curves for Al-Cu system in 1.0M NaCl, pH = 4.7

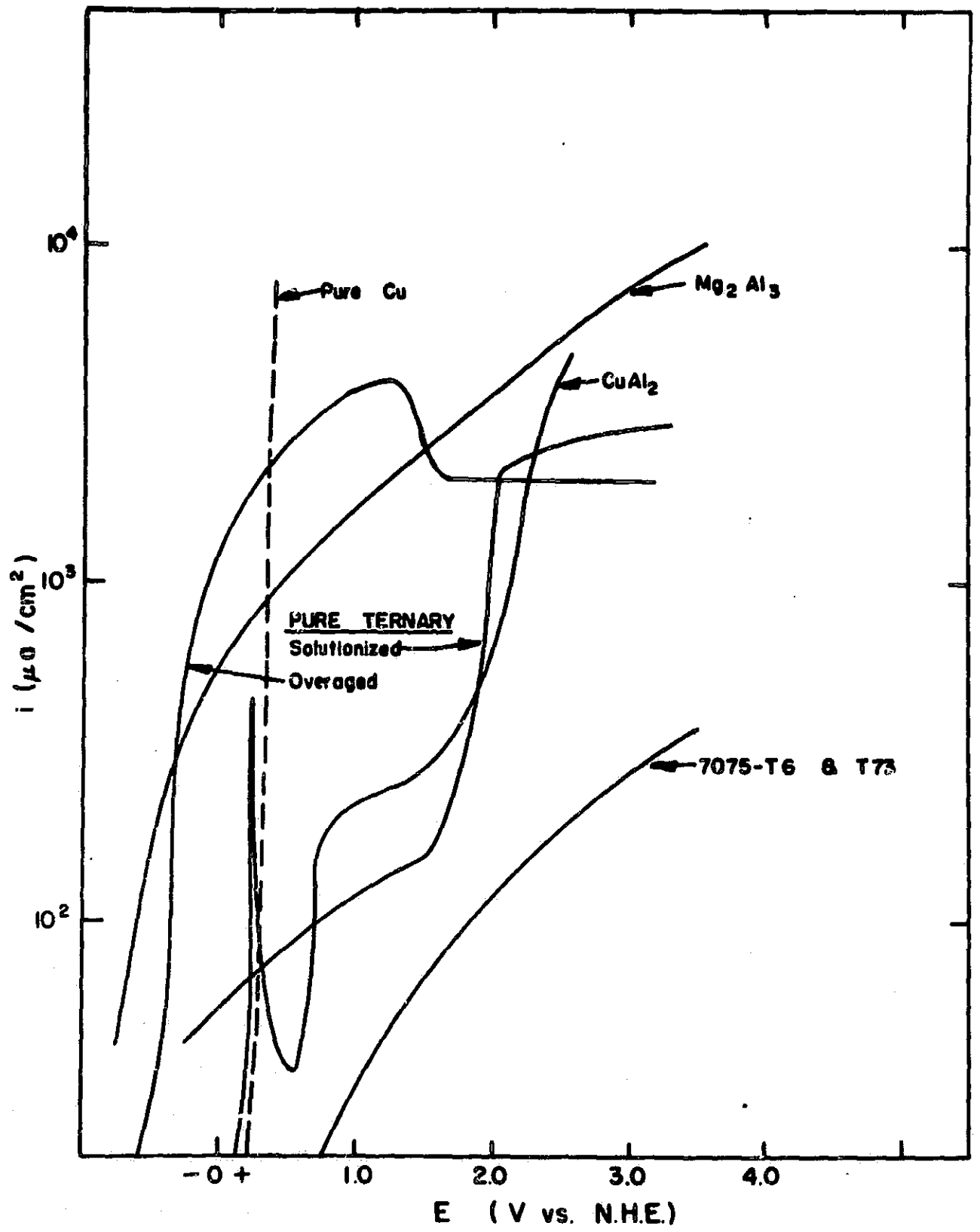

Fig. 12. Anodic polarization curves for ternary systems in 1.0M Na_2SO_4, pH = 4.7

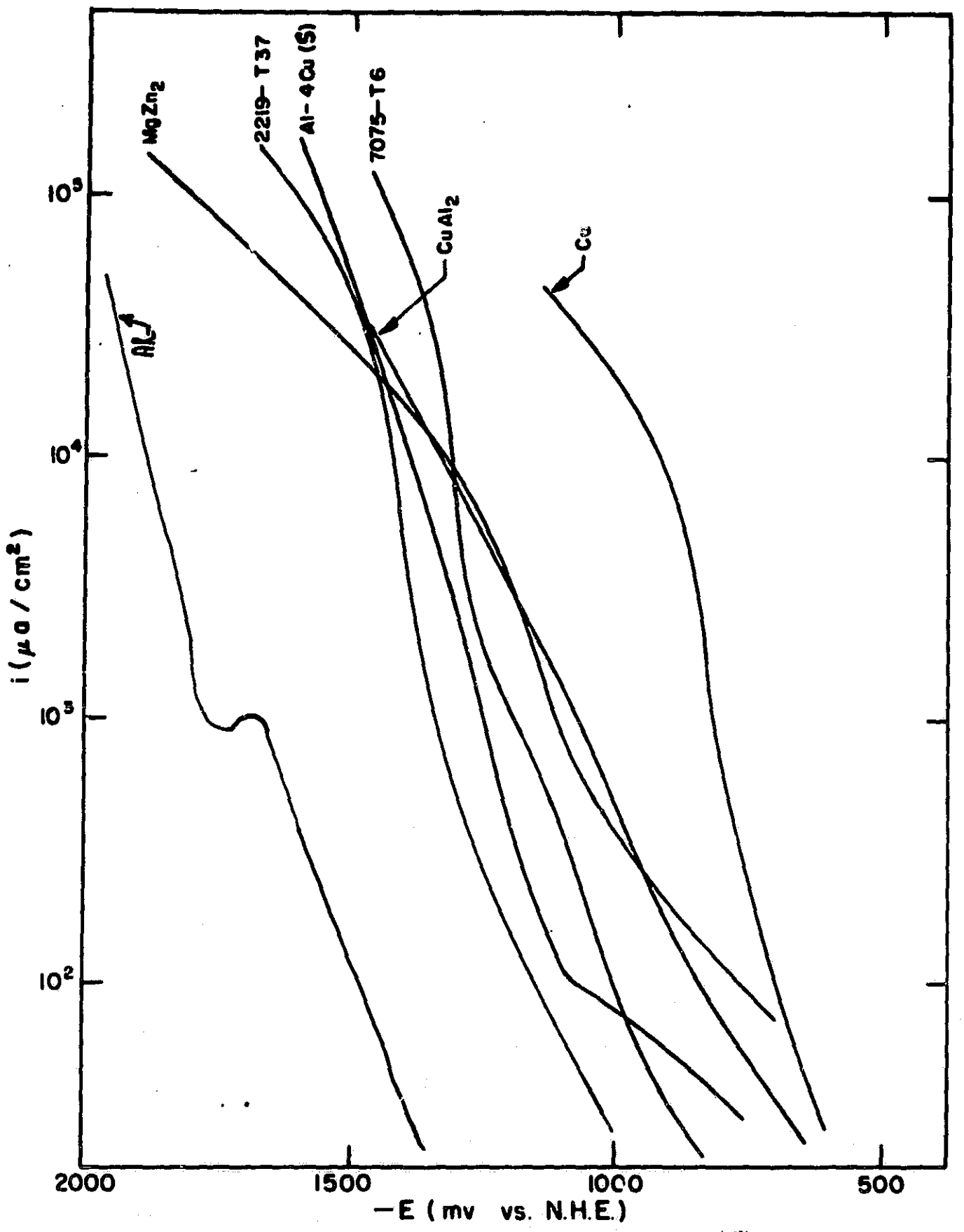

Fig. 13. Cathodic polarization curves for binary and ternary systems in 1.0M NaCl, pH = 4.7

While it appears that Cu, homogeneously distributed through the Al matrix, exerts a pronounced effect on the anodic polarization curves, the magnitude of this effect is, again, not simply related to the amount of Cu. This is brought out by the proximity of the curves for 2219-T37 and $CuAl_2$, even though the latter contains 14 times the quantity of Cu. The considerably more noble position of the curve for pure Cu suggests that the maximum effects of composition on the polarization curves occur at low Cu levels.

In SO_4^{2-}, there is essentially no difference between the anodic polarization behavior of either the commerical or pure binary alloy and pure Al. When present in larger amounts, Cu does disrupt the passivating effect on the Al oxide to some degree. Thus, in $CuAl_2$ the anodic polarization behavior differs markedly from that in Cl^-. The sharp peak around +300 mV versus NHE, which is very time dependent, is considered to be due to the dissolution of Cu. The removal of surface Cu atoms during this anodization in SO_4^{2-} evidently results in enrichment of the surface in Al. This Al is subsequently passivated at higher potentials, greatly retarding further Cu dissolution.

An extensive study of $CuAl_2$ involving galvanostatic, potentiostatic, and linear voltage scan techniques had been carried out previously. These results were reported in the Fifth Quarterly Report (Figs. C. 1 to C. 10).

The anodic polarization curves for the ternary system (Fig. 10) reveal a marked dependence on both the nature of the secondary alloying constituents as well as the metallurgical state of the alloy. Two ternary systems, kindly supplied to us by Dr. D. O. Sprowls of Alcoa, have been investigated. The first is a pure ternary alloy containing Al, Zn, and Mg only in the amounts indicated in Table II. This is referred to as the pure "ternary." The second consists of two alloys having compositions similar to that of 7075, with the exception that one of them does not contain Cu. This system is referred to as the "ternary," with or without Cu. The limits of the system are defined by $MgZn_2$, the most active

Table II. Alloy Compositions

	Element									
	Mg	Zn	Cu	Cr	Ti	Fe	Si	Mn	Zr	V
7075	2.5	5.6	1.6	0.25						
Pure ternary	2.4	7.5								
Ternary plus Cu	2.47	5.64	1.61	0.20	0.02	0.00	0.01			
Ternary (no Cu)	2.49	5.68	0.01	0.19	0.02	0.00	0.01			
2219			6.2		0.021			0.32	0.023	0.059
Pure Al-4Cu			4.1							

component, and pure Cu, the most noble. Two tempers of 7075 (-T73 and -T651) as well as two series of pure alloys are included. The open circuit potentials for the series are consistent with the relative positions of the respective curves and have been listed in Table I. The compositions of the alloys are given in Table II.

It was found, as in the case of the binary Al-4Cu system, that solutionization shifts the polarization curve towards that of the minor alloying constituent. The curve for solutionized Al-4Cu is closer to that of Cu than is the curve for the overaged alloy. In the ternary system, also, the curves for the solutionized alloys lie closer to that for $MgZn_2$ than those for the corresponding overaged materials. The addition of Cu to the ternary drastically shifts the curves more noble, but does not alter their relative positions.

The presence of a secondary passivation phenomenon which appears to coincide with the formation of a thick white oxide film is characteristic of the overaged alloys not containing Cu. The difference between the curve for the pure ternary and that for the ternary can be ascribed to either the trace alloying components (Cr, Ti, and Si) or, more likely, to the 0.01% Cu. It was suggested in the previous discussion of the Al-4Cu system that the maximum change in curve position with Cu content occurs at low Cu concentrations. This would be supported by the observed difference between the pure ternary and ternary containing the 0.01% Cu. Not only does Cu (presumably) cause a shift in the polarization curves, but it also suppresses the secondary passivation effect. For the solutionized and maximum susceptibiltiy forms of the ternary, addition of Cu has less effect and merely shifts the curves slightly in the noble direction.

The effect of Cu in suppressing the activating influence of Mg and Zn is demonstrated in SO_4^{2-} media as well. Although the curves for the ternary with and without Cu are not available, the likely effect can be seen on comparing the plots for 7075-T6 and -T73 with those for the pure ternary. In the case of the latter, heat treatment has a marked effect on the subsequent anodic behavior, whereas no significant difference

was found between the -T6 and -T73 tempers. In Fig. 10, the effect of heat treatment on the curve separation decreases with increasing Cu content. On this basis, it would be expected that in SO_4^{2-} a detectable difference would be found between solutionized and overaged ternary containing Cu.

It can be seen from Fig. 13 that the alloy composition has only a slight effect on the cathodic polarization behavior. In addition, the curves are almost independent of the nature of the anion. The hydrogen overvoltage is highest for pure Al, as evidenced by the very negative position of the curve, whereas it is lowest for pure Cu. With the exception of the Al curve, there are no distinguishing features. The sensitivity of the cathodic polarization behavior of Al to anions and the prior anodization was discussed in our First Annual Summary Report.

C. Mode of Corrosive Attack

The mode of attack in pH 4.7 Cl^- following corrosion at two current densities (constant charge) has been established for most of the materials. The two current densities employed were 21 mA/cm^2 for 50 or 100 sec and 2.1 mA/cm^2 for 500 or 1000 sec. These experiments were done galvanostatically in order to have better control of the amount of attack than is readily possible in a potentiostatic experiment. The resulting photomicrographs for the 2219 and pure binary alloy systems are shown in Figs. 14 through 20.

In the 2219 system, intergranular corrosion is conspicuous only in the -T37 temper and is accompanied by pitting (Fig. 19). Following anodic polarization measurements, in which much larger amounts of charge were involved, -T37 specimens shows severe intergranular attack and much more extensive pitting. The -T851 alloy, on the other hand, (Fig. 20) shows no intergranular corrosion even on samples used for polarization curve determinations. Although the pit density is lower on the -T851 alloy than on the -T37, the discolored patches around the pits suggest considerable internal corrosion. The weight loss studies on 2219-T851 (First Annual Summary Report) clearly revealed that the bulk of the corrosion on this alloy occurs under the surface and extends both inwardly and laterally.

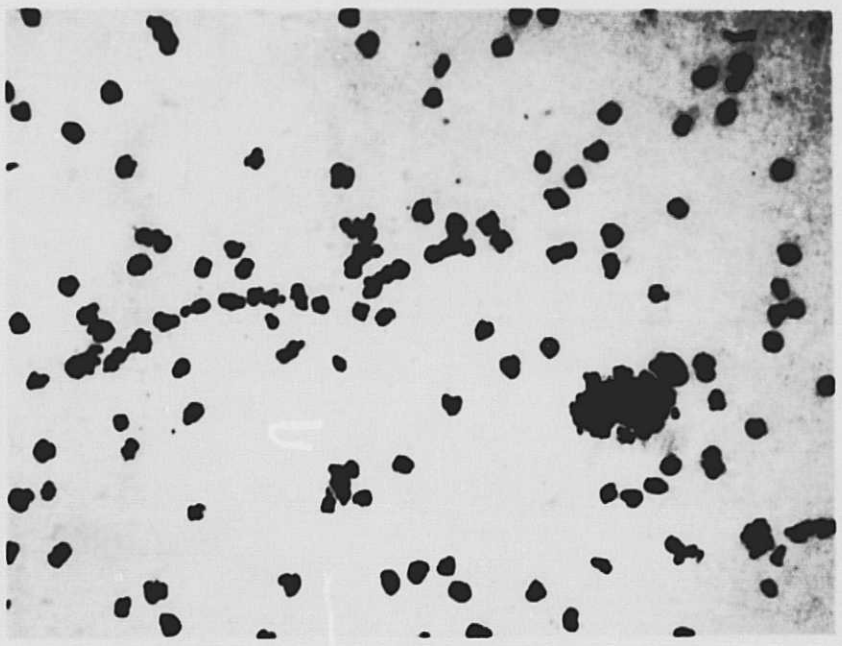

(a) Solutionized Al-4 Cu

(b) Maximum susceptibility Al-4 Cu

Fig. 14. Photomicrographs of Al-4 Cu alloys following anodic polarization at +50 mV to the respective open circuit potentials in 1.0M NaCl, pH = 4.7

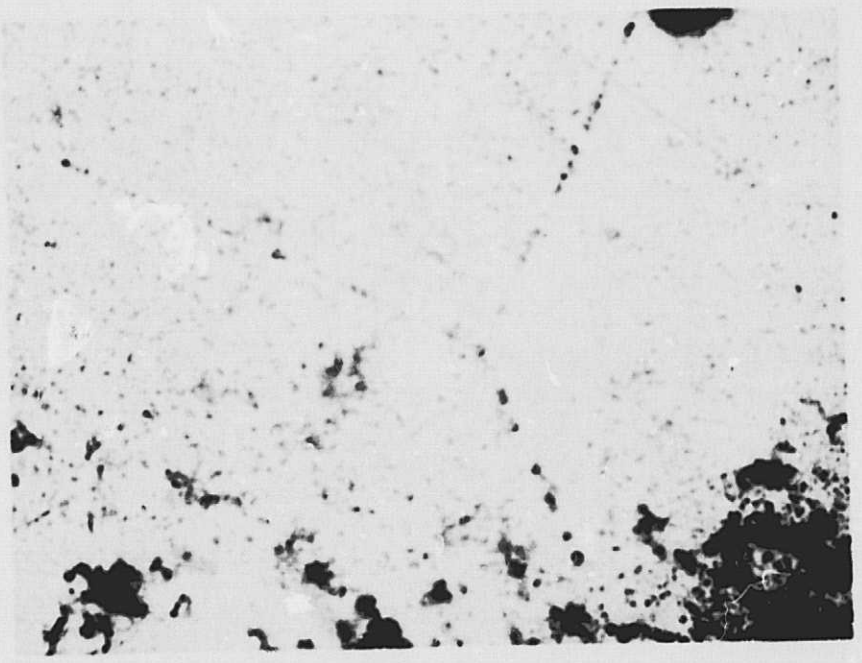

(a) 66X

(b) 95X

Fig. 15. Photomicrographs of overaged Al-4 Cu alloys following anodic polarization at +50 mV to the open circuit potential in 1.0M NaCl, pH = 4.7

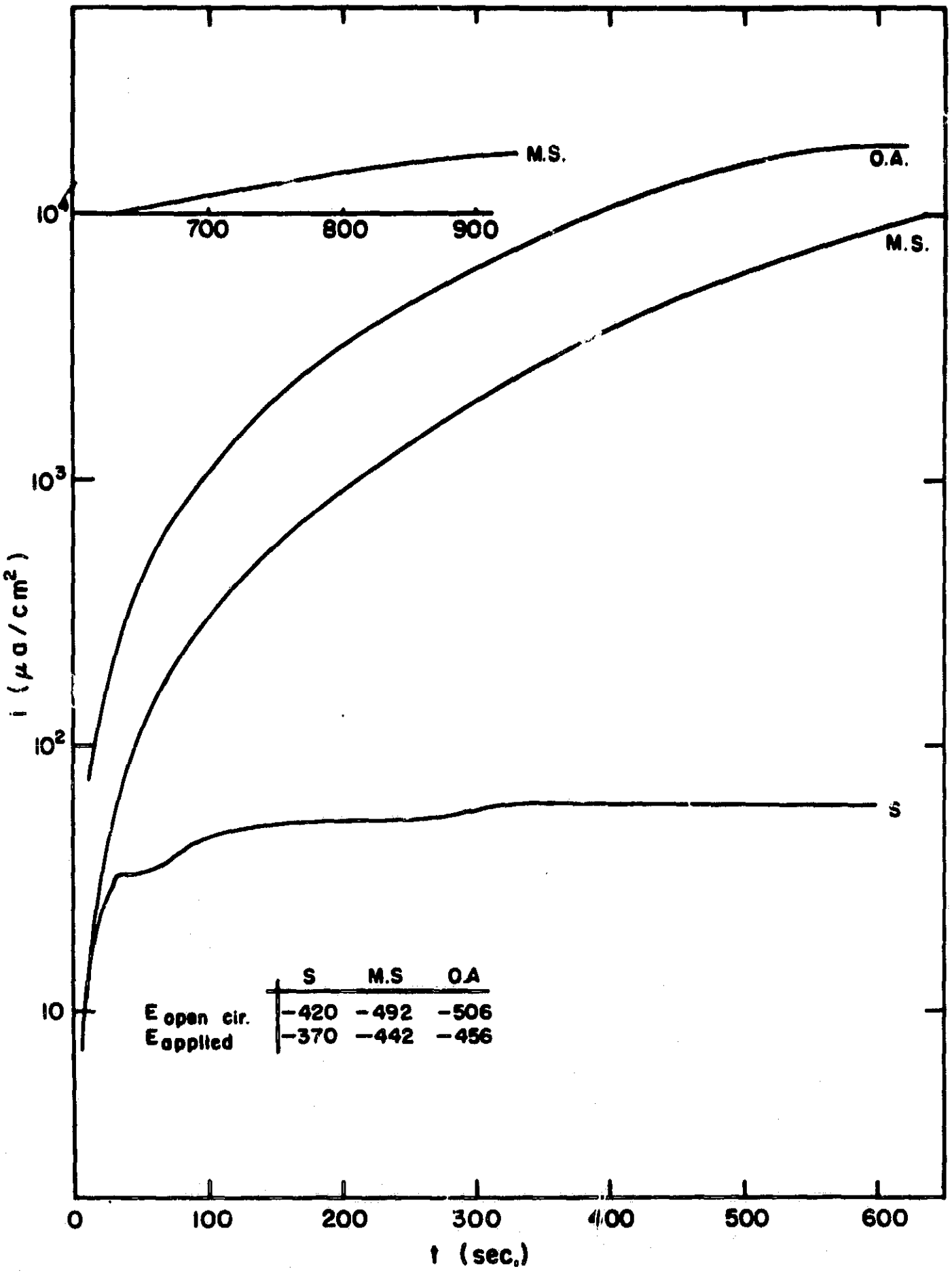

Fig. 16. Current-time curves for pure Al-4 Cu in 1.0M NaCl, pH = 4.7 (E (applied) = E (open circuit) +50 mV)

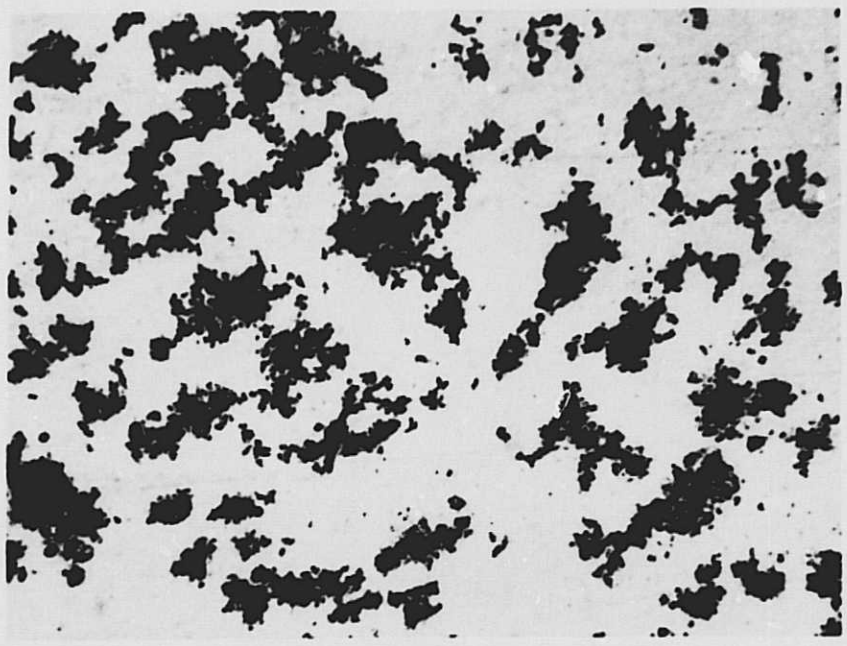

(a) Solutionized Al-7.5Zn-2.4Mg (66X)

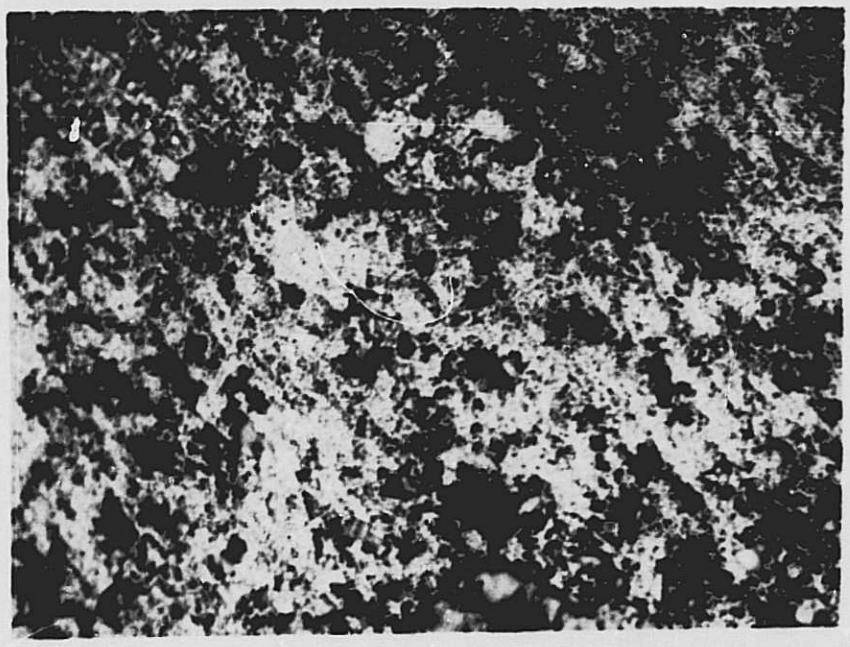

(b) Overaged Al-7.5Zn-2.4Mg (533X)

Fig. 17. Photomicrographs of ternary alloy (no Cu) following galvanostatic corrosion in 1.0M NaCl, pH = 4.7

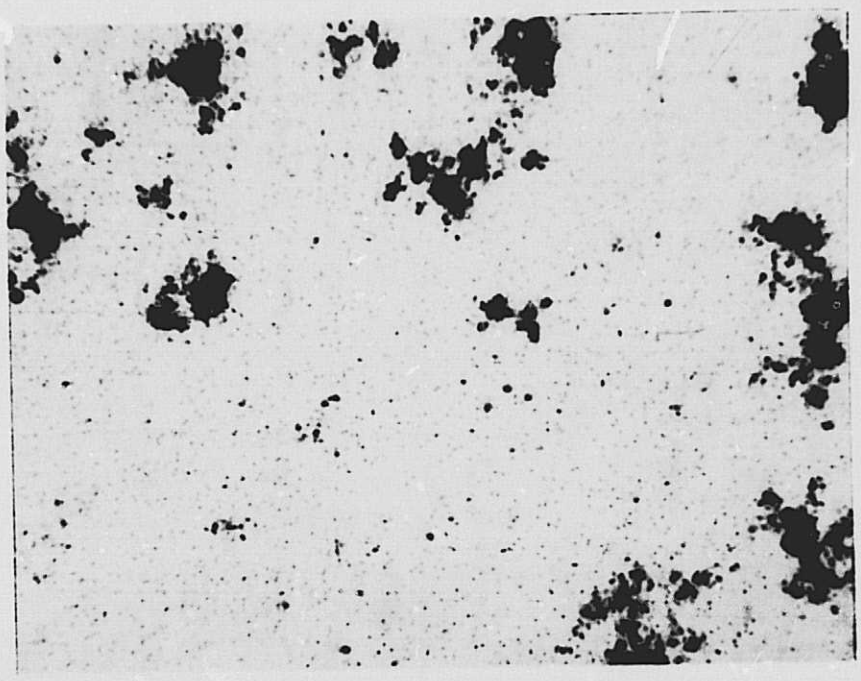

(a) Solutionized Al-7.5Zn-2.4Mg (66X)

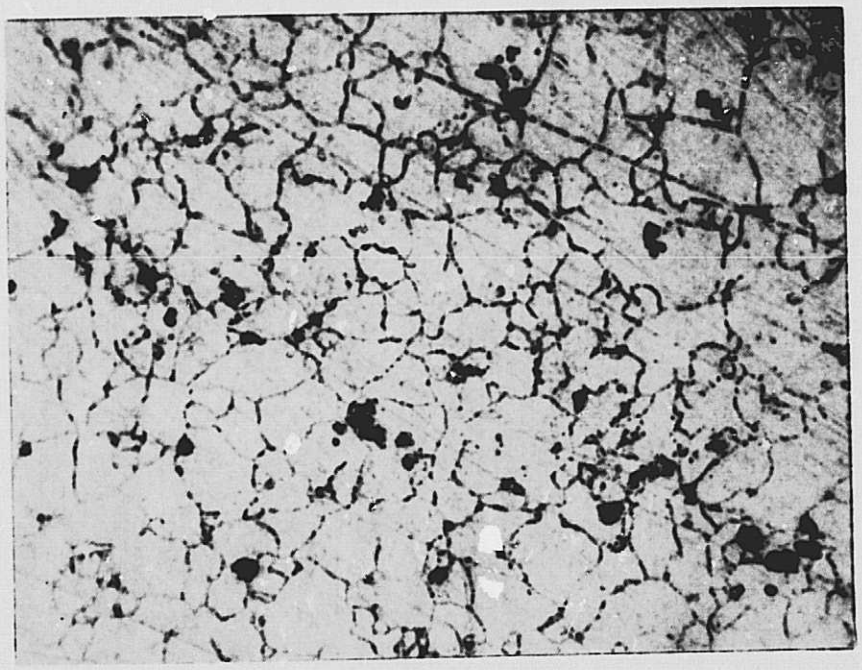

(b) Overaged Al-7.5Zn-2.4Mg (533X)

Fig. 18. Photomicrographs of ternary alloy (with Cu) following galvanostatic corrosion in 1.0M NaCl, pH = 4.7

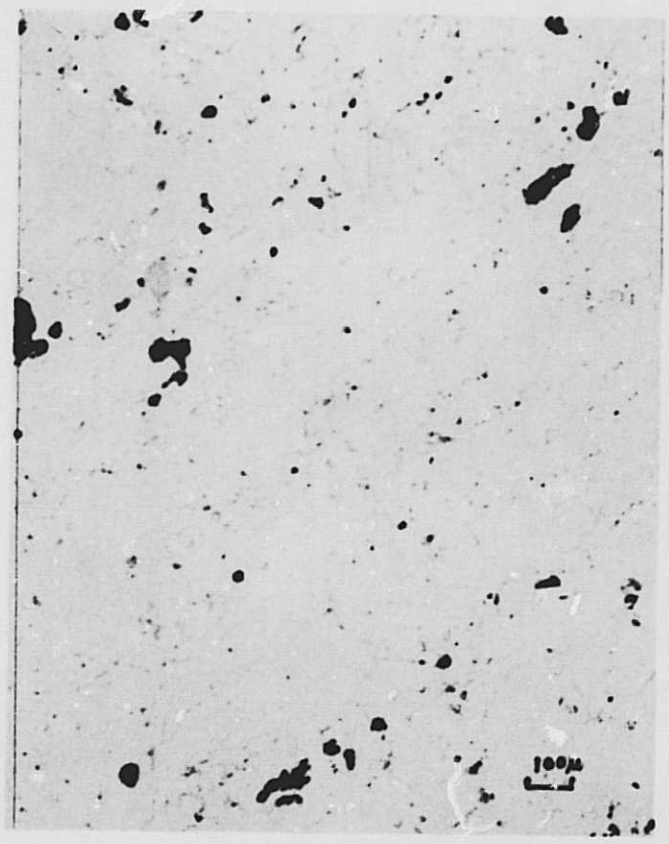

(a) 50X

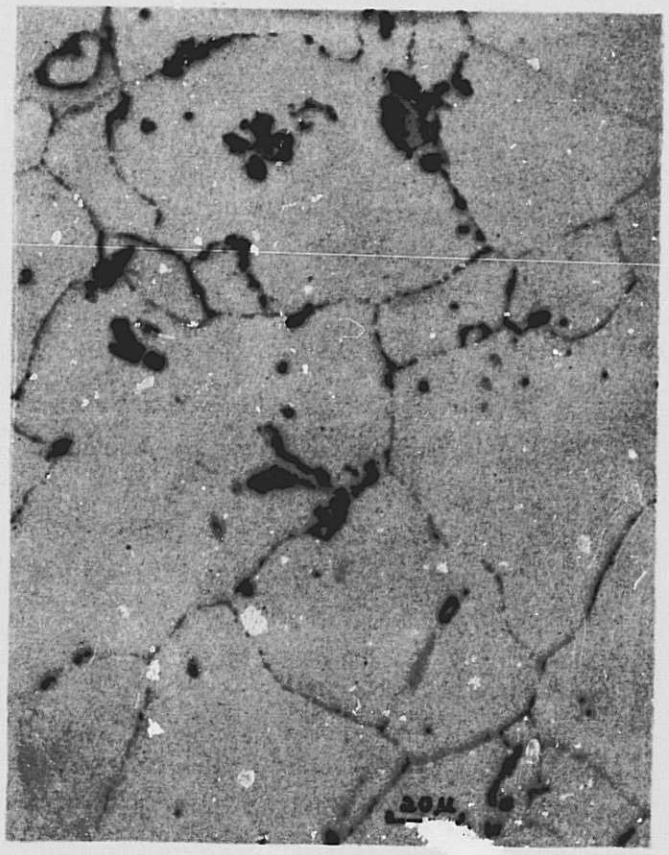

(b) 400X

Fig. 19. Photomicrographs of 2219-T37 following corrosion at 21.0 mA/cm^2 for 100 sec in pH 4.7 Cl^-

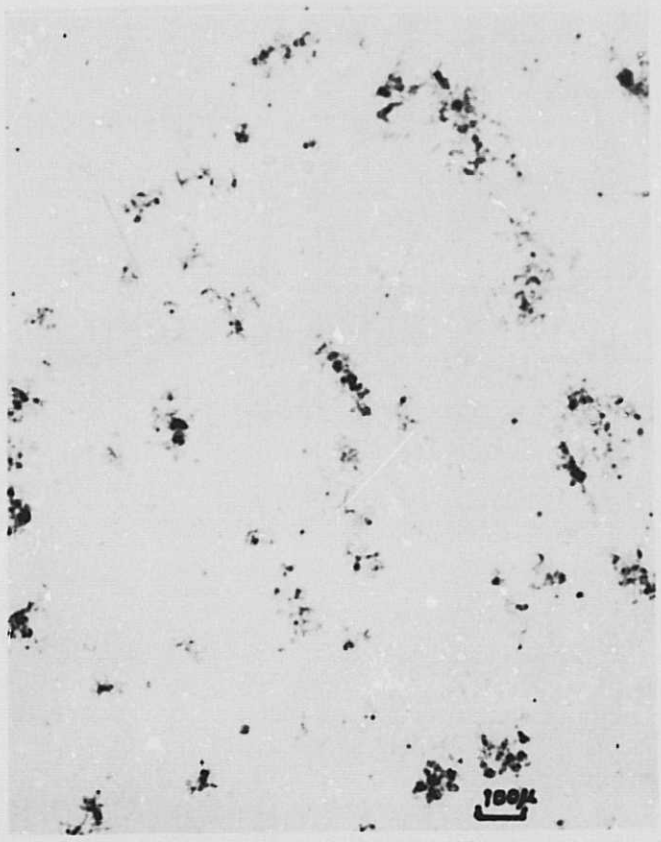

(a) 2.10 mA/ cm^2 for 500 sec

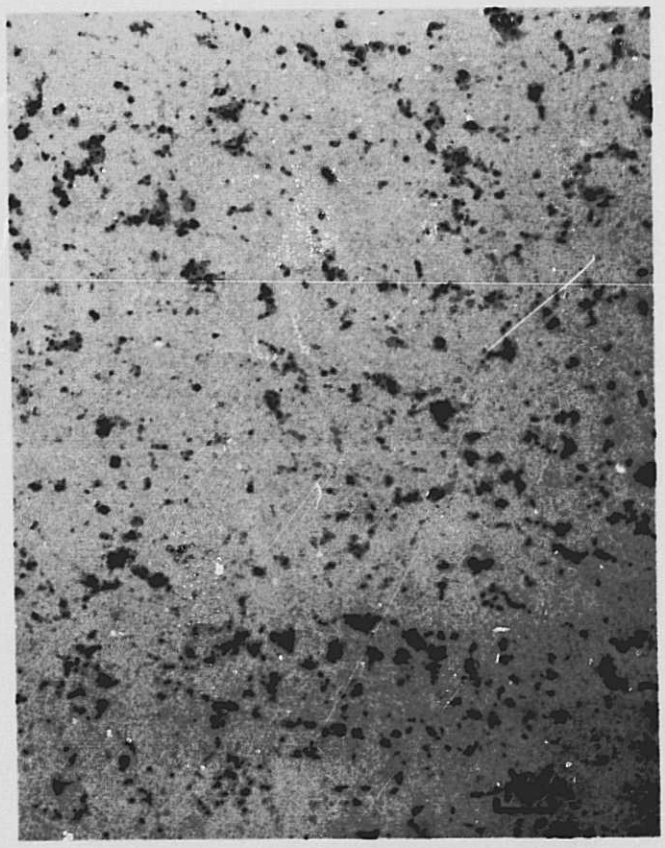

(b) 21.0 mA/ cm^2 for 50 sec in pH 4.7 Cl^-

Fig. 20. Photomicrographs of 2219-T851 following corrosion (50X)

The lack of intergranular attack in the -T851 material, which is in an overaged condition, is not consistent with the results obtained on the pure binary alloys. The maximum susceptibility and overaged pure alloys both underwent visible grain boundary corrosion. It is difficult to say which of the two aged forms shows the greater grain boundary attack. The denuded zone is apparent in the maximum susceptibility form due to the much lower density of pits in this region adjacent to the grain boundaries. Neither this nor slip lines were visible in corroded overaged material. The denuded zone was far more conspicuous on specimens which had been corroded at constant potential during the current versus time studies. Figs. 14 and 15 are photomicrographs of the three pure binary alloys following corrosion in pH 4.7 Cl^- at a potential 50 mV anodic to their respective open circuit potentials. The current-time plots are shown in Fig. 16.

The corrosion morphology of the two 7075 tempers and the pure ternary system were also investigated by corroding them galvanostatically. The ternaries with and without Cu were not examined this way, but photomicrographs of these alloys after anodic polarization curve determinations are included in this section.

The photomicrographs of 7075-T6 and -T73 following galvanostatic corrosion were presented in the Fifth Quarterly Report (Figs. C. 23 and C. 24). In neither temper was there clear evidence of intergranular corrosion. Film formation was heavy on the -T6 temper, becoming heavier with increasing current density, but was almost entirely absent on the T-73. Although the film on the -T6 alloy tended to obscure surface features such as pits, it appears that pitting is more severe on the -T73 material.

The corresponding data on the pure alloy system were presented in Sixth Quarterly Report (Figs. C. 5 through C. 9). Oxide formation was evident on all three forms of the alloy but, in the overaged form, grain boundaries could easily be seen. It is uncertain whether or not this involves preferred corrosion at the grain boundaries, since it is only discontinuity in the oxide film which makes them visible (Fig. C. 8 and C. 9, Sixth Quarterly Report). Changes in the direction of striations in the film above the overaged material served to define the individual grains. This was not the

case with the maximum susceptibility form although, in this case, pits terminating at grain boundaries served to accentuate some of the grains (Fig. C. 6, Sixth Quarterly Report).

Entirely different modes of attack were observed in the ternary plus Cu. The ternary without Cu was similar to the pure ternary, as might be expected, especially in the solutionized condition (see Fig. 17). The ternary containing Cu showed a greater tendency to pit in the solutionized form and underwent intergranular corrosion (Fig. 18) when overaged.

Studies of the localization of corrosive attack have also been made using electron microscopy. This study has been made with foils of pure Al-7. 5Zn-2. 4Mg and Al-4Cu. Corrosion studies have been carried out in both buffered 1M NaCl and also 1M NaCl containing 1% H_2O_2 by volume. These studies have led to several important conclusions concerning the manner in which attack occurs on these two alloys.

There is a major difference between the ternary and the binary alloys with regard to the behavior of the precipitate particles. With Al-Zn-Mg, these precipitates are $MgZn_2$, while for Al-Cu they are $CuAl_2$. Our electrochemical measurements on the pure compounds, as described in the previous section, show that $MgZn_2$ is more active than the matrix, while $CuAl_2$ is more noble. Hence, in the case of the ternary alloy, the precipitate particles should dissolve preferentially; in the binary alloy, however, the matrix will dissolve.

These predictions have been verified by direct observation in the electron microscope where the preferential dissolution of the $MgZn_2$ particles can be clearly seen (Fig. 21a). The stability of the $CuAl_2$ particles is also evident from their continued existence, even along grain boundaries which have cracked apart (Fig. 21b), $MgZn_2$ precipitate particles dissolve first leaving the matrix behind, however. Fig. 22 a shows a grain boundary in Al-7. 5Zn-2. 4Mg after solutionization at 480 °C, followed by water quenching and aging for 89 hr at 100 °C. This photograph is a very good example of the precipitate structure developed in this alloy, expecially with regard to precipitates at the grain boundary. Fig. 22b shows the appearance of the

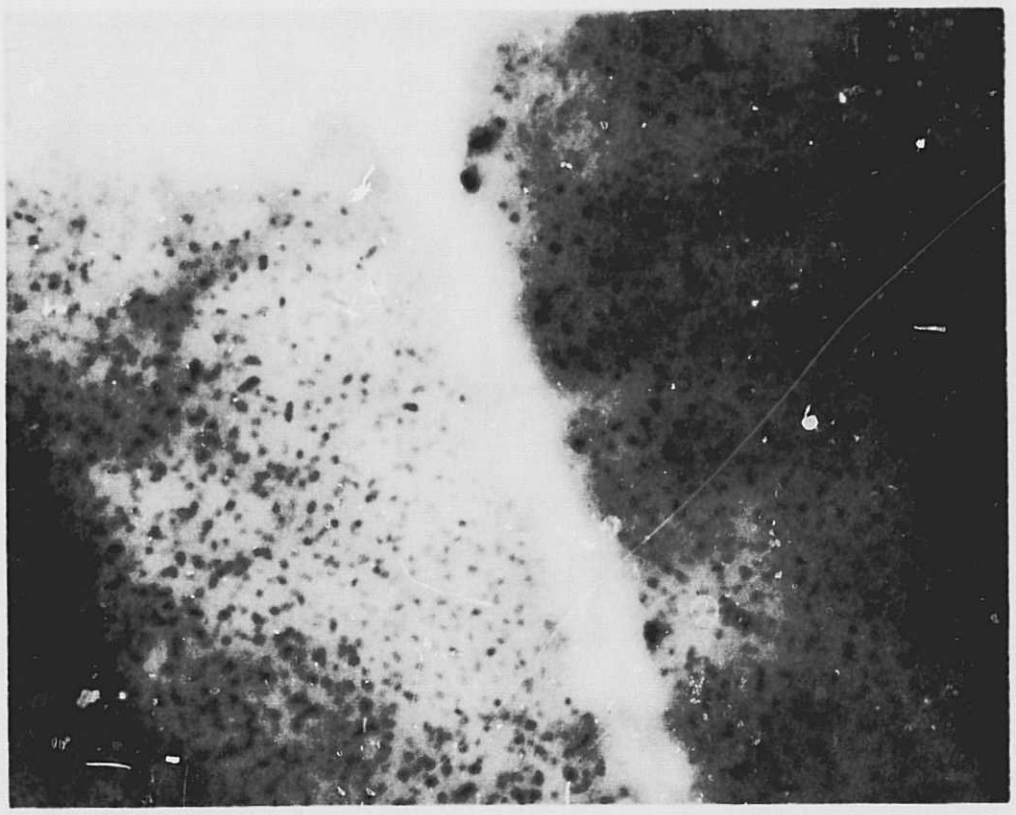

(a) Al-7.5 Zn-2.4 Mg (37000X)

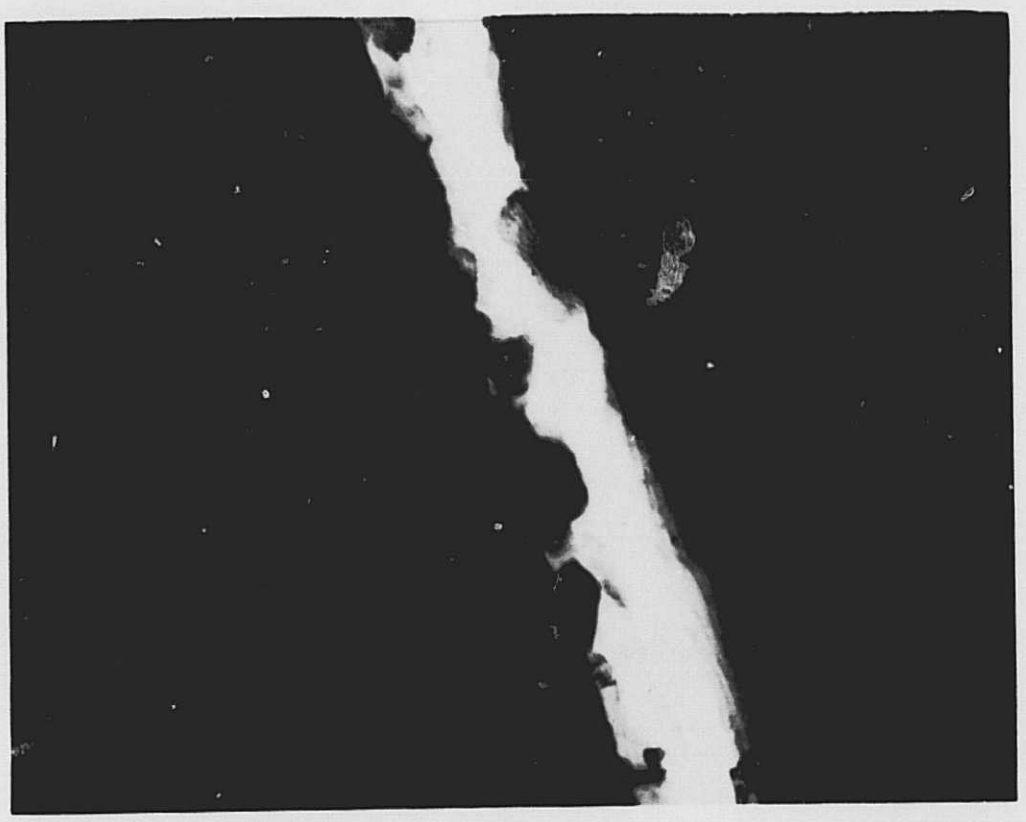

(b) Al-4 Cu (100000X)

Fig. 21. Electron micrographs of thin foils after corrosion

(a) Alloy aged 89 hr at 100 °C

(b) Alloy after corrosion in buffered 1.0M NaCl for 3 hr

Fig. 22. Grain boundary in Al-7.5 Zn-2.4 Mg (37000X)

boundary after exposure for 3 hr in 1M NaCl buffered to pH 4.7. As can be seen, most of the precipitate particles have been leached out and a crack has developed along the boundary.

The electron microscope investigation has shown the influence of precipitates on the effectiveness of the surface oxide layer in retarding corrosion. It was found that the oxide formed immediately above the grain boundary was very much less protective than that elsewhere on the alloy. That is, the oxide immediately above the grain boundary showed a strong tendency to fracture under circumstances in which the oxide on other parts of the surface did not (see Fig. 23b). This weakness of the oxide over the grain boundary is considered to be related to the grain boundary precipitates. This assumption is supported by the appearance of oxide over the matrix areas after corrosion. These areas showed symmetrically shaped patches, whose symmetry corresponded to that of the particles in the matrix (see Fig. 23a).

Fig. 24a shows the square pattern of attack that has been found repeatedly in aged Al-4Cu. This photograph shows also a fine background pattern indicative of a solution and redeposition mechanism. The apparent association of these square areas with precipitates should also be noted. This relationship is also shown in the lower magnification of Fig. 24b. If attack is allowed to continue, these localized areas of attack lead eventually to complete perforation, as shown in Fig 25. It should be noted in this figure that the diagonals of all the square pits are parallel, indicating the crystallographic nature of the attack.

With regard to the actual mechanism of anodic dissolution, very high magnification (greater than 200000X) work on Al-4Cu has given evidence of a tubular pitting mechanism as proposed by Pickering and Swann.[4] In this mechanism, which was developed specifically for the case of an alloy consisting of one noble component and one much less noble component, the bottom of the pit is pure matrix material and is anodic to the noble-metal-rich cathode which has been formed around the mouth of the pit. Fig. 26 is an electron micrograph showing such a structure. Further evidence for solute transport has been obtained by the detailed examination of grain boundary precipitate

(a) In matrix (37000X)

(b) Along grain boundary (14000X)

Fig. 23. Electron micrographs showing effect of precipitates on oxide formation

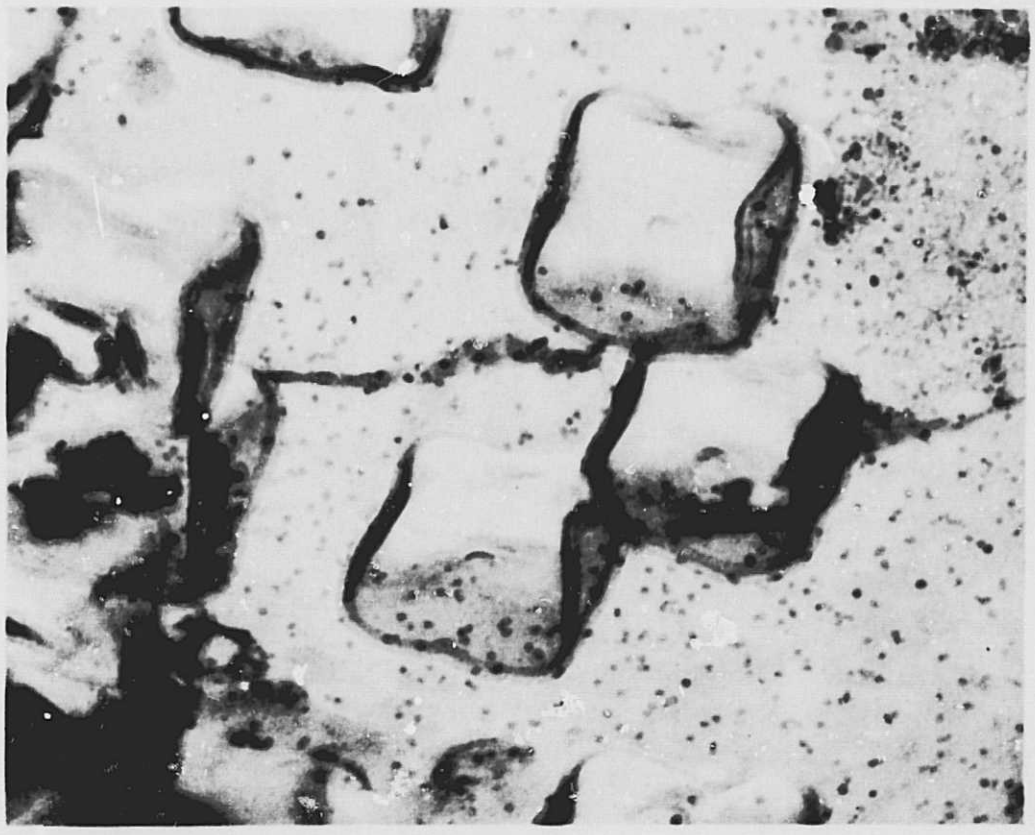

(a) Corrosion patterns on Al-4Cu (100000X)

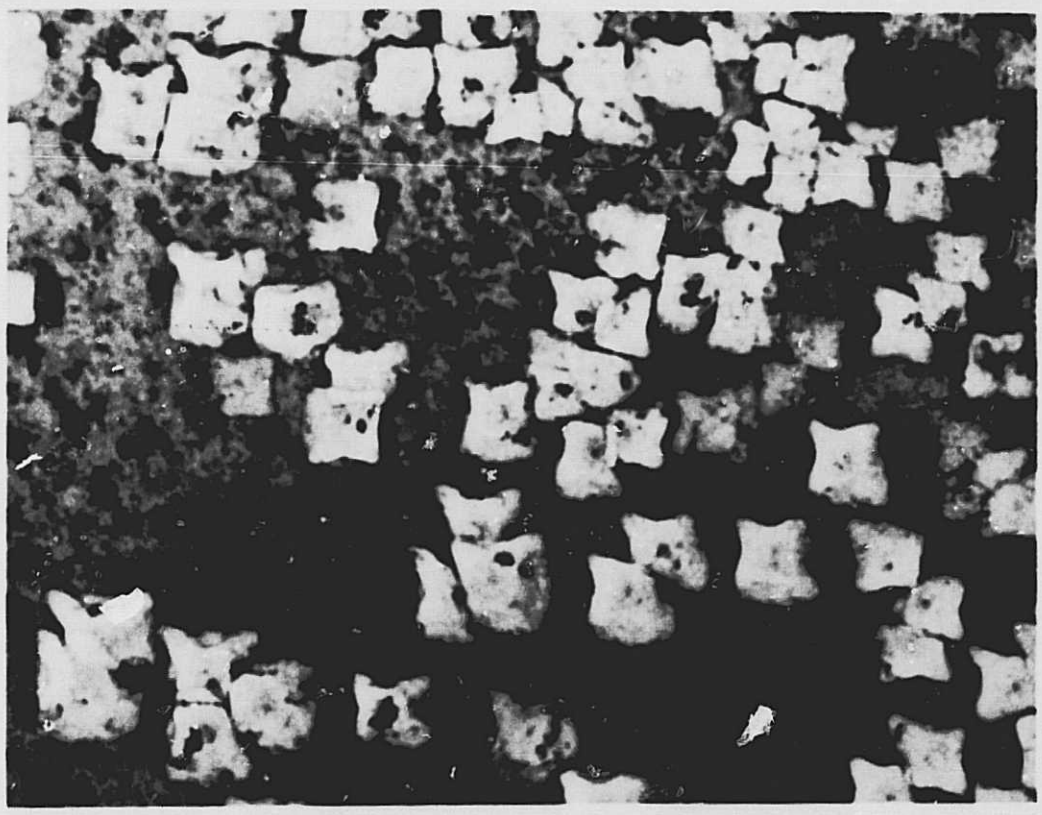

(b) Further evidence for specific pattern attack (37000X)

Fig. 24. Effects of corrosion on Al alloys

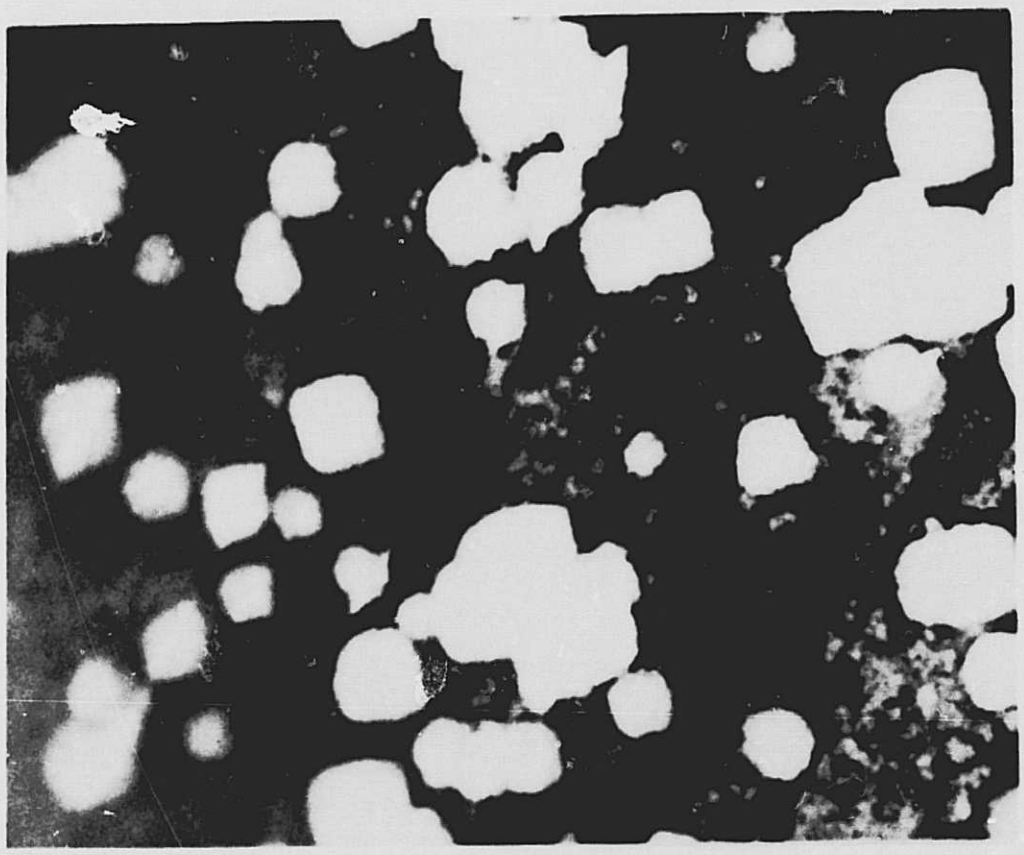

Fig. 25. Geometry of corrosion pits in Al-Mg-Zn (7500X)

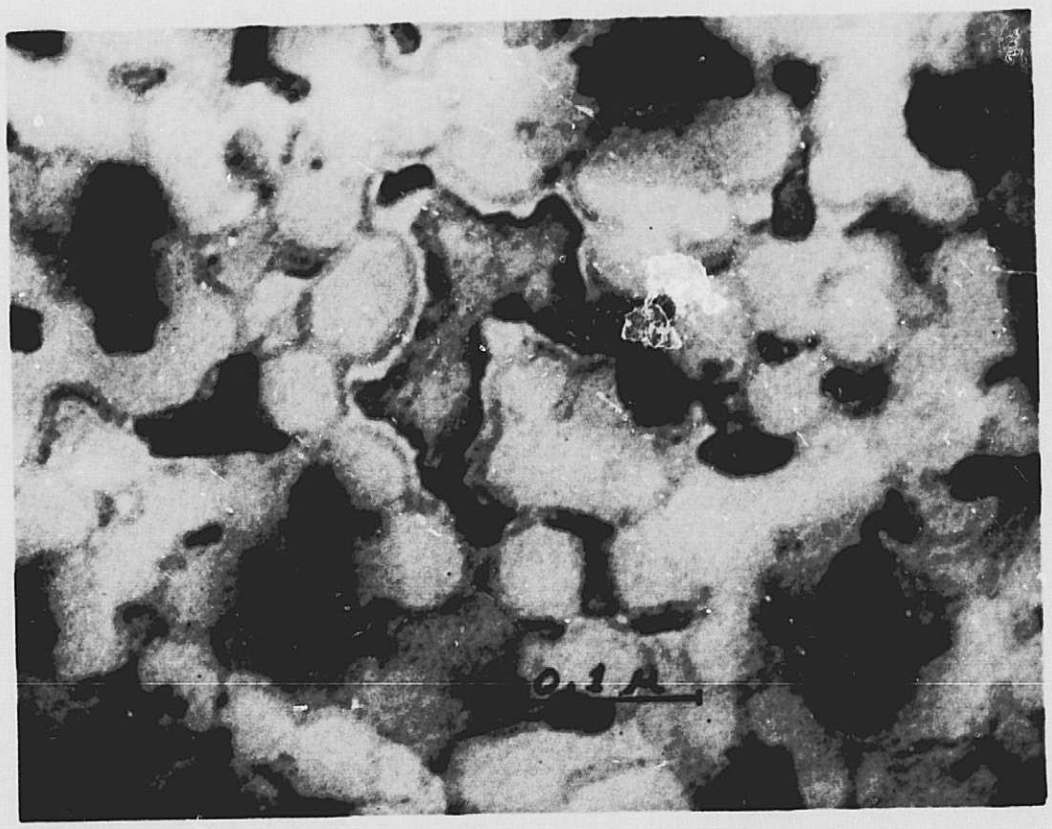

Fig. 26. Electron micrograph of aged Al-4 Cu after dissolution (250000X)

particles after particle dissolution. This examination has revealed a class of smaller precipitate particles which would not be expected to have been stable during the aging heat treatment, and must therefore have been formed during dissolution (most probably by a solution and redeposition mechanism).

Further electron microscopy work concentrated on the study of the interaction of the dislocation substructure and the corrosion processes. The prepared specimens containing dislocations were strips of Al-7.5Zn-2.4Mg solutionized for 30 min at 480 °C and quenched. After aging, the strips were rolled to 0.006-in. foil, re-solutionized, and aged for 24 hr at 130 °C. After aging, the foils were then rolled to 4 mils. It is important, of course, that this final rolling operation be carried out after aging to generate dislocations after precipitation. In this way, any special dislocation arrangements such as planar arrays which might be associated with the effect of precipitation could be observed. The 0.004-in. foil was then thinned electrochemically, as usual.

The appearance of a foil after this treatment is shown in Fig. 27a. This photograph clearly shows the development of planar arrays of dislocations both in the body of one grain and also intersecting the grain boundary. A higher magnification photograph of the intersection of these arrays with grain boundaries is shown in Fig. 27b. Note that the array is completely stopped by the boundary and that there is no evidence of slip across the boundary. Hence, the expected stress concentration effect of these arrays at the boundary is high.

Fig. 28a shows the same area as Fig. 27 after exposure to a solution of 20 g/l NaCl adjusted to a pH of 3.7 by addition of HCl. The exposure time was 2 hr. Particularly in the higher magnification photographs of Fig. 28b, there can be seen the development of a background of areas of preferential attack and the formation of masses of corrosion products. The planar arrangement of this material suggests that this attack is associated with the dislocation arrays shown previously. The change in the appearance of the grain boundary itself should also be noted. In Fig. 27, the individual precipitate particles along the grain boundary can be seen, while in Fig. 28,

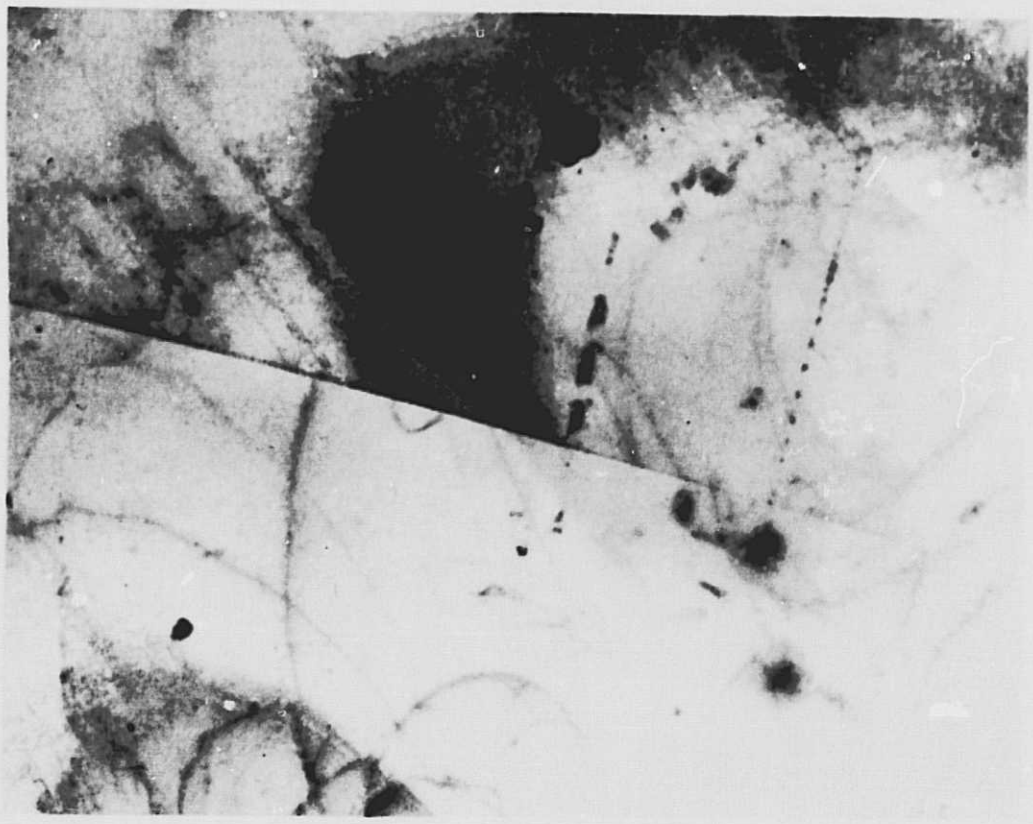

(a) 6200X

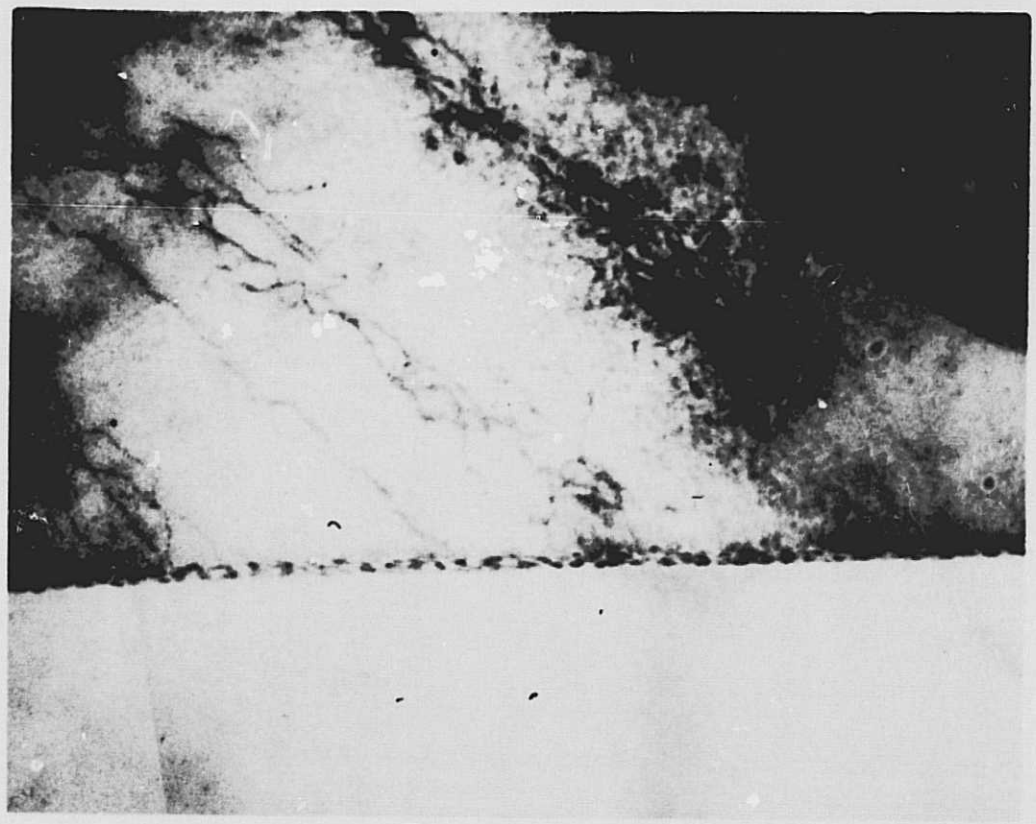

(b) 37000X

Fig. 27. Electron micrographs of aged Al-7.5 Zn-2.4 Mg foil before corrosion

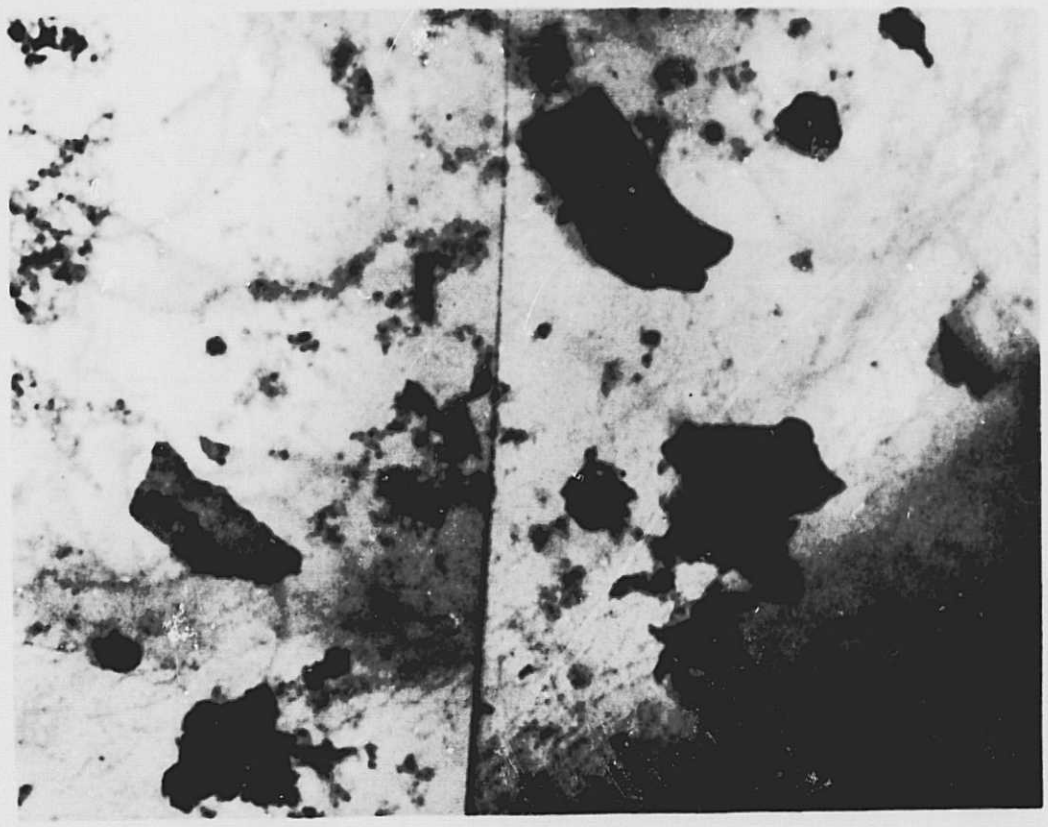

(a) 6200X

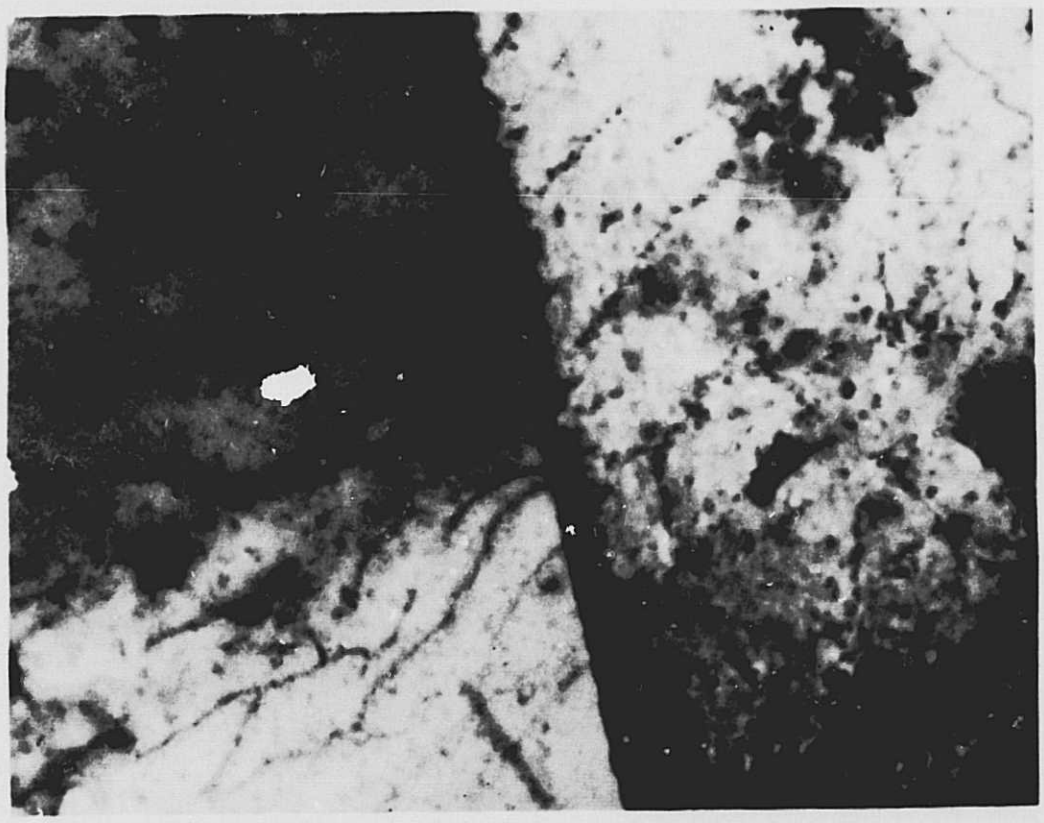

(b) 37000X

Fig. 28. Electron micrographs of aged Al-7.5 Zn-2.4 Mg foil after corrosion

only a homogeneous band of corrosion product can be distinguished.

Because of the significant nature of this conclusion concerning the preferential dissolution of planar arrays of dislocation, further confirmation of data was sought. As before, specimens of Al-7.5Zn-2.4Mg were solutionized for 30 min at 480 °C, quenched, and aged for 24 hr at 130 °C. After aging, the foils were rolled to 4 mils to generate the dislocation structure in the presence of the precipitate particles. After this treatment, planar arrays of dislocations were again found, as shown in Fig. 29a. A similar specimen, after corrosion for 13 min in a solution of 1M NaCl containing 1% H_2O_2, is shown in Fig. 29b. Here the increased rate of attack at the region of the planar arrays is clearly visible.

Fig. 30 shows the appearance of a grain boundary, indicating the selective dissolution of the $MgZn_2$ particles along this boundary. This foil was also corroded for 13 min in a solution of 1M NaCl containing 1% H_2O_2. The photograph also shows what appears to be a preferentially dissolved dislocation pileup, similar to those shown in Fig. 29b.

The consistency of our results gives strong indication that dislocation pileups on planar arrays do occur in Al-7.5Zn-2.4Mg alloys under certain conditions of heat treatment and deformation, and that these arrays do constitute sites for preferential corrosive attack.

D. Summary of Corrosion Characteristics and Relation to Stress Corrosion Susceptibility

The heavy filming and secondary passivation phenomena observed only on alloys devoid of Cu are particularly significant with regard to the nature of the effect of minor alloying constituents on the polarization and corrosion behavior of Al alloys. A further, more detailed discussion is appropriate, since it is intimately related to both the corrosion and stress corrosion behavior of Al alloys.

We have distinguished the effects of secondary alloyants such as Mg, Zn,and Cu on the electrochemical behavior of the alloys into local oxide disruption effect and general disruption effect. These will be discussed further in this section.

In summary, we have made the following observation. Pure Al,

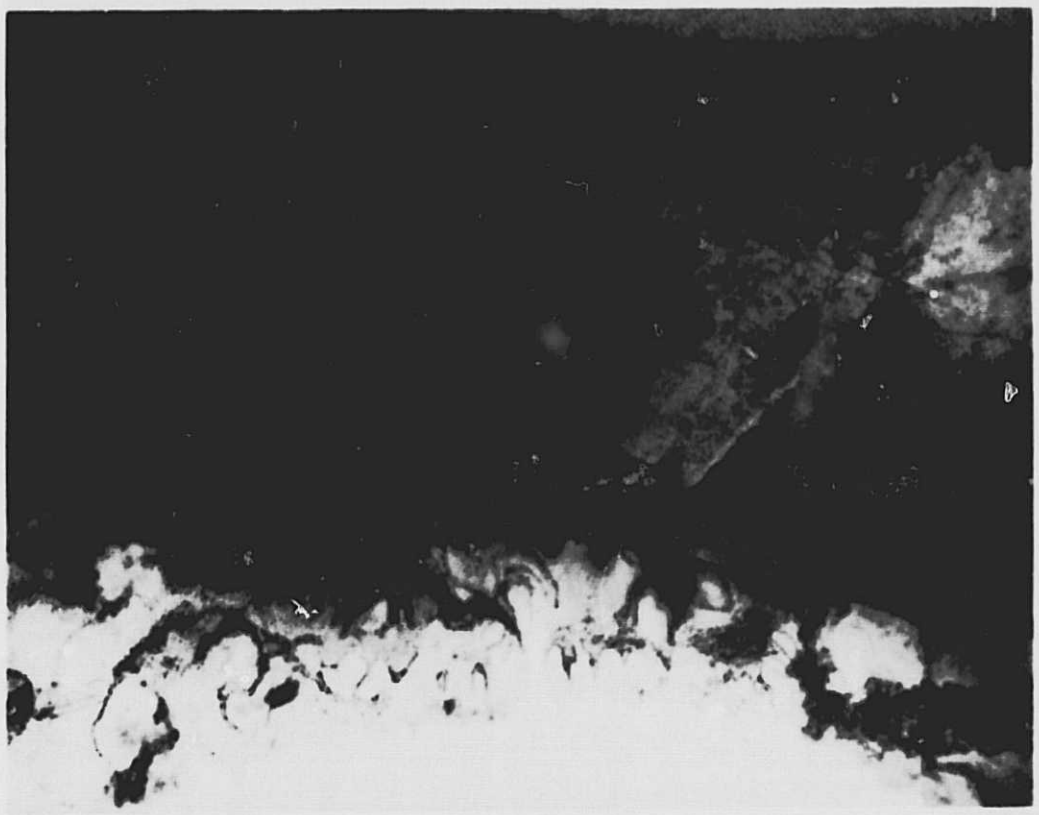

(a) Before corrosion

(b) After corrosion

Fig. 29. Electron micrographs of aged Al-7.5 Zn-2.4 Mg foil (6200X)

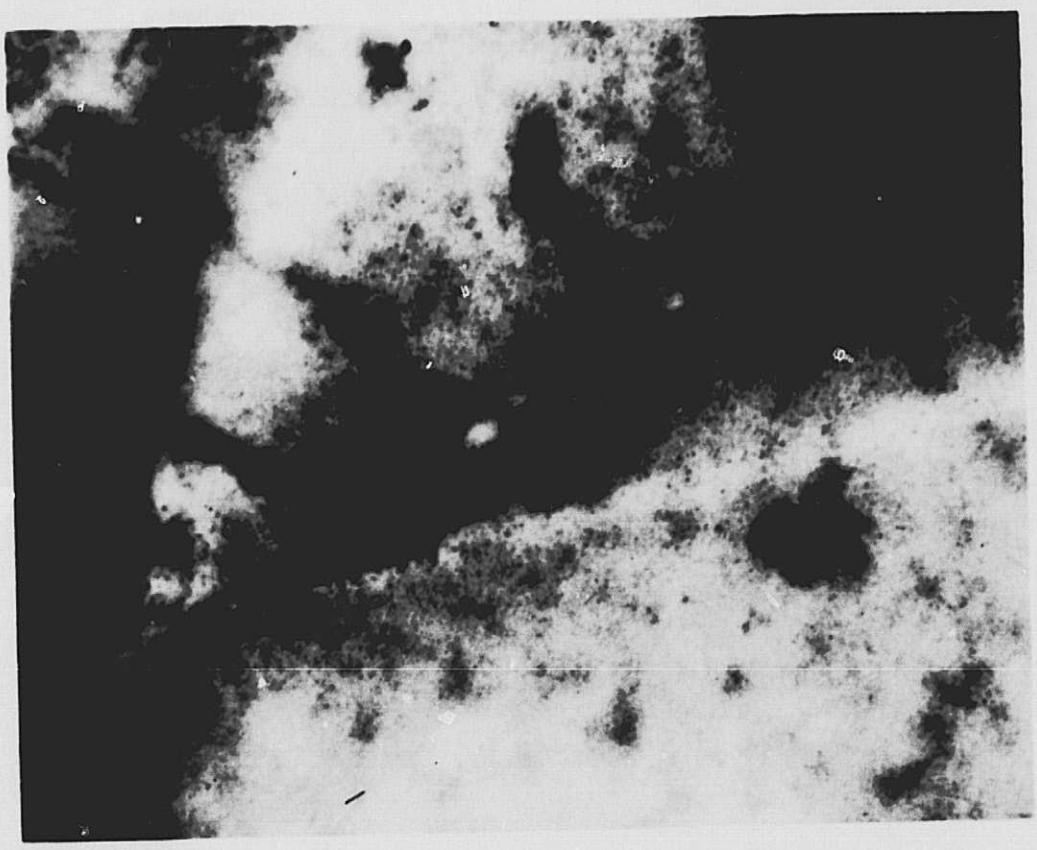

Fig. 30. Electron micrograph of aged Al-7.5 Zn-2.4 Mg foil after corrosion (37000X)

which is covered by a protective film of Al_2O_3, dissolves transpassively in Cl^- because of interaction between the oxide and Cl^-. Since there is essentially no interaction between SO_4^{2-} and Al_2O_3 the rate of dissolution is orders of magnitude lower in this medium. With Mg and Zn present, the dissolution rate is increased in both SO_4^{2-} and Cl^-. With Cu present, there is a trend in the opposite direction; i.e., the oxide is made more protective.

The overall effect of alloying, when all three elements are present, depends on the nature of the heat treatment. Indeed, the degree of change in the polarization and corrosion behavior from that of pure Al is more dependent on heat treatment than upon the quantity of Zn, Mg, and/or Cu. There is strong evidence to suggest that extreme sensitivity to the quantity of Zn, Mg, and/or Cu occurs at very low alloying concentrations of these elements.

This behavior has been interpreted in terms of two distinct mechanisms. The first, which has been called the local disruption effect, pertains exclusively to the aged alloys where the bulk of the secondary alloyants is present in the form of a second phase such as $CuAl_2$ and $MgZn_2$. This hypothesis assumes that above such particles the alumina film will be either nonexistent or at least considerably weaker and more strained than above the Al-rich matrix. The oxide above the Al-rich matrix will be weakened in the vicinity of these particles. The degree of weakening will increase with the size of the particles and with their proximity to one another.

Where we have $MgZn_2$ precipitates, which of course have no Al_2O_3 film of their own, the result will be an enhancement in the overall rate of dissolution of the alloy. This is espcially true in SO_4^{2-}, since $MgZn_2$, unlike Al, dissolves with great ease in both SO_4^{2-} and Cl^-. Experimentally, it is seen that the anodic current in SO_4^{2-} for the overaged pure ternary is orders of magnitude greater than that for 7075 and pure Al and, initially, is also significantly greater than the anodic current for the solutionized pure ternary.

As seen from the polarization curves for $CuAl_2$, its dissolution rate

is much lower in SO_4^{2-} than in Cl^-, suggesting that a strong protective effect is exerted by the Al present. Thus, for the Al-Cu system, the local disruption effect would be expected to be considerably less important than for the Al-Zn-Mg system. Indeed, it is observed that the polarization behavior of the Al-Cu alloys does not differ significantly from that for pure Al in either Cl^- or SO_4^{2-}.

The behavior of aged alloys containing all three alloyants (Mg, Zn. and Cu) seems at first glance to be at variance with the local disruption theory, but this need not necessarily be the case. These cases will be examined in terms of the general disruption effect.

The general disruption effect has been formulated to explain the changes produced in the polarization behavior of the solutionized alloys and also, to some extent, of the aged forms of some of these materials. In general terms, it suggests that the secondary alloyants cause changes in the physical and chemical properties of the passivating oxide (alumina) film through changes in ionic conductivity and/or changes in the structure of the oxide film as it forms in air after polishing and, subsequently, in solution.

Referring to the anodic polarization curves obtained in Cl^- and SO_4^{2-} (summarized in Figs. 10 — 12) it can be seen that the presence of Zn, Mg, and Cu affects the corrodibility of Al to a degree seemingly out of proportion to the amounts present. In Cl^-, the potential difference between solutionized pure ternary and solutionized ternary plus Cu is more than 150 mV. In SO_4^{2-}, the anodic current for solutionized pure ternary is orders of magnitude greater than the current for 7075 or pure Al.

In terms of the general disruption effect, Cu modifies the oxide film above the solutionized alloys, resulting in increased resistance to the passage of Al ions, whereas Mg and Zn have the reverse effect. When all three are present, the result depends on the metallurgical state, probably on grain size, and on amounts of the elements.

It is certainly more difficult to characterize the exact nature of the general disruption effect. Is it due to a change in ionic conductivity, a change in the morphology of the film, or a varying combination of the two?

There are difficulties associated with each theory. The ionic conductivity hypothesis is appealing, but has difficulties with regard to Cu, since at the potentials encountered in Cl^- media, Cu(I) or Cu(II) cannot exist.

As far as the second alternative is concerned, although it is easy to visualize Cu, Mg, and Zn atoms as altering the oxide nucleation and growth processes, it seems unlikely that the resulting polarization behavior could be so strongly affected, and in either direction at that. With regard to this hypothesis, however, it is significant to note again that heavy filming accompanying anodic dissolution in Cl^- is observed only on the Cu-free alloys. Such an oxide is undoubtedly very porous, possessing none of the protective characteristics of the more compact invisible films formed in air and in SO_4^{2-}. The 0.01% Cu present in the "ternary without copper" is believed to be responsible for the partial suppression of the secondary passivation peak and filming. Thus, this second theory is somewhat more credible than the first, although changes in ionic conductivity must still be of considerable importance in the ternary system.

The main purpose of the corrosion investigation has been to relate the corrosion morphology to the stress corrosion susceptibility of the materials and to examine the Dix theory[5] in the light of these results. Briefly, Dix theory of SCC is purely electrochemical, requiring a nearly continuous path of corrodible material for susceptibility. This path can be the precipitate phase in the ternary system or the more anodic denuded zone adjacent to precipitate in the binary (Al-Cu) system.

It has been shown that $MgZn_2$ is very active in both Cl^- and SO_4^{2-}. It can be concluded from this that anodic polarization of aged ternary alloys will result in dissolution of the exposed $MgZn_2$ at the fastest rate possible. Even at open circuit, the exposed $MgZn_2$ should dissolve within a short time. In Cl^-, under conditions of anodic polarization, the Al under the $MgZn_2$ particles should be more reactive than the exposed matrix Al, since corrosion can occur on an initially unfilmed surface The process of crack propagation may well involve a repetitive two stage process such as this. In SO_4^{2-} on the other hand, there will be negligible dissolution of the Al under the corroded $MgZn_2$ particles. As a result,

crack propagation will not be likely. Thus, the great corrodibility of $MgZn_2$ is not in itself sufficient to produce stress corrosion susceptibility. This can be understood to be the case from our observation that 7075 is more susceptible to SCC in Cl^- than in SO_4^{2-}, whereas $MgZn_2$ corrodes equally well in both. Also, in 7075-T6, small changes in potential cause large changes in the lifetime; yet thay cannot have a significant effect on $MgZn_2$ dissolution. If a continuous line or zone of $MgZn_2$ existed through an alloy, cracking would be expected to occur in both SO_4^{2-} and Cl^-. However, such a continuous line of precipitate, over any significant distance, never occurs. The Dix theory cannot be maintained, then, for this alloy system.

The binary alloys offer a somewhat different situation. The required continuous anodic path is more readily achieved because the denuded zone is the more anodic region. $CuAl_2$ particles will, of course, dissolve, but only at fairly anodic potentials. Of the two commercial 2219 alloys studied, the nonsusceptible -T851 temper gave no evidence of intergranular corrosion, whereas the susceptible -T37 was found to have undergone severe grain boundary corrosion. At high magnification, the corroded grain boundaries appear to be continuous, and the particulate $CuAl_2$ is visible. On the basis of the Dix theory, the stress corrosion susceptibility of the binary system should tend to increase with the degree of intergranular attack.

There is a contradiction between the results of the visible examination of corrosive attack and those in the electron microscopic study, however. We noted in the latter that all tempers of Al-4Cu are susceptible to intergranular corrosion, although the rate of trenching increases with aging. The light microscope reveals only very deep trenches. These results may in a sense be more relevant, since it may be necessary to have a deep trench for the Dix theory to apply. We should point out, however, that stress corrosion in this system requires the continuous application of stress during the whole process. It is difficult to see how susceptibility to pure intergranular corrosion can then be the dominant factor.

E. Stress Corrosion

1. Introduction

The stress corrosion tests have concentrated on the commercial alloys 2219 and 7075. Unless otherwise specified, tests were carried out in 1N NaCl buffered to a pH of 4.7 with 0.05N acetate buffer. All tests were carried out at a constant strain equivalent initially to 90% of the 0.2% offset yield stress, as determined from the mechanical tests described in Section II.

2. Test cell

These stress corrosion tests[6] were all carried out in the cell shown in Fig. 31.

The cell consists of a heavy walled Pyrex tube, fitted with smaller inlet and outlet tubes which terminate in ball joints. The working volume is about 70 ml. The inlet tube is fitted with a perforated ring of glass which directs the incoming flow uniformly against the gauge section of the specimen. Provision for controlled stirring is not commonly provided in stress corrosion studies, but it has been found that under certain circumstances the stirring rate can be an important variable. The outlet has an extension tube which is bent upward to draw off any gas produced during the corrosion process. The solution is circulated by means of a peristaltic pump operating on Viton tubing and connected to the system via Teflon tubing and ground glass ball joints. Before entering the cell, this solution is thermostated by being passed through a water-jacketed reaction kettle. There it is also deoxygenated by purging with nitrogen before being pumped into the cell itself.

The samples themselves are short, 1.5-in. standard tensile specimens which are threaded at each end into 3/8-in. steel extension rods. By using small specimens, samples from the short transverse direction of rolled material can be tested, and this is usually the direction of interest in stress corrosion studies.

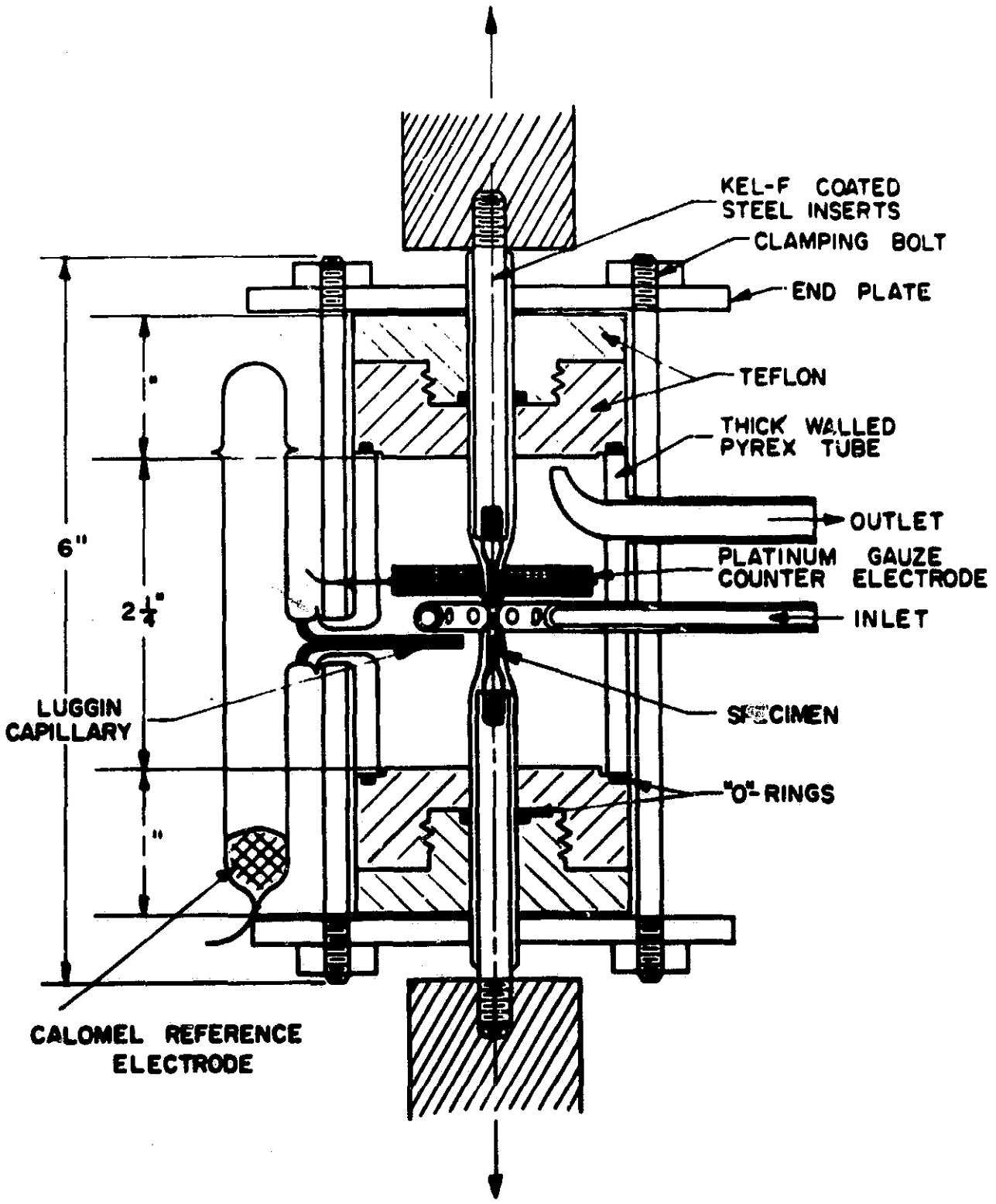

Fig. 31. Schematic diagram of stress corrosion cell

This assembly, sample and grips, is dipped into a molten mixture of Kel-F no. 200 and no. 210 waxes to mask off all but a 1/8-in. section on the gauge length, to which corrosion is consequently restricted. Masking the grips is necessary to eliminate corrosion of the steel extension rods. These are passed through the Teflon end pieces of the cell by means of deformable O-ring seals, as shown in Fig. 31. Because the end pieces are threaded, these seals can be independently tightened even after the cell is fully assembled. The Teflon end pieces are also sealed onto the flat ends of the cell by means of O-rings together with three long bolts which pass through circular Al clamping plates at each end of the cell. The O-ring seals have been found to be extremely effective, and leakage of solution does not occur even after violent specimen failure.

The use of a sealed and purged system eliminates effects due to dissolved air or oxygen and is, therefore, an improvement over other cells for use with testing equipment which has been open to the air. By using standard tensile bar samples, many of the problems associated with the use of wire specimens are avoided.

3. Charge required for failure of 7075

Initially, tests were carried out to determine the effect of galvanostatic current density on the charge (in C/cm^2) which had to be passed before failure occurred. Current densities of between 0.1 and 20 mA/cm^2 were used. Over this range, the charge per unit area which is necessary to cause failure increased from 1.5 to 5 C/cm^2. Hence, it may be concluded that at the higher currents, the corrosion reactions cannot proceed fast enough in localized regions to accommodate all the currents, and a higher percentage of the current is involved in general uniform corrosion attack.

At the lower currents, however, it is possible to localize the corrosion reaction to pits and to crevices; thus, each unit of charge has a greater effectiveness in causing failure. Such a curve showing C/cm^2 to failure versus applied corrosion current must, of course,

go through the origin, since if no current at all were applied, the specimen would still fail finally through free corrosion. However, when current is plotted on a linear scale, it is very easy to extrapolate the linear part of the curve to a positive intercept. Our interpretation of the value of this intercept is that it must represent the minimum amount of mass which must be lost for failure to occur. For 7075-T651, this value is 1.35 C/cm^2 or about 1.35×10^{-4} g/cm^2. If such a mass loss were evenly distributed, it would amount to the removal of only about 2500 monolayers.

It is suggested that this procedure and the values of C/cm^2 or g/cm^2 which this procedure produces might provide useful parameters for quickly sorting different materials with respect to their stress corrosion susceptibility. For example, 2219-T851 in similar tests absorbs several hundred coulombs before failure (not by stress corrosion in fact, but by general attack), while 7075-T6(51) absorbs less than 1.5 C/cm^2 under the same conditions before failure occurs. These tests have as a very great advantage the fact that they can be carried out relatively quickly compared with normal environmental exposure tests. In addition, solutions of practical interest could be utilized, with the impressed current only accelerating the naturally occurring reaction.

4. Stirring rate effects for 7075 SCC

The time to failure has also been shown to depend on the rate at which the corrosion solution is circulated around the test specimen. This effect is most reasonably attributed to the sweeping away of corrosion products from the surface of the specimen. In particular, localized pH changes might still occur, in spite of buffering, in regions such as pits of corrosion crevices, and it is precisely these areas which would have the greatest effect on the failure time. By circulating fresh buffered solution, we would expect these effects to be reduced. Anodic corrosion of Al removes OH^- from solution, hence making the solution more acidic. Failure times decrease as acid concentrations increase, and conversely. Hence, increasing the stirring rate would be expected to increase the failure time, because with greater stirring more buffer would be supplied to keep the pH constant.

This expected result is in fact observed, as shown in Fig. 32, and we have found that the time to failure at 0. 1 mA/cm^2 increases by more than a factor of two as the flow rate was increased from 100 to 600 mℓ/min. This effect, while relatively straightforward in interpretation, has generally not been taken into account in general stress corrosion testing. This may be the reason for some part of the very large scatter which is associated with these tests. In our own testing program, the observation of the above results has led to the adoption of a standard condition of stirring for all tests (220 mℓ/min, unless otherwise stated).

5. Load relaxation rate

Because the load is monitored continuously during our tests, the relaxation rate, that is, the change in load with time at constant strain, is automatically measured. In the absence of stress corrosion, Al alloys at room temperature are still expected to show relaxation under load. Anodic dissolution accelerates this effect markedly, and the increased rate of relaxation gives a measure of the extent of such damaging attack.

This conclusion is confirmed by the experiment shown in Fig. 33 (a plot of the relaxation rate versus time for a specimen of 7075-T6 under either cathodic protection or anodic dissolution). This figure shows that under cathodic protection the initial high relaxation rate after loading rapidly decays to a low value, but that when the current is reversed so that anodic dissolution is occurring, the relaxation rate begins to increase. These data are presented here to demonstrate a novel method for determining whether or not a cathodic protection treatment is indeed preventing metal dissolution. Since this method does not require a measurement of the time to failure, it is inherently more rapid than those which do require such a measurement. As such, it could be of value in an accelerated testing program.

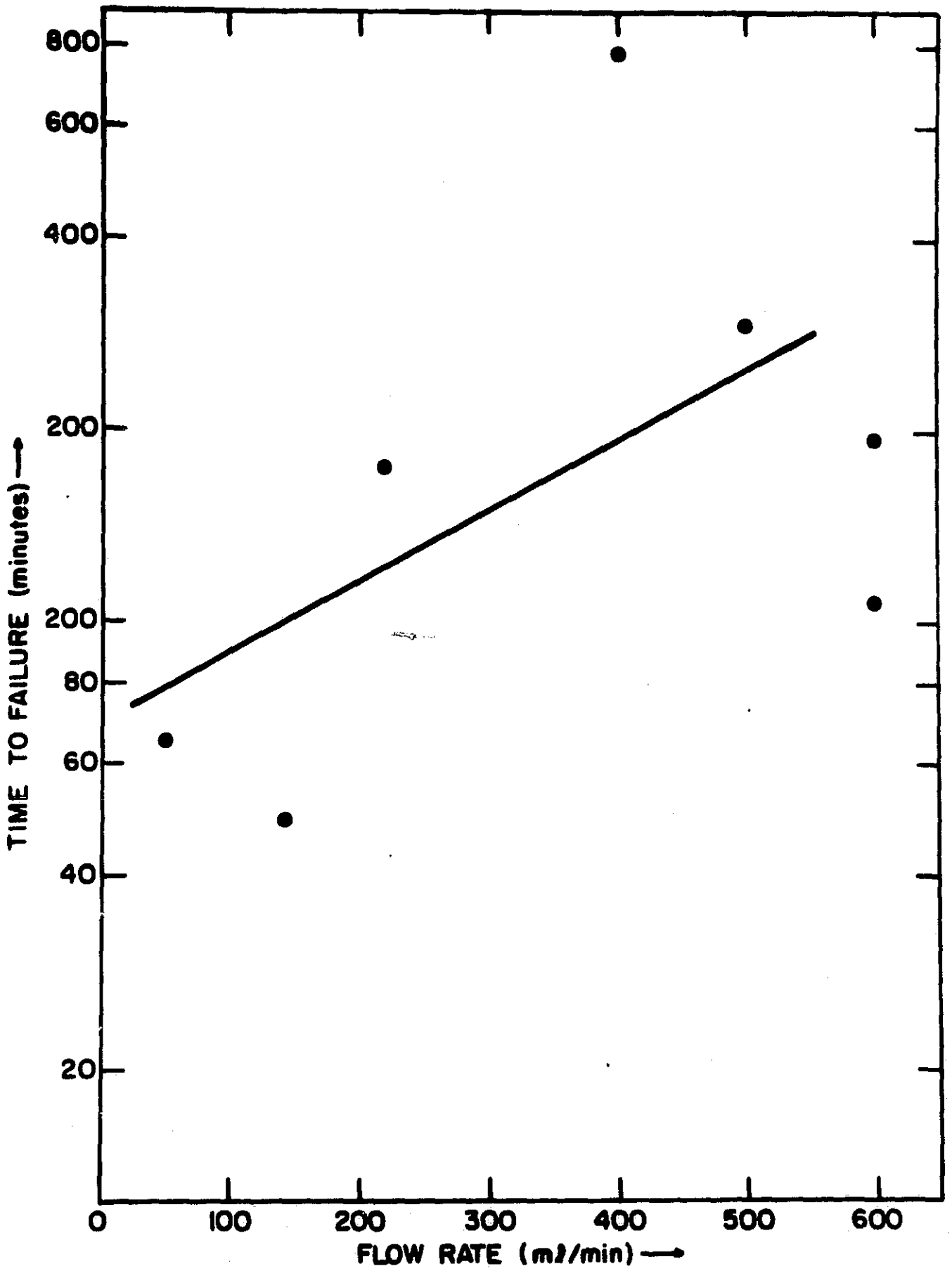

Fig. 32. Time to failure versus stirring rate for 7075-T6 short transverse specimens (j = 0. 1 mA/cm^2)

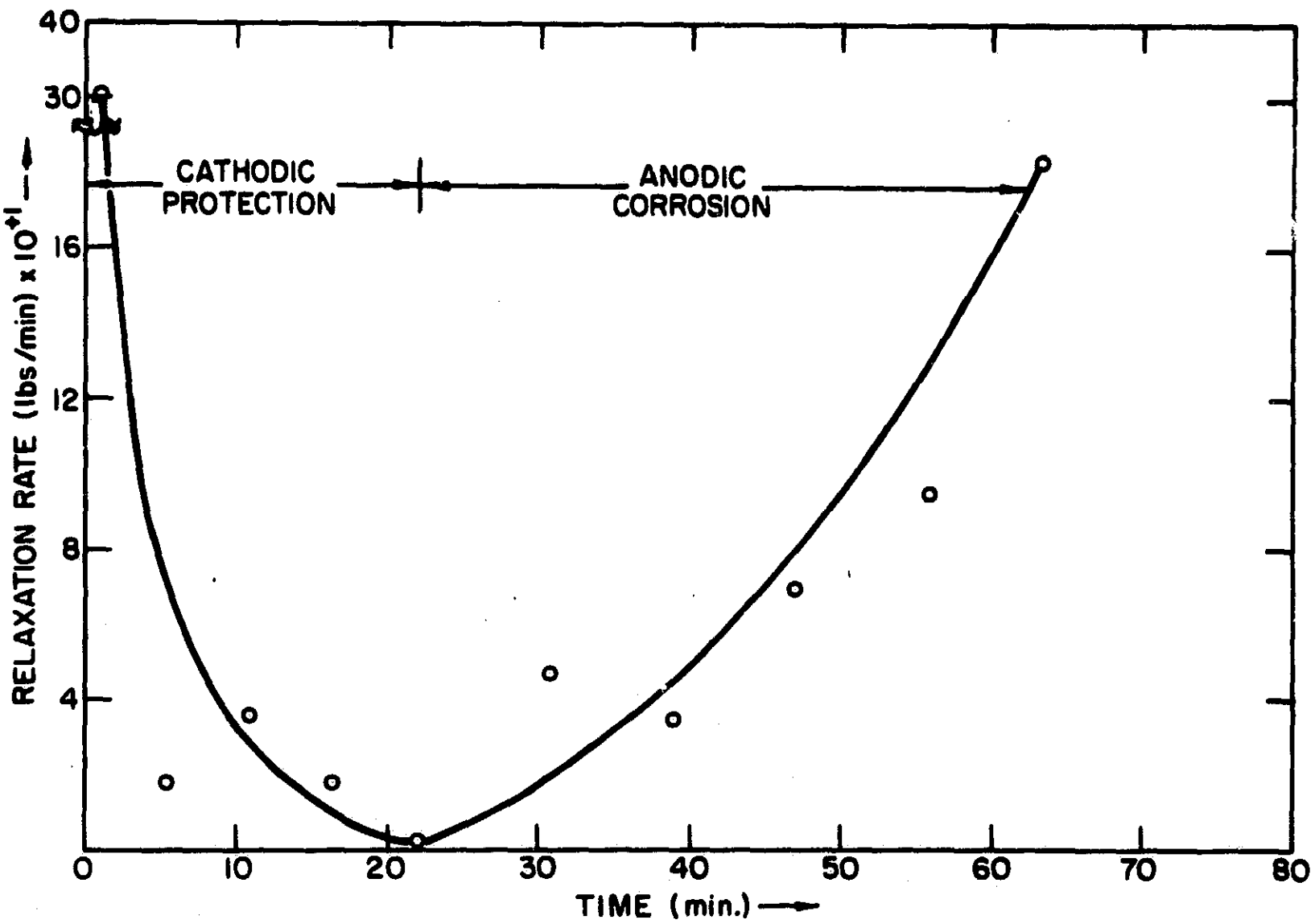

Fig. 33. Relaxation rate versus time during both cathodic protection and anodic corrosion for specimen initially stressed in the same manner used for stress corrosion test

6. Failure modes of 7075 and 2219

Continuous monitoring of the load during testing has revealed a substantial difference in the mode of failure of 2219-T37 compared with 7075-T651. This difference occurred in experiments where the alloys were kept at constant strain under loads which were initially 90% of the 0.2% offset yield strength. In the case of 7075-T651, failure was catastrophic. That is, after a period of only moderate change with time, the load would drop suddenly to zero, and the fracture would propagate continuously across the specimen. This is shown in Fig. 34. This sudden failure is, in general, preceeded by a period only amounting to 15 to 30 sec, during which the load would relax at an ever accelerating rate.

For 2219-T37, an entirely different behavior was observed. Instead of failing catastrophically, the specimens failed discontinuously in a stepwise manner. It is reasonable to associate that part of the step where the load does not fall off rapidly with the halting of crack advance at a grain boundary intersection, especially since this was observed with Al-4Cu.

This would be consistent with the observed microstructures of 7075-T651 and 2219-T37. In the case of 7075-T651, transverse sections show the grains to be severely elongated so that specimens strained in the short transverse direction will be stressed normal to these elongated grain boundaries. This will have the effect of providing very long regions of low cleavage energy (the grain boundaries) along which cracks can propagate. In the case of 2219-T37, however, the grain elongation is not as extreme. Hence, even in the short transverse direction, the number of available grain boundaries oriented normal to the direction of stressing is not as large as in 7075-T651. In addition, the grain boundaries themselves are partly irregular due to the fact that the -T37 temper is not a temper induced by precipitation heat treatment. Rather, it is a temper which is produced by mechanical treatment. Hence, a greater irregularity of grain boundaries is to be expected.

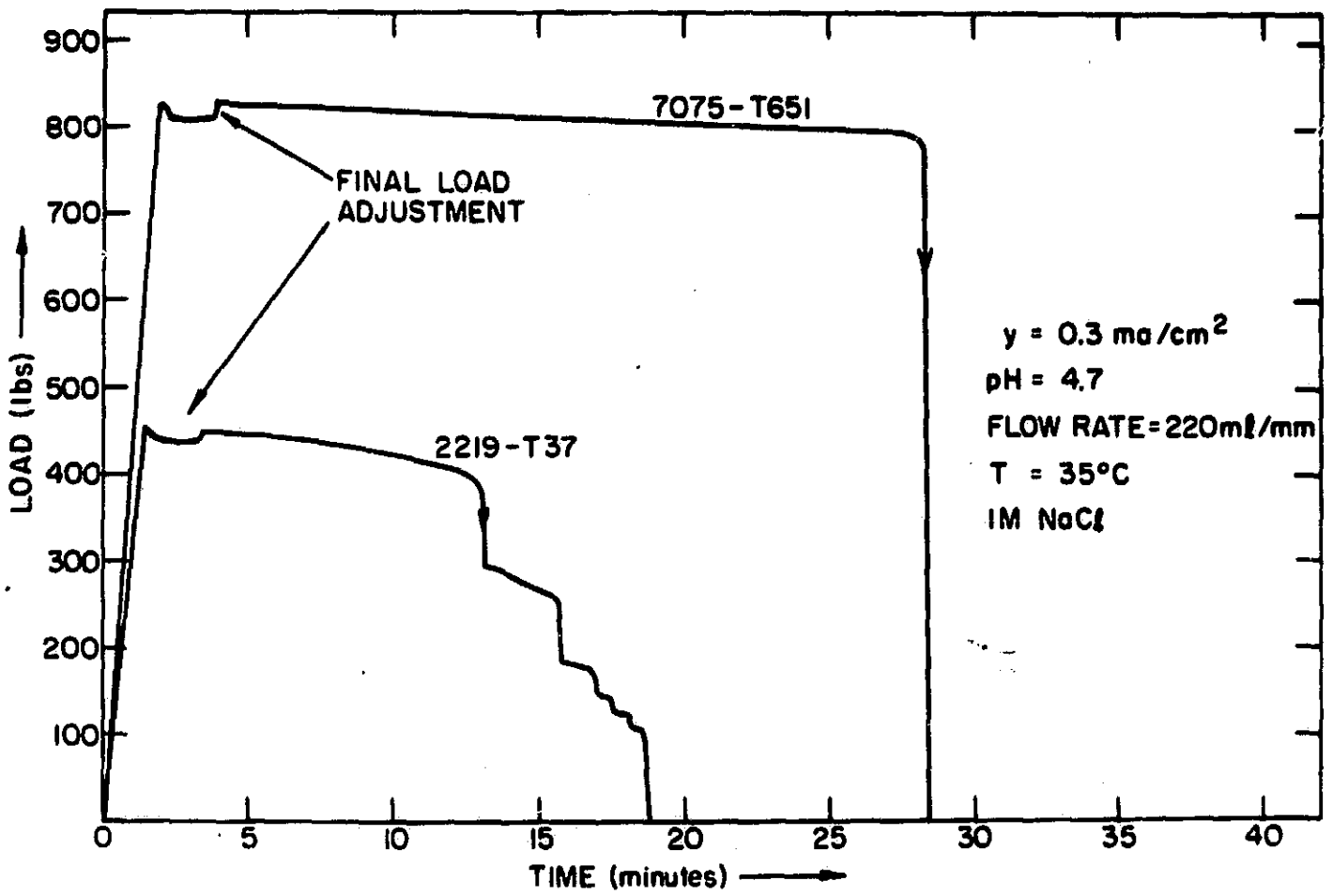

Fig. 34. Load versus time during stress corrosion tests on aluminum alloys 2219-T37 and 7075-T651

The grain boundaries in 2219 which are suitably oriented do not have as low a cleavage energy as those in 7075. This can be concluded from the fact that large grained samples of high purity Al-Mg-Zn fracture along grain boundaries, while similar specimens of Al-Cu do not. In addition, since a yield strength of 75000 psi in 7075-T651 (as opposed to 44000 psi for 2219-T37) is found, the elastic energy available for crack propagation is much greater in the former than in the latter. This fact, combined with the lower grain boundary cleavage energy and greater yield stress in the high strength alloys, serves to explain the differences in fracture modes satisfactorily.

Further proof that crack advance in the 2219-T37 alloys is associated with the halting of crack advance at grain boundary intersections was obtained by testing large grained specimens of Al-Cu. For these specimens, crack advance could be observed visually, since the samples were in the form of strips 0.020 by 0.25 by 4 in., and the individual grains extended through the sample thickness. It was noted that load dropoffs coincided with sudden crack advance and that this periodic crack advance was associated identically with change in crack direction of a single crack as it advanced from grain boundary to grain boundary.

7. Precorrosion effects on the SCC of 7075 and 2219

It is fundamentally assumed in the study of stress corrosion that there must be conjoint action between the applied stress and the corrosion process for this phenomenon to occur. In other words, the extent of damage must be greater when both stresses and corrosion are applied simultaneously than when each is applied separately. In the past, this distinction has seldom been rigorously examined even though, as discussed below, some preliminary work has been done. It is apparent that two aspects are crucially important: (1) the separation of the effects of stress and of corrosion in stress corrosion, and (2) the demonstration of the conditions under which it is appropriate to investigate

experimentally the atomistic mechanisms for each process. Furthermore, from the engineering standpoint, it is also of practical importance to isolate mechanical from chemical effects.

As will be shown, large differences exist in the behavior of different Al alloys in the extent to which these two parameters must be separated. This separation, it turns out, is of critical importance in establishing meaningful measures for the kinetics of crack growth in Al alloys. Hence, in the experiments on the SCC of 7075-T6, 2219-T37, and Al-4Cu described below, we focused on this important problem. It will appear that for 7075-T6(51), for example, only a very small part of the failure time in a stress corrosion test corresponds to the real stress corrosion phenomenon. The remainder of the time (80%) comprises a "sensitization" of the material by pure corrosion and, finally, rapid crack propagation.

The usual definition of stress corrosion requires that stress and corrosion acting together must lead to greater damage than if they act separately. The extent of damage is usually measured as a decrease in mechanical strength. The American Society for Metals Committee on stress corrosion[7] has suggested taking the ratio of the differences in breaking loads of uncorroded, corroded but not stressed, and corroded while stressed specimens as a means of determining whether or not stress corrosion does occur in a given alloy system. This method thus gives a measure of the extent to which mechanical properties are impaired by pure corrosion relative to that produced by corrosion under stress. As discussed by Sprowls,[8] a stress corrosion index (SCI) may be defined as

$$SCI = \frac{TS_u - \sigma}{TS - \sigma} \tag{1}$$

where σ = engineering stress applied to stressed and exposed specimen resulting in its failure

TS_u = engineering tensile strength of unstressed specimen exposed for the time to failure of the stressed specimen

TS = engineering tensile strength of unexposed specimen

If a material undergoes true stress corrosion, then exposure to the corrosive environment without the application of stress would not lead to a significant reduction in failure time in a subsequent normal stress corrosion test. * If, however, pure corrosion were important initially in the failure process, then exposure to the corrosive environment without stress (precorrosion) would be expected to lead to a decrease in the subsequent time to failure, which is measured from the time when the stress was applied. These two cases are illustrated schematically in Fig. 35. In this figure, the ordinate is the time to failure (measured in each case from the time the load was applied), and the abscissa is the precorrosion time (i.e., the time during which the specimen was exposed to the environment without load).

The horizontal dashed line (A) shows the result to be expected if precorrosion has no effect, while the 45° dashed line (B) shows the result for the case in which precorrosion is exactly as effective in leading to final failure as corrosion under applied load.

To provide a quantitative measure of the effect of precorrosion, one can define a precorrosion susceptibility index (PSI). This index is most reasonably taken as the negative of the derivative of the subsequent time to failure (measured from the time of load application) with respect to the time of precorrosion; that is

$$\text{PSI} \equiv \frac{-\text{d (time to failure after precorrosion)}}{\text{d (time of precorrosion)}} \qquad (2)$$

If the time to failure does not change with precorrosion, the PSI value is zero and the specimen has not undergone damage from the precorrosion treatment. If, however, corrosion without load is just as effective in leading to failure as corrosion with load, then the PSI value is unity. In this case, the decrease in subsequent time to failure is just as great for one unit of precorrosion time as for one unit of corrosion while under load.

---

*A normal stress corrosion test designates a test in which load and the corrosive environment are applied simultaneously.

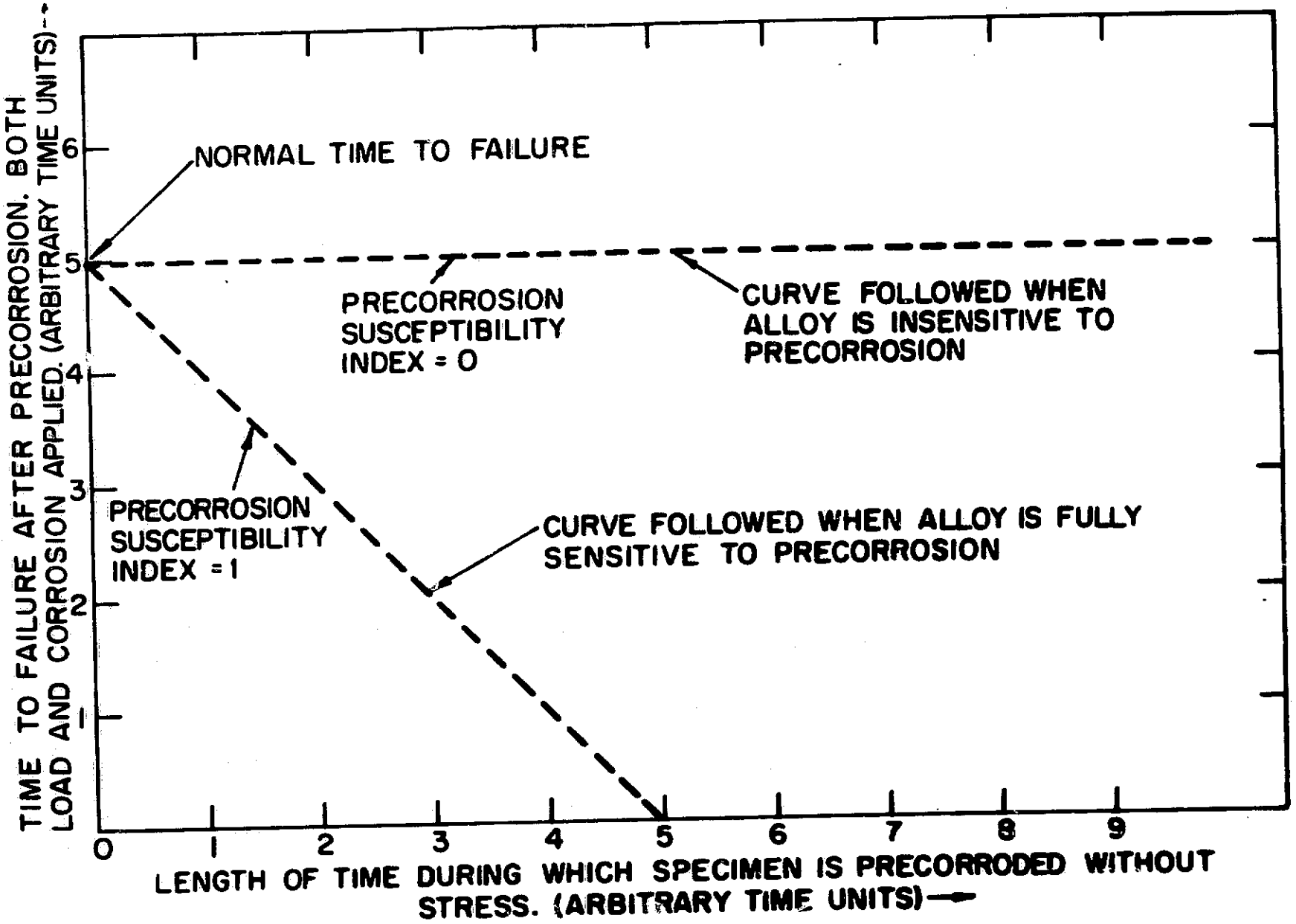

Fig. 35. Schematic diagram of precorrosion test results

The PSI value need not remain constant over the whole range of precorrosion treatments. As will be shown, an initial PSI value of unity is found for certain alloys. After precorrosion for a period of greater than the normal time to failure, however, the PSI value becomes zero, indicating a transition from a corrosion process that is unaffected by the load to one which is accelerated by the applied stress.

The results of precorrosion tests on both Al alloys (2219-T37 and 7075-T651) are shown in Fig. 36. Precorrosion was carried out galvanostatically at a current density of 0.3 mA/cm^2. This current density was chosen because this is approximately that which could be supplied by oxygen reduction in air saturated solutions. By using galvanostatic conditions, however, the corrosion could be more directly controlled.

The surface of the gauge section was machined to a 25-μ in. surface finish. The load was applied without removing the specimens from the solution. Fig. 36 is normalized, that is, the ordinate and abscissa values of each point were divided by the normal time to failure for the alloy represented by that point. For 2219-T37 and 7075-T65, these normal times to failure were 16.5 and 31.5 min, respectively.

As can be seen in the figure, the specimens of 2219-T37 showed a PSI value of approximately zero. This indicates that true stress corrosion was occurring throughout the failure process. The specimens of 7075-T651, however, initially showed a PSI value of unity, indicating that the first stage of the failure process in these specimens is a corrosion process that is unaffected by the application of the load. This initial pure corrosion stage is followed by a true stress corrosion process which leads to final failure. This transition can be seen from the change in the PSI value from unity for precorrosion treatments of up to approximately one times the normal time to failure, to zero for precorrosion treatments of from one to more than ten times the normal time to failure. As shown, the period of true stress corrosion amounts to only 20% of the total failure time. Of the normal time to failure, 80% is associated with a process that is not accelerated by the application of the load.

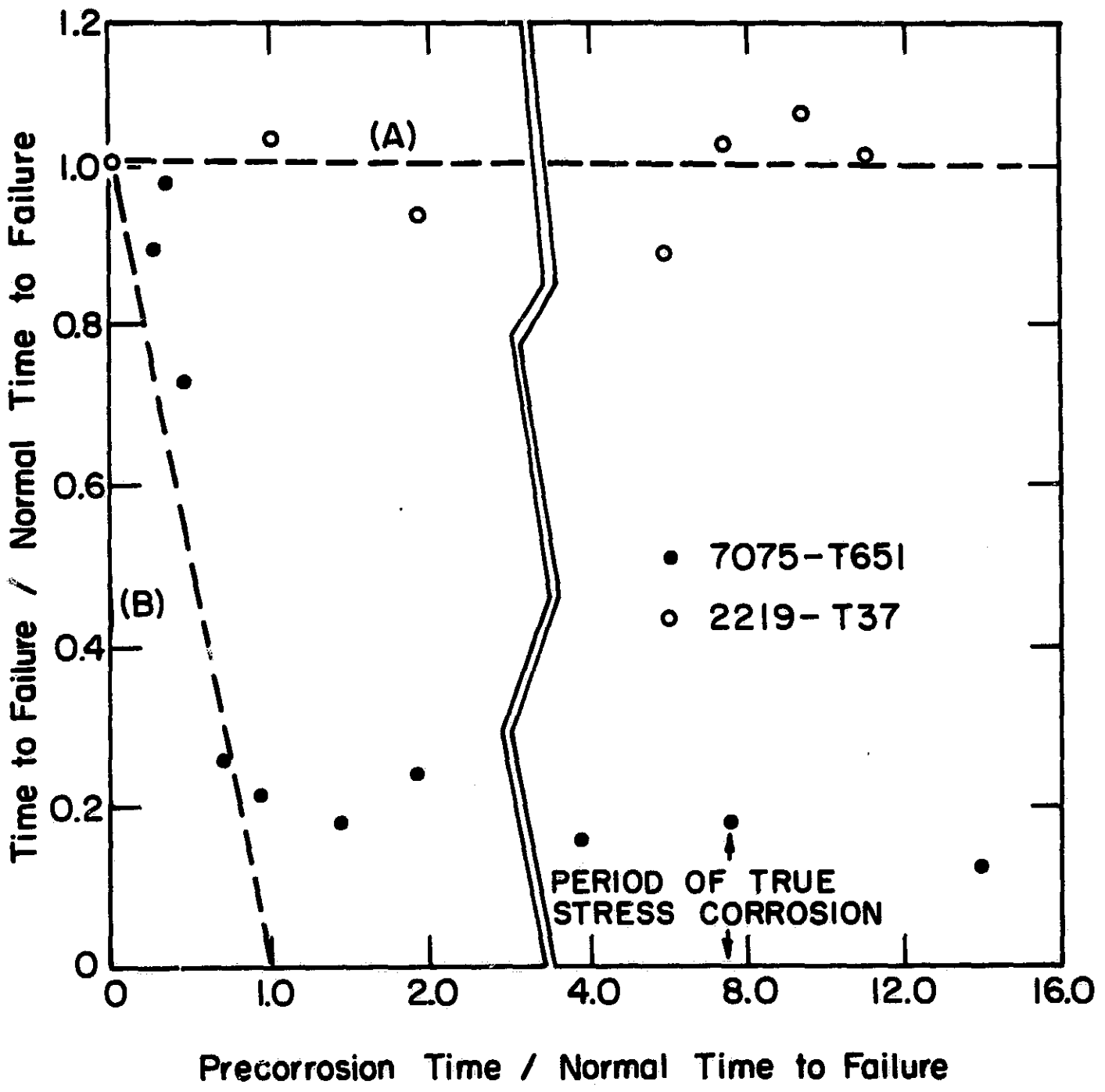

Fig. 36. Precorrosion time versus time to failure

To obtain a comparison between the method described here and the stress corrosion index (SCI) method, tests have been carried out to determine the quantities needed to calculate the SCI value from Eq. (1). For both 2219-T37 and 7075-T651, the SCI values were found to be approximately 0.97, which indicates that the mechanical properties of both alloys were hardly affected by the corrosion without applied stress. Hence, using the SCI method the very large difference between the behavior of these two alloys would not be observed.

To determine if the effect found for 7075-T651 was due to residual stress, specimens were solutionized for 1 hr at 480 °C in argon (this treatment removes all residual stress). The specimens were then quenched in oil at 121 °C and aged for 24 hr to approach the -T651 temper. * By quenching in hot oil, any thermal stresses are minimized. If present at all, they would be expected to be compressive at the surface layer and hence would not assist stress corrosion. The results obtained on these heat treated specimens are shown in Fig. 37. As before, the coordinates of each point have been normalized by dividing by the normal time to failure, which for these samples was 13 min. These results also show a sharp initial decrease in time to failure resulting from the precorrosion treatment. The initial PSI value is unity as before. Hence, the marked susceptibility to precorrosion of this alloy cannot be entirely attributed to residual stress.

Since Fig. 37 is a normalized plot, it is also significant that the period of true stress corrosion is very nearly the same for both the as machined and the reheat treated specimens, even though their normal times to failure differ by a factor of more than two. Thus, it is possible to study the influence of such factors as pH and temperature on the stress corrosion process, in a manner that is independent of the surface condition of the alloy, using these tests.

---

*The -T651 temper is obtained from the -T6 temper by slight stretching after quenching. Stretching was not needed in this case, because quenching was carried out in hot oil.

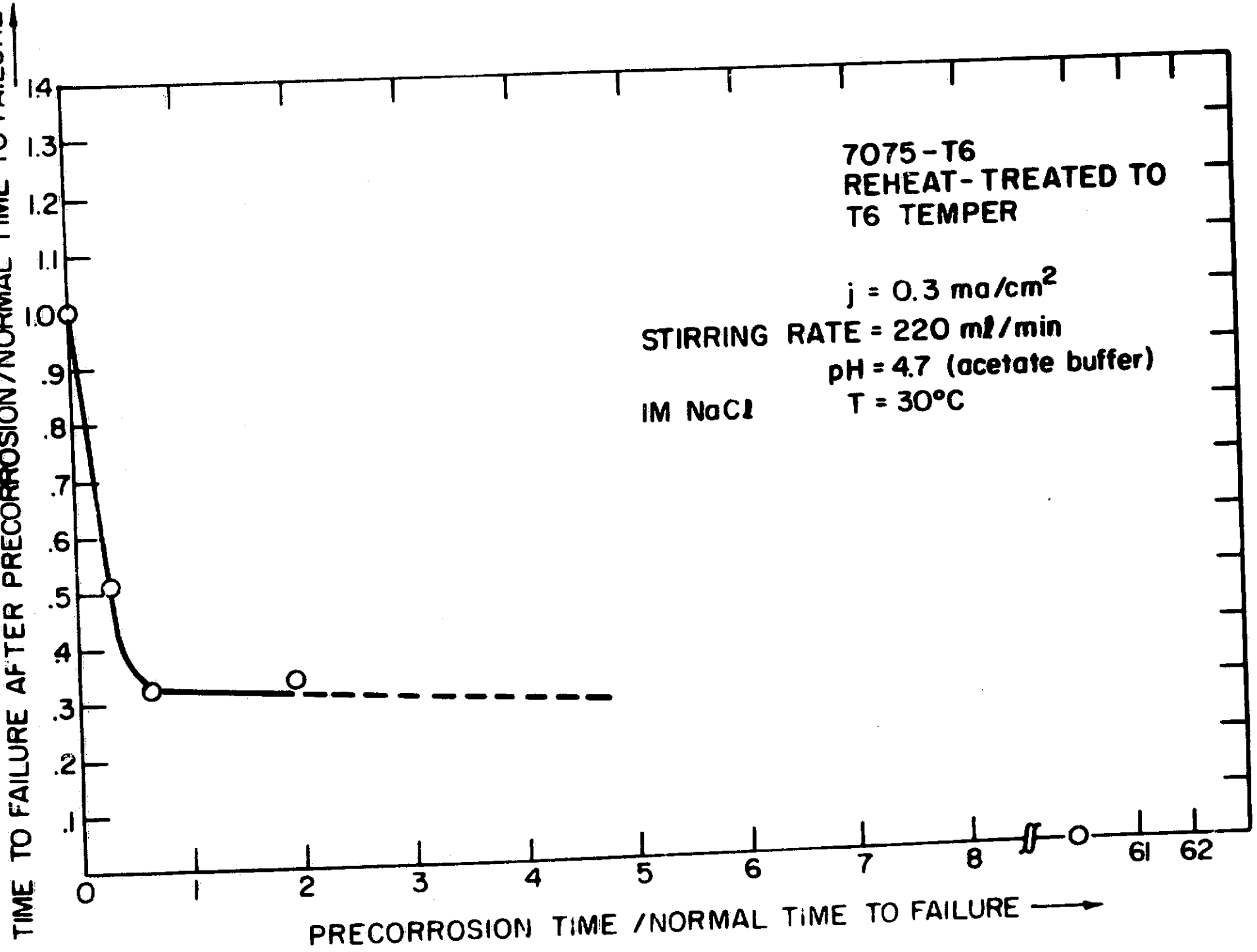

Fig. 37. Normalized time to failure versus precorrosion time for reheat treated 7075-T6

8. Effects of heat treatment on the SCC of 7075

To determine whether or not any of the above results could be due to the presence of residual stress, specimens were solutionized for 1 hr at 900 °F to remove any possible residual stress. This was followed by quenching in oil preheated to the proper temperature (250 °F) for aging the -T6 temper, and aging for 24 hr as before.

Mechanical tests were then run on the 7075 specimens which were reheat treated to the -T6 temper to verify that this temper was indeed reproduced. Similarly, mechanical tests were also made on those specimens which were overaged at 350 °F. These tests (Fig. 38) show that on initial overaging the yield stress actually increased slightly, and that indeed in overaging for times of about 8 hr, the strength would be slightly above that for the -T6 condition.

The results of stress corrosion and precorrosion tests as a function of overaging are shown in Fig. 39. We see that after 10 hr of overaging, the normal time to failure is almost two orders of magnitude higher than for 7075-T6. Hence, this heat treatment procedure provides a means of increasing the resistance to failure without decreasing the strength. It also has the advantage that it can be applied to already fabricated parts.

In addition, we may note that this increase in SCC resistance derives entirely from a precorrosion phenomenon, indicating that the latter cannot derive from residual tensile stresses.

9. Effects of Cl^- concentration on the SCC of 7075

Fig. 40 shows the results of tests to determine the effect of Cl^- concentrations in solutions of 1M Na_2SO_4 buffered to a pH of 4.7 with sodium acetate and acetic acid. It is evident that Cl^- concentration exercises a critical influence. Below a concentration of 10^{-3}M Cl^-, failure does not occur in more than 18 hr, while for a concentration of 10^{-2}M Cl^-, failure occurs in slightly over 3 hr. It should also be noted that for a solution 1M in both SO_4^{2-} and Cl^-, failure occurs in 41 min, which is only slightly higher than the 32-min normal time to failure determined in 1M NaCl alone.

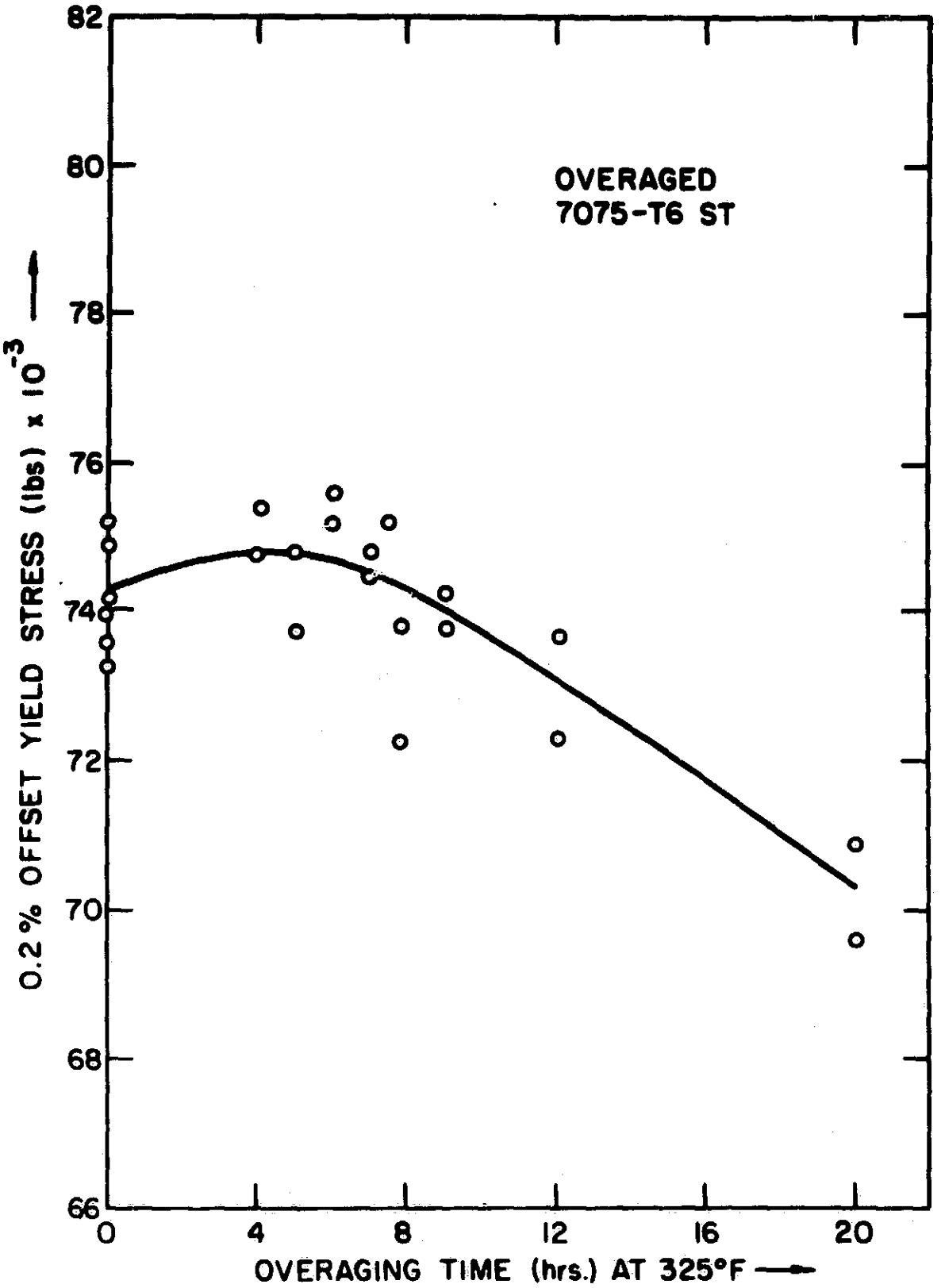

Fig. 38. Yield strength versus overaging treatment

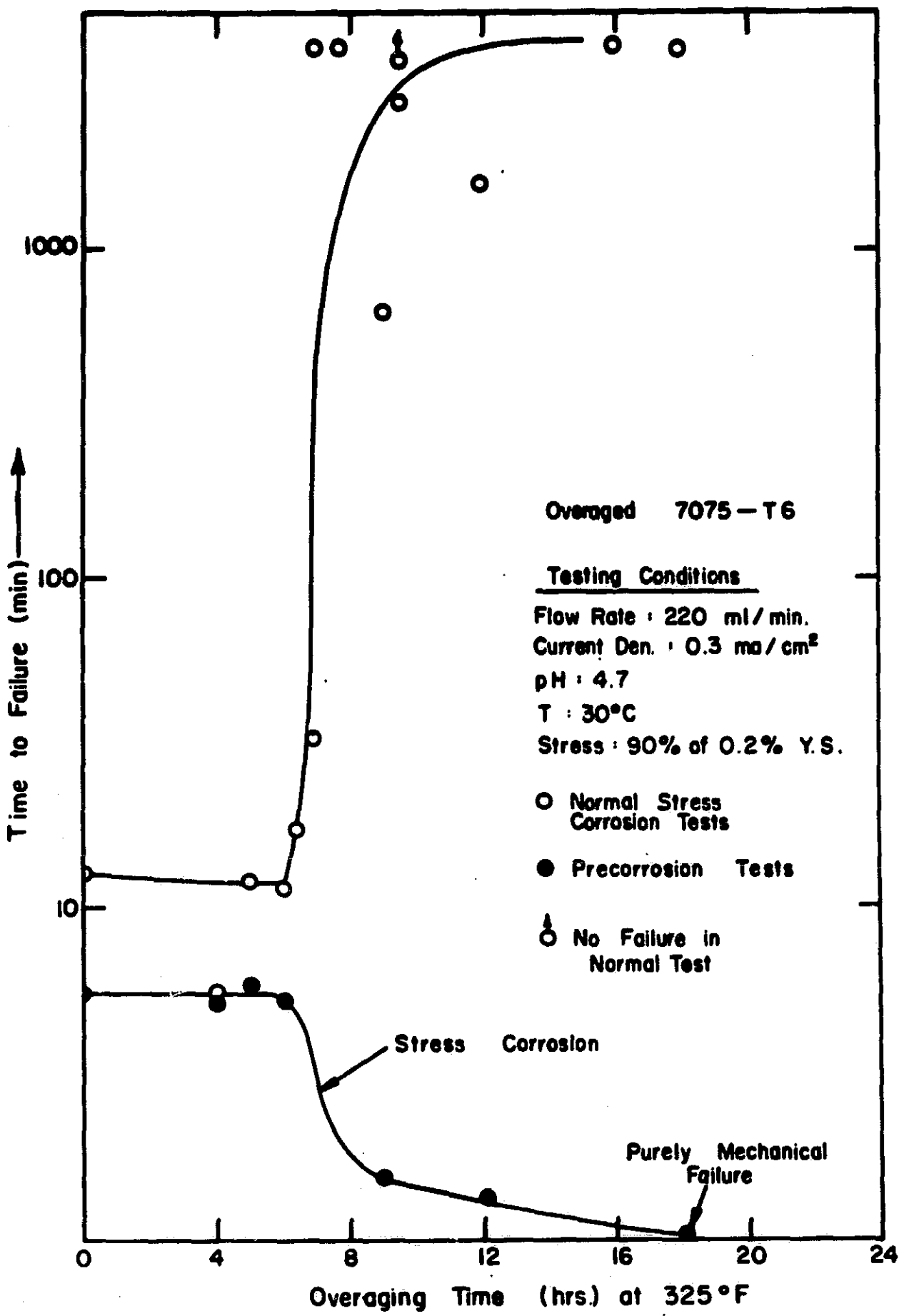

Fig. 39. Time to failure versus overaging time for 7075

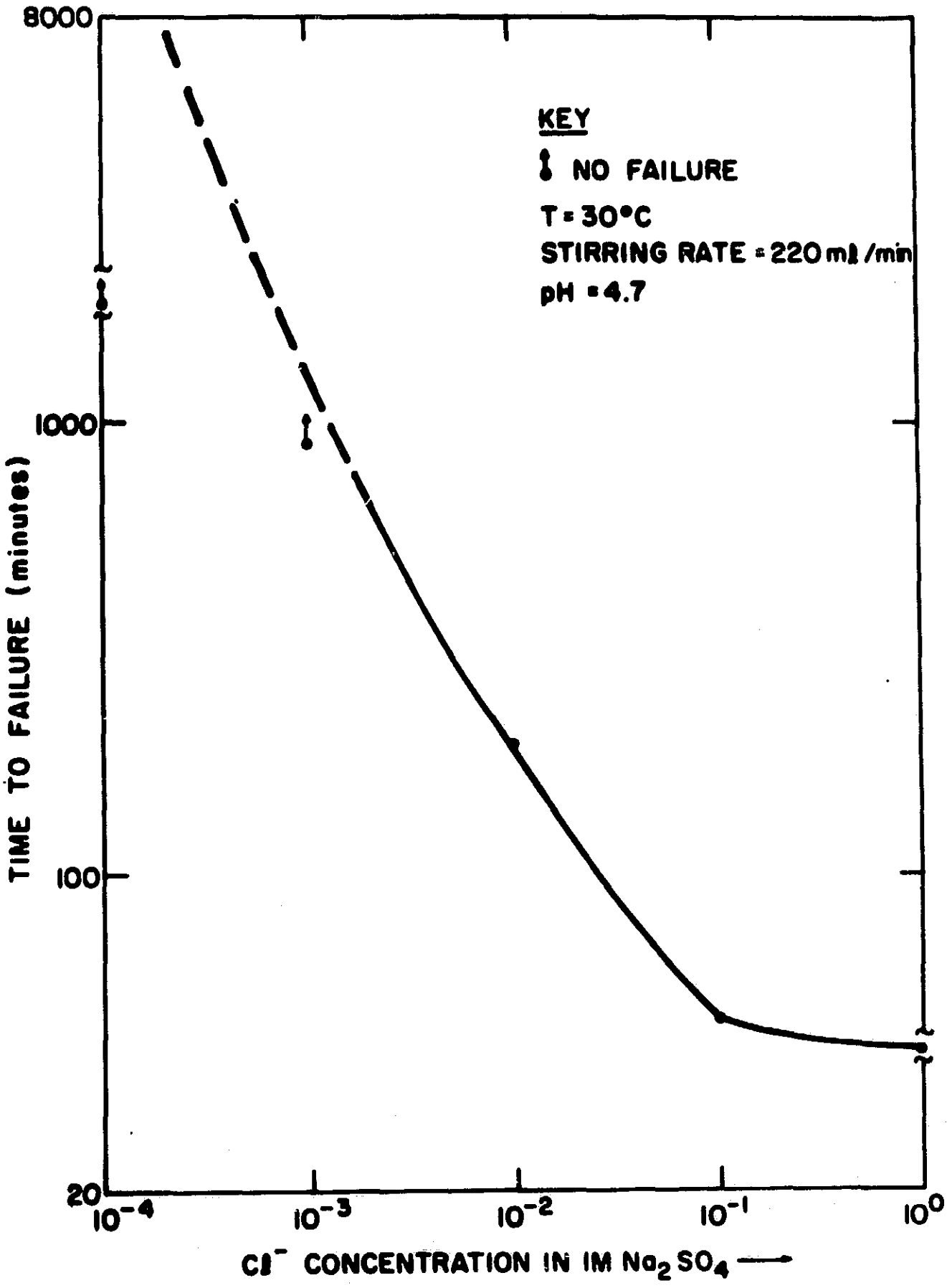

Fig. 40. Time to failure versus Cl^- concentration for 7075-T6 ($j = 0.3$ mA/cm^2; stress = 90% of yield stress; 1M Na_2SO_4)

Using the results of Fig. 40, precorrosion tests have been carried out in 1M Na_2SO_4 containing 10^{-2}M NaCl, in order to determine the effect of reduced Cl^- concentration on the precorrosion and true stress corrosion processes. The results of these tests are shown in Fig. 41. This curve shows an initial, almost level region (PSI near zero) followed by a steep region (PSI near unity). This result should be compared with that found for 1M Cl^- where there is no initial level region. Apparently, the effect of the lower Cl^- concentration has been to introduce an incubation period during which the presence of stress is necessary for damage to occur. The overall scatter of the data is also substantially greater than that of the 1M Cl^- case. This may be because, under less severe environmental conditions, specimen preparation and condition become more critical in determining time to failure. The point shown as the normal time to failure, for example, is the average of four tests which gave values between 68 and 192 min.

10. Effects of load interruption on SCC

These experiments were designed to provide further insight into the processes occurring during the period of true stress corrosion in 7075. The sequence of loading during galvanostatic corrosion for these tests is shown in the lower right-hand corner of Fig. 42. Note that the galvanostatic current is kept constant throughout the tests. First, the specimen was precorroded without stress for a period OA, long enough to bring the specimen into the region of true stress corrosion. The load was then applied for a period AB during which, according to our previous conclusions, true stress corrosion occurs. However, this load was not maintained for a time long enough to cause failure. The load was then removed for a time BC (the corrosion current was still maintained constant). The load was finally reapplied and the time until failure, CD, measured.

By plotting this latter fracture time, CD, against the second load interruption, BC, one can obtain information on the type of corrosion which is occurring during the interval BC. The results of tests of this type on

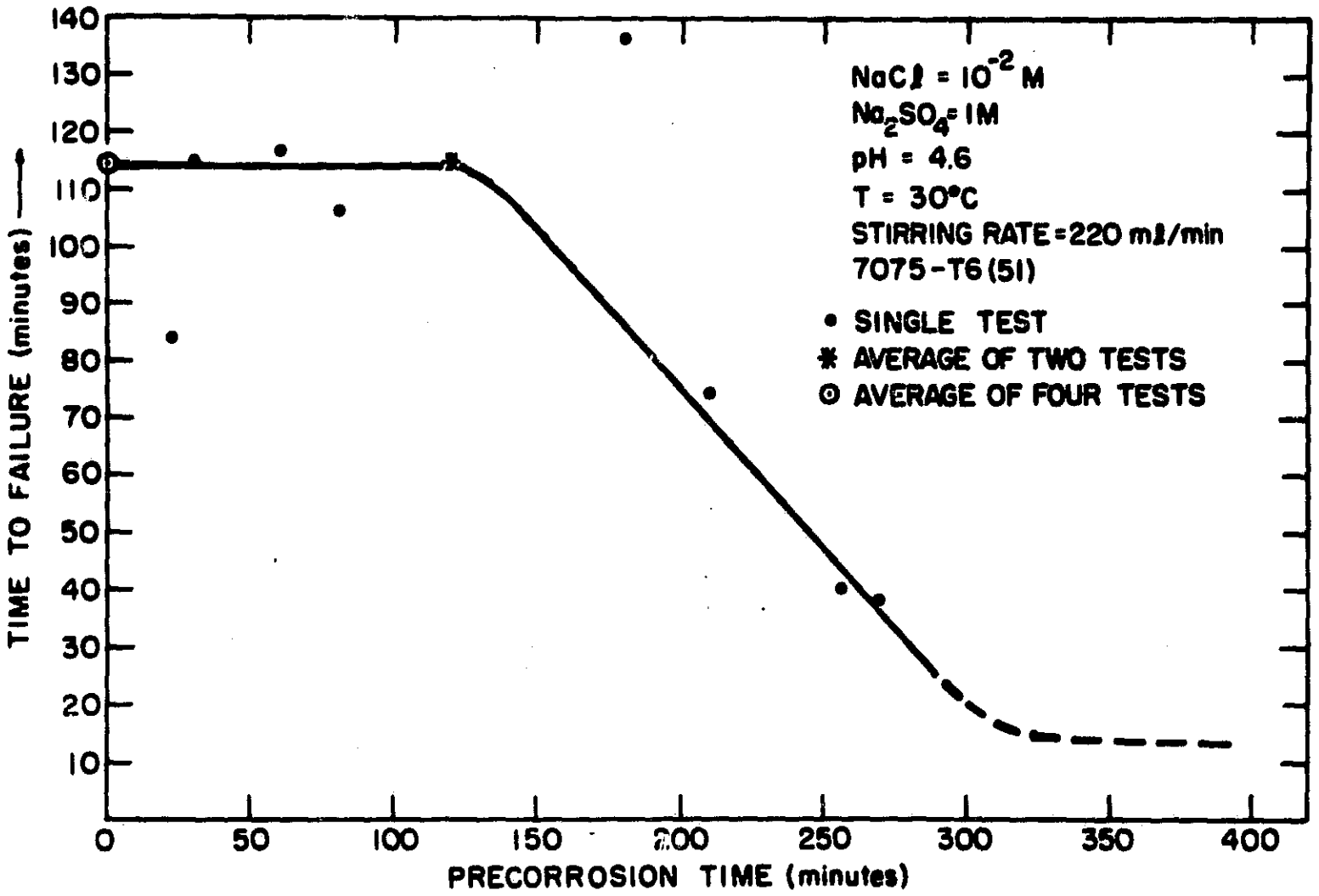

Fig. 41. Time to failure versus precorrosion time for 7075-T6

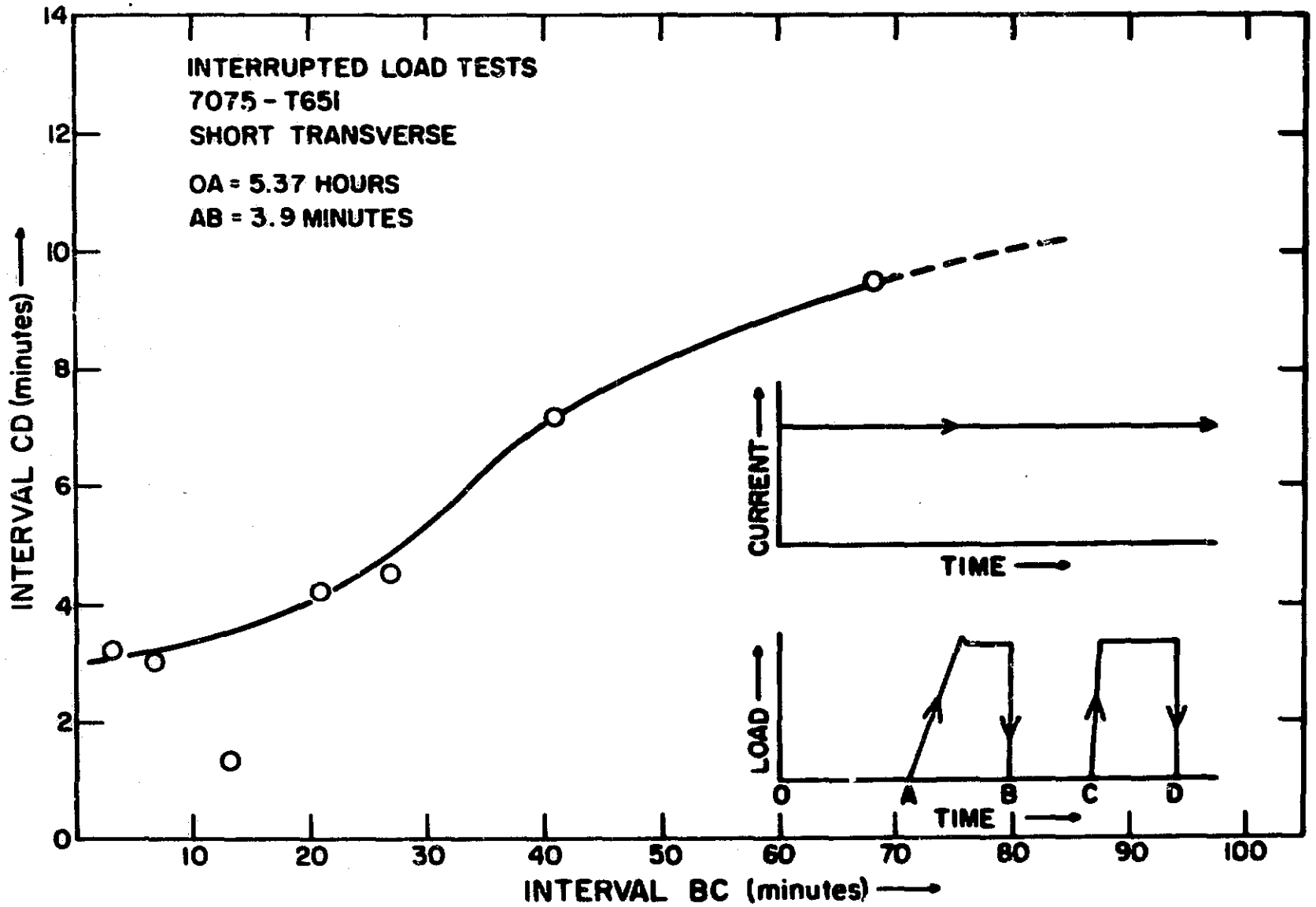

Fig. 42. Interrupted load tests on 7075-T651

7075-T651 short transverse specimens are also shown in Fig. 42. For these tests, the period AB was made equal to one-half the normal period of true stress corrosion. The period BC was then varied, and the resulting time CD plotted. This figure shows that initially corrosion between intermittent loading has no effect on the total time of failure under load (= AG + CD, i.e., 3.9 + 3 = 6.9 min, about that normally found without load interruption). This indicates that once cracks have been initiated, the presence of stress is essential to keep them propagating. The whole loaded period is then a true stress corrosion period, as previousiy assumed.

Eventually, as the period BC is extended, the total failure time under load increases. This result indicates that the effect of much corrosion without stress during the period BC is to blunt the cracks which were beginning to form during the true stress corrosion period AB.

Photomicrographs taken of specimens subjected to this interrupted loading treatment also show that flaw sharpening under stress does occur (Fig. 43). In these photographs, the initial blunt corrosion fissures caused by the precorrosion treatment can be seen, together with an apparent sharpening of the roots of these flaws by the action of the applied stress. The localization of this sharpening effect at the grain boundary is clearly seen in the higher magnification photograph, Fig. 43b.

11. Effects of oxygenation on precorrosion

The aim of these experiments has been to establish whether the precorrosion effect is a special feature of our rather unusual testing procedure, i.e., carried out galvanostatically. We should say that the logic of electrochemical theory argues very strongly against any such special consideration. However, in discussion with other workers, the possible specificity of our testing conditions has been repeatedly suggested as the reason for our precorrosion phenomenon Correspondingly, tests have been carried out in the absence of applied current, depolarizing the corrosion reaction by saturating the solution with O_2. Under these conditions, the normal time to failure was found to be 14.4 min.

(a) 200X

(b) 800X

Fig. 43. Photomicrographs of interrupted load test specimen

A complete series of precorrosion tests were carried out; the results are shown in Fig. 44. As can be seen, the initial behavior under these conditions is very near to that which was observed previously using a galvanostatic current of 0.3 mA/cm^2. Initially, the PSI index is almost unity, but becomes zero after precorrosion equal to one times the normal time to failure. The period of true stress corrosion, as has been found to be the case for galvanostatic testing, is equal to only 10 to 20% of the time to failure as determined in a normal stress corrosion test (load and corrosion applied simultaneously).

These oxygen tests confirm the validity of the galvanostatic testing procedure by demonstrating that the precorrosion effect is not dependent upon the method of corrosion (e.g., whether from oxygen reduction or from an external battery). The precorrosion phenomenon is not then a special phenomenon associated with our specific testing conditions, but is a property of the material, 7075-T651.

12. Effects of precorrosion and drying

The objective of these experiments is to examine the possibility that the cause of the precorrosion phenomenon is the production of a hostile environment in corrosion crevices. This hostile environment would, of course, be eliminated if the specimen were washed and dried after precorrosion but before the normal stress corrosion test.

Specimens have been precorroded for varying lengths of time, removed from solution, vacuum dried, replaced in solution, and the time to failure in a normal stress corrosion test determined. The results of these tests are shown in Fig. 45. It is clear that there is considerably more scatter in these results than has usually been the case. Nevertheless, there is a fairly discernible trend. First, it is evident that after drying the effect of the precorrosion treatment is, to a large extent, altered. Indeed, it appears that for certain combinations of precorrosions and drying time, the subsequent time to failure may be significantly increased. This is especially well demonstrated by the combination of precorrosion for 200 min followed by desiccation for 15 hr, after which the specimen did not fail for 1375 min.

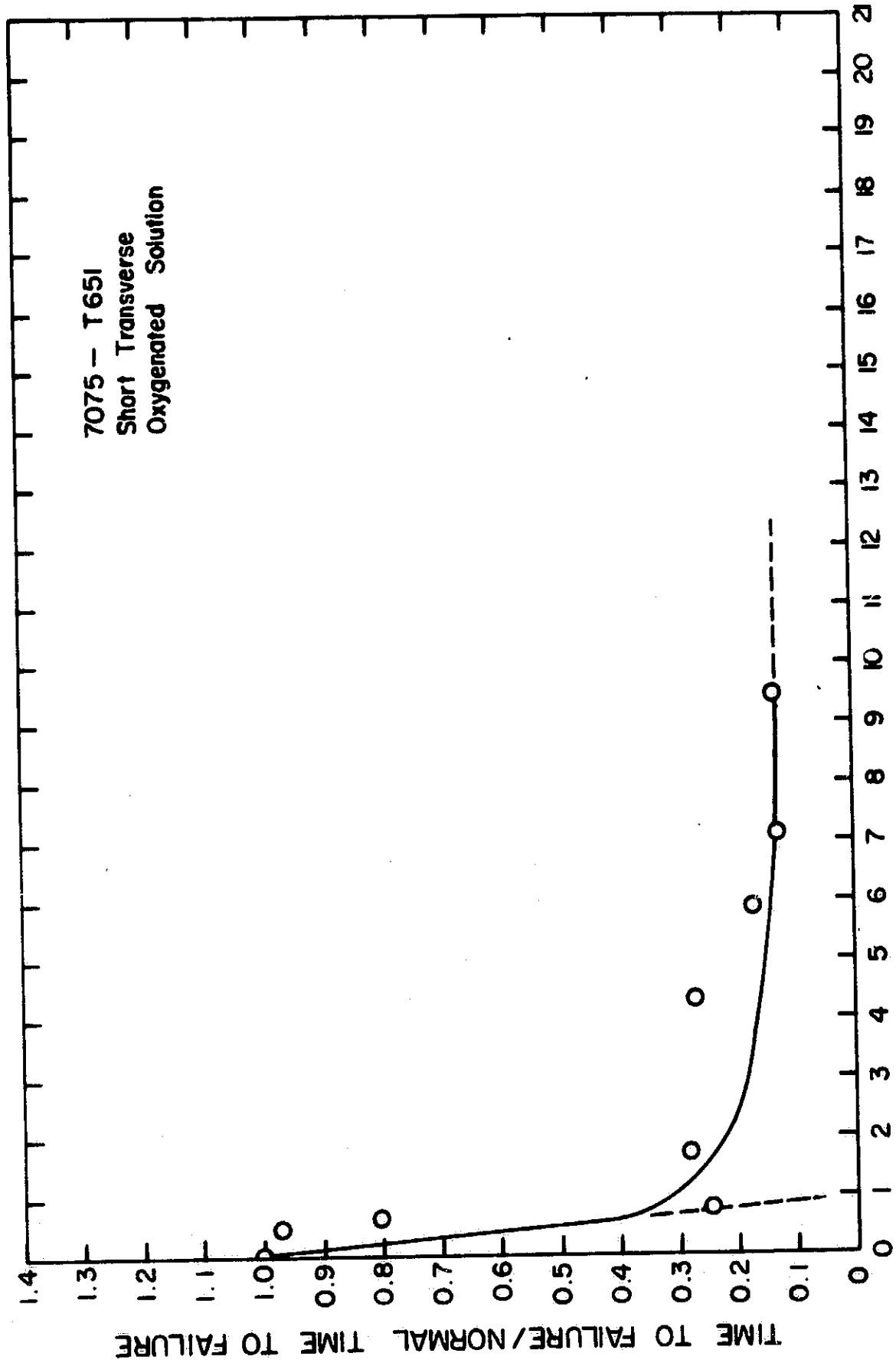

Fig. 44. Precorrosion test on 7075-T651 in oxygenated solution

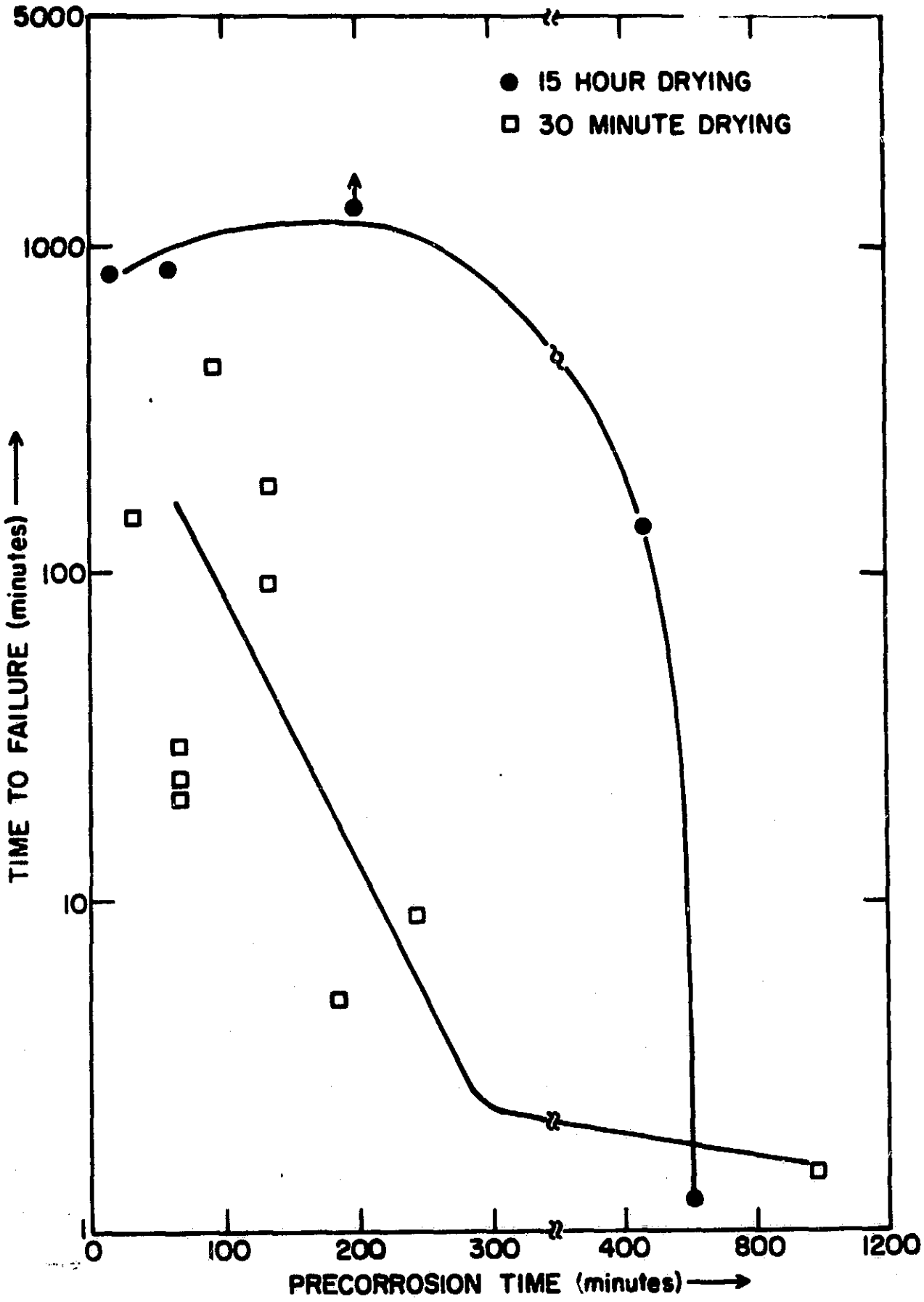

Fig. 45. Normal time to failure versus precorrosion time for 7075-T651 dried after precorrosion treatment

These experiments suggest that the precorrosion effect is not the result of buildup of a hostile environment, since it would not then be possible to obtain failure times longer than normal by drying. Rather, the following theory seems possible. We assume that there are some areas that are more prone to attack than others, and that these areas are attacked first during the initial precorrosion. However, there is evidence from the literature[9] that once cracking has been halted in a particular location, it is not likely to reinitiate at this same position immediately. The reasons for this behavior are not entirely clear; however, one possible cause would be the formation of particularly heavy corrosion product layers at points of maximum initial attack. Once the corrosion environment is removed by desiccation, re-penetration of the environment into these initial sites of attack could be slow. Corrosive attack would then be forced to proceed on secondary sites which are only slowly attacked.

13. Effects of surface preparation on precorrosion of 7075

Our results have demonstrated that for machined specimens of 7075-T651 tested in the short transverse direction, about 80% of the time to failure is taken up by a process that is not accelerated by the application of a load. Similar results have been reported by Gruhl.[10] Recently, Borchers and Tenchoff[11] reported on an extensive study of the effect of surface preparation on the time to failure of stress corrosion specimens. They concluded that the increase in time to failure, resulting from such surface treatments as shot-peening, came about not from any residual stress effect, but rather from the disruption of the grain boundary structure at the surface of the specimen. Although not referred to as such by Borchers and Tenchoff, this surface layer is in fact a modified Beilby layer,[12] i.e., a layer of severe crystallographic distortion. Beilby's original concept was particularly directed towards the crystallinity of the surface; however, it is appropriate and reasonable that this concept of surface distortion be applied specifically to the case of grain boundaries as well as grain interiors.

To test this hypothesis, we have carried out a two-fold program. First, we have tested specimens with elaborately prepared surfaces for the precorrosion effect. The aim of this careful surface preparation was toensure, as far as possible, that the only surface layer present was the 25-Å oxide layer which cannot be avoided. Secondly, we have carried out differential surface etching experiments. These have been done on as-machined, reheat treated, and reheat treated and electropolished specimens of 7075-T651 to determine if significant destruction of the surface grain boundary structure is responsible for the precorrosion effect, particularly in the as machined samples.

The results of the precorrosion tests on these three types of samples (as machined, reheat treated, and reheat treated and electropolished samples) are shown in Fig. 46. The data on the as machined and the reheat treated samples are, of course, the same as those given in Figs. 36 and 37, and are repeated here for convenience. This figure is not normalized: each point represents the actual time to failure as ordinate and the actual time of precorrosion as abscissa. These tests were carried out under the same conditions as previously described, i. e., with an applied anodic current density of 0. 3 mA/cm^2, at 30 °C, in a 1M NaCl solution buffered to pH 4. 7 with sodium acetate and acetic acid.

There are three principal features of Fig. 46. First, it is apparent that the normal time to failure (that is, the time to failure at zero precorrosion) of the as machined specimens is approximately five times that of the reheat treated and then electropolished samples, and about twice that of the reheat treated specimens. Secondly, it is apparent that after about 0. 5 hr of precorrosion, the subsequent time to failure under load is the same for all specimens. Thirdly, the reheat treated and then electropolished specimens do not show a precorrosion effect, while the simply reheat treated specimens show an effect intermediate in magnitude to the others.

These observations are consistent with the hypothesis that the precorrosion effect arises from the presence of some form of surface layer. To investigate this possibility, we have used the method of direct

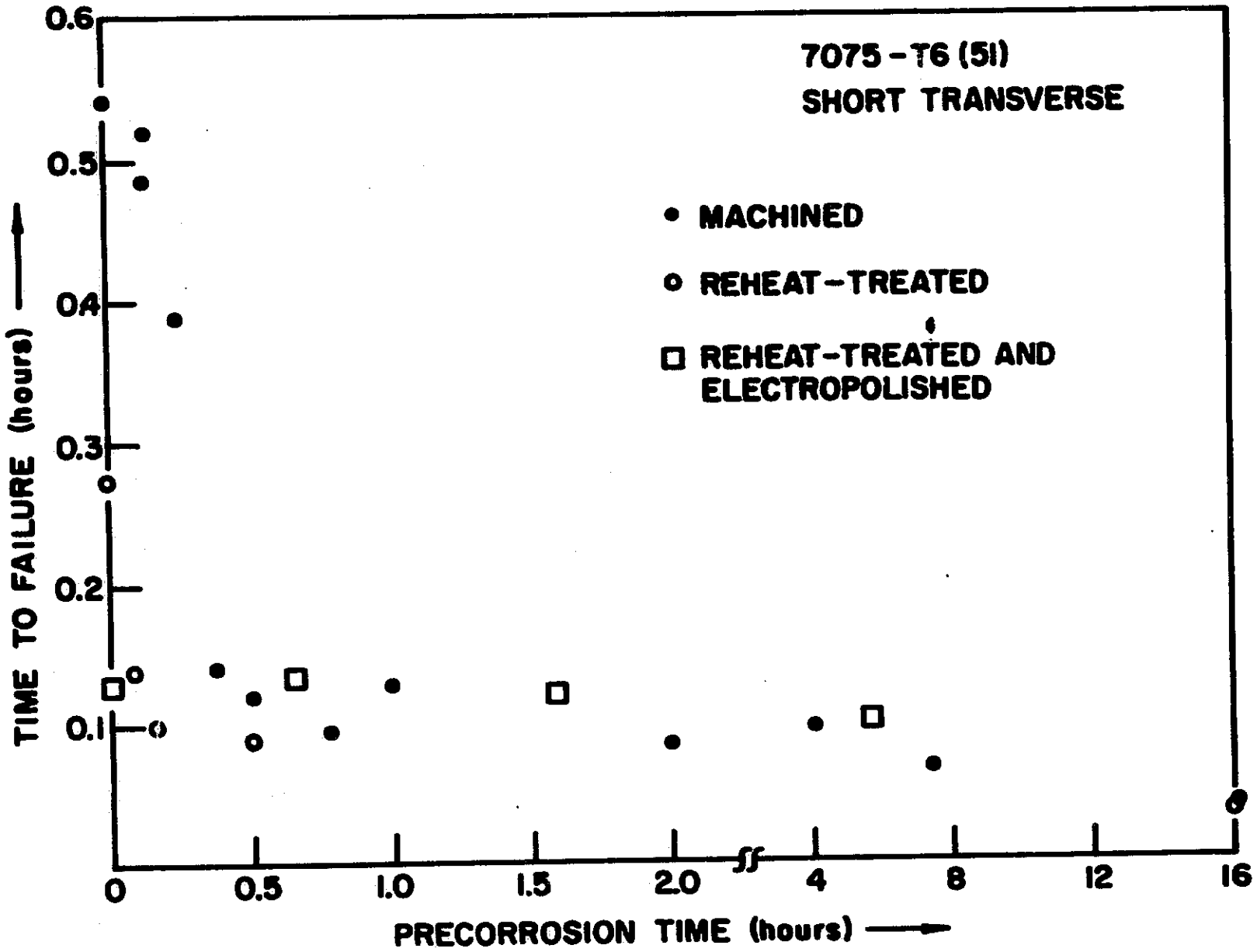

Fig. 46. Results of precorrosion tests on as machined, reheat treated, and reheat treated and electropolished samples of 7075-T651 (short transverse samples)

etching of the surfaces of each of the specimens to see if there is a significant difference in the development of etch patterns between the different methods of surface preparation. It may be, for example, that the as machined specimens will not show a developed grain boundary pattern after an etching treatment which was sufficient to reveal grain boundaries on the specimen which had been electropolished. This behavior would constitute very strong evidence that the grain boundaries in the as machined specimen had been disrupted near the surface.

The results of our experiments in the three types of alloys are shown in Fig. 47. This figure shows the appearance of the surface of each specimen after an exposure of 25 sec to an etch which is composed of 1% HF, 1.5% HCl, 2.5% HNO_3, balance H_2O. It can be plainly seen that after this treatment the grain boundary structure on the reheat treated and then electropolished specimen is clearly developed, while the as machined specimen still shows no evidence for grain structure. By using an etchant which reveals grain boundaries while not obscuring the surface with corrosion product, one is able to see what type of surface is exposed to the solution without having that surface obscured by corrosion products, as would be the case for exposure to an actual salt solution.

From this study, one may draw a rather important practical conclusion. It is clear now why mechanically disruptive surface treatments are effective in improving stress corrosion resistance: the grain boundary at the very surface is destroyed. Because there are no grain boundaries where stress corrosion can begin, true stress corrosion attack must wait until pure corrosion, unaccelerated by stress, has penetrated this surface layer. By knowing that this is the case, one may now undertake investigations of different surface mechanical treatments and know what sort of structure must be produced if good resistance to stress corrosion is to be achieved.

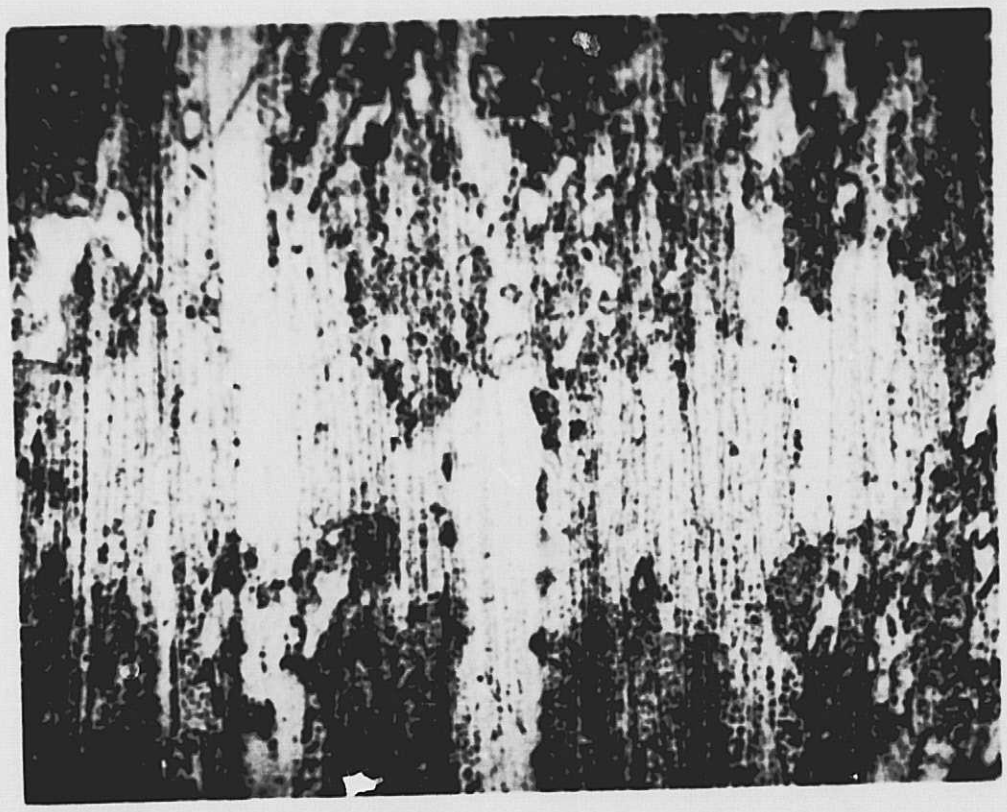

(a) As-machined

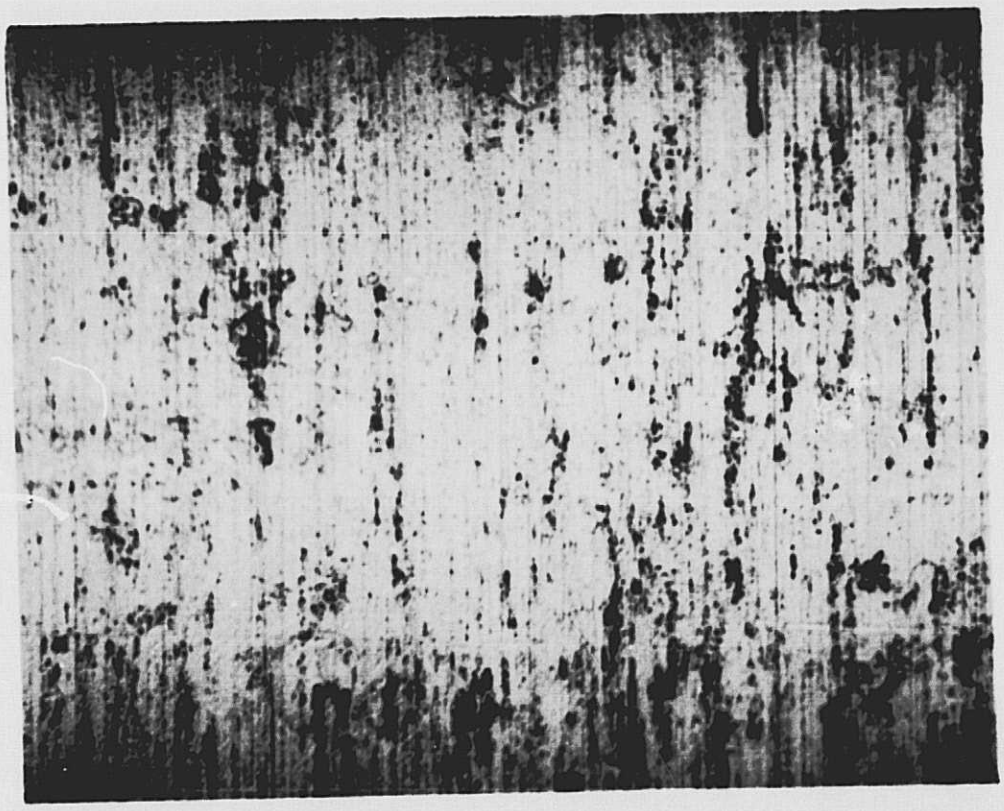

(b) Heat treated

Fig. 47. Photomicrographs of sample surfaces (200X)

(c) Reheat-treated and electropolished samples after etching

Fig. 47. Photomicrographs of sample surfaces (200X) (Cont.)

In addition, in combination with the drying experiments described in Section 12, it is possible to increase the ability of a mechanically deformed layer to effect such protection. Such a procedure would be very effective for surface protection of already fabricated parts.

14. Effects of temperature on the SCC of 7075

These experiments have been carried out to determine the effect of temperature on the normal time to failure of 7075-T651. They have been carried out in very carefully deaerated solutions to eliminate any possible effects arising from the change in oxygen solubility with temperature. The solution was, as before, 1M NaCl buffered to pH 4.7 with sodium acetate and acetic acid. The applied current was 0.3 mA/cm^2. Temperature was measured with a mercury thermometer mounted through the cell wall.

We have shown previously that for as machined specimens of 7075-T651, over 80% of the normal time to failure is taken up by a process which does not involve stress corrosion. Only during the last 20% of the failure time is it necessary to apply a load to cause damage. Thus, in determining the effect of temperature on the time to failure, it is important to distinguish between the effect of the temperature on the pure corrosion process, which destroys the Beilby layer, and the effect of temperature on the true stress corrosion process. To achieve this separation of effects, we have carried out tests to determine the normal time to failure of 7075-T651 specimens in both the as machined and electropolished conditions.

These tests were carried out using a slightly different specimen configuration than had been used. All tests, as before, used specimens which had a gauge length of 9/16 in. This section was then covered with wax until only a 1/8-in. section was left exposed. For these high temperature runs, however, we have found that the wax used had a slight tendency to run at the elevated temperatures. To avoid problems associated with this, a new set of samples has been prepared in which the

gauge section was increased to 1 3/4-in. In this case, no wax is required, since the specimen extends completely through the cell.

Tests were carried out on both as machined and electropolished samples for the following reasons. We have previously shown that, for the electropolished specimens, the whole period of the normal time to failure is taken up by a true stress corrosion process. For the as machined samples on the other hand, only 20% of the total time to failure is taken up by stress corrosion. Therefore, by comparing the behavior of these two types of samples, one obtains an indication of the extent to which the change in time to failure depends on each process.

The results of these tests are shown in Fig. 48. The main feature of note in this figure is the increase in the normal time to failure of the as machined specimens with temperature.

Since these tests were carried out in deoxygenated solution, it is not possible to attribute this increase to a change in oxygen solubility (decreasing with T) combined with a H_2-depolarized corrosion reaction (increasing with T). Rather, it is more likely that the increase shown by the as machined samples results from the changing nature of pitting-type corrosion attack. That is, at 50 °C, the pitting corrosive attack is less sharp than at 30 °C. Then, the pitting corrosion attack does not lead to an increased rate of penetration of the modified Beilby layer. Rather, the attack is more rounded at the pittings. This is shown in Fig. 49.

On the other hand, in the case of the electropolished specimens, an increase in temperature leads to a slight decrease in the failure time. This result is to be expected since, for these samples, there is no surface layer which must be penetrated by pure corrosion. Enough attack can be located immediately at grain boundaries, cutting the surface, and an increase in temperature will not destroy this localization because a pitting-type process is not involved.

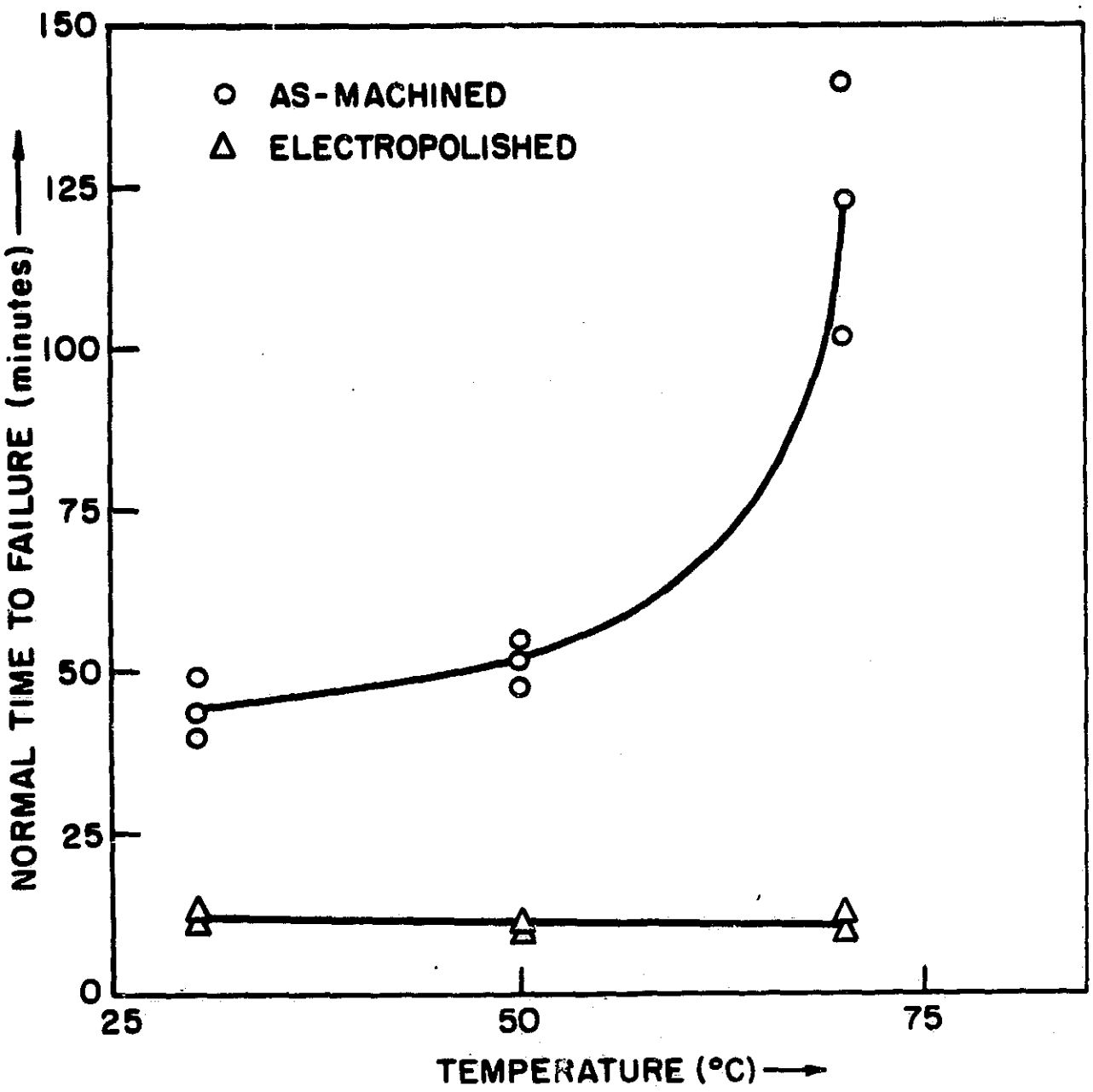

Fig. 48. Normal time to failure versus temperature for 7075-T651

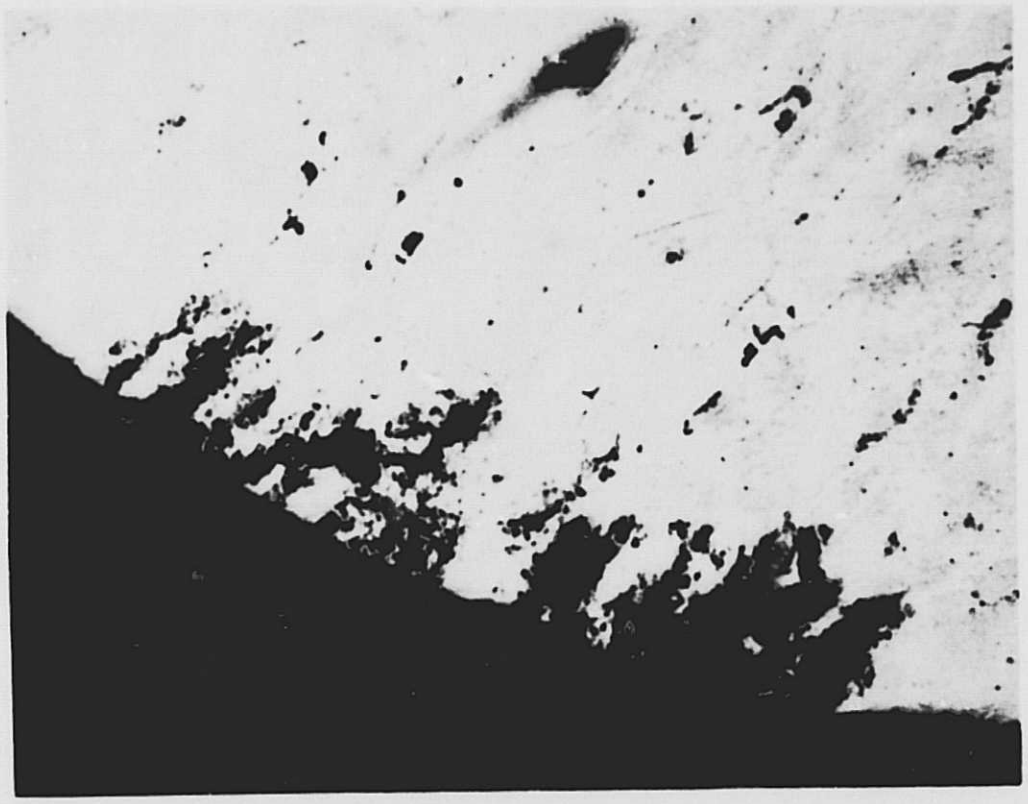

(a) T = 30 °C

(b) T = 70 °C

Fig. 49. Specimens of 7075-T651 precorroded 4 hr at 0.3 mA/cm^2 (120X)

15. Effect of shot-peening on the precorrosion of 2219-T37

It has previously been mentioned that 2219-T37 in the as machined condition does not show an appreciable precorrosion effect (Fig. 42). It may be speculated that this result arises because of the increased grain boundary cleavage energy of this alloy. That is, because cleavage of 2219-T37 would not be expected to be nucleated until a large fissure had been formed by corrosion, it could be that the deformed layer introduced by machining would be too thin to substantially affect the time required to form the corrosion crevice to stimulate cleavage. In this case, however, the added depth of the deformed layer introduced by shot-peening might be expected to cause an appreciable shot-peening effect.

To examine this possibility, short transverse samples of 2219-T37 have been shot-peened, precorroded, and tested. The results of these tests are shown in Fig. 50. No precorrosion effect is observed. One is thus led to the conclusion that in this alloy a true stress corrosion process occurs even in the presence of disrupted grain boundaries.

F. Electrochemical Investigations of Localization of Deformation of Al-Zn-Mg-(Cu) Alloys

We have carried out a series of experiments to investigate the apparent brittleness of the oxides on Al alloys, and to observe transient currents during the propagation of cracks. The reasons for a study of the mechanical properties of the protective oxides on our alloys are fairly straightforward. It is well known that the corrosion of Al is dominated by a breakdown of its protective oxide film. Dissolution of Al, when not covered by oxide, is extremely rapid in aqueous environments. In stress corrosion, oxide rupture is inevitably involved, and a number of theories of stress corrosion discuss oxide rupture as the limiting step.[13-16] A careful study of the correlation of oxide rupture with stress corrosion susceptibility is therefore of great interest.

An experimental approach to the determination of oxide ductility has recently been suggested by Bubar and Vermilyea.[17] They examined current

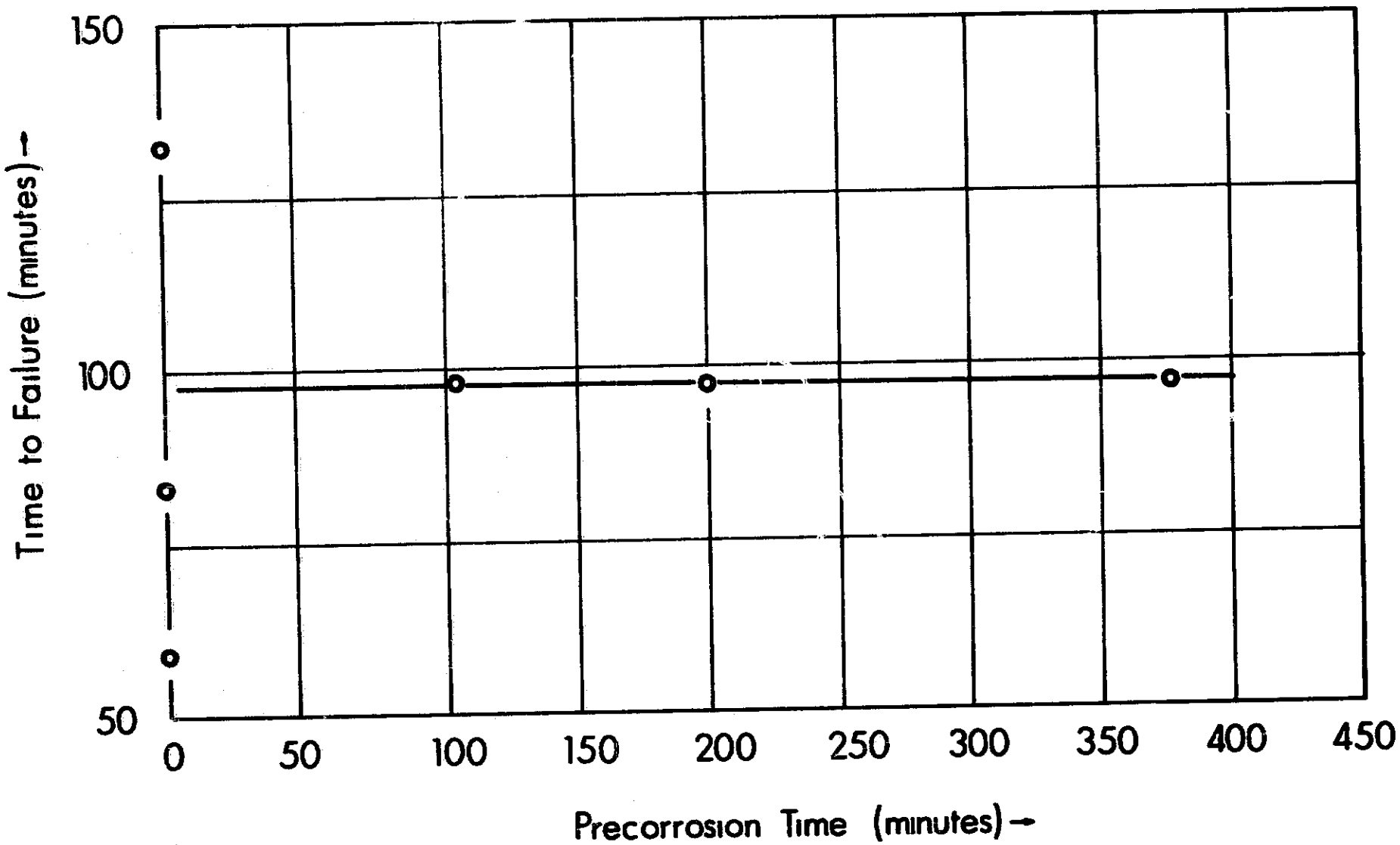

Fig. 50. Time to failure versus precorrosion time (shot-peened 2217-T31; $j = 0.30$ mA/cm^2)

transients during straining of oxide covered metals. The principle of their method is as follows. If a passive metal is held at constant potential (E_1), a steady state oxide is formed and the dissolution current falls to a very low value. If the metal is strained, the oxide will thin or crack, depending on its ductility. The current will then increase, corresponding either to oxide thickening or to its repair. These cases will not be readily distinguishable experimentally. If a passive film is grown at a higher potential (E_2), it will be thicker. If the metal, covered with the thicker E_2 oxide is strained at E_1, it will, if the oxide is ductile, thin and no current will flow until it has thinned to the steady state thickness corresponding to E_1. If, on the other hand, the E_2 oxide is brittle, it will crack when the metal is strained at E_1 and a current, corresponding to oxide repair, will be obtained.

This technique clearly provides a method for examining the ductility of protective oxides. It was found by Bubar and Vermilyea that on Al, thin oxides (<40 Å) of Al_2O_3 have some ductility, but that thicker oxides are entirely brittle. An extension of these experiments to Al alloys would be of great interest. Thus, our aim has been to carry out Bubar and Vermilyea's experiment on Al alloys and to look for a correlation between apparent oxide brittleness and stress corrosion susceptibility. The specific effect of Cl^- ion in enhancing SCC may, for example, find its explanation in a modification of the ductility of the protective oxides.

One possible reason why oxides on some stress corrosion susceptible alloys (e.g., 7075-T6) may appear unusually brittle is localization of the deformation of the metal. Thus, if when the metal is strained it deforms preferentially in narrow regions (e.g., the grain boundary margins), the local protective oxide will thin or crack (depending on its ductility) more than the oxide on the remainder of the metal. Such localization of the deformation of the metal has been suggested[18, 19] to be intimately involved in the stress cortosion of Al-Zn-Mg. Thus, we can turn the oxide ductility experiment around. We can deliberately put a brittle oxide on the alloy and use its rupture to investigate the localization of deformation within the metal.

Experiments to explore the phenomena of straining electrodes were carried out in buffered NaCl before undertaking the detailed studies outlined

above. To perform these experiments, we have used the cell arrangement which was developed for the stress corrosion tests with two modifications: (1) new Teflon end caps were prepared so that rectangular strip specimens could be accommodated, and (2) a platinized platinum hydrogen reference electrode replaced the calomel reference electrode. This was because the Hg from the calomel electrode disturbed the behavior of the Al.

Using this system, the procedure was to allow the specimen to come to its steady state rest potential and then to apply a small anodic current, on the order of microamps per square centimeter, to the specimen. This current was applied potentiostatically, that is, the potential of the specimen was controlled via a potentiostat at a few millivolts more positive than the rest potential, and the current which was required to maintain this potential was measured continuously. The sample was then strained (this straining ruptures the oxide and exposes fresh metal). This fresh surface would be substantially more active than the oxide-filmed alloy, and so the current required to maintain the potential constant increased.

By measuring this increase as a function of the deformation, one may determine in a quantitative way the amount of charge that was passed in repairing the ruptured oxide. By continuing to record the current after the sample has stopped being strained, the rate of repair of the oxide may also be determined. In this manner, the brittleness or protective nature of the oxide was determined. Furthermore, this method was applicable not only to air formed films, but also to other films as well, e.g., those films formed by anodization or films of corrosion products. Tests with this technique were initially carried out with high purity Al. This was done to provide a standard against which the results with alloy specimens could be compared. To ensure that the only oxide present was an air formed oxide, the sample was first cleaned and then exposed for 48 hr to the oxide thinning solution of Heine and Pryor.[20]

The sample was strained at a rate of about 3×10^{-3}%/min and the potential held constant to produce an initial current density of approximately $2 \mu A/cm^2$. As can be seen from Fig. 51, this current density did not change significantly during straining until a load sufficient to cause plastic deformation was reached. At this load, the current increased markedly. When straining was

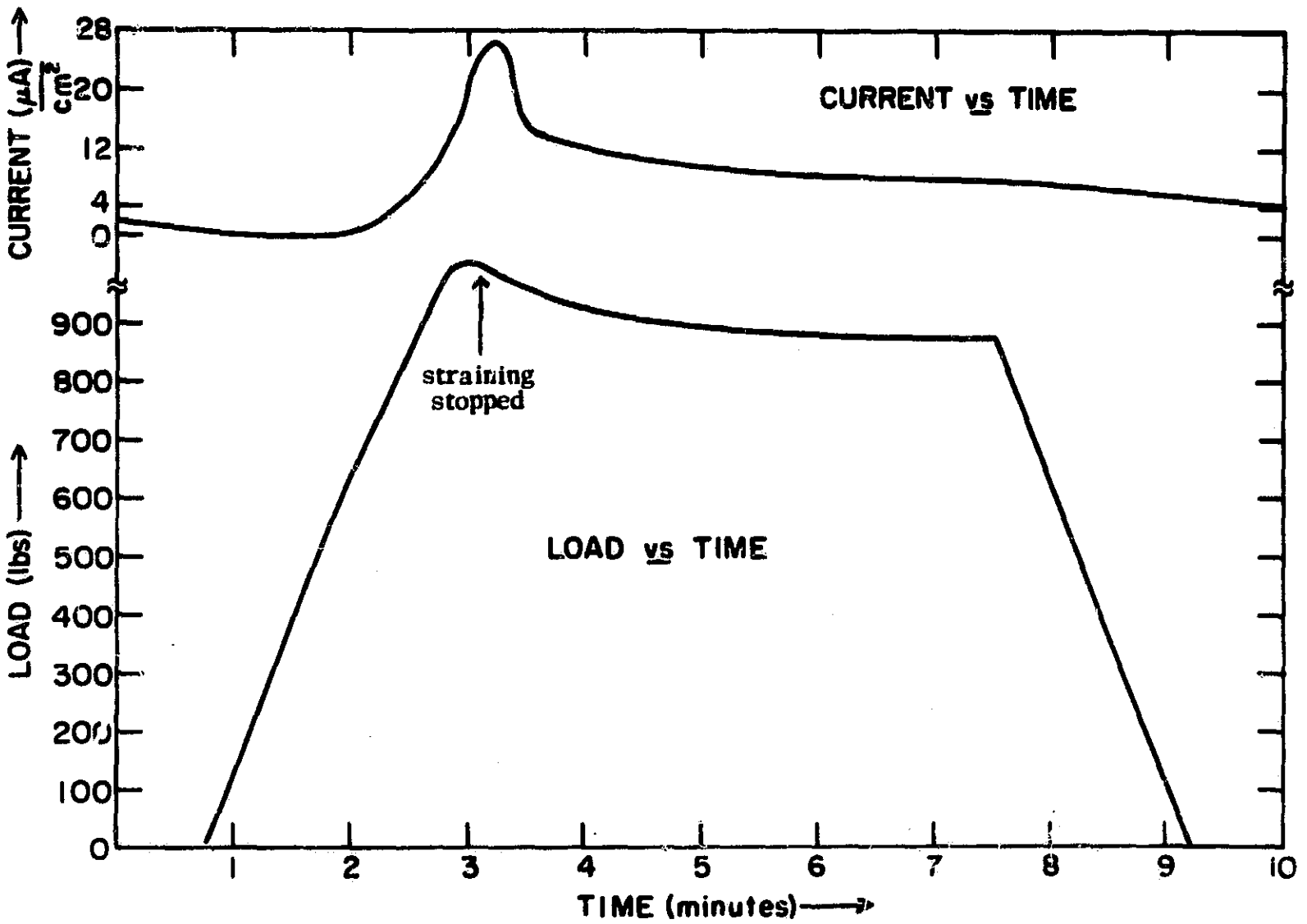

Fig. 51. Current density versus time and load versus time for potentiostatically controlled specimen of pure Al during straining in 1M NaCl

stopped so that the load was allowed to decrease slightly as creep occurred, this current again rapidly decreased, though it did not quite return to its original level. This behavior will be shown to be typical of strained Al alloys. When the elastic limit is reached and the materials deform so that the load no longer increases linearly, there is always a rapid increase in current density, indicating that fresh metal is being exposed to solution.

Fig. 52 shows the results of a similar test made on a specimen of 7075-T651. The film on this specimen was again air formed, although Heine and Pryor's solution was not used. Just as before, the current necessary to maintain the potential of the specimen constant remains steady until the elastic limit is reached (after 6.5 min on the abscissa in Fig. 52). When plastic deformation begins and the load stops rising, then just as in the pure Al case, the current increases sharply. It falls immediately when straining ceases and the load is allowed to relax slightly. When the load is removed, there is no detectable change in current, indicating that by this time the oxide film is completely repaired.

A particular feature of these tests is the fact that the current does not increase until the onset of plastic flow. This observation remains true, even when a specimen has been strained elastically and then unloaded so many times that it is nearing its fracture point. No change in current is observed until fracture, at which point the current rises sharply due to the formation of the two fresh fracture surfaces.

Our previous work on 7075-T651 has shown that the stress corrosion of 7075-T651 short transverse specimens may be divided into two distinct regions: (1) an initial region during which corrosion without applied load is just as effective in leading to final failure as is corrosion with load, and (2) a terminal region of true stress corrosion during which significant additional damage does not occur unless the load is applied. The previous strain tests described for 7075-T651 specimens were carried out in conditions corresponding to the initial region. It is therefore of considerable interest to see if there is any difference between the behavior of these specimens and the behavior of specimens which have been brought into the region of true stress corrosion by a precorrosion treatment.

Fig. 53 shows the results of a straining test on a specimen of 7075-

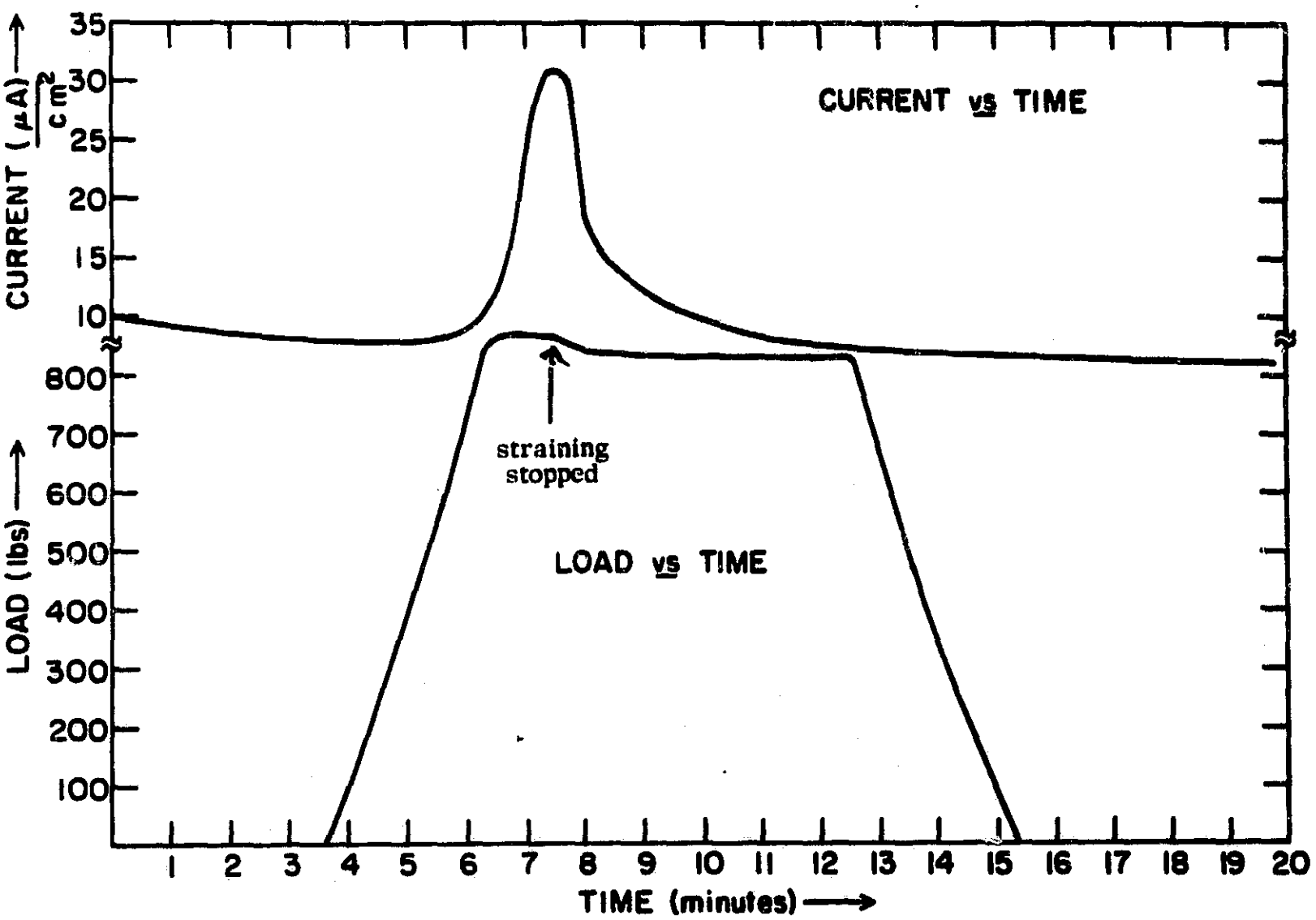

Fig. 52. Current density versus time and load versus time for potentiostatically controlled specimen of 7075-T651 during straining in 1M NaCl

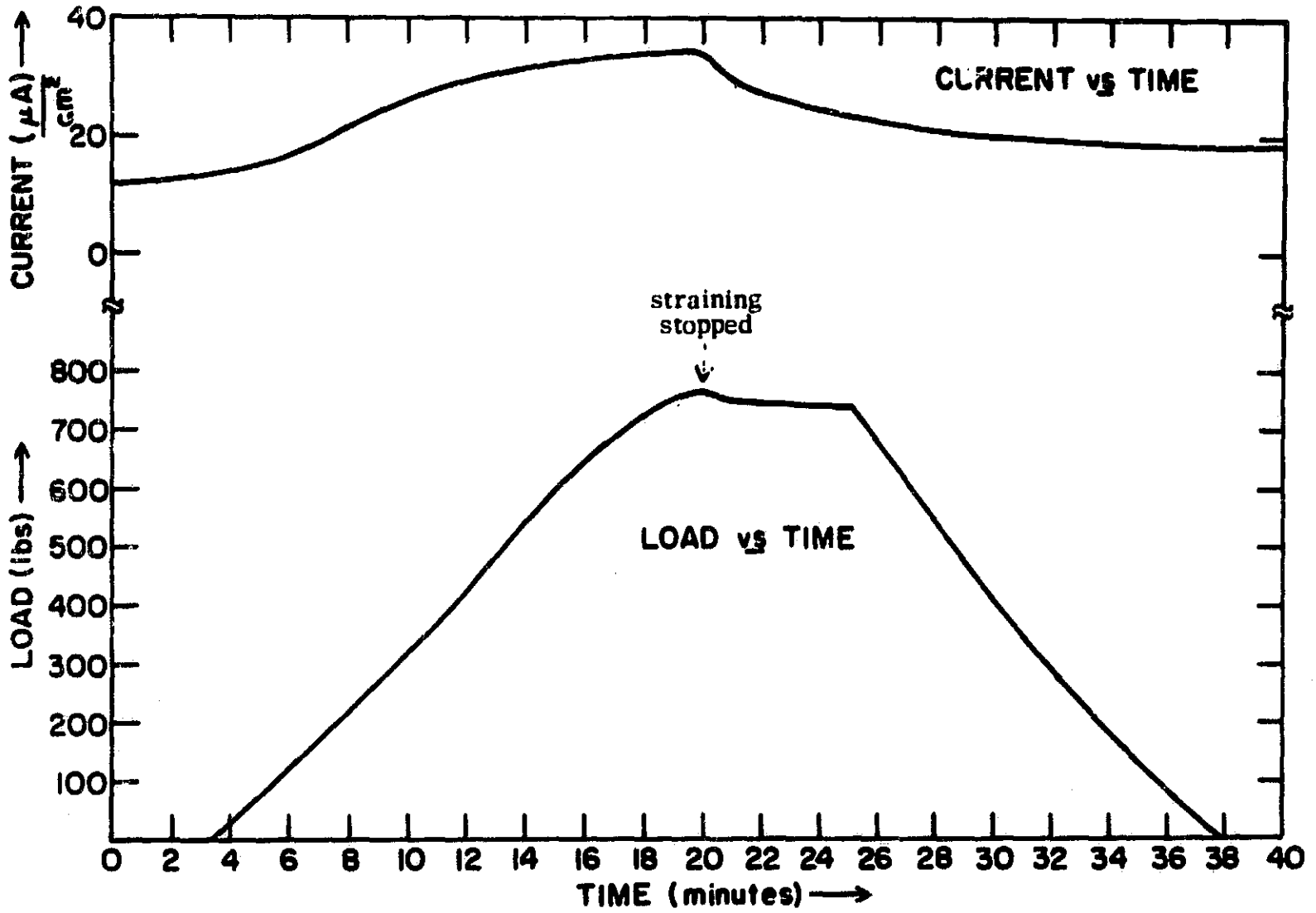

Fig. 53. Current density versus time and load versus time for potentiostatically controlled precorroded specimen of 7075-T651 in 1M NaCl

T651 which was precorroded for 180 min with a current density of 0.3 mA/cm^2 (sufficient to bring the sample into the region of true stress corrosion). It is apparent from the figure that the current necessary to maintain the potential of this specimen constant begins to increase substantially before the onset of plastic deformation. This is to be compared with the behavior in Fig. 52, which shows no increase in current before the beginning of plasticity. Evidently, one of the effects of the precorrosion treatment has been to increase the effective brittleness of the oxide film, either through chemical or morphological change, or by altering the stress level for the underlying metal to flow. The last is the most likely explanation, and for instance should correspond to the situation at the root of a corrosion pit.

Because of the reactivity of Al, its corrosion rate is dominated by the characteristics of its oxide film. Without the presence of an oxide film, Al reacts extremely rapidly, thus, oxide rupture is most likely involved in the stress corrosion of Al based alloys. The previous results were for experiments conducted on specimens in 1M NaCl solution. The method was extended to a film forming medium, i.e., a medium in which Al when anodized forms a protective oxide rather than dissolving. Following Bubar and Vermilyea, these tests were carried out in a 1% (by weight) solution of ammonium tetraborate [$(NH_4)_2 B_4O_7 . 6 H_2O$)]. Specimens were treated initially by lapping with no. 600 grip silicon carbide paper and were then etched for 3 min in 1N NaOH solution.

The results of our tests on pure Al strained in borate solution are shown in Figs. 54 through 58. Fig. 54 shows results for a sample anodized at +71 V versus a saturated calomel electrode (sce). The oxide here was about 1000 Å thick. In this case, as in all others reported here, no current transient was observed until the onset of plasticity. Hence, as indicated, the deformations plotted as abscissa are purely plastic deformations. In this case, as in all subsequent cases, the potential at which the specimen was strained was -0.30 V versus sce (or +0.445 V versus the RHE). This is the same straining potential as that used by Bubar and Vermilyea. The anodizing and test solutions were also the same, and thus our results may be directly compared with those which they obtained.

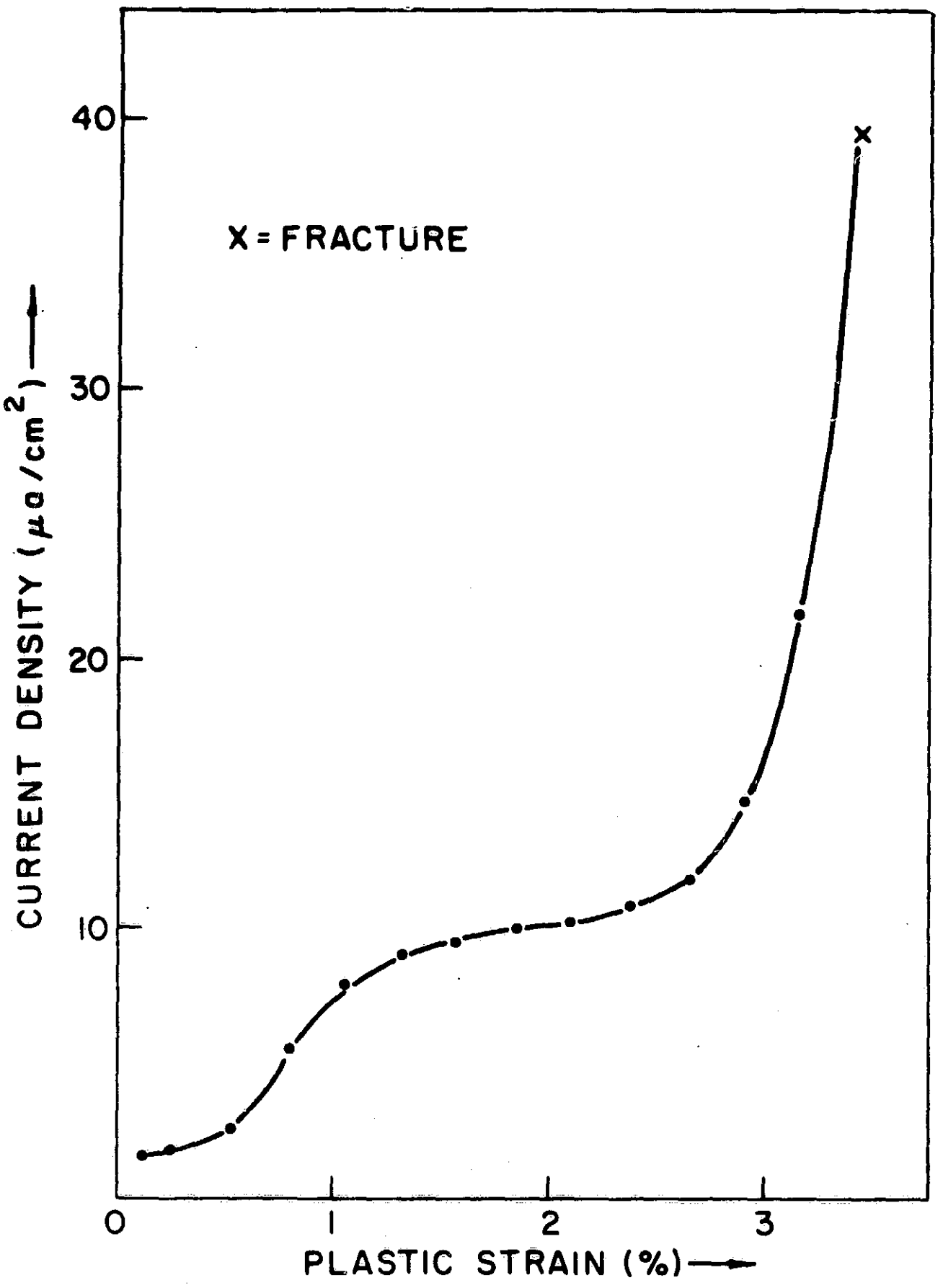

Fig. 54. Current density versus strain for pure Al anodized at +71 V versus sce and strained at –0. 3 V versus sce

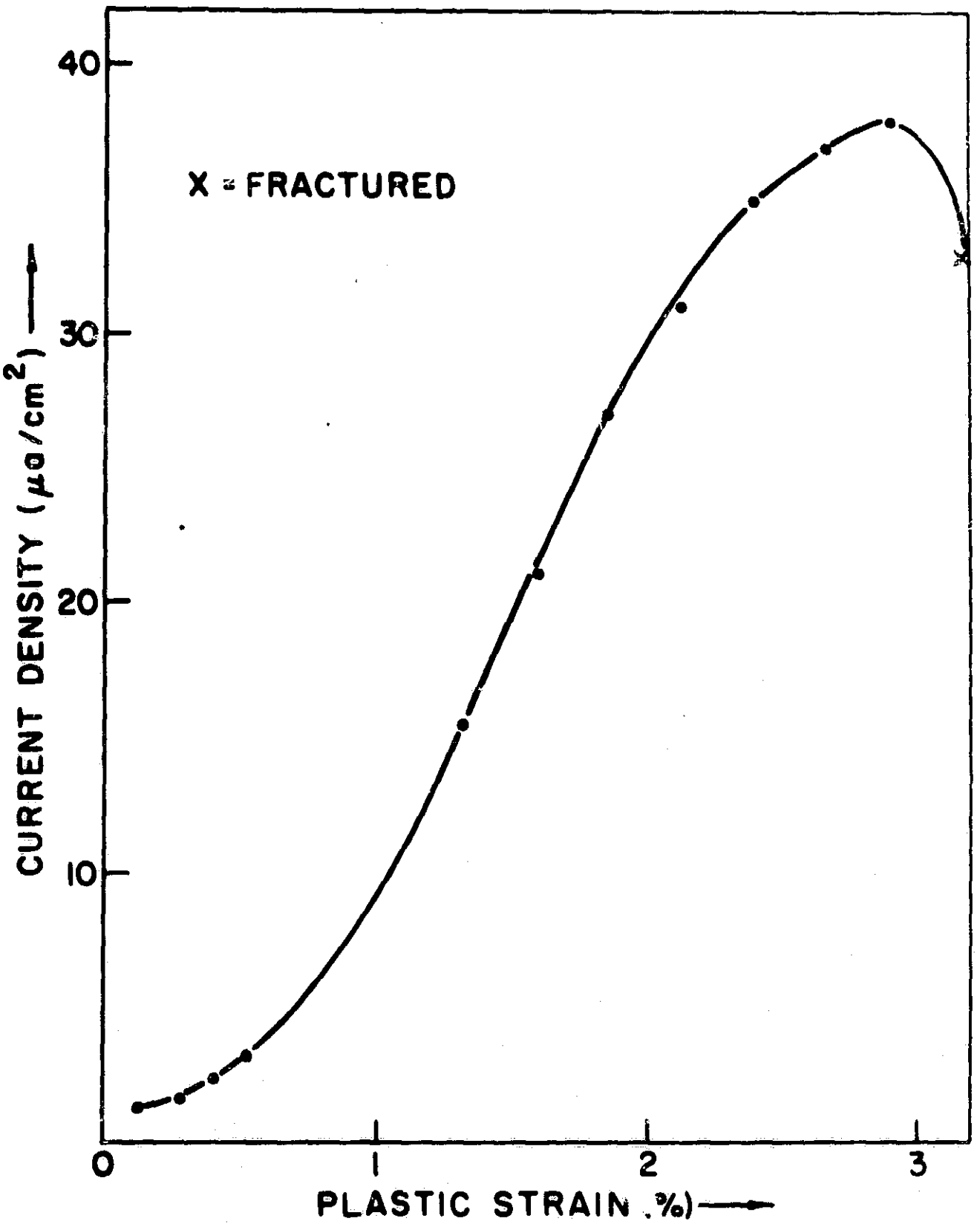

Fig. 55. Current density versus strain for pure Al anodized at +35 V versus sce and strained at –0.3 V versus sce

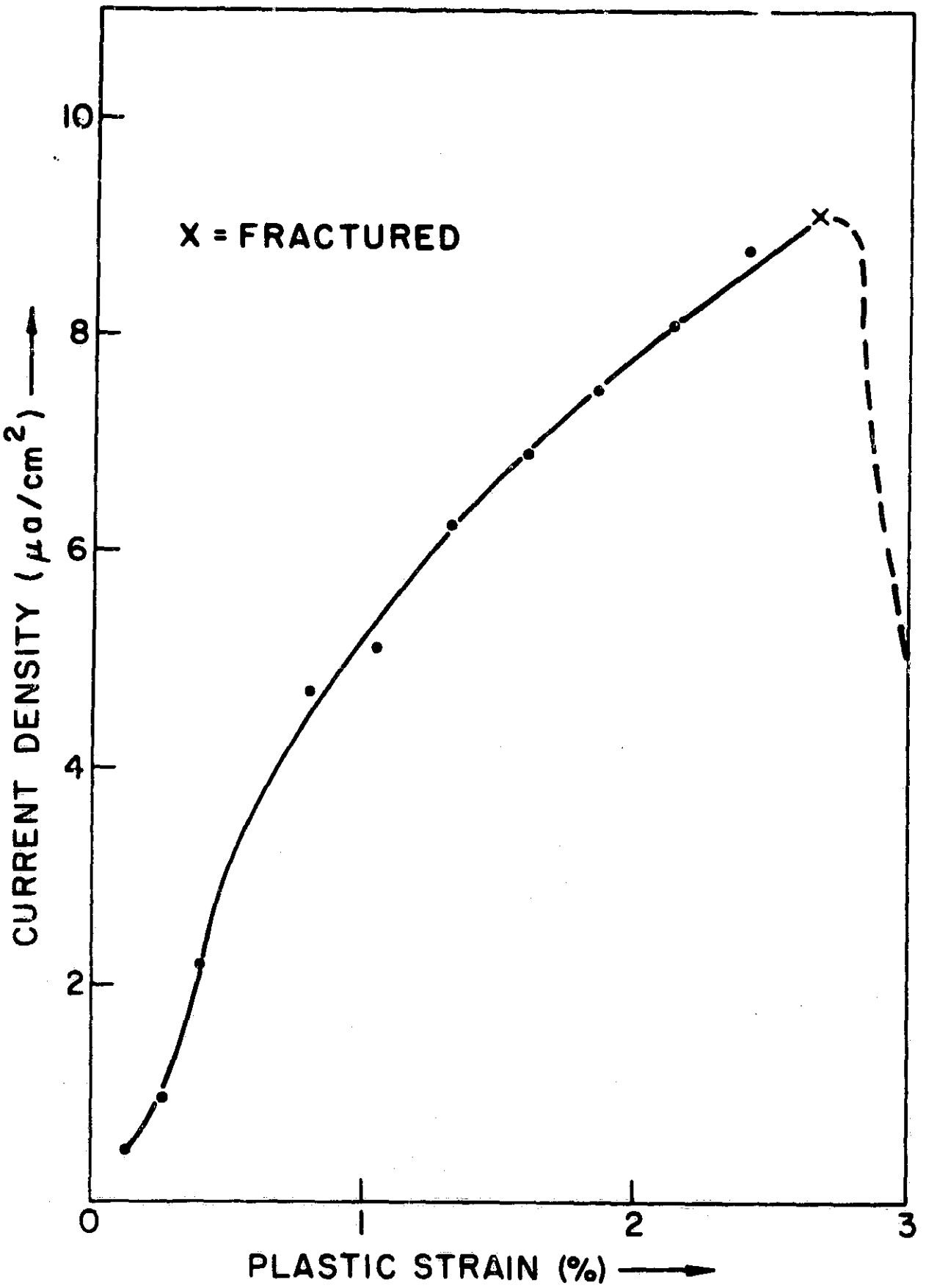

Fig. 56. Current density versus strain for pure Al anodized at +0. 8 V versus sce and strained at –0. 3 V versus sce

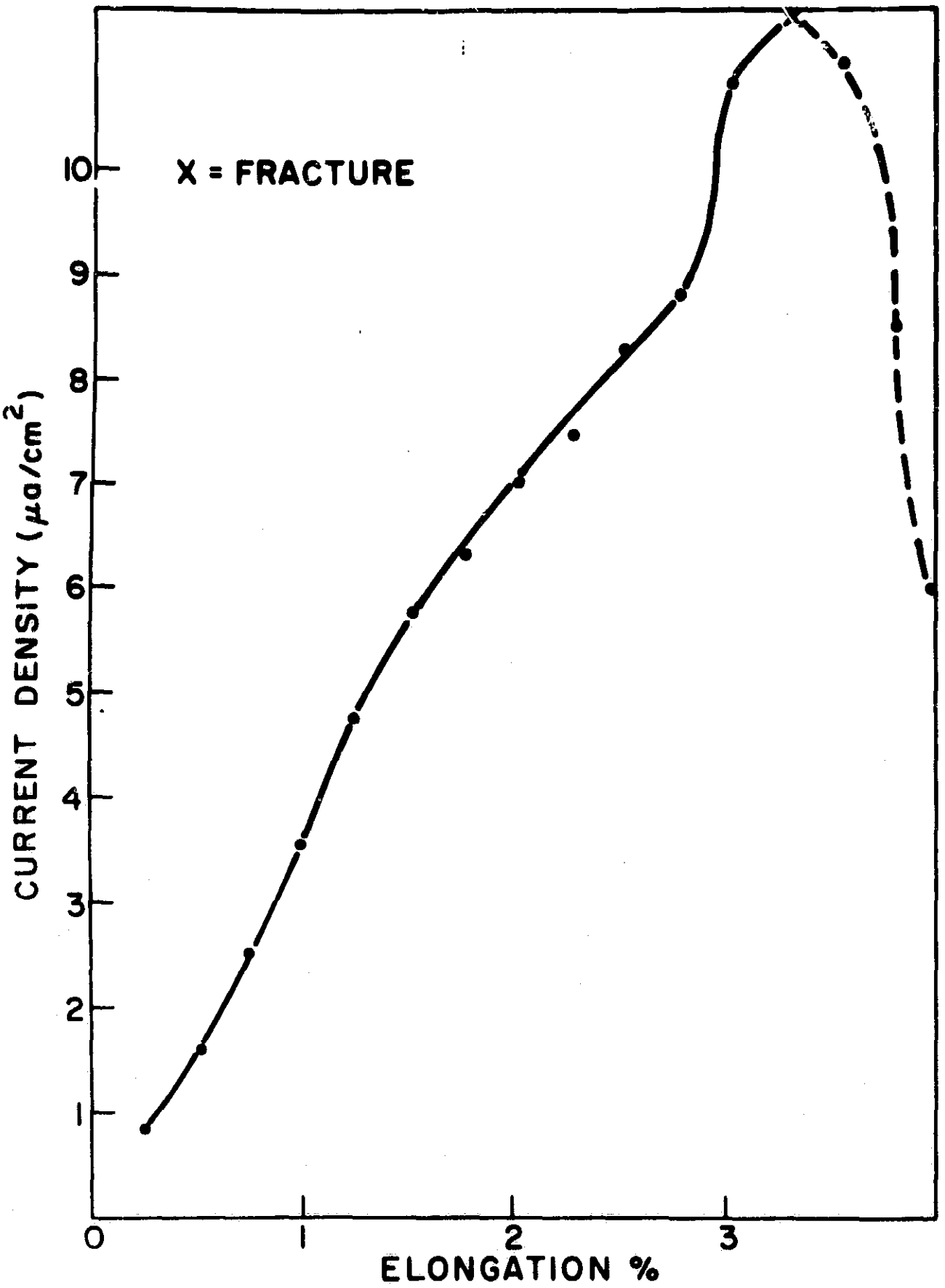

Fig. 57. Current density versus strain for pure Al anodized at +0.5 V versus sce and strained at –0.3 V versus sce

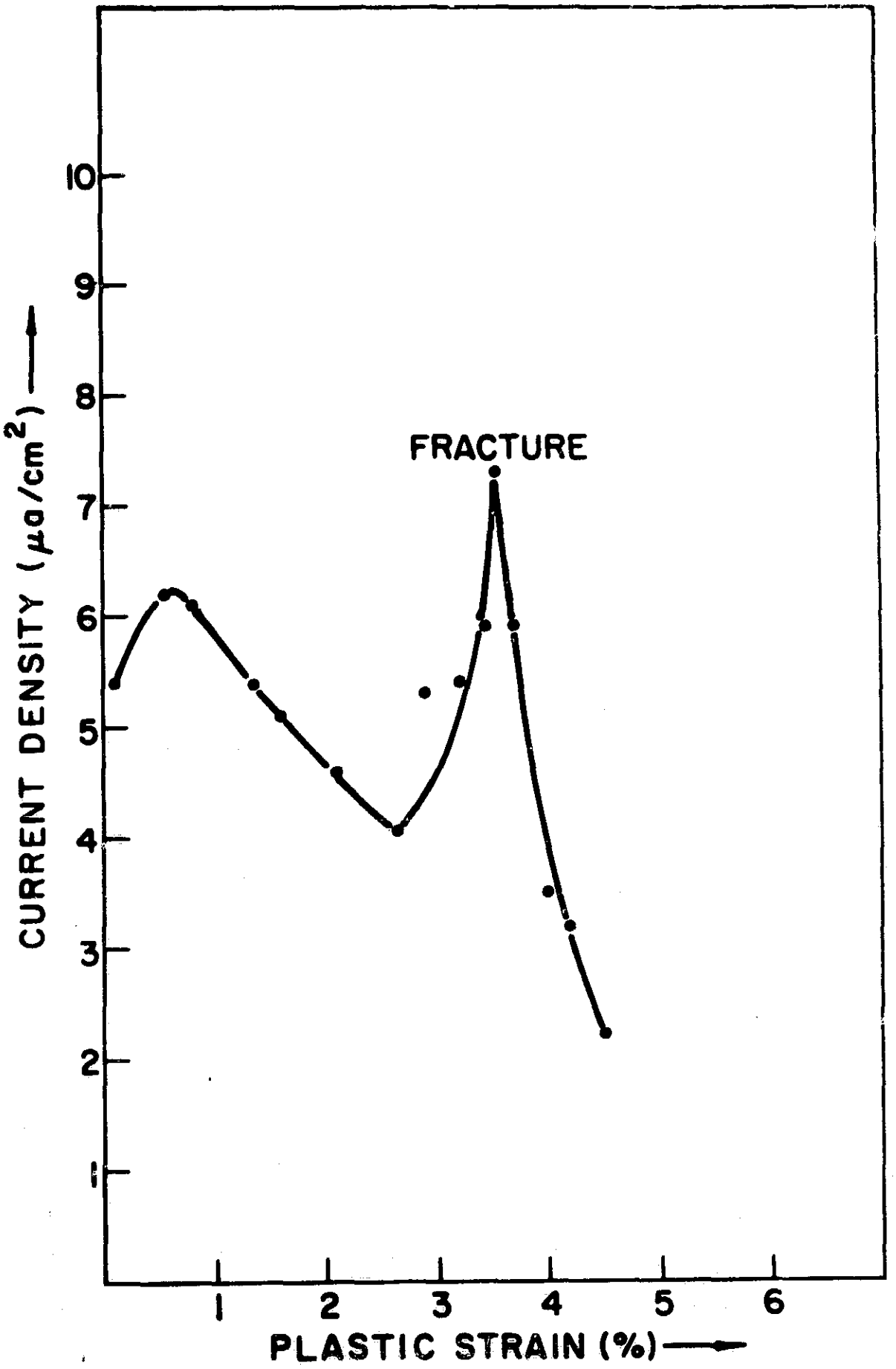

Fig. 58. Current density versus strain for pure Al anodized at –1.395 V versus sce and strained at –1.395 V versus sce

Fig. 54 shows that during the initial plastic strain, up to 1%, the current increases by a factor of about four. This is followed by a fairly level plateau region extending to about 2.5% strain, at which point the current increases very sharply until fracture of the specimen occurs at about 3.4% strain. The interpretation of these results is as follows. The initial increase in current at strains less than 1% is associated with initial oxide rupture. The plateau region between 1 and 2.5% is associated with uniform deformation maintaining the current at the increased level, and the final sharp rise in current is associated with localized deformation ("necking") and final fracture.

Fig. 55 shows results for a specimen anodized at +35 V versus sce. In this case, the oxide was ~ 500 Å thick. Here, the behavior up to 1% plastic strain is similar to that for the 1000 Å oxide. Between 1% plastic strain and 2.0% plastic strain, however, the current continues to increase steadily. Only in the last 0.3% strain does the current fall. This last effect is most likely due to the fact that the entire region of localized deformation is no longer yielding, but rather only the leading edge of the fracture area is yielding. The absence of a platueu region indicates that at no point is the rate of repair equal to rate of generation of fresh surface.

Fig. 56 and 57 show results for a film anodized at +0.8 V (43 Å) and +0.5 V (natural film, ~ 27 Å) versus sce, respectively. For these samples, the behavior is substantially similar to that of the sample anodized at +35 V, with the exception that the anodic current is substantially less throughout the test. Again, no plateau region is observed.

Fig. 58 shows the result for the specimen anodized at −1.395 V versus sce and strained at this same potential. Unlike previous tests, therefore, oxide thinning can contribute to the observed current as well as oxide fracture. As seen from the figure, the initial current is relatively high. Within 1% plastic strain, it rises slightly and then declines until the onset of necking and final fracture. The reasons for the intermediate decline are not clear.

Comparison of these results with those of Bubar and Vermilyea reveals both similarities and differences. The current does decrease as the anodizing potential is decreased in both sets of results. In the case of the anodization at 71 V versus sce, the maximum current observed is approximately the same in both cases. However, the plateau region noted in our case does not appear in

the case of the results of Bubar and Vermilyea. In the case of the specimen anodized at 35 V versus sce, the agreement between our results and those of Bubar and Vermilyea is quite good with regard to maximum current and shape of the current versus strain relation. Our results show the increase in current beginning in the region of 0.5% plastic strain, while Bubar and Vermilyea show the current increase to begin in the region of 2% strain. It is likely, however, that this difference results from inaccuracies in the Bubar and Vermilyea strain measuring system, since they used only gross position measurements to measure strain on their wire samples. In our case, tensile specimens were used and the crosshead position was known accurately. For samples anodized at 0.5 V versus sce, Bubar and Vermilyea show a substantial increase in the range over which current increases only slowly with strain. In the case of our specimens, however, no such effect is observed.

For the specimen strained at the oxide formation potential, both our results and those of Bubar and Vermilyea show a substantially earlier increase in current with straining than in those cases where straining was carried out at a lower potential than the anodization potential. This behavior results since in this case both oxide thinning and oxide fracture contribute to the observed current.

Using the same borate solution that was used for the pure Al samples, similar tests have now been carried out on commercial alloy 7075 in a series of heat treated and surface conditions. These treatments are the same as those that have been described previously. The surface treatments are of two kinds: (1) as machined, and (2) electropolished. The heat treatment used consisted or overaging material in the -T6 temper by heating at 325 °F for either 3 or 12 hr.

It is of particular interest in these experiments to examine the way in which the condition of the sample is reflected by its response in the elastic deformation region. This is because we are anxious to correlate surface condition with the very smallest localized deformations leading to oxide rupture. These, we believe, are likely to be the most relevant to SCC. The oxides were formed by constant potential anodization in the borate solution. Then, as before, the potential of the samples was controlled potentiostatically at -0.3 V versus sce and the sample was strained elastically. The current necessary to

maintain the sample potentials constant was then recorded as a function of the elastic strain.

The results of these tests on as machined, electropolished, and heat treated alloys for different oxide thicknesses are shown in Figs. 59, 60, 61, and 62. We see that there is a tendency for the electropolished and the overaged samples to show more apparent oxide brittleness than for the as machined or the overaged 12 hr samples. This tendency is more evident in Fig. 63 which shows the elastic strain at which there is a current increase of 5 μA as a function of oxide thickness.

From this figure it can be seen that, especially for thinner oxides, the two samples with highest SCC susceptibility show the greatest apparent oxide brittleness. Thus, these data permit the conclusion that there is a direct relationship between apparent oxide brittleness and stress corrosion. Since the oxide properties per se are unlikely to vary with these surface treatments, the important conclusion is that the apparent "brittleness" of the oxides results from localized deformation of the underlying metal. The latter evidently correlates with SCC susceptibility.

Thus, for the overaged speciments, the denuded grain boundary zone will be the same in each case, since the initial part of their heat treatments which would be expected to substantially fix the precipitate free zone is the same for both overaging treatments. In this case, it is most likely that change in dislocation structure from planar arrays (in the case of overaging for 3 hr) to a distributed network (in the case of overaging for 12 hr) dictates the effective oxide ductility . In the case of the as machined sample, the machining process introduces a distorted layer in whch defined grain boundaries do not exist. It has been shown previously that within this layer stress corrosion does not occur. Thus, although the time to failure of these samples is only 30 min, initially they are effectively immune to stress corrosion. This is consistent with the concept of nonlocalized plastic flow favoring immunity to stress corrosion, since relatively high elastic strains are required to initiate breakage of the film.

In addition to these experiments, tests of the effect of elastic strain cycling have been carried out on specimens of 7075-T6 overaged for 12 hr. at 325 °F. These tests were carried out exactly as before, except that the

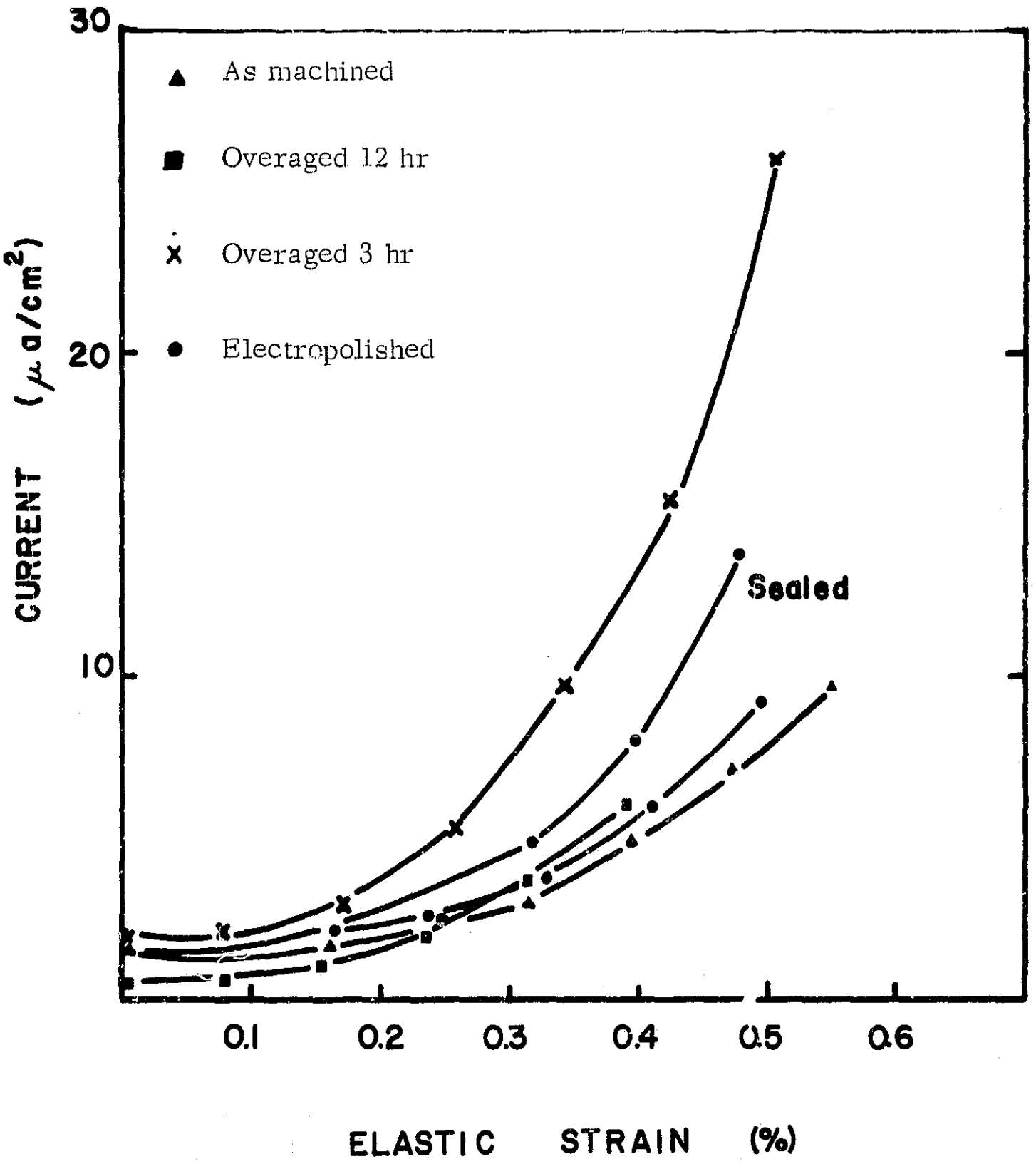

Fig. 59. 7075-T651 anodized at +71 V versus sce (1000-Å-thick film)

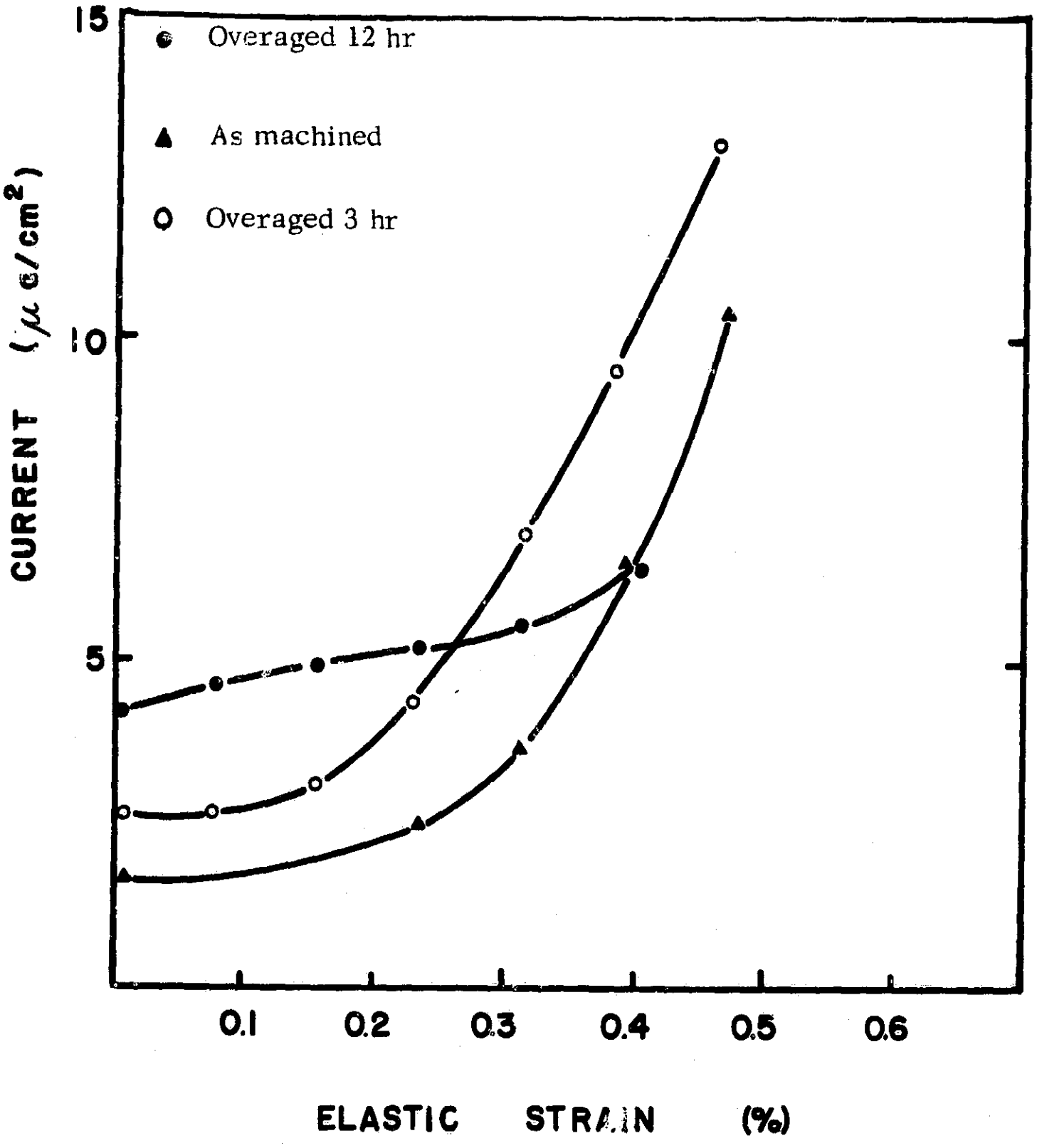

Fig. 60. 7075-T651 anodized at +33 V versus sce (500-Å-thick film)

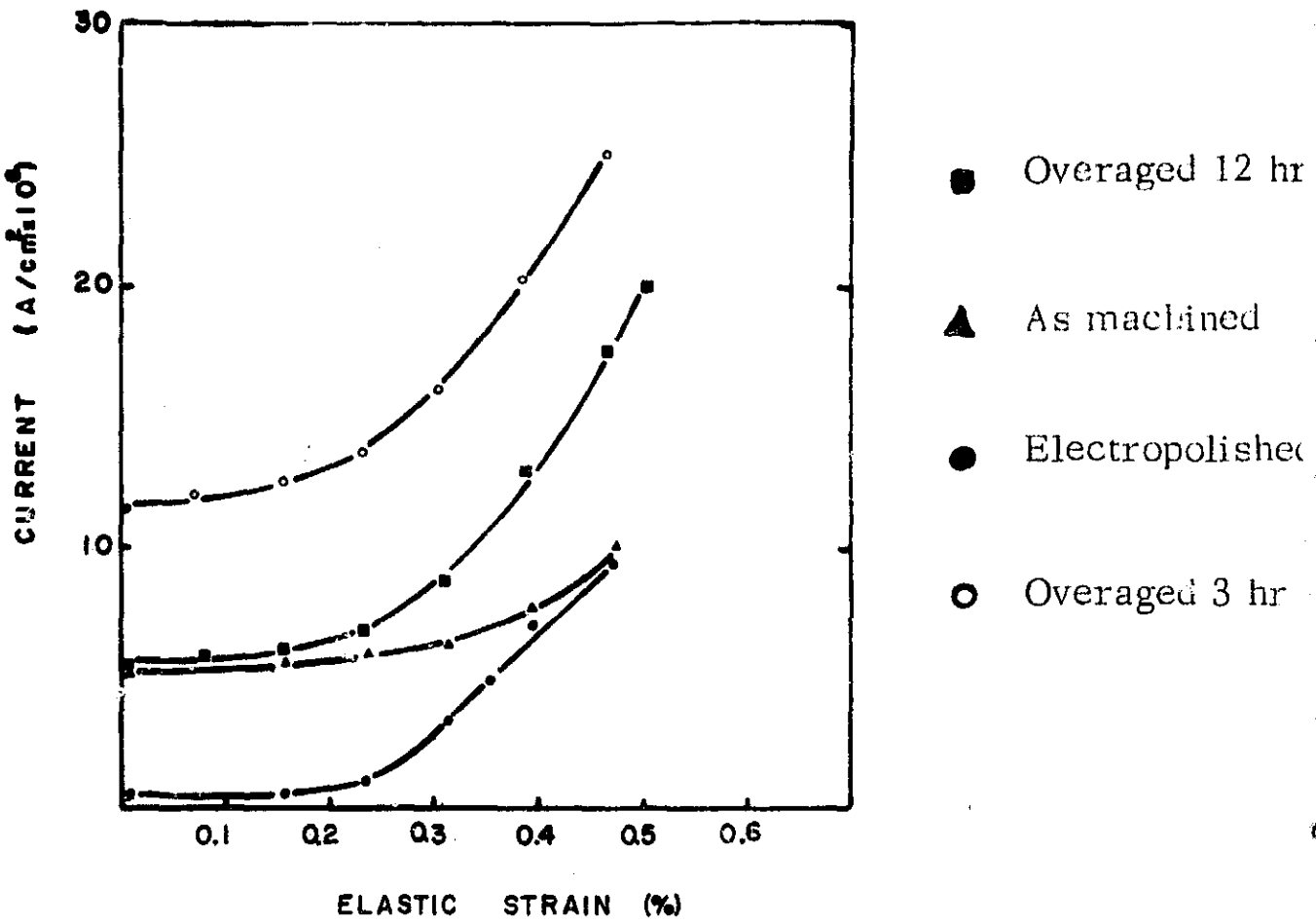

Fig. 61. 7075-T651 anodized at +4.7 V versus sce (100-Å-thick film)

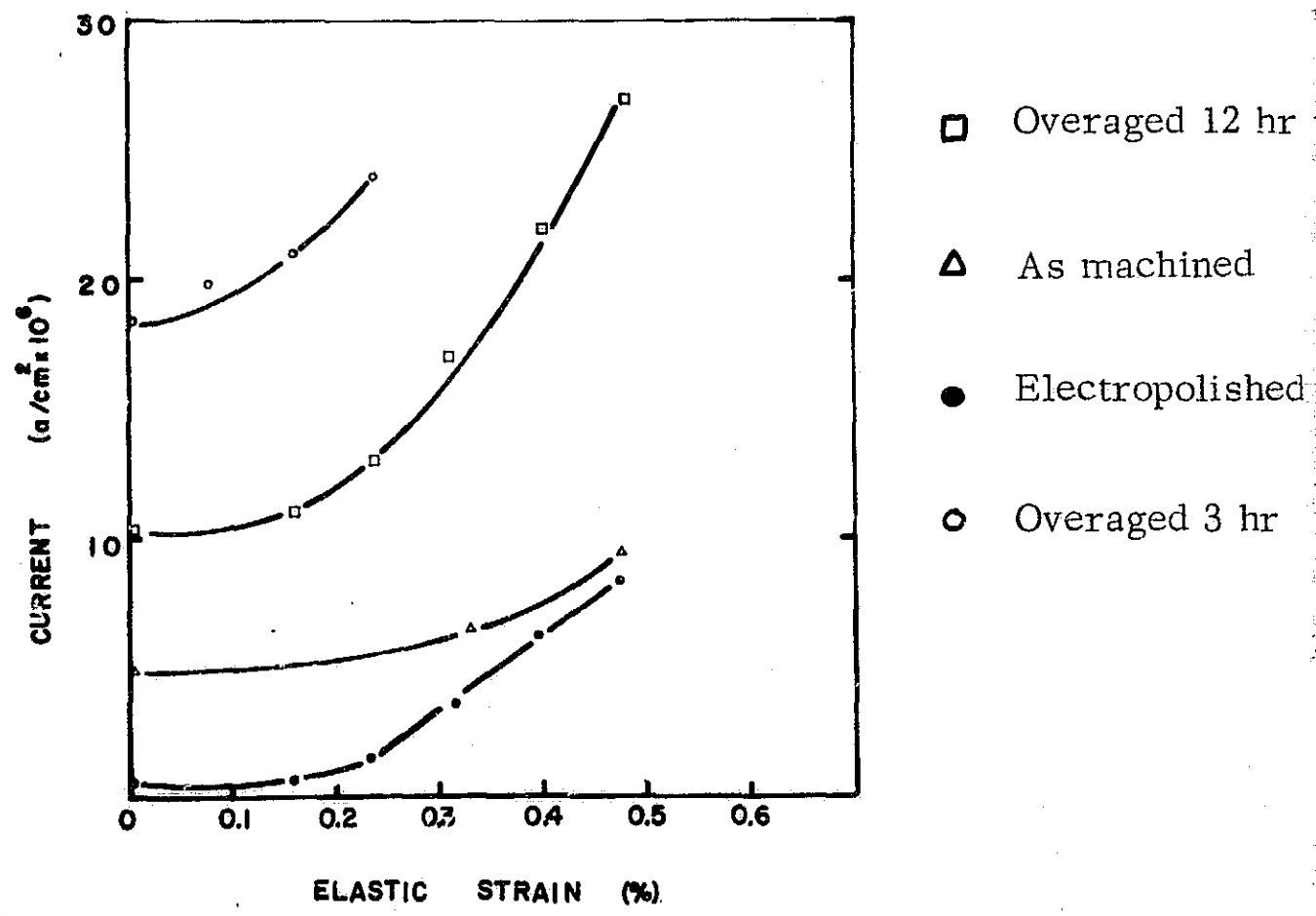

Fig. 62. 7075-T651 anodized at 0.8 V versus sce (43-Å-thick film)

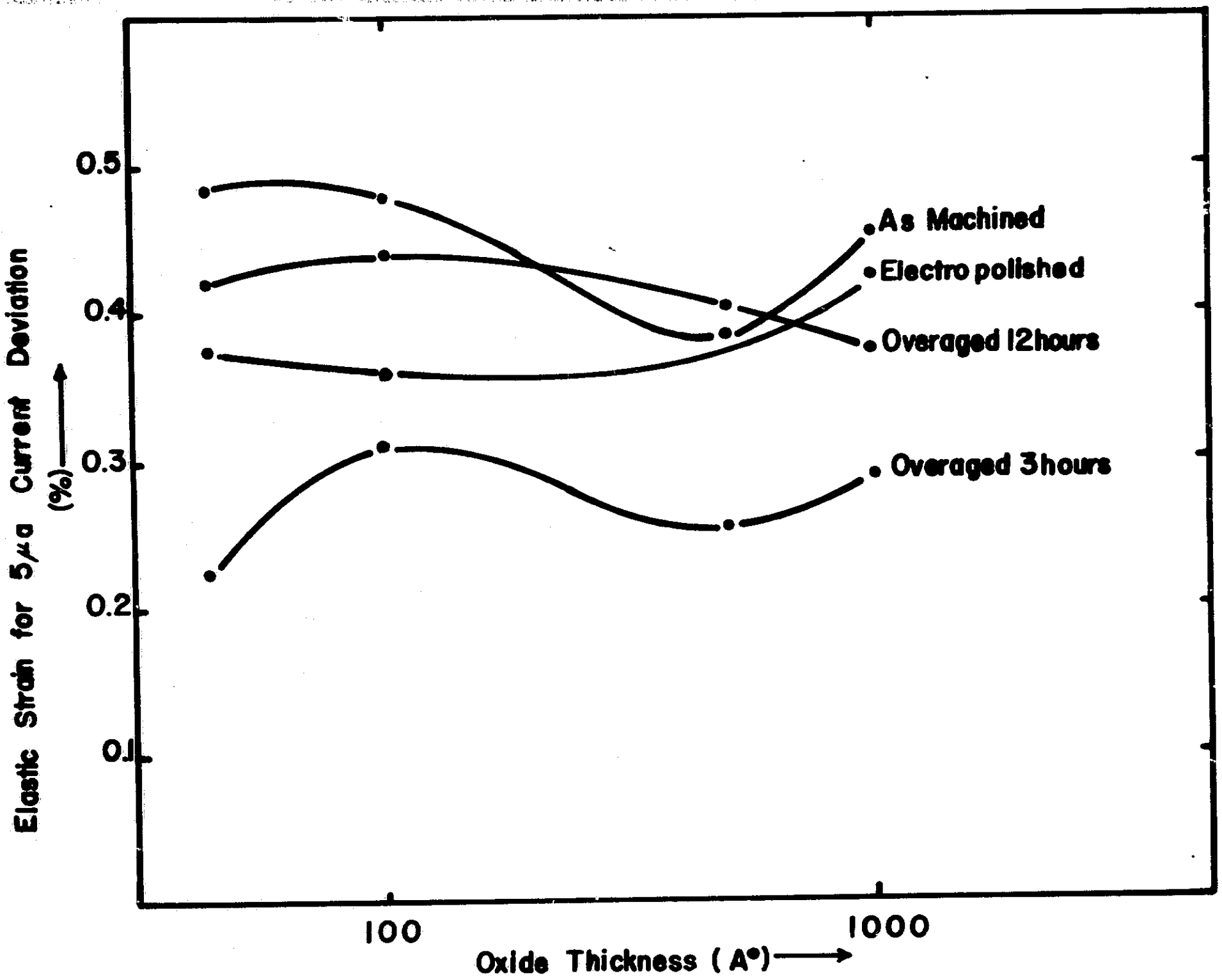

Fig. 63. Oxide thickness versus elastic strain (alloy 7075)

elastic strain was applied in a cyclic fashion. That is, after reaching the maximum elastic strain, the direction of straining was reversed, and the cycle was repeated. The results of these tests as a function of oxide thickness (anodization voltage) are shown in Figs. 64, 65, and 66. We see that the thinner the oxide, the greater the current increase during each cycle. This indicates that oxide rupture is more permanent and less repairable if the oxide is thin.

These conclusions are supported by the results on specimens of Al-7.5Zn-2.4Mg heat treated to have the same bulk hardness (Rockwell B 71-74) but different grain boundary depleted zones. This heat treatment consisted of a solution heat treatment at 480 °C for 1 hr followed by water quenching and then aging at either 2 hr at 130 °C (narrow zone) or for 1.25 hr at 180 °C (wide zone).

These results are shown in Fig. 67. In this case, it is evident that the wide depleted zone samples show a greater increase in control current than the narrow zone samples. However, the latter are more susceptible to stress corrosion. This result is consistent wtth our previous finding, because in this case we have kept the condition of the dislocation in the bulk constant (hardness constant) while varying the precipitate free zone (PFZ). Under these conditions, easier deformation of a zone at a grain boundary would be expected to blunt the effedts of dislocation planar arrays at that boundary. Thus, in this case, greater ease of plastic deformation implies a greater blunting effect, and therefore less stress corrosion susceptibility.

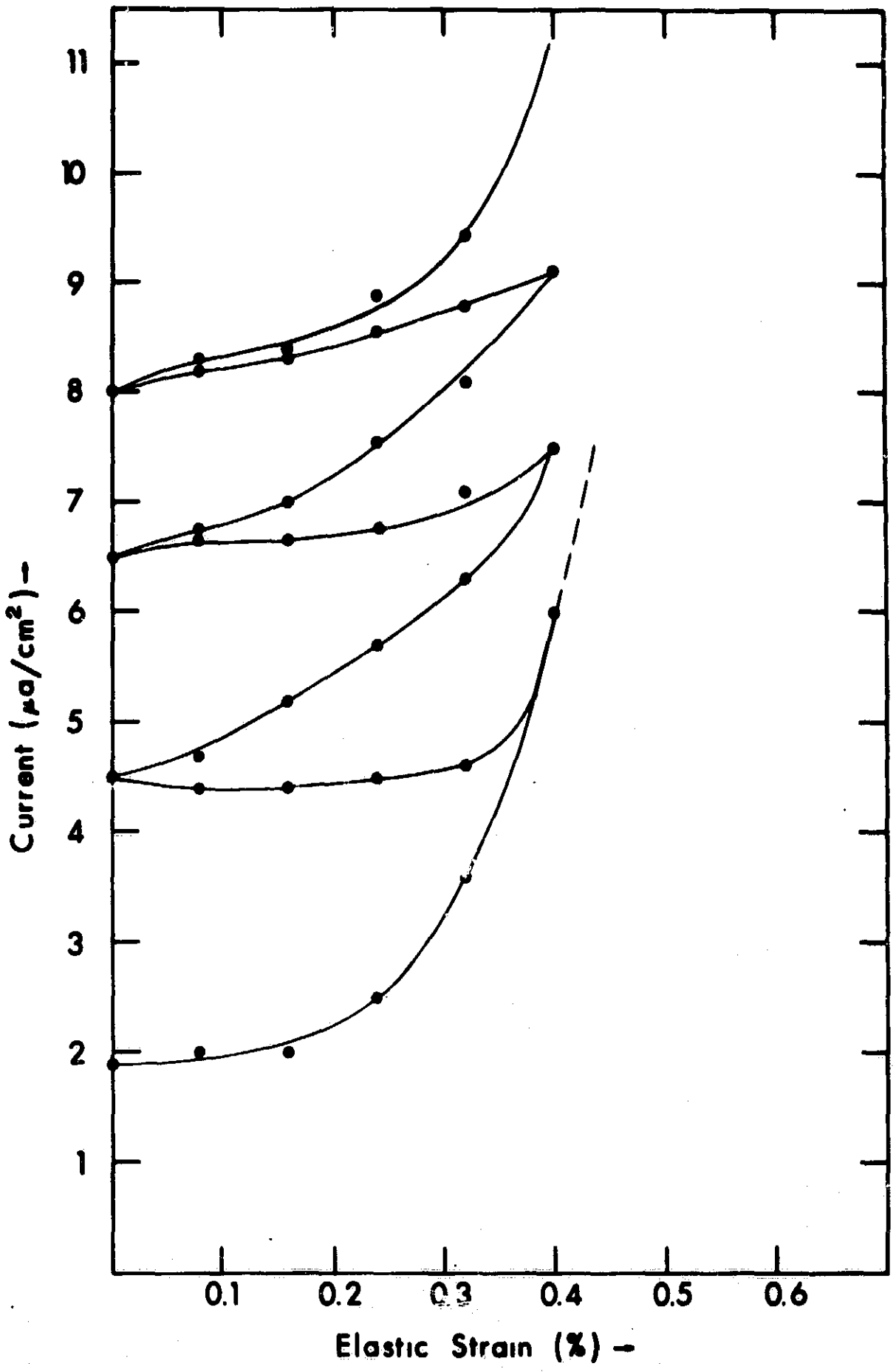

Fig. 64. Alloy 7075 overaged 12 hr and anodized at +0. 8 V versus sce

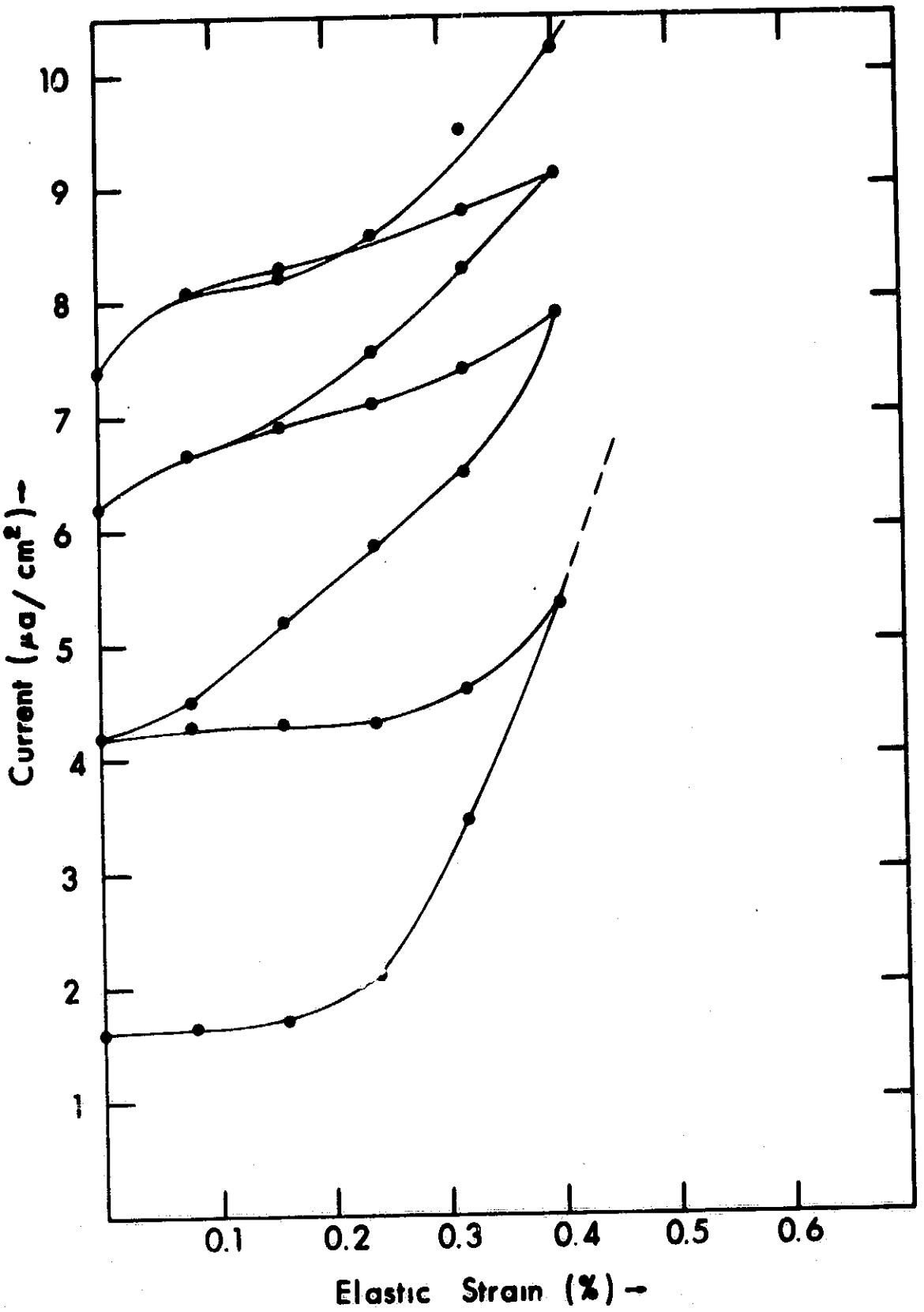

Fig. 65. Alloy 7075 overaged 12 hr and anodized at +4.9 V versus sce

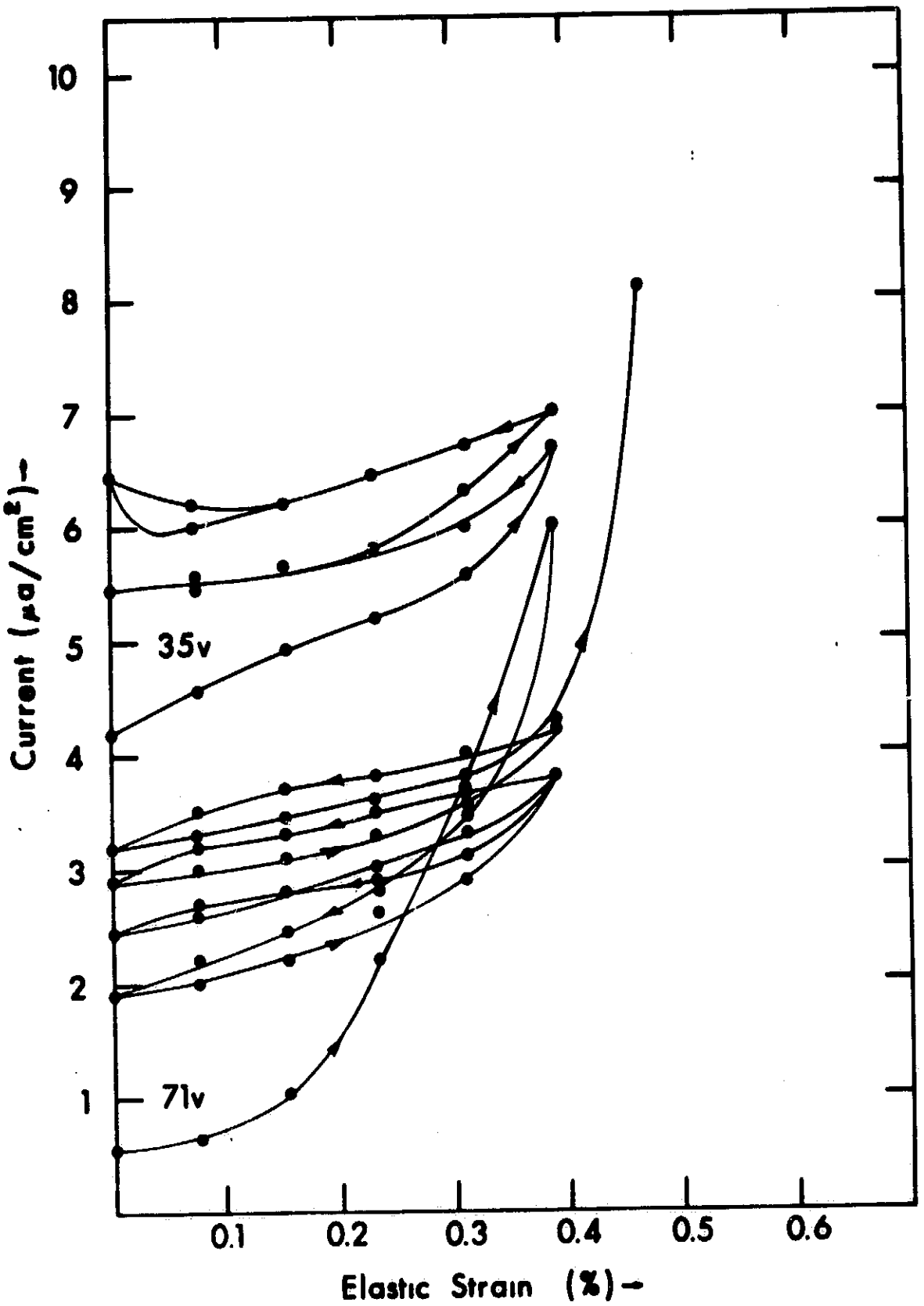

Fig. 66. Alloy 7075 overaged 12 hr

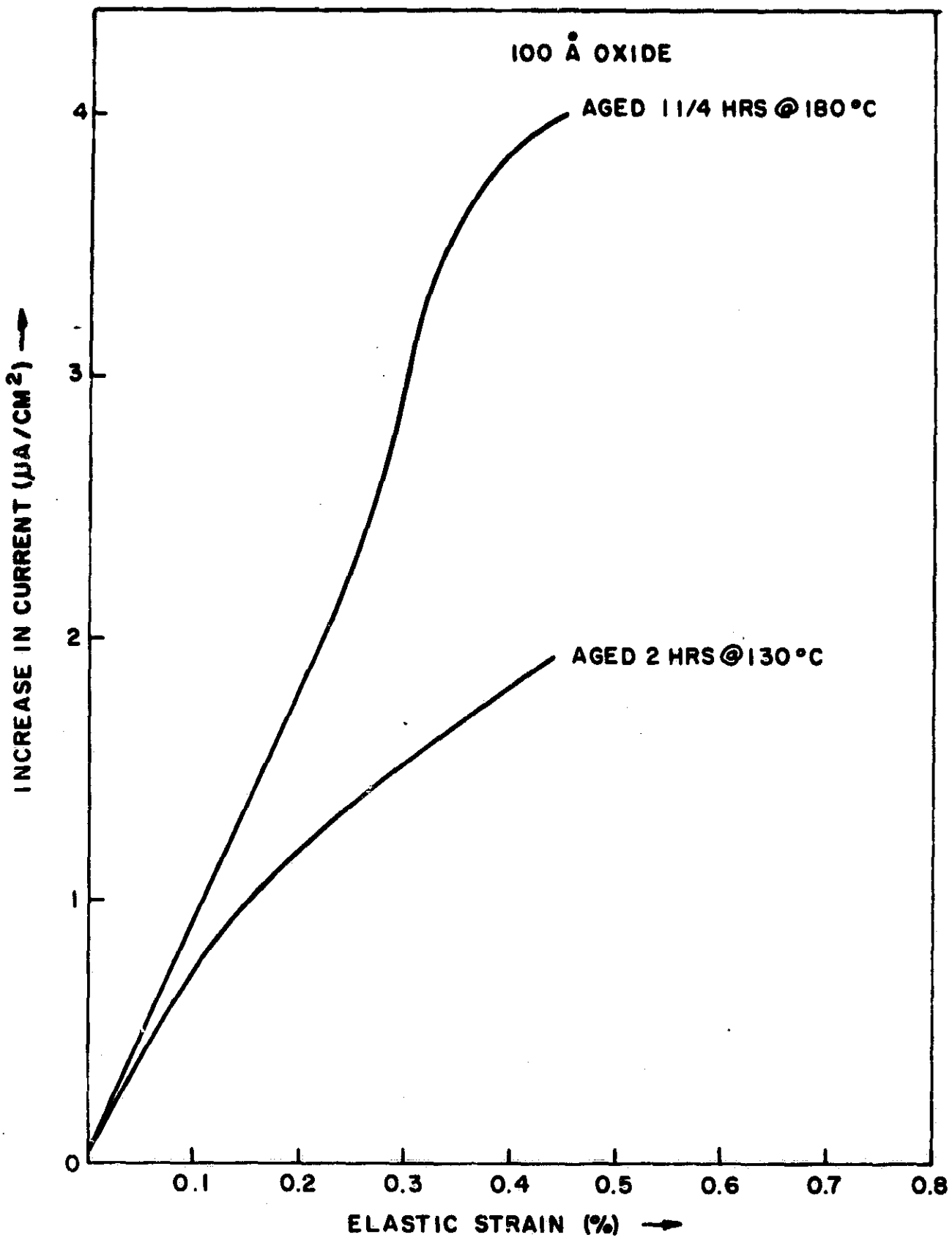

Fig. 67. Current increase versus elastic strain for aged Al-7.5 Zn-2.4 Mg

IV. NONDESTRUCTIVE TESTING TECHNIQUES FOR THE DETECTION OF STRESS CORROSION

A. Introduction

This section is concerned with the second phase of the program, the development of nondestructive techniques for the detection of stress corrosion damage in Al alloys.

Part B summarizes the literature survey carried out on available techniques (the complete survey is presented in the Second Quarterly Report). Part C deals with the detection of SCC using eddy currents. The remainder of this section is concerned with the detection of SCC with ultrasonic surface (Rayleigh) waves. Part D deals with the general principles involved and with the experimental procedures. Part E gives the results for SCC produced under various environmental conditions, and part F is concerned with the instrumental design parameters for SCC detection.

Finally, the Appendix presents the results of the investigation of simulated defects with Rayleigh waves.

B. Survey of Nondestructive Testing Techniques for the Detection of Surface Flaws

All nondestructive methods for the detection of SCC involve the measurement of a physical property sensitive to stress corrosion damage. Since this damage is initially signaled by the formation of surface microcracks, useful techniques are those inherently sensitive to such surface defects. In most cases, it is difficult to predict theoretically the precise effect of stress corrosion damage on the physical property being measured, particularly for specimens of arbitrary geometry. Therefore, the emphasis in the literature survey is to enumerate empirical relationships and to include only that theory necessary to the understanding of these relationships.

Of all the techniques available, only those involving ultrasonic surface (Rayleigh) waves and those involving surface conductivity measurements using eddy currents appeared to be really promising.

The survey, therefore, was primarily concerned with these two methods (however, internal friction, magnetic, thermal, radiographical, and laser methods were also investigated).

C. Detection of SCC With Eddy Currents

1. Basic principles

In eddy current testing, a piece of metal is characterized by its permeability, dimensions, and electrical conductivity. The permeability for nonmagnetic metals is constant, and for all practical purposes is equal to that of free space ($4\pi \times 10^{-7}$ H/m). Therefore, this parameter does not yield information about the physical conditions of nonmagnetic samples such as Al alloys. The dimensions of the sample do not affect the measurements if they are large compared to the penetration of eddy currents and the area of the probe.

The third property, effective electrical conductivity, is a function of many parameters including presence of irregularities, impurities, grain size, and mechanical and thermal treatment. The presence of cracks or variations in physical, chemical, or metallurgical structure can be detected using the change in the apparent conductivity (or resistivity), because such irregularities alter the distribution of surface currents within the specimen. This results from the fact that cracks, pits, or any other defect will change the effective conductivity of a piece of metal by crowding eddy currents into a smaller volume. Currents cannot cross the microscopic voids and, in being diverted around them, will raise the current density in the surrounding metal and thereby lower the effective conductivity detected by an outside observer.

This suggests that the observed changes in apparent conductivity (or resistivity) may be utilized to identify the kind, size, and distribution of defects. This is generally accomplished by the use of calibration curves.

2. Eddy current instrumentation

The investigation of eddy currents (electrical conductivity) for the detection of SCC was made with the Dermitron Thickness Tester at four frequencies: 100 kHz, 500 kHz, 2 MHz, and 6 MHz. The 6-MHz channel was mostly used, because at this frequency the smallest defects will be detected (other frequencies were used for some tests).

This instrument was designed as a thickness tester (e. g. , for paint, etc.), but it can also be used for measuring the electrical conductivity of metals. The probe induces eddy currents in a metallic surface; the depth of penetration, δ, of the eddy currents is measured on a linear scale (0 to 100) through the magnetic field which opposes the inducing current. The readings on the linear scale of the Dermitron are used with calibration curves to correlate relative Dermitron readings with actual physical characteristics. The accuracy of this instrument is generally quoted as $\pm$ 5%.

For the eddy current measurements, the special microprobe MID was used. This microprobe requires an area of a 1/16-in. -diameter circle for magnetic materials, but for nonmagnetic materials such as Al the necessary area is that of a 1/8-in. -diameter circle. The inner and outer coils of this microprobe are 38 and 50 mils in diameter, respectively.

The Dermitron has three OPERATE positions which apply to the different combinations of materials and thicknesses. However, for the purpose of crack detection, OPERATE-1 and OPERATE-3 have been used. Fig. 68 shows the Dermitron, the microprobe MID, and a stage constructed to test 1/8-in.-diameter cylindrical tensile specimens.

3. Depth of penetration

Before proceeding with the actual measurements, the depth of penetration, δ, was calculated for different pure metals which were used to calibrate the instrument. The depth of penetration is given by

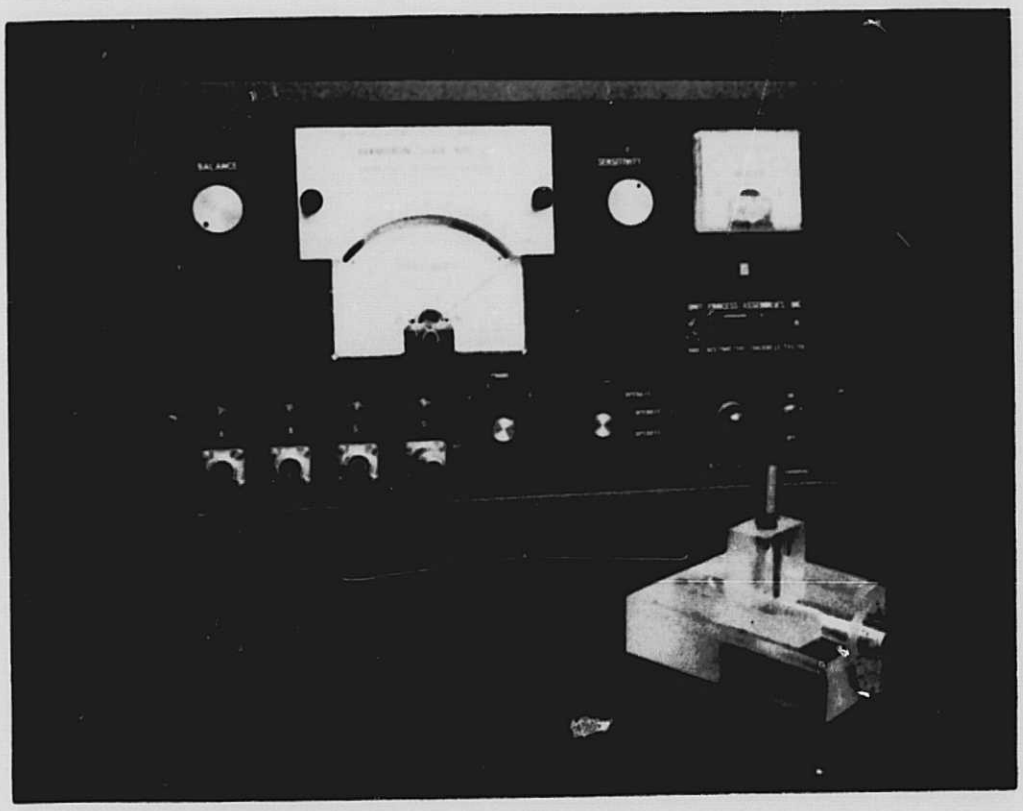

Fig. 68. Eddy current instrument (Dermitron), microprobe, and stage for testing 1/8-in. -diameter cylindrical tensile specimens

$$\delta = (\pi f \mu \sigma)^{-\frac{1}{2}}$$

where δ = depth of penetration, m

f = frequency, Hz

μ = magnetic permeability, $4\pi \times 10^{-7}$ H/m for nonmagnetic materials

σ = volume electrical conductivity, mho/m

Table III gives the resistivity and conductivity at 20 °C and the depth of penetration at 6 MHz of the pure metals used to calibrate the Dermitron. Al (2024) and Al (2219) have the same δ as Al (7075) shown in Table III. Fig. 59 is a plot of the depth of penetration at 6 MHz versus resistivity and conductivity. The important point is that the penetration into Al (7075) at 6 MHz (50 μ) is sufficiently small that the detection of very small surface flaws should be easy.

Table III. Resistivity, Conductivity, and Depth of Penetration at 6 MHz for the Pure Metals Used to Calibrate the Dermitron

Metal	Resistivity (20 °C), μohm-cm	Conductivity (20 °C) mho/cm x 10^5	% IACS	Depth of Penetration at 6 MHz Microns	Mils
Silver	1.6	6.25	104	26.1	1.03
Copper	1.673	5.92	100	26.7	1.05
Aluminum	2.69	3.72	62	33.9	1.33
Magnesium	3.9	2.56	43	40.8	1.60
Al 7075 alloy	5.7	1.76	29.4	49.5	1.93
Zinc	5.92	1.69	28.2	50.3	1.98

Table III lists conductivity in conventional conductivity units and also as a percent of the International Annealed Copper Standard (IACS) commonly used in the literature and expressed by:

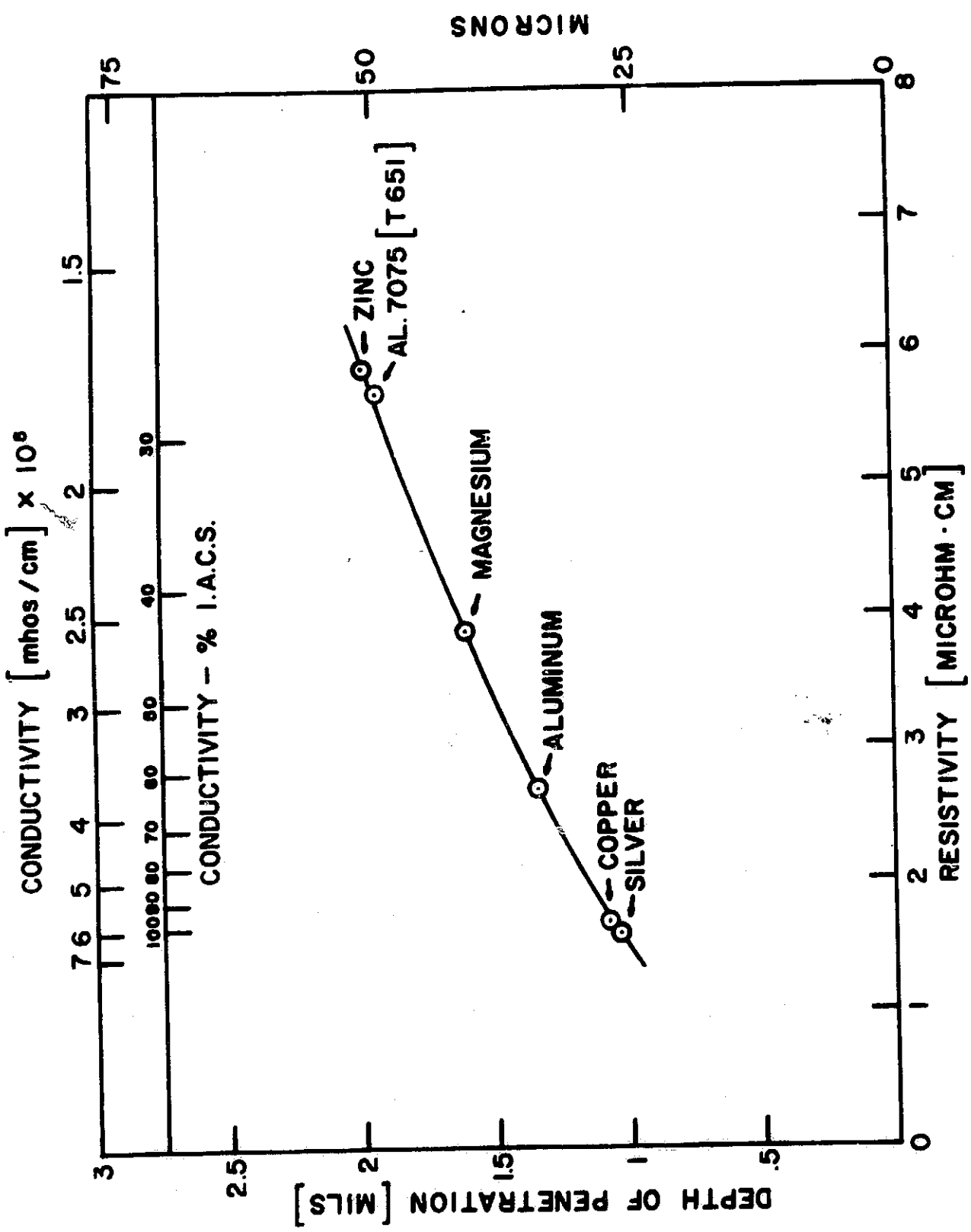

Fig. 69. Depth of penetration as a function of resistivity and conductivity at 6 MHz

$$\text{Conductivity in \% IACS} = \frac{\rho \text{ (of pure Cu at 20 °C)}}{\rho \text{ (of the sample at 20 °C)}} \times 100$$

where ρ is the resistivity. The resistivity of pure Cu (100% IACS) at 20 °C is 1.673 μ ohm-cm.

4. Effect of surface roughness

To investigate the effect of surface roughness on Dermitron readings, measurements were made on flat surfaces with different surface finishes. For this purpose, test blocks were prepared from 7075-T6 plates. The geometry of these test blocks showing the different directions and planes is given in Fig. 70.

The notation used is as follows:

STD: short transverse direction
TD: transverse direction
RD: rolling direction
ST-T plane: plane determined by the ST and T vectors
ST-R plane: plane determined by the ST and R vectors
R-T plane: plane determined by the R and T vectors.

The dimensions of the test blocks were much greater than the depth of penetration and the area of the microprobe. The effect of an edge is easily demonstrated by moving the probe toward the end of the test block and observing the change in position of the pointer on the linear scale.

The different surface finishes of the test blocks were obtained using various abrasive materials. The fine grinding was performed with 180, 240, 320, 400, and 600 grit silicon carbide paper. Polishing was done with aluminum oxide by successive polishes using Polishing Alumina no. 1 (5.0 μ), no. 2 (0.3 μ), and no. 3 (0.05 μ).

Ten readings were taken on each of the three coordinate planes (ST-T, ST-R, and R-T), for all surface finishes. Each reading was an average over ten different trials. Typical results are given in Fig. 71 and Table IV.

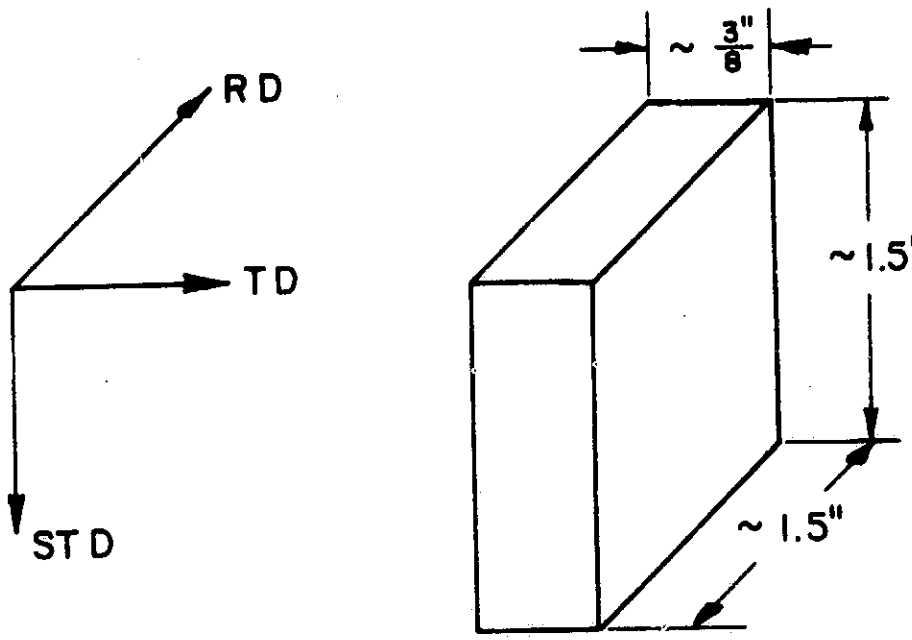

Fig. 70. Typical test block used to investigate surface roughness (shows different coordinate directions)

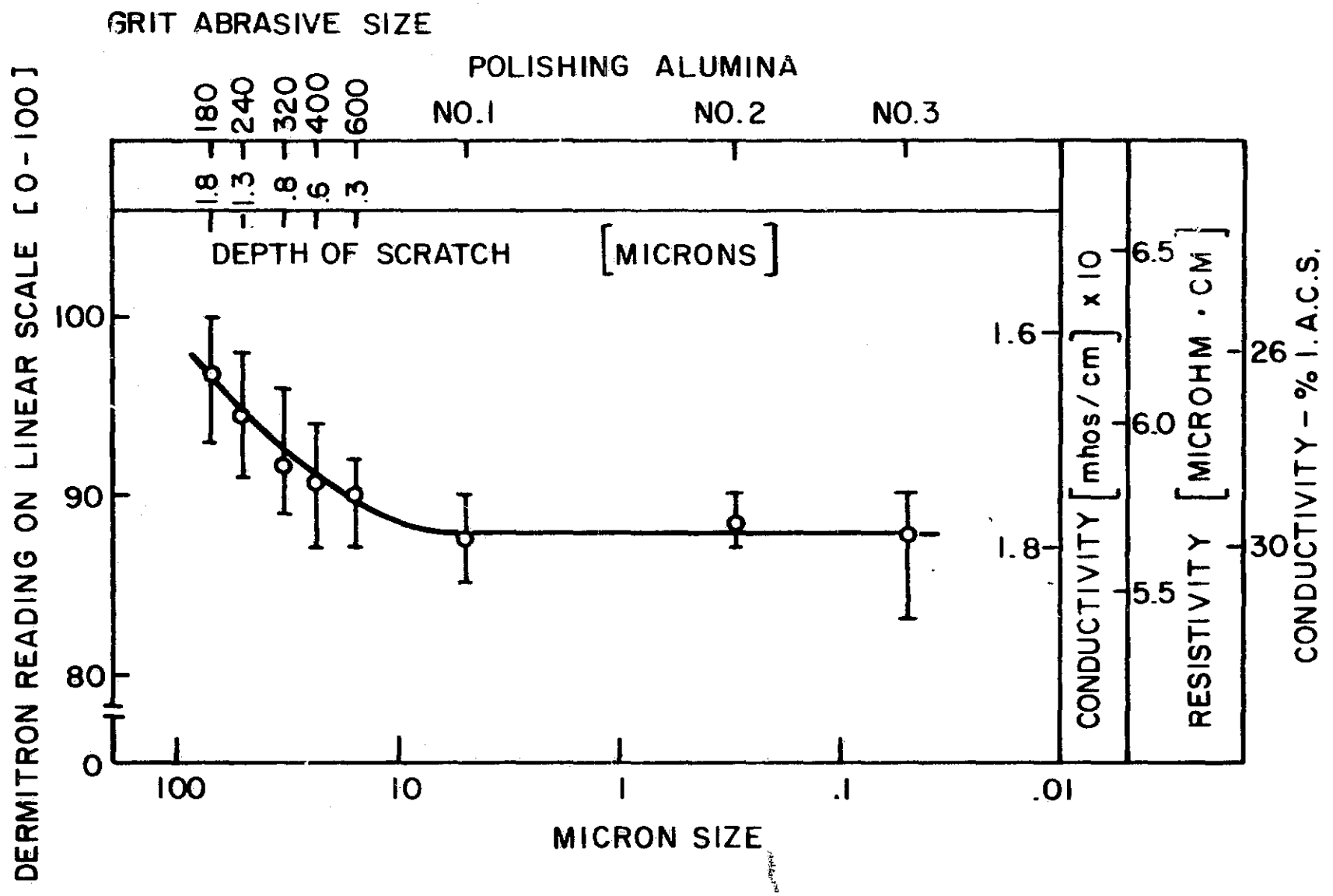

Fig. 71. Surface roughness as a function of Dermitron reading for OPERATE-3 position

Table IV. Dermitron Readings in the OPERATE-3 Position for the Three Planes of an Al 7075 Test Block (Surface Finished with 5 μm Polishing Compound)

	R-ST	T-ST	R-T
Maximum	90	90	88
Average	88. 1	87. 2	86
Minimum	86	84	85

Fig. 71 is a plot of the Dermitron reading versus surface finish. The Dermitron reading was the average reading on all three planes (R-S, S-ST, R-ST) having the same finish. The surface finish is given in terms of three different quantities: (1) abrasive size (which produced the scratch), (2) particle size in microns, and (3) average depth of scratch produced in terms of the rms roughness.[21] The rms roughness is the root mean square height of all the peaks and valleys. The relationship between the various types of abrasive grits and polishing compounds and the average depth of scratch (rms roughness) is given in Fig. 72.

The other coordinate is either the Dermitron reading on the linear scale (0 to 100), the resistivity in μohm-cm, the conductivity in mho/cm, or the % of IACS. Fig. 72 shows that when the surface finish is better than that produced by a 600-grit silicon carbide paper, the Dermitron reading is constant. This surface we will call a "standard surface finish." The shallowest scratch depth that can be detected is 0. 3 μ. For the subsequent measurements, and in particular for calibration, the samples to be tested were given the standard surface finish to hold this parameter constant. For these measurements, the sensitivity control was set to maximum value, the OPERATE-3 position was used, and the balance control was adjusted so that the instrument read 88 on the linear scale when the probe was placed on the standard surface finish. In the OPERATE-1 mode, the Dermitron reading was independent of surface finish up to and including surfaces finished with no. 180 grit.

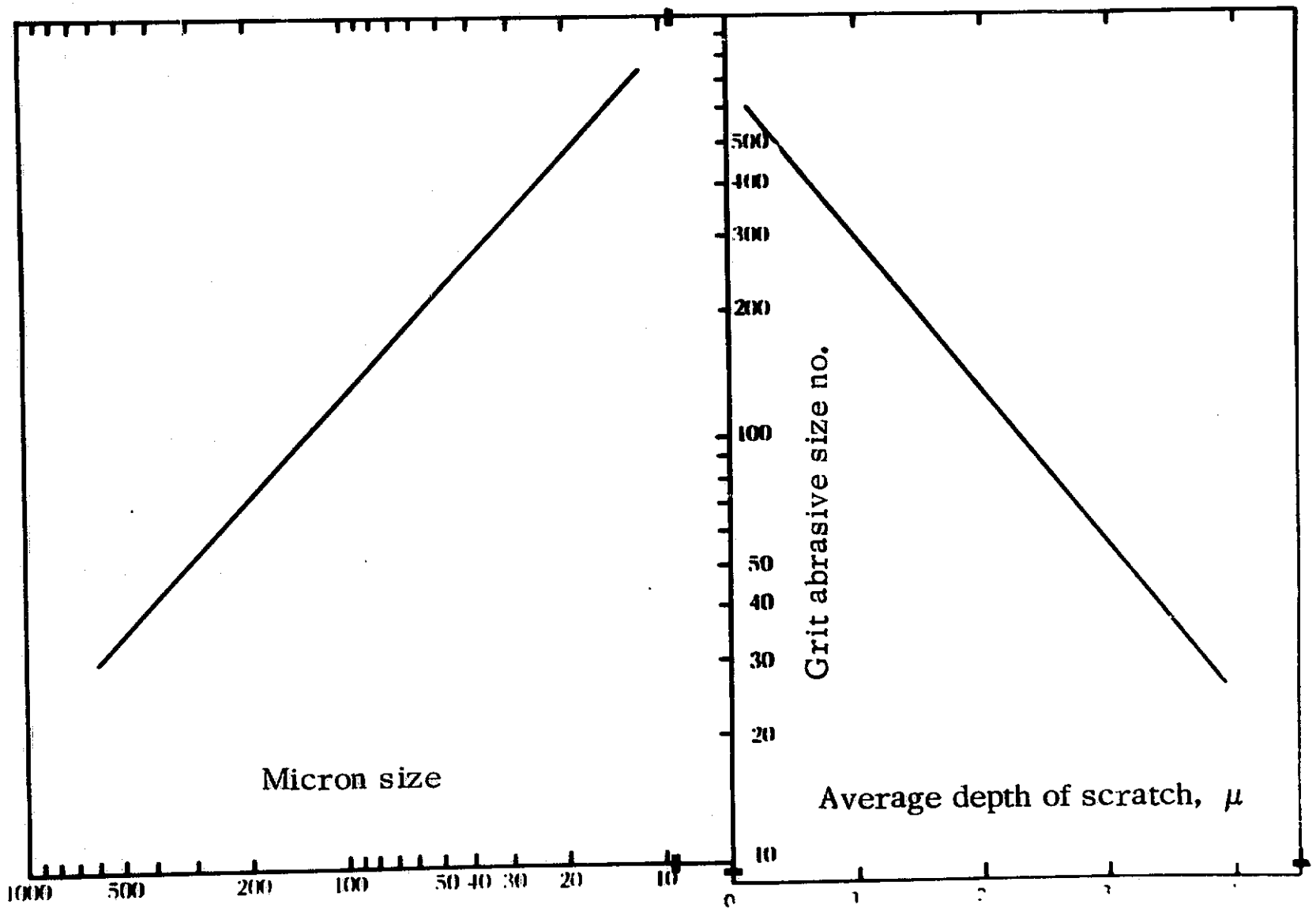

Fig. 72. Relationship between grit size, micron size, and average depth of scratch

Because of the variability of the Dermitron readings, the average, minimum, and maximum values are given in the figures. This gives a better idea as to whether two sets of readings overlap than would just the average. Examples of the scatter in the data are given in Table IV. Here, we give the Dermitron readings for the three planes of a test block with surface finished with no. 1 polishing alumina. If we take 10 readings at the same position of the R-ST plane of the same test block, we find a maximum reading of 89, an average of 87. 8, and a minimum of 86. However, the fluctuations of a set of 10 readings are much smaller than the changes in readings, due to changes in other parameters. These fluctuations produce an average change in apparent resistivity of less than 3%.

In general, the change in effective resistivity due to surface roughness is much smaller than the change produced by defects. For example, the resistivity of Al (7075) with a standard finish is 5. 7 μohm-cm and the apparent resistivity for 180-grit finish (the roughest finish used) is 6. 1 μohm-cm, a 7% increase in effective resistivity. However, data obtained on surfaces exposed to various amounts of stress corrosion showed increases in apparent resistivity ranging from 16 to 120%, which gives an indication of the excellent sensitivity of the Dermitron to SCC.

5. Instrument calibration

In order to relate the Dermitron readings to known physical characteristics of a specimen, calibration curves were prepared. For this purpose, different pure metals were given the standard finish, and the Dermitron reading was plotted against their resistivity or conductivity. Fig. 73 is a plot of the Dermitron reading versus resistivity. Approximately a linear relationship between Dermitron reading and resistivity was obtained. The sensitivity control was set to a maximum and the balance control was set to read 11 on the linear scale when placed on Ag. Position OPERATE-3 was used.

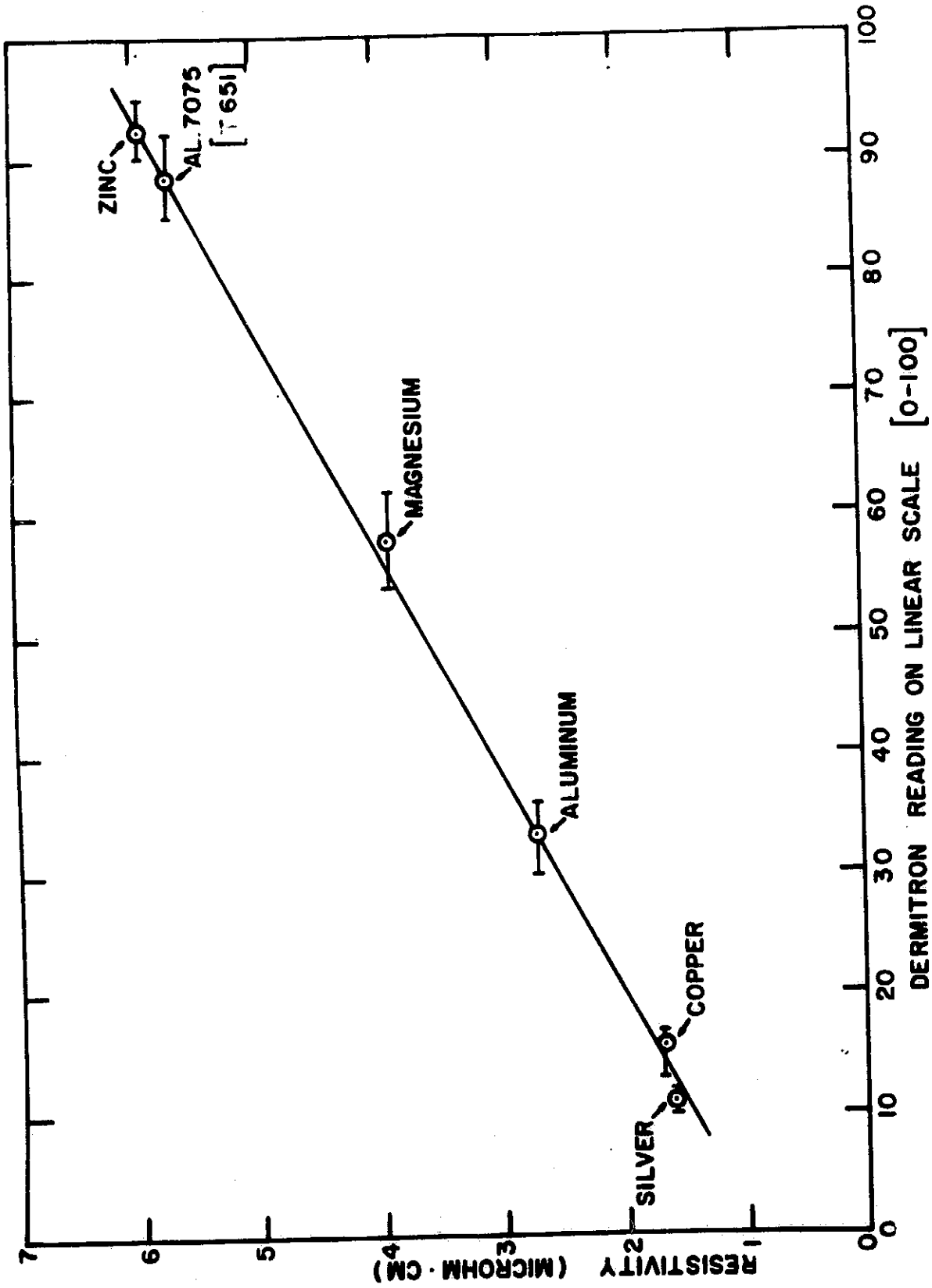

Fig. 73. Dermitron reading versus resistivity (using OPERATE-3 position) for flat surfaces

Fig. 74 is another plot of the Dermitron reading versus resistivity, including measurements on two magnetic materials: Co and Ni. This curve was obtained by adjusting the balance control to read 7.5 on the linear scale when placed on Ag and then adjusting the sensitivity control to read 94 on the linear scale when placed on Ni. The curve is not continuous because of the different nature of the samples. The first part of the curve is linear, in agreement with Fig. 73. Using this figure, the change in effective resistivity of specimens can be measured directly from the Dermitron reading.

6. Effect of simulated flaws

The first type of artificial flaws was longitudinal grooves cut on the surface of Al 7075 (T651) with a standard finish. The length of these grooves was much larger than the dimensions of the eddy current probe, thus eliminating end effects. The average of a number of readings are presented in Figs. 75 and 76 with a schematic of the cross section of the grooves and microprobe. All measurements were made using the OPERATE-3 position of the Dermitron. The ordinates of these figures are given in (1) relative Dermitron reading (which is the difference in the instrument readings when the probe is placed on a groove and on a flawless surface of standard finish), and (2) apparent resistivity increase. The abscissa is the depth of the grooves in microns, mils, and also in percent of depth of penetration (1.93 mils or 49.5 μ for Al-7075 at 6 MHz). For the grooves of Fig. 77, the S-N (silver-nickel) scale was used because the instrument proved to be much too sensitive for grooves of these dimensions on the S-Z (silver-zinc) scale. These figures indicate that the apparent resistivity increases with increasing depth and width of the groove. In Fig. 75, the curves seem to converge in the vicinity of 10 μ, indicating that the threshold of detectability of narrow grooves with the microprobe at 6 MHz is in that vicinity. However, the microprobe itself, when dragged on a standard finish surface under the normal pressure provided by the probe guide, will produce a

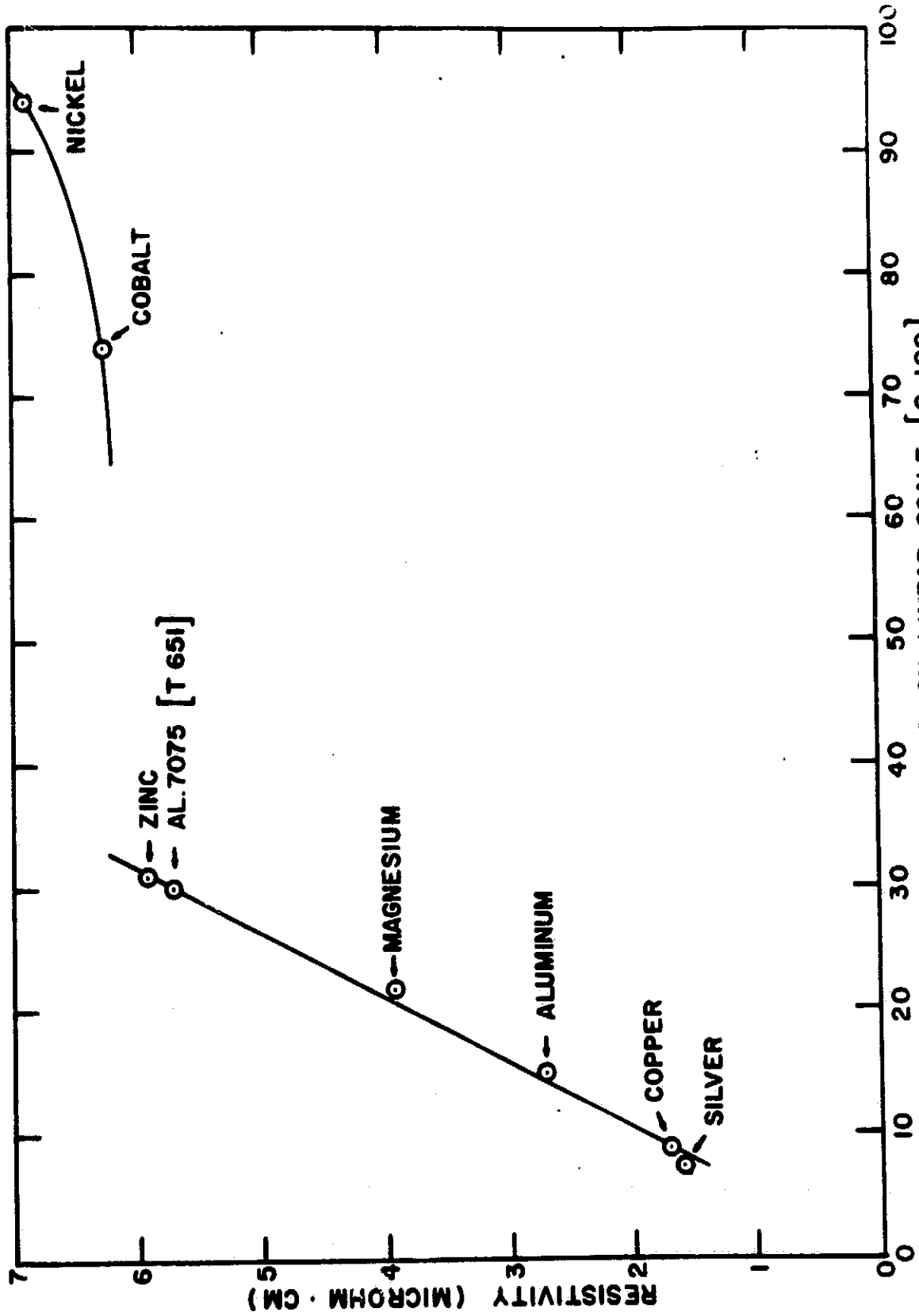

Fig. 74. Dermitron reading versus resistivity (using OPERATE-3 position) for flat surfaces including magnetic materials

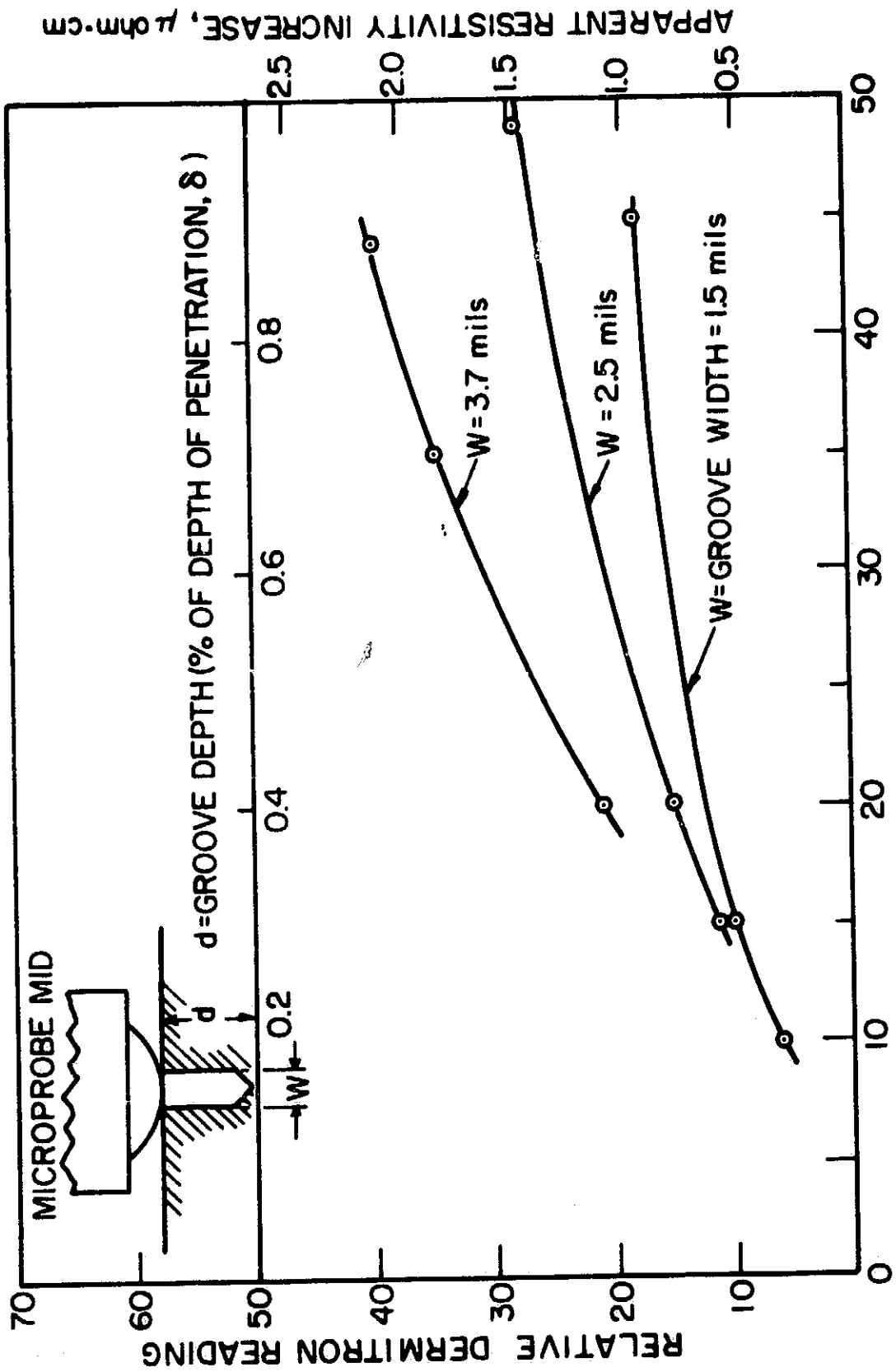

Fig. 75. Effect of artificial grooves on the eddy current instrument reading as a function of depth (S-Z scale)

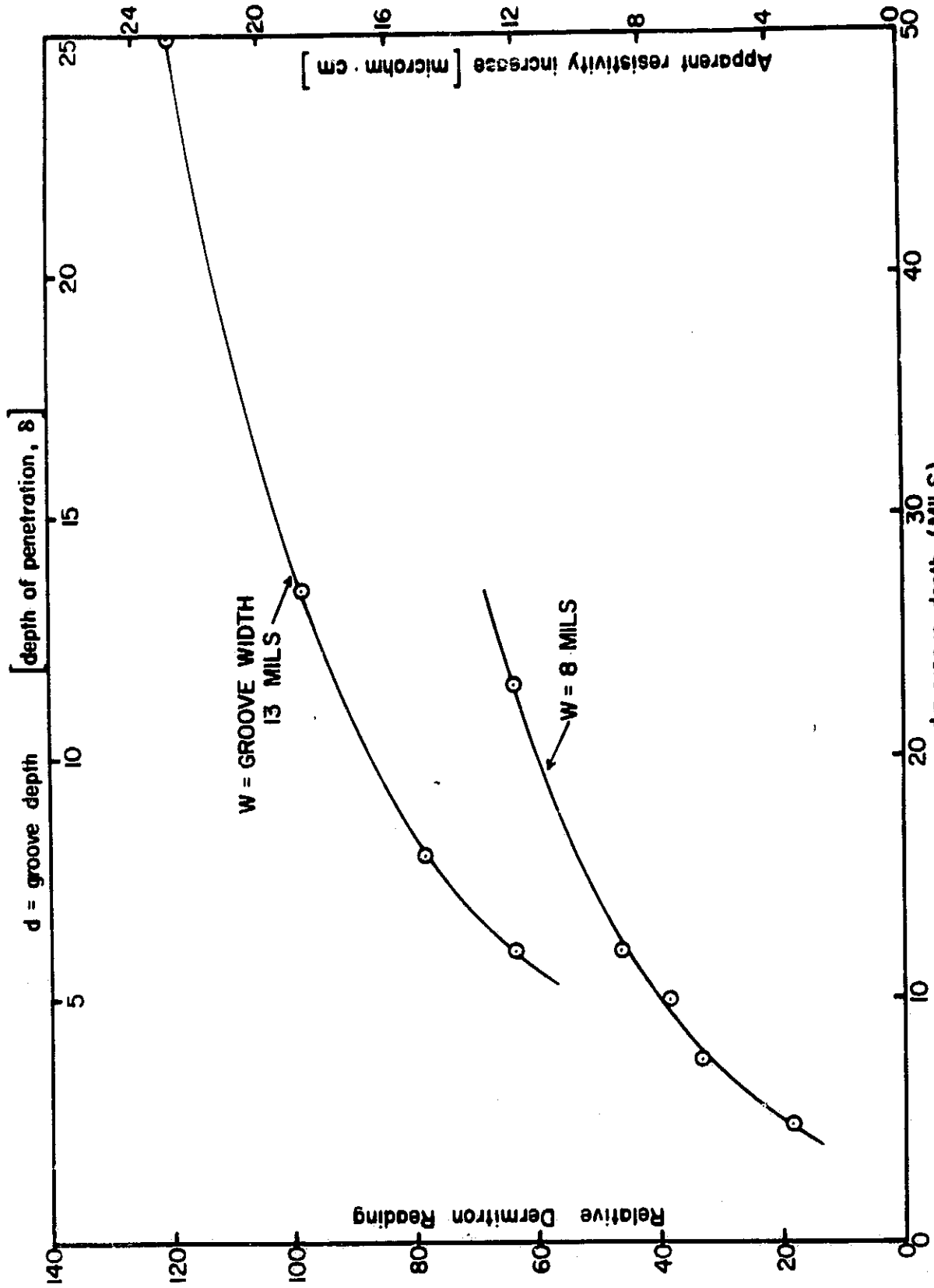

Fig. 76. Effect of artificial grooves on the eddy current instrument reading as a function of depth (S-N scale)

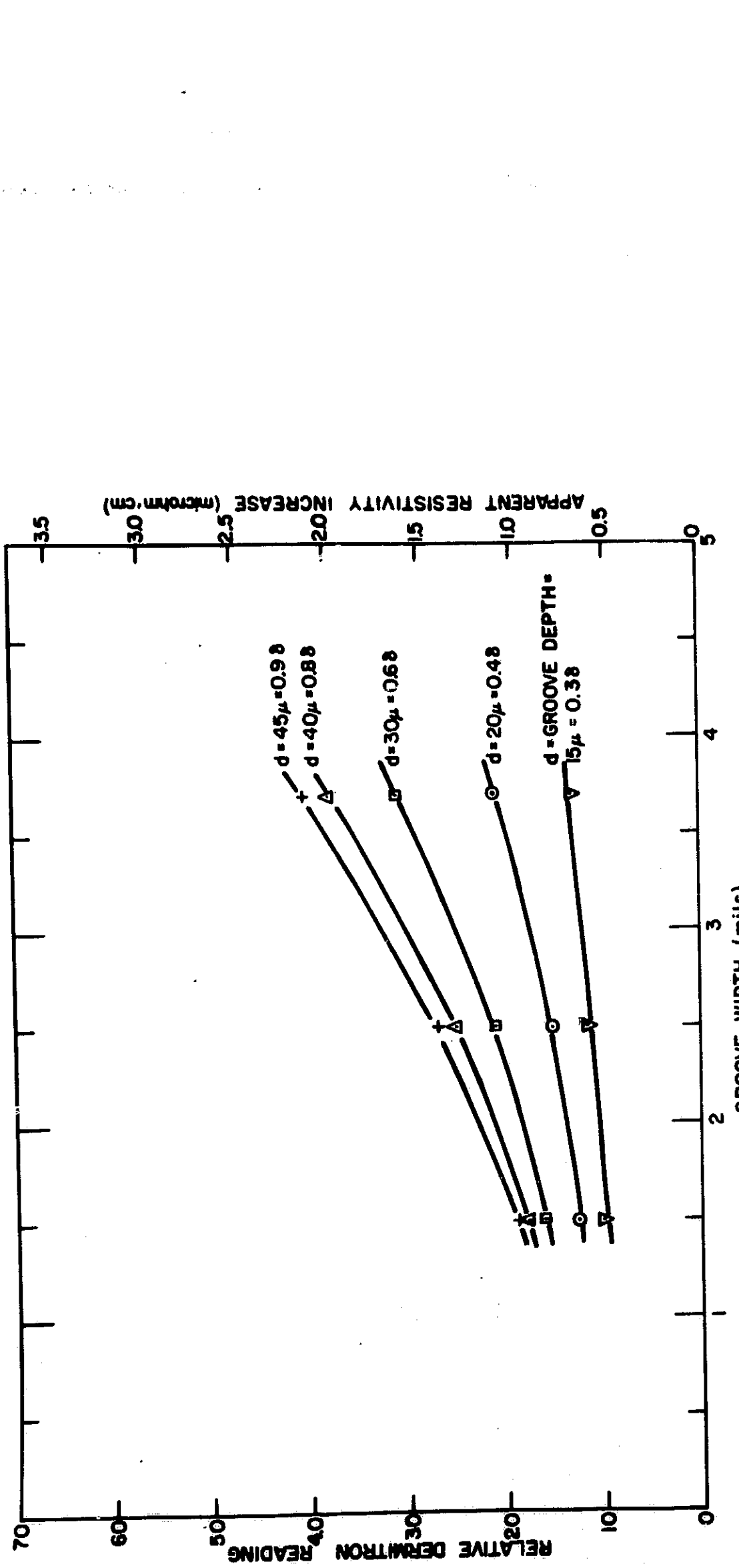

Fig. 77. Effect of artificial grooves on eddy current instrument reading as a function of width (S-N scale)

groove of about 40 μ (1.5 mils) in width and about 10 μ in depth. To protect the microprobe from wear, a thin film of oil which did not affect the Dermitron reading was used. In Fig. 77, the data of Fig. 75 are replotted with the width of the groove as abscissa.

Table V gives the effect of cylindrical V-bottom holes on the eddy currents. The data indicate that the change in effective resistivity is independent of the hole depth and proportional to the hole diameter. The minus sign in the data of Table V means that the deflection of the meter needle was to the left, opposite the deflection when the microprobe is used on grooves.

7. Effect of surface curvature

In order to investigate the effect of curvature on eddy currents and to prepare calibration curves for the cylindrical tensile specimens, cylindrical rods of varying diameter were prepared. Material used included Cu, Al, Al 7075, and Zn. The results are given in Figs. 78, 79, 80, and 81. For Figs. 80 and 81, which are detailed regional expansions of Figs. 78 and 79, respectively, the sensitivity setting was at a maximum. In Figs. 78 and 79, the sensitivity setting was the same as for the S-N scale used for flat surfaces. Figs. 78 and 80 are plots of relative Dermitron reading versus resistivity with varying rod diameter. The plots indicate that the lines of equal rod diameter are similar to the corresponding curves for flat surfaces for various materials. Figs. 79 and 81 are plots of rod diameter versus relative Dermitron reading for various resistivities (different materials). These graphs illustrate the effect of curvature on eddy currents. The relative Dermitron reading decreases with increasing rod diameter. In addition, Fig. 81 shows that the rate of decrease of the relative Dermitron reading is inversely proportional to rod diameter. These graphs can be used for calibration when measuring cylindrical tensile stress specimens.

Table V. Effect of Cylindrical Holes Perpendicular to the Surface on Eddy Current Instrument (Dermitron) Reading

Diameter, mils	Depth		Change in Relative Dermitron Reading
	Mils	% of Depth of Penetration, δ	
5	1 to 2	0.5 to 1.0	Undetected
7	3 to 4	1.5 to 2	Undetected
22	16, 25, 47	8, 12.5 23.5	All induced same reading: –57 on S-N scale
26	13, 30, 45	6.5, 15, 22.5	All induced same reading: –96 on S-N scale

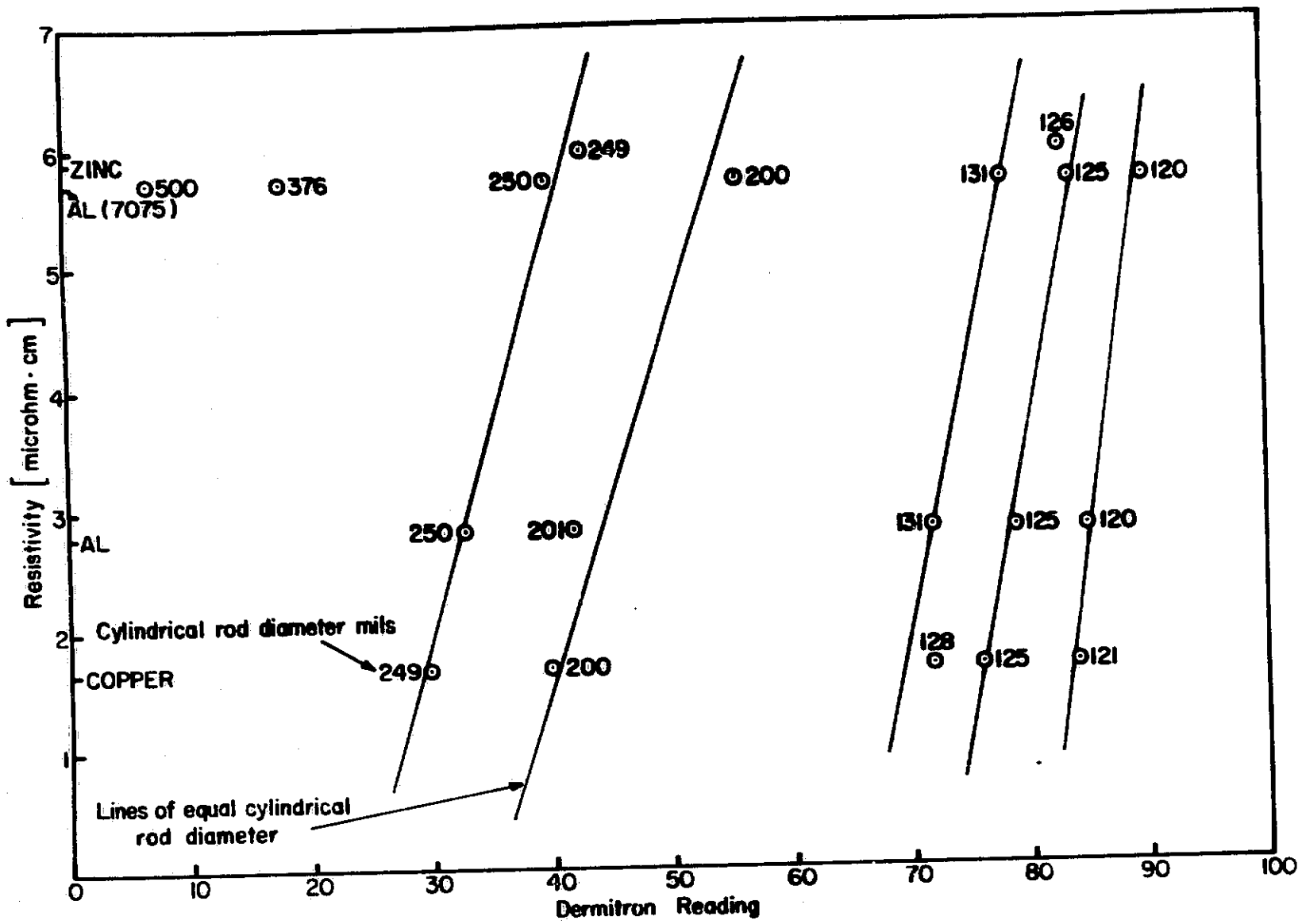

Fig. 78. Dermitron reading versus resistivity for cylindrical rods of varying diameter (same instrument sensitivity as that used for S-N scale)

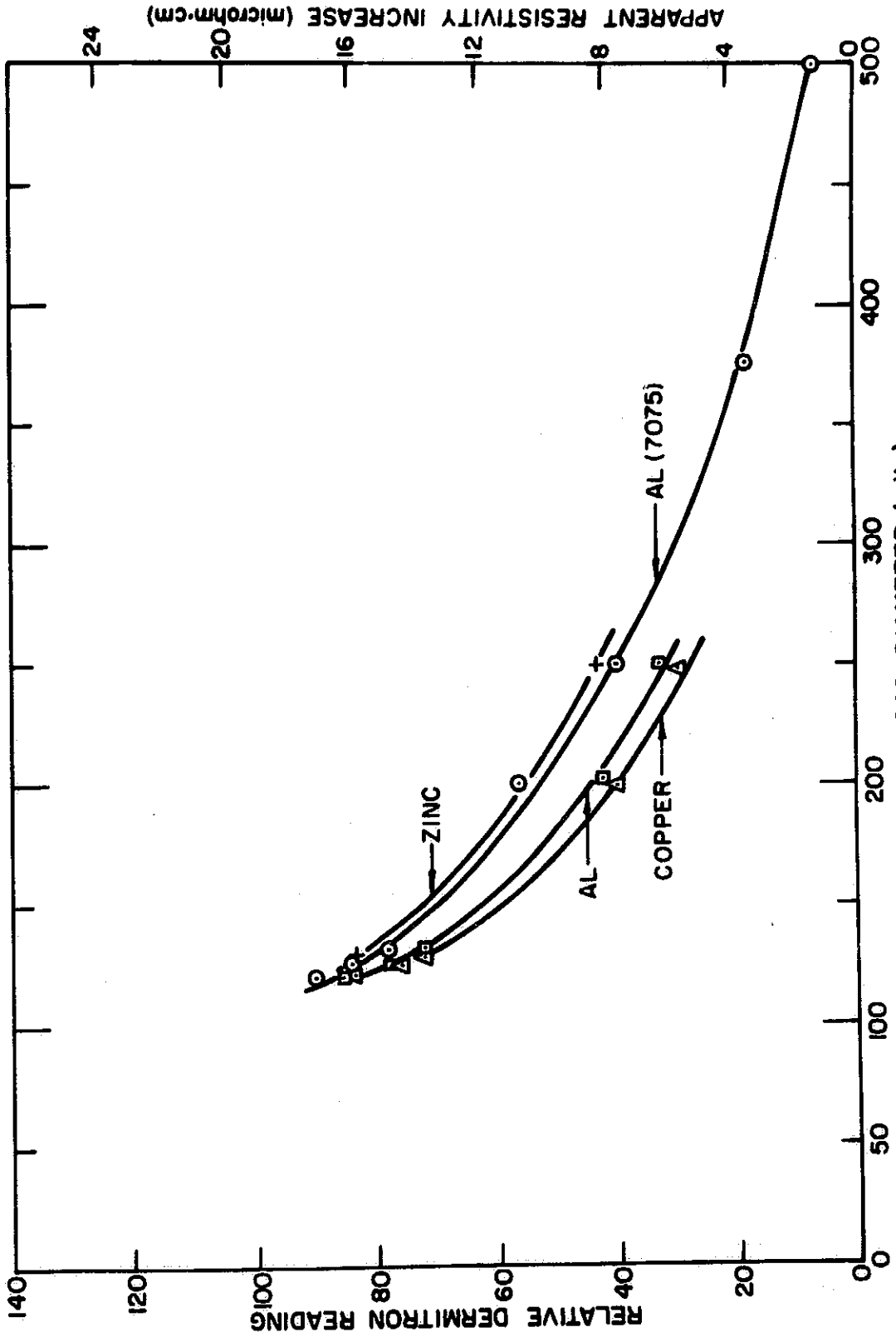

Fig. 79. Effect of surface curvature on eddy current instrument reading as a function of cylindrical rod diameter (same instrument sensitivity as that used for S-N scale)

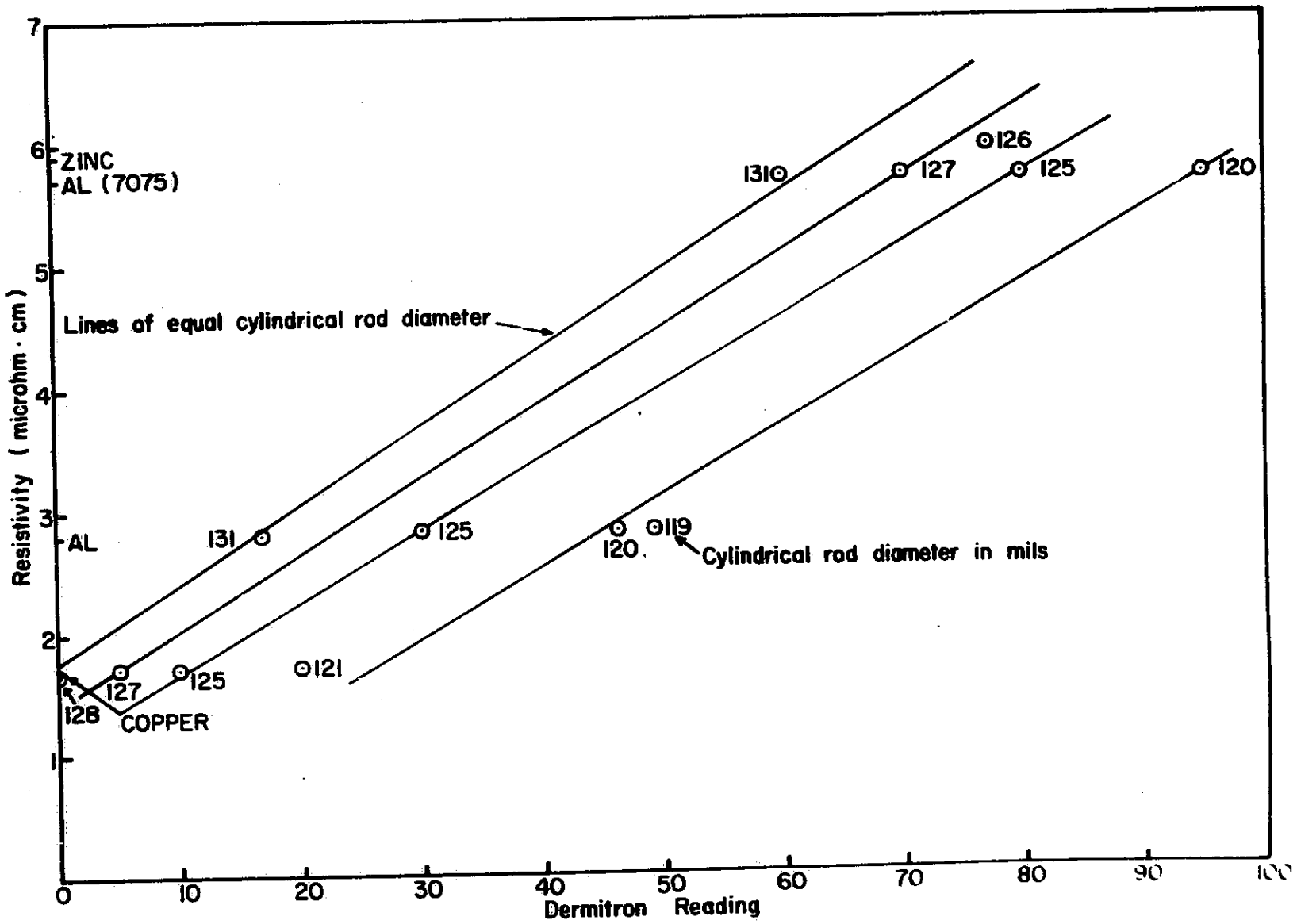

Fig. 80. Dermitron reading versus resistivity for cylindrical rods of varying diameter (same instrument sensitivity as that used for S-Z scale)

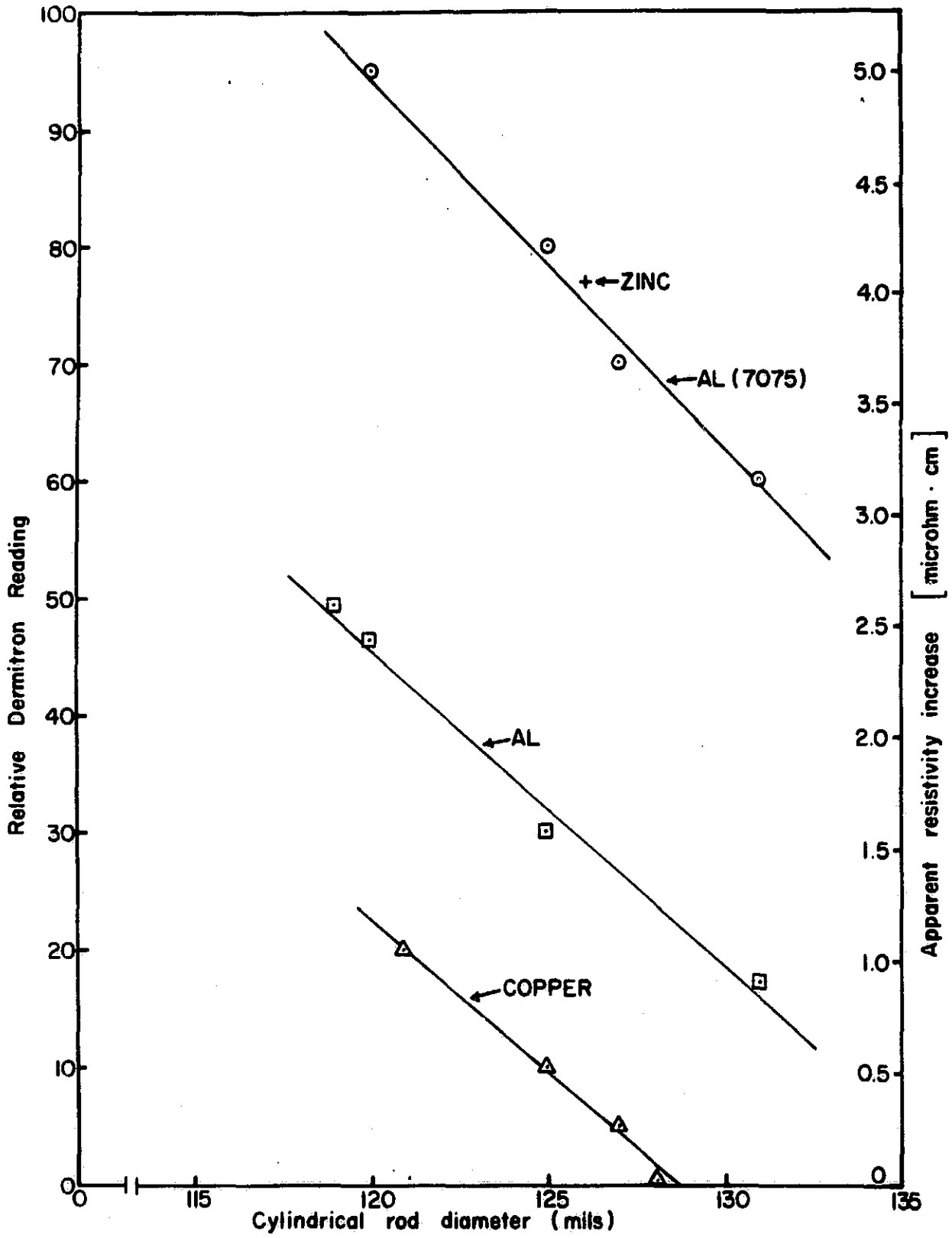

Fig. 81. Effect of surface curvature on eddy current instrument reading as a function of cylindrical rod diameter (same instrument sensitivity as that used for S-Z scale)

8. SCC detection

Eddy currents were used to detect stress corrosion cracks on cylindrical and U-bend specimens. Data obtained on surfaces exposed to various amounts of stress corrosion indicated increases in apparent resistivity ranging from 16 to 120%. The results demonstrated the sensitivity of eddy currents to SCC.

One of the disadvantages of eddy currents is the small area checked (1/8-in.-diameter circle for the microprobe used) at each measurement. This implies that if an area of practical dimensions is to be tested, a large number of measurements or some sort of elaborate assembly consisting of a large number of eddy current probes would be required. Correspondingly, the investigation of SCC detection with eddy currents was discontinued and ultrasonic (Rayleigh) surface waves were used for the remainder of the program.

D. Detection of SCC With Rayleigh Waves: Basic Principles and Experimental Data

1. Basic principles

A detailed description of Rayleigh waves, their properties and practical applications, was published in the literature survey in the Second Quarterly Report. However, a brief review with respect to the detection of SCC is presented in the following paragraphs.

In general, SCC starts at the surface of an originally flawless material; the detection of SCC in its very early stages involves studying the surface. Ultrasonic Rayleigh waves are an excellent means for detecting SCC in a nondestructive manner and are adaptable for field testing of parts in service, because they are very sensitive to surface conditions.

Rayleigh waves can propagate on the surface of a solid whose thickness perpendicular to the surface is large compared with the wavelength. Their amplitude decreases exponentially with increasing depth below the surface. At a distance of 1 wavelength below the surface, the amplitude of vibration is less than 10% that at the surface. Further, the amplitude of the waves is attenuated as it travels over the surface of the material.

In the early stages of SCC, pits and microcracks appear on the surface of the part. Once initiated, these microcracks join together to form larger cracks which eventually, under the applied tensile stress, cause the final fracture of the part. These microcracks are capable of reflecting most of the ultrasonic energy directed against them, thus rendering themselves detectable.

The ultrasonic technique for the detection of SCC may be explained as follows: A radio frequency (RF)signal generator emits electric pulses which are applied to a piezoelectric crystal and produce sound wave pulses at the RF. In this work, the crystal was barium titanate and the frequency was 4 MHz. However, if higher frequencies are used, a thinner layer of the surface is probed and smaller defects are detectable. The probe containing the transducer is brought into contact with the test specimen through a coupling medium, and the ultrasonic waves enter the specimen. If there are any flaws or discontinuities in the direction of sound propagation, part of the sound energy will be reflected back to the transducer where it will be transformed to an electrical pulse for display on the oscilloscope screen of the ultrasonic apparatus.

Of the different methods used for the production of Rayleigh waves, the so-called "wedge method" produces the strongest surface waves in this frequency range. The wedge angle is chosen so that refraction at a right angle results. By the application of Snell's law, the wedge angle, θ, is given by

$$\theta = \sin^{-1} \frac{V_1}{V_2}$$

where V_1 = wave velocity in the wedge material
V_2 = wave velocity in the test specimen

The longitudinal waves, which the barium titanate crystal generates, travel through the plastic wedge (Lucite, in the Krautkrämer MOB probe used in the work) and are transformed at the interface between the plastic and the test specimen into surface waves. There must be a coupling

liquid between the probe and the test specimen or the waves will be reflected almost 100% by the air gap.

2. Equipment

A Krautkrämer ultrasonic flaw detector type USIP 10W with a frequency range of 0.5 to 15 MHz was used. The instrument has the amplification calibrated in decibels, which makes it possible to compare the heights of two echoes directly.

For the determination of the optimum wedge angle, which process is described in detail in the next section, the Krautkrämer miniature universal variable angle probe type MUWB was used. Following the determination of the optimum angle, a Krautkrämer miniature fixed angle surface wave probe type MOB, which is much smaller than the MUWB, was used.

Both of these probes generate surface waves which travel in a beam with very small divergence. Fig. 82 shows the Krautkrämer ultrasonic flaw detector with the miniature fixed angle surface wave probe type MOB affixed to a U-bend tensile specimen. In addition, the Krautkrämer miniature universal variable angle probe type MUWB is shown at the left-hand side. Some measurements were made with an Arenberg PG-650 high power pulse RF generator.

3. Transducer wedge angle and coupling medium

V_1 for the Lucite coupling block is 2730 m/sec, and V_2 for shear waves in Al-7075 is 3080 m/sec. Thus, θ is about 62°. The best experimental value of θ lies close to this value.

Lucite was selected as coupling block because it meets the requirement that $V_2 \geq V_1$ for the generation of surface waves, and also has high attenuation: 7.0 db/cm at 5.0 MHz. This high attenuation will minimize most of the disturbing echoes in the probe between the starting pulse and the coupling medium echo which result from reflections of the ultrasonic beam within the coupling block.

The theoretical angle determined above will not produce pure surface waves. One of the experimental factors, shown in Fig. 83, is

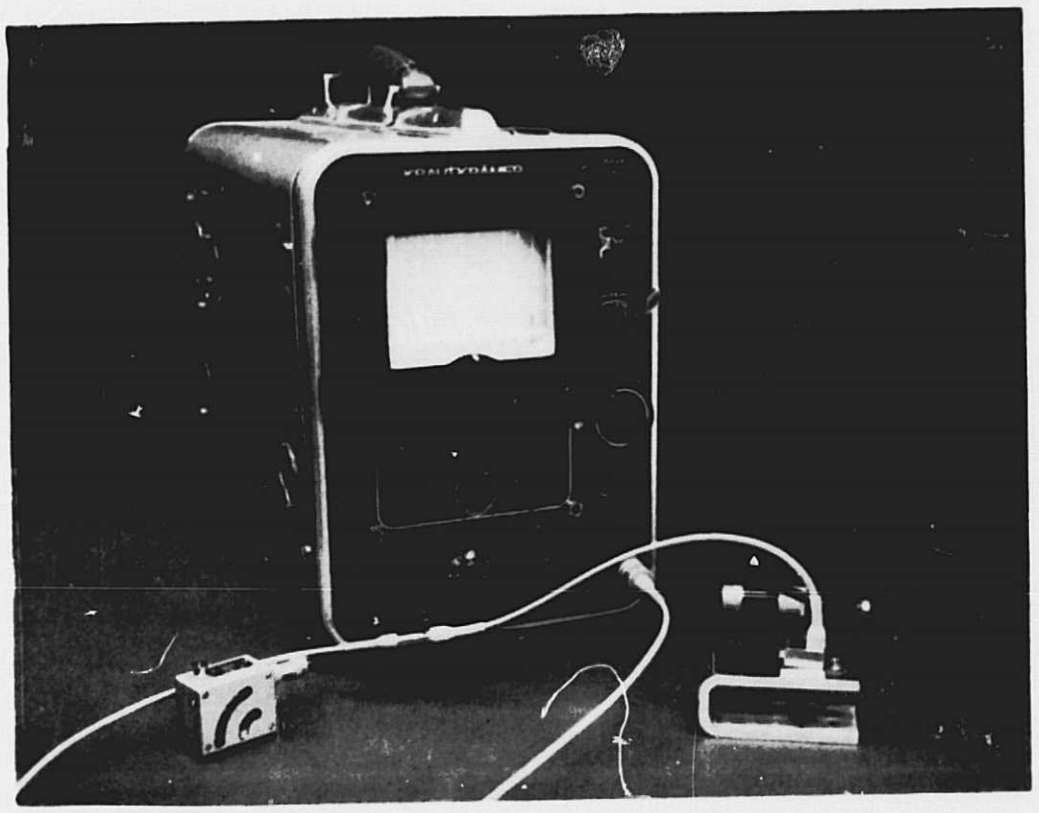

Fig. 82. Ultrasonic apparatus used (Krautkrämer), flaw detector type USIP-10W; miniature fixed angle surface wave probe type MOB (positioned on U-bend specimen); and miniature universal variable angle probe type MUWB (on the left)

Krautkrämer miniature universal variable angle probe, type MUWB

Krautkrämer miniature fixed angle surface wave probe, type MOB

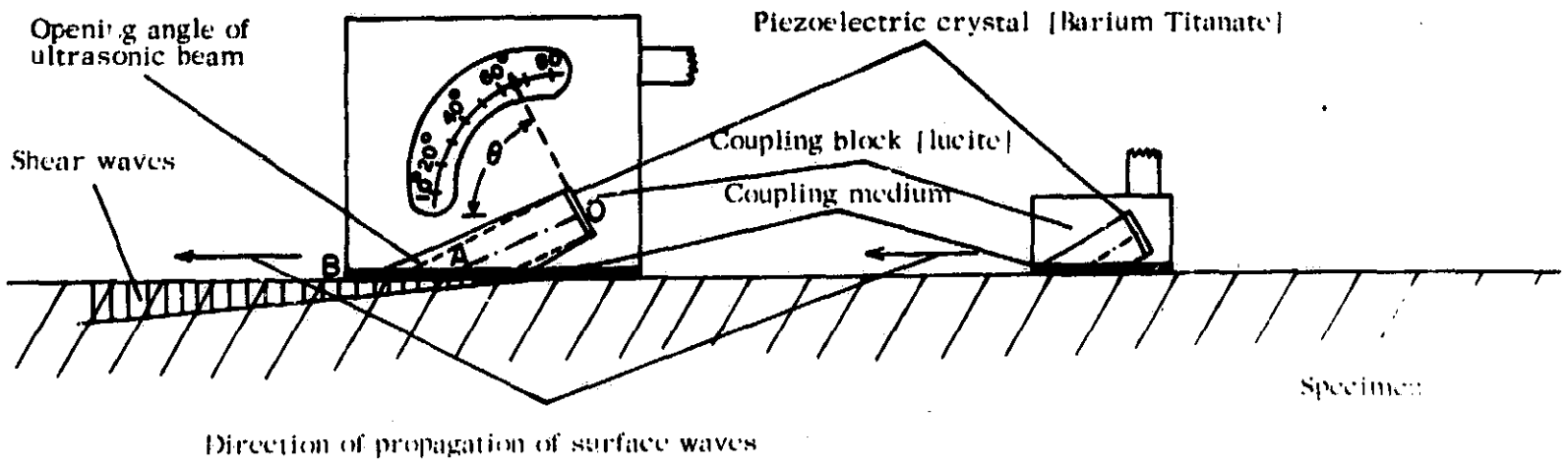

Fig. 83, Schematic diagram of surface wave probes used

the divergence of the longitudinal sound beam in the probe determined by the frequency, size, and shape of the crystal, and the distance OA. That is, part of the ultrasonic beam in the probe will produce shear waves in the test specimen.

The optimum angle was determined empirically with the variable angle probe MUWB, which is shown schematically in Fig. 83. To determine when pure surface waves are present, the extreme sensitivity of surface waves to damping is used. If the surface of the specimen over which the surface waves pass is touched with a wet fingertip, all echoes on the screen due to pure surface waves will disappear. This technique can be used to trace the location of an echo appearing on the screen due to a flaw or any other disturbance. To determine the optimum angle, θ is varied until the heights of the echoes from the surface of the test specimen are a maximum. The maximum energy in the surface waves was obtained at angles between 66 and 69°. An explanation for a range of values for θ instead of a single angle is that at different angles the path lengths to the free surface are unequal. This variable distance is indicated in Fig. 83 by the line AB. Surface waves traveling under the probe are greatly attenuated. The compensation between the efficiency of surface wave generation and the surface wave attenuation thus gives a range of angles. In the fixed angle probe, this distance (AB) is much less. The miniature fixed angle surface wave probe, type MOB, operating at 4 MHz was used in the subsequent work.

The following media were tested for acoustic coupling: water, glycerol, water and glycerol, "3-in-1" electric motor oil, white petroleum jelly, silicon lubricants, "Apiezon" vacuum greases, soft green Keer impression coumpound no. 2, and rubber cement. Even though most of these media were efficient, rubber cement proved the most suitable. The amount of ultrasonic energy transmitted to the test specimen is strongly dependent on the thickness of coupling medium and on the medium chosen. In addition, reproducibility is a problem. Rubber cement showed the best reproducibility and was used for the subsequent work. However, additional transducer design work could reduce some of the coupling problems.

4. Attenuation of surface waves

One of the most important parameters in ultrasonic testing is the attenuation of the Rayleigh wave as it propagates over the surface. The attenuation in general is caused either by the divergence of the ultrasonic beam or by the interaction the wave undergoes as it propagates through or over the medium. Measurements made included data on surface finish ranging from that produced by no. 36 grit paper to that produced by no. 2 polishing alumina (aluminum oxide, particle size 0.3μ) over distances up to 22 in.

The U-bend specimens used were highly polished but not optically flat. Their finish was designated as "buffed" in the attenuation investigation and was similar to the finish produced by no. 2 polishing alumina. A surface having a finish designated "as rolled" or "as received" in these measurements is the surface condition of the aluminum plates as received.

The relationship between the various types of abrasive grits and polishing compounds and the average depth of scratch (rms roughness) was given in Fig. 73. Results were obtained in both the long transverse and the rolling directions, and also included painted surfaces. In addition, data were obtained when the direction of propagation of Rayleigh waves was perpendicular and parallel to the direction in which the abrasive paper was moved to produce the surface finish.

A few typical experimental results will illustrate the attenuation investigation. Fig. 84 is a series of oscillograms showing the results for different probe-to-edge distances. Echoes A and B are from two successive edges of the test blocks. The decrease in the height of echoes from the edges of the test block shows the increasing attenuation with increasing path length. Plots of the relative amplitude of the echoes of the Rayleigh waves reflected from the edge of the test plates as a function of distance from the probe to the edge of the test block (with the surface finish as a parameter) were made. The relative amplitudes are the ordinates and are given in db as normalized with respect to the echo from the edge of the block. The probe-to-edge distances in inches are the abscissas.

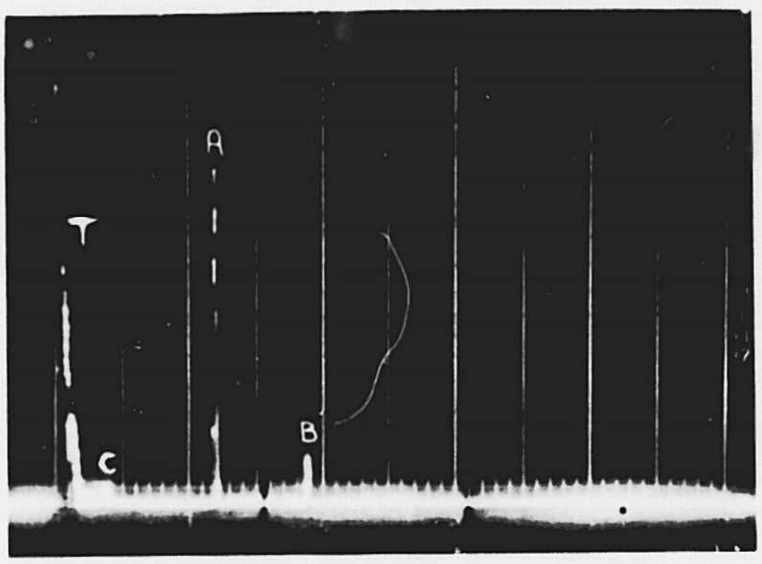

(a) Propagation distance = 1.625 in.

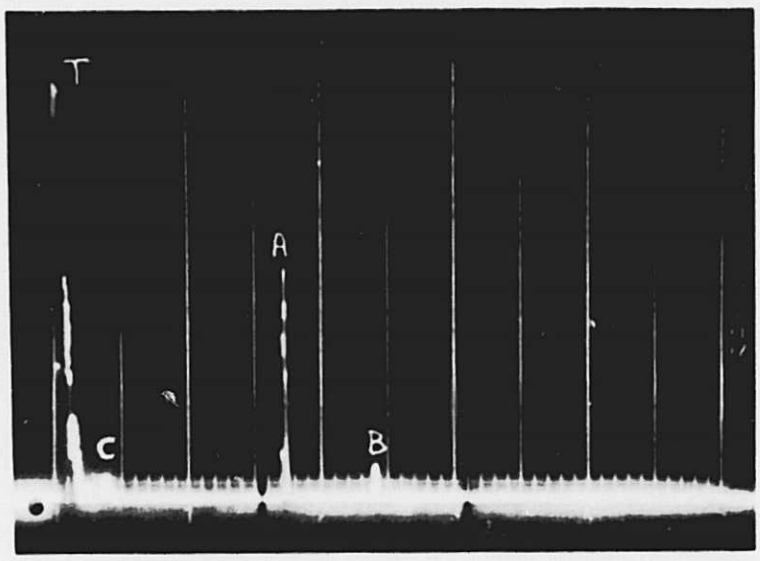

(b) Propagation distance = 2.875 in.

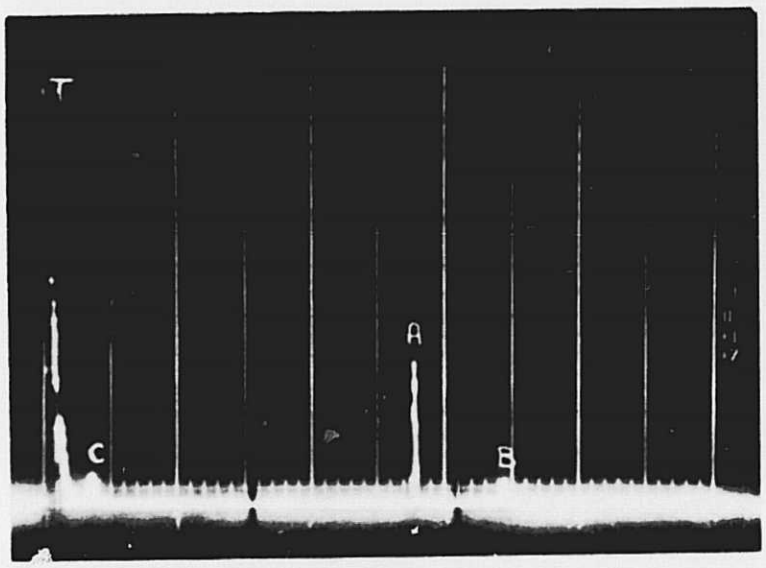

(c) Propagation distance = 5.313 in.

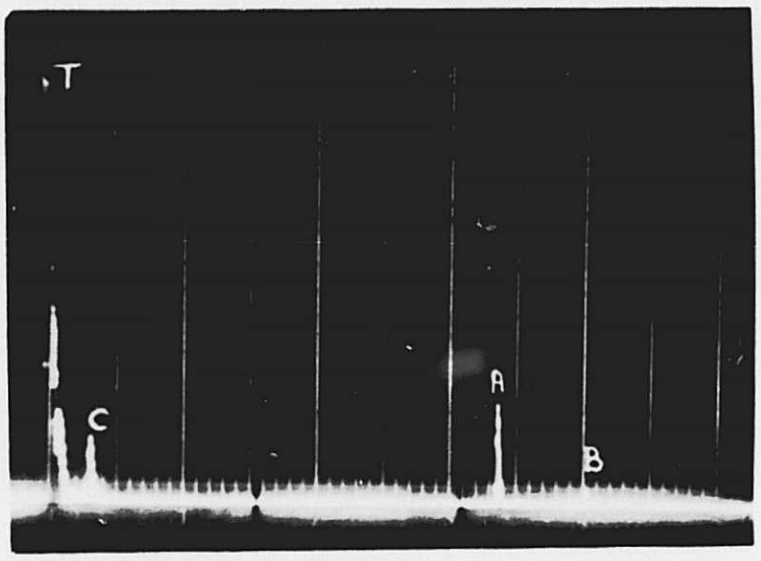

(d) Propagation distance = 6.750 in.

Fig. 84. Oscillograms indicating the reduction in height of echoes from two successive edges of the test block due to surface attenuation

Fig. 85 shows measurements in the long transverse direction for surface finishes produced by abrasive paper ranging from no. 36 to no. 180 grit, for the "as received" finish, and for painted surfaces. The Rayleigh waves propagated parallel to the scratches produced by the abrasive paper. The painted surface was produced by spray painting 320 grit finished surface with 2 mils of glossy white enamel (no. 1501 Krylon). The data show some scatter, but fall approximately on a straight line.

Fig. 86 illustrates the difference when the direction of propagation of Rayleigh wave is perpendicular or parallel to the direction in which the abrasive paper was moved to produce the surface finish. Fig. 86a is the oscillogram for a low gain setting of the oscilloscope, and shows the amplitude of these echoes compared to the big echo (on the right-hand side of the oscillogram) produced by the reflection from the edge of the test block. Fig. 86b is the same configuration as (a), but with the gain increased by 20 db. It shows details of the small echoes. Fig. 86c is the same as (b), but the direction of propagation of Rayleigh waves was along the lay of the surface finish. Comparison of Fig. 86b and c shows the difference in attenuation when the waves travel parallel and perpendicular to the lay of the same surface. The surface finish involved in parts (a), (b), and (c) was produced by no. 36 grit paper (average depth of scratch about 3.1 μ). For further comparison, an oscillogram (Fig. 86d) was obtained where the test conditions were identical to (c), except that the surface finish was produced by no. 320 grit paper (average depth of scratch about 0.8 μ). A considerable decrease of the small echoes is evident. These considerations could become crucial in the interpretation of small echoes relating to the detection of stress corrosion or other minute cracks.

Preliminary studies have also been made to investigate the propagation of Rayleigh waves at the boundaries of solid and liquid media. It was found that thin layers of liquids of finite extent (e.g., a drop of water, rubber cement, machine oil, and melted wax) give reflections with echoes of varying height, whereas a layer of hardened wax or rubber cement will partially or totally attenuate the surface waves depending on the area of

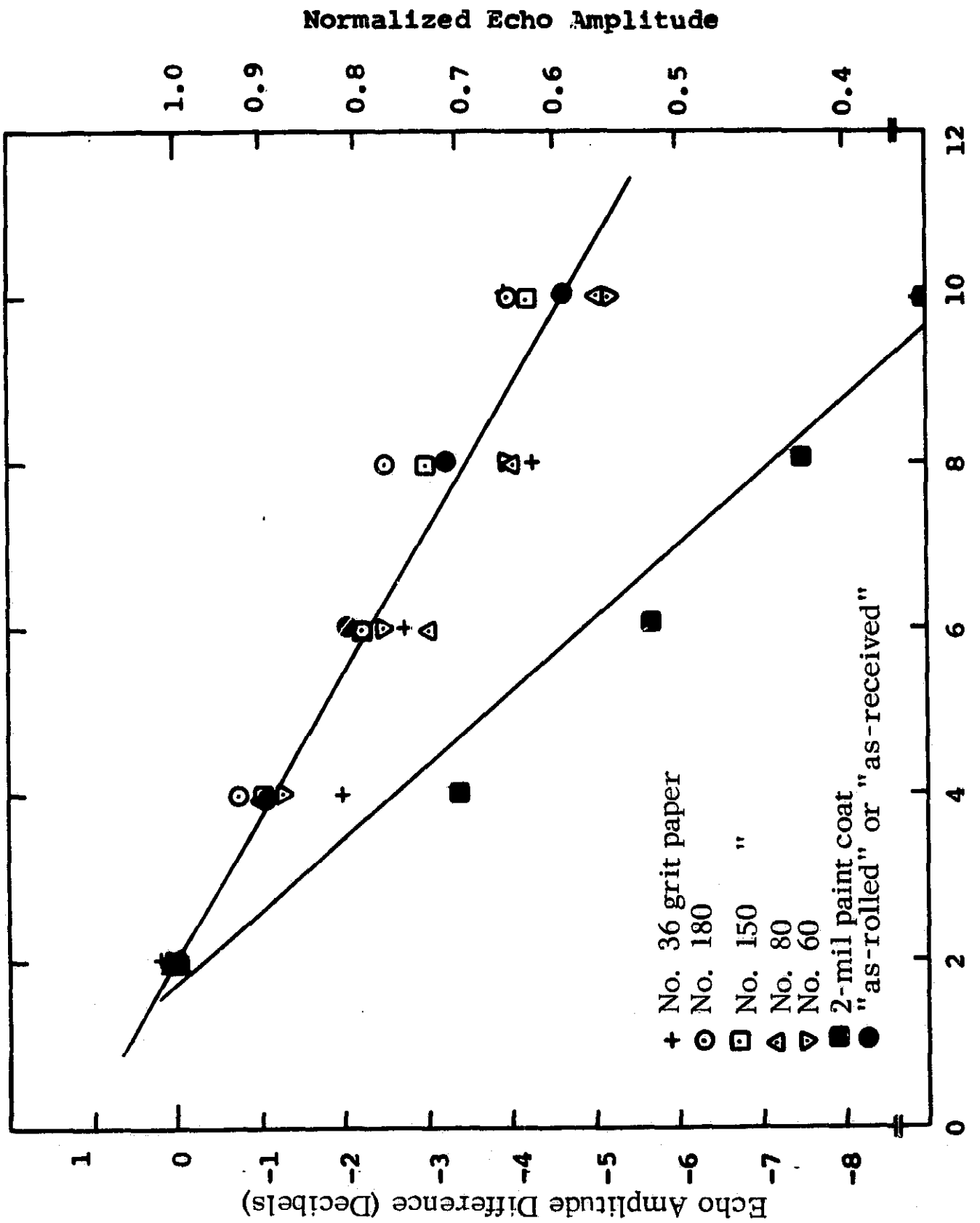

Fig. 85. Attenuation of Rayleigh waves in the long transverse direction

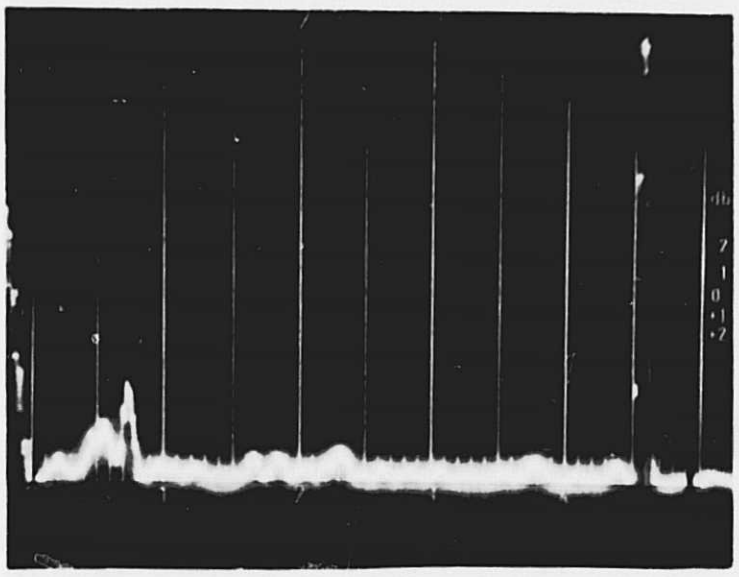

(a) Direction of propagation of Rayleigh waves perpendicular to lay of surface finish produced by no. 36 grit abrasive paper at low gain setting

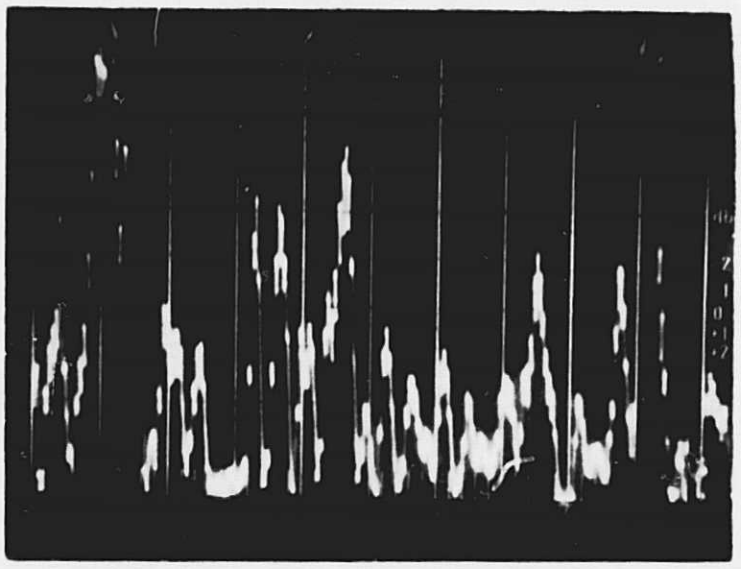

(b) Same as (a), but with a gain increase of 20 db

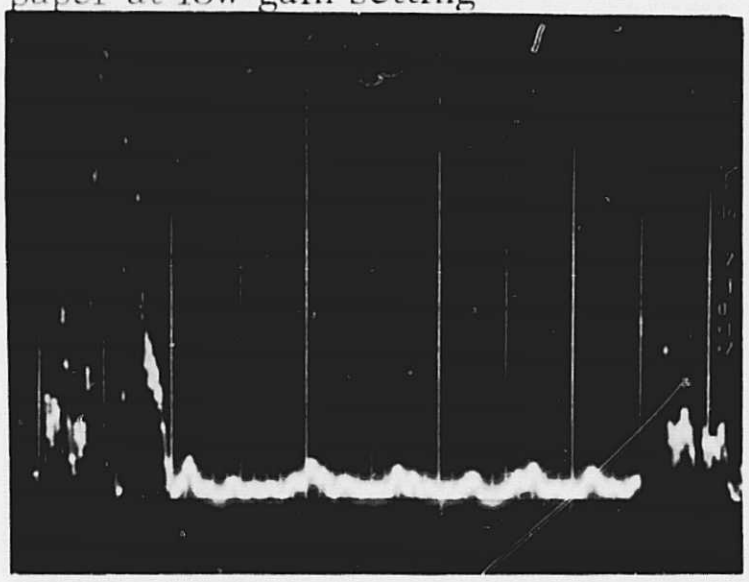

(c) Same as (b), but with the direction of propagation of Rayleigh waves parallel to the lay of the surface finish

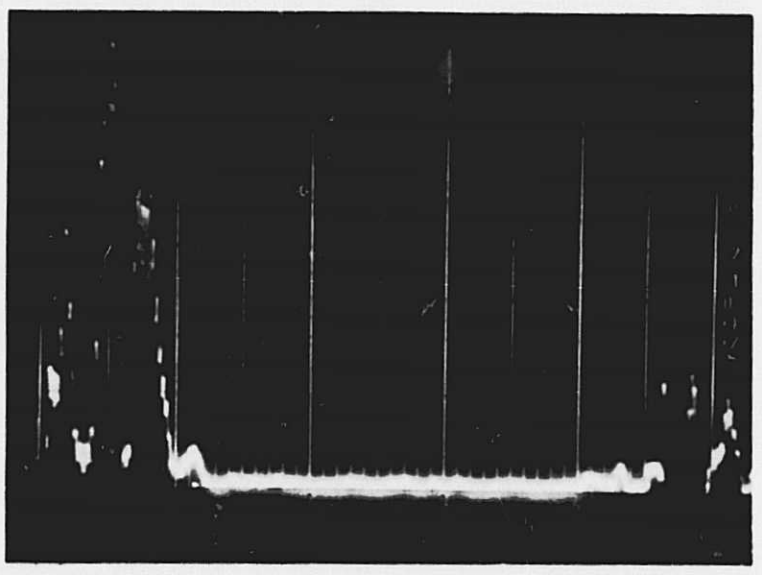

(d) Same as (c), but with the surface finish produced by no. 320 grit abrasive paper

Fig. 86. Oscillograms indicating the effect of the direction of the lay of the surface finish on Rayleigh waves

surface covered. It was also found that the Rayleigh waves were strongly attenuated with no reflection when the solid was covered with a liquid such as water on Al 7075. Monitoring of SCC in a liquid environment thus was not possible.

A synopsis of all our attenuation data for 7075 and 2219 is given in Table VI. From this table it is seen that the value of attenuation in the rolling direction for both alloys is about the same: 0. 15 db/cm for 7075 and 0. 14 db/cm for 2219. We also see that for 2219 the attenuation is greater in the rolling direction than in the long transverse, as expected, but the difference (0. 03 db/cm) is smaller than the corresponding difference (0. 09 db/cm) for 7075. A possible explanation is in the grain structure of these alloys. In the case of 7075, the grains are somewhat elongated, thus resulting in more grain boundaries per unit distance in the long transverse direction. This would increase the scattering for propagation in that direction.

We should note at this point that whereas the Rayleigh waves are not particularly sensitive to the different types of surface finish, eddy currents used in previous similar investigations were as shown in Fig. 71.

Several important conclusions may be drawn. The surface finish has a remarkably small effect on the attenuation, especially if the direction of finish is parallel to the direction of propagation. Even with a very rough grit (no. 36), attenuations of only 0. 3 db/cm were obtained. This is small compared with that produced by SCC (see Figs. 106, 107, and 108 for typical SCC attenuation data). The painted surfaces used here introduced an increase in attenuation of approximately two. Still, this is fairly small when compared with SCC.

To summarize: we can say that for most reasonably finished surfaces the exact character will not be too important in observing SCC effects. Even if the surface finish of parts to be tested is unknown or rougher than surface conditions investigated here, an attenuation curve can readily be obtained before actual testing begins.

Table VI. Attenuation of Rayleigh Waves on Plane Surfaces of Al Alloys at 4 MHz

Al Alloy	Propagation Direction	Surface Finish	Attenuation, db/cm	Remarks
7075 (T651)	Rolling	No. 36 grit paper and finer, and "as rolled"	0. 15	Rayleigh waves parallel to lay of finish
7075 (T651)	Rolling	No. 36 to no. 80 grit paper	0. 30	Rayleigh waves perpendicular to lay of finish
7075 (T651)	Long transverse	No. 36 grit paper and finer, and "as rolled"	0. 24	Rayleigh waves parallel to lay of finish
7075 (T651)	Long transverse	2-mil paint coat	0. 45	Rayleigh waves parallel to lay of finish
2219 (T37)	Rolling	No. 180 grit paper and "as rolled"	0. 14	Rayleigh waves parallel to lay of finish
2219 (T37)	Long transverse	No. 150 to no. 180 grit paper, and "as rolled"	0. 17	Rayleigh waves parallel to lay of finish

5. Stress calibration of U-bend specimens and creeping and relaxation

Measurements were made using a U-bend tensile specimen. The stress in the outer fiber of the bend of the U-bend samples can be calculated from the formula

$$\sigma_m = \frac{3\,LP}{2\,Wd^2}$$

where σ_m is the maximum stress, P is the applied load, and L, W, and d are the dimensions shown in Fig. 87. Values of the stress were found by elastically deforming the U-bend specimen using known loads and measuring the resulting deflection of its legs. Fig. 88a shows a stress corroded U-bend specimen still under stress, and Fig. 88b shows a fractured sample. The stress calibration curve was a straight line (see Fig. 89). A schematic diagram of the experimental procedure is also shown. The abscissa of this plot is the change in D and is given in terms of distance (mils) and also as a percent of the original separation (D) corresponding to zero load. The ordinate is given in terms of load applied, stress in outer fiber, and percent of yield strength which is 75,000 psi for Al-7075.

To investigate any possible deformation hysteresis caused by stressing the U-bend samples to the vicinity of 90% of the yield strength, the data for the stress-calibration curve were plotted as shown in Fig. 90. One set of points in this graph corresponds to the deflection of the legs of the U-bend sample when the load was increasing and the other when the load was decreasing. The plot is a straight line, indicating that the U-bend specimen returns to its original dimensions with no elastic energy trapped.

To investigate the effect of creeping and relaxation, the value of applied load was measured as a function of time at fixed stress levels. Typical results of this preliminary study are shown in Fig. 91. Stress calibration and sample geometry are crucial parameters in the SCC tests.

One problem is that different samples have different metallographic characteristics. We have even found small differences in tensile strengths of samples cut from different parts of the same plate. It was not possible to measure the strength of every U-bend, and some variation seems likely.

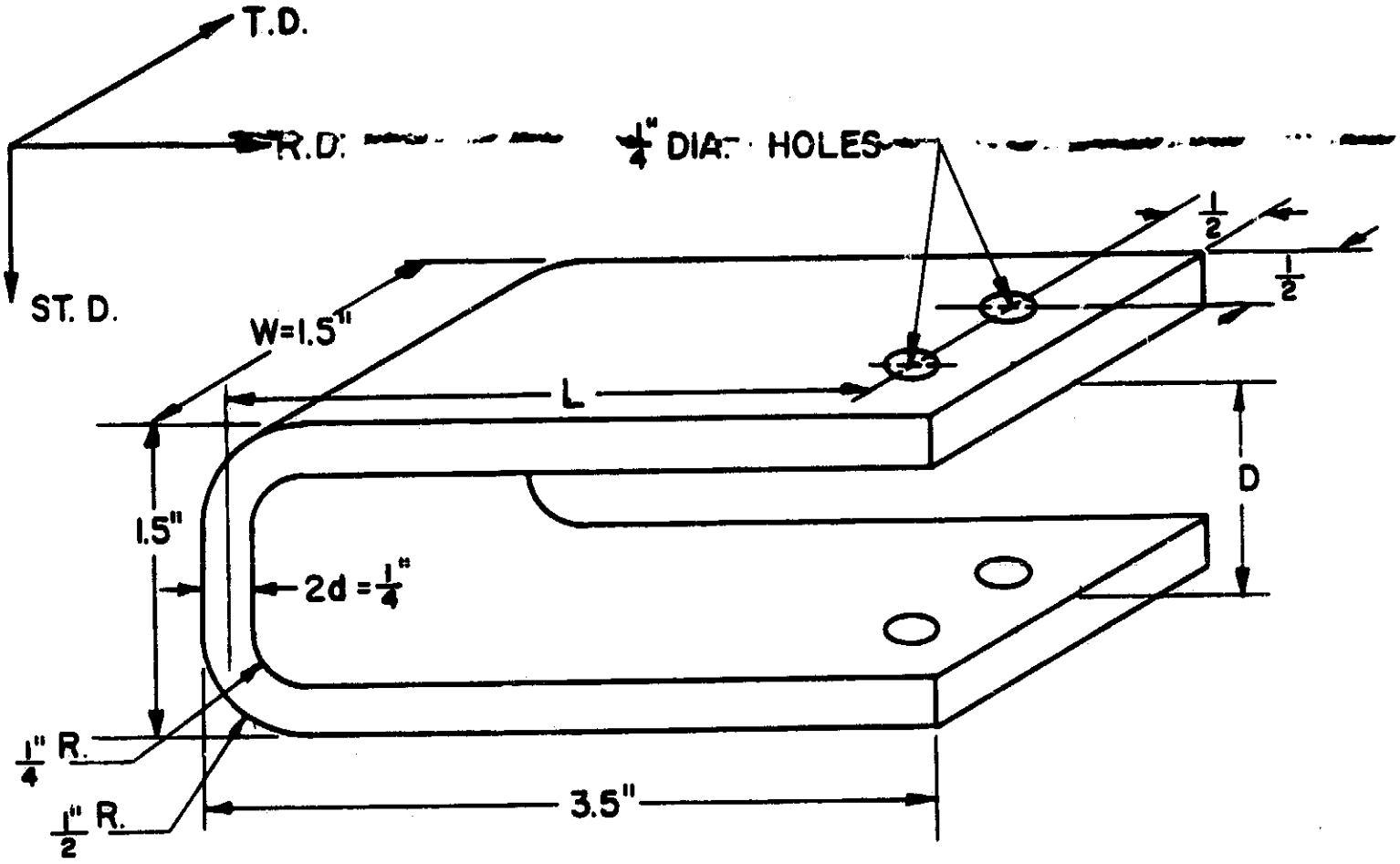

Fig. 87. U-bend tensile specimen and coordinate directions

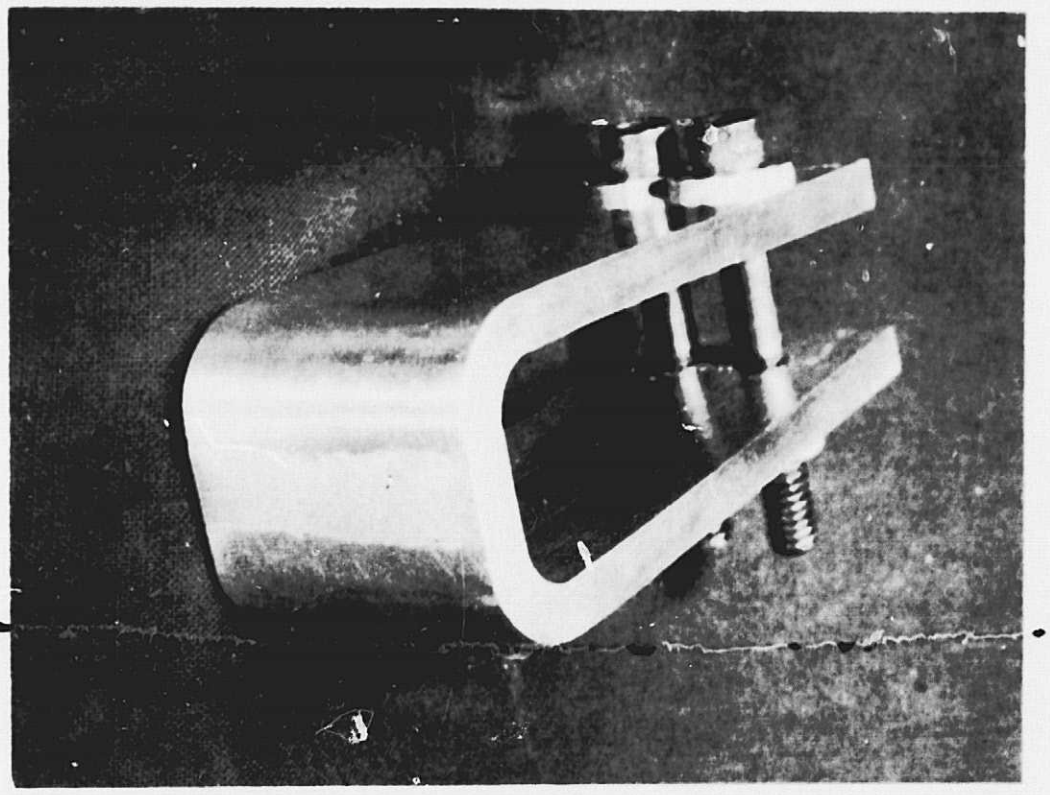

(a) After charge of 17.5 C/cm^2 (stress = 50000 psi)

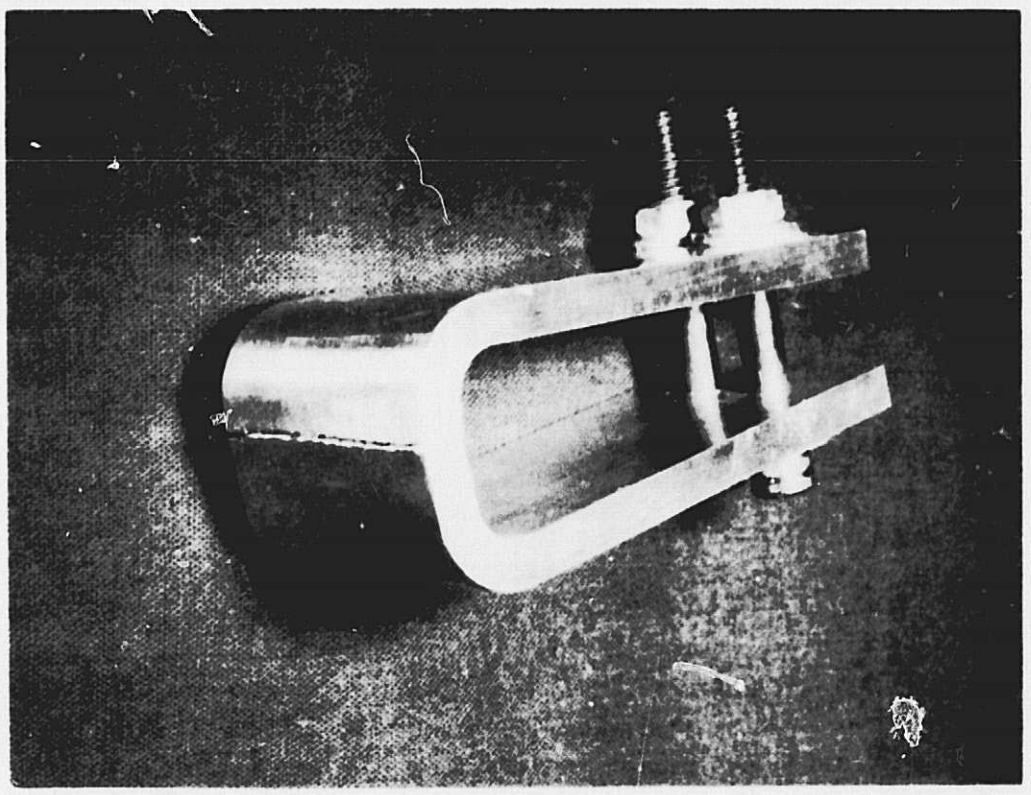

(b) 5 days after removal from solution

Fig. 88. U-bend specimen

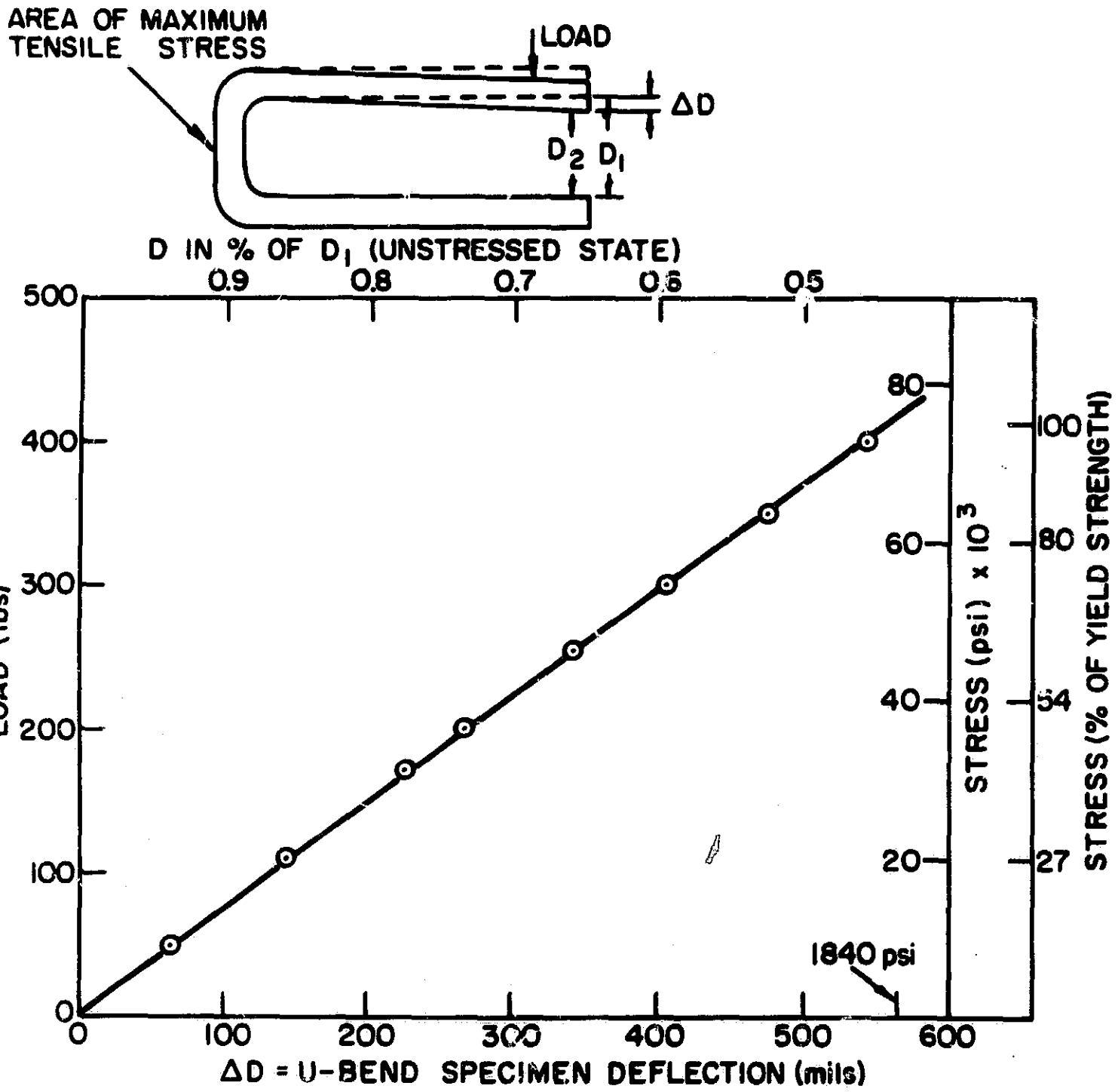

Fig. 89. Calibration curve relating deflection of U-bend tensile specimen to the stress applied on the outer fiber (experimental procedure shown)

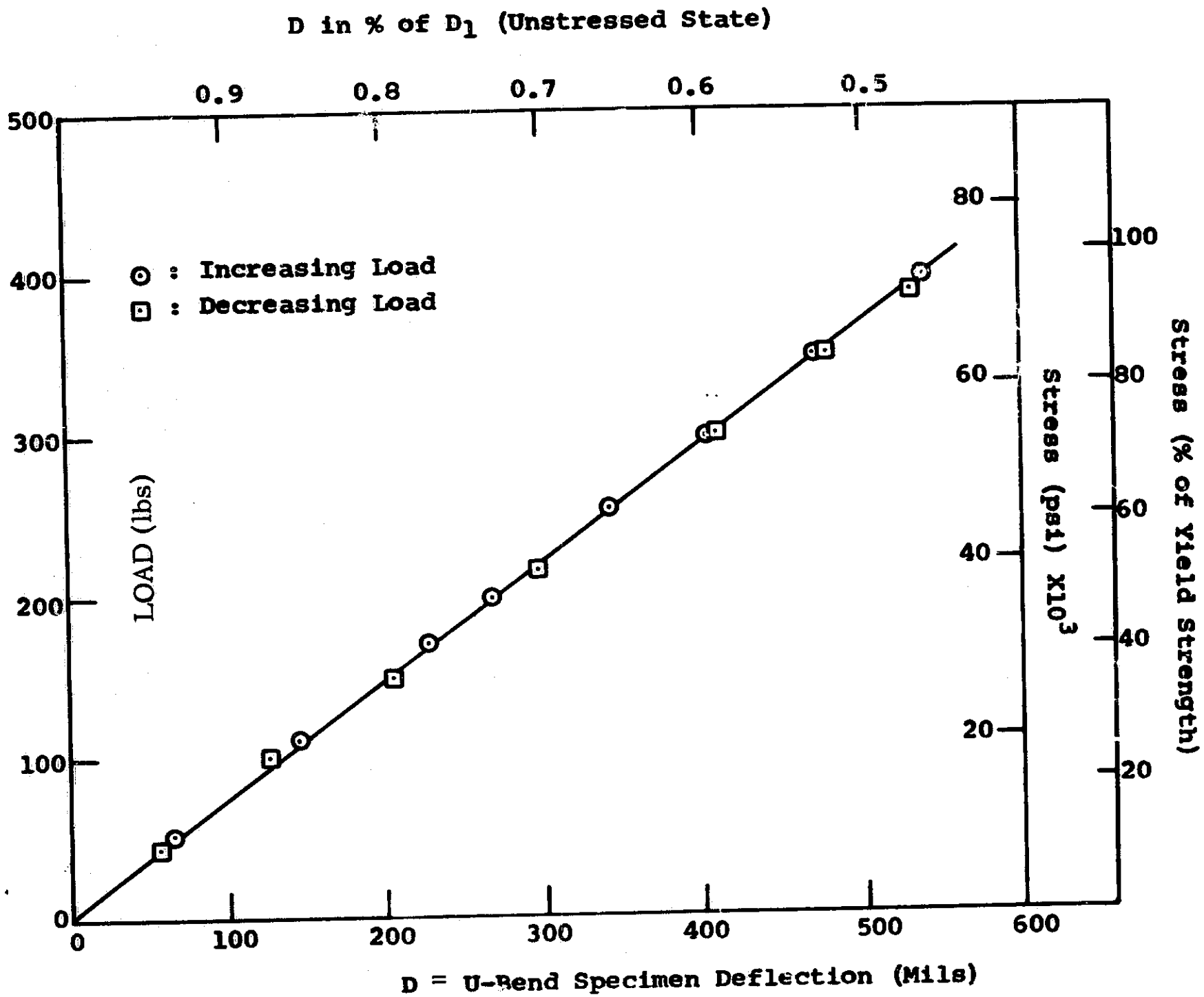

Fig. 90. Stress-calibration curve for U-bend specimens (indicates no deformation hysteresis)

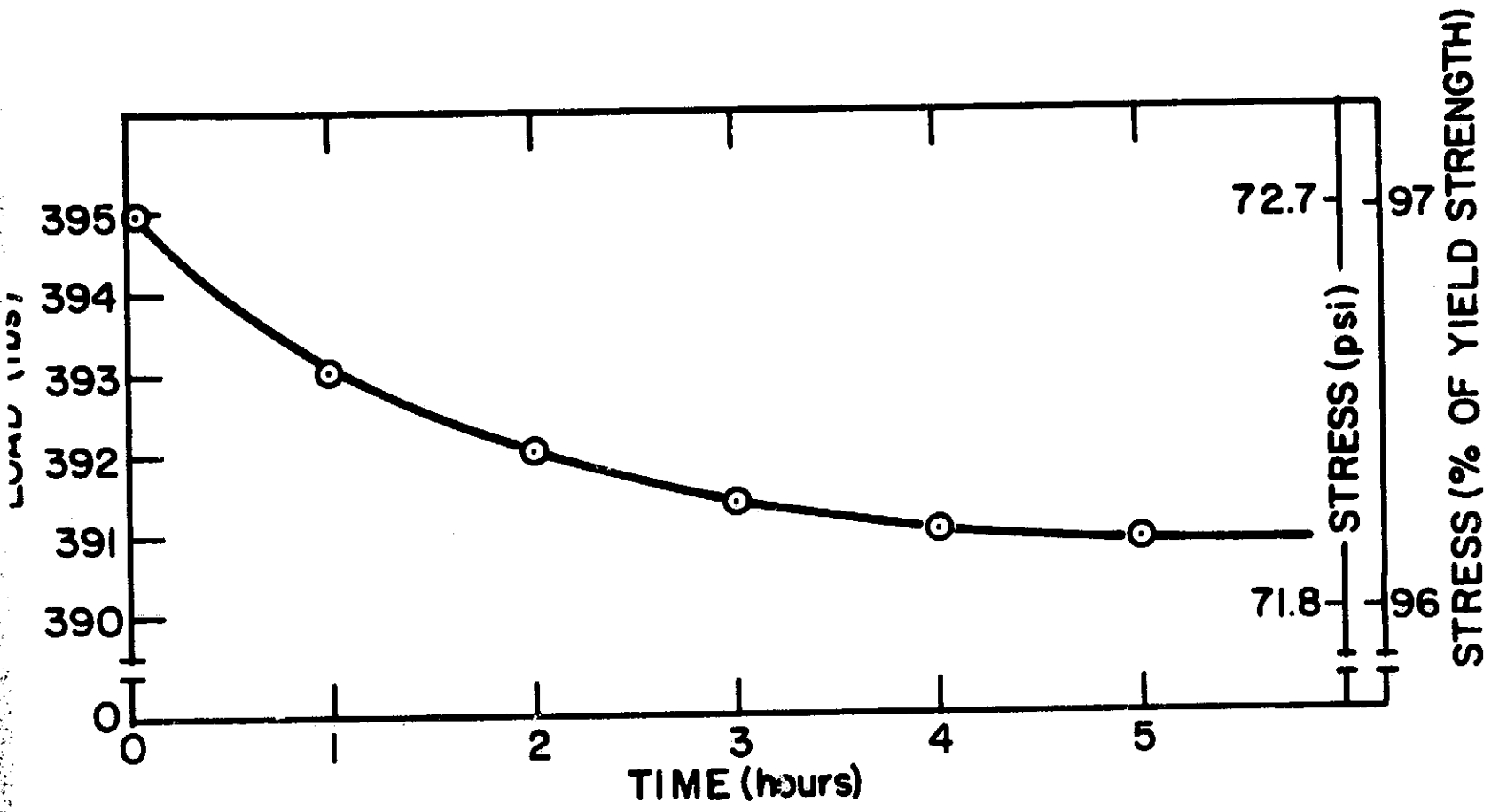

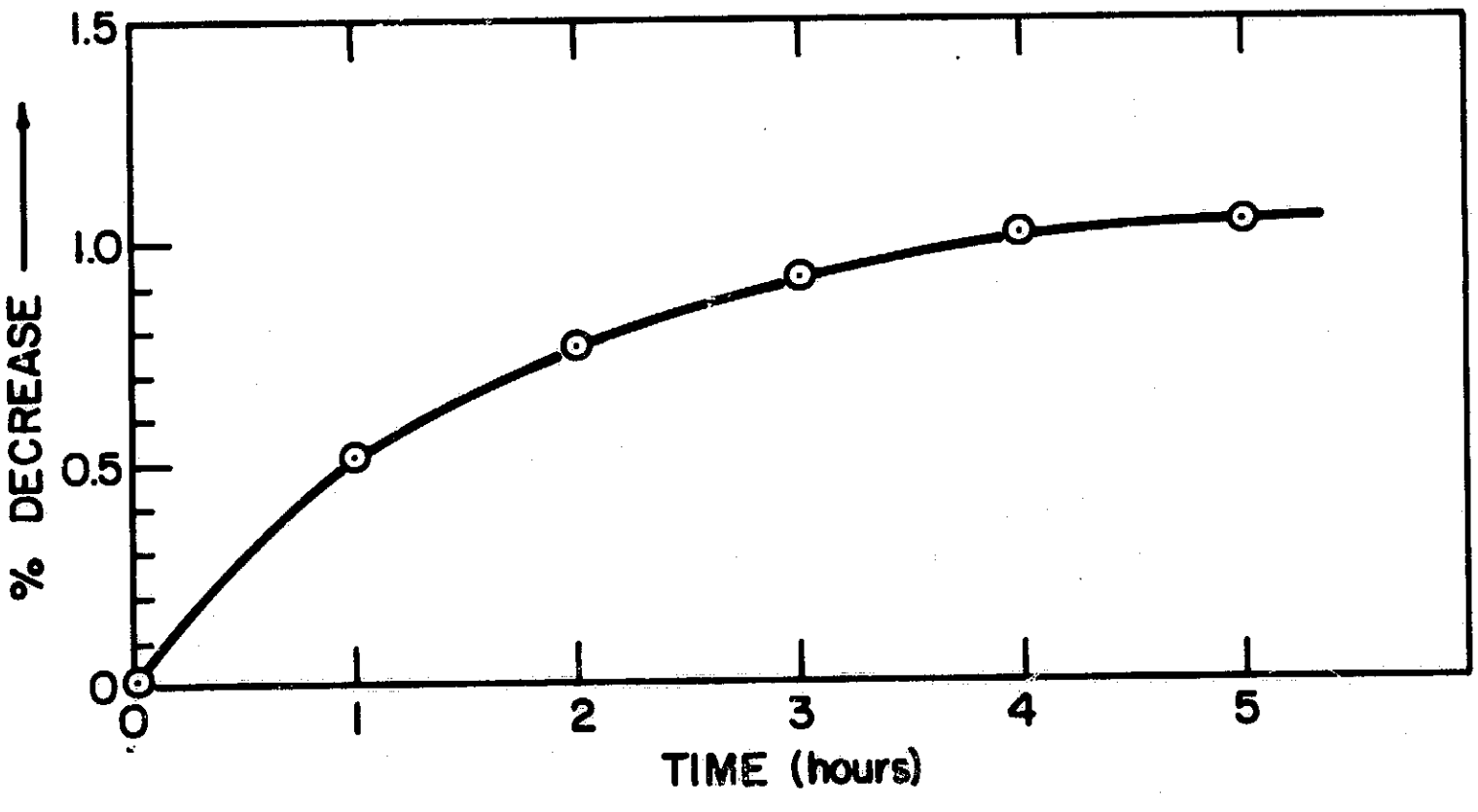

Fig. 91. Typical results of creeping and relaxation measurements

An example of the variability depending on the source of the material is illustrated in Fig. 92 which is a stress-calibration curve for the U-bend specimens. The abscissa of this plot is the change in D (separation between the legs of the U-bend sample) and is given in terms of mils, and also as a percentage of the original separation at zero load. The ordinate is given in terms of applied load, stress in the outer fiber, and percentage of yield strength. The three U-bend specimens tested for this plot came from three different plates of 7075 used during this contract and designated as series A, B, and C. The thickness of these samples at the bend was the same and equal to the nominal value of 0. 250 in. The graph indicates that even though the samples were geometrically identical, their stress-calibration curves were not. For instance, at 90% of the yield strength, the corresponding deflections for U-bend specimen series A, B, and C are 0. 507, 0. 525, and 0. 493 in. Thus, if a series C sample is to be stressed to 90% of the yield strength using the calibration curve for series B, the actual stress of the specimen will be about 96% of the yield strength, and its SCC life will be drastically shortened.

Stress-calibration curves were also prepared for 2219 (T37). The 0. 2% offset yield strength was taken as 44000 psi. The load deflection curves for this alloy are shown in Fig. 93. Three of the curves correspond to U-bend specimens no. 6D, 18D, and 42D, which originated from the sample plate, but with thicknesses at the bend of 0. 248, 0. 250, and 0. 252 in. , respectively. The fourth curve is for a sample coming from a different plate with a thickness at the bend of 0. 251 in. The dashed line in this graph, included for comparison, is the average for series A, B, and C of the 7075 U-bend specimens.

The graph illustrates the effect of the different origins of the samples and the shifting of the load-deflection curves due to differences in specimen thickness at the bend. The deflection of the legs, D, is proportional to σ_m (assuming $d \ll L$)

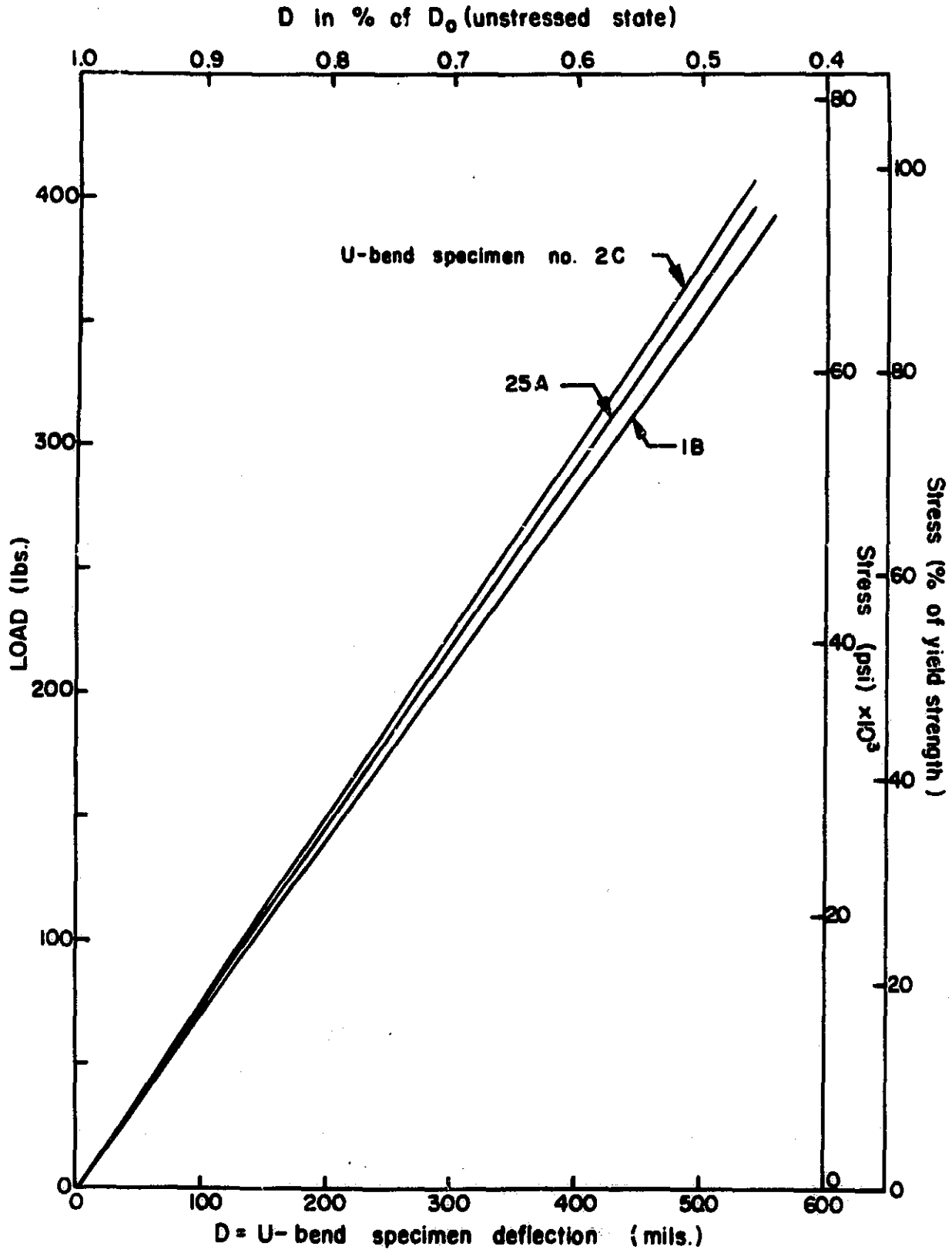

Fig. 92. Calibration curve relating the deflection of U-bend specimens to the applied stress on the outer fiber at the bend for 7075 (T651) (curve illustrates variability of plates A, B, and C)

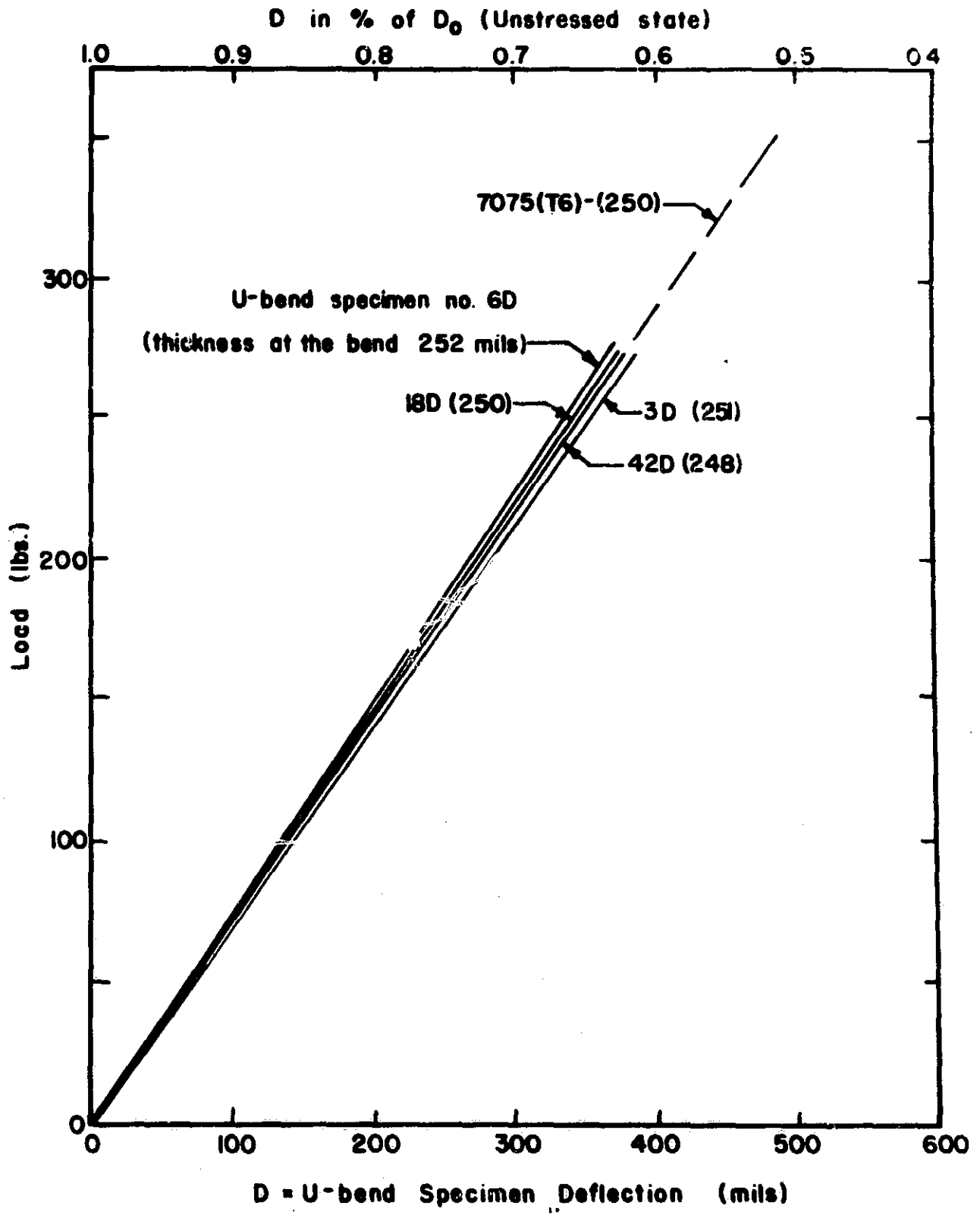

Fig. 93. Calibration curve relating the deflection of U-bend specimens to the applied stress on the outer fiber at the bend for 2219(T37)

$$D = \alpha \frac{L}{d} \sigma_m$$

where to first order α is a numerical constant depending only on the elastic properties of the material. Note that σ_m is only linearly dependent on d instead of quadratically as in the equation for the stress in the outer fiber of the bend of the U-bend samples (Section 5). Thus, the best way to stress the U-bends is to use a predetermined deflection rather than load. As a general practice, the thickness of the U-bend specimens was 0.250 ± 0.002 in., which would produce not more than a ± 1% variation in stress.

Another observation that can be made from Fig. 93 is that the average stress-calibration curves for 7075 and 2219 are very close. This implies that any errors in the determination of stress will be more severe for 7075 than for 2219, because of the spreading of the curves and the fact that the 0.2% offset yield strength of 7075 is almost double the corresponding value for 2219 when expressed in psi. In both alloys, the error will be smaller for low stress levels because of the smaller spread of the calibration curves. The machined U-bend samples were assumed to be free of internal stresses.

6. SCC testing of U-bend specimens

To investigate the effect of SCC, U-bend specimens were corroded galvanostatically at different levels of stress, current density, and time of exposure. The last two parameters can be combined to obtain the total charge producing the corrosion (C/cm^2). For this purpose, a constant rectangular area (3.5 cm^2) on the outside surface of the sample at the bend is exposed to a corrosive environment of 1N NaCl plus 0.05 acetate buffer (pH 4.7). Tests at a pH of 2.1 and 11.8 were also carried out.

The counter electrode in the SCC cell was a platinum wire in the form of a ring at the bottom of the cell. This helped to ensure a symmetrical current distribution in the cell. In some of the tests, the SCC cell was

enclosed in a bag which was filled with a nitrogen atmosphere while nitrogen was bubbled through the solution to remove any dissolved oxygen. No differences between this more elaborate procedure and leaving the cell exposed to air were detected. Most of the work was done at a frequency of 4 MHz, but other frequencies were also investigated.

The principles involved in detecting SCC ultrasonically in a U-bend specimen are as follows. Either the attenuation of the surface waves in going over the corroded area can be measured, or a reflection from developing microcracks can be observed on the screen of the ultrasonic apparatus, or both. For this purpose, two reference grooves were cut on the outside surface of the U-bend specimen where the Rayleigh waves were propagating. One of these was cut in front of, and the other behind, the area to be corroded. A schematic diagram of the experimental procedure, along with the expected oscillogram, is shown in Fig. 94. In this figure, groove G_1, cut in front of the area to be corroded, will give an echo of constant height which serves as a reference echo to compare with other echoes. Groove G_2, cut behind the area to be corroded, will give an echo of varying height depending on the amount of attenuation that the Rayleigh waves underto in propagating over the corroded area. The height of this echo will be compared with the height of the reference echo G_1 to determine the amount of attenuation and, in turn, the amount of SCC.

The pulses behind the echo of groove G_2 are from the holes at the end of the legs of the U-bend sample and from the edge of the specimen. However, these echoes do not disturb the results, because they are outside the area of interest in the oscillogram which is confined between the echoes from grooves G_1 and G_2. If any microcracks develop during stress corrosion, echoes will appear in the position corresponding to the area to be corroded in the oscillogram.

The procedure used in carrying out the tests was as follows. Reference grooves were cut on the U-bend specimens in the appropriate positions. Then the samples were stressed to a specific value for the

(A) EXPERIMENTAL PROCEDURE

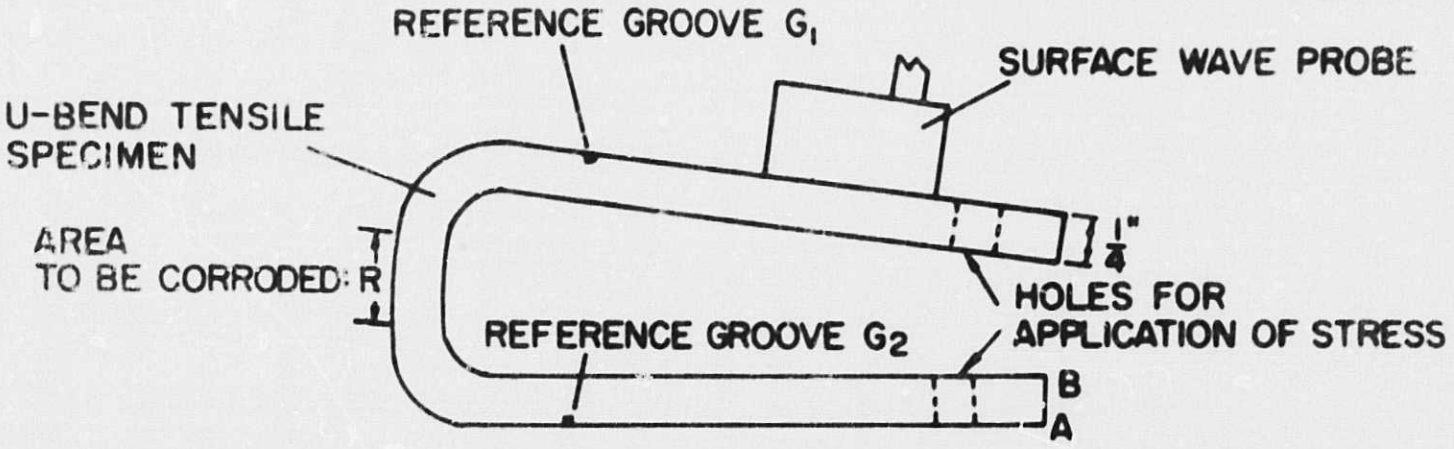

(B) EXPECTED OSCILLOGRAM

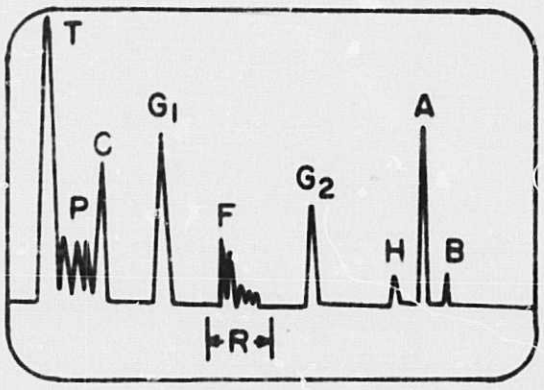

(C) ACTUAL OSCILLOGRAM

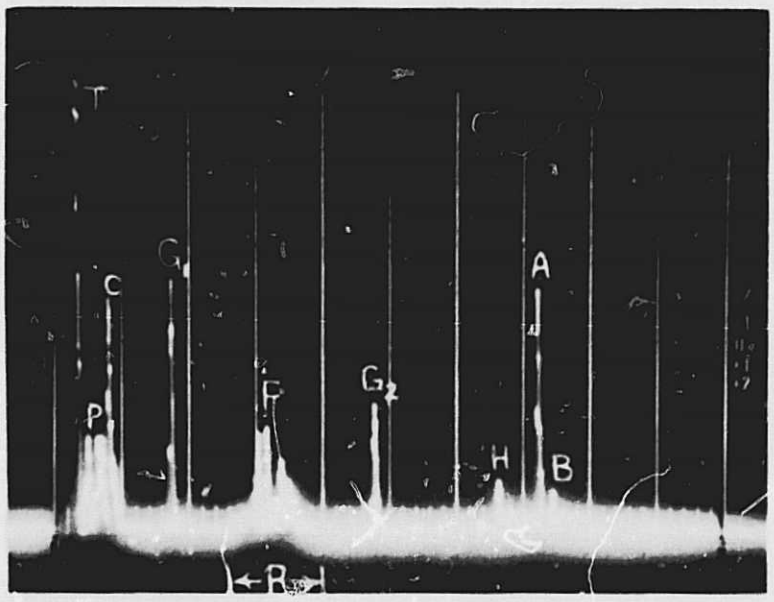

T = TRANSMITTED PULSE
P = ECHOES FROM PROBE
C = ECHO FROM COUPLING MEDIUM
G_1 = ECHO FROM REFERENCE GROOVE G_1
F = ECHOES FROM MICROCRACKS ON CORRODED AREA R
G_2 = ECHO FROM REFERENCE GROOVE G_2
H = ECHO FROM HOLE
A = ECHO FROM CORNER A
B = ECHO FROM CORNER B

Fig. 94. Test principle of detecting surface flaws with Rayleigh waves

particular test, taking into consideration creeping and relaxation. At that point, an oscillogram was taken for reference purposes. The U-bend specimen was corroded for the specific values of the parameters (current, exposure time) for the particular test. The sample was removed from the corrosive environment, cleaned, and tested ultrasonically and with eddy current. The measurements after each set of corrosive conditions were first taken with the stress applied and then after the stress was removed, so that the results of the "loaded" and "unloaded" states could be compared. The specimen was then corroded for another period of time and the measurements were repeated.

Three methods of ultrasonically measuring SCC damage are schematically illustrated in Fig. 95. In the first method, shown in part (a) of Fig. 95, the relative difference between the echoes of the two reference grooves G_1 and G_2 for various SCC states is measured. The second method can be used when echo G_2 is completely attenuated due to the SCC. In this method, shown in part (b) of Fig. 95, the relative height of the major flaw (echo F) above the average "grass" in the corroded area R is measured. Alternatively, the difference in echo amplitude between echo G_1 and the flaw echo F can also be used. The third method, which is shown in part (c) of the same figure and is not as consistent, is used when a number of flaw echoes are present. In this method, the sum of all relative echo heights is used as a measure of SCC damage. Of the three methods, method (a) proved to be the most consistent and sensitive to SCC and was generally used subsequently.

A special assembly was used to ensure a fixed position of the ultrasonic transducer during the tests. This assembly consists of a jig which can be clamped rigidly to the U-bend samples. The ultrasonic probe is coupled to the surface of the sample using a thin layer of a coupling medium (rubber cement) and is held rigidly in position by the adjusting screws of the jig. This assembly ensures that there is no linear or rotational displacement of the probe during the experiments, and thus successive oscillograms can be taken with the exact same probe position. This is essential in observing changes of echoes and comparing successive

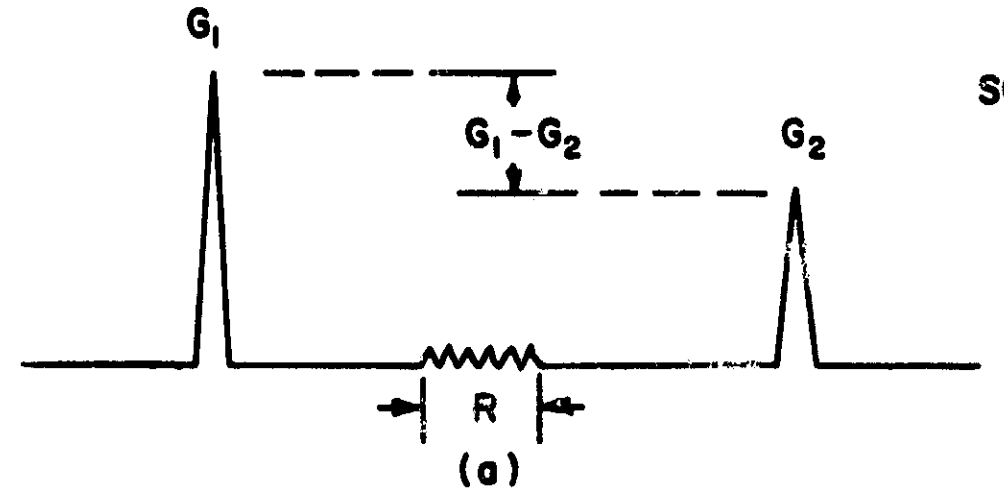

SCC MEASURE : $G_1 - G_2$

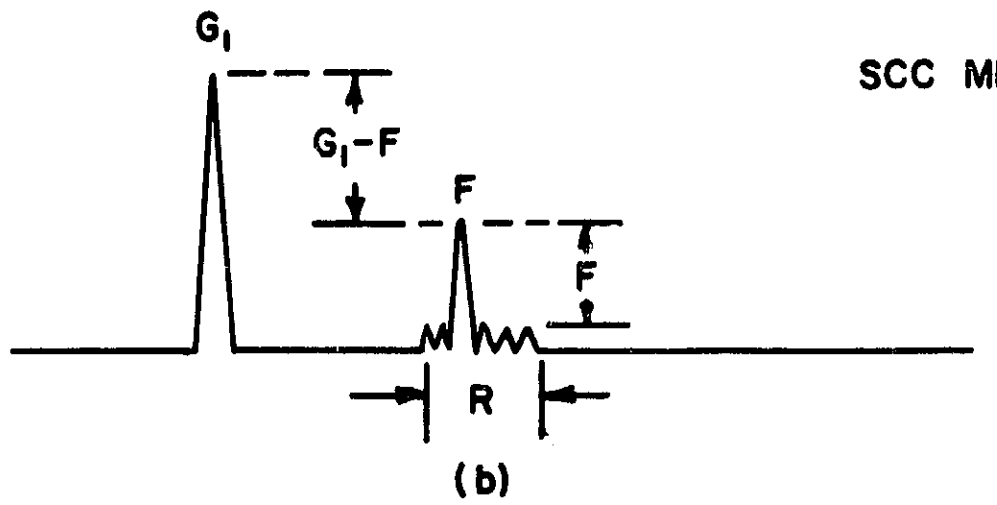

SCC MEASURE : F or $G_1 - F$

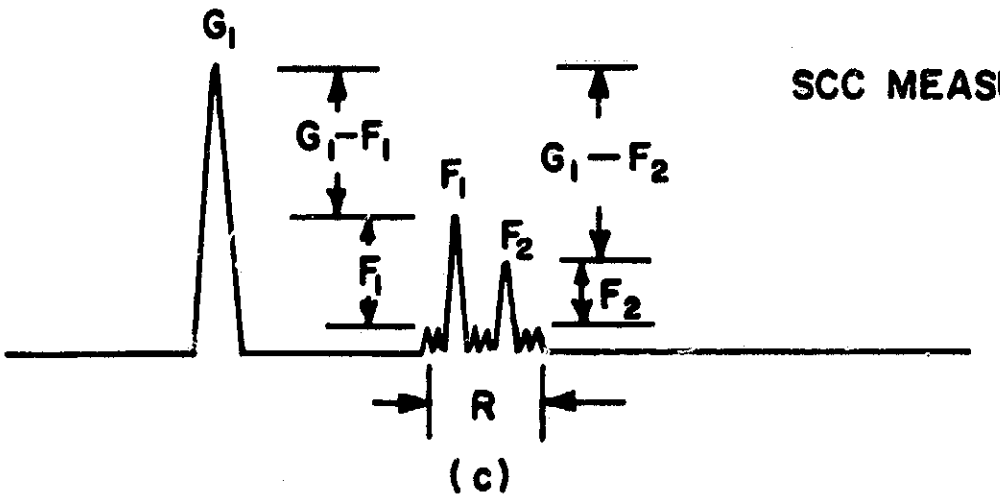

SCC MEASURE : $(G_1 - F_1) + (G_1 - F_2) + \ldots + (G_1 - F_n)$

or

$F_1 + F_2 + \ldots + F_n$

G_1 , G_2 = ECHOES FROM REFERENCE GROOVE
F_1 , F_2 = ECHOES FROM FLAWS
R = CORRODED AREA

Fig. 95. Schematic representation of three methods of quantitatively measuring SCC damage with ultrasonic surface waves

oscillograms, since a slight probe movement will alter the echoes and result in erroneous readings. An idea of the rotational sensitivity of the probe can be obtained by examining Fig. A-17 of the Appendix which illustrates the effect of reflector orientation on Rayleigh waves. It can be seen from that figure that the echo amplitude decreases to half its initial value at an angle of only 3°.

If the position of the probe is changed during the experiment, or if the probe is removed and then replaced, early detection of SCC damage is not quite as easy for the loaded and unloaded states. This is because any change in the oscillogram might not be distinguished from small changes in the coupling. One of the first ultrasonic indications of SCC is an echo comparable in amplitude to reflections from grain boundaries. The appearance of these reflections is strongly dependent on the position of the probe. To be detectable, the reflection from the SCC must be larger than that of the grain boundaries.

7. General galvanic corrosion (GGC)

In order to help differentiate between the effects of general galvanic corrosion (GGC) and SCC, tests were performed using exactly the same procedure as in the SCC case, except for absence of stress.

The results of ultrasonic measurements for 7075 and 2219 are plotted in Fig. 96. This figure shows the GGC damage, as measured by ultrasonic attenuation, versus the amount of corrosion in C/cm^2. The ultrasonic attenuation is measured in loss per unit distance (db/cm) rather than in terms of a round trip loss as is sometimes done. The graph indicates that the data for 2219 fall on a straight line and are even more consistent than the data for 7075 which also show a linear dependence on corrosion. No data could be obtained for 7075 after an exposure of 13 C/cm^2 (or 6.5 hr), because the reflection from the second reference groove was totally attenuated. The data for both 2219 and 7075 have approximately the same slope (0.67 db/cm per C/cm^2), but the 7075 has a slightly smaller x-axis intercept (0.3 C/cm^2). This implies that appreciable surface disturbance from GGC results from less attack in 7075 than in 2219. The x-axis intercepts are about 0.3 and 1.0 C/cm^2 for 7075 and 2219, respectively.

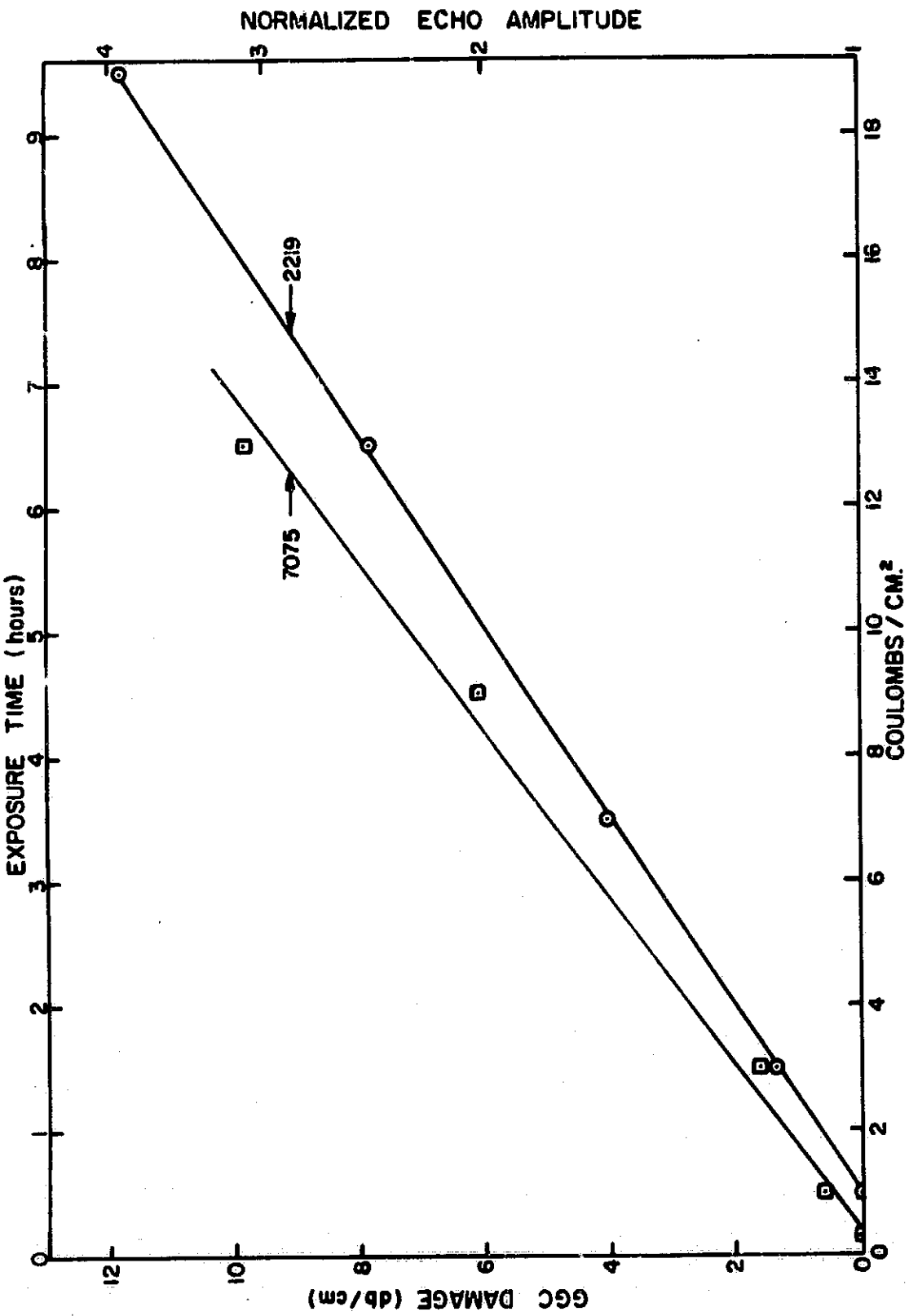

Fig. 96. Ultrasonic attenuation due to GGC as a function of charge at 0.53 mA/cm^2

This intercept should not be interpreted completely as the period that the alloy is not attacked by corrosion (incubation period), but rather in part as the threshold of ultrasonic detectability. This is illustrated by the photomicrograph (Fig. 97a) which shows the surface condition on the corroded area after an exposure of 1.0 C/cm^2 or 30 min (x-axis intercept) at a current density of 0.53 mA/cm^2. This picture clearly demonstrates the existence of corrosion damage (pits) even though it could not be detected ultrasonically. Part (b) of Fig. 97 shows the surface condition after an exposure of 19 C/cm^2 or 9.5 hr. The dark areas in this photomicrograph are deep pits that produced definite echoes and drastically attenuated the second reference echo.

Fig. 98 is a typical series of GGC oscillograms for 2219 showing the attenuation of the Rayleigh waves with increasing corrosion. Part (a) of this figure is the reference oscillogram showing the unattenuated echo from the reference groove (the tall echo to the far right), and parts (b) and (c) correspond to exposures of 7 and 13 C/cm^2 or 3.5 and 6.5 hr, respectively. Note the decrease in echo from the reference groove.

E. Detection of SCC With Rayleigh Waves: Results and Discussion

1. SCC tests at 90 and 60% of yield strength for 7075 and 2219

Investigations of SCC using ultrasonic surface waves have been made on U-bend specimens (both 7075 and 2219 alloys). For 7075, 90 and 60% of the yield strength correspond to 68000 and 45000 psi, respectively (75000 psi yield strength). For 2219, 90 and 60% of the yield strength correspond to 39500 and 26300 psi, respectively (44000 psi yield strength).

Typical results of ultrasonic examination are shown in Fig. 99 which is a series of oscillograms indicating the effect of SCC on 7075. The four oscillograms of this figure correspond to: (a) initial reference state, (b) "loaded" state after 15 min exposure, (c) stress just released, and (d) well relaxed state. The effect of this short exposure is readily seen in oscillogram (b), where a number of echoes are present from the corroded area, and the echo from the reference groove G_2 is greatly attenuated. When the stress was released, however, oscillograms (c) and (d) do not reveal any definite echoes from the exposed area, but echo G_2 is attenuated. This

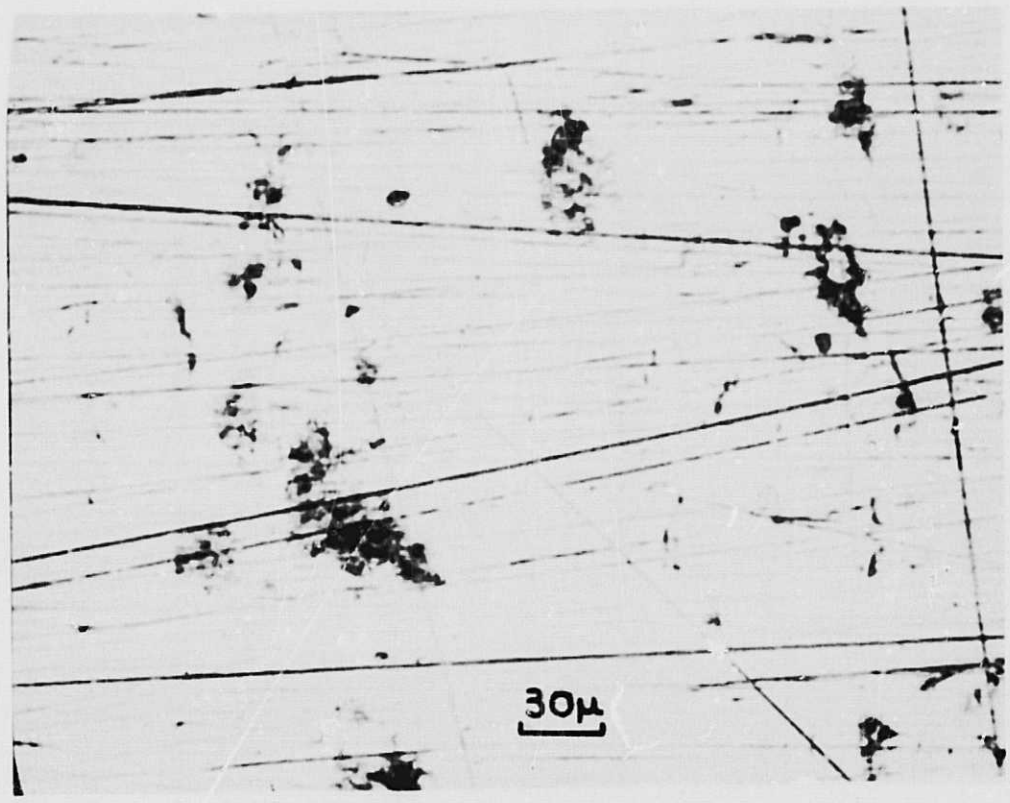

(a) After exposure of 1.0 C/cm^2 or 30 min

(b) After exposure of 19.0 C/cm^2 or 9.5 hr

Fig. 97. Photomicrographs of the surface condition of a 2219(T37) U-bend specimen illustrating the effect of GGC at 0.53 mA/cm^2 (300X)

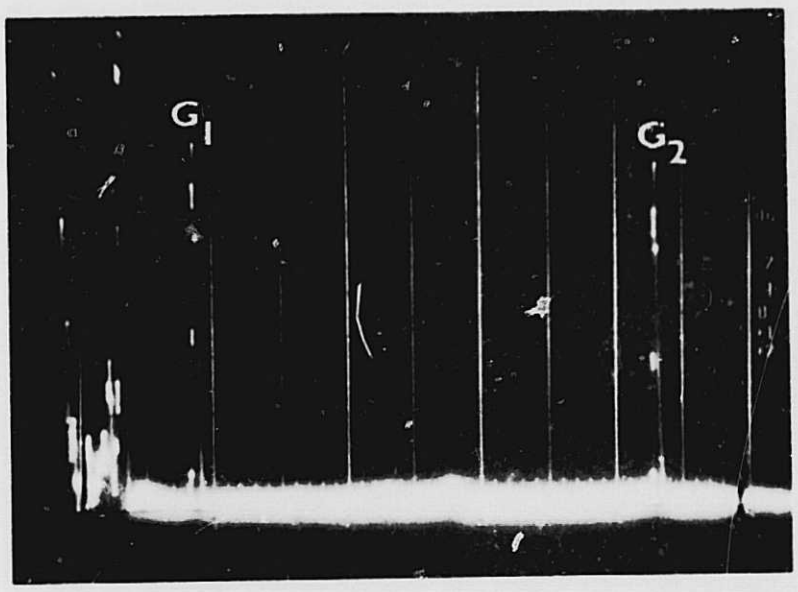

(a) Reference oscillogram

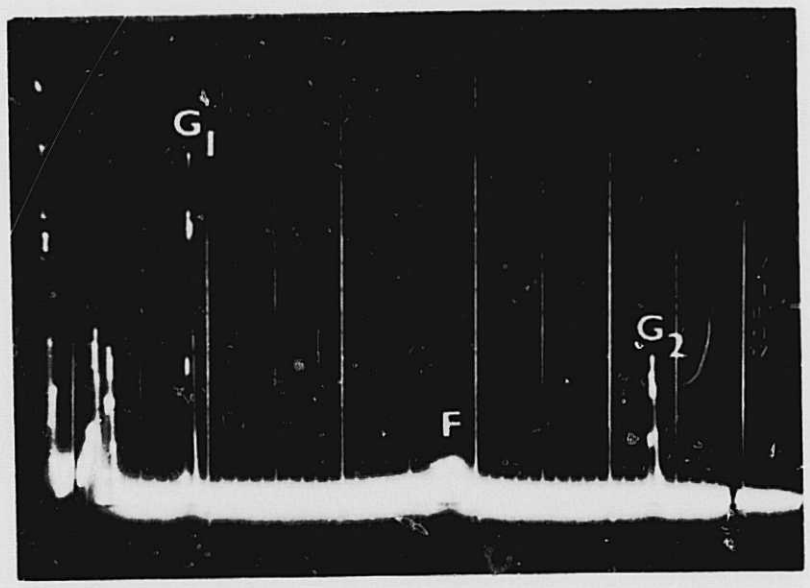

(b) After 7.0 C/cm^2 or 3.5 hr

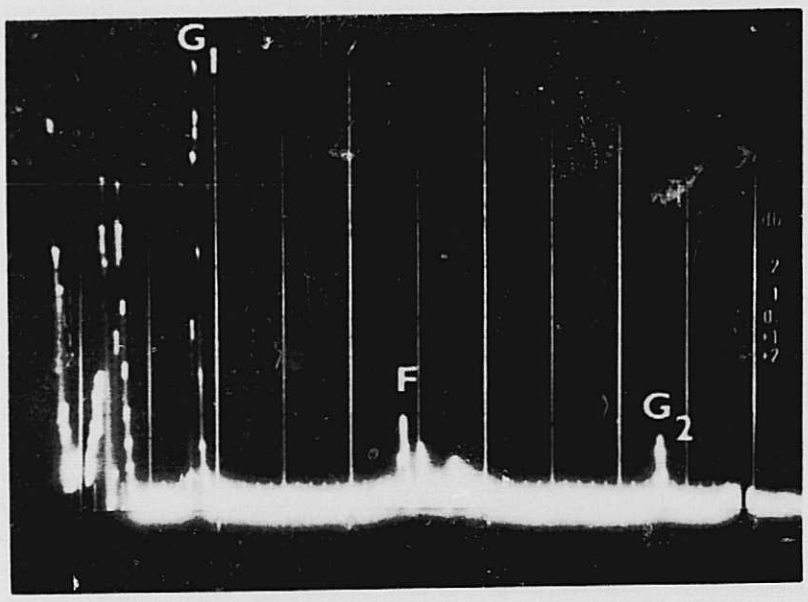

(c) After 13.0 C/cm^2 or 6.5 hr

Fig. 98. Oscillograms illustrating the effect of GGC for 2219(T37) at 0.53 mA/cm^2

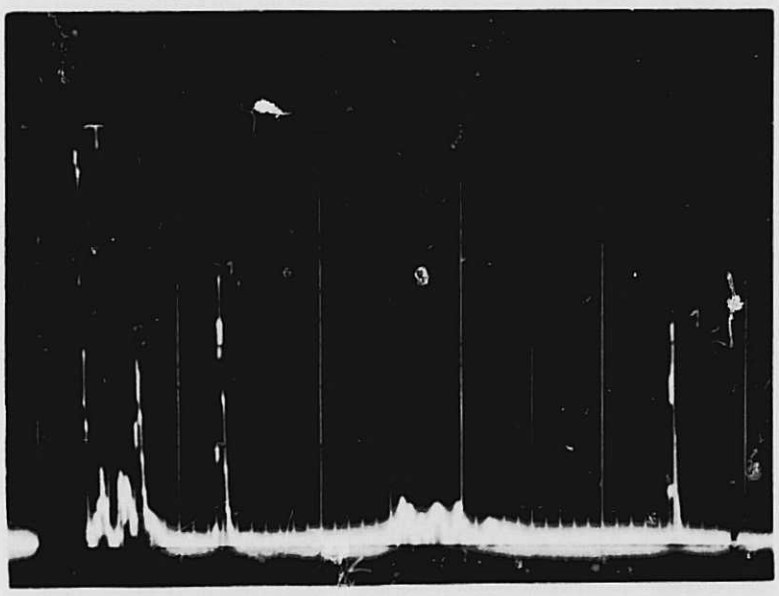

(a) Reference oscillogram

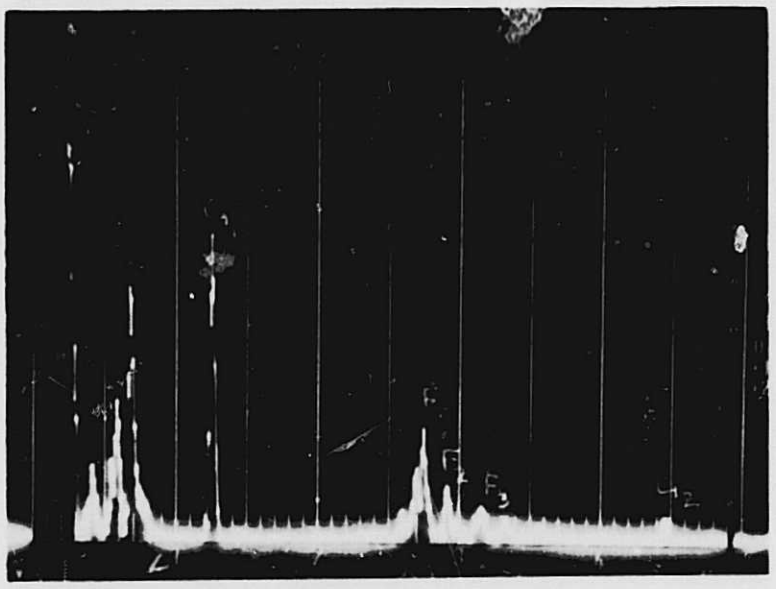

(b) After 0.5 C/cm^2 had passed at 90% of the yield strength ("loaded" state)

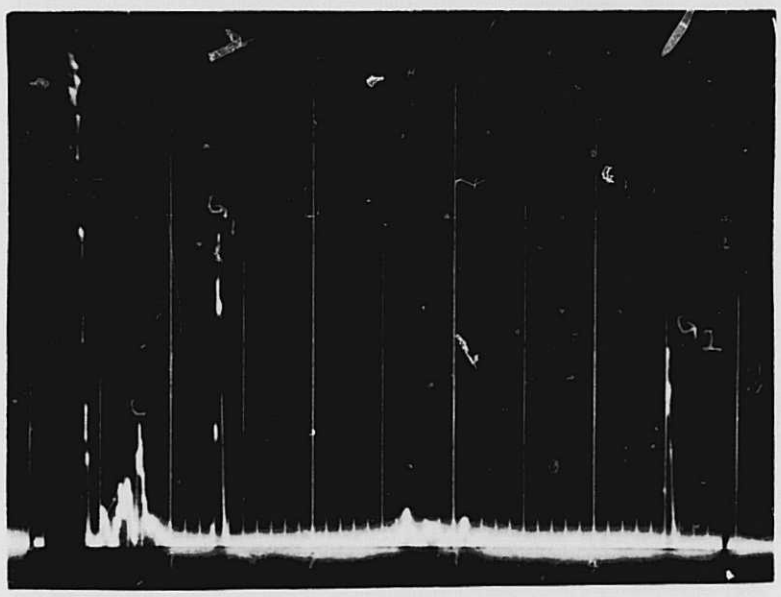

(c) Just after stress was released (just released "unloaded" state)

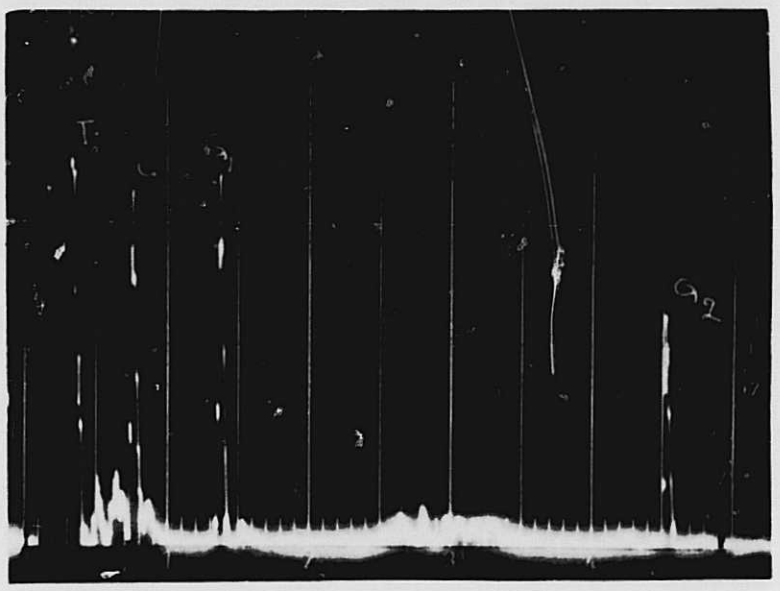

(d) Well after stress was released (well relaxed "unloaded" state)

Fig. 99, Oscillograms illustrating the effect of SCC (U-bend specimen no. 5A)

demonstrates that SCC is revealed clearer and faster in the "loaded" state.

The nature and size of microcracks responsible for the echoes from the exposed area are shown in Fig. 100. These photomicrographs were obtained in the well relaxed "unloaded" state after the 15-min exposure. Part (a) of this figure indicates the approximate location where the ultrasonic beam entered the corroded area, and illustrates the surface condition of the exposed and unexposed areas. In the same picture, two approximately parallel microcracks, pits produced by GGC, and small areas that were not attacked by the corrosive environment are shown. The small areas were caused by gas bubbles produced during corrosion, that prevented some areas from being attacked. Photomicrograph (b) shows the nature and size of a number of connected microcracks and pits inside the corroded area. The width of these microcracks is only a few microns. They run perpendicular to the stress direction with a number of steps. The straight lines are caused by scratches.

Another example of the ultrasonic examination is the series of oscillograms of Fig. 101 for the 60% of the yield strength case. These oscillograms illustrate the behavior for a longer exposure time. Here, after an exposure to 1.86 C/cm^2 (Fig. 101b), the complete attenuation of the second reference echo is evident. Echoes from the corroded area are also shown. Even after the release of the stress, an appreciable attenuation of the second reference echo is noted, and also well defined echoes from the corroded region (Fig. 101c).

The effect of stress on microcracks is shown in Fig. 102. Part (a) of this figure is a typical microcrack with no stress applied. Part (b) is the same microcrack under stress. Stress pulls the microcrack apart, thus exposing a greater effective depth to the ultrasonic beam and causing higher attenuation. This is evidenced in the difference in attenuation of the loaded and unloaded states.

The results for 7075 at 90% of the yield strength are shown in Fig. 103. Also included are the results of GGC tests for which the current density was the same. The GGC curves are an expansion of the lower left-hand corner of Fig. 96. In this figure, the increase in attenuation per unit distance

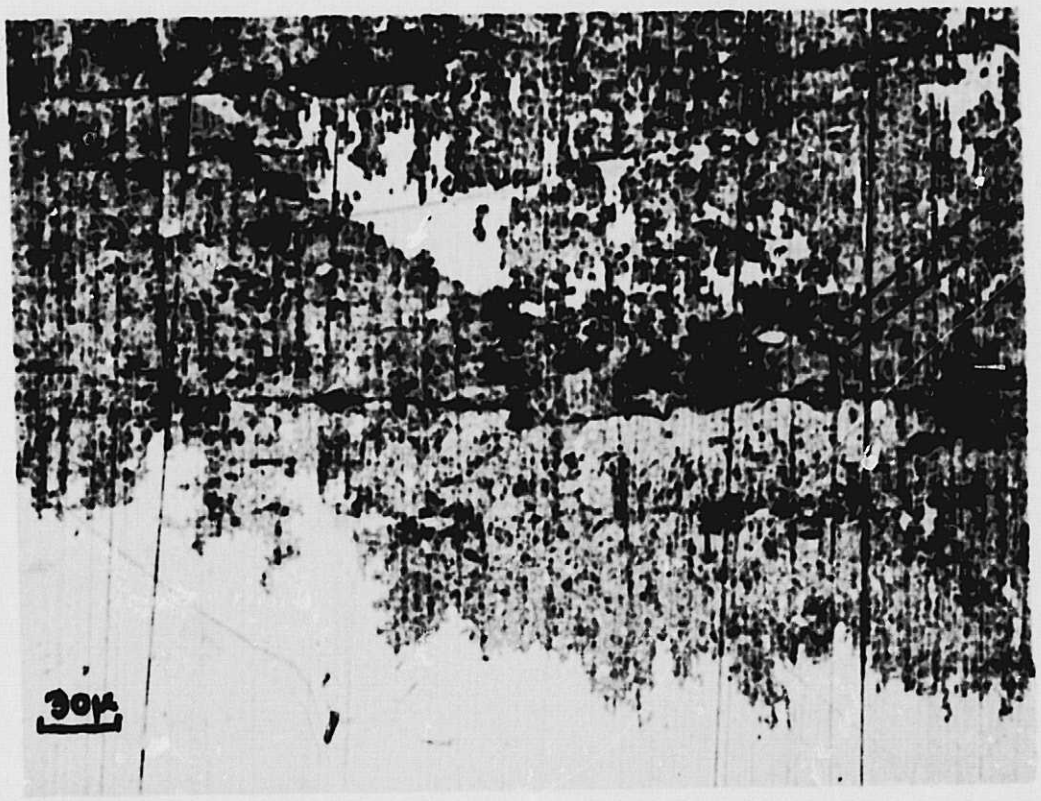

(a) Approximate location where the ultrasonic beam entered the corroded area (illustrates nature of the boundary between exposed and unexposed areas)

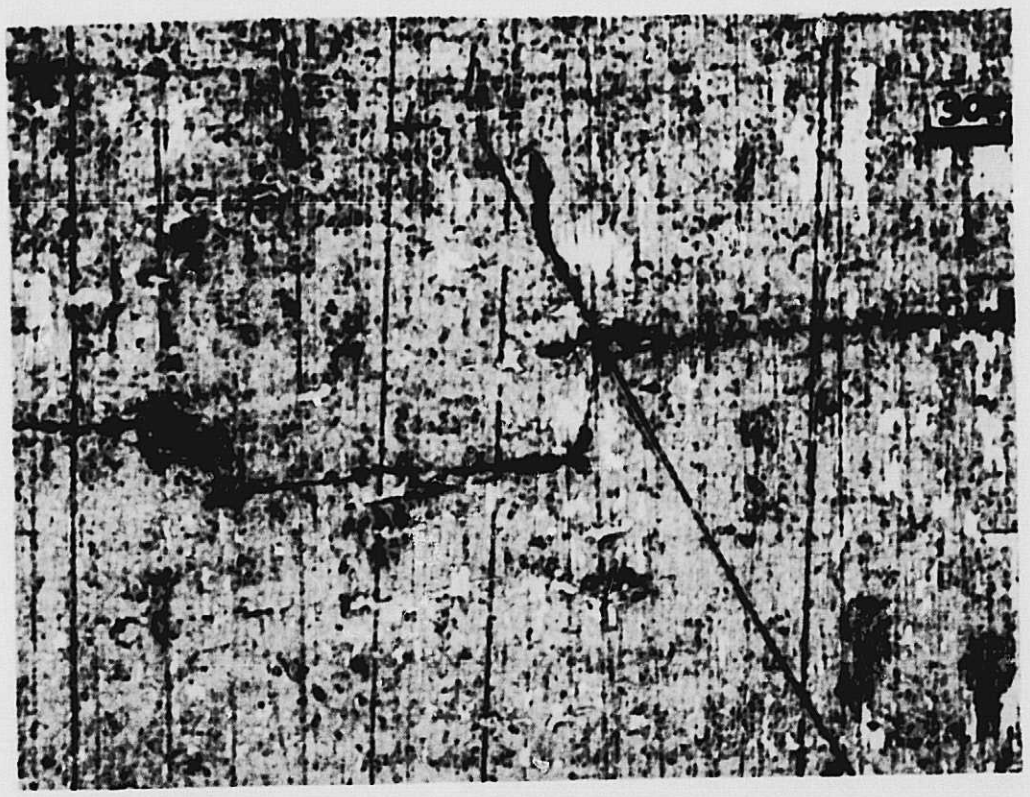

(b) Location well inside the corroded area (indicates number of connected microcracks)

Fig. 100. Photomicrographs of typical regions on the surface of U-bend specimens illustrating the effect of SCC at 90% of the yield strength and after 0.5 C/cm^2 had passed (well relaxed "unloaded" state at 300X)

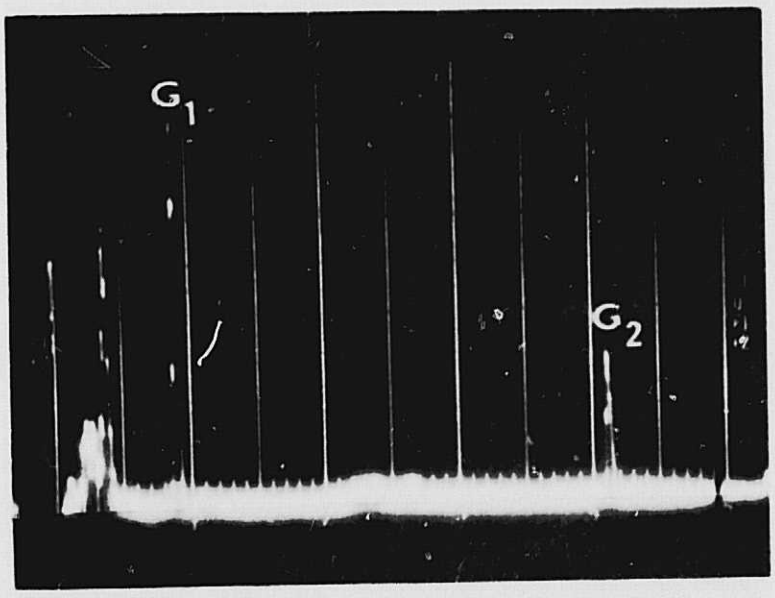

(a) Reference oscillogram

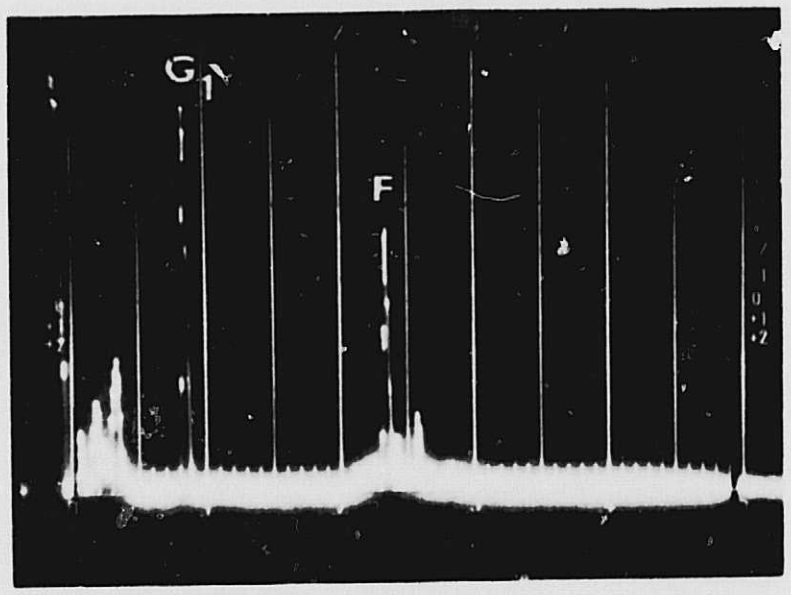

(b) After 1.86 C/cm^2 had passed in the loa state

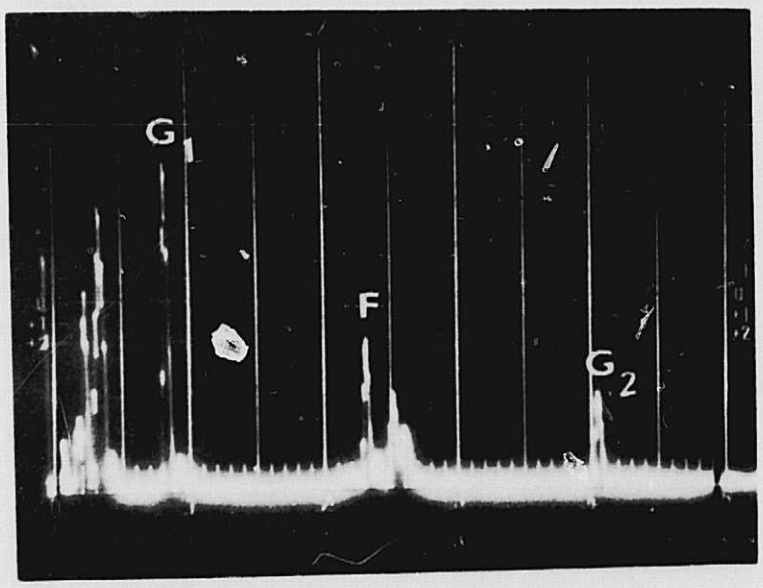

(c) After 1.86 C/cm^2 had passed in the unloaded state

Fig. 101. Oscillograms illustrating the effect of SCC at 60% of yield strength and 0.52 mA/cm^2

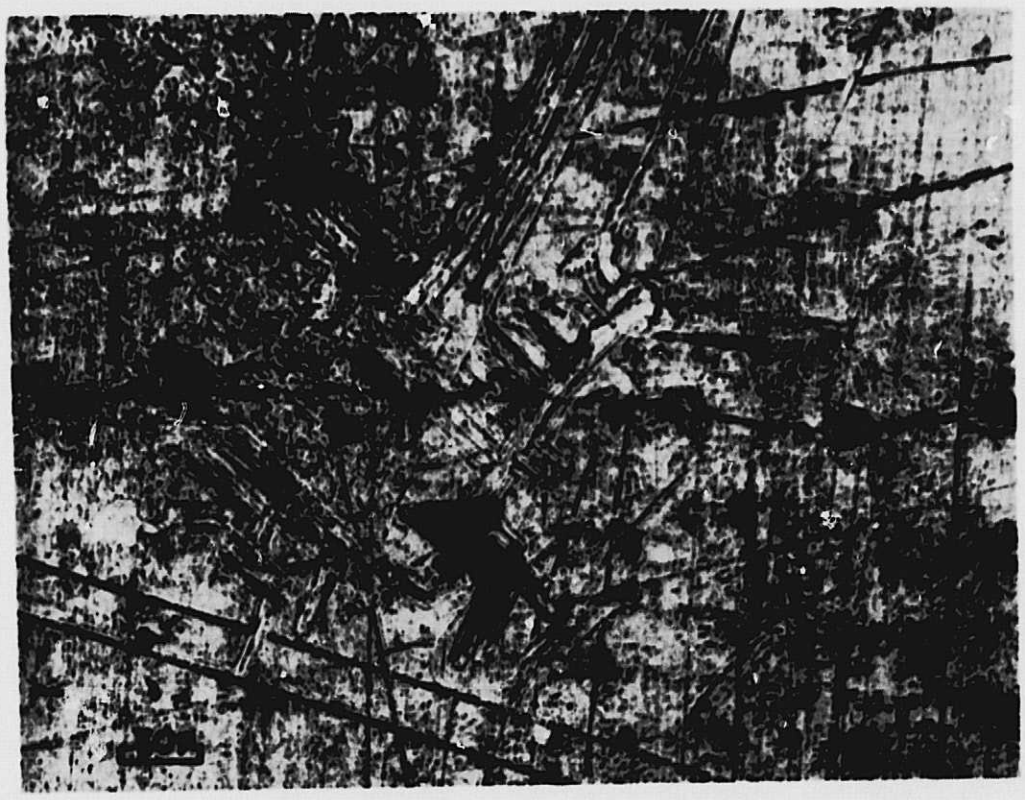

(a) No stress applied ("unloaded" state)

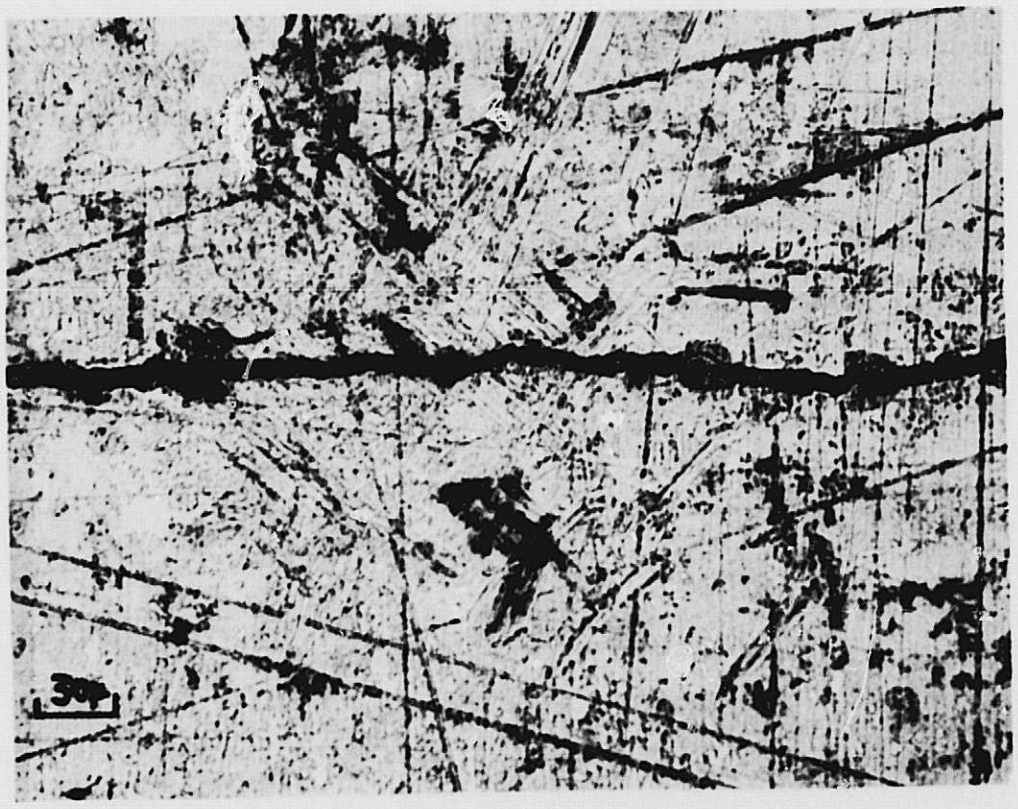

(b) 4×10^4 psi tensile stress ("loaded" state)

Fig. 102. Photomicrographs of typical microcracks illustrating the effect of crack opening under tensile stress (taken after a total of 60 min exposure to corrosive solution at 1 mA/cm^2 and 4×10^4 psi; U-bend specimen no. 4A)

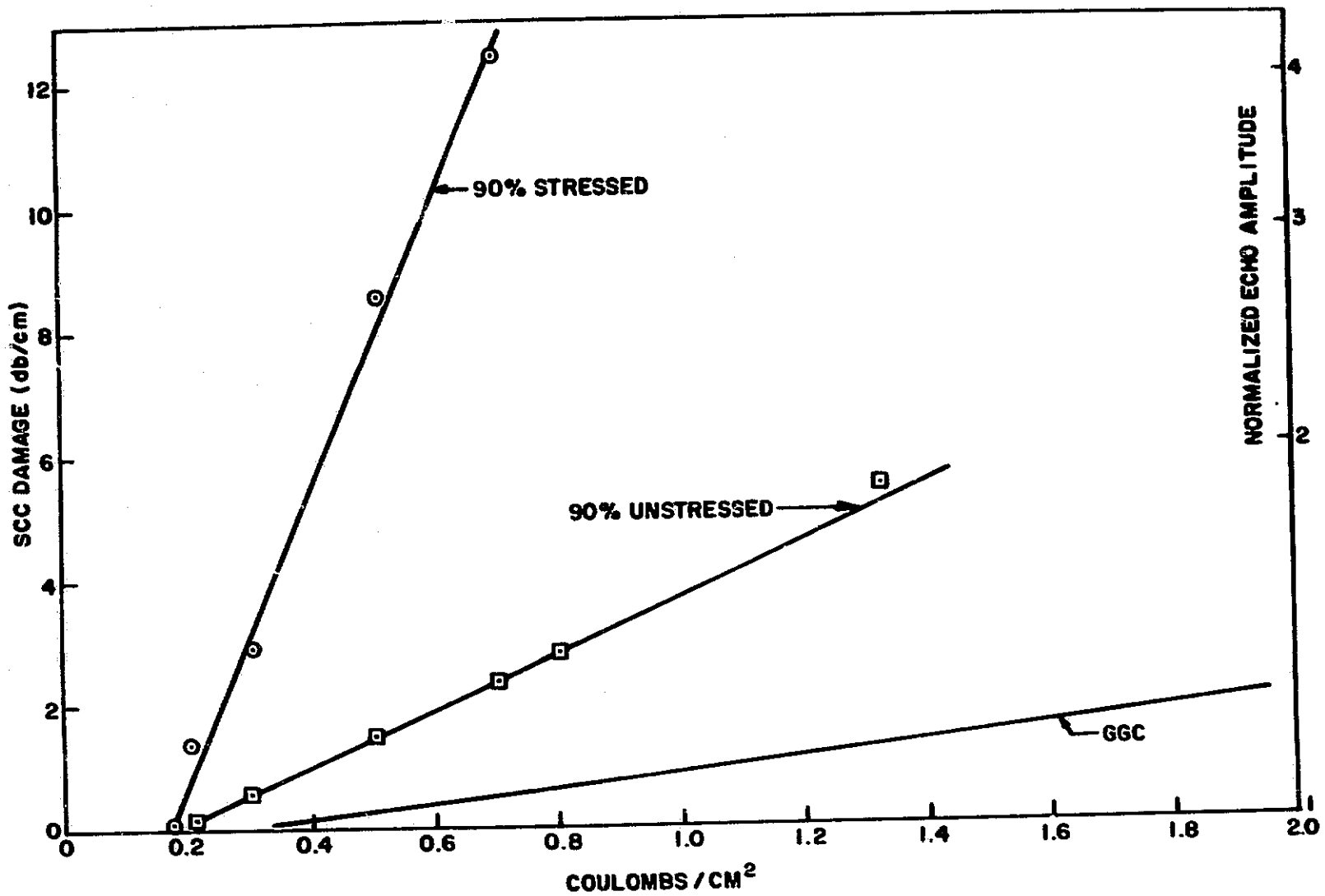

Fig. 103. Attenuation due to SCC damage at 60 and 90% of the yield strength of 7075 (T651)

is plotted as a function of the amount of corrosion.

The ordinate of Fig. 103 is the SCC damage determined ultrasonically for the 90% of the yield strength case, and is expressed as a change of echo amplitude and of normalized echo amplitude. The abscissa of this plot is expressed in C/cm^2 and in exposure times. The current density was constant at about $0.52\ mA/cm^2$. This graph illustrates the effect of SCC damage in both the loaded and unloaded states. In the unloaded state, it was not necessary to differentiate between just relaxed and well relaxed conditions, because the ultrasonically measured difference was of the order of 1 db, which is the experimental error. No attenuation data could be obtained for the point at $0.8\ C/cm^2$, because the very high attenuation did not allow the echo from the second reference groove to be detected. All the data were consistent with differences of the order of 1 db.

The results for the three sets of data are all straight lines within experimental error, and indicate a linear increase of SCC damage with increasing exposure, as evidenced ultrasonically. The ultrasonic sensitivity is much greater for the loaded state (approximately by a factor of 5), and thus can detect damage earlier. The line for the GGC data has a much smaller slope. The ratios of slopes for loaded SCC, unloaded SCC, and GGC are 23.4:1, respectively. All three lines have a nonzero intercept and tend to converge to the same value of $0.2\ C/cm^2$. The distance between 0 to $0.2\ C/cm^2$, indicated in the graph by the dashed line, can then be interpreted as an incubation period. This is verified by the fact that the data obtained after 0.185 C/cm^2 exposure showed no attenuation.

The results for the case of 7075 samples stressed to 60% of the yield strength are shown in Fig. 104. The ultrasonic and microscopic examination for this case is similar to that for the 90% of the yield strength case, and thus photographs are omitted. Finally, Fig. 105 illustrates the results for 7075 for both 90 and 60% of the yield strength cases for easier reference.

Fig. 106 illustrates the results for 2219 at 90% of the yield strength. The ultrasonic attenuation is plotted as a function of the amount of corrosion. No SCC attenuation data in the stressed state were obtained beyond an exposure of $0.8\ C/cm^2$, because the second reference echo was so highly attenuated. In general, the graph indicates an increase in the SCC damage with increasing exposure where the stressed state has a much greater ultrasonic

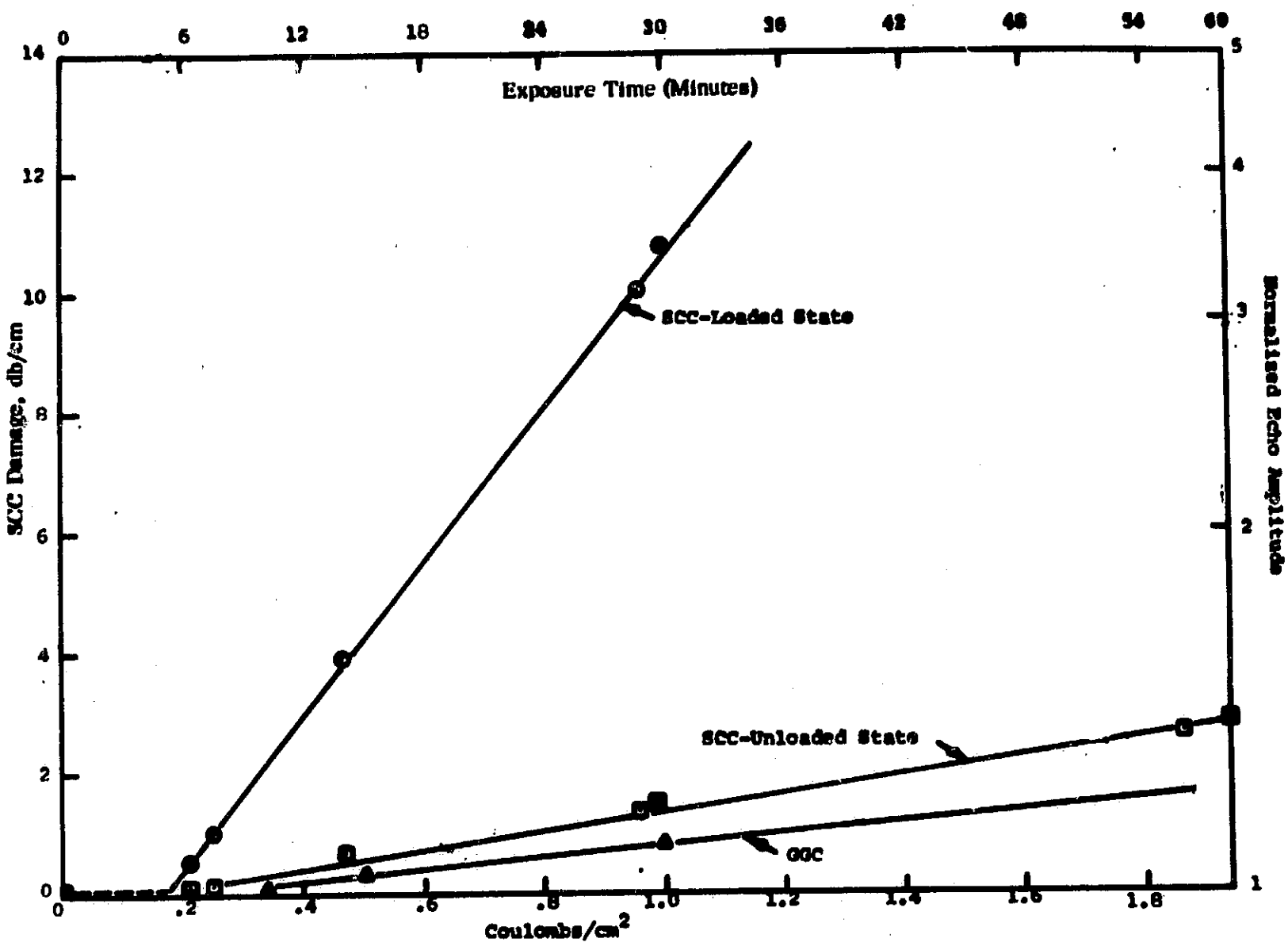

Fig. 104. SCC damage measured ultrasonically as a function of charge at 0.52 mA/cm^2 and 60% of the yield strength (GGC results also included for comparison)

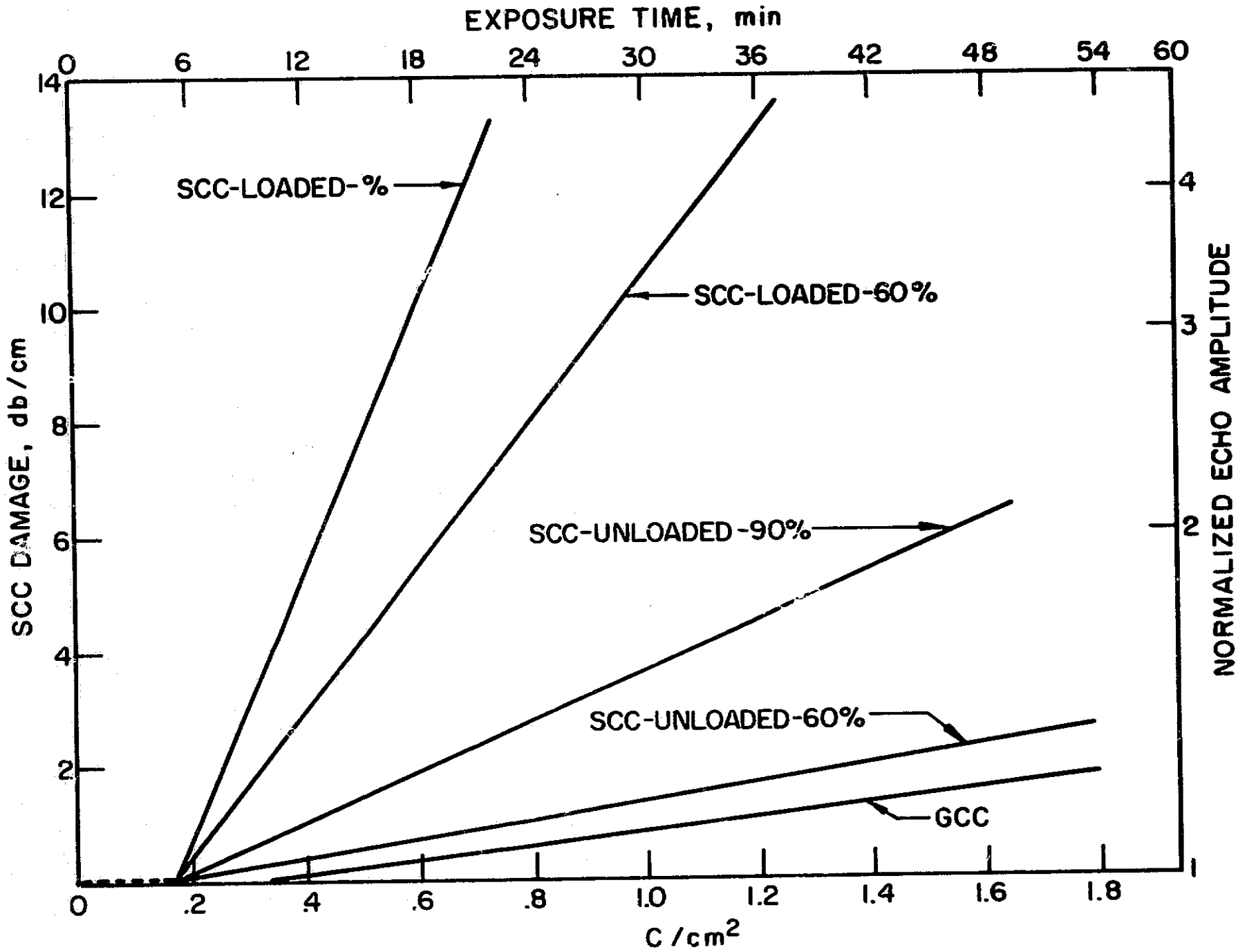

Fig. 105. Ultrasonic attenuation due to SCC and GGC as a function of charge at 0.52 mA/cm^2

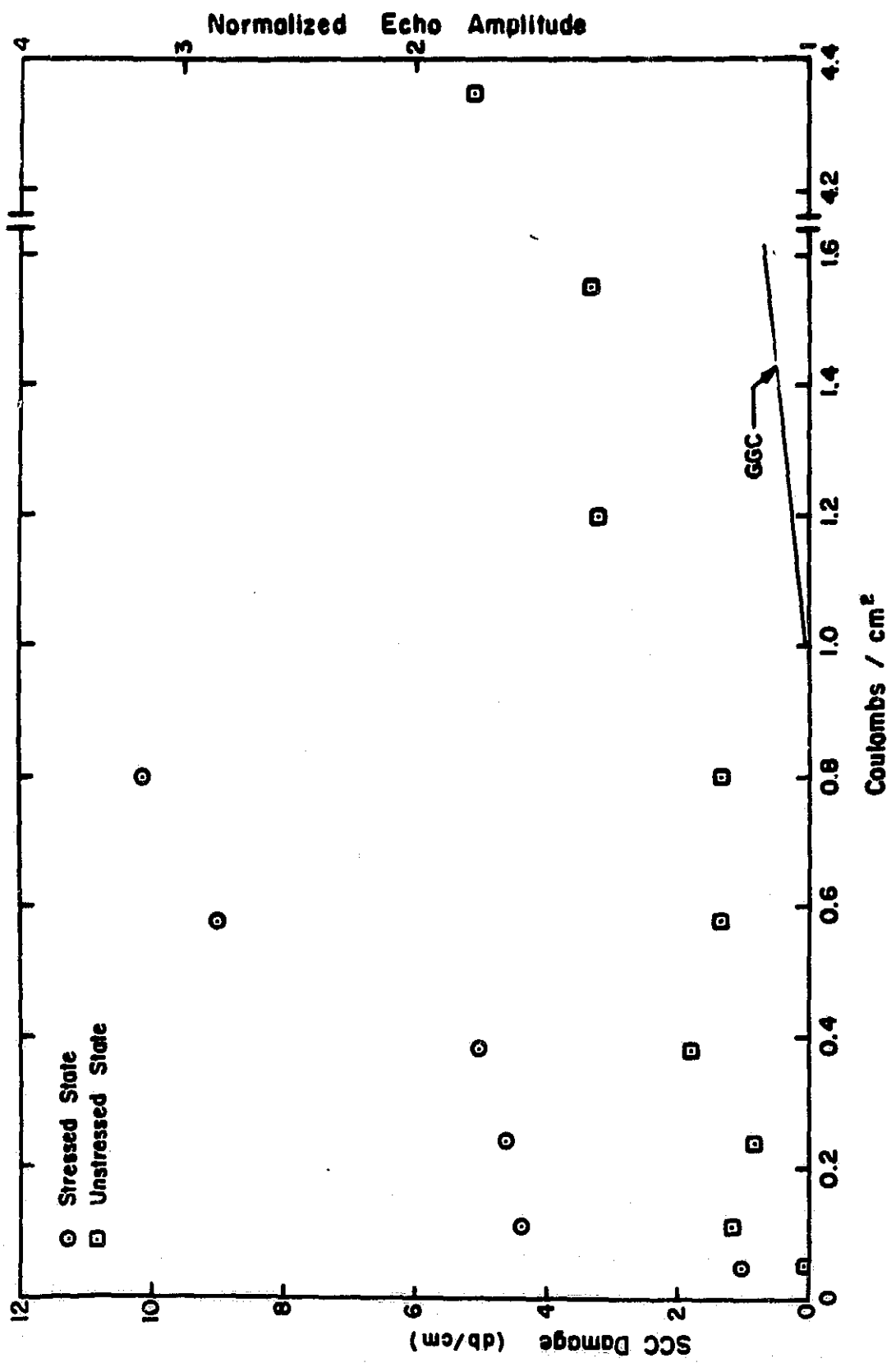

Fig. 106. Ultrasonic attenuation due to SCC damage for 2219 (T37) as a function of corrosion charge at 0.62 mA/cm^2 and 90% of the yield strength

sensitivity than the unstressed state.

The results for 2219 at 60% of the yield strength are shown in Fig. 107. Again no SCC attentuation data could be obtained beyond an exposure of 1.1 C/cm^2, because the second reference echo was totally attenuated. In general, Fig. 107 indicates an increase in the SCC damage with increasing exposure with a much greater ultrasonic sensitivity in the stressed than in the unstressed state. However, the relative slopes of the stressed and unstressed states are smaller than the corresponding slopes of Fig. 106 for the case of 90% of the yield strength.

Photomicrographs of the corroded area of the same U-bends when unstressed were made (magnification 300X). Pictures were taken after exposures of 0.058 (Fig. 108a), 0.38 (Fig. 108b), and 4.35 C/cm^2 (Fig. 109). Fig. 109a is in the approximate position where the ultrasonic beam entered the corroded area, and Fig. 109b shows the surface condition well inside the corroded area.

These photomicrographs illustrate the zig-zag morphology of microcracks and the absence of extensive general galvanic corrosion in 2219. From Figs. 106 and 107, and 108 and 109, we note that the region in which most of the data were taken (up to ~1.5 C/cm^2) is practically free of GGC.

The results indicate that for equal amounts of corrosion the attenuation was largest for the sample stressed to 90%, probably because of the more rapid development of the microcracks. The attenuation in both the 90 and 60% cases, while still under stress, is higher by approximately a factor of 5 than when the stress is released. Even when the U-bend specimen is not under stress, the attenuation is substantially higher than that produced on samples subjected to GGC.

The ultrasonic analysis showed two differences between 2219 and 7075. These are:

(1) Relation of damage to exposure. The data for 2219 show more scatter and seems to indicate a steplike increase in the SCC

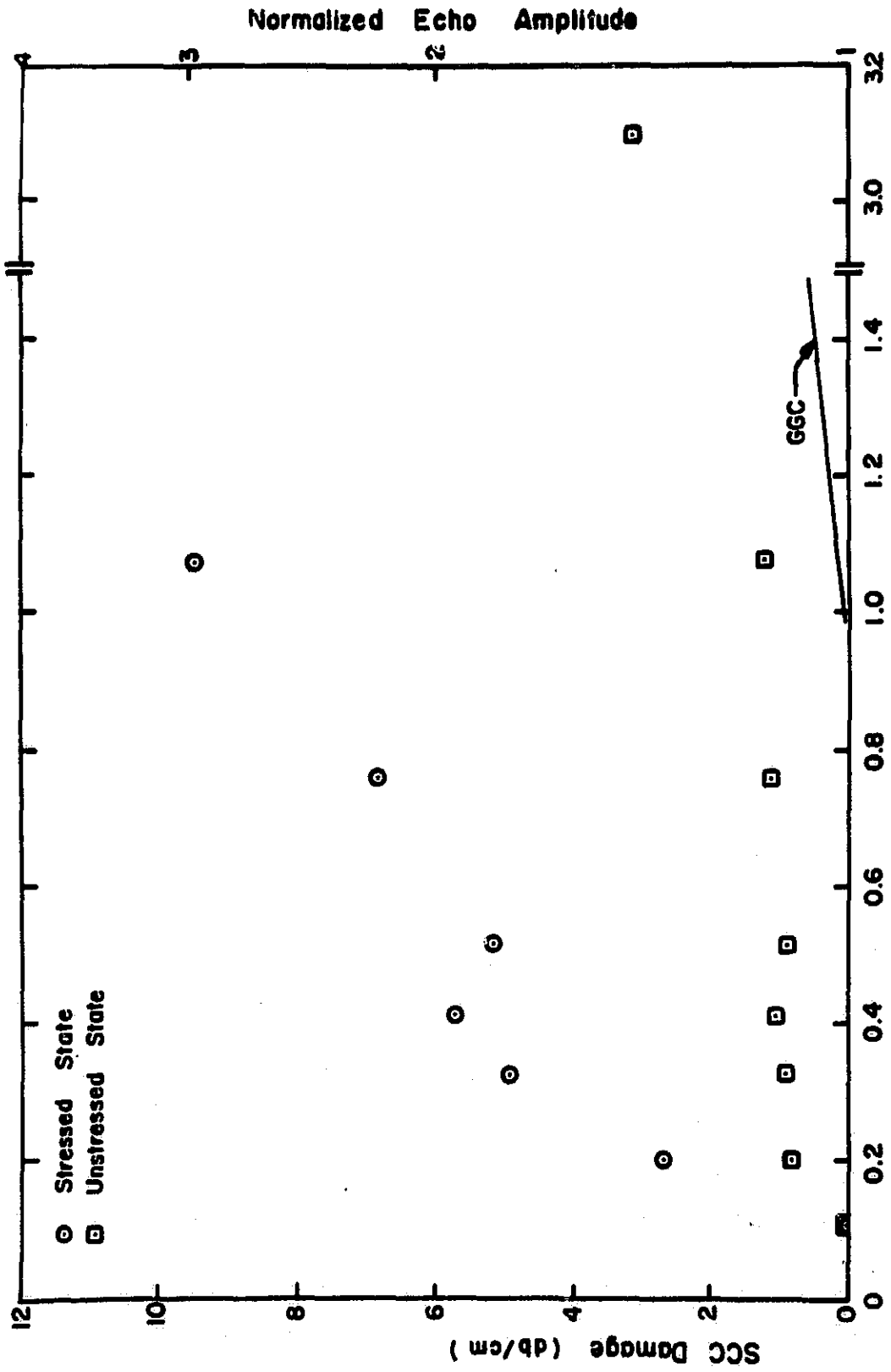

Fig. 107. Ultrasonic attentuation due to SCC damage for 2219 (T37) as a function of corrosion charge at 0.57 mA/cm^2 and 60% of the yield strength

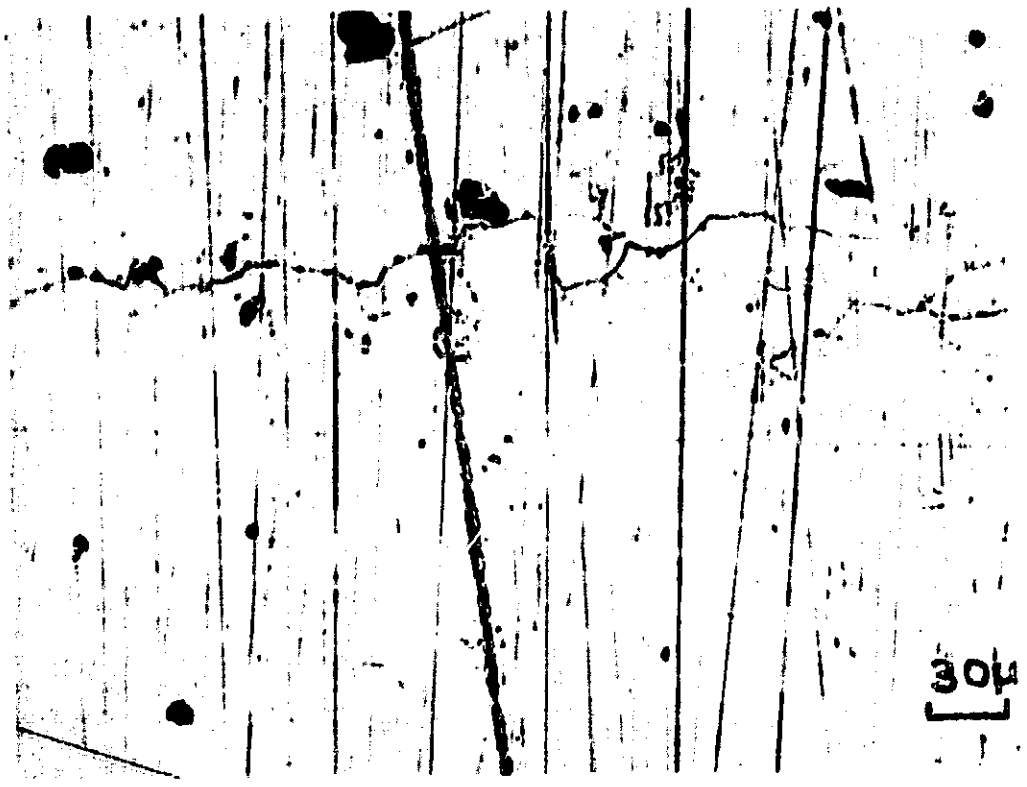

(a) After 0.058 C/cm^2

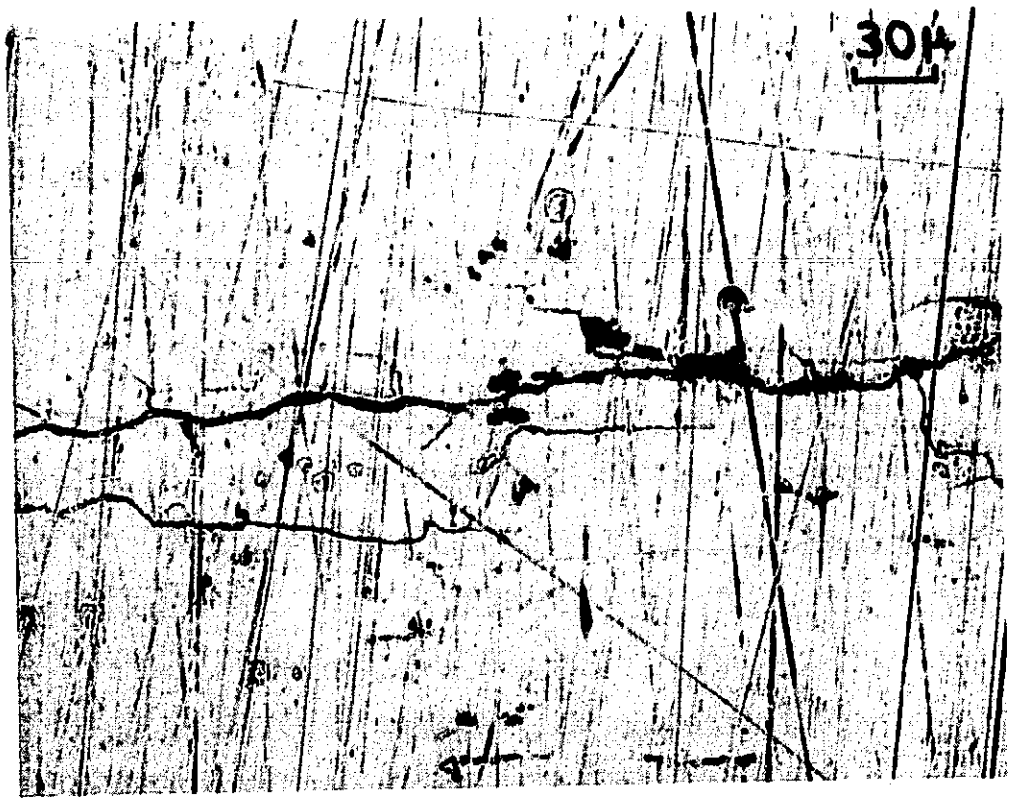

(b) After 0.38 C/cm^2

Fig. 108. Photomicrographs of typical regions on the surface of 2219 (T37) U-bend specimens illustrating the effect of SCC (unstressed state, 300X)

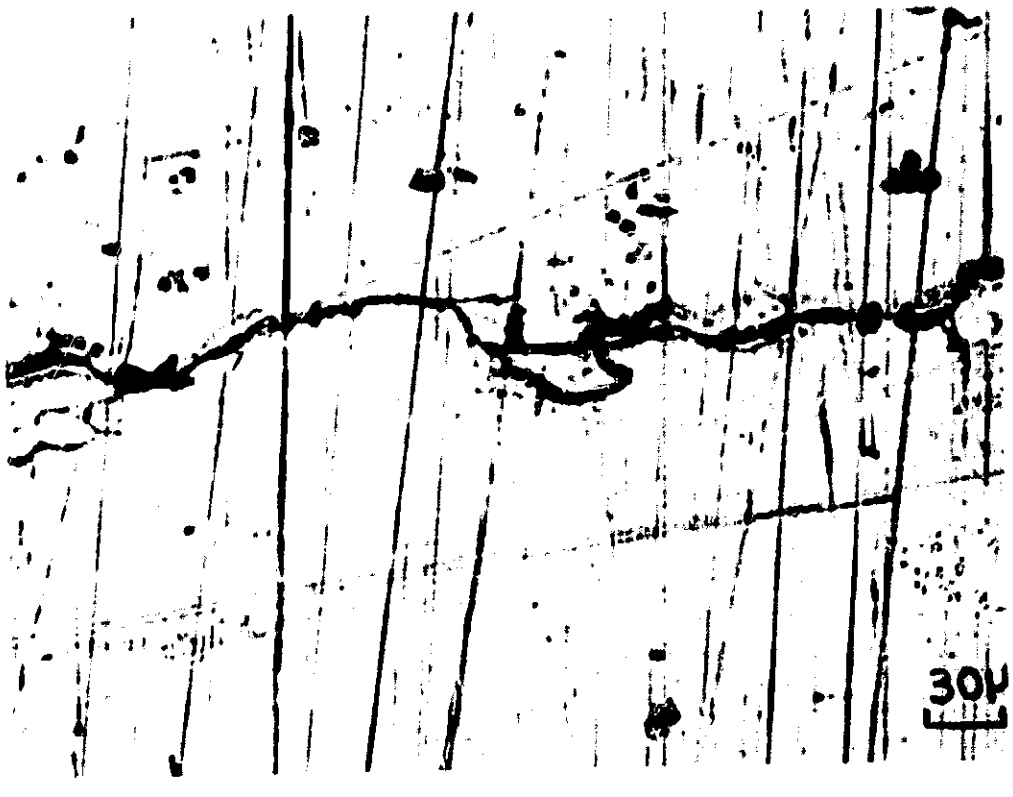

(a) Approximate location where ultrasonic beam entered the corroded area

(b) Location well inside corroded area

Fig. 109. Photomicrographs of typical regions on the surface of 2219 (T37) U-bend specimens illustrating the effect of SCC at 90% of the yield strength after 4.35 C/cm^2 (unstressed state, 300X)

damage with increasing exposure. This was not observed in the case of 7075 which rather showed a smooth, monotonic increase.

(2) Incubation period. There does not appear to be any incubation period for 2219 stressed to 90% of the yield strength, except for possibly a small (~ 0.04 C/cm^2) ultrasonic detectability threshold in the unstressed state. The corresponding incubation period or threshold for 7075 is about 0.2 C/cm^2.

For 2219 stressed to 60% of the yield strength, analysis of small echoes from microcracks indicated that the incubation period is less than 0.1 C/cm^2. This is shown in Fig. 110. Part (a) of this figure is the reference oscillogram, and part (b) is the oscillogram obtained in the stressed state after an exposure of 0.1 C/cm^2. The small echoes are clearly shown in part (b), even though they did not contribute much to the attenuation of the echo from the reference groove. The microscopic examination of this sample showed a few very small microcracks that apparently did not cause a detectable attenuation.

The microscopic examination of the specimens of 2219(T37) also show a mode of cracking different from that of 7075(T651). These differences are:

(1) Nature of microcracks. The photomicrographs of 2219 indicate that the microcracks for this alloy are of a zig-zag nature compared with the relatively straight cracks of 7075. A possible explanation may be the shorter and somewhat rounded grain boundaries of 2219 compared with the elongated grain boundaries of 7075.

(2) Density of microcracks. For 2219, the microcracks appeared to be uniformly distributed on the corroded area, whereas for the 7075, most of the microcracks were located at the edges of the rectangularly corroded area with only a few scattered in the central region.

(3) GGC. There was more GGC attack for 7075 than 2219.

2. SCC tests at 30% of the yield strength

The tests described here were performed at a stress

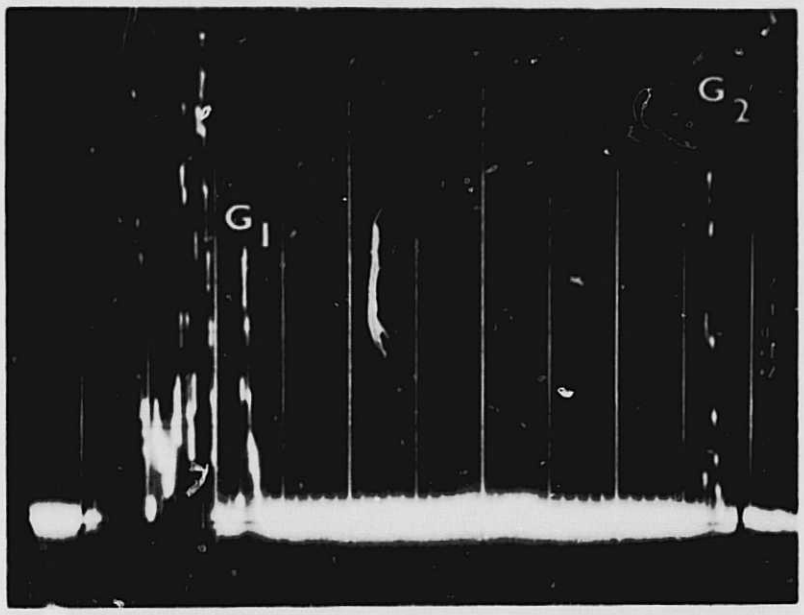

(a) Reference oscillogram

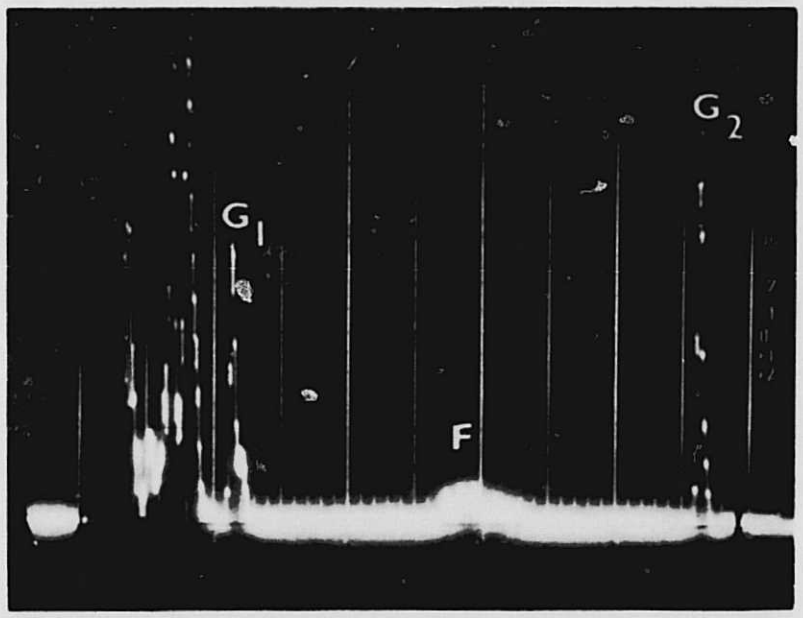

(b) After 0.1 C/cm^2 at the stressed state

Fig. 110. Oscillograms illustrating the effect of SCC for 2219 (T37) at 60% of the yield strength after 0.53 mA/cm^2

level of 30% of the yield strength, or 22500 psi on U-bend specimens of 7075. This value is approximately three times the threshold for SCC.

The results are shown in Fig. 111. This figure is the usual plot of the ultrasonic attenuation per unit distance (db/cm) versus the amount of corrosion (C/ cm^2). Fig. 111 also shows, for comparison, results for the 90 and 60% cases as well as the GGC results. The current density for these tests was 0.53 mA/cm^2, the same as used in earlier experiments. Oscillograms and photomicrographs were similar to those discussed earlier, and are not included here.

The results for the 30% case indicate a linear increase of attenuation with increasing exposure in both the stressed and unstressed testing states. As expected, the attenuation-corrosion slopes are smaller than both the 90 and 60% cases. The ratio of slopes for 90, 60, and 30% cases in the stressed state are 2.9:1.6:1, respectively. For the unstressed 30% state, the line is close to the GGC case which is the threshold for dectecting attenuation caused by SCC. This means that it would be difficult to differentiate ultrasonically between SCC in the unstressed testing state and GGC in the tests where the stress level during stress corrosion was smaller than 30% of the yield strength, unless a microscopic examination of the surface is performed which would reveal the presence of microcracks in the SCC case and their absence in the GGC case.

The x-axis intercept of the lines for the 30% case again indicates an incubation period of about 0.2 C/cm^2, which is the same as has been observed in other cases. The results of the ultrasonic and microscopic examinations for the 30% case were very similar to those for the 90 and 60% cases.

In order to express the threshold for ultrasonic detection of cracking in terms of SCC life for the 30% case, time to failure data would be necessary. However, for the 60% case, the threshold is of the order of 1% of the SCC life. This would indicate that the threshold for the 30% case should be even lower, and we could say that the SCC damage is effectively detected (in terms of SCC life) nearly from the onset.

3. SCC tests at a current density of 1.5 mA/cm^2

Most of the SCC investigations described previously

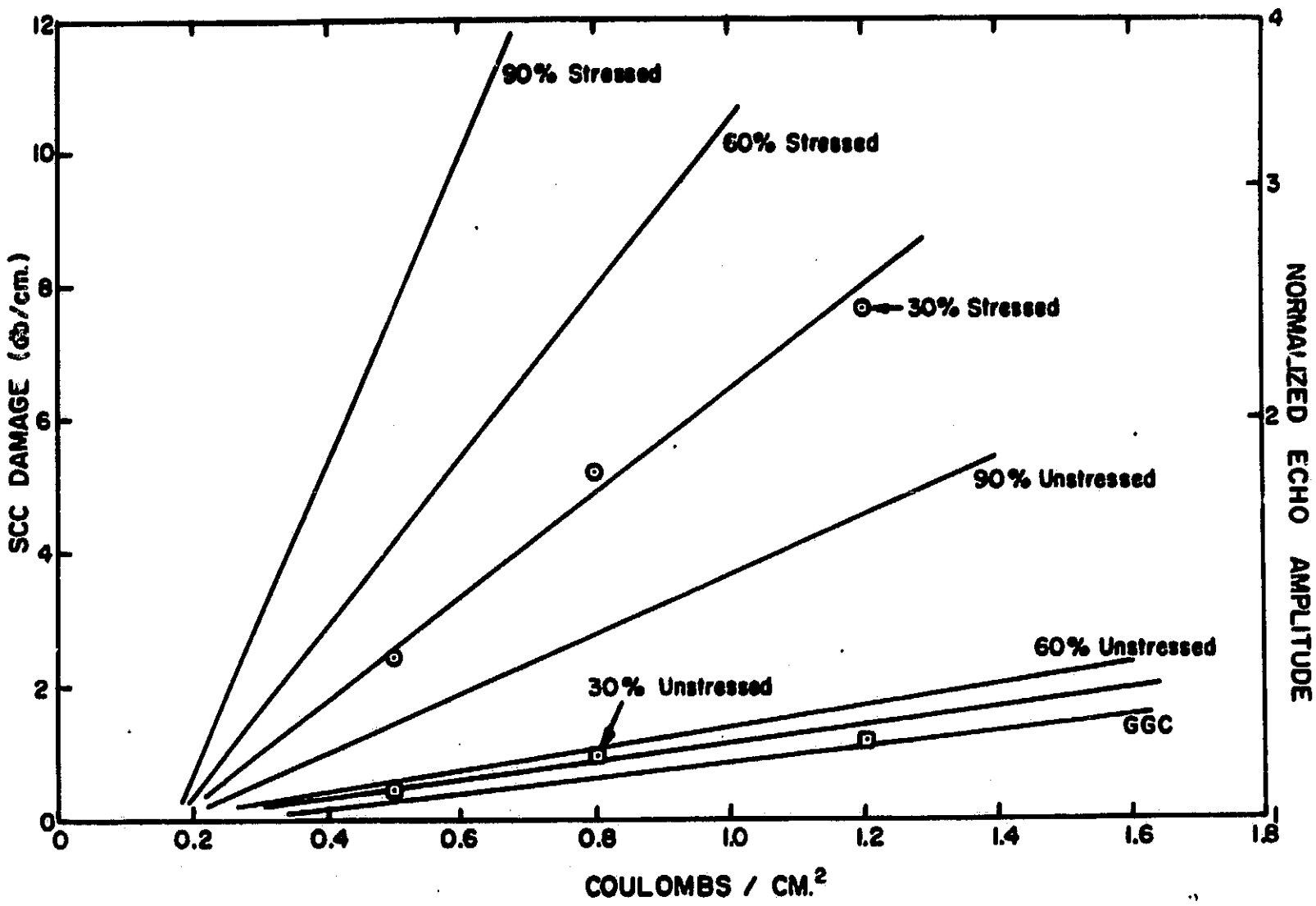

Fig. 111. Ultrasonic attenuation due to SCC and GGC for 7075 as a function of charge at 0.53 mA/cm^2 and 30% of the yield strength

were performed at a current density of approximately 0.5 mA/cm^2. The tests described here were carried out at a current density of 1.5 mA/cm^2 on U-bend specimens of 7075. SCC life tests indicate that the time to failure decreases with increasing current density.

The results of the investigation with 1.5 mA/cm^2 at 90 and 60% of the yield strength are shown in Fig. 112. This figure is a plot of the ultrasonic attenuation per unit distance (db/cm) versus the amount of corrosion (C/cm^2), and shows for comparison the results of 90%, 60%, and GGC cases performed at 0.55 mA/cm^2. These results indicate excellent agreement between tests performed at 0.55 and 1.5 mA/cm^2 for both 90 and 60% cases when the ultrasonic attenuation is plotted as a function of total charge. Naturally, if the ultrasonic attenuation is plotted as a function of exposure time, the slopes of lines corresponding to 1.5 mA/cm^2 are greater than those for 0.55 mA/cm^2, as shown in Fig. 113. Note that in such a plot (damage versus exposure time) the origins of the family of lines (incubation periods) do not coincide as they do in a damage versus charge plot.

The results of the ultrasonic and microscopic examinations for the 1.5 mA/cm^2 case were very similar to those for the 0.55 mA/cm^2 case.

4. SCC tests at pH = 2.1 and pH = 11.8

Most SCC and GGC studies performed were carried out in a 1M solution of NaCl buffered to a pH of 4.7. In order to investigate the effect of SCC performed with different pH's, tests were performed at pH = 2.1 and pH = 11.8. These tests were mostly carried out at a stress level of 60% of the yield strength on 7075.

The solution for the pH = 2.1 tests was prepared by adding HCl to 1M NaCl until the desired pH was obtained (a pH of 2 corresponds to 0.01N HCl). The solution for the pH = 11.8 tests was prepared by adding NaOH (a pH of 12 corresponds to approximately 0.01N NaOH). Although the solutions were not buffered, checks of the pH during and after corrosion showed no change.

The results of this investigation are shown in Fig. 114, the standard plot for the ultrasonic attenuation per unit distance (db/cm) versus the amount of corrosion (C/cm^2). This figure includes for comparison the results obtained with a pH of 4.7 at the same current density (0.53 mA/cm^2) and stress level (60% of the yield strength). The ultrasonic examination was

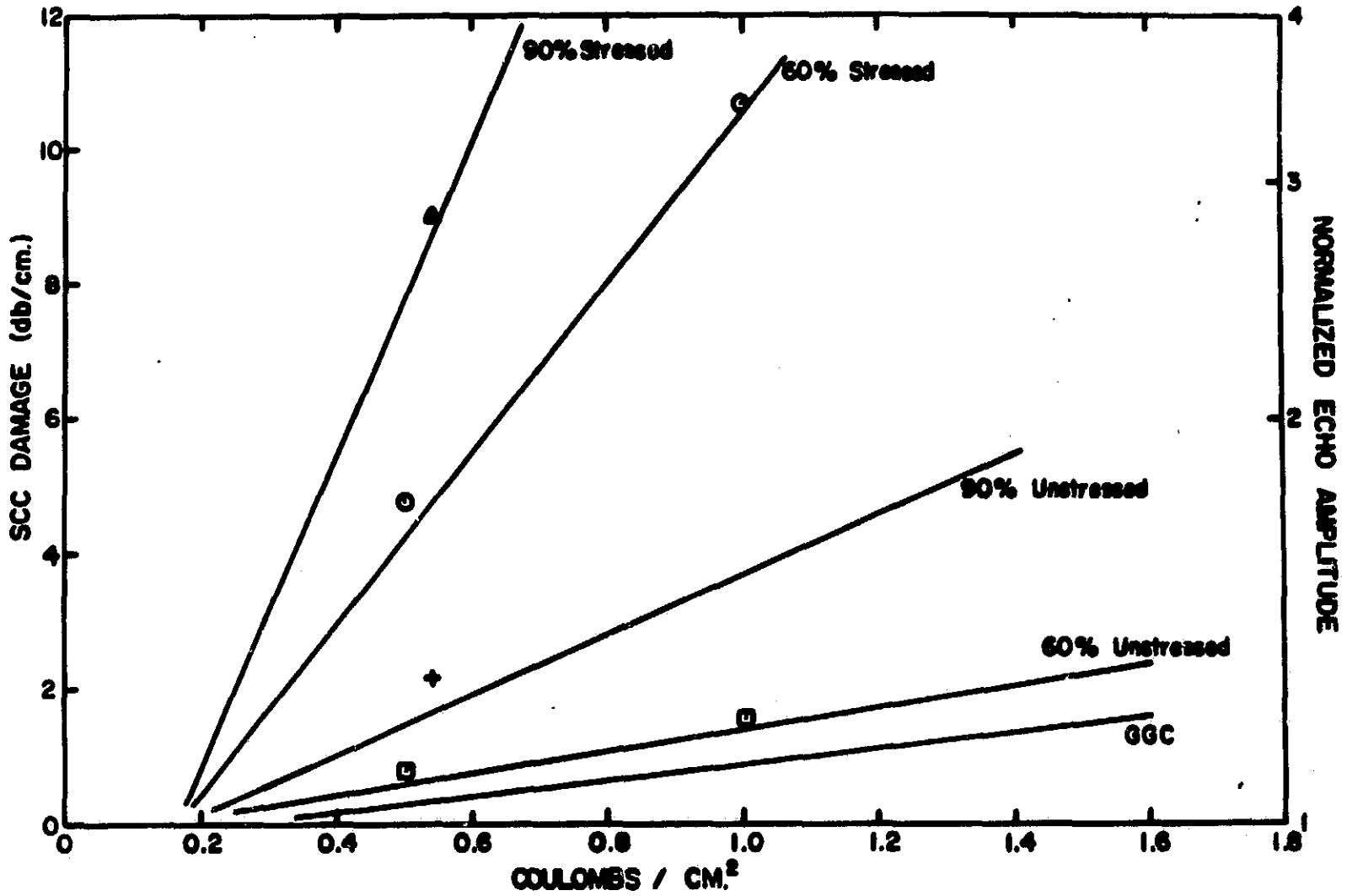

Fig. 112. Ultrasonic attenuation due to SCC and GGC for 7075 as a function of charge (straight lines correspond to 0.55 mA/cm^2 and data points to 1.5 mA/cm^2)

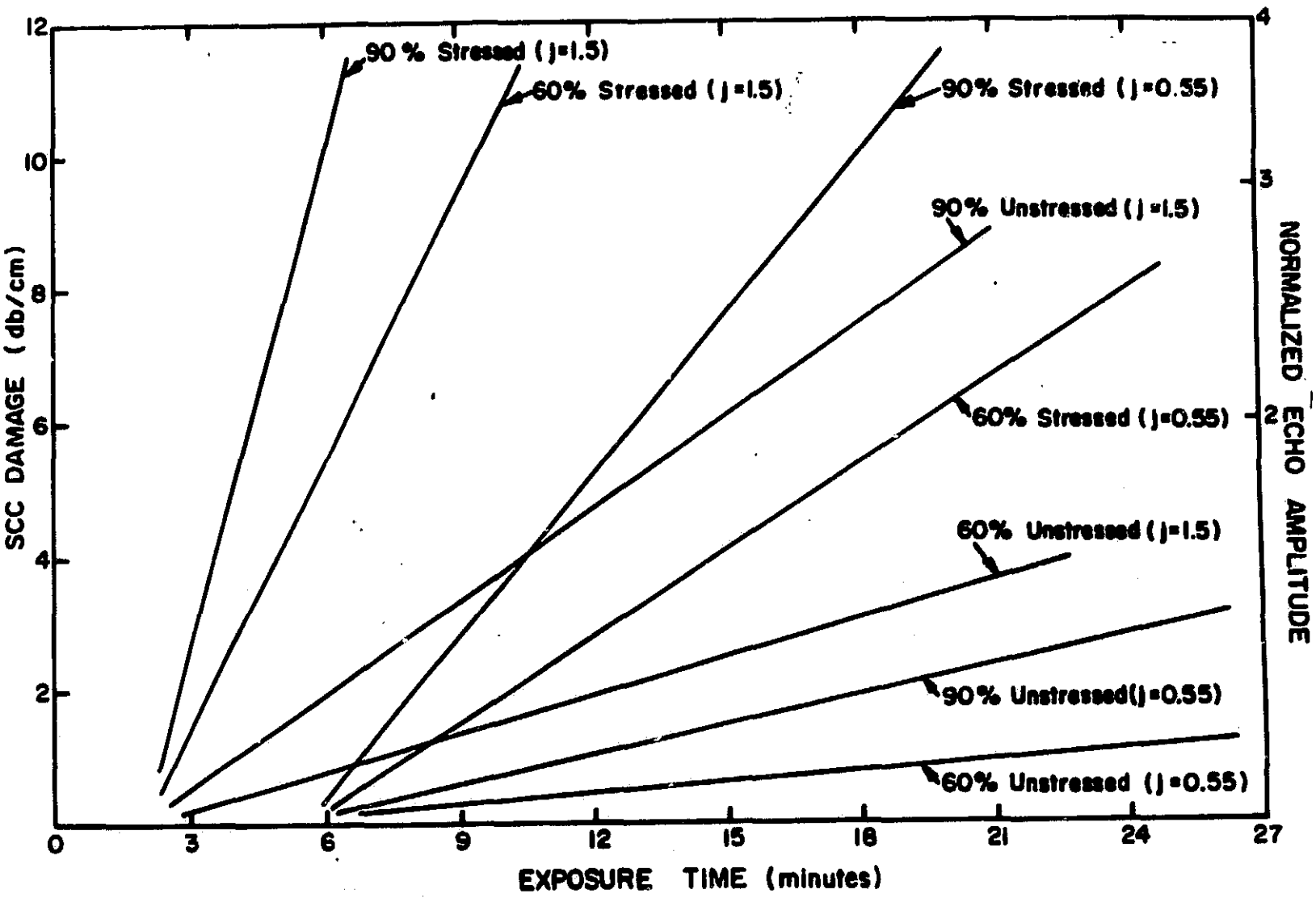

Fig. 113. Ultrasonic attentuation due to SCC for 7075 as a function of exposure time at 0.55 and 1.5 mA/cm^2

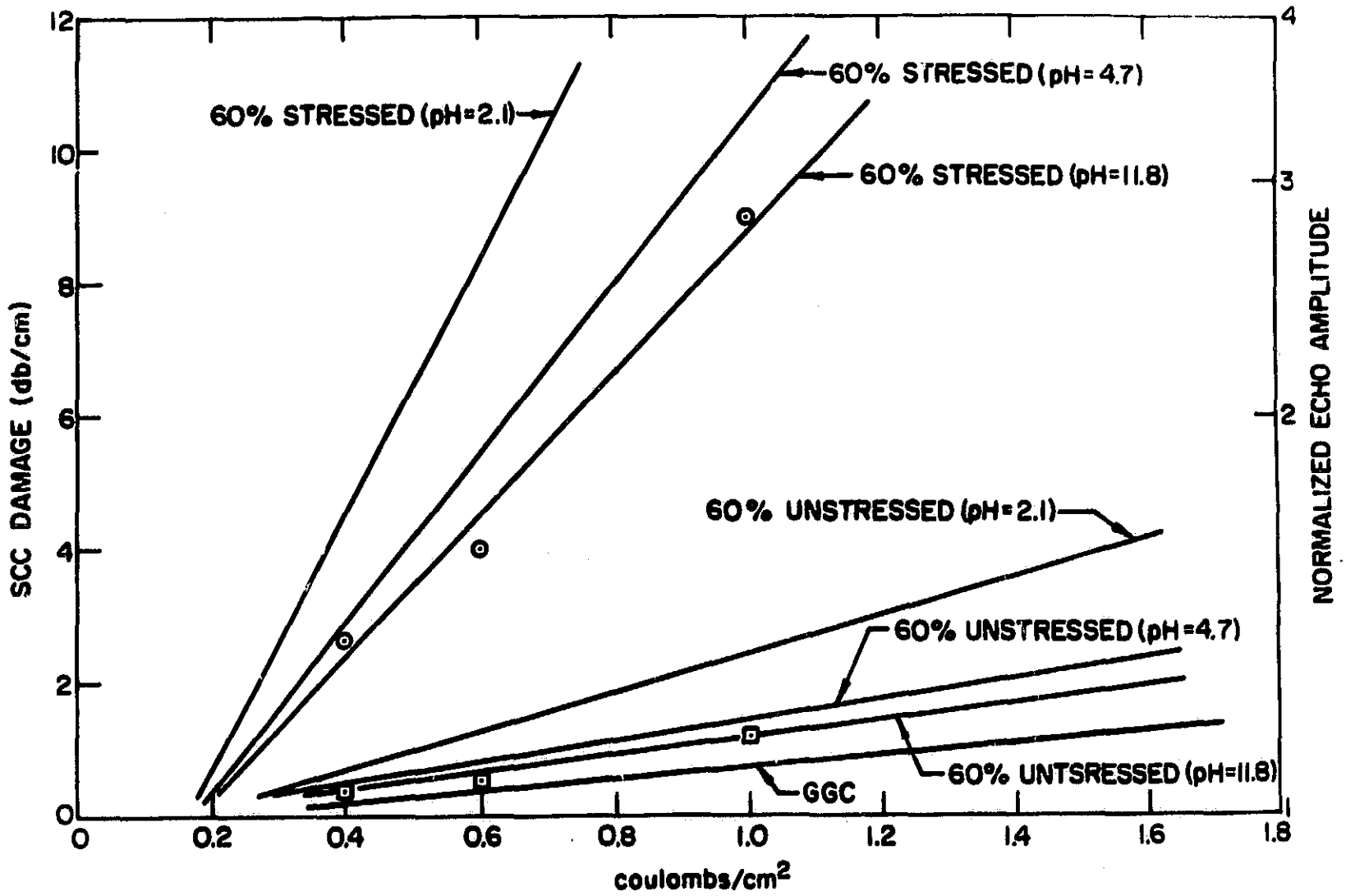

Fig. 114. Ultrasonic attenuation due to SCC and GGC for 7075 as a function of charge at 0.53 mA/cm^2 and 60% of the yield strength (solutions used had pH of 2.1, 4.7, and 11.8, respectively)

quite similar to the other cases, and thus no details, such as oscillograms, are included here.

The data indicate a linear increase in ultrasonic attenuation with galvanostatic charge ir all cases. However, the slopes of the lines for both the stressed and unstressed states are different than the corresponding slopes at a pH of 4.7: larger for a pH of 2.1 and smaller for a pH of 11.8. The slopes for pH = 2. , 4.7, and 11.8 cases in the stressed state are in the ratios of 2:1.2:1, respectively. The x-axis intercepts for the lines of the pH = 11.8 and 2.1 cases again indicate an incubation period of about 0.2 C/cm^2.

The effect of increasing the pH is to reduce the amount of SCC damage (attenuation) at an equivalent amount of galvanostatic charge, whereas decreasing the pH increases the amount of SCC. When plotted in terms of SCC lifetime, the cases of pH = 2.1, 4.7, and 11.8 will probably coincide, since Rayleigh wave NDT is really a measure of the depth of cracks and not the process producing them.

Photomicrographs of the corroded surfaces for a pH of 11.8 and 2.1 were indistinguishable from those with a pH of 2.1 and of 4.7 and thus are not presented in detail here.

5. SCC tests in salt-dichromate solutions

In order to compare our SCC results obtained by galvanostatic methods to other types of environmental tests, we applied an accelerated laboratory test to our U-bend specimens of 7075. The test was performed by continuous immersion in a salt-dichromate solution of 1% NaCl - 2% $K_2Cr_2O_7$ with a pH of 3.7 at a temperature of 60 °C (140 °F). The solution was prepared on a wt % basis using reagent grade chemicals and distilled water. The test solution was placed in a glass container and the temperature was maintained within ± 1 °C of 60 °C. Distilled water was added periodically to compensate for the small evaporation losses. Details of the testing procedure were similar to those by Helfrich.[22]

Although chemical etching was part of the procedure recommended in the reference, initial tests were performed without etching the exposed area before immersion of the specimen. The surface finish of the fabricated U-bend specimens has a high degree of polish, but is not optically flat. This surface finish is referred to as "buffed." Rayleigh wave measurements showed that this surface has a low attenuation (0.15 db/cm at 4 MHz).

The initial tests were performed at a stress level of 60% of the 0.2% offset yield strength, and exposures to the salt-dichromate solution ranged from 15 min to 23.5 hr. The examination of the surface with Rayeligh waves at 4 MHz did not indicate any increase in attenuation, even for the relatively long exposure of 23.5 hr. Microscopic examination of the exposed areas also did not show any evidence of microcracks, and there was negligible evidence of general corrosion. This is somewhat surprising, since tests by Helfrich showed failure of samples stressed to approximately 40% of the yield strength within a 1-hr period.

Following these negative results, the effect of chemically etching the exposed area before commencing the SCC test runs was investigated. The etching was performed in the unstressed state by immersing the area to be corroded first in a 5% NaOH solution at 75 °C (about 170 °F) for 30 sec, and then in cold concentrated HNO_3 for 20 sec, with a final rinse in distilled water. The area to be corroded was a rectangular surface (1 by 3.8 cm) on the outside face of the U-bend specimen.

During all stages of the chemical etching and SCC testing, the samples were checked both with ultrasonic surface waves and with a microscope. The 4-MHz transducer was attached with rubber cement on the U-bend specimen. A special mechanical assembly was used to ensure that the position of the probe on the sample did not shift during the tests. No change of ultrasonic attenuation was observed during the chemical etching. The microscopic examination showed that the highly polished finish had been dulled, but no other form of attack was evidenced.

Following the etching, the U-bend specimen was stressed to 3000 psi or 40% of the 0.2% offset yield strength. The sample was then exposed to the salt-dichromate solution with the temperature again at 60 °C. Exposures ranging from 1 to 11 hr again produced no change in the ultrasonic attenuation. The microscopic examination was also consistent with the ultrasonic results, and did not show any signs of attack.

Thus, it was concluded that either the salt-dichromate solution was not effective for our studies, or the exposure times were too short for this particular corrosive enviroment, even though they were long compared to our galvanostatic times. No explanation of the negative SCC results can be proposed at this time.

6. Determination of SCC life (time to failure)

One of the important parameters in SCC investigation is the time to failure or SCC life. In this study, we measured the failure time in order to express the first detectable SCC damage as a fraction of this time. Usually, this lifetime was determined in a separate test, not with the actual samples used for the SCC measurements. Unfortunately, considerable variability is observed in this time to failure, and this introduces uncertainty as to when SCC damage can first be detected in terms of a fraction of the lifetime.

A possible method to avoid this variability would be to obtain the SCC life for the particular U-bend used in an NDT study. This could be done in principle by continuing its corrosion until failure (after the appropriate ultrasonic measurements had been made), thus eliminating any variability of the U-bend geometry. Since the measurements cannot be carried out in situ, the U-bend must first be removed and cleaned. Restarting the corrosion could then lead to erroneous results.

The results of the tests on U-bend specimens are given in Fig. 115. For this study, the stress was 90% of the yield strength. Fig. 115 is a plot of corrosion charge per unit area (C/cm^2) as an ordinate versus the current density (mA/cm^2) as abscissa. Many tests decribed in this report were performed at a current density of about 0.53 mA/cm^2 where the average value of the SCC life is 1.6 C/cm^2. This value is slightly less than the corresponding point on the straight line (2.0 C/cm^2) in Fig. 115, but is in best agreement with the data at that particular current density. Using 1.6 C/cm^2 as the SCC life at 90% of the yield strength of 7075, the threshold for ultrasonic detection (incubation period 0.2 C/cm^2) is 13% of the SCC life.

For the 7075 case at 60% of the yield strength, preliminary tests indicated SCC life in the vicinity of 14 C/cm^2. Assuming this value, the threshold for detection is 1.5% of the SCC life. However, more sophisticated mechanical tests reported in a previous section with cylindrical tensile specimens at a slightly smaller current density (0.3 mA/cm^2) indicate that for 7075 at 60% of the yield strength the SCC life is twice as long. This value would give an ultrasonic threshold of about 0.7% of the SCC life. However, both values (i.e., the one obtained with the U-bend specimen and the

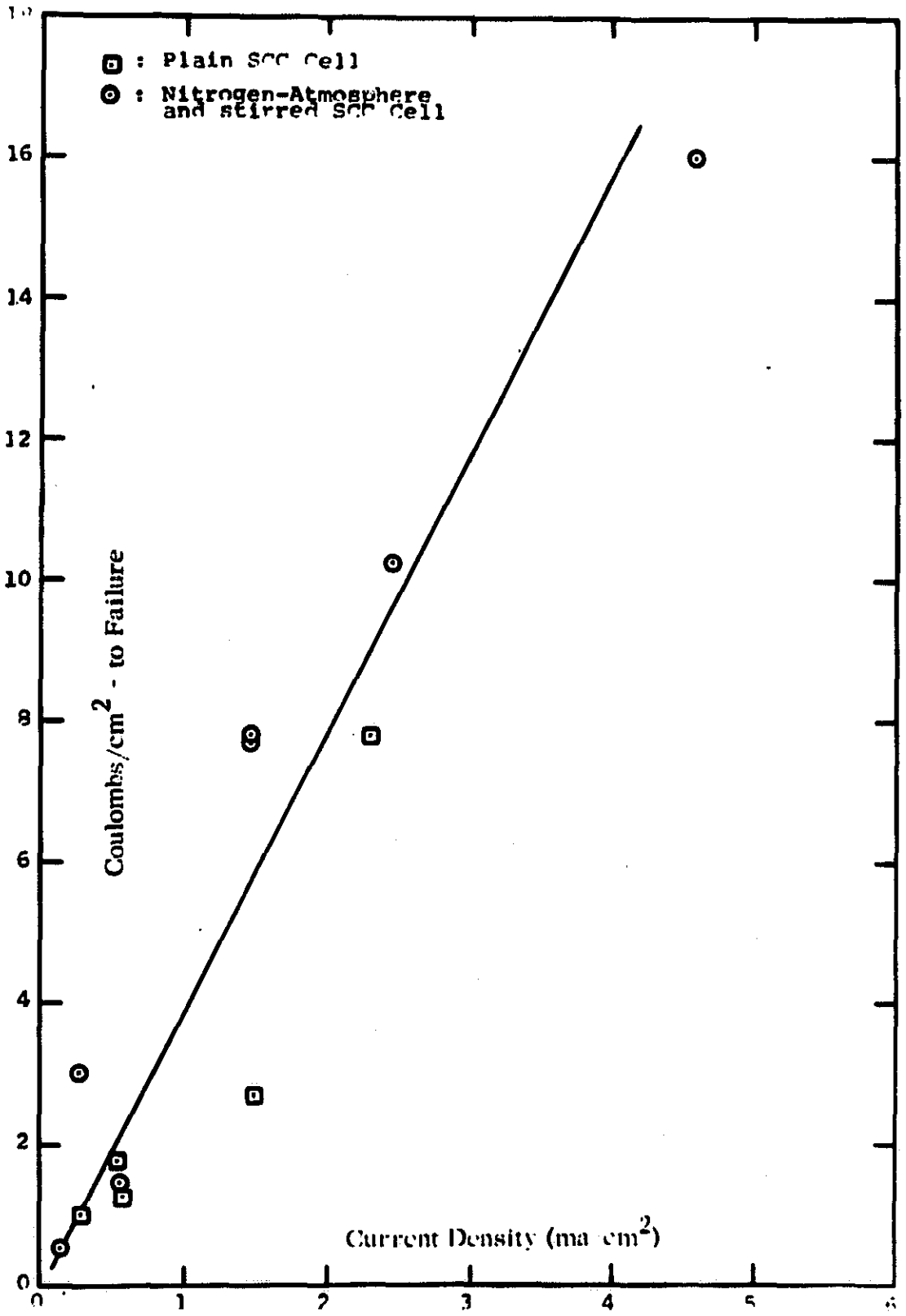

Fig. 115. Determination of SCC life (graph indicates number of C/cm^2 required for fracture of U-bend specimens as a function of current density)

one obtained with the cylindrical specimen) are only a small fraction of the SCC life. Thus, we could say that for the 7075 case at 60% of the yield strength, the SCC damage is effectively detected in terms of SCC life right from the onset.

The tests of SCC life of 2219 showed that the time to failure for U-bend specimens is longer than for 7075. Also, the samples do not fail in the same catastropic way as the 7075, but rather in a stepwise manner. Catastropic failure of 2219 U-bend specimens (i.e., fracture into two pieces) did not occur even for exposures up to 3 days; however, lifetime tests on 2219 at 60% of the yield strength performed on cylindrical tensile specimens in the main SCC cell showed that the time for the load to drop to 80% of the initial value is only 37 min. These tests were carried out at a current density of 0.3 mA/cm^2, thus giving a total charge of 1.1 C/cm^2 for the stress to drop to 80% of its original value. There is practically no incubation period for 2219, and thus the threshold for ultrasonic detection is very small.

The failure behavior of 2219 (T37) was discussed in Section III of this report and is shown in Fig. 61, which was a typical load versus time relationship. We pointed out that the discontinuous failure of 2219 possibly results from the halting of crack propagation when a crack comes to the end of a suitably oriented grain boundary. An additional period of time is then required to nucleate a crack in the new grain boundary. In 7075, once a crack has begun to propagate it continues until the failure is complete. This periodic behavior of 2219 is a possible explanation for the steplike scatter of the data of the SCC attenuation shown in Fig. 74. Another implication of the periodic behavior of this alloy is the definition of the SCC life. In the experiments reported in Section III of this report, the time to failure for 2219 was taken as the time for the applied load to drop to 80% of its original value, rather than the time to complete failure.

7. Precorrosion damage of 7075 and variable load SCC

As discussed earlier in this report (Section III), precorrosion is almost as effective in shortening the life of 7075 as SCC. Such precorrosion could lead to rapid failures of stored parts upon use. The investigation reported in this section is concerned with the study of the development of cracks after precorrosion and their detection by surface waves under application of a load to the precorroded U-bend samples. This is also of interest for

the mechanism study.

The precorrosion studies performed in phase I of the program were characterized in terms of times to failure. For the NDT investigation of the detection of precorrosion damage, U-bend specimens were precorroded for fixed lengths of time followed by stress corrosion. The specimens were not corroded to failure, but rather the damage was monitored ultrasonically and microscopically throughout the test. This method is apparently quite successful in giving us information about precorrosion. Even though the SCC cell used for the U-bend is quite simple, the damage produced by increasing exposures in SCC and GGC tests can be accurately monitored ultrasonically.

The experiments were performed under "standard" conditions, i.e., current density of 0.53 mA/cm^2 in a corrosive environment of 1M NaCl plus 0.05M acetate buffer (pH = 4.7) at a stress level of 60% of the 0.2% offset yield strength. The principle of these precorrosion tests is illustrated in Fig. 116.

The experimental procedure for the precorrosion tests is best illustrated by describing in detail a test and the corresponding oscillograms of the ultrasonic reflections taken at various stages.

The procedure is as follows. The U-bend specimen was prepared by cleaning and cutting grooves for reference reflections, after which a reference oscillogram was taken with the U-bend unstressed (Fig. 117a). The surface wave transducer was attached with rubber cement to one leg of the specimen and secured with a mechanical assembly to prevent any movement of the probe throughout the complete precorrosion test. The unstressed U-bend was then corroded under "standard" conditions for a particular length of time (31.5 min or 1 C/cm^2 for the particular test described). After this precorrosion exposure, the sample was removed from the solution, cleaned, and microscopically examined. Then another oscillogram was taken (Fig. 117b). Next, the stress was applied (60% of the 0.2% offset yield strength) and followed by microscopic examination and another check of the ultrasonic reflectivity in order to observe any possible changes during the stressing procedure (Fig. 117c). Following the application of stress, the sample was stress corroded under standard con-

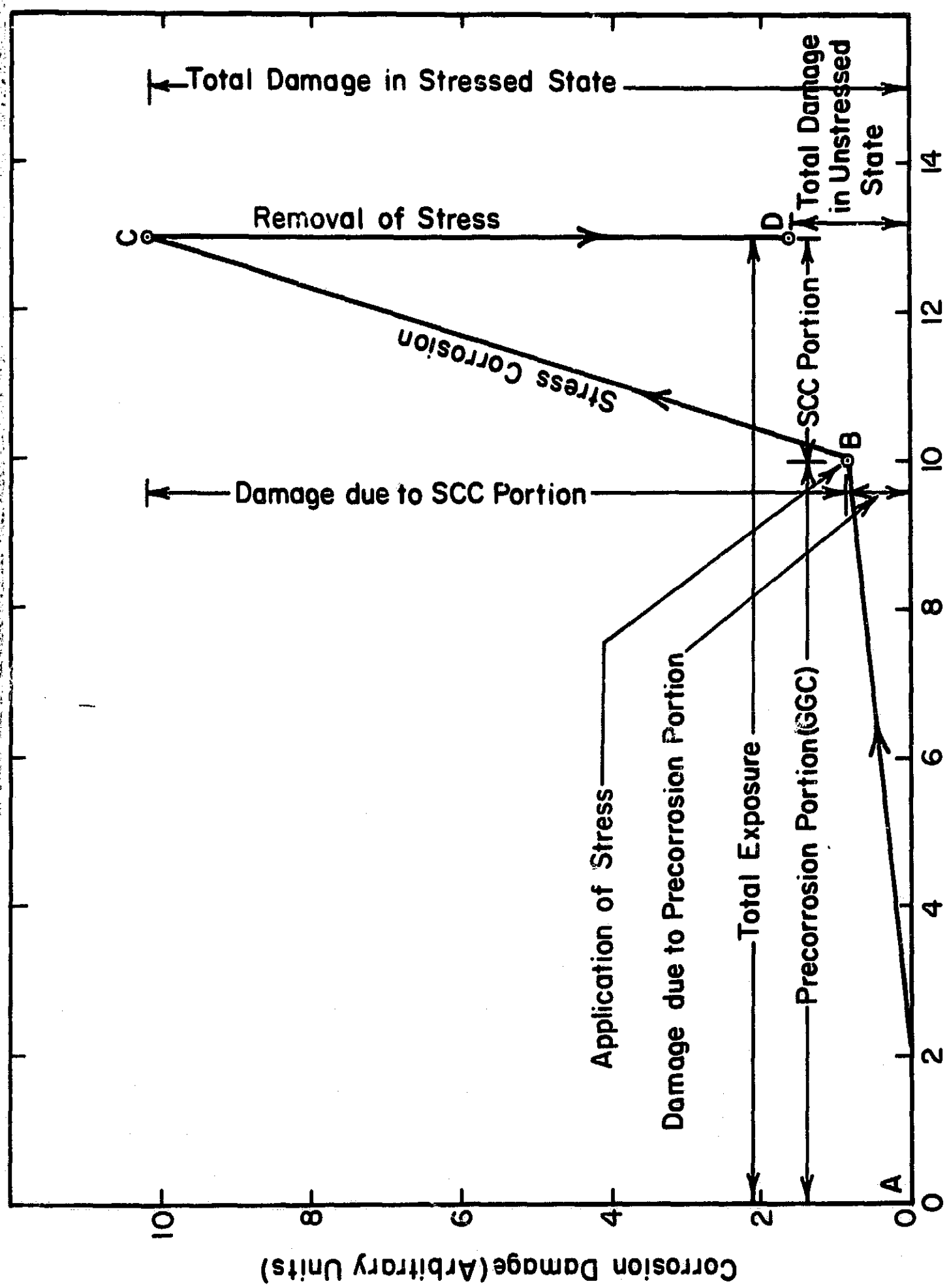

Fig. 116. Typical ultrasonic attenuation d
at various stages of the test

on due to precorrosion

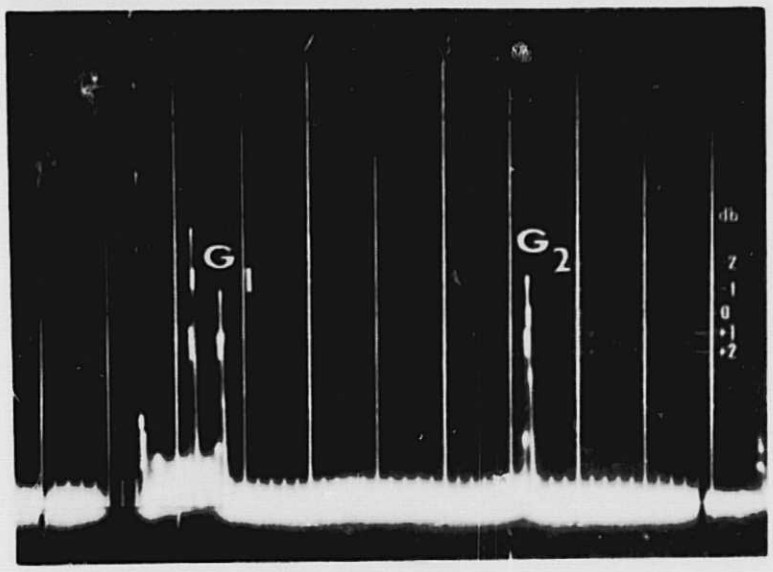

(a) Reference oscillogram

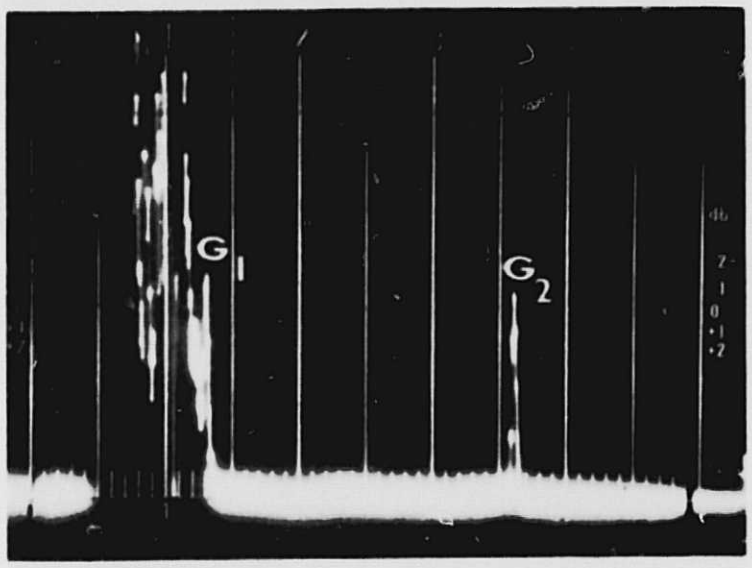

(b) After precorrosion of 1 C/cm^2

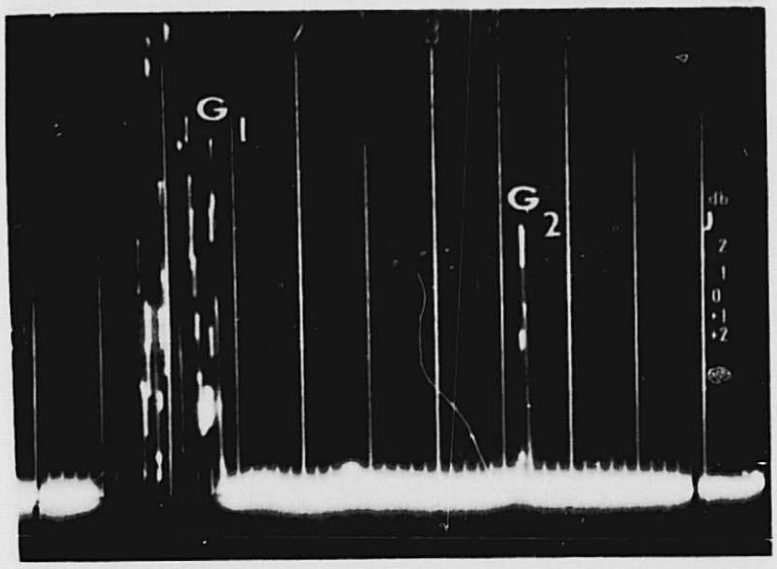

(c) After application of a stress of 60% of the yield strength

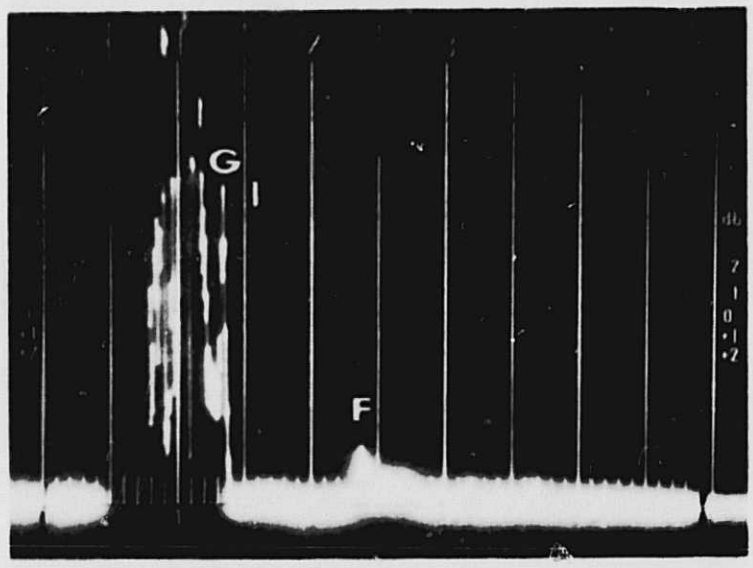

(d) After additional corrosion of 0.3 C/cm^2 but still under stress

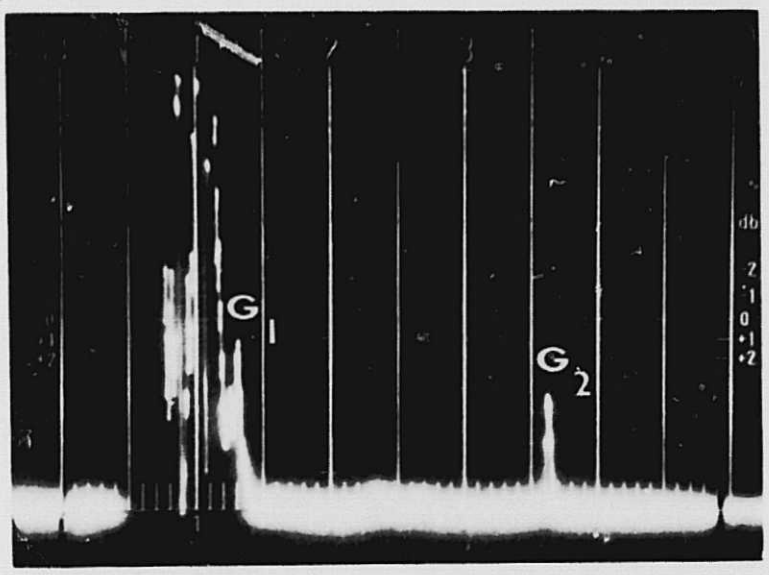

(e) Unstressed state

Fig. 117. Oscillograms illustrating the effect of precorrosion of 7075

ditions for a predetermined time (9.5 min or 0.3 C/cm^2), removed from the solution, cleaned, microscopically examined, and ultrasonically tested (Fig. 117d). The stress was released, and final examinations were made (Fig. 117e).

A summary of the ultrasonic results is shown in Fig. 118. This figure is the usual plot of the ultrasonic attenuation per unit distance (db/cm) versus the amount of corrosion (C/cm^2). The same figure contains the results of corrosion for the cases of samples stressed to 60% of the yield strength and examined in both the stressed and unstressed states, and also for GGC.

Now, with the aid of the oscillograms of Fig. 117, the microscopic examination, and the plotted results of Fig. 118, we are in a position to discuss the precorrosion results. Beginning with the precorrosion of 1 C/cm^2, oscillogram (b) of Fig. 117 indicates a small increase of attenuation due to GGC. The microscopic examination at this point, of course, showed the exposed area to be corroded with pits but with no microcracks present. The change of ultrasonic attenuation (about 0.6 db/cm) is naturally in excellent agreement with the GGC line of Fig. 118. The oscillogram for the U-bend immediately after stressing (Fig. 117c) indicates that an increase in attenuation of about 1 db occurred during the stressing process; however, the microscopic examination did not reveal any visible changes in the surface condition of the exposed area. This increase in attenuation during the stressing process was less than 1 db/cm, and was probably caused by changes in the transducer coupling.

Following the precorrosion exposure of 1 C/cm^2 and a cumulative exposure of 1.3 C/cm^2, the oscillogram of the U-bend in the stressed state indicated a striking increase in attenuation. The corresponding microscopic examination complemented the ultrasonic results by revealing the presence of microcracks. Finally, the stress was removed and the oscillogram in Fig. 117e was taken in the unstressed state. The microscopic examination in this state revealed the partially closed microcracks.

Two basic kinds of precorrosion test were performed. The first was done by varying the presorrosion portion (GGC) of the exposure while holding the SCC portion constant. The second test involved a constant pre-

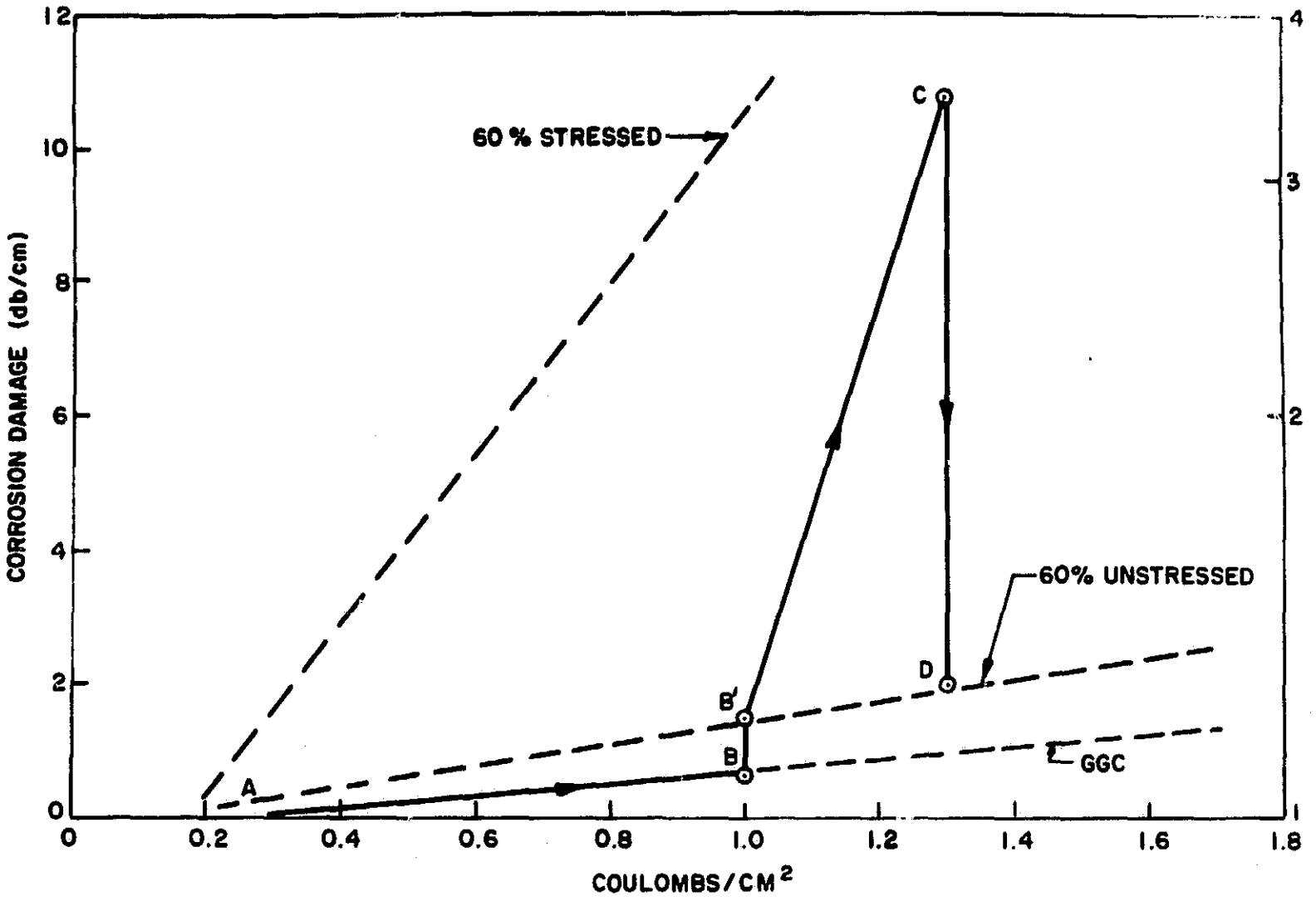

Fig. 118. Ultrasonic attenuation due to precorrosion at various stages of the test (also shown are lines for normal SCC at 60% of the yield strength and GGC)

corrosion and a varying SCC exposure.

A summary of the ultrasonic results is shown in Figs. 119 and 120. These figures are the usual plots of the ultrasonic attenuation per unit distance (db/cm) versus the amount of corrosion (C/cm^2). The same figures show the results of conventional SCC for the cases of samples stressed to 60% of the yield strength and examined in both the stressed and unstressed states, and also for GGC. The microscopic examination was in agreement with previous GGC and SCC tests.

Fig. 119 contains the results of the first type of precorrosion test, that is, constant SCC portion and varying precorrosion. The constant SCC exposure was 0.3 C/cm^2 or 9.45 min. The change in Rayleigh wave attenuation at various stages of the precorrosion test is shown by the heavy, thick lines.

Fig. 119 indicates that the damage produced during the SCC portion of the test (segment BC) is always greater than that produced during conventional SCC for the same exposure. In other words, the slopes of the BC segments are always greater than the conventional SCC-60% stressed line. For example, in Fig. 119, AB represents typical precorrosion (in this case, 1 C/cm^2). Segment BC is due to an additional 0.3 C/cm^2 of SCC exposure. This additional exposure increased the attenuation by about 9.4 db/cm. The attenuation produced in a U-bend stressed to 60% should be at most 3.8 db/cm for 0.3 C/cm^2 of SCC, if we disregarded the initial incubation period of 0.2 C/cm^2, and 1.7 db/cm if we take it into account. Finally, segment CD shows the decrease of attenuation when the stress is removed. The results dramatically demonstrate the effect of precorrosion.

Fig. 119 can be divided into two regions. By drawing a line through point C parallel to the GGC line (dotted line), we obtain its intercept (point I) with the 60% stressed line for conventional SCC tests. The value of point I is 0.95 C/cm^2. The amount of precorrosion and of SCC corresponding to point I would be 0.65 and 0.3 C/cm^2, respectively, giving a combined exposure of 0.95 C/cm^2. The region to the left of I involves total exposures (GGC and SCC) smaller than 0.95 C/cm^2, whereas the second region to the right of I involves total exposures greater than 0.95 C/cm^2.

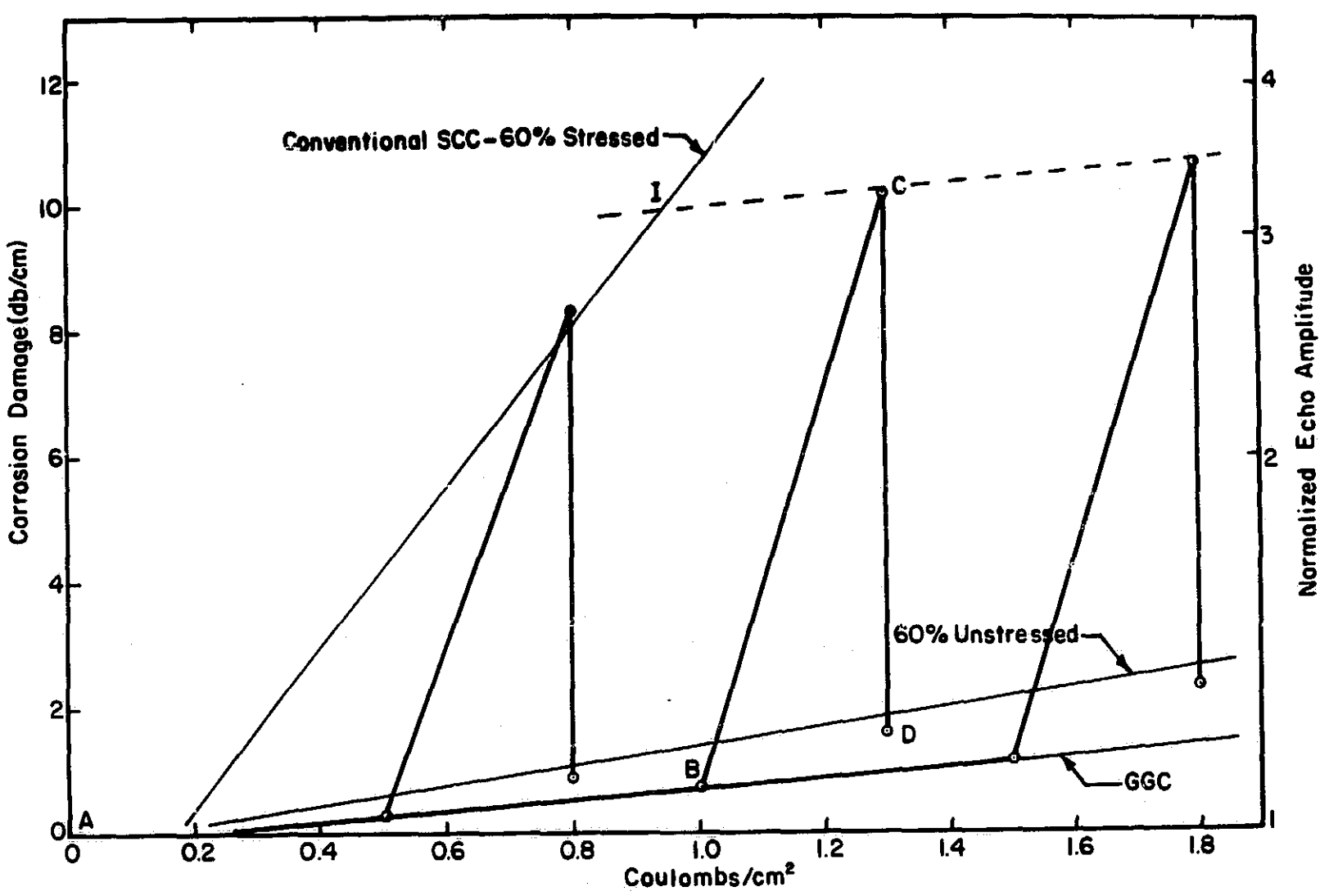

Fig. 119. Ultrasonic attenuation due to precorrosion (heavy lines) at various stages of the test (constant SCC exposures)

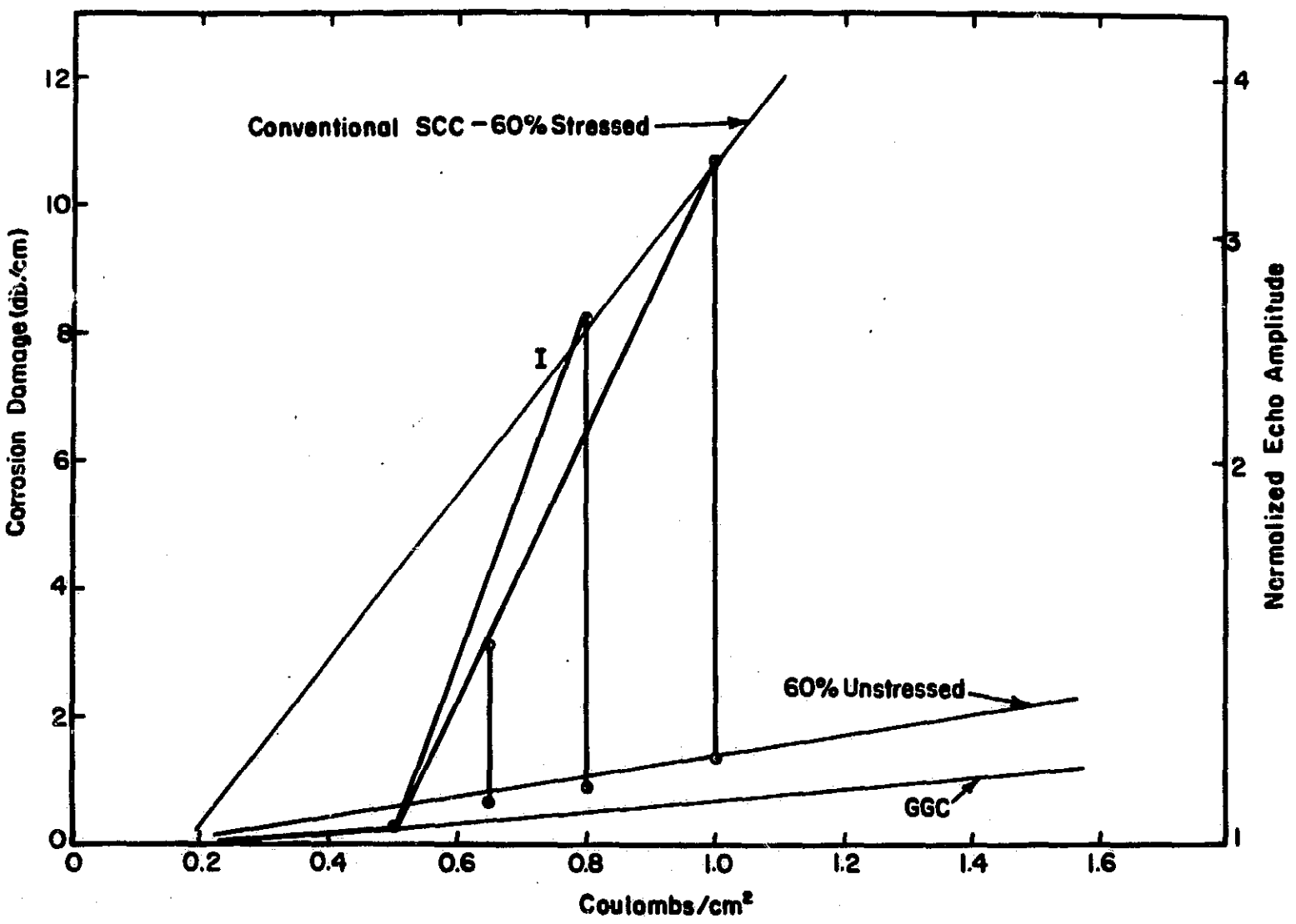

Fig. 120. Ultrasonic attenuation due to precorrosion (heavy lines) at various stages of the test (constant GGC exposures)

To the right of point I, i.e., for precorrosion greater than 0.65 C/cm^2, the damage produced by the SCC portion (0.3 C/cm^2) is constant (9.4 db/cm), but the total damage is smaller than the damage from conventional SCC for the same combined exposure. To the left of point I, i.e., for precorrosion exposures less than 0.65 C/cm^2, the damage produced by the constant SCC portion decreases as we move from point I to the incubation threshold (0.2 C/cm^2). However, at any time this damage would be greater than the damage expected for conventional SCC for the same pure SCC exposure time (0.3 C/cm^2) without precorrosion. The total damage would be equal to or smaller than the damage from a conventional SCC exposure for the same combined exposure. In general, point I in Fig. 119 will move to the right or to the left of its present position (0.95 C/cm^2) as the SCC portion of the exposure (0.3 C/cm^2) increases or decreases.

Fig. 120 contains the results of the second type of precorrosion test, i.e., constant precorrosion portion and variable SCC portion. The constant precorrosion was 0.5 C/cm^2 or 15.75 min. This figure indicates that increasing SCC exposure produces increasing damage. This damage is always greater than the damage from a similar exposure to conventional SCC. As in Fig. 119, the results fall into two distinct regions. We observe that for total exposure (GGC and SCC) greater than 0.8 C/cm^2 (point I), the combined damage equals the damage expected for conventional SCC tests. For total exposures less than the value of I, the damage is less than that produced in conventional SCC tests. Again, as in Fig. 119, point I in Fig. 120 will also move to the right or left as the precorrosion portion of the exposure (0.5 C/cm^2, in this case) increases or decreases, respectivel

The results of the precorrosion investigations given in Figs. 119 and 120 have been combined in Fig. 121 as follows. The horizontal axis is the ratio, r_e, of the precorrosion portion of the exposure (GGC) to the total exposure (GGC + SCC). The vertical axis is the ratio, r_d, of the damage produced by the combined exposure (GGC + SCC) to the damage caused by conventional SCC applied for a time equal to the total exposure (GGC + SCC). Both r_d and r_e can range from zero to one.

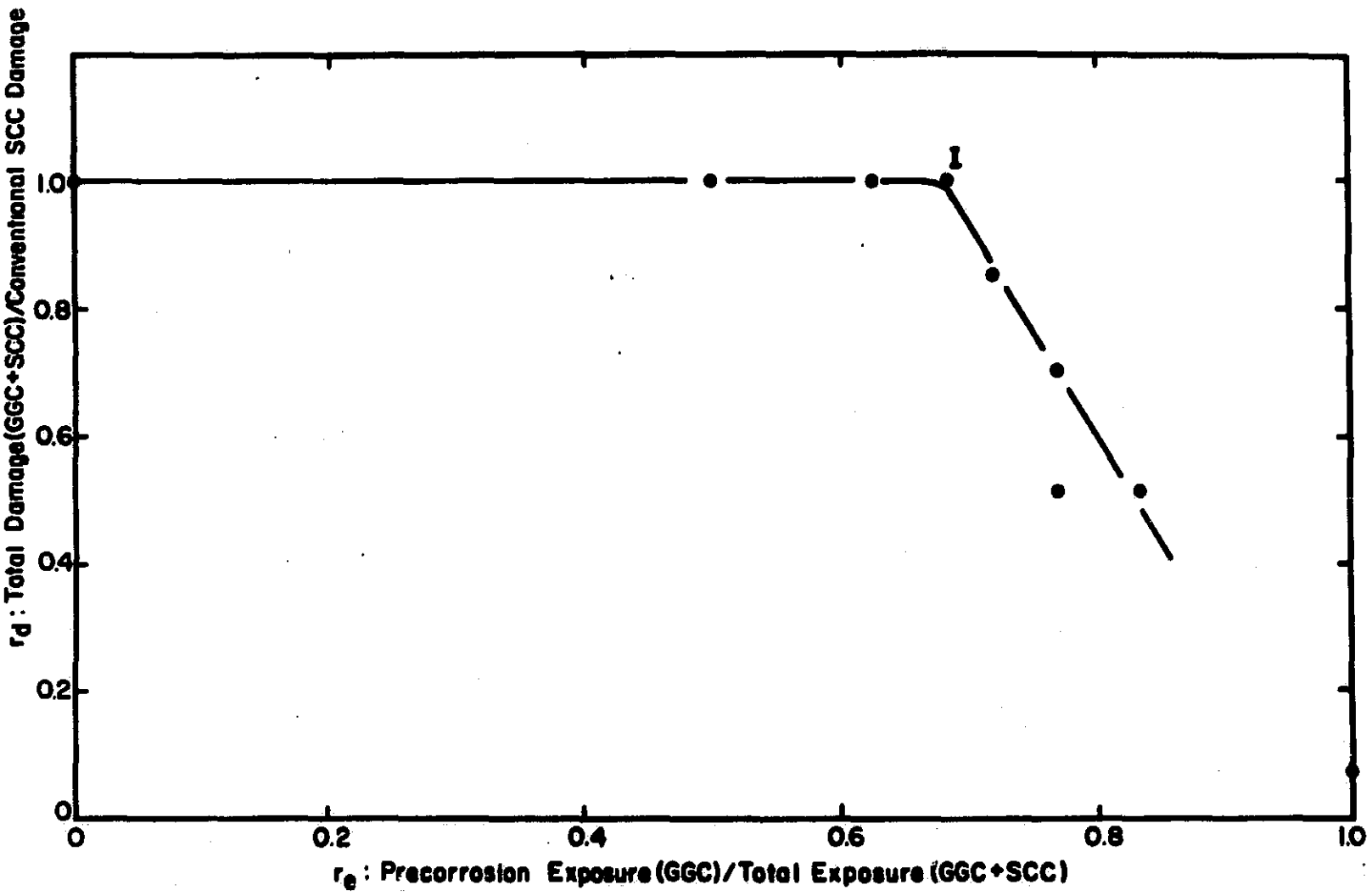

Fig. 121. Normalized corrosion damage versus precorrosion exposure for 7075 (T651)

Such normalization of the axes was carried out in order to plot and evaluate the results of both Figs. 119 and 120 simultaneously and independently of the type of precorrosion test (varying precorrosion or SCC). When r_d is one, the damages produced in the precorrosion test and conventional SCC tests for the same charge are identical. For r_d less than one, the damage in the precorrosion test is less than the SCC test.

If we refer to Fig. 121, we see that a distinct break in the graph occurs at $r_e = 0.685$. If the precorrosion portion of the exposure is less than about 0.7 of the total exposure, the final total damage (GGC and SCC) will be equal to the damage expected for conventional SCC, i.e., $r_d = 1$. However, to the right of the break, or when the precorrosion portion of the exposure is greater than 0.7 of the total exposure, the final damage will be smaller than the damage expected from conventional SCC, decreasir with increasing GGC exposure. The minimum value of r_d occurs when $r_e = 1$. At this point, $r_d = 0.07$ and corresponds to the case of simple corrosion (GGC) without stress.

The general nature of the results of Fig. 121 strongly resembles the results of Fig. 36 of this report. The principal difference in these two figures is that previously the precorrosion tests were characterized by time to failure, whereas here the damage was monitored ultrasonically and measured in terms of an acoustic attenuation. Also, the stress level used here was 60% of the yield strength, whereas earlier it was 90%.

The conclusions drawn from the two studies are similar. In the mechanism study it was concluded that for 7075-T651, about 80% of the time to failure of as machined specimens in conventional SCC tests corresponds to pure precorrosion. According to Fig. 121, for precorrosion exposures up to 70% of the total exposure, the total damage is equal to the damage produced by conventional SCC for the same total exposure. For precorrosion exposures greater than 70% of the total exposure, the total damage is smaller than for conventional SCC, and decreases with increasin precorrosion exposure.

Fig. 122 can be used to illustrate the connection between the two studies. It is a general plot (arbitrary units) of corrosion damage versus exposure. The plot is over exposures ranging from zero to time to failure. The results of phase I were obtained at fracture. In the NDT part, however, exposures were less than the time to failure and the situation at fracture is extrapolated. We see, for example, that a total exposure smaller than the fracture time produces damage equal to conventional SCC if the pre-corrosion portion (say, GGC_1) is less than or equal to 70% of the total exposure ($GGC_1 + SCC_1$). Then, at the fracture time, i.e., with the total exposure equal to the time to failure ($GGC_2 + SCC_2$ in Fig. 122), we can say that if the precorrosion exposure (GGC_2) is equal to or less than 70% of the fracture time ($GGC_2 + SCC_2$), the damage on the specimen will be the same as in a conventional SCC test. That is to say, the specimen will fracture. If, at the normal fracture time, GGC_2 is greater than 70% of the total exposure, the total damage will be less than that normally found at this time, i.e., the sample will not fracture. Then we can say that 30% of the normal fracture time is pure SCC, the other 70% of the damage at failure can be derived from pure corrosion.

The general conclusion of the precorrosion investigation is that we can arrive at a particular amount of damage, points C_1 or C_2 in Fig. 122, via two paths. First, by following the conventional SCC path directly to points C_1 or C_2 in Fig. 122 (lines AC_1 or AC_2) by conventional SCC. The second path is precorrosion followed by SCC, i.e., initially along the GGC line (line AB_1 or AB_2) and then up to the conventional SCC line (line B_1C_1 or B_2C_2). This important result shows that the role of precorrosion may be to sensitize the surface to the development of microcracks during the SCC portion of the exposure. In phase I, it was shown that precorrosion is probably the result of the disruption of the grain boundary structure at the surface of the specimen.

In addition to the types of precorrosion tests discussed in the foregoing paragraphs, another type of intermittent test was performed. This consisted of additional GGC to the test specimens used previously. That is, the U-bends were subjected to additional plain corrosion (GGC) after the

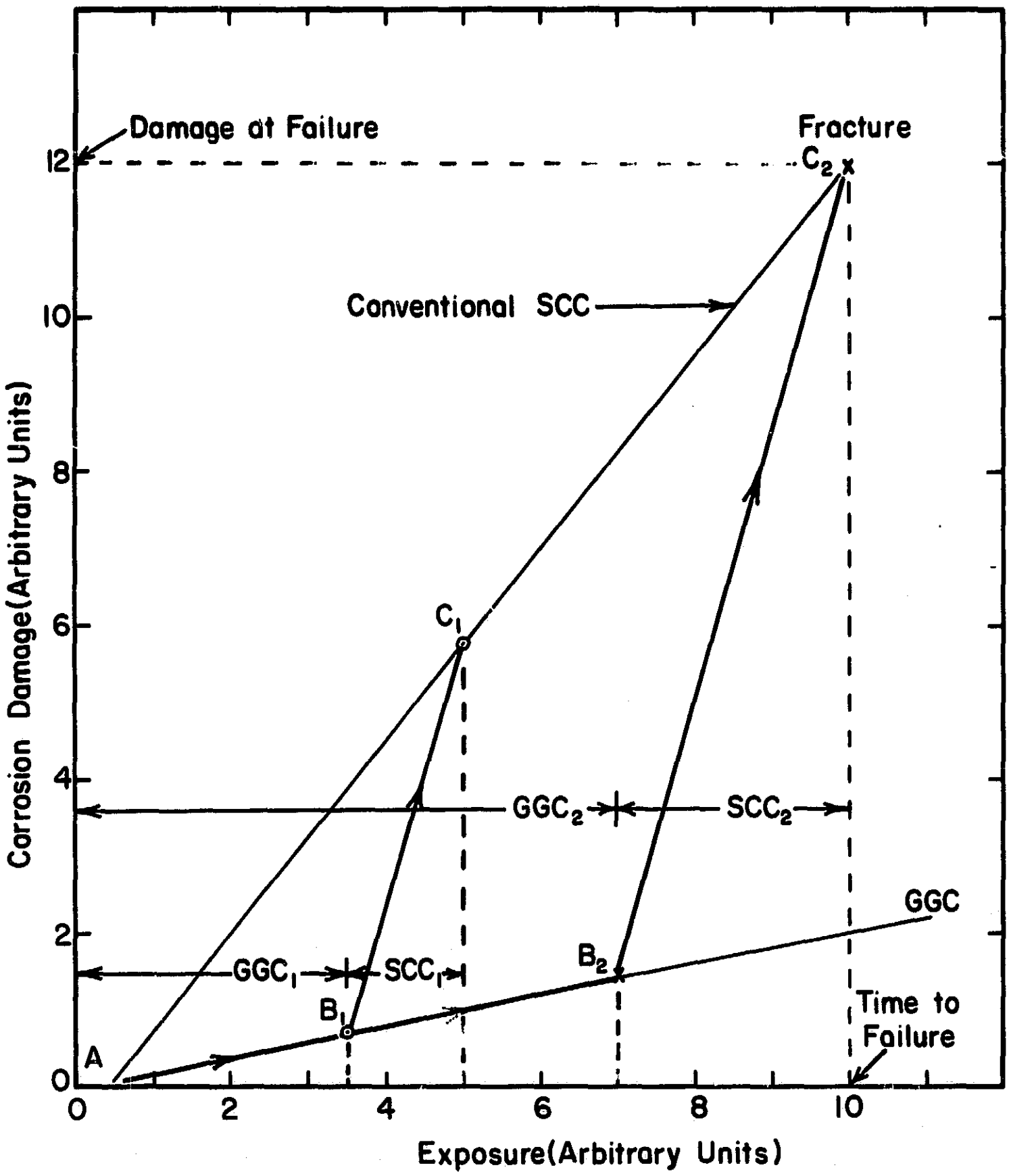

Fig. 122. Typical corrosion damage versus precorrosion exposure curves for exposures up to fracture

stress applied during the SCC portion was released. A typical test is outlined in Fig. 123. The precorrosion portion is represented by line AB; line BC is the SCC part, line CD represents release of the stress, and line DE represents the additional GGC. The results indicate that subsequent GGC produces additional damage at a rate equal to conventional GGC, i.e., segment DE is parallel to the conventional GGC line.

A brief study was made of the effect of SCC tests where the stress level varies during the test. The principle involved in the variable load SCC tests is similar to that of precorrosion tests. Here, the initial GGC part of the precorrosion exposure is substituted by an SCC part. That is, the test consists of two SCC periods at different stress levels.

Only preliminary data were obtained in this study, However, the results were similar to those expected on the basis of the precorrosion studies. A typical test is shown in Fig. 124. Here, the U-bend (7075) was initially stress corroded at 20% of the yield strength for 0.6 C/cm^2 (segment AB). Then, the sample was stressed to 60% of the yield strength (segment BB'). The small increase in attenuation during the stressing process was probably due to mechanical deformation of microcracks already produced in the first part of the test (segment AB). Next, the U-bend was stress corroded at 60% of the yield strength for 0.4 C/cm^2 (segment BC) for a total exposure of 1.0 C/cm^2. Then, the stress was removed (segment CD).

From Fig. 124 we see that the damage caused by the second exposure (segment B'C) is greater than the damage expected from a conventional SCC test at the same stress level and exposure, i.e., 60% of the yield strength and 0.4 C/cm^2, respectively. Further, the total damage after a cumulative exposure of 1.0 C/cm^2 was equal to that expected from conventional SCC tests at 60% of the yield strength. This indicates a behavior similar to that exhibited by precorrosion.

Additional tests need to be made to determine if an exposure of less than 0.4 C/cm^2 would move point C to the SCC 60% yield strength curve. With more tests, a figure similar to Fig. 121 should be able to be constructed.

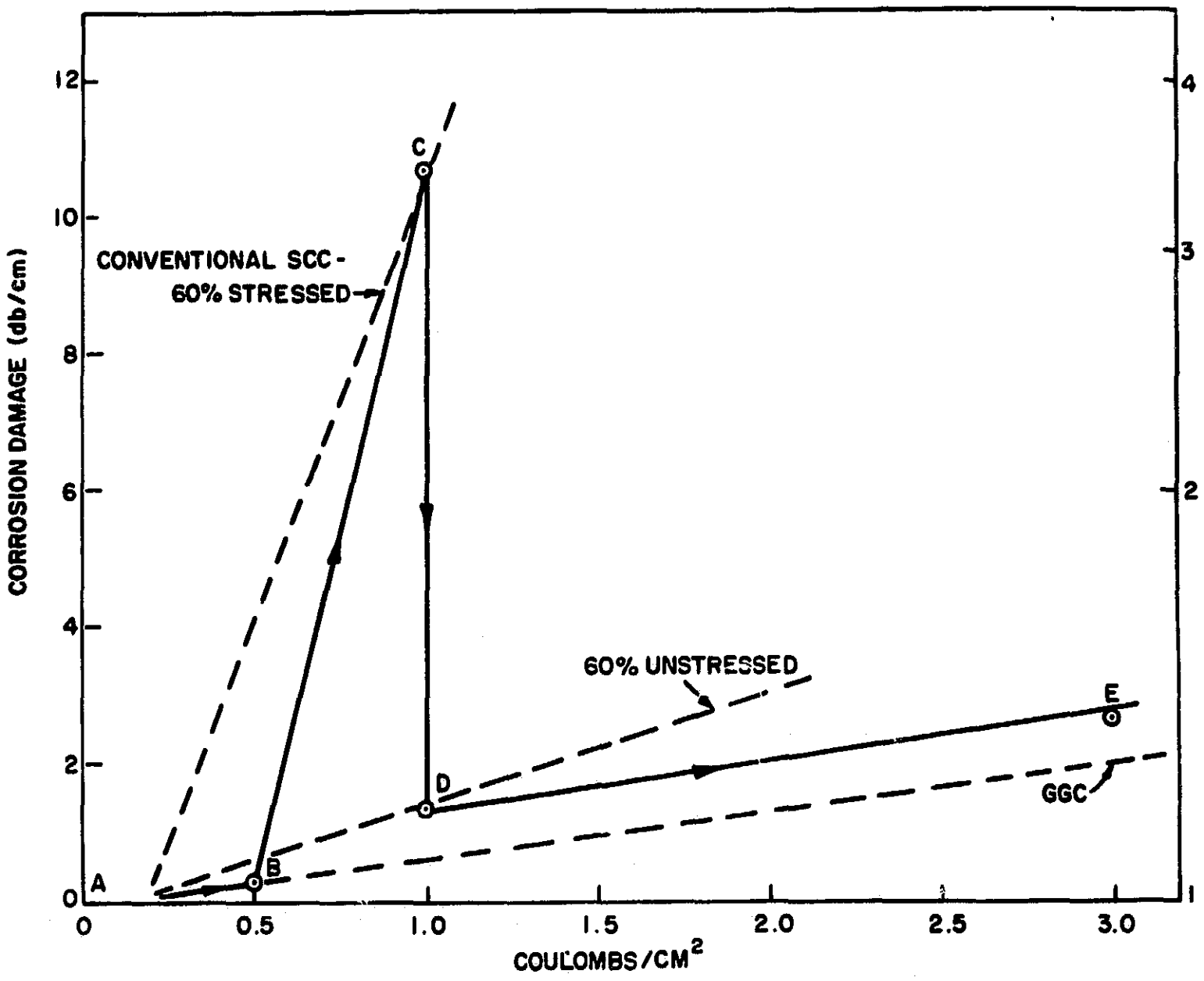

Fig. 123. Ultrasonic attenuation due to intermittent precorrosion (heavy lines) at various stages of the test

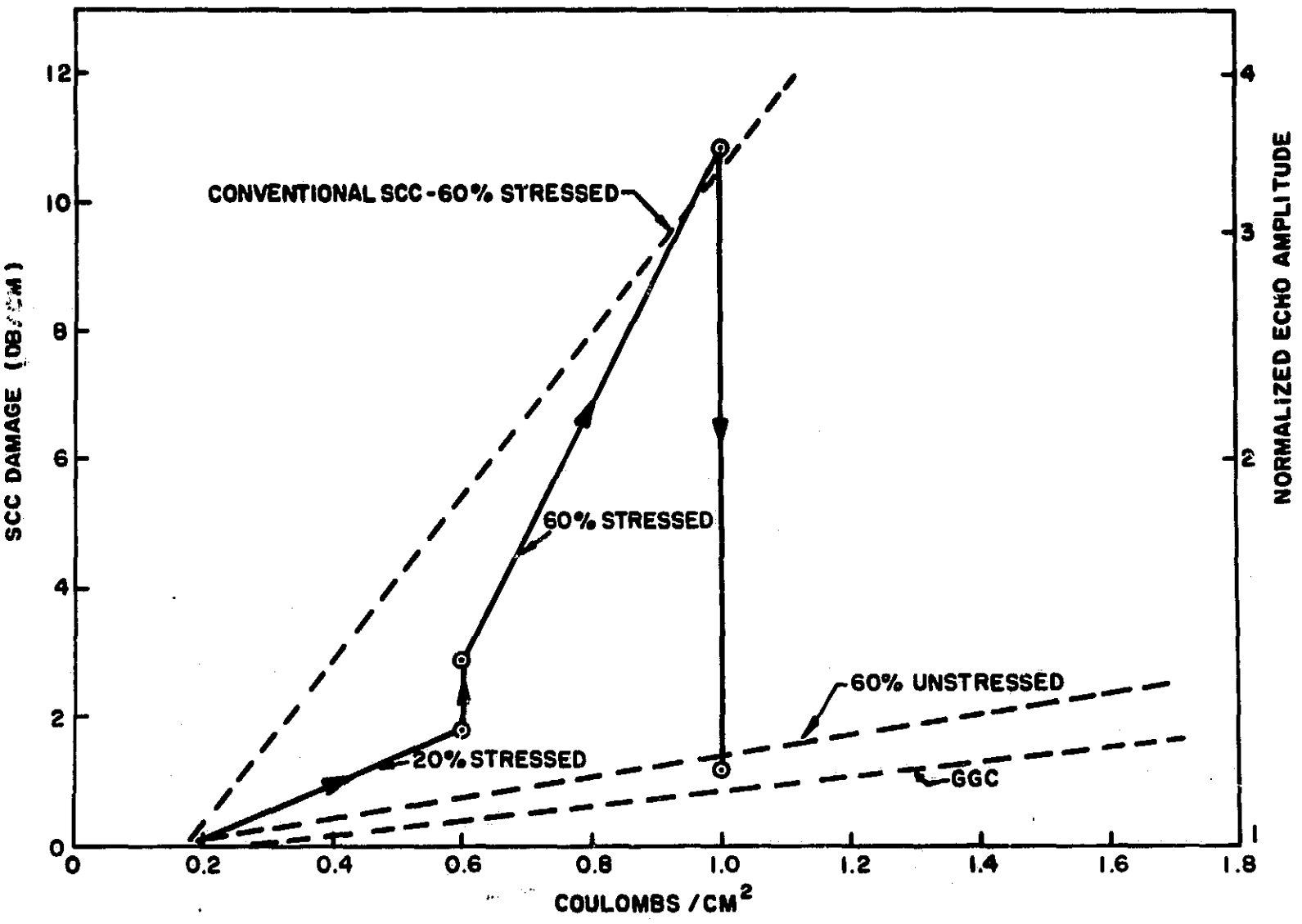

Fig. 124. Typical test of 7075 U-bend specimen under various conditions

8. Resolution of ultrasonic measurements

In the examination of the oscillograms in the SCC studies, small echoes were observed from the corroded area at the bend of the U-bend specimens. These echoes were present before the samples were stressed, and are possibly associated with the slight anisotropy of the aluminum plate produced by the rolling or machining process. Normally, polycrystalline aluminum should be an isotropic medium, but since the elastic moduli change slightly with stress, the medium loses its isotropic character to some degree. The velocity of Rayleigh waves is stress dependent;[23] however, the change in velocity is only of the order of 0.1%, which is below the limit of measurement for ordinary pulse-echo ultrasonic instruments.

An investigation of the nature of these echoes as a function of stress was made to avoid misinterpreting them as small echoes originating from microcracks. This was done by continuously monitoring these echoes with the fixed position probe assembly while the U-bend specimen was being stressed. The results are shown in Figs. 125 and 126 for 7075(T651) and 2219(T37), respectively. These figures are oscillograms of the echoes obtained with high instrument gain and are very similar in nature. In Fig. 125, the four oscillograms were taken at stress levels of 0, 20%, 85%, and 100% of the yield strength of 7075. In Fig. 126, part (a) corresponds to no stress, part (b) to 90% of the yield strength, part (c) to a stress well beyond the yield point, and part (d) to the well relaxed state after the stress was released. In the last stage, part (d), the U-bend specimen had been permanently deformed, since its leg separation had decreased by 10% of the original value.

Examination of both figures indicates that essentially the nature of these small echoes does not change with increasing stress. The change in their relative amplitude, which was monitored through reference echoes, was not more than 2 db. In order to differentiate between these echoes and those from microcracks, especially at the early stages, photographs of the original echo distribution would be necessary. In practice, at high instrument gain, reflections from such surface features would have to be taken

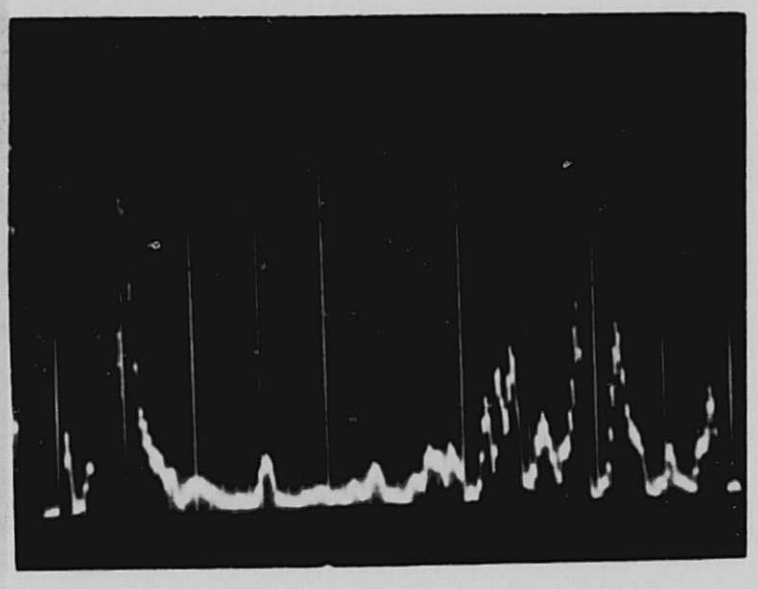

(a) 0% of the yield strength

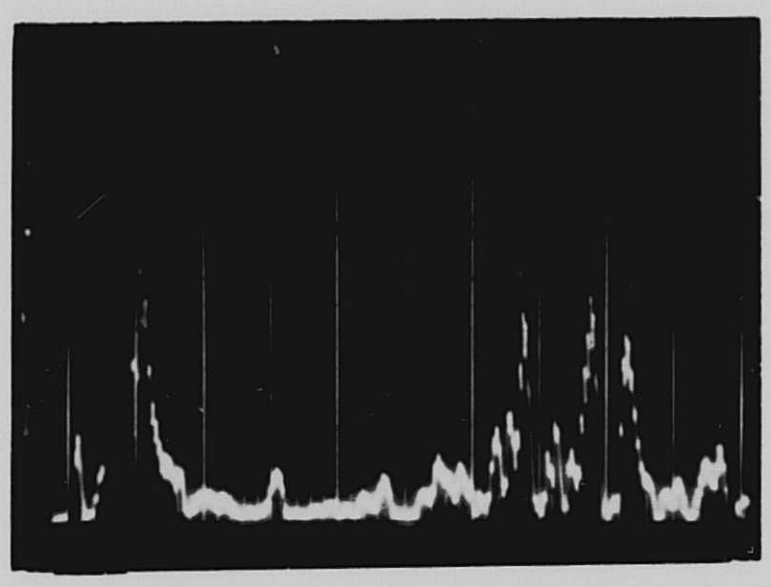

(b) 20% of the yield strength

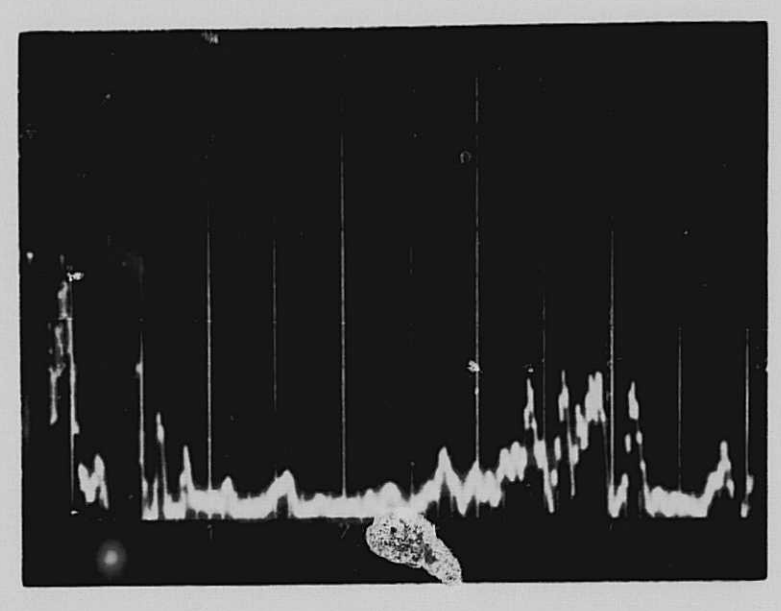

(c) 85% of the yield strength

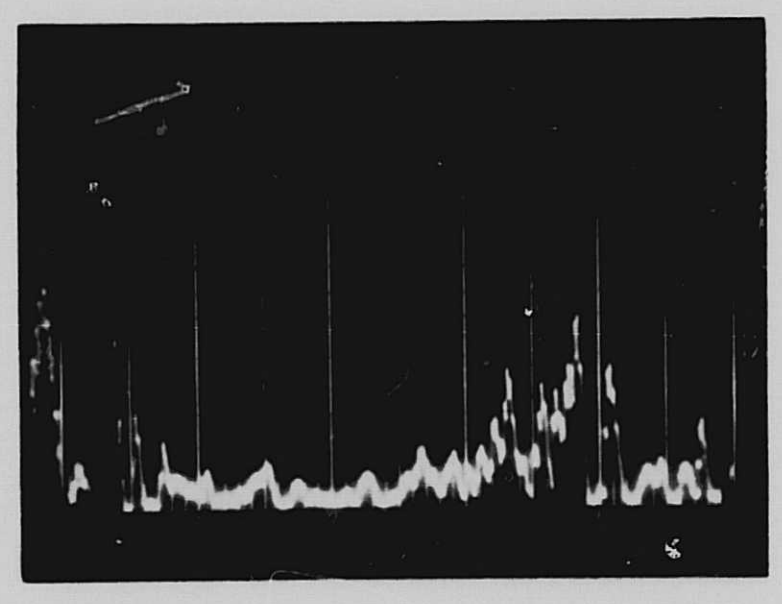

(d) 100% of the yield strength

Fig. 125. Oscillograms indicating the effect of applied stress on small echoes present in the area to be corroded before commencement of SCC tests for 7075 (T651)

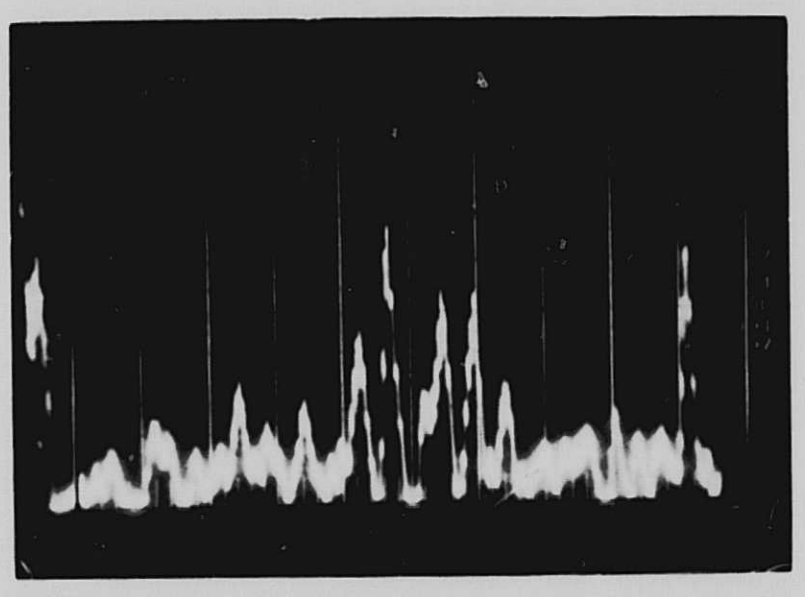

(a) 0% of the yield strength

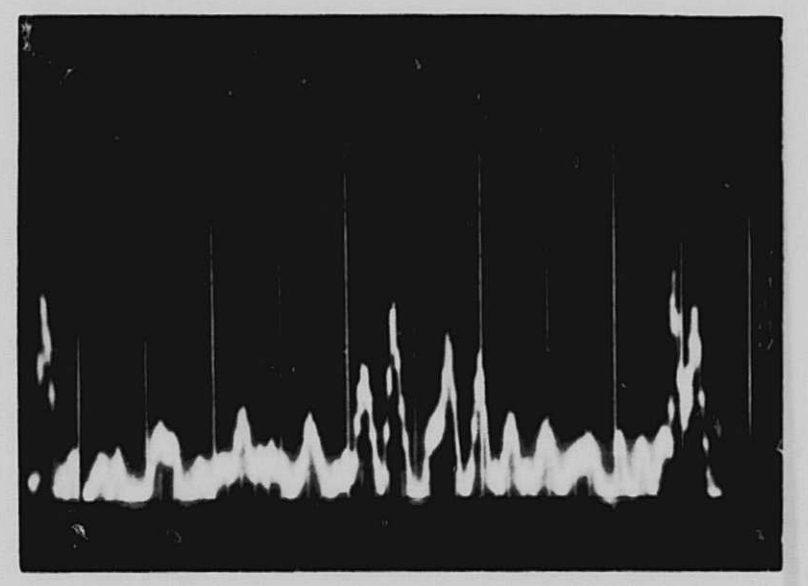

(b) 90% of yield strength

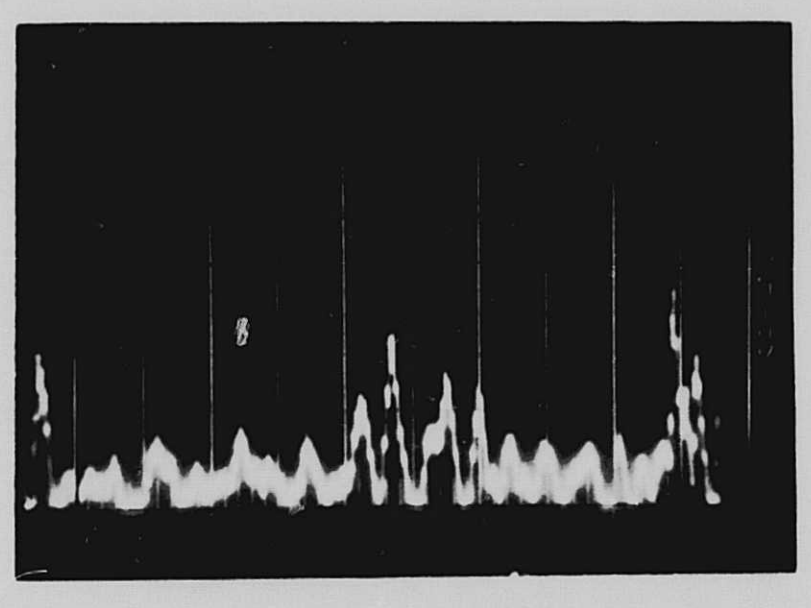

(c) Well beyond yield point

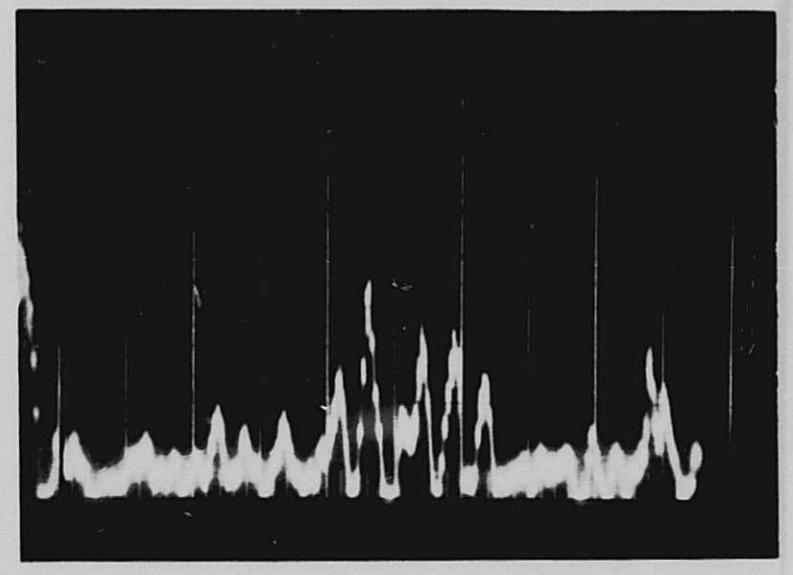

(d) After stress was relieved and U-bend specimen had been permanently defor

Fig. 126. Oscillograms indicating the effect of applied stress on small echoes present in the area to be corroded before commencement of SCC tests for 2219-T37

into account. For most SCC detection purposes, one would not need to use such high gains, and no serious difficulty would arise.

No change in the conductivity was detected with stress as indicated by the Dermitron eddy current tester.

The general nature of SCC involves closely spaced microcracks which, depending upon their relative separation, can produce either single or distinct echoes. Ideally, two isolated parallel grooves have to be a finite distance apart before they can produce two distinct signals on the screen of the ultrasonic flaw detector. This is the "resolving power" of the instrument and is defined as the ability to distinguish between two closely spaced grooves. This depends, among other things, on the pulse width of the emitted wave, on the bandwidth of the signal amplifier, and on the oscillator frequency.

To determine the actual resolving power of the instrument used in this investigation (Krautkrämer type USIP 10W, 4-MHz probe), two 1.5-mil-wide parallel grooves with varying separations were cut on a flat surface of 7075, and the corresponding oscillograms observed.

The results are shown in Fig. 127. Parts (a) and (c) of this figure were taken with a scale of 0.66 cm of aluminum per division, while (b) and (d) were taken with 0.055 cm of aluminum per division. Echoes A and B on parts (a) and (b) are from two grooves 1/16 in. (1.5 mm) apart. This separation was well resolved. When the groove spacing was 1/32 in., the echoes were not resolved. This spacing is shown in parts (c) and (d) of Fig. 127. Thus, the resolving power of the instrument is roughly 1.5 mm and is about the same as for similar instruments reported by other experimenters.[24] Since similar settings were used in the SCC investigations, echoes from microcracks were not necessarily completely resolved. A single echo from the corroded area could easily come from several closely spaced microcracks or pits.

High resolution NDT ultrasonic instruments[25] have been developed with resolving powers of the order of 0.4 mm.

9. Effective crack depth

Originally, the corroded U-bends were cleaned by a simple rinse in distilled water followed by acetone. It was observed that if the

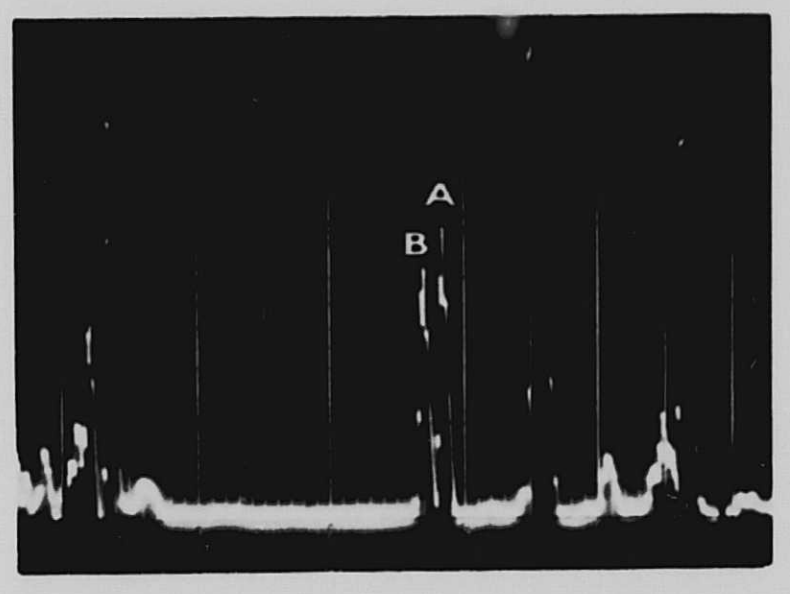

(a) Groove separation ~ 1/16 in., scale = 0.66 cm Al/div

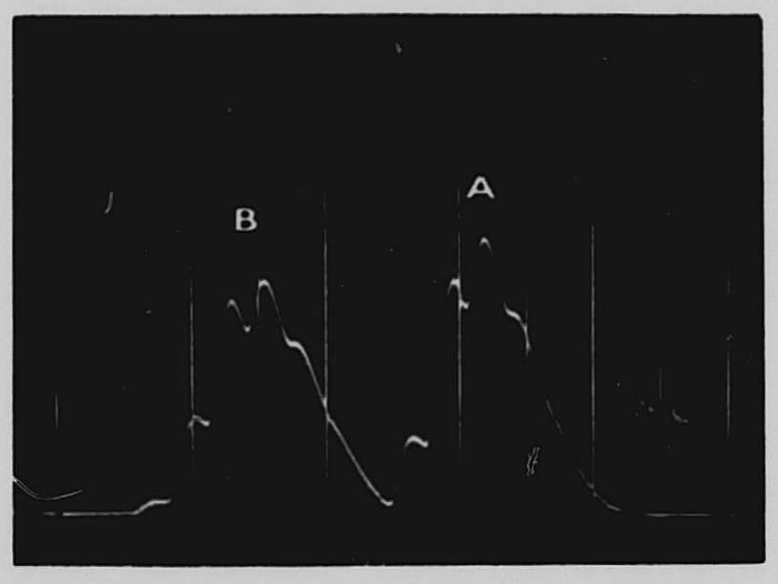

(b) Groove separation ~ 1/16 in., scale = 0.055 cm Al/div

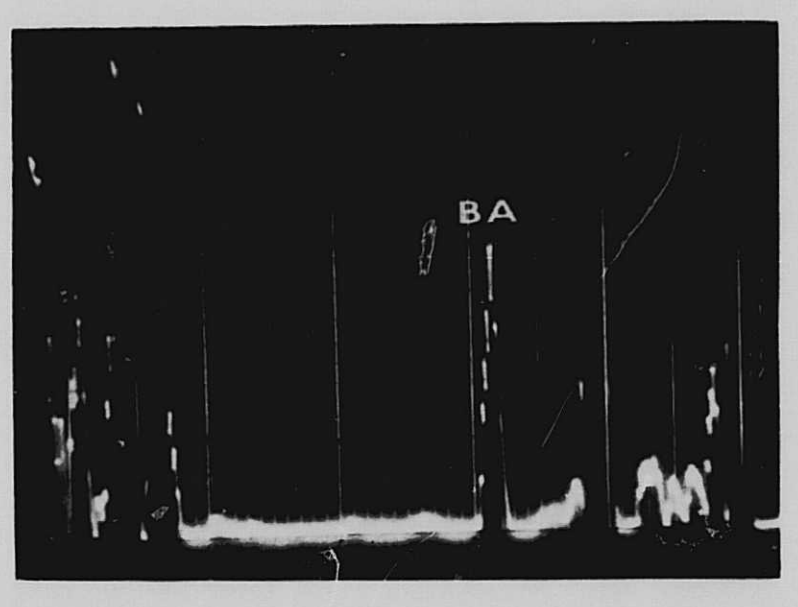

(c) Groove separation ~ 1/32 in., scale = 0.66 cm Al/div

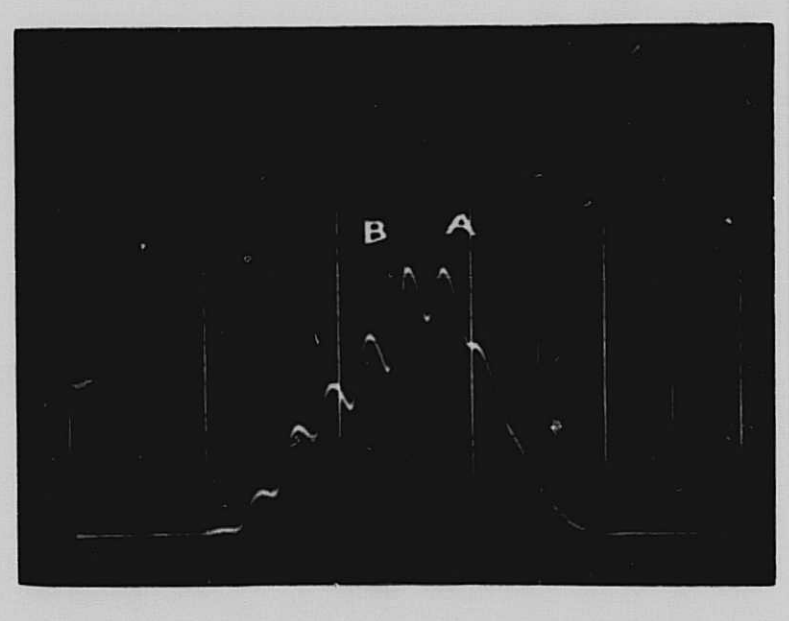

(d) Groove separation ~ 1/32 in., scale = 0.055 cm Al/div

Fig. 127. Resolving power of ultrasonic instrument (Krautkrämer type USIP 10 W, 4-MHz probe)

sample was ultrasonically agitated while being rinsed in water (followed by acetone), the Rayleigh wave attenuation was found to be slightly higher. This seems to indicate that liquid trapped in the tip of the cracks can decrease the effective attenuation.

Table VII shows the increase in attenuation when ultrasonic agitation is used for cleaning U-bends corroded under various conditions. The samples were still under stress when the measurements were made.

To rule out the possibility that the increase in attenuation was caused by continued corrosion of the U-bend which was still under stress by trapped solution, the U-bend was immersed in the original solution and the original cleaning procedure was repeated. Excellent agreement with the first data (no ultrasonic agitation) was obtained. This is demonstrated in Fig. 128 which is a series of oscillograms obtained at different stages of the experiment. Part (a) is the reference oscillogram, part (b) corresponds to initial removal from the corrosive bath and cleaning, and part (c) is the oscillogram obtained after the U-bend specimen has been ultrasonically cleaned. Parts (d) and (e) correspond to oscillograms obtained after the reimmersion. Part (d) was taken immediately after removal and simple cleaning, and part (e) after ultrasonic cleaning. Finally, part (f) was taken when the stress was released (unstressed state). It is seen that oscillograms (b) and (d), and (c) and (e) are identical, which implies that when the solution reenters the tip of the cracks it reduces the attenuation by exactly the same amount as when the sample was initially removed from the corrosive bath.

The following explanation is proposed. When the U-bend specimens were initially cleaned, the solution trapped in the tips of the cracks acted as a coupling medium between the two sides of the crack, thus allowing more energy to be transferred across the sides of the cracks. In other words, the effective depth of the crack is decreased. When the specimen is cleaned by ultrasonic agitation, the solution at the tip is replaced by acetone which may easily evaporate. This illustrates that some care should be taken in SCC tests with regard to the cleaning of SCC specimens. The higher attenuation does not materially affect previously reported results. The primary result would be to increase the slope of the attenuation versus SCC damage by approximately 15%.

Table VII. Increase in the Amplitude of the Reference Echo After Cleaning Using Ultrasonic Agitation

Stress Level, % yield strength	Current Density, ma/ cm^2	Charge, C/ cm^2	pH	Increase of Echo, db
30	0.53	0.50	4.7	1.5
30	0.53	0.80	4.7	2
30	0.53	1.00	4.7	2
60	1.50	0.50	4.7	2.5
60	1.50	1.00	4.7	4
60	0.53	0.35	2.1	2
60	0.53	0.50	2.1	3
60	0.53	0.70	2.1	3
90	1.50	0.54	4.7	4

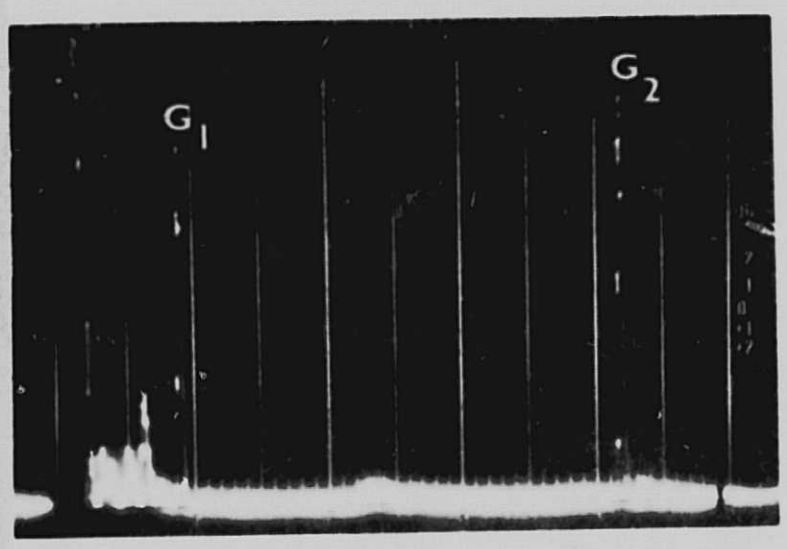

(a) Reference oscillogram

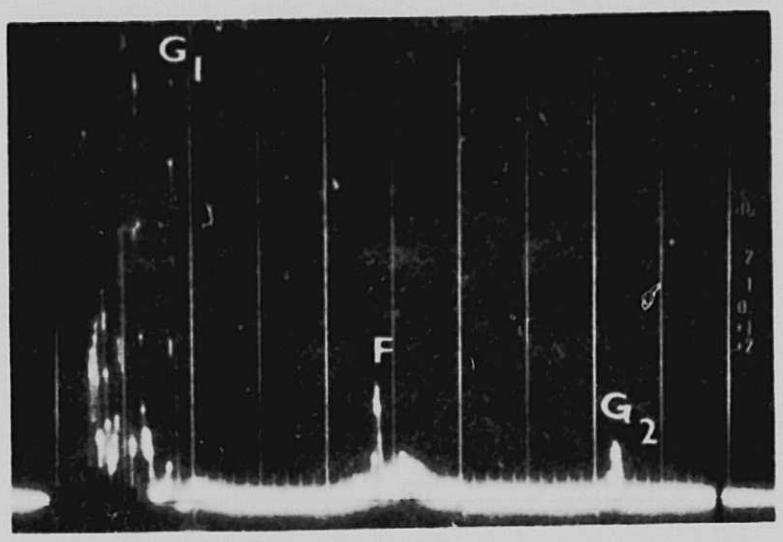

(b) After initial removal from corrosive bath and plain cleaning

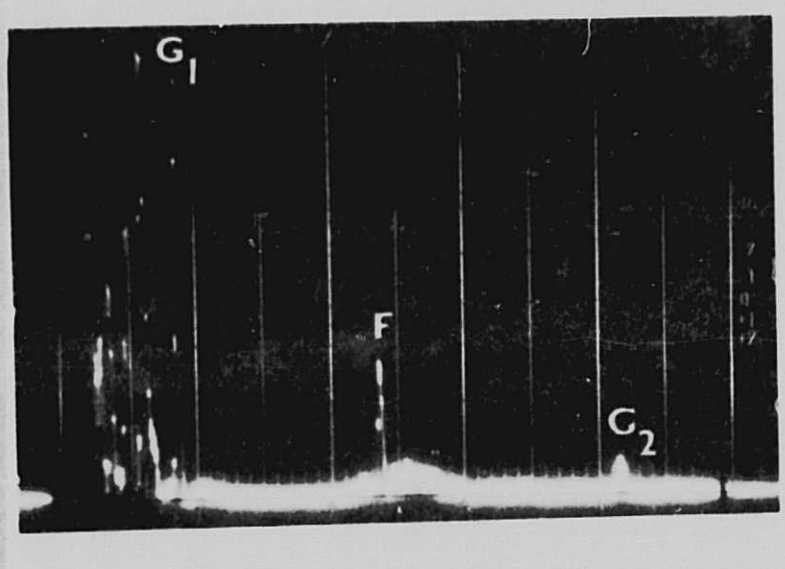

(c) After ultrasonic cleaning

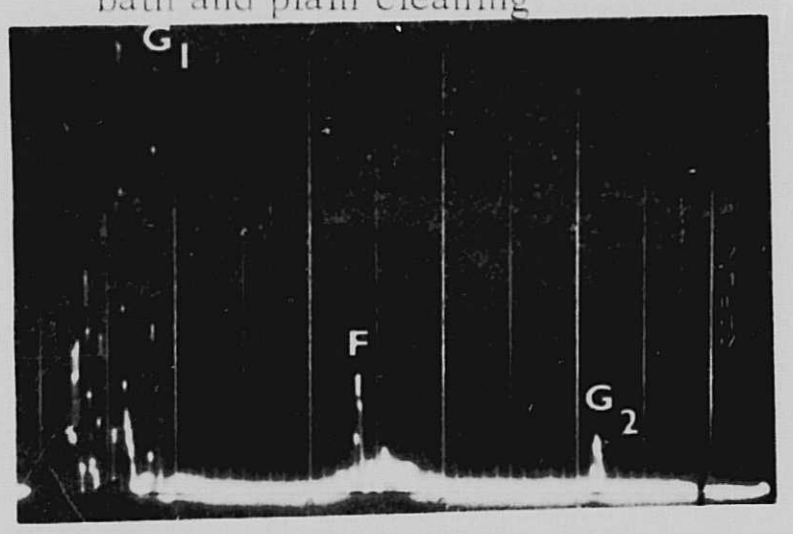

(d) After reimmersion removal and plain cleaning

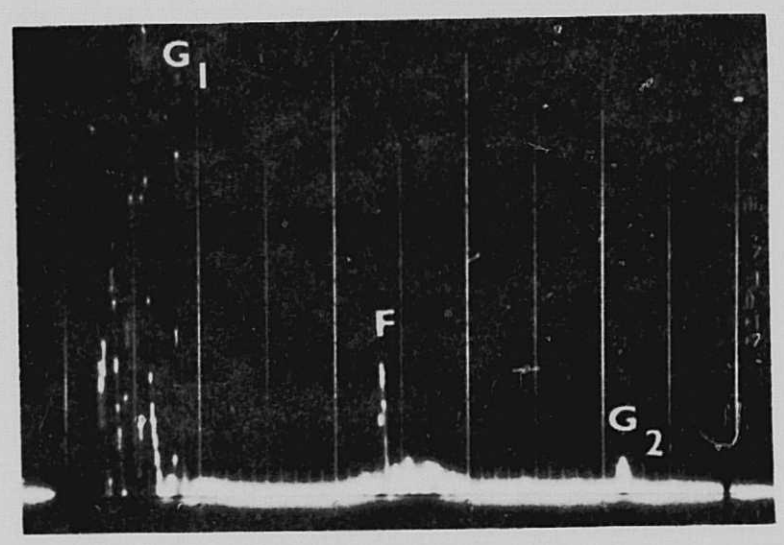

(e) After second ultrasonic cleaning

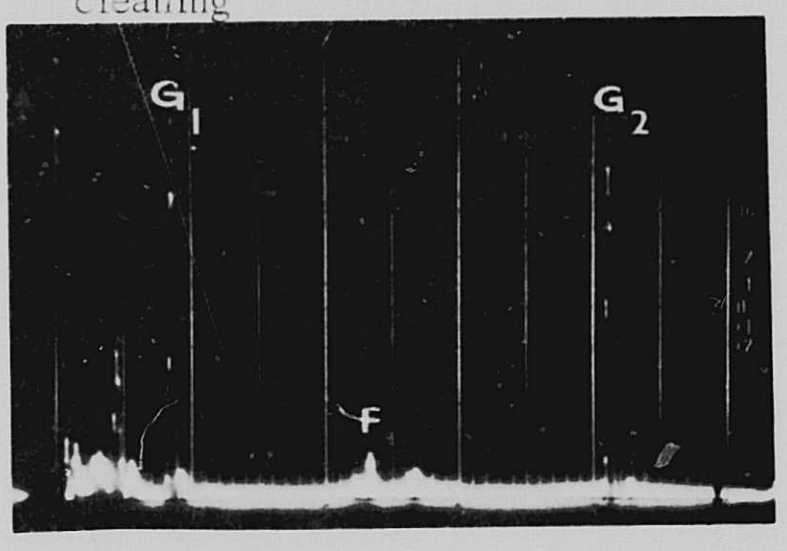

(f) Unstressed state

Fig. 128. Oscillograms illustrating the effect of cleaning by ultrasonic agitation for 7075 at 30% of the yield strength and 0.53 mA/cm after 1.0 C/cm^2 charge

It has been observed that U-bends left under stress fail after hours or a few days following removal from the corrosion bath. This can probably also be understood in terms of the corrosive solution which is apparently trapped in the tip of the cracks.

10. Anisotropy of Rayleigh wave echoes from SCC

In this investigation, the anisotropy of reflections from stress corrosion cracks was studied as a function of the angular rotation of the probe. This measures the sensitivity of the Rayleigh waves to defects on a corroded area not perpendicular to the ultrasonic beam. The tests included both 7075 and 2219 alloys, SCC and GGC, stressed and unstressed states, 60% and 90% of the yield strength stress levels, and different amounts of exposure to the corrosive environment. Because of geometry, the maximum allowed rotation of the probe on the U-bend specimens was about 40°. Fig. 129 shows the results. The amplitude of the highest echo originating from the corroded area was measured with respect to the corresponding echo at normal incidence. That is, the echo at normal incidence is taken as 0 db and all other echoes were referenced to it.

Fig. 129 also includes the results for a single artificial, straight reflector and multiple short parallel grooves. A complete discussion of artificial defects is presented in the Appendix. The principal observations of this investigation and some appropriate explanations are listed below.

1. The scatter between points of different specimens is of the order of that observed between points of the same sample. Most of the data points are correct within 2 db.

2. SCC and GGC are detectable over a wider angular range than a set of multiple short parallel grooves or a single isolated groove. This, for the case of SCC, is probably due to the fact that some cracks or segments of cracks make an angle with the transverse direction and are thus favorably oriented to a particular probe angle. This increases the angular sensitivity of the probe and makes possible the detection of stress corrosion cracks from wide angular limits. For the GGC case, the pits offer reflectors at all possible angles and this, in principle,

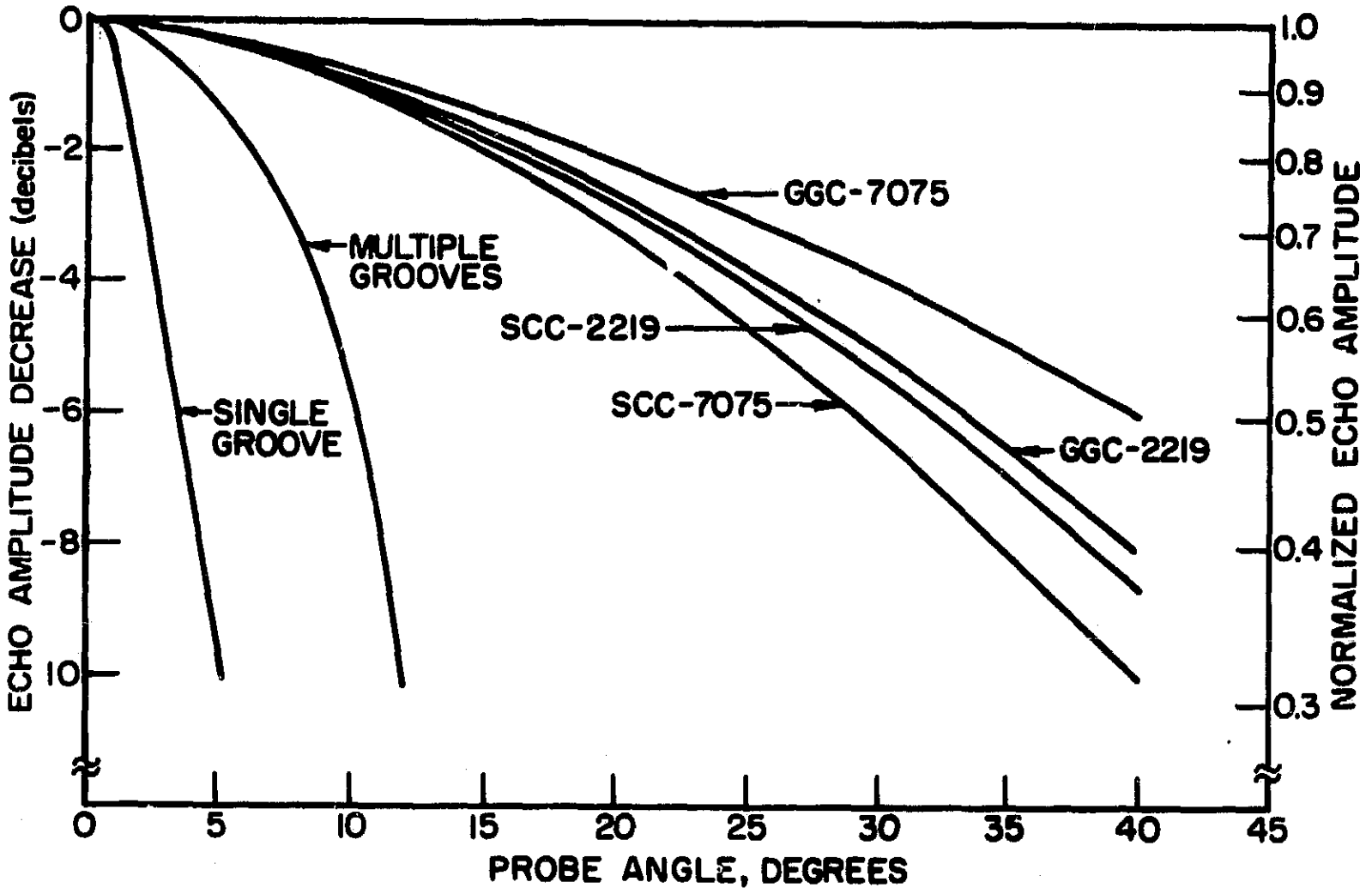

Fig. 129. Anisotropy of Rayleigh wave echoes from SCC, GGC, and artificial defects as a function of probe angle

makes GGC easier to detect than SCC. However, SCC is almost always accompanied by some plain corrosion. The best approximation to pure SCC would be the short exposures of 2219 specimens where the GGC attack is minimum.

3. GGC has a smaller variation of reflectivity with angle than SCC. The fact that there is any angular dependence of reflectivity with GGC probably arises through interaction of pit formation and the anisotropy of the aluminum produced by rolling in the fabrication process.

4. The angular dependence is independent of the amount of corrosion of the specimens for both GGC and SCC.

5. For the case of GGC, the relative reflectivity at any angle is less for 2219 than for 7075.

6. The results did not depend on whether or not the specimens were stressed or unstressed during ultrasonic investigation.

7. For SCC, the angular dependence of reflectivity was independent of the stress level (60 or 90% of the yield strength).

8. The greater decrease in reflectivity for 7075 than for 2219 at a given angle was possibly due to the zig-zag nature of the 2219 stress corrosion cracks.

11. Morphology of microcracks

The surface appearance of some SCC microcracks is shown in Figs. 102 and 109. The width of these microcracks was measured to be a fraction of a mil. In order to obtain an estimate of the depth of these microcracks as well as the morphology of their depth profile, destructive testing was used. Their profile in a plane perpendicular to the crack plane was obtained by sectioning U-bends. This profile is not necessarily at the deepest point of the microcrack.

Fig. 130 shows typical depth profiles (at a magnification of 250X) of microcracks on fractured 7075 U-bends stress corroded at 90% of the yield strength. Fig. 131 is the microcrack of Fig. 130a at 150X after the area had been etched to show the nature of grain boundaries. Fig. 131 indicates that the direction of propagation of the microcrack is indeed along the grain boundaries. The depth and width at the surface of these microcracks is about 300 and 15 μ, respectively, as measured from the photomicrographs.

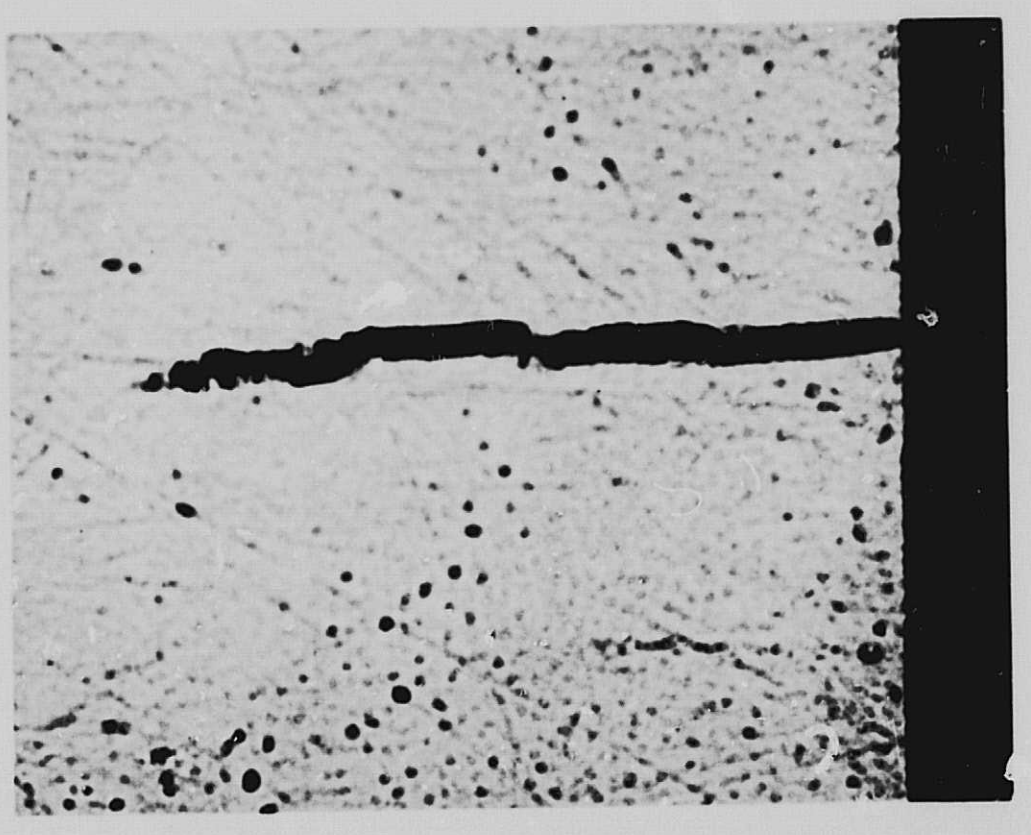

Fig. 130. Typical depth profiles of microcracks on 7075 U-bends stress corroded at 90% of the yield strength (250X)

Fig. 131. Microcrack of Fig. 130 (a) after area had been etched to show the nature of the grain boundaries (150X)

Another observation is that the tips of the microcracks are somewhat blunt instead of sharp. This can possibly be explained by the continued general corrosion at the tip by trapped NaCl solution. The U-bends had been stored for several months after fracturing without being cleaned and dried.

Fig. 132 is a complete fracture profile at 100X of the same plane as Figs. 130 and 131. The fracture profile of this figure as well as the depth profiles shown in the other photomicrographs indicate a stepwise propagation. The dimensions of these steps are of the order of the grain size. Fig. 132 indicates that fracture to the depths of the order of the microcracks is due to SCC, whereas the rest is due to mechanical failure.

Fig. 133a is a cross section of a fractured 7075 U-bend at low magnification (10X), and shows the morphology. The brittle fracture region is shown at the top. More detail at a higher magnification (25X) is given in Fig. 133b. Most of the brittle fracture regions measured were around 1 mm.

Finally, Fig. 134 shows in detail the surface morphology of a nucleated microcrack on a 7075 U-bend at 3. 2X. Of particular interest are the ends of the microcrack which uniquely show the process of crack propagation. The length of this crack is about 3 mm and the width at the center about 20μ.

12. Monitoring of crack growth

Some preliminary data were obtained on crack growth by ultrasonic monitoring. This was done by cementing the Rayleigh wave transducer on the U-bend and monitoring the propagation of existing microcracks while the sample was in the stressed state.

Fig. 135 indicates the results for a single microcrack nucleated on a 7075 U-bend specimen stressed to 60% of the yield strength and monitored through reference grooves similar to those used for the SCC investigation. The monitored microcrack is the one shown in Fig. 134. The data were obtained after the microcrack had increased to a length of about 1/ 8 in., and it was monitored for 35 days. The attenuation was

Fig. 132. Complete fracture profile on the same plane as Figs. 130 and 131 (100X)

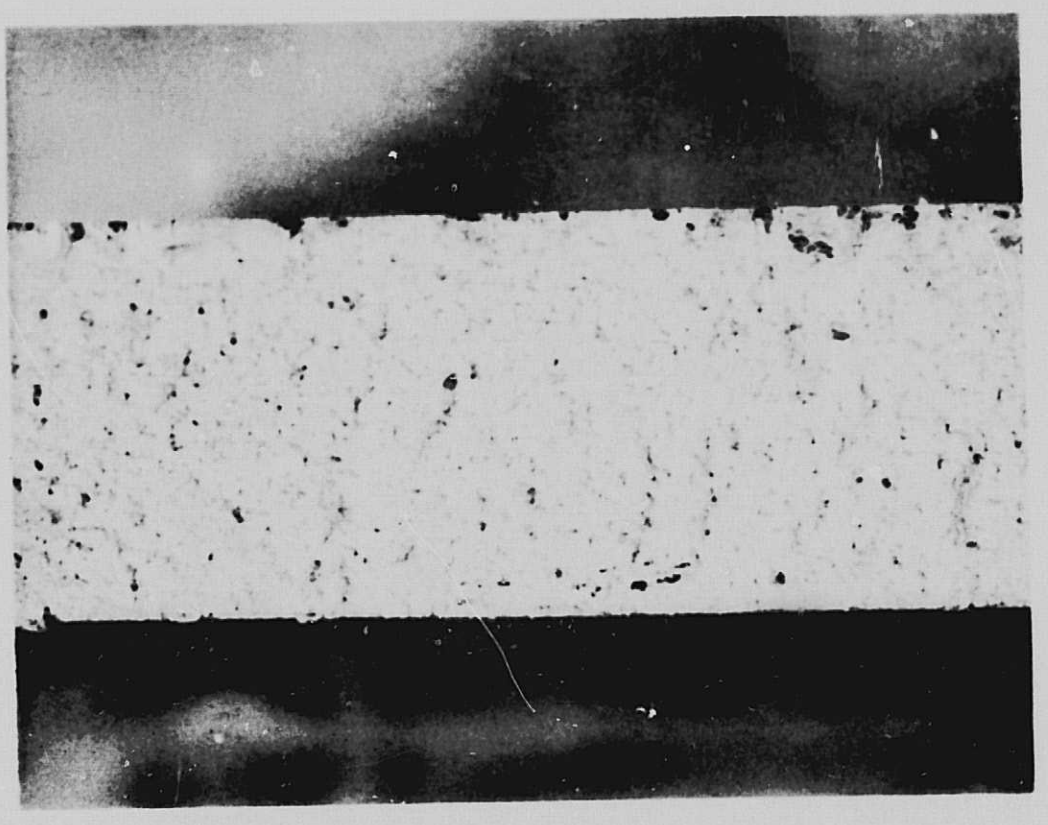

(a) Cross section showing brittle fracture region in upper part of photograph (10X)

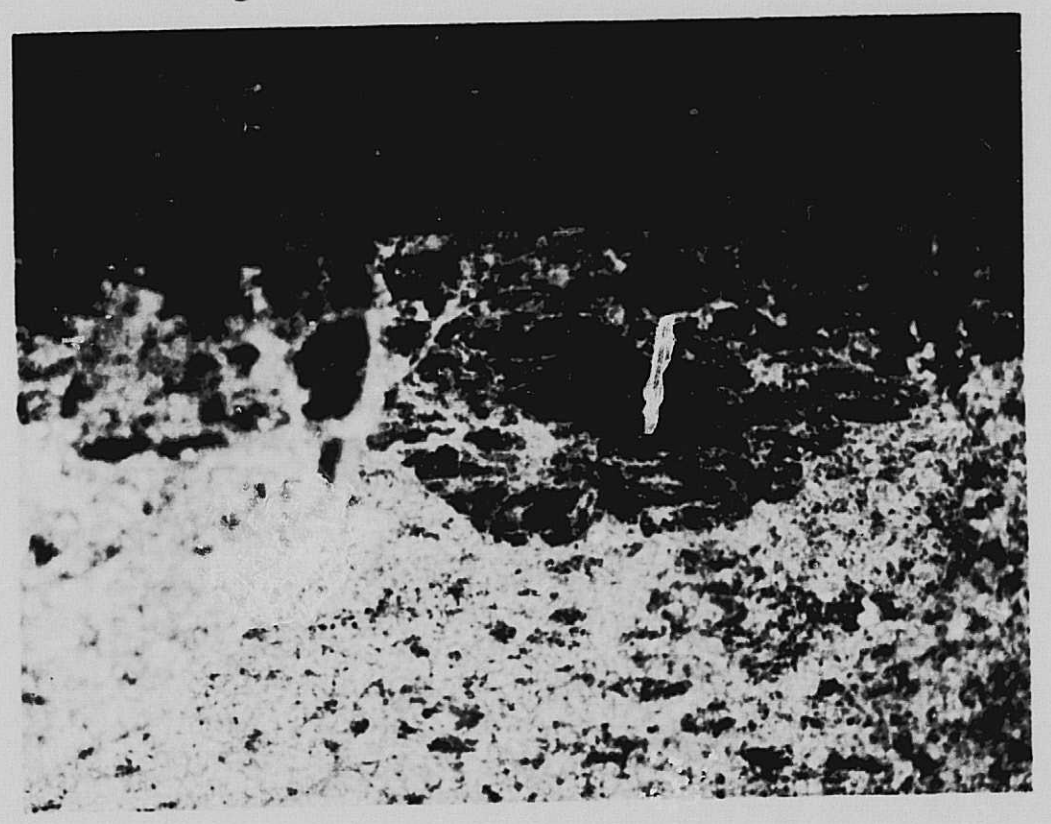

(b) Detail of brittle fracture region (25X)

Fig. 133. Morphology of fractured U-bend tensile specimen

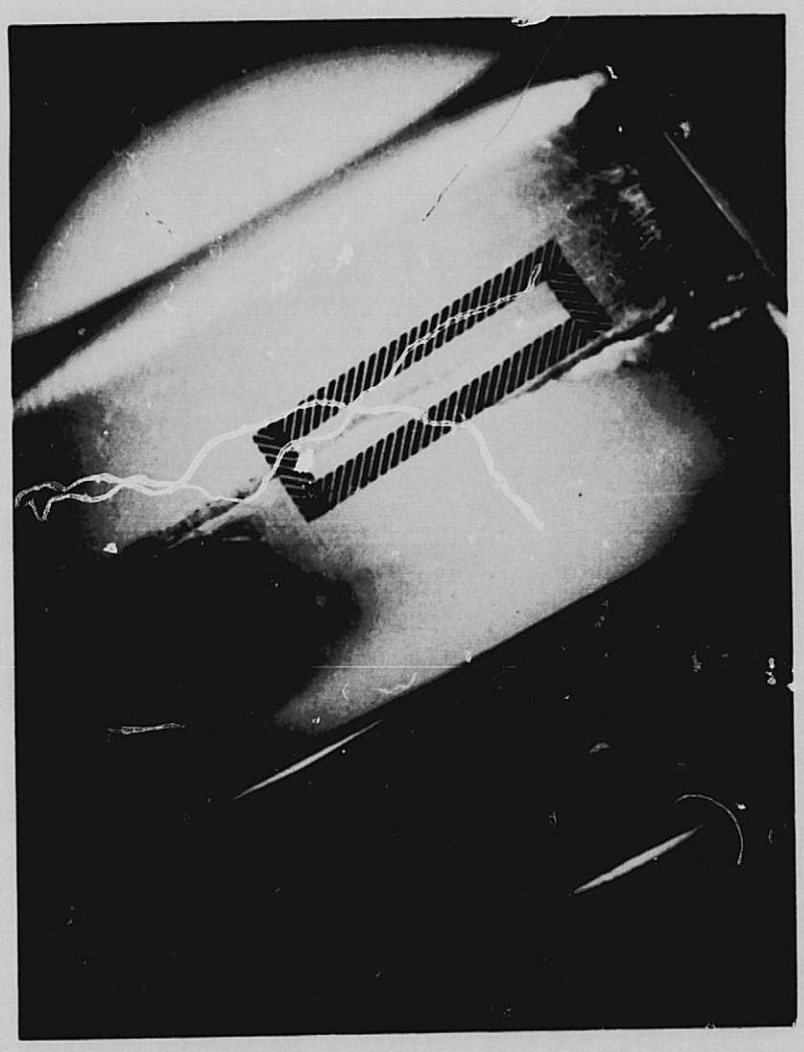

Fig. 134. Detail of the surface morphology of a nucleated microcrack on 7075 U-bend specimen (3. 2X)

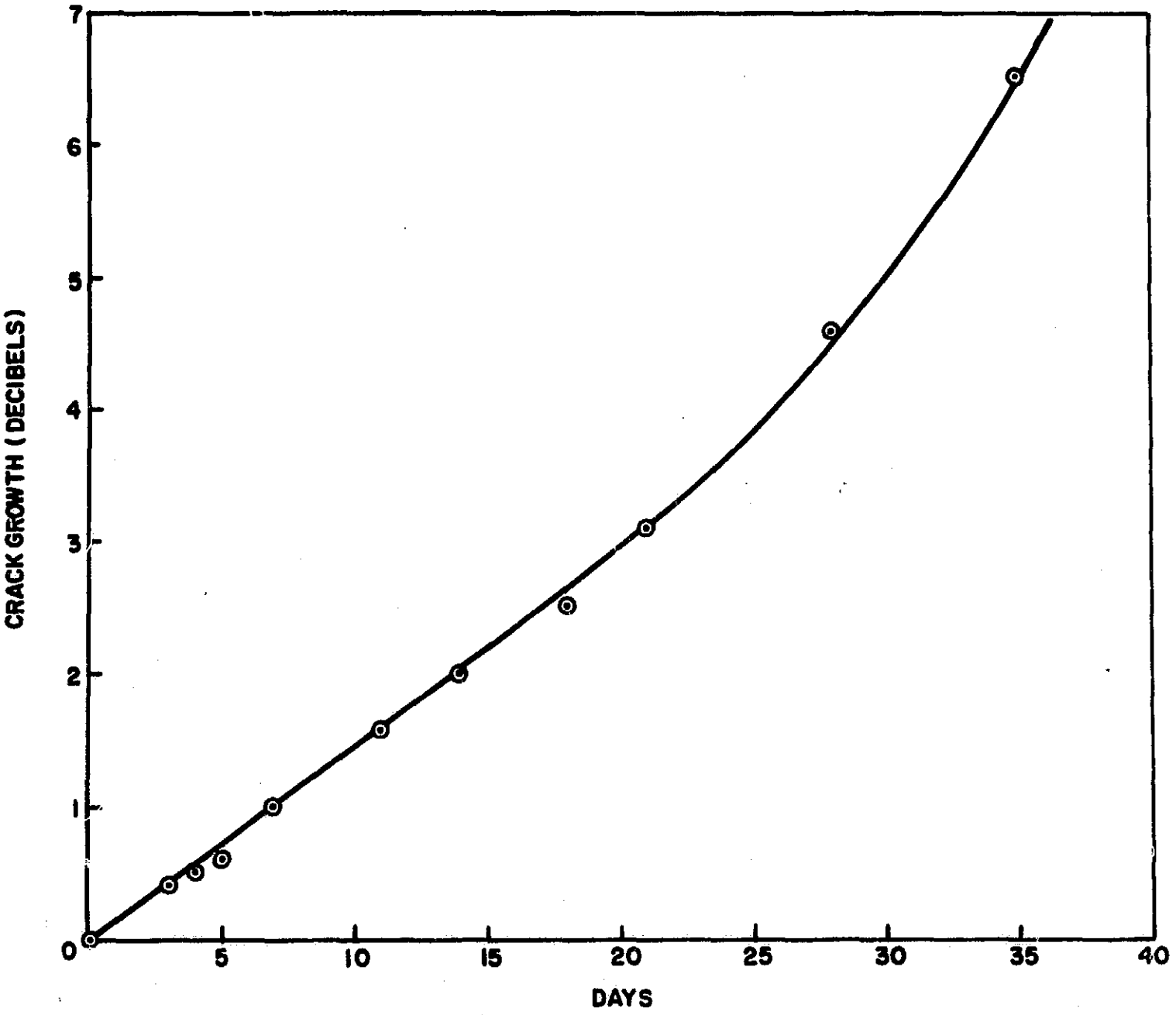

Fig. 135. Growth of nucleated microcrack of a 7075 U-bend specimen stressed to 60% of the yield strength

normalized to zero for the initial measurement, and it was expressed as a round trip loss instead of loss per unit distance. This was done because here only one microcrack was measured and not a stress corroded area of finite dimensions.

From the graph, we observe that the initial part of the curve is a straight line with a slope of 1.5 db per 10 days, whereas the latter part has a slope of twice as much. This suggests that the rate at which the crack propagates increases with time. However, additional tests would be required to establish the nature of crack growth for both isolated microcracks and general SCC damage extended over finite areas.

G. Instrumental Design Parameters for SCC Detection

1. Detection of SCC in finished parts

In order to use Rayleigh waves for the detection of SCC, it is necessary either to observe reflections from the cracks or to measure the associated increase in attenuation. For reflection measurements, a transducer attached to the surface of the part is all that is necessary.

We have found that commercial "rubber" cement gives a reproducibl bond with a high coupling coefficient. Variations of less than 1 db are generally obtained. We can take advantage of the ability of Rayleigh waves to propagate around rounded corners to detect cracks over a large area of surface. By making use of the different anisotropy of the reflection from SCC and GGC, it is possible to differentiate between SCC and the more general attack of GGC.

The determination of SCC damage by attenuation is slightly more complicated, but this method is more sensitive. As was discussed earlier, it is necessary that a known discontinuity be present to reflect part of the ultrasonic energy back to the transducer. The reflection coefficient of the discontinuity must be known. Several means of introducing an artificial reflector were tried, including liquids on the surface, a razor blade, and a brass block attached with rubber cement. Of these, the latter is by far the most reproducible and also gives the largest reflection coefficient.

Preliminary studies of externally attached reflectors indicate that the reflectivity is strongly influenced by the coupling medium, but the am-

plitude of the return signal could be reproducible within 2 db. With this type of sensitivity, it is possible to detect SCC on 1 or 2 cm of materials. The sensitivity is increased, since the surface wave passes over the corroded region twice. Of course, it is assumed that the attenuation per unit distance is known for the unaffected surface. Another possibility would be to use separate sending and receiving transducers to measure the surface attenuation. Since Rayleigh waves are not extremely sensitive to surface finish, compared with SCC effects, is appears that this technique of measuring surface attenuation is very promising for routine detection of SCC damage.

In the following paragraphs, some practical considerations that arise when making measurements on fabricated parts are discussed. These include the actual technique and the geometrical arrangement and positioning of the transducers.

2. Measurement methods

There are basically two ways in which SCC can be detected using ultrasonic Rayleigh waves: (1) either the reflection from the cracks may be observed, or (2) the reduction of energy in the main ultrasonic beam may be determined after passing over the corroded area.

When a Rayleigh wave propagates, most of the energy is confined to within 1 wavelength of the free surface. Any discontinuity or acoustic impedance mismatch in this volume will result in the reflection or refraction of some portion of the mechanical energy associated with the plane wave. Practically, the simplest way to observe discontinuities is to look for scattered energy. Depending upon the type of defect and its geometrical shape and composition, a characteristic pattern of reflections will occur which should enable the artifact to be identified. For example, we have found that SCC in aluminum will produce cracks whose reflection coefficient varies as that shown in Fig. 136. Other types of defects such as artificial grooves and holes are discussed in the Appendix.

The second method of detection depends on measuring the change in amplitude of plane waves after passing over the irregular region. (It is also possible to examine changes in phase or, equivalently, in delay time

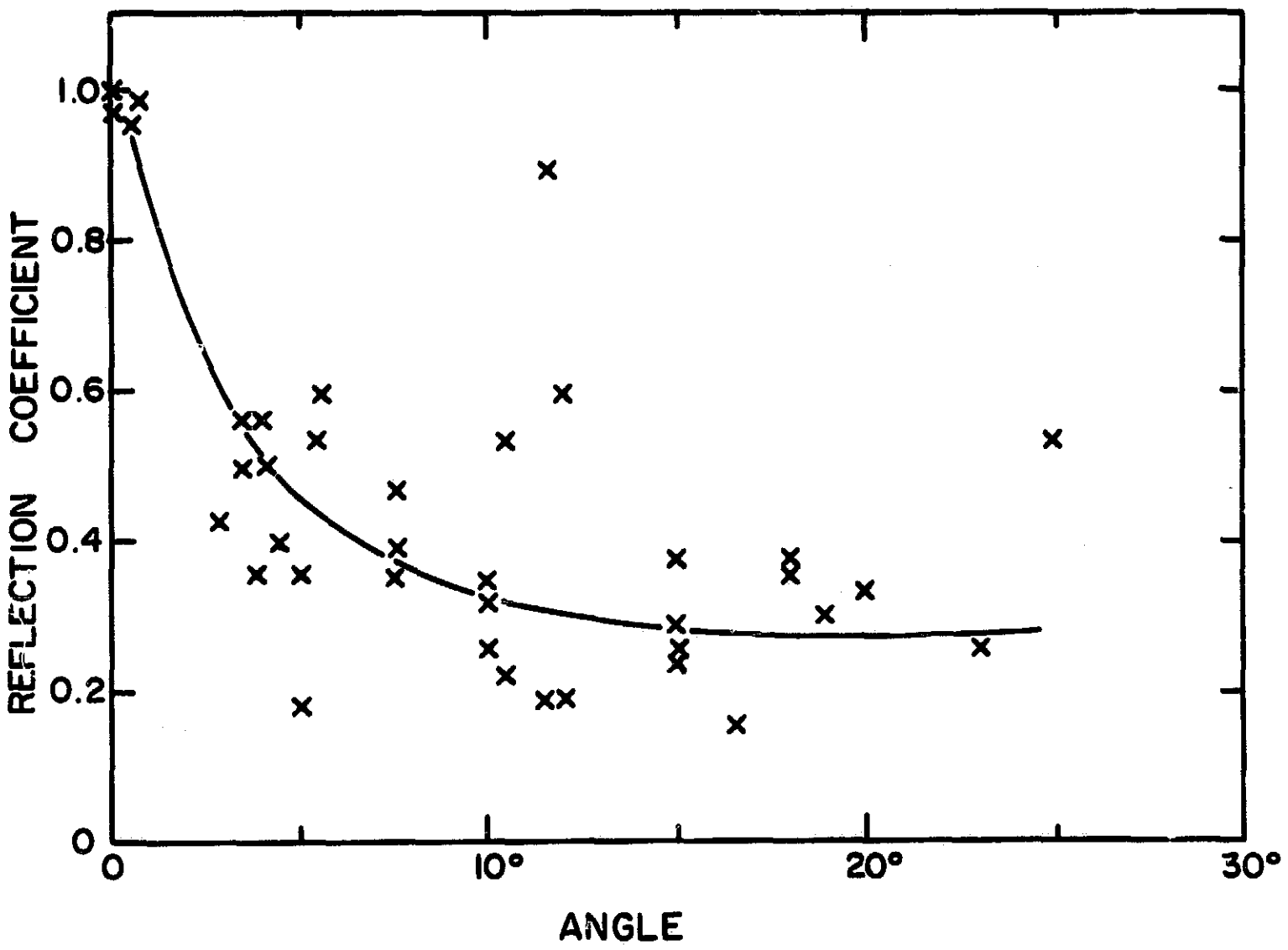

Fig. 136. Ultrasonic reflection coefficient as a function of angle from normal incidence to the direction of SCC for four different U-bends (data for each U-bend has been normalized to unity for 0°)

of the wave, but experimentally this is more difficult.) A fairly large change must occur to be easily detectable. For example, the variability of coupling and of orienting transducers can introduce errors of the order of 1 to 2 db (50% variation in power) with our present experimental techniques. A variation on this technique is to reflect the Rayleigh wave back to the transmitting transducer which is then used as a receiver. Only one transducer need be attached and the surface wave now makes two passes through the SCC region. The major drawback is that now either the reflector must be bonded to the surface or a permanent groove or ridge must be used as the reflector.

All previous surface attenuation measurements made during this contract have used the same transducer for transmitting and receiving. A reflecting groove was used to return the acoustic wave to the transducer. One advantage of this method is that the wave transverses the corroded region twice, which makes small attenuations easier to detect. Some preliminary measurements have been made where two separate transducers were used.

A number of different U-bends were examined in the unstressed, well relaxed state by bonding one transducer on one leg and the other on the opposite side. Rubber cement was used as the coupling media. A jig was available to hold only one transducer; thus, the second was held in position only by the bonding material. The measurements were easily reproducible to within ± 1 db. The transducers were oriented to obtain maximum transmission.

One difficulty was that the surface wave probes are resonant at different frequencies: one for 4 MHz, where $\lambda = 0.7$ mm in Al, and the other for 2.25 MHz, where $\lambda = 1.25$ mm. There is enough overlap of the passbands, however, to work. Results in approximate agreement with previous measurements were found by comparing SCC samples to uncorroded U-bends. Because the samples were unstressed and the ultrasonic wave made only one pass through the SCC region, the increase in attenuation was relatively small.

The technique with the best reproducibility, and hence highest sensitivity, is that in which a permanent reflector is on the far side of the material under study and a reference groove is nearby. The acoustic properties of the intermediate region can be determined by looking at the relative change of amplitude of the signal from the two reference reflectors. This method is independent of the transducer coupling loss, and is essentially the technique that has been used for our U-bend measurements.

3. Number of transducer attachments

One consideration in a practical situation is the number of times a transducer must be coupled to and decoupled from the surface of the part under test. The larger the number of attachments, the more time consuming and the more subject to error the test becomes. For the sake of discussion, we will consider a rectangular plate of dimensions D_1 by D_2, and assume that the stress corrosion cracks are to be detected by technique (1) as discussed above.

In the simplest case, if the transducer or search unit is W units wide, then D_1/W steps would be necessary to completely check the plate (Fig. 137a). If a separate reflector were to be used, then up to two D_1/W attachments would be needed. To check the plate completely in both directions, $(D_1 + D_2)/W$ attachments would be needed.

Another more complicated case is if we desire to determine the anisotropy of the reflection coefficient for diagnostic purposes, i.e., for distinguishing SCC from other surface defects. Then, we might use three transducers as shown in Fig. 137b. The areas common to all the transducers, A, is shaded and is given by

$$A = W^2(1 - 1/2 \cos \theta)/\sin \theta$$

The number of separate attachments needed to cover the whole surface would be $3 D_1 D_2/A$. For a more detailed look at the surface, we must pay for it with many more steps in the procedure. Generally, the method that uses the fewest steps and still gives the required information about the SCC condition of the surface will be favored. At this time a definite choice of technique is not possible.

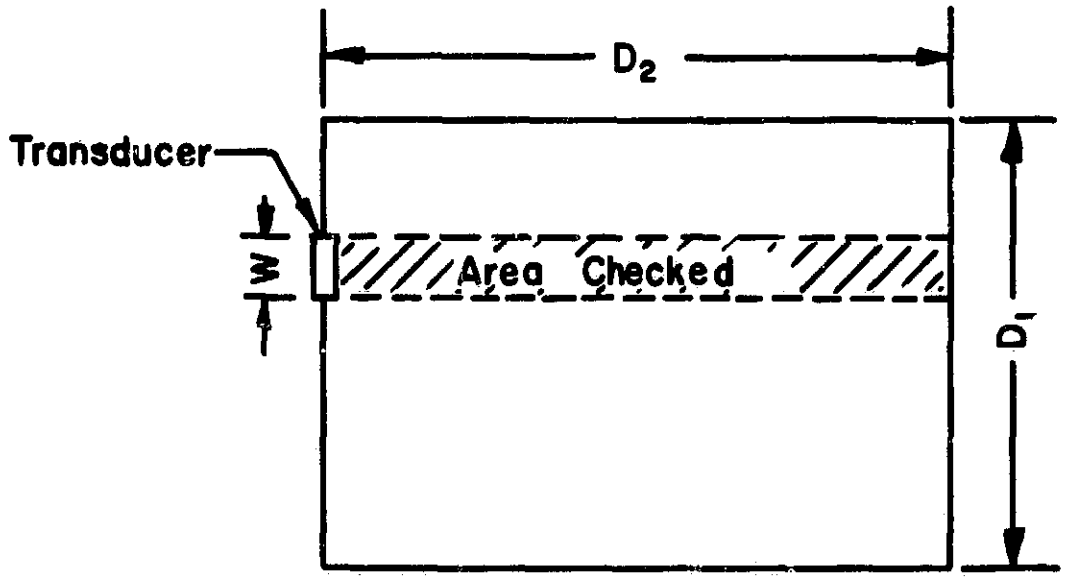

(a) Rectangular plate (D_1 by D_2 units)

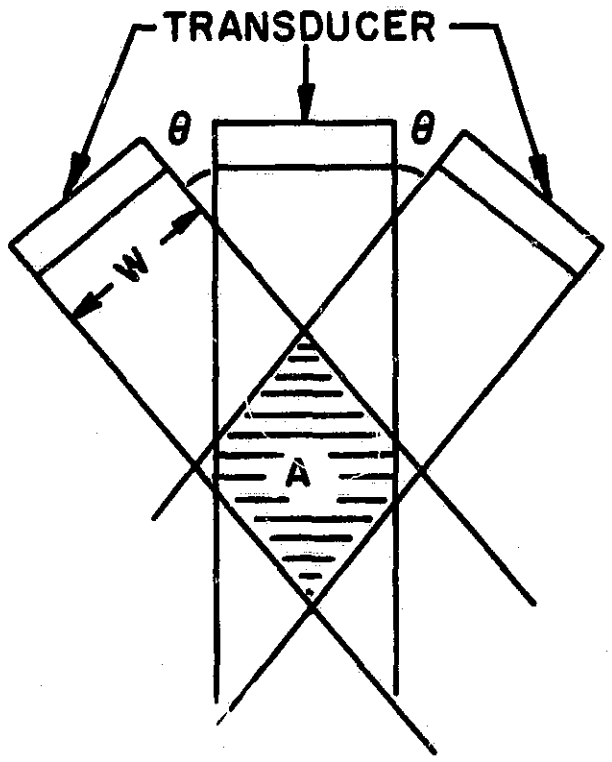

(b) Arrangement of three transducers to determine the anisotropy of the reflection coefficient

Fig. 137. Apparatus to be used for the identification of SCC

4. Angular dependence of reflection

Another consideration is the angular dependence of the reflection coefficient. For example, if the defect behaved purely as a specular reflector, then the reflectivity, R, would vary as

$$R = \left(1 - \frac{B}{W} \tan 2\alpha\right) \qquad \text{for } \frac{B}{W} \tan 2\alpha \leq 1$$

$$R = 0 \qquad \text{for } \frac{B}{W} \tan 2\alpha \geq 1$$

where B is the distance to the defect and α is the angle of incidence. If the reflection were more nearly diffuse, then the reflectivity of a crack which is long compared with W would be independent of α. Experimentally, we have found the behavior to be somewhere in between. Fig. 136 shows a plot on a linear scale of the relative reflection coefficient as a function of angle for four different U-bends. The plot has been normalized to one for each U-bend at normal incidence. We note that the reflectivity appears peaked in the forward direction and flattens out and looks approximately diffused beyond 3°.

Some additional work is needed to define more accurately the anisotropy of SCC, such as measurements at higher and lower frequencies and on rougher surfaces.

5. Probability of crack detection

In some cases it might be possible to examine only a fraction of the surface. We then want to know what is the probability of detecting a crack. Let us assume as a model that the SCC has an effective or average length L and is located on a rectangular plate. The cracks are oriented with an angle β with respect to an incident Rayleigh wave from one transducer. The testing is to be done by affixing the transducer of width W at a position near one side and checking for a reflection from any crack across the plate. The transducer will then be moved a distance K down the plate and the test will be repeated (Fig. 138). We assume that if the

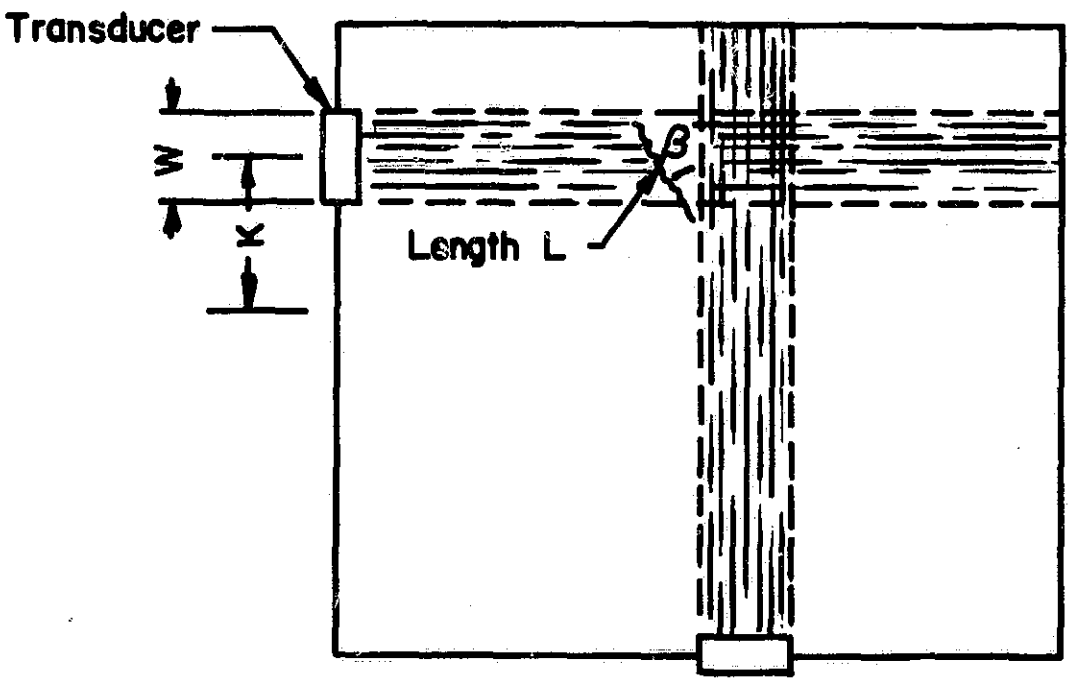

Fig. 138. Model of rectangular plate to determine the optimum angle to search for cracks (crack is L units long and the transducer of width W is moved a distance K along an edge for successive measurements)

crack is anywhere within the search beam, it will be detected. Since the reflection is diffuse, the acoustic wave will be scattered in all directions.

The probability of detecting the crack, P_1, will be

$$P_1 = (W + L \cos \beta) / K \qquad \text{for } L \cos \beta \leq K - W$$

$$P_1 = 1 \qquad \text{for } L \cos \beta \geq K - W$$

If we now scan along the other edge, the probability of detecting the defect, P_2, will be

$$P_2 = (W + L \sin \beta) / K \qquad \text{for } L \sin \beta \leq K - W$$

$$P_2 = 1 \qquad \text{for } L \sin \beta \geq K - W$$

The total probability of detecting the crack, P_T, will be

$$P_T = 1 - [1 - (W + L \sin \beta) / K] \; [1 - (W + L \cos \beta) / K]$$
$$\text{for } L \cos \beta \text{ and } L \sin \beta < K - W$$

$$P_T = 1$$
$$\text{for either } L \cos \beta \text{ or } L \sin \beta \geq K - W$$

From this expression, we note that for short cracks, $L \leq (K - W)/(2$ the maximum value of P_T occurs at $\beta = 45°$; i.e., the best angle to search for short cracks would be at +45° and −45° with respect to the probable crack orientation.

In the case of "long" cracks, $L \geq (K - W)$, the optimum procedure is to look at normal followed by parallel incidence to the possible cracks.

The intermediate case is slightly more complicated, with the condition that

$$\sin 2\beta = \left(\frac{K - W}{L}\right)^2 - 1$$

when $K - W > L > (K - W) / (2)^{\frac{1}{2}}$ for a maximum value of P_T.

Let us examine P_T for several different values of W, L, and K. If we assume that W/K = 0.5 and L/W = 0.1 (i.e., the transducer is moved twice its width each step and the cracks are only 0.1 as long as the width of the transducer), the results in Table VIIIa are obtained. This table is the output of a computer program designed to calculate P_T. The probability is only weakly dependent on angle, but it has a maximum at 45°. In all cases, P_T is symmetrical about the 45° angle.

If relatively long cracks are present (L/W = 1 and W/K = 0.5), the maximum P_T now occurs at 0° (Table VIIIb). An intermediate case occurs when W/K = 0.3 and L/W = 2. Here the maximum probability occurs at 10.6° (Table VIIIc).

In all cases, P_T is only weakly dependent on angle. As noted earlier, Rayleigh wave reflections exhibit an angular dependence which is peaked in the forward direction. This anisotropy should be enough to outweigh the angular dependence of P_T and to make the normal incidence direction, $\beta = 0$, favored for NDT purposes.

6. Effect of frequency on detectability of SCC

One of the most important parameters associated with Rayleigh or surface wave propagation is the frequency of operation. The depth of penetration of these waves is only of the order of the wavelength, λ. It is this limited penetration that makes these waves valuable in the investigation of phenomena which occur very close to or on the surface. In order to make an investigation as a function of depth, it is only necessary to vary the frequency, f, since $\lambda = V_R/f$. The Rayleigh wave velocity, V_R, in aluminum is about 2.8×10^5 cm/sec.

Most of our investigations were made using a frequency of 4 MHz, which gives a wavelength of 0.7 mm (28 mils). This frequency has proved to be quite satisfactory for most experiments. For work at other frequencies (1 MHz), a lower frequency transducer was obtained from Krautkrämer. For studies at 4, 12, and 20 MHz, a transducer has been purchased from Panametrics (Waltham, Massachusetts). The 1-MHz (really 1.1 MHz) transducer is of the conventional plastic wedge design, but the other probe uses a flint glass prism.

Table VIIIa

PROBABILITY OF OBSERVING A CRACK

ANGLE(DEG)	PROBABILITY
0.0	.7750
5.0	.7760
10.0	.7785
15.0	.7800
20.0	.7812
25.0	.7823
30.0	.7831
35.0	.7836
40.0	.7840
45.0	.7841

THE ANGLE FOR MAXIMUM PROBABILITY IS 45.000 DEGREES

W/K= .500 L/K= .050 (K-W)/L= 10.000

Table VIIIb

PROBABILITY OF OBSERVING A CRACK

ANGLE(DEG)	PROBABILITY
0.0	1.0000
5.0	.9991
10.0	.9969
15.0	.9937
20.0	.9901
25.0	.9865
30.0	.9833
35.0	.9807
40.0	.9791
45.0	.9786

THE ANGLE FOR MAXIMUM PROBABILITY IS 0.000 DEGREES

W/K= .500 L/K= .500 (K-W)/L= 1.000

Table VIIIc

PROBABILITY OF OBSERVING A CRACK

ANGLE(DEG)	PROBABILITY
0.0	.9300
5.0	.9338
10.0	.9350
15.0	.9344
20.0	.9326
25.0	.9303
30.0	.9278
35.0	.9258
40.0	.9244
45.0	.9240

THE ANGLE FOR MAXIMUM PROBABILITY IS 10.534 DEGREES

W/K= .300 L/K= .600 (K-W)/L= 1.167

Most conventional Rayleigh wave wedge transducers are made out of Lucite or some other plastic in which a longitudinal acoustic wave is launched. The plastic is necessary, since one requirement for Snell's law is that the velocity in the incident medium be less than the Rayleigh wave velocity in the test material. Only in some plastics and liquids is this condition fulfilled for incident longitudinal waves on metals such as aluminum. Snell's law states that the angle of the wedge, θ, is given by

$$\theta = \sin^{-1} (V_1 / V_2)$$

where V_1 is the wave velocity in the wedge material and V_2 is the Rayleigh wave velocity in the test specimen. Rather than a longitudinal wave, it is possible that a shear or transverse wave be used. This enables a somewhat wider range of material to be used and still satisfy Snell's law since, in general, the shear wave velocity in a solid is less than the longitudinal velocity (quite often only 1/2 or 1/3).

The shear wave-wedge surface wave probes we are using are made of flint glass with quartz transducers (Fig. 139). Because of the relatively low acoustic loss in quartz, it is generally necessary to separate the transmit and receive functions into different units. If one transducer is to be used for both, the high acoustic Q of flint glass compared to aluminum does not damp out internal reflections fast enough to prevent interference with the reflected Rayleigh waves unless very long path lengths are used.

The major advantage of going to such a transducer structure is that the quartz shear transducers may easily be driven in overtone modes. That is, if f_T is the fundamental resonant frequency of the transducer, then acoustic waves of 3 f_T, 5 f_T, etc., may be excited by changing only the frequency of the exciting RF generator. This allows the wavelength to be varied, although in discrete steps, with only one transducer.

Fig. 140 shows the experimental arrangement that was used to test the transducers at the fundamental and harmonic frequencies. The signal exciter is an Arenberg model PG-650 which is a high power, pulsed RF generator specifically designed for ultrasonic work. The attenuator is used to set the level. The output of the amplifier section of the Krautkrämer

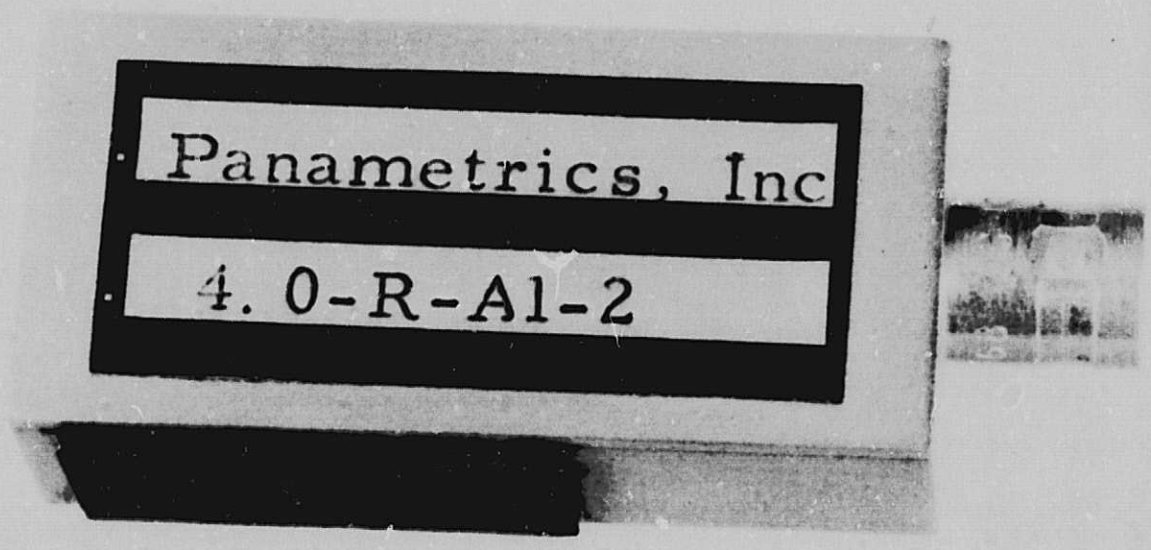

Fig. 139. Ultrasonic Rayleigh wave transducer with flint glass prism

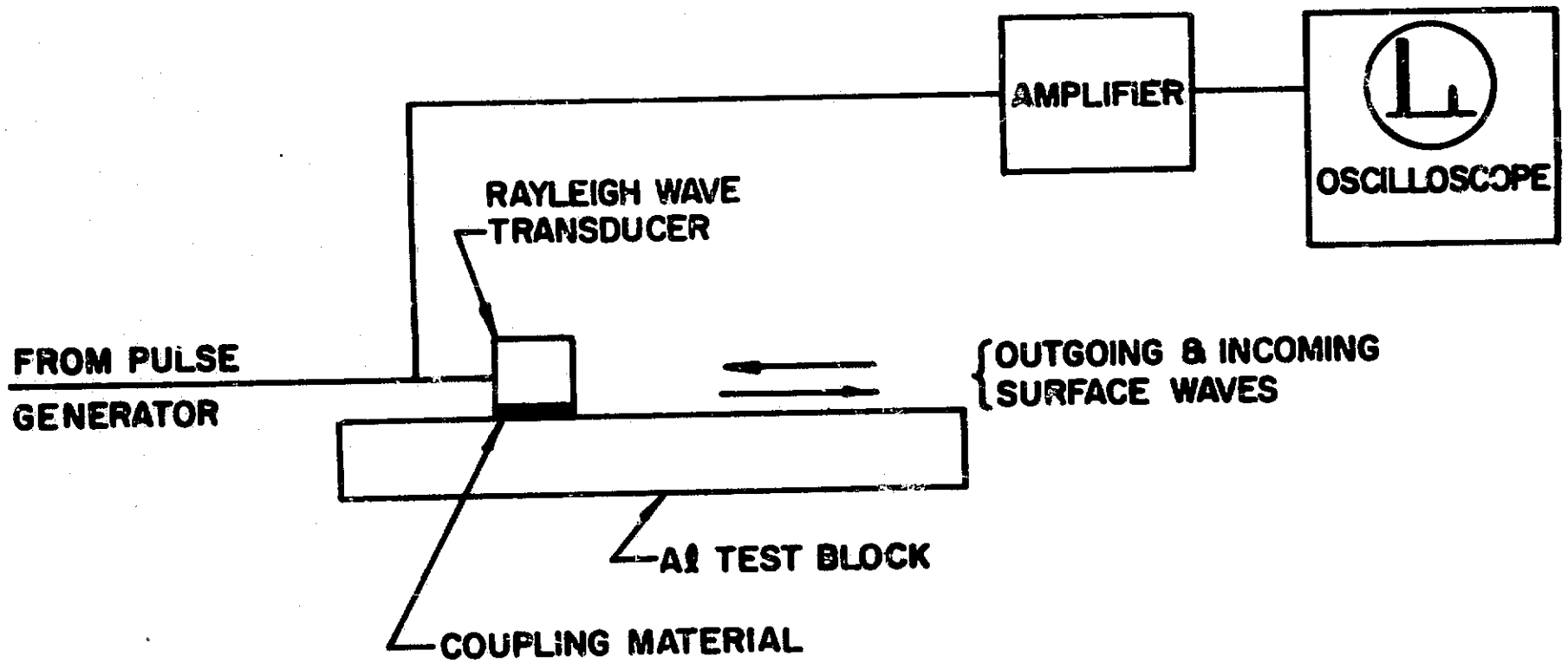

Fig. 140. Experimental setup used to measure the relative transducer loss for various frequencies and means of coupling at the surface

USIP 10 W was displayed on an oscilloscope. Surface waves were observed at 4 MHz which is the fundamental, as well as 12 and 20 MHz. At the highest frequency, the transmitted signal was only a few db above the noise, but with the Arenberg model WA-600 amplifier, which is designed for operation at these frequencies, a large improvement in the signal to noise ratio was obtained.

During the course of these experiments, we determined that the Krautkrämer probe could be made to work not only at its 4-MHz fundamental but at its first overtone of 12 MHz. The actual efficiency was as good as the flint glass transducer, although at higher frequencies the loss in the plastic wedge became quite high.

Measurements were made on SCC with the 1-MHz surface wave probe. As expected, because of the large depth of penetration (approximately 1/8 in.), essentially no reflections could be seen from SCC in the unstressed state. As a first approximation we might expect the reflections to be only 1/4 as large as for the 4-MHz signals.

7. Transducer coupling

In this program (NDT), the surface wave transducer has been coupled to the test sample via thin layers of rubber cement. We have found that commercial rubber cement gives a reproducible bond with a high coupling coefficient. Variations of less than 1 or 2 db are generally obtained. However, in some relatively long laboratory corrosion tests, the durability of the rubber cement coupling for long exposures becomes important. This was the case with the SCC tests in the salt-dichromate solution and the precorrosion investigation.

During these tests, the Rayleigh wave probe is coupled to the surface of the U-bend by rubber cement and is kept in a fixed position by a special jig. This was necessary for accurate ultrasonic monitoring. (The sample and the probe are often handled during the test, with danger of disturbing the bond.) This is because the U-bend (with the attached probe) is exposed to the corrosive environment, removed, ultrasonically cleaned, and stressed or unstressed. This procedure must be repeated when re-exposure is necessary.

The data and discussion presented in the following paragraphs are intended to demonstrate the behavior of the rubber cement bond versus time for different laboratory conditions. Times involved in these data vary from a few minutes to a few hundred hours. They are helpful in determining the expected changes in coupling losses for tests of different periods of time. They are also of interest for instrumental design for on-site SCC detection.

When first applied to the surface of the U-bend and the transducer, the rubber cement is viscous and as it slowly dries the coupling decreases (see Fig. 141). This figure and those remaining in this section contain data from different tests and are plots of the decrease in coupling in decibels versus time. The data in Fig. 141 represent the situation in which the transducer was attached to the U-bends and the coupling was constantly monitored ultrasonically while the samples were undisturbed. This figure indicates that initially there is a rapid increase in coupling loss (steep slope) followed by a tapering off to a nearly horizontal line. This initial loss of about 14 db which occurs during the first 20 hr is probably due to drying of the rubber cement bond.

A second cause of changes in coupling is the handling of the U-bend and the attached probe during the test. This, however, proved to be not as important as the drying of the rubber cement bond. Fig. 142 contains data taken from short duration tests (< 1 hr), and represents the situation in which the transducer was attached to the U-bends which were in turn exposed to the corrosive environment at room temperature, removed from the solution, and ultrasonically cleaned. The relatively scattered data can be approximated by a straight line with a slope equal to 2 db/hr. From Fig. 141 we note that the slope of the curve due to the drying of the rubber cement at 1 hr is about 1 db. Comparing this value to the slope of 2 db/hr of Fig. 142, we can possibly attribute the difference (~1 db) to the handling of the samples and attaching the probe during the test.

Fig. 143 gives data obtained from intermittent tests in which the U-bend specimens were subjected to corrosion at a temperature of 60 °C and were undisturbed during alternate time intervals; i.e., both the drying

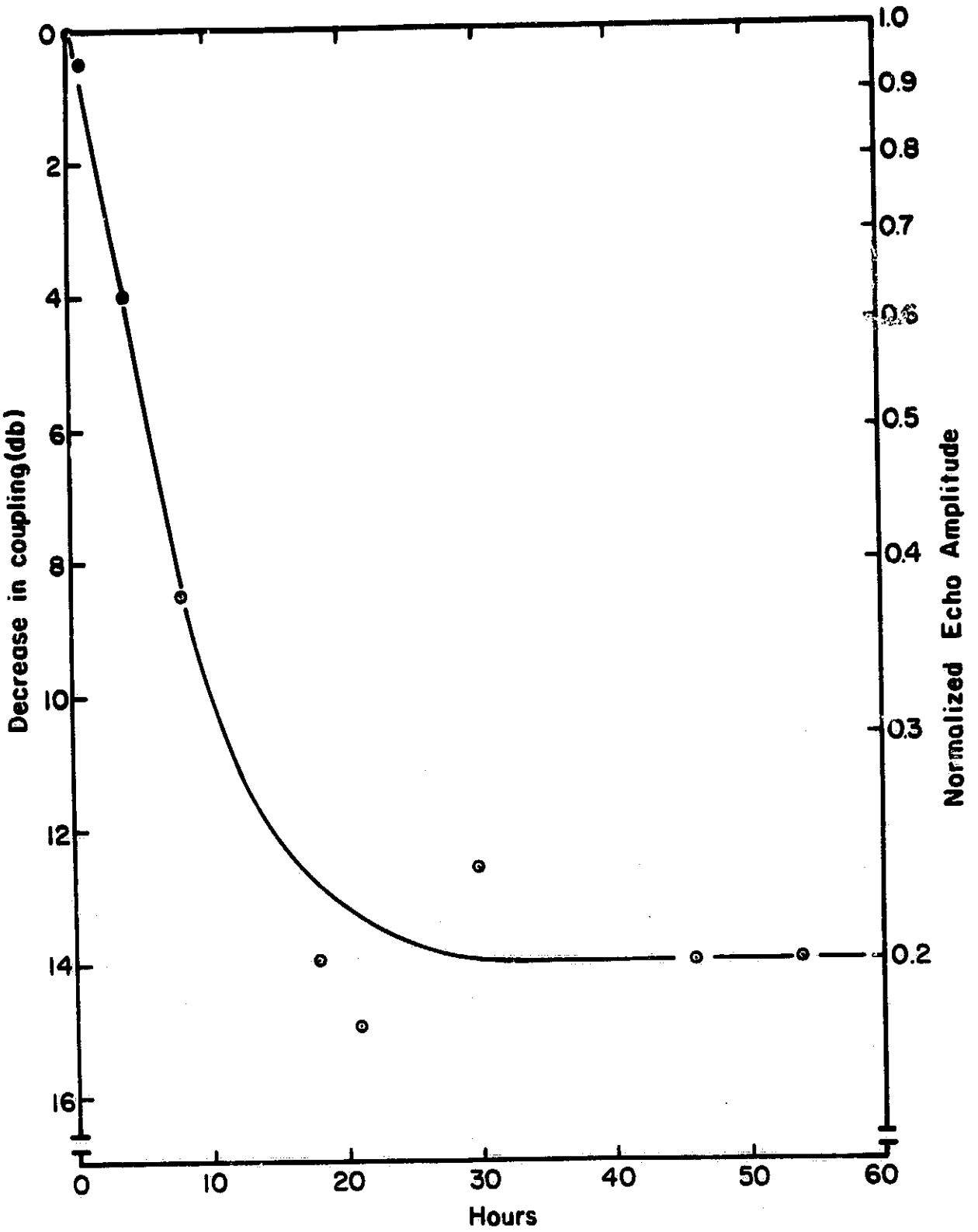

Fig. 141. Decrease in coupling versus time when both the transducer and the U-bend specimen are at rest

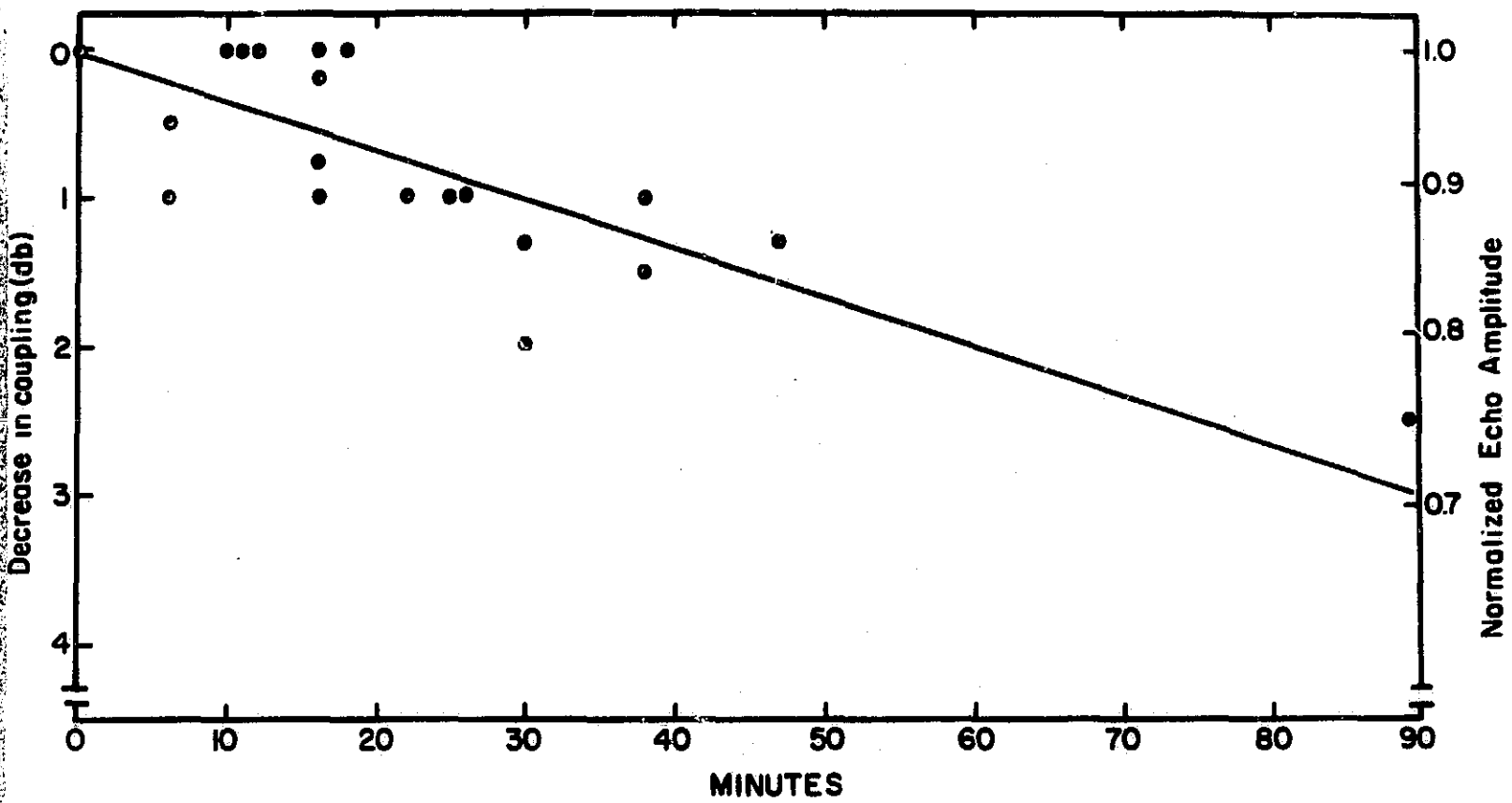

Fig. 142. Decrease in coupling versus time during conventional corrosion tests

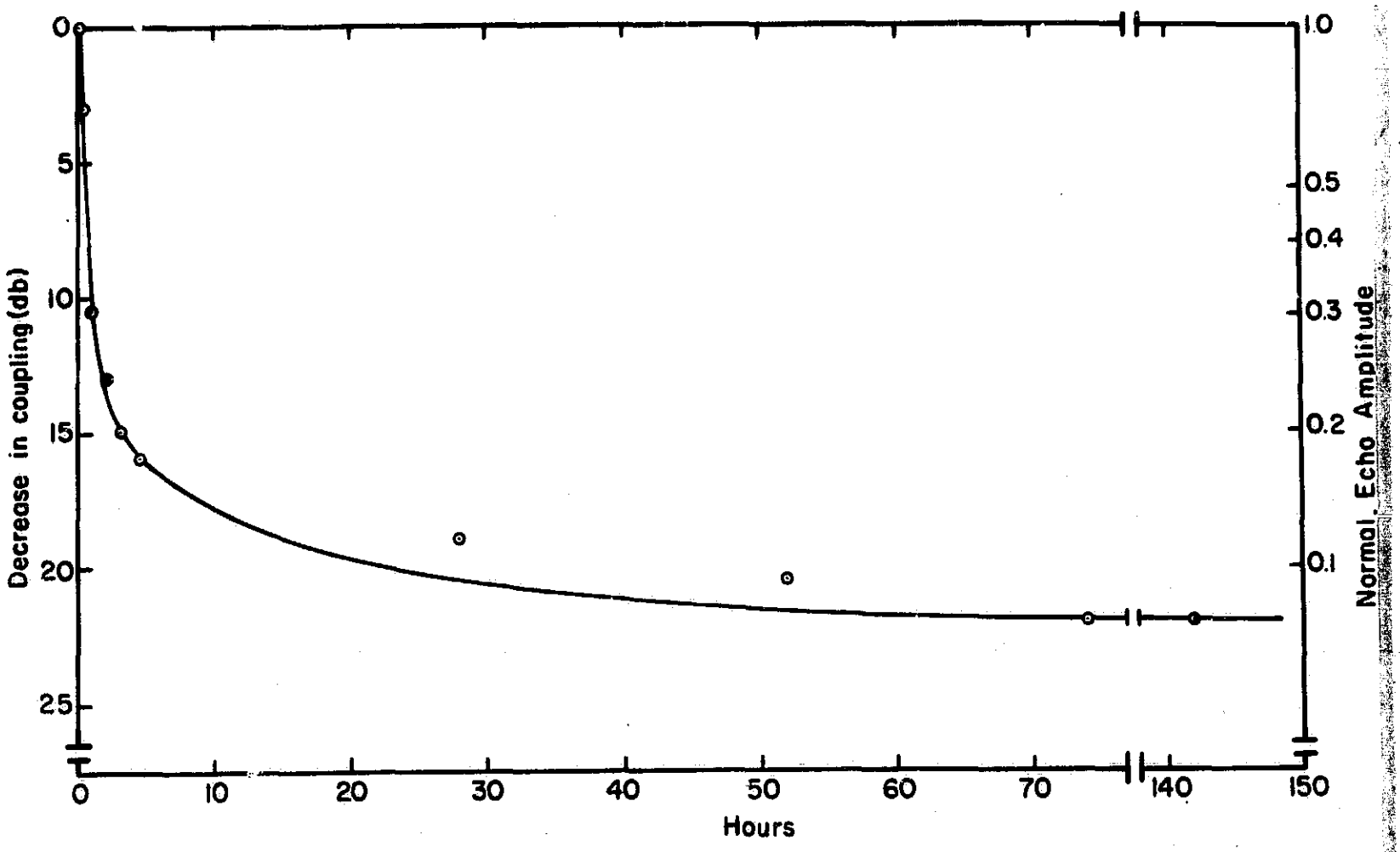

Fig. 143. Decrease in coupling versus time for intermittent corrosion tests at 60 °C

of the rubber cement bond and the handling of the sample contributed to coupling losses. This figure indicates similar behavior to Fig. 141 except for two features. One is the asymptotic value of about 22 db in Fig. 143. The other is the steeper initial slope of this figure. The terminal value of 14 db in Fig. 141 is reached after about 20 hr, whereas the value of 14 db is reached within 3 hr in Fig. 143. Both differences are possibly attributable to handling of the U-bend and transducer and to the higher testing temperature (60 °C) causing faster drying of the cement. However, Fig. 143 verifies the leveling off suggested by Fig. 141 for exposures as long as 142 hr. This effect could be explained by the argument that as soon as the outside of the coupling rubber cement dries, the inside remains unchanged, thus resulting in no increased losses.

Fig. 144 shows data obtained from intermittent tests. During these tests, the initial bond between the U-bends and the transducer was allowed to dry before the commencement of the tests in which the U-bends were both corroded and undisturbed during successive time intervals. The time allowed for drying was about equal to the time to reach the terminal value in Fig. 141 (~20 hr). Fig. 144 indicates an initial decrease in coupling of about 15 db for the first 20 hr due to drying of the bond. This is in excellent agreement with Fig. 141. Then, there is an additional loss of about 5 db due to handling during the test. The coupling of the bond decreased by about 21 db and stayed at this value for times as long as 342 hr. The flat regions in the figures of this section would probably extend to much longer times, but the tests were discontinued.

From the above discussion we can draw the following conclusions:

1. When the rubber cement bond dries without being disturbed (without handling), it reaches a terminal value of about 14 db after approximately 20 hr. Then there is no further change in coupling.

2. If the sample is tested while the bond is drying, this value (~14 db) is reached after approximately 3 hr.

3. During intermittent tests in which the U-bend is both corroded and at rest for successive time intervals, the terminal value due to the combined losses of drying of the rubber cement bond and handling is about 21 db.

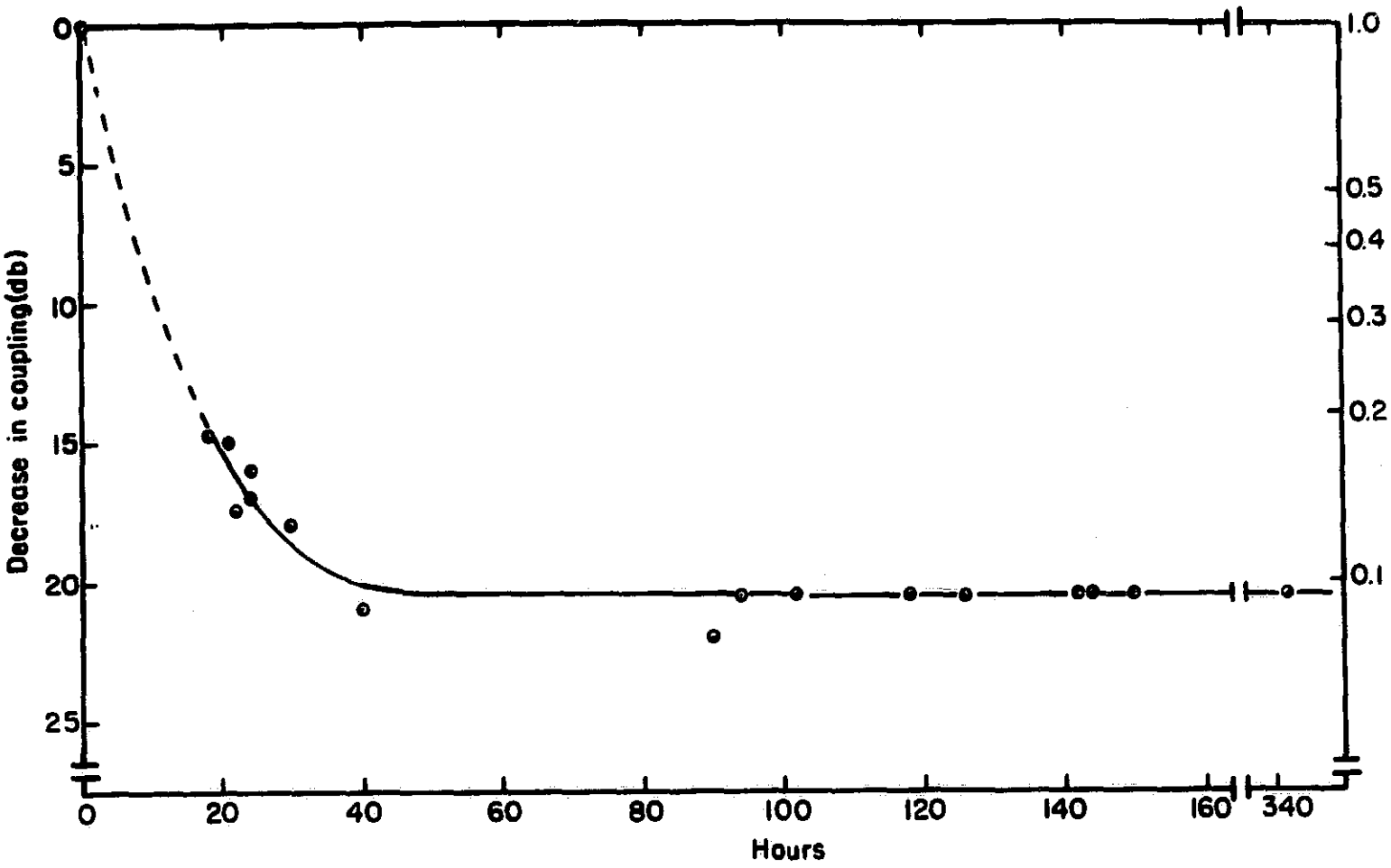

Fig. 144. Decrease in coupling versus time for intermittent corrosion tests

4. The coupling loss of about 21 db can easily be compensated for during a relatively long experiment by changing the gain and power settings of the ultrasonic instrument. Because of these changes in ultrasonic coupling, it is clear why it is necessary to use a reference reflection against which to measure all changes in attenuation.

8. Studies of rapid and reproducible coupling of transducers and reflectors to surfaces

Over the course of this work, we have found that commercial rubber cement is a very easy and effective means of coupling ultrasonic transducers to the surface of test specimens. As a laboratory technique it has been very satisfactory, fulfilling a number of requirements of a good bonding material. These include low acoustic loss, reproducibility without excessive care, and long lifetime (on the order of days) without extreme changes in characteristics. In addition, the technique makes it easy to remove the transducer and easy to clean the test part and transducer.

For use in the field and performing tests in situ, though, it would be much more desirable if a liquid coupling could be avoided, for obvious reasons. We have made some tests using sheets of rubber between the foot of the probe and the test surface to see if the liquid can be eliminated.

The principal function of a coupling medium is to make intimate acoustic contact between the two surfaces under consideration. This is done by "filling in" all the air gaps and voids between the phases with some material which has compatible acoustic properties such as low attenuation and a reasonable acoustic impedance. Generally, it is desirable that the bond thickness be thin compared with the wavelength of the ultrasonic wave. Acoustic matching, using various thicknesses of materials with selected properties to transform the acoustic impedances, is possible, but we will not consider it here because of its complications.

The results of a series of experiments are summarized in Table IX. Results are expressed relative to a "standard" rubber cement bond. The transducer, the 1.1-MHz fundamental probe operating at 3.3 MHz and driven by the Arenberg PG-650 pulse generator, was used as a sender and receiver to observe echoes from the edge of an unfinished, as received aluminum block.

The first column of the table gives the coupling material which was used in between the shoe of the probe and the test surface. The second column indicates the increase in signal level required to obtain the same size echo as was observed with rubber cement. The decrease in efficiency of the coupling of the transducer is half this number. The third column gives some comments, mainly about the pressure.

Table IX. "Dry" Coupling of a Rayleigh Wave Transducer to an Aluminum Block (Measurements Are Referenced to Commercial Rubber Cement as a Standard)

Material	Signal Level, db	Comments
Rubber cement	0	Used as standard
Rubber sheet (1/2 mm thick)	10	Hand pressure
Rubber sheet (1/2 mm thick)	14	Pressure of 1 kg/cm^2
Rubber sheet (1 mm thick)	23	Hand pressure
Rubber sheet (0.1 mm thick)	22	Hand pressure
Nothing	> 43	No coupling observed

In no case was a very good result obtained. A wider range of rubber could be tried. For example, a somewhat softer grade might not require as high a pressure. The thin rubber (0.1 mm) was evidently too thin for the relatively rough test block.

9. Liquid filled transducer

Another type of structure that might be used for a practical transducer for Rayleigh waves is a liquid filled cell with a longitudinal transducer at one end and a thin piece of rubber at the other (Fig. 145).

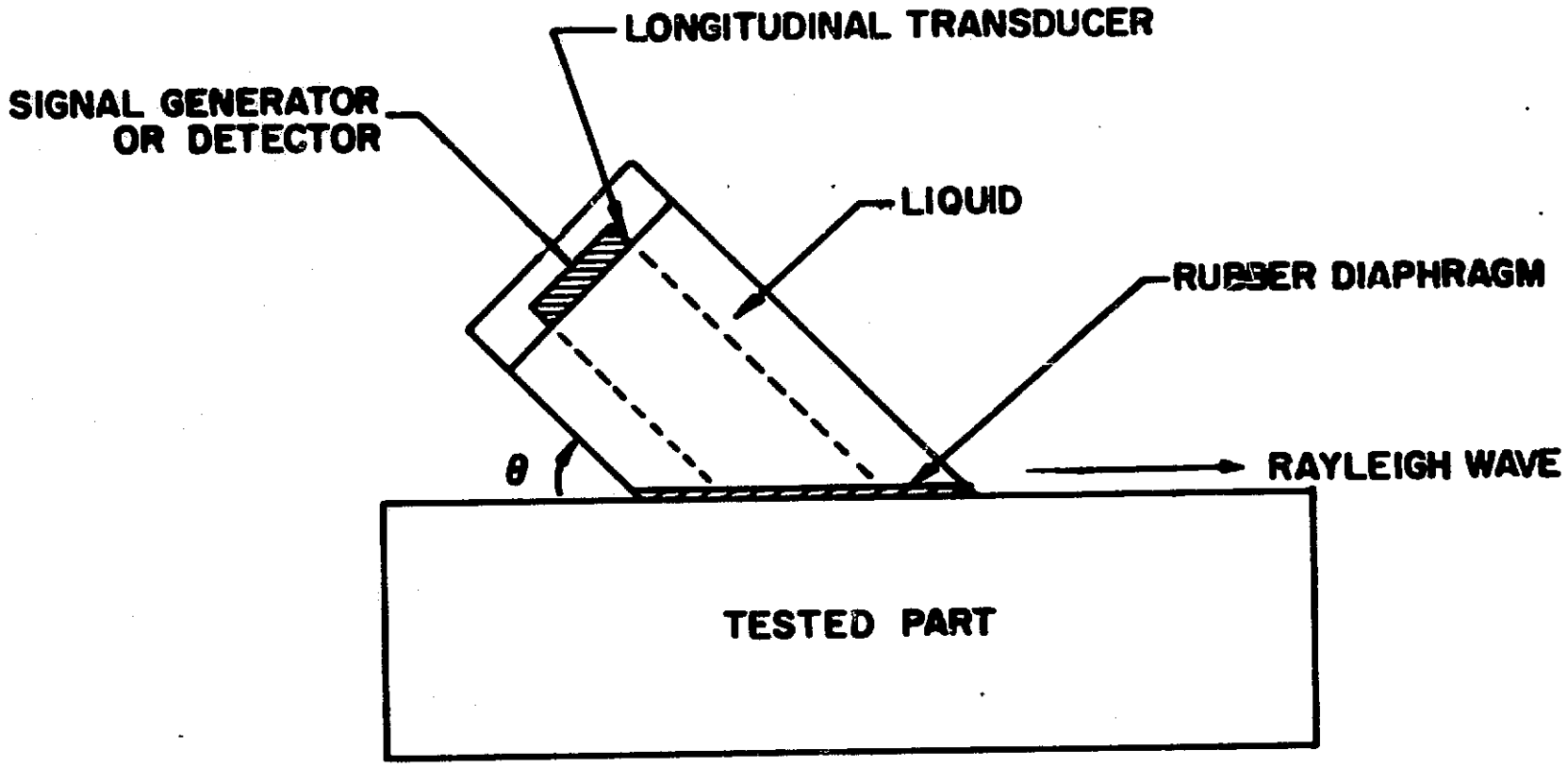

Fig. 145. Ultrasonic surface wave transducer using liquid rather than plastic for the incident media

Because of the relatively small velocity of propagation of longitudinal acoustic waves in water, the criterion that the longitudinal velocity be less than the Rayleigh velocity is satisfied. The probe would essentially be equivalent to the wedge transducer we have used, except that a liquid would be substituted in place of the plastic.

The foot of the probe must be able to conform to relatively rough and even to slightly curved surfaces. By varying the liquid, and thus the longitudinal acoustic wave velocity, the angle θ can be changed. For example, for carbon tetrachloride, $V_L = 0.92 \times 10^5$ cm/ sec and for glycerol, $V_L = 1.9 \times 10^5$ cm/ sec. This means the angle for launching Rayleigh waves can range at least from 70.5 to 47° in aluminum. This angle would be determined by the angle at which the tube was cut.

The path length in the acoustic liquid medium can be adjusted so that the attenuation will damp out internal reflections before the reflected Rayleigh wave returns. This length will depend on the type of liquid, the frequency, and the range of delays to be investigated. The liquid chosen for the first transducers was distilled water. The tube is made of copper and the angle θ, shown in Fig. 145, should be 58°.

The longitudinal transducer was a PZT-4 ceramic with a resonant frequency of 5 MHz. It was bonded to the end plate of the tube by soldering with indium which has a melting point of 155 °C. An Arenberg PG-650 pulsed oscillator was used for excitation and a WA-600 wide-band amplifier was the detector.

The liquid filled transducer was tested by looking for reflections from the edge of an aluminum block, as indicated in Fig. 145. Surface waves were successfully excited and reflected from the edge of the test block, although considerable interference from bulk waves and multiple reflections in the walls of the tube was observed. A transducer with a larger diameter would eliminate these difficulties.

10. Determination of final SCC condition of used fabricated parts

In this section we present the results of an investigation of the feasibility of determining the amount of SCC damage in a fabricated part

with a minimum of knowledge of the corrosion parameters. In this study, parts were simulated by U-bend specimens that had been stress corroded under various conditions. For SCC studies, the three most important parameters are the corrosion charge (q), in C/cm^2, stress (σ), in % of the yield strength (% of YS), and the corrosion damage as measured by the attenuation of a surface wave in db/cm.

During the initial experiments on the U-bends, the SCC damage was monitored by the ultrasonic technique as the stress of the U-bend was gradually released after the sample had been stress corroded. This was done to determine the path that the attenuation curve follows as the stress is reduced to zero. Typical results are shown in Fig. 146 which is a plot of attenuation versus stress. The arrowheads in this figure indicate whether measurements were made when the stress was decreasing or increasing. The attenuation was normalized to zero db/cm for zero applied stress. Sample one was reduced from the SCC stress level of 30% of YS to zero. The stress in sample two was increased from zero back to 30% of YS, which was the stress level for the SCC tests. The stress in sample three was reduced to zero from 60% of YS after it had been used in a precorrosion experiment. In all cases, i.e., either decreasing or increasing stress and SCC or precorrosion studies, the attenuation has a linear dependence on stress.

Fig. 147 indicates the behavior of attenuation versus increasing stress for U-bend specimens with various amounts of corrosion (all were stress corroded at 60% of the YS). At least for stress levels of 30% of the YS, the attenuation is proportional to the stress level and, also, the amount of corrosion.

Fig. 148 illustrates the situation when a corroded U-bend is stressed to a higher stress level than that at which it was corroded. The two samples shown in this figure were stress corroded at 30% of YS for different amounts of exposure, and then restressed to a value more than double the original value. The most striking feature is the hysteresis of the attenuation-stress curves. The initial path (indicated in Fig. 148 by "1" under the arrowhead) is the same as for sample one in Fig. 146. Segment 1

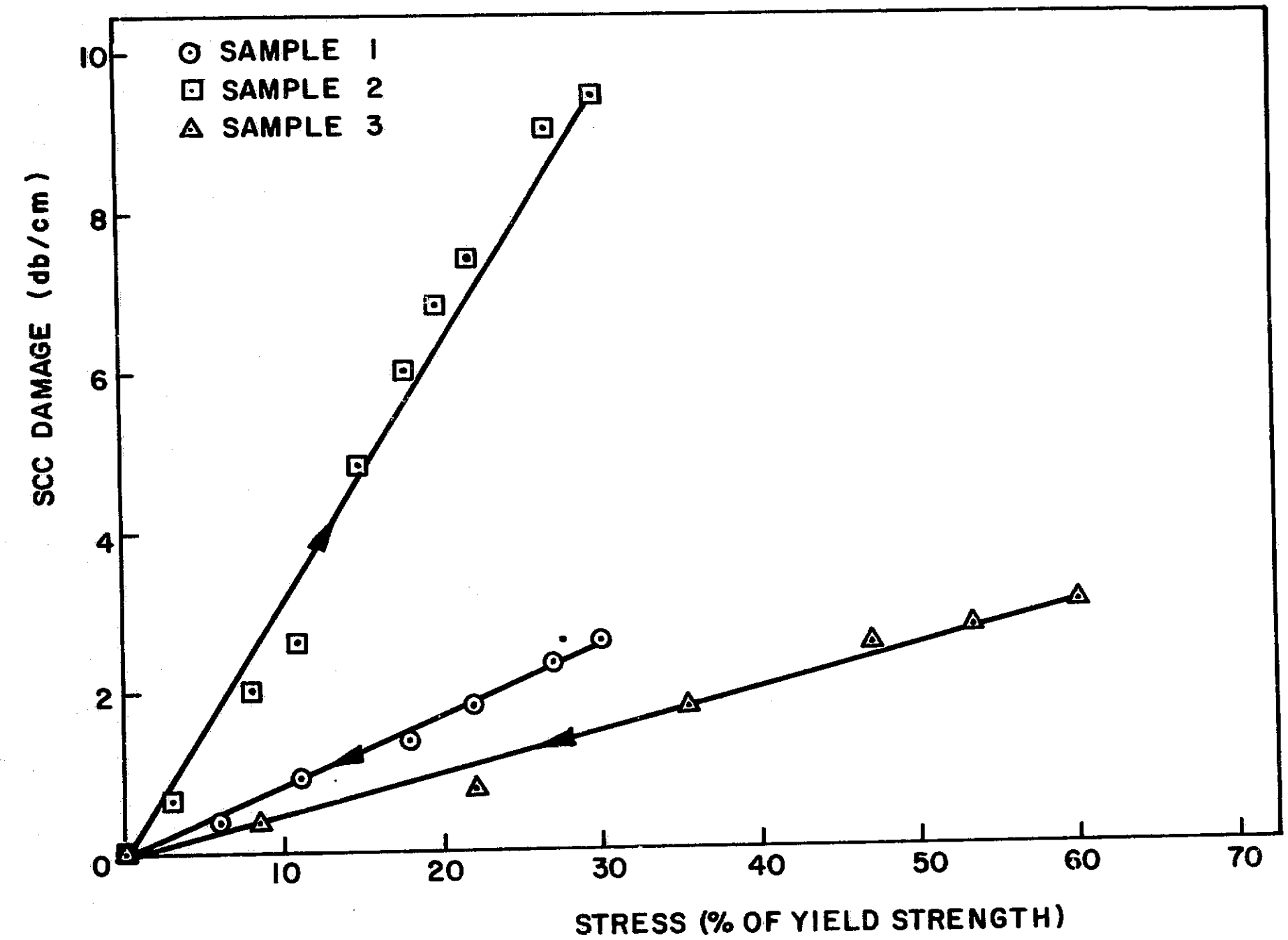

Fig. 146. Plot of attenuation versus stress on three U-bend specimens

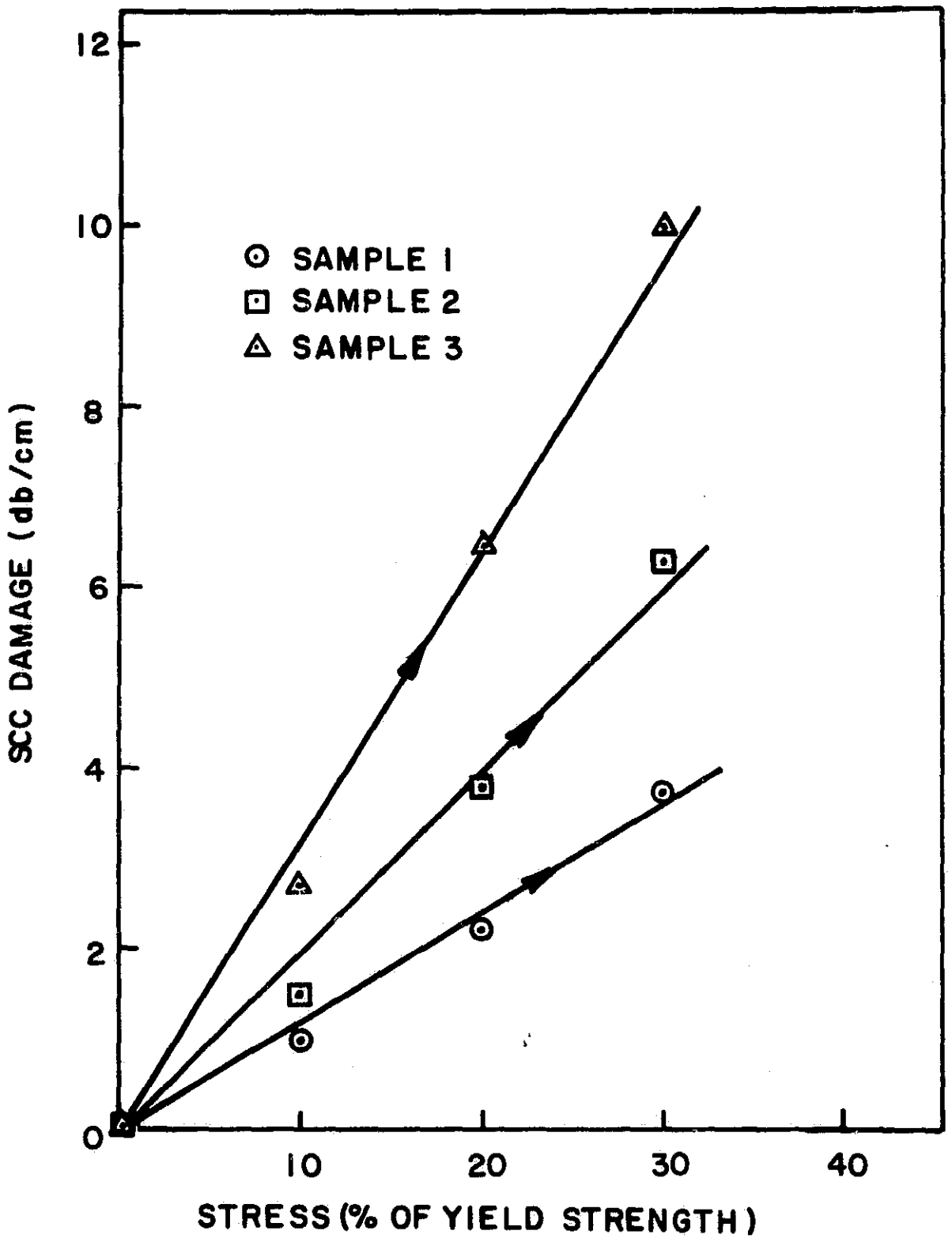

Fig. 147. Plot of attenuation versus stress on U-bend specimens with various amounts of corrosion (all were stress corroded at 60% of the yield strength)

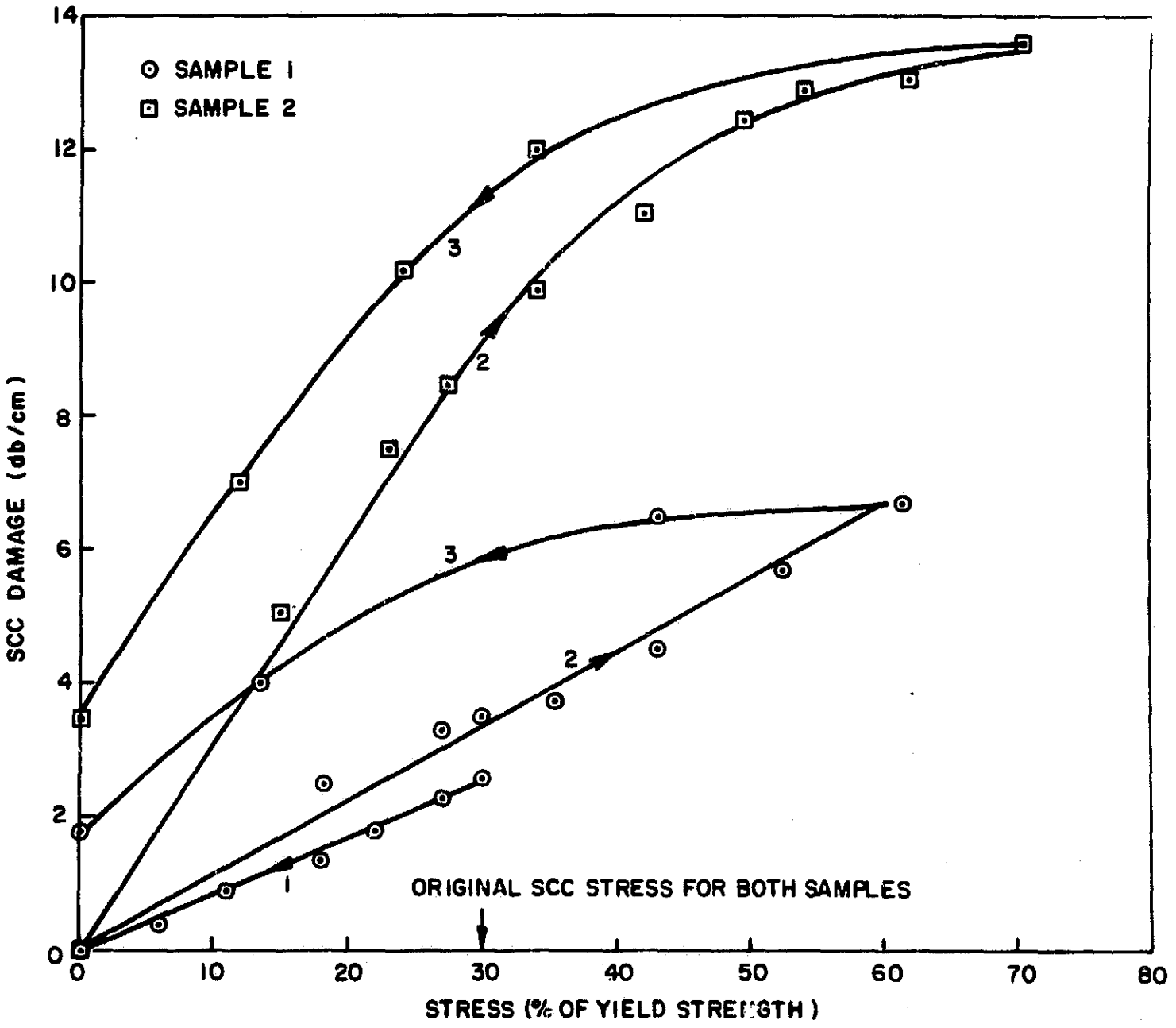

Fig. 148. Corroded U-bend specimen stressed to higher stress level than that at which it was corroded

traces the gradual release of stress from the original 30% of YS level to zero. The sample was left in an unloaded state for some time, and then it was restressed to about 60% of YS via path "2." Finally, it was brought back to zero stress following curve "3."

For sample two in Fig. 148, the original stress release curve from 30% of YS to zero (cf. path 1 for sample one) was not measured. Path 2 is again the stressing process that brings the sample from the unloaded state to a stress of 70% of YS, and path 3 is the stress released curve. The results for both samples are very similar, except for the steeper slopes of sample two which is due to longer SCC exposure. We note that curve 2 for both samples is linear, at least up to the stress corrosion level (30% of the YS), but beyond this deviations from straight lines are noted especially for the second sample. In general, the attenuation increases with stress as we pass the 30% of YS mark, suggesting that there is a further mechanical rupture and growth of the microcracks under the influence of the applied stress, i.e., the effective depth of damage increases. This explanation is also strongly supported by the hysteresis of curve 3, which is everywhere above curve 2, and the increased attenuation at zero stress.

In the foregoing analysis an observation was made that deserves further comment concerning path 2 in Fig. 148 and similar curves (increasing stress) in Figs. 146 and 147. It was observed that paths 1 and 2 for sample one in Fig. 148 do not coincide. Path 2 has a larger slope and a difference of attenuation of about 1 db at the SCC stress level of 30% of YS.

Even though path 1 was not measured on sample two in particular, we know from the usual attenuation-exposure curves (Fig. 111) that an attenuation of 4.5 db/cm would be measured immediately after corrosion. This is only half the 9 db/cm that was measured at 30% of the YS (Fig. 148). Similar differences have been observed for a number of samples.

A possible explanation of this increase in attenuation is the fact that the U-bends used in this study had been stored for some time after being stress corroded without being carefully cleaned and dried. It is

thus possible that small amounts of corrosive solution and water could be trapped at the tips of microcracks and would produce additional damage even though the U-bends are stored away unloaded. A few U-bends that had been stored while under load fractured after a few hours (i.e., overnight). This could also be explained in terms of trapped solution at the tips of microcracks.

We can now proceed to show how the SCC state of a precorroded sample may be determined. Fig. 111 shows the standard attenuation versus charge (exposure) curves with stress as a parameter. Fig. 149 was obtained from Fig. 111 by replotting attenuation versus stress with charge as the parameter. The attenuation shows a linear dependence on stress within experimental error. It would be quite useful if we can determine the final amount of SCC damage (attenuation) and the corresponding loaded state at which it occurred. The damage can easily be obtained from Figs. 111 or 149 if both stress and charge are known. However, in practical situations only the stress might be known. As it turns out, the SCC conditions and the effective charge of a used part can be determined if only the stress is known (by effective charge we mean the corrosion as measured by the initial slope of the surface wave attenuation under an applied stress, e.g., Figs. 147 and 148). This is used to eliminate from consideration any increased damage for large stresses as evidenced in Fig. 148.

To determine the SCC damage of a used sample, we would stress it to a small fraction (10 to 20% of YS) of the stress used in the SCC test. The resulting straight line should be superimposed on Fig. 149 and the charge determined from the line parallel to it. The intercept of this line in Fig. 111 with the known stress value will give the final damage on the attenuation axis. That is, if the SCC stress of a used part is known, the charge and damage in terms of acoustic attenuation can be determined.

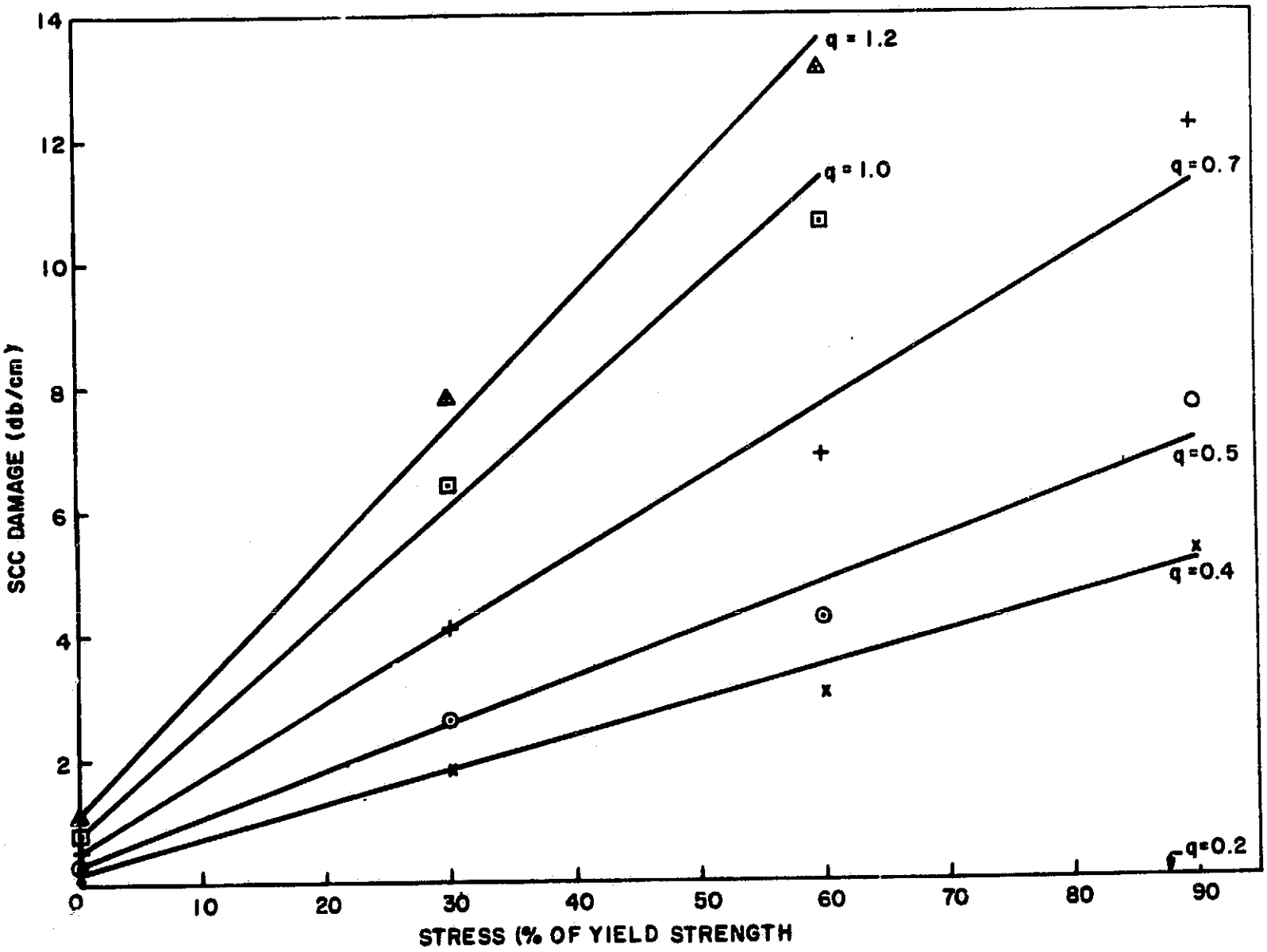

Fig. 149. Plot of attenuation versus stress (charge is parameter)

V. REFERENCES

(1) H. A. Holl, Corrosion 23, 173 (1967).

(2) M. O. Speidel, Ohio State Conference on Stress Corrosion, Columbus, Ohio, Sept. 11–15, 1967.

(3) A. J. Sedricks, P. W. Slattery, and E. N. Pugh, Trans. ASM, 62, 238 (1969).

(4) H. W. Pickering and P. R. Swann, Corrosion, 19, 369t (1963).

(5) E. H. Dix, Trans. AIME, 137, 11 (1940).

(6) F. H. Cocks and M. W. Krebs, J. Electrochem. Soc., 115, 722 (1968).

(7) Metals Handbook, American Society for Metals, Metals Park, Ohio, 1948, p 227.

(8) P. O. Sprowls, in "Stress Corrosion Testing," ASTM STP 425, ASTM, Philadelphia, 1967, p 292.

(9) H. K. Farmery and U. R. Evans, J. Inst. Metal., 88, 81 (1959-60).

(10) W. Gruhl, Z. Metallk. 54, 86 (1963).

(11) H. Borchers and E. Tenchoff, Z. Metallk., 59, 58 (1968).

(12) G. Beilby, "Aggregation and Flow of Solids," MacMillan Co., London, 1921.

(13) F. A. Champion, Symposium on Internal Stresses in Metals and Alloys, Inst. of Metals, London, 1948, p 468.

(14) H. Logan, J. Res. Nat. Bur. Stds., 61, 503 (1958).

(15) P. R. Swann and J. D. Embury, in "High Strength Materials," John Wiley Inc., New York, 1965, p 327.

(16) T. P. Hoar and J. G. Hines, in "Physical Metallurgy of Stress Corrosion Fracture," Interscience, New York, 1959, p 107.

(17) S. F. Bubar and D. A. Vermilyea, j. Electrochem Soc., 114, 882 (1957).

(18) E. N. Pugh and W. R. D. Jones, Metallurgia, 63, 3 (1961).

(19) G. Thomas and J. Nutting, J. Inst. Metals, 88, 81 (1959-1960).

(20) H. A. Heine and M. J. Pryor, J. Electrochem. Soc., 114, 882 (1967).

(21) Buehler, Ltd., Metals Digest, vol. II, no. 2 (1965) p 5.

(22) W. J. Helfrich, Kaiser Aluminum & Chemical Corp., "Final Summary Report on Development of a Rapid Stress-Corrosion Test for Aluminum Alloys," for NASA, Contract No. NAS8-20285, George C. Marshall Space Flight Center, Huntsville, Alabama.

(23) R. W. Benson and V. J. Raelson, Prod. Engr., 30, 94 (1959).

(24) G. J. Binczewski, "Standardization and Application of Surface-Wave Inspection," Nondestructive Testing, Jan. —Feb. 1957, pp 36-40.

(25) R. J. Botsco, "High Resolution Ultrasonics," Materials Evaluation, April 1967, pp 76-82.

VI. CONCLUSIONS AND RECOMMENDATIONS FOR FURTHER WORK

Our investigation of the mechanism of SCC of Al alloys has demonstrated that there are large differences between the Al-Cu (e. g., 2219) and the Al-Mg-Zn-Cu (e. g., 7075) systems.

In the Al-Cu system, stress corrosion susceptibility is associated with the presence of paths at the grain boundaries which are preferentially attacked by corrosion. Mechanical properties are relatively unimportant. In the Al-Mg-Zn-Cu system, however, the opposite is true. There is little correlation of stress corrosion susceptibility with specific corrosion properties and little obvious tendency for intergranular corrosion. However, there is strong correlation with mechanical properties and with the tendency for cleavage to occur along the grain boundaries. This conclusion has been corroborated by observing the apparent oxide ductility on the alloy as a function of surface treatment.

A major finding has been that for Al-Mg-Zn-Cu most of the normal stress corrosion failure time is not taken up by a stress corrosion process, but by a pure stress corrosion process: the precorrosion effect. It has been shown that this precorrosion effect is the direct consequence of a layer in which grain boundary structure at the surface of the metal has been destroyed by mechanical deformation. In effect, it is such layers which account for most of the resistance shown by existing structures. Furthermore, mechanical deformation of alloy surfaces followed by an anodic electrochemical treatment could substantially increase the stress corrosion life of finished Al alloy structures even further. Thus, a program to perfect both mechanical and electrochemical surface treatments to maximize stress corrosion resistance is proposed. A primary consideration should be the applicability of these treatments to existing structures.

In addition to surface treatments, two types of treatments designed to affect bulk properties are proposed on the basis of the results. The first method consists of modifications in heat treatment, with particular emphasis on quenching rate, e. g., by quenching in oil. The aim in this case would be to increase stress corrosion resistance while retaining strength. The second method has the possibility of achieving complete protection from

stress corrosion without loss in strength. This would be achieved through the destruction of a clear, well defined grain boundary structure throughout the bulk of the metal by the combination of mechanical and thermal treatments.

With regard to nondestructive testing, it has been shown that both eddy currents and ultrasonic surface waves are suitable for the very early detection of stress corrosion damage. The ultrasonic surface wave technique is the more practical, however, since it can readily distinguish stress corrosion damage from other kinds of surface defects. A major area for further investigation to develop a practical instrument for use in the field is to explore the practicability of liquid filled surface wave probes.

Appendix

INVESTIGATION OF SURFACE RAYLEIGH WAVE RESPONSE WITH SIMULATED DEFECTS

A. Introduction

When surface defects occur in the path of propagation of Rayleigh surface waves, a scattered Rayleigh wave is produced, as well as bulk waves (longitudinal and shear) which propagate into the medium. One result of this scattering is the attenuation of the main Rayleigh wave beam. This is easily demonstrated by damping echoes with a fingertip, as illustrated in Fig. A-1. The experimental arrangement for this test is shown in part (a) of Fig. A-2. Groove G_2 was about 8 mils wide and 4 mils deep. Part (a) of Fig. A-1 is the reference oscillogram, part (b) is the oscillogram obtained when a fingertip was used to damp the ultrasonic beam just before it reached groove G_2, and oscillogram (c) was obtained when a fingertip was placed between groove G_2 and corner A. Part (b) indicates that the ultrasonic beam consists only of Rayleigh waves, because no echoes are present after echo G_1. However, when the Rayleigh waves reach groove G_2, bulk waves indicated in oscillogram (c) by echoes B_1 and B_2 are generated which are not damped by a fingertip.

To determine the effect of surface defects on the propagation of Rayleigh waves, real defects such as cracks and pits were approximated as isolated artificial defects of known geometry. Cracks can be simulated by grooves, and pits by hemispherical indentations or cylindrical holes with their axes perpendicular to the surface. In the investigation described in the following paragraphs, isolated U-shaped grooves were used as a first approximation to stress corrosion cracks. The measuring frequency of the sound was 4 MHz.

U-shaped grooves of varying width and depth, and with a length longer than the width of the transducer crystal to avoid end effects, were cut on flat surfaces of 7075. The direction of propagation of the Rayleigh waves was perpendicular to the grooves and parallel to the rolling direction.

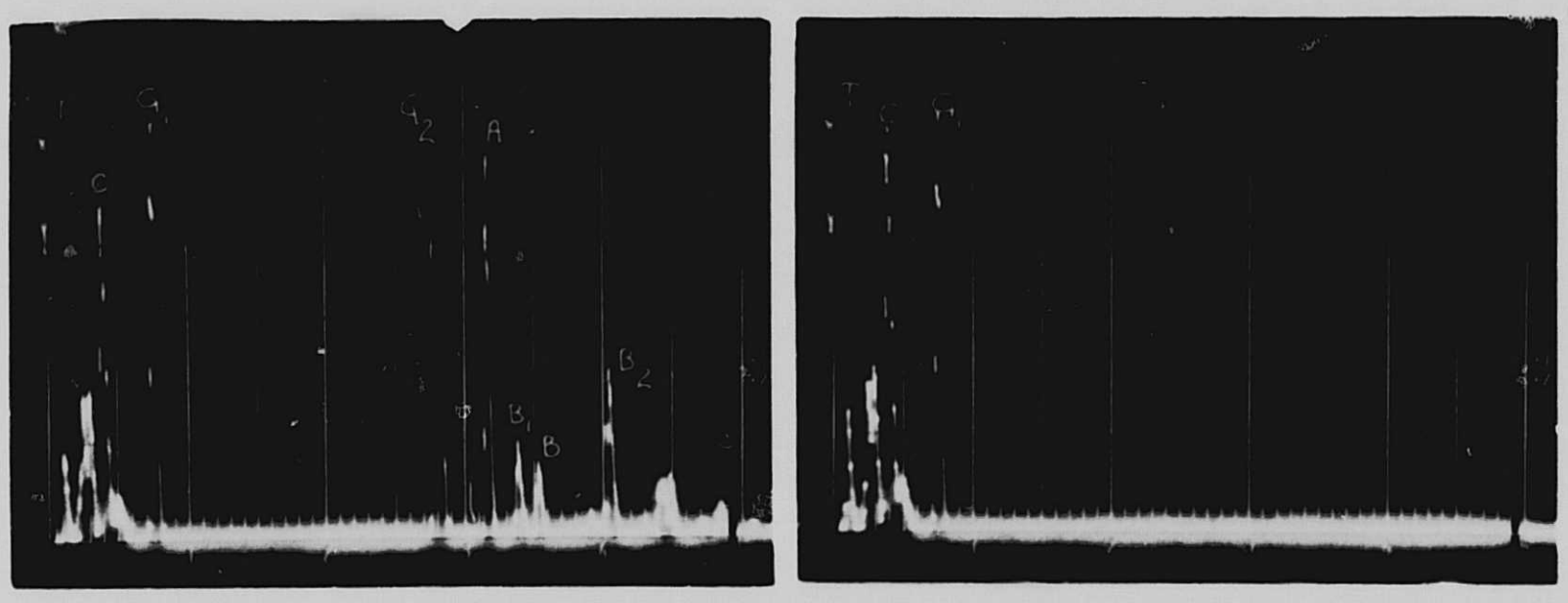

(a) Reference oscillogram

(b) Oscillogram obtained when a fingert is used to damp the ultrasonic beam just before reaching the groove

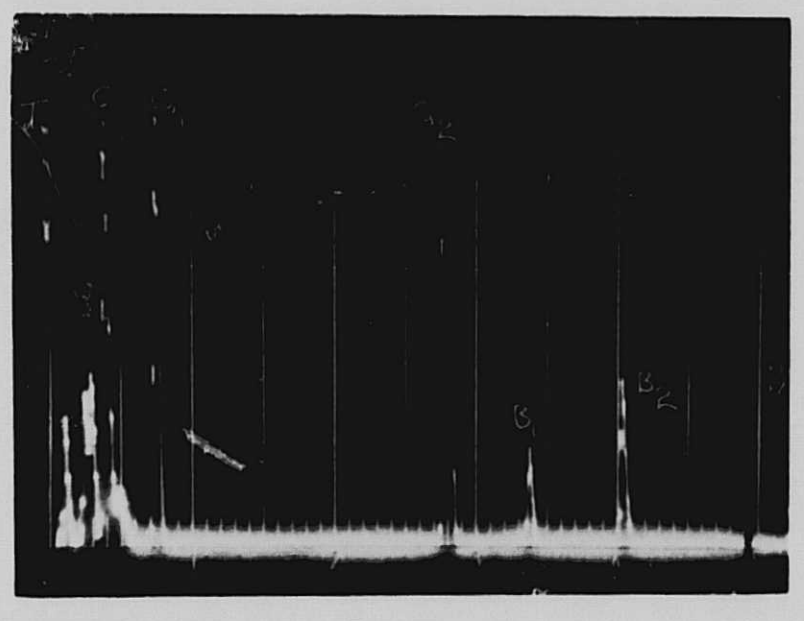

(c) Oscillogram obtained when a fingertip is used to damp the ultrasonic beam just after reaching the groove (shows bulk waves B_1 and B_2)

Fig. A-1. Oscillograms illustrating the transformation of a part of the Rayleigh wave beam into bulk waves by a surface groove

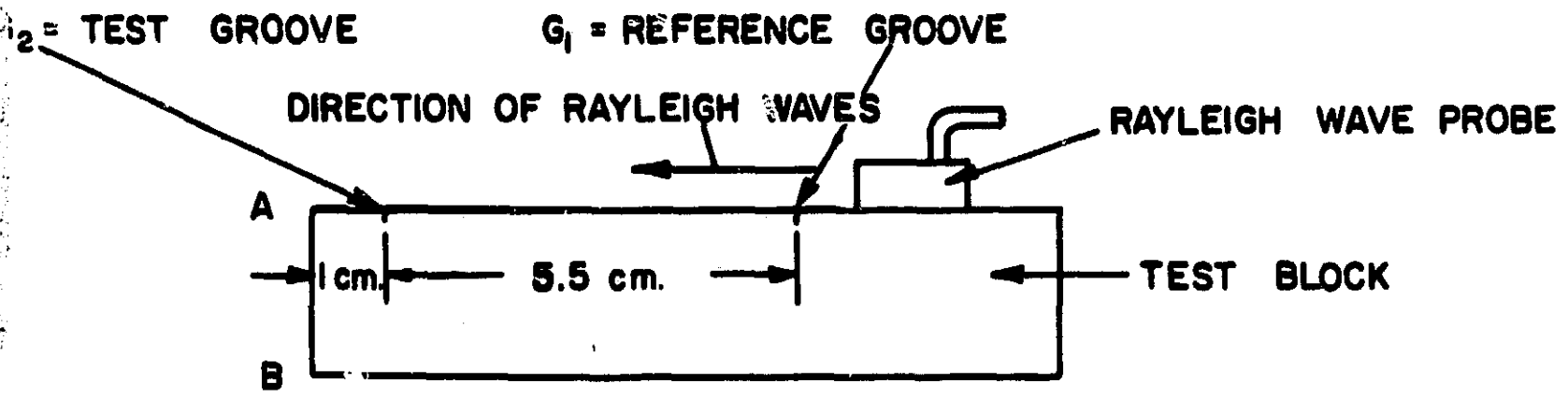

(a) EXPERIMENTAL PROCEDURE

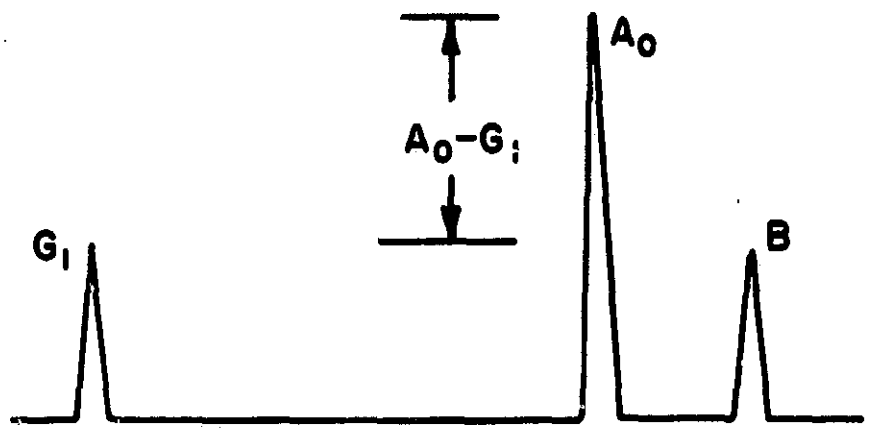

(b) REFERENCE OSCILLOGRAM

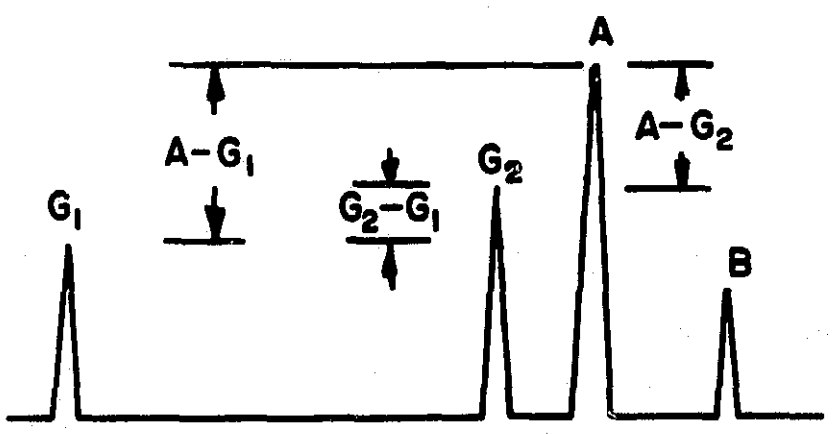

(c) TEST OSCILLOGRAM

Fig. A-2. Test principle for the effect of depth of artificial flaws on Rayleigh wave response

B. Effect of Depth of Artificial Flaws and Penetration of Rayleigh Waves Below the Surface

In the investigation of SCC, it is necessary to know how deep a flaw must be before it can be detected. Another important parameter to know is how far below the surface a flaw or defect can be and still be detected. This is important if only surface defects are to be considered. Artificial grooves were used, since to first order they approximate a crack produced by SCC. Of course, cracks produced by SCC are quite irregular, but the general results are similar. The following procedure was used. A reference groove was cut and an oscillogram taken showing the reflection from this groove. Then the test groove was cut and additional oscillograms were taken. The depth of the groove was measured by noting the change in focal distance when a Leitz Metallograph (model MM5) was first focused on the bottom of the groove and then on the surface. The reference groove was introduced for normalization to eliminate any variation of the coupling of the transducer to the test material. Fig. A-2 shows the test arrangements and reference and test oscillograms.

The data may be analyzed in several ways. One is to determine the ratio, G_2/A. Since G_2 and A are in db, this is done by subtracting them. If we refer to Fig. A-3, the difference is then proportional to

$$\log \frac{r_2}{(1 - r_2)^2}$$

where we assume that the transmission coefficient of the groove is equal to $(1 - r_2)$, and r_2 is the reflection coefficient of the groove.

As the depth of the grooves was increased, echo G_2 increased and echo A decreased. Figs. A-4 and A-5 are plots of reflection of the Rayleigh wave from the test goove at a constant transducer distance versus depth of groove. Fig. A-5 is an expansion of the lower left part of Fig. A-4, including additional data. The ordinates of these plots are the differences of echoes G_2 and A expressed in db and relative echo amplitude. The abscissas are the groove depths expressed in mils, microns, and D/λ, where D is the depth of the groove and λ is the wave length of the Rayleigh wave.

λ is obtained from the relationship

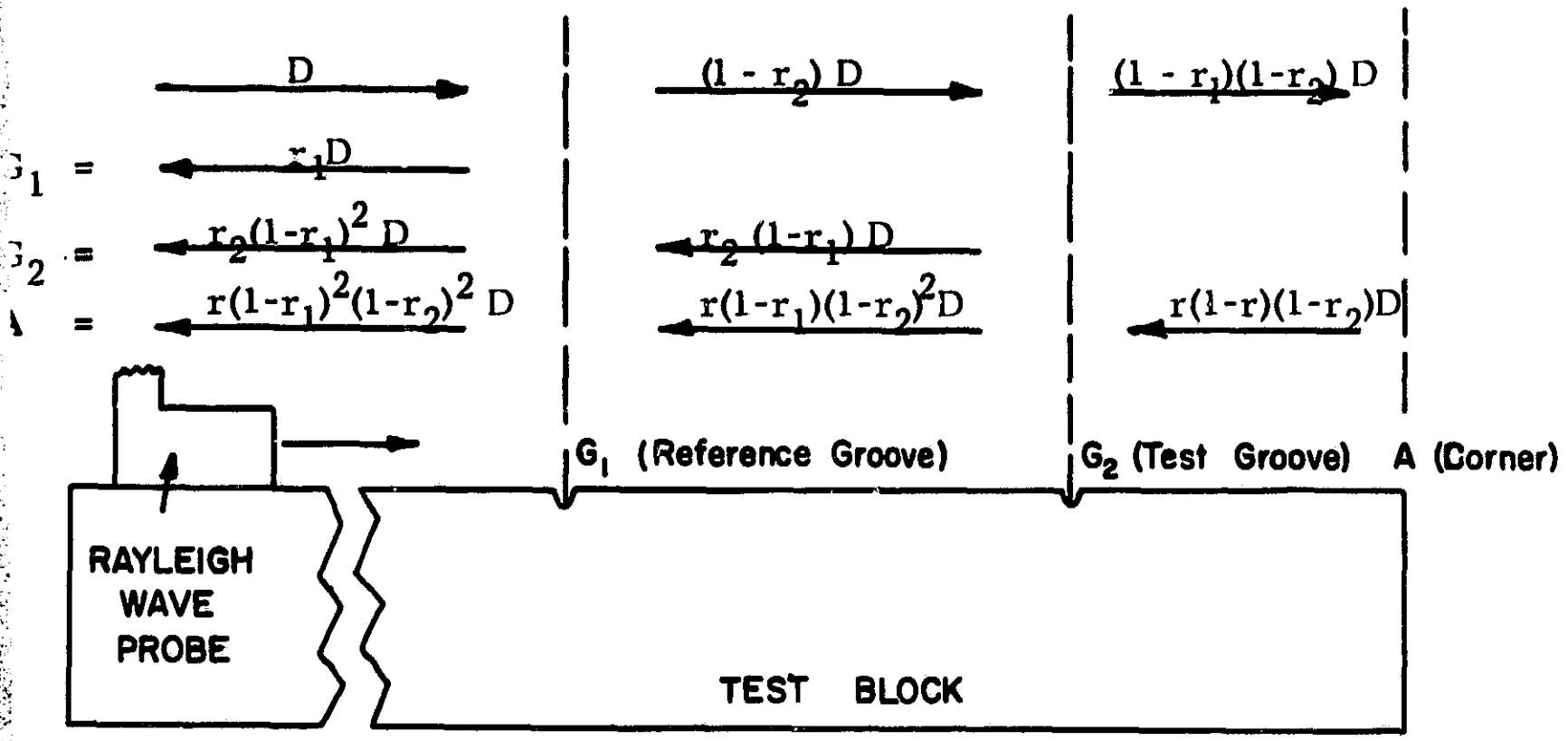

is the output amplitude from the transducer

is the reflection coefficient of the edge

is the reflection coefficient of the reference groove

is the reflection coefficient of the test groove

is the return signal from the edge

is the return signal from the reference groove

is the return signal from the test groove

is the return signal from the edge when G_2 is absent (i. e. for $r_2 = 0$)

$$\frac{G_2}{A} = \frac{r_2}{(1-r_2)^2} \quad \frac{1}{r}$$

$$\frac{G_2}{A_o} = \left(\frac{G_2}{G_1}\right) \quad \left(\frac{G_1}{A_o}\right) = \frac{r_2}{r}$$

Fig. A-3. Idealized model of the effect of a groove in the path of Rayleigh waves

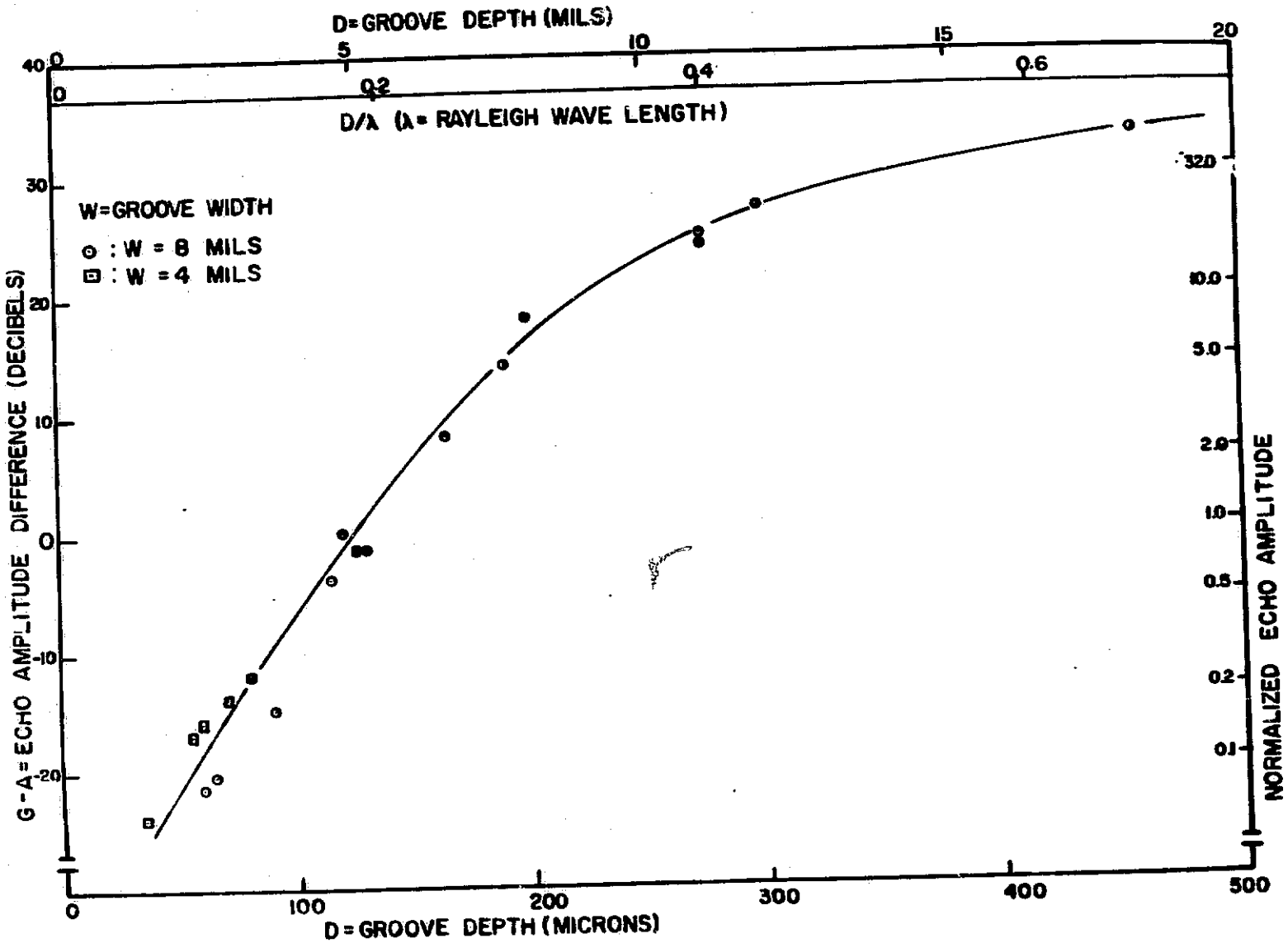

Fig. A-4. Effect of depth of artificial flaws on Rayleigh wave response

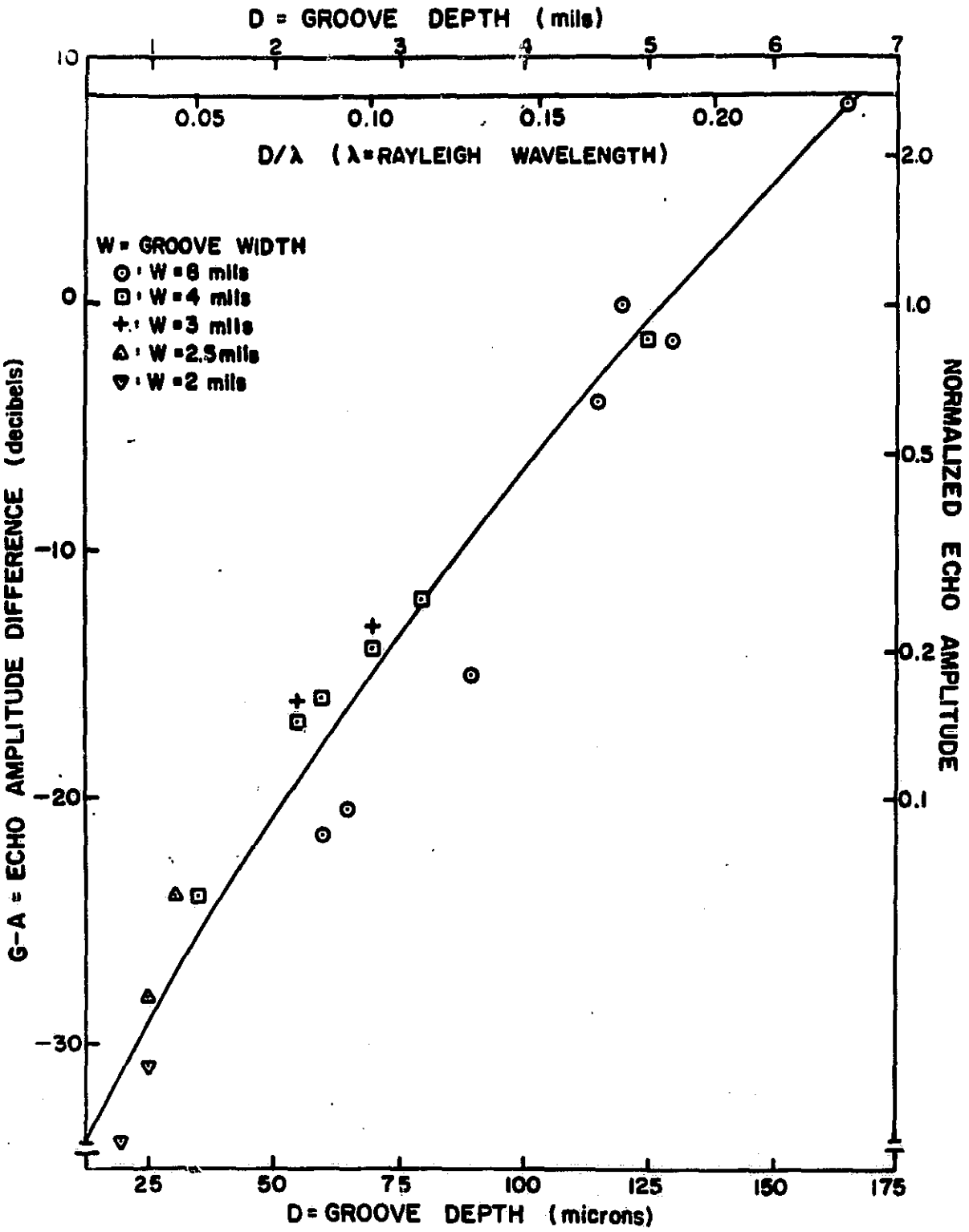

Fig. A-5. Effect of depth of artificial flaws on Rayleigh wave response (expansion of lower left part of Fig. A-4, including additional data)

$$\lambda = \frac{V}{f}$$

where λ = wave length of Rayleigh waves

V = velocity of Rayleigh waves

f = frequency of Rayleigh waves

If V equals 1.11×10^5 in./sec and the frequency is 4 MHz, then $\lambda = 27.5$ mils or 700 microns.

Another plot can be made by comparing the echo from groove G_2 with the edge reflection A_0 before the groove was cut. This is done by using the reference groove reflection as indicated in Fig. A-3. This ratio is directly proportional to log r_2 and is shown in Fig. A-6, where A_0/G_2 is plotted versus $1/D$. As can be seen, the data are fit relatively well by a straight line.

If all the energy in the incident Rayleigh wave between the surface and a depth D is assumed to be reflected and the remaining energy is transmitted, then we would find that

$$r = e^{-\alpha \lambda / D}$$

because the energy density of a Rayleigh wave decreases approximately exponentially from the surface. We find that $\alpha = 0.55$ for this particular geometry.

In this investigation, the following assumptions were made: (1) the reflectivities of the leading edge of the groove and of the edge of the test block were constant, and (2) the groove and the edge of the test block were both perpendicular to the ultrasonic beam. The last assumption was verified by obtaining a maximum reflection for both groove and edge at the same angular position of the transducer. If two reflecting edges are parallel, their maximum reflections with respect to the orientation of the probe occur simultaneously. Another factor that could also affect the results is the profile of the grooves. In this study, U-shaped grooves were assumed. However, in theory, a V-bottom groove has three reflecting edges and a square-bottomed groove has four, thus raising the question of the possibility of constructive or destructive interference effects. An additional factor to be considered is the width of the grooves which becomes increasingly important when its value is of the order of its depth or greater. In the plots of the data (Figs. A-4 and

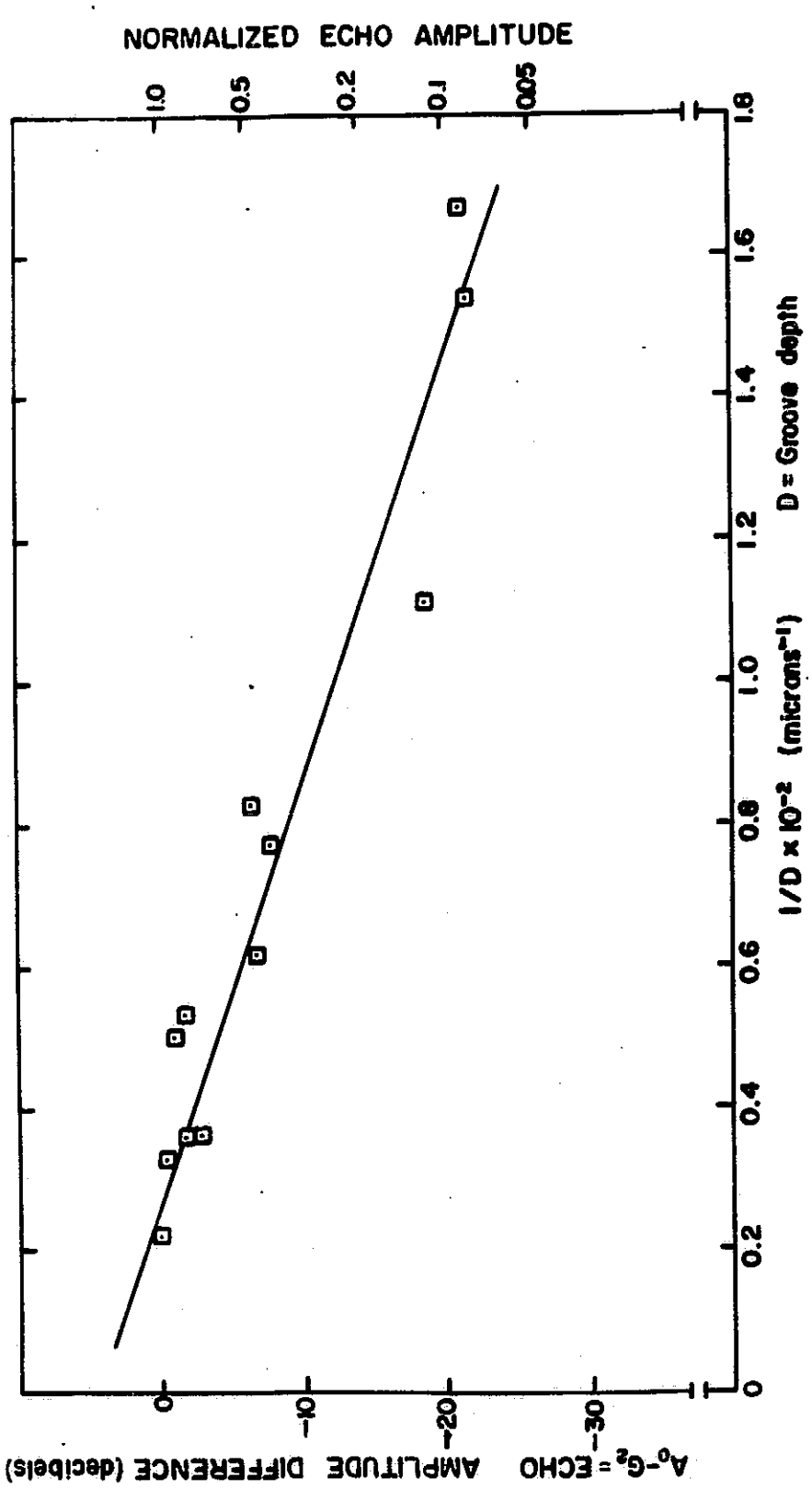

Fig. A-6. Reflection of Rayleigh waves from a groove as a function of the reciprocal of depth

A-5), the width was recorded as a parameter.

Examination of Fig. A-5 indicates that for grooves of the same depth their reflecting power decreases with increasing width. This can be explained by the fact that the bottom of a narrow groove scatters part of the incident wave, thus causing reflection, while the bottom of a wide groove allows a part of the incident wave to propagate over its contour. Additional results plotted in a different manner are shown in Figs. A-7 and A-8. The ordinates of these plots are the amplitudes of the echoes from the grooves and from the test block edges, expressed in db, and the normalized echo amplitudes. The abscissas are groove depths expressed in mils, microns, and D/λ, where D is the depth of the groove and λ is the Rayleigh wavelength. Both figures indicate that as the depth of the groove increases, the echo from the test groove increases and the echo from the edge of the test block decreases. However, below a depth of the order of a wavelength, both echoes approach a limiting value. Total reflection is not observed even for the deepest grooves, which implies that when the groove is several wavelengths deep, part of the Rayleigh wave beam propagates around the bottom of the groove.

Data from Fig. A-4 are replotted in Fig. A-9. The reflection coefficient, of the grooves is shown as a function of the reciprocal of the depth of the grooves (Fig. A-10). The reflected signal is normalized with respect to the echo from the edge before the test groove was cut (the behavior is described reasonably well by $r = \exp [-\alpha \lambda / D]$. We would expect α to be of the order of one or one-half, since the energy density of a Rayleigh wave decreases exponentially from the surface. A least squares fit gives a value of $\alpha = 0.43 \pm 0.04$.

In order to obtain data on the effective depth below the surface at which a defect that does not intercept the surface might be detected, a groove was cut in the back side of a test block. This groove, about 12 mils wide, was successively cut to greater depths, approaching the side of the test block on which the Rayleigh waves propagate.

Fig. A-11 illustrates the reflection from the subsurface groove and test block edge as normalized with respect to the reference groove. It is plotted as a function of the depth of the groove edge below the surface

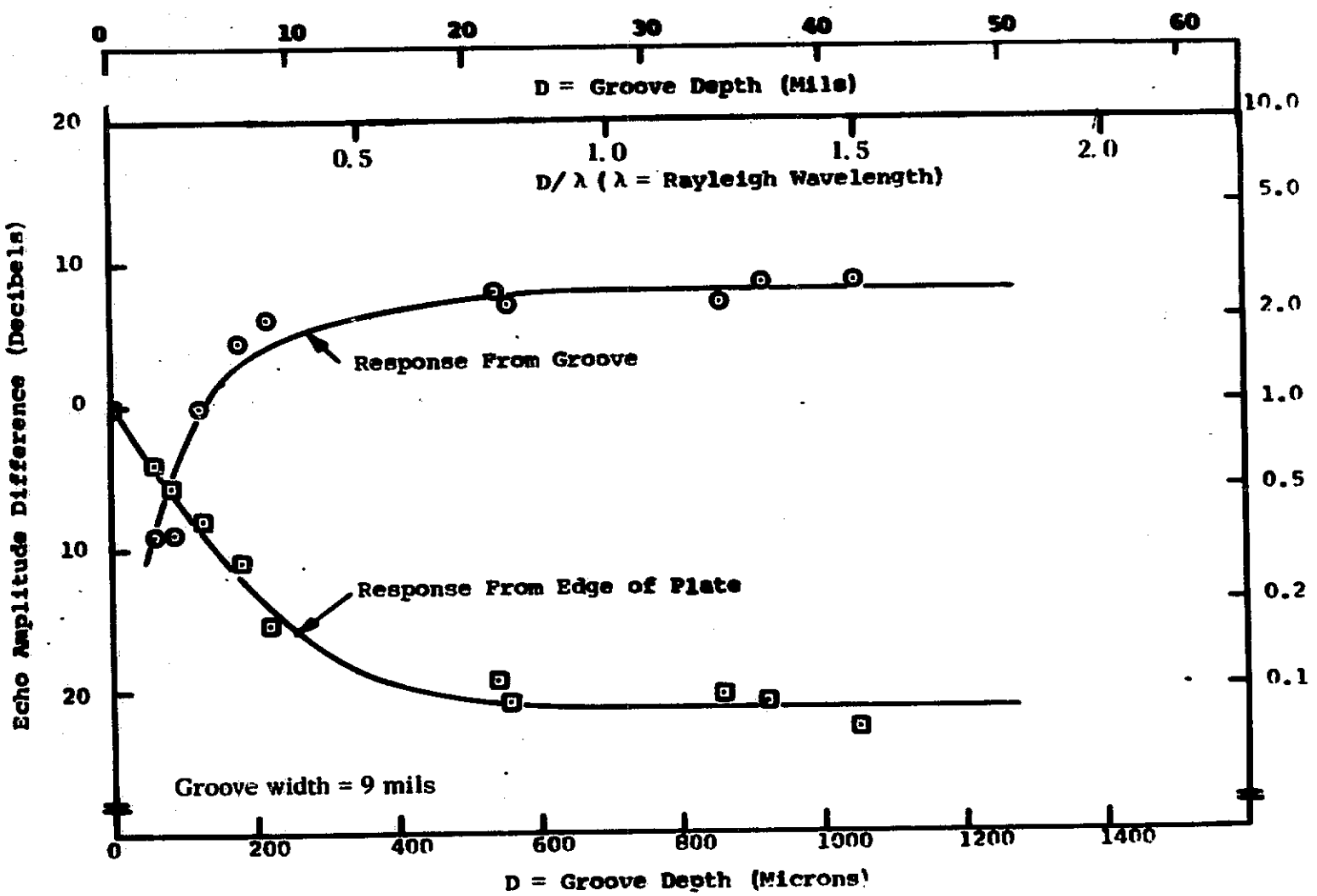

Fig. A-7. Effect of depth of artificial grooves on Rayleigh wave reflection (groove width = 9 mils)

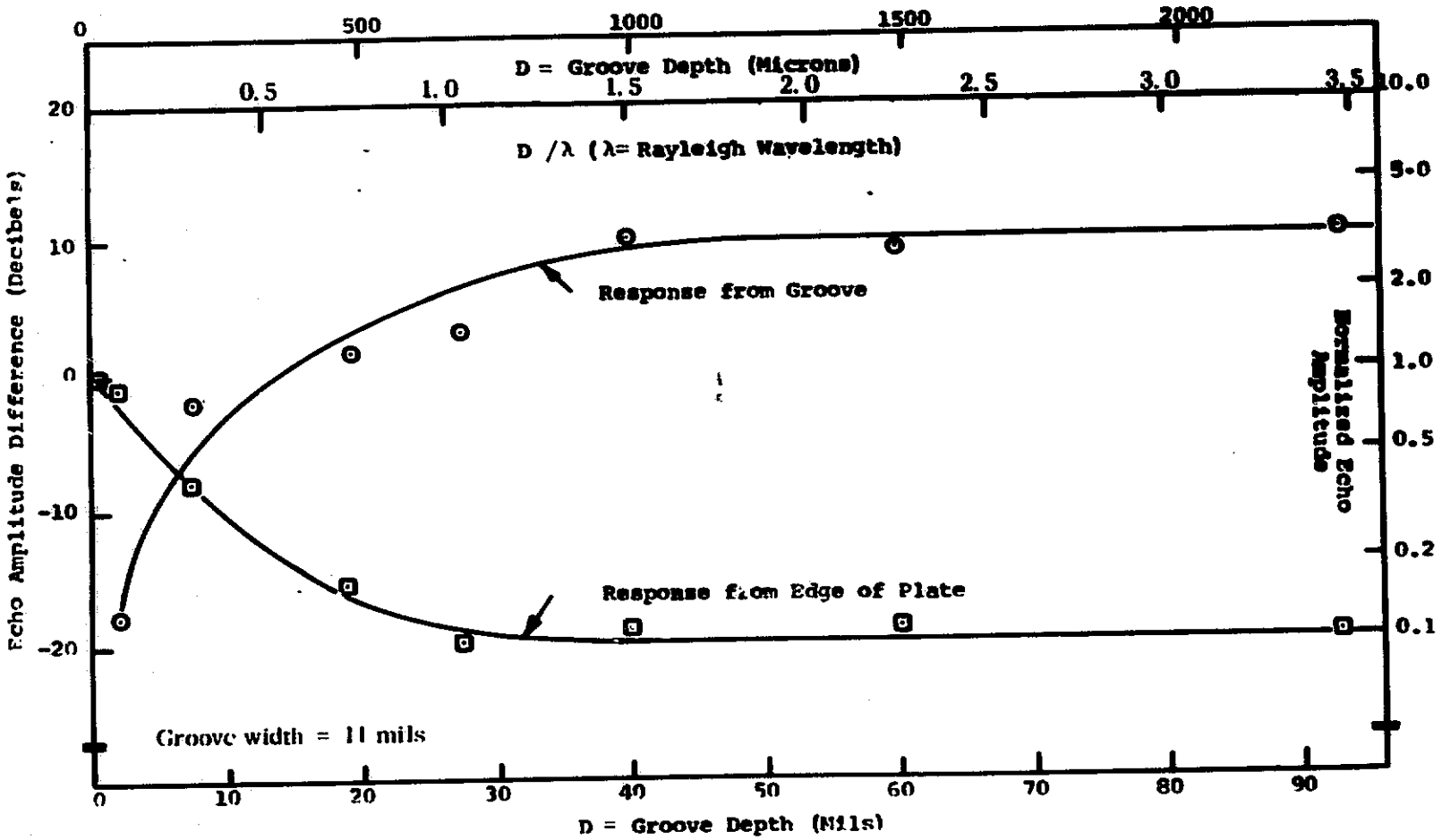

Fig. A-8. Effect of depth of artificial grooves on Rayleigh wave reflection (groove width = 11 mils)

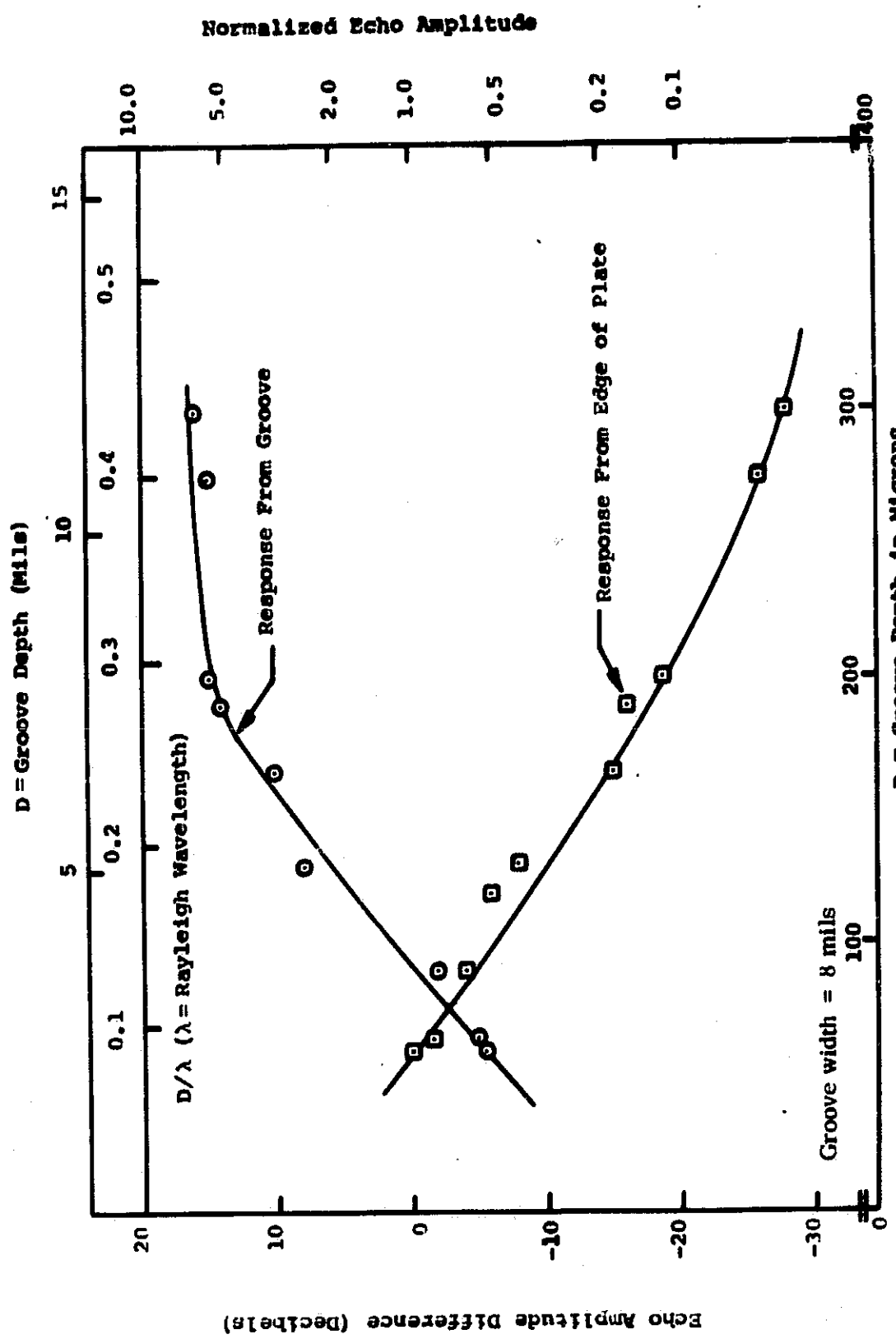

Fig. A-9. Effect of depth of artificial grooves on Rayleigh wave reflection (groove width = 8 mils)

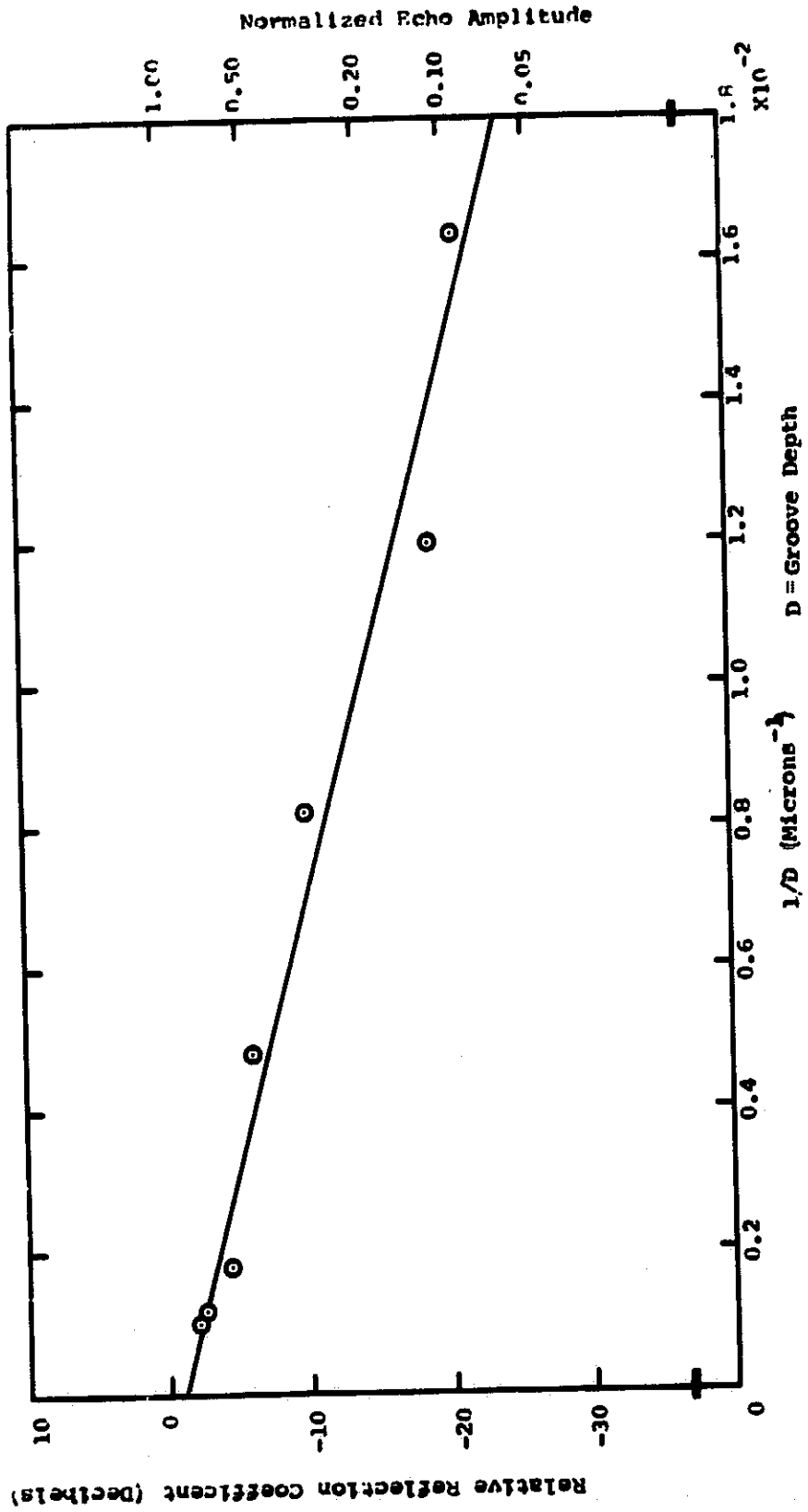

Fig. A-10. Reflection of Rayleigh waves from a groove as a function of the reciprocal if depth

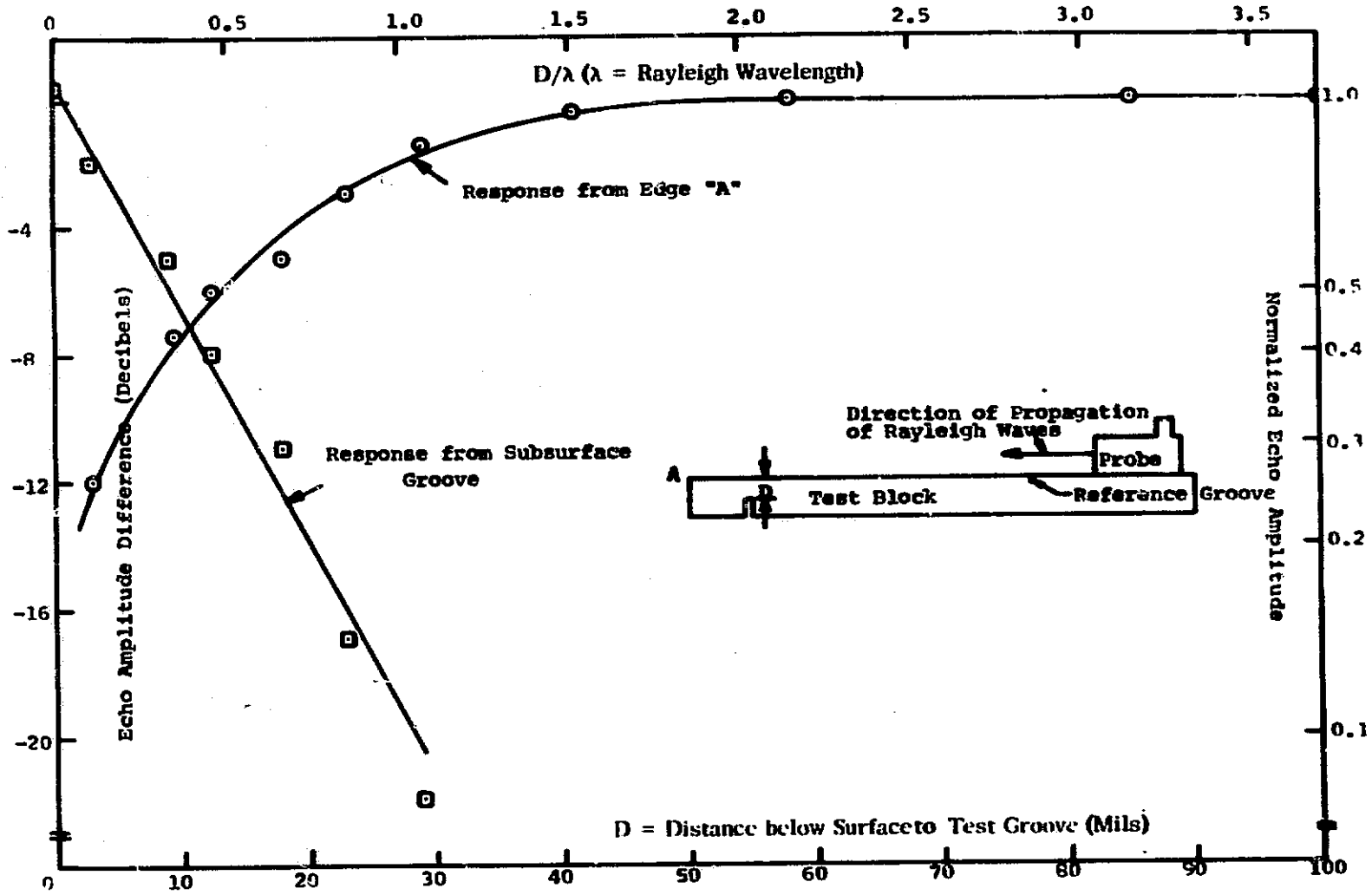

Fig. A-11. Effect of subsurface groove on Rayleigh wave reflection (experimental procedure also illustrated)

in mils and units of D/λ. This figure shows that as the distance below the surface to the edge of the groove decreases, the echo from the edge of the test block decreases and the echo from the groove increases rapidly. A few points were taken for D greater then 100 mils (not shown in Fig. A-11), but no effect on the echo from the edge of the test block could be observed. Reflections comparable to the noise level of the ultrasonic system were obtained from the subsurface groove, when the distance below the surface to the groove was slightly over 1 λ (27 mils at 4.0 MHz).

We find that grooves only a few tenths of a wavelength (100 μ) are readily detectable. Defects located deeper than 1 to 1.5 mm were not detectable. This means that Rayleigh waves are indeed very sensitive, but only to defects within 1 λ of the surface.

C. Effects of Cylindrical Holes

The first-order approximation to pits are cylindrical holes. By studying reflections from holes, an estimate of the detectability of pits such as those produced by GGC can be obtained. Holes were cut on flat surfaces of test blocks with axes perpendicular to the surface. In this investigation, corrections to the amplitudes of echoes due to the change in path length caused by the increasing hole diameters were not made, since they were small.

Fig. A-12 is a plot of Rayleigh wave reflection as a function of the diameter of a V-bottomed hole of constant depth. The same figure also shows the experimental procedure and a typical test oscillogram. The ordinate is the amplitude of the echoes normalized with respect to the reflection from the edge of the test block (A-H), and the abscissa is the diameter of the hole expressed in mils and units of D/λ. The graph indicates that as the diameter of the hole increases, the amplitude of the echo also increases up to a diameter of 175 mils or 7 λ, after which it apparently becomes constant. The echo from the edge of the test block decreases, becoming constant for diameters greater than 175 mils.

To investigate the effect of a flat-bottomed hole on the Rayleigh waves as the probe moves parallel to the edge of a test block behind the hole, the experimental procedure indicated in Fig. A-13 was used.

(a) Experimental procedure

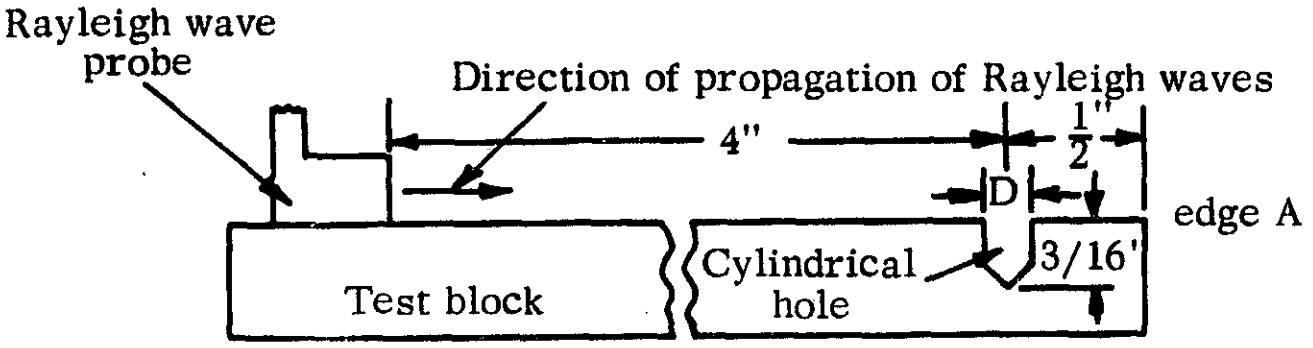

(b) Test oscillogram

A: echo from edge A

H: echo from cylindrical hole

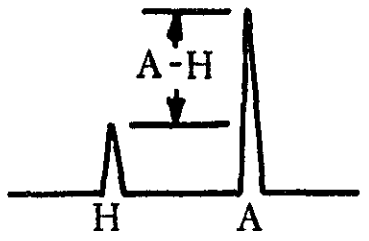

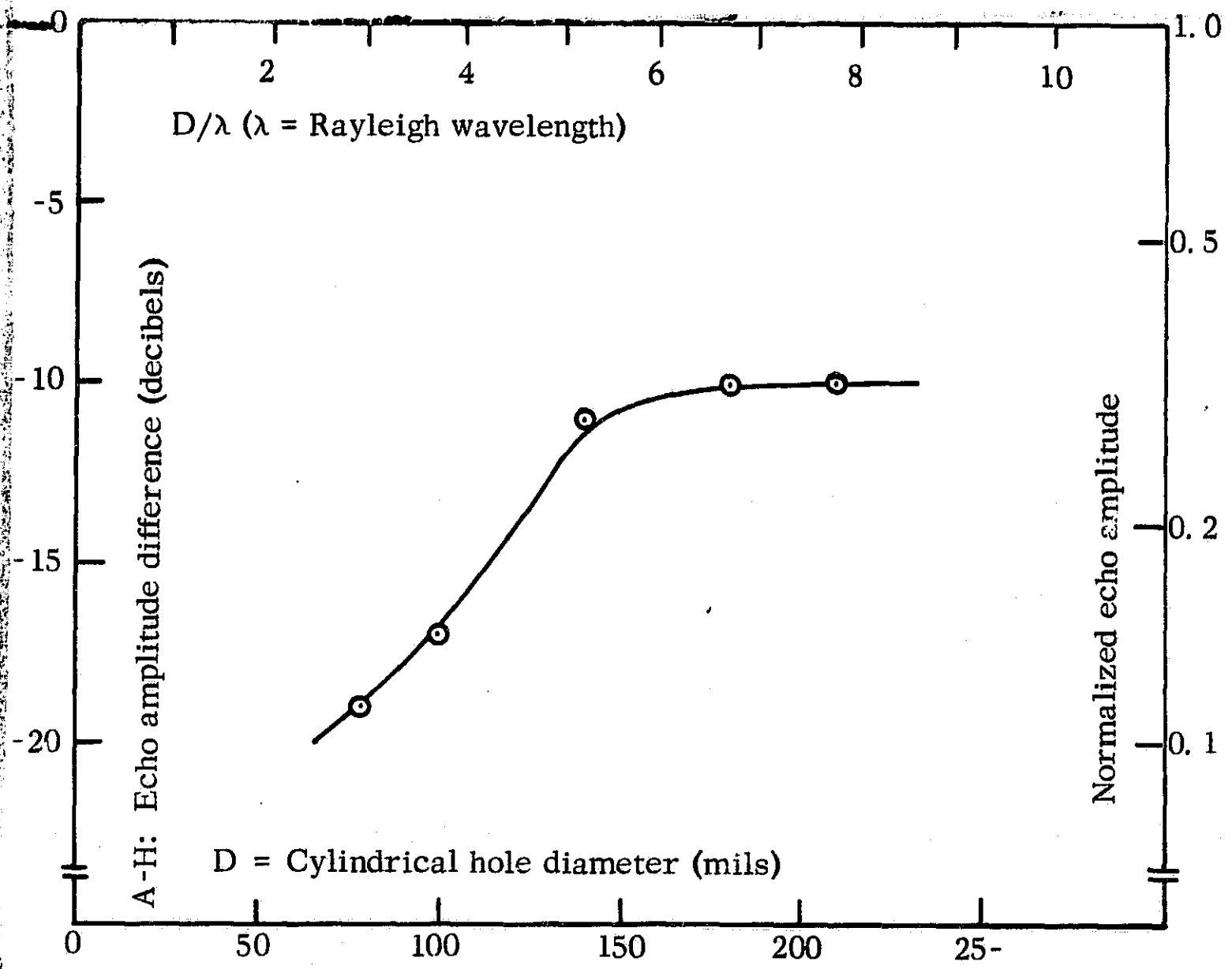

Fig. A-12. Effect of cylindrical holes with axes perpendicular to the surface on Rayleigh wave reflection as a function of hole diameter (experimental procedure also illustrated)

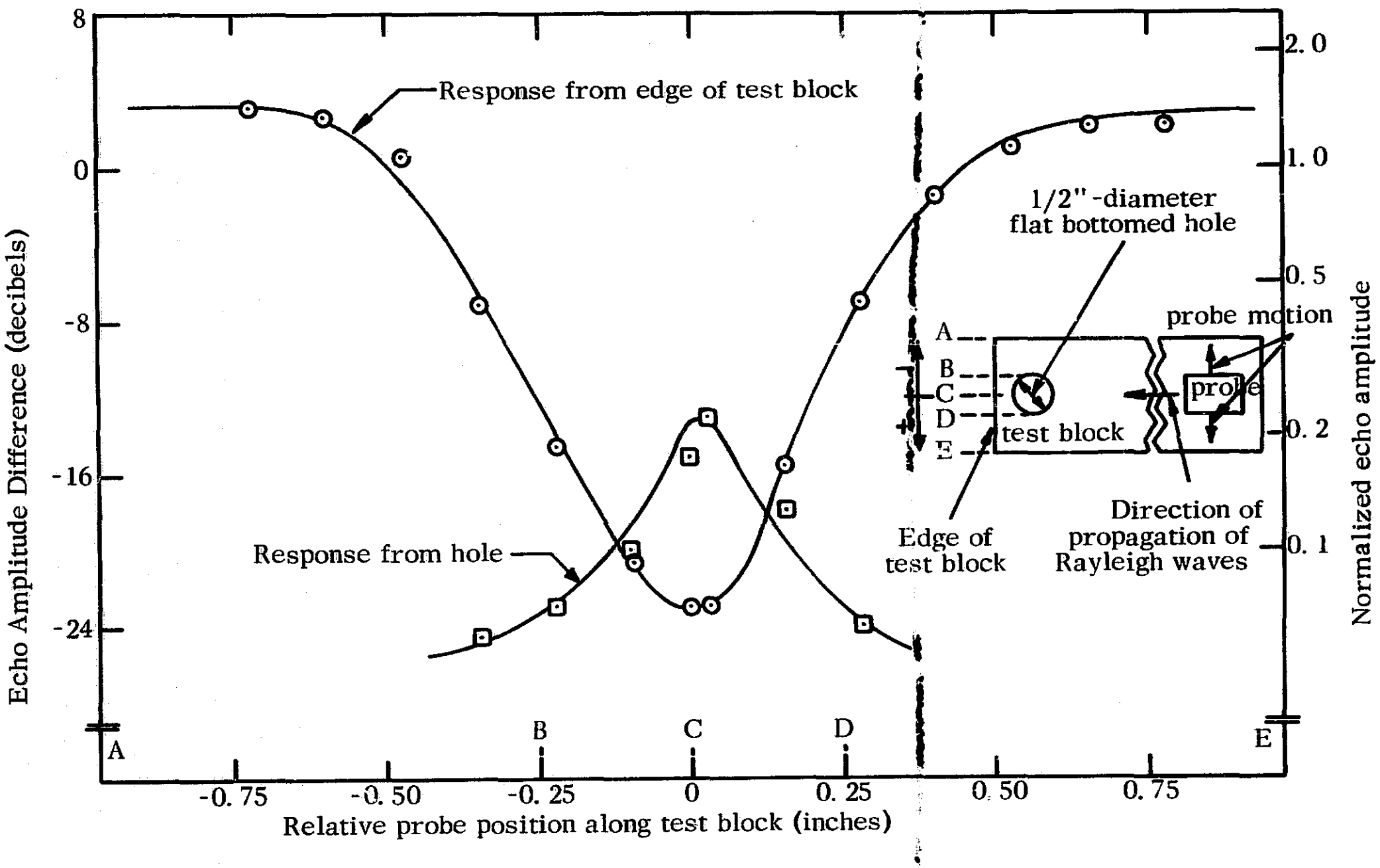

Fig. A-13. Effect of cylindrical hole with axis perpendicular to the surface on Rayleigh waves as a function of probe position (experimental procedure also illustrated)

The results are shown in the same figure. The depth of the hole was 3/16 in. As the probe approaches the hole, the echo from the hole increases and that from the edge of the test block decreases. However, even when the center of the Rayleigh wave beam has completely passed the hole, there is a small echo present which is due to the spreading of the ultrasonic beam.

To investigate the effect of a variable hole diameter and probe position, a series of holes of constant depth (1/8 in. deep and V-bottomed) were drilled, in order of increasing diameter, parallel to the corner of the test block. The probe was then moved parallel to the edge of the test block. The results and experimental details are shown in Fig. A-14. The amplitude of the echo from the holes and from the edge of the test block with respect to a reference groove is plotted as a function of the position of the probe. With the help of Figs. A-12 and A-13, an oscillating curve was drawn to fit the data. The values of the maxima of the oscillations, which occur when the ultrasonic beam is perpendicular to the center of holes of constant depth, increase with increasing hole diameter. The minima of the oscillations occurred when the ultrasonic beam passed between the holes and was reflected from the edge of the test block. The small echoes present between the holes are due to the spreading of the ultrasonic beam.

In the study of the different effects shown in Figs. A-12, A-13, and A-14, the depth of the holes was constant. An investigation of the reflectivity as a function of the depth of the hole was made. A 1/8-in.-diameter, flat-bottomed hole was cut on a flat surface of a test block to increasing depths and the Rayleigh wave response was measured. The results and experimental procudure are shown in Fig. A-15. The amplitude of the echoes from the hole and from the edge of the test block, normalized with respect to a reference groove and expressed in db, is plotted versus the depth of the hole in mils and in units of D/λ. The results indicate that up to 40 mils or 1.5 λ, the echoes from the hole rapidly increase with increasing hole depths, while the echo from the edge decreases. Deeper than 40 mils, both echoes remain roughly constant.

Again, as in the case with artificial grooves, holes were detectable

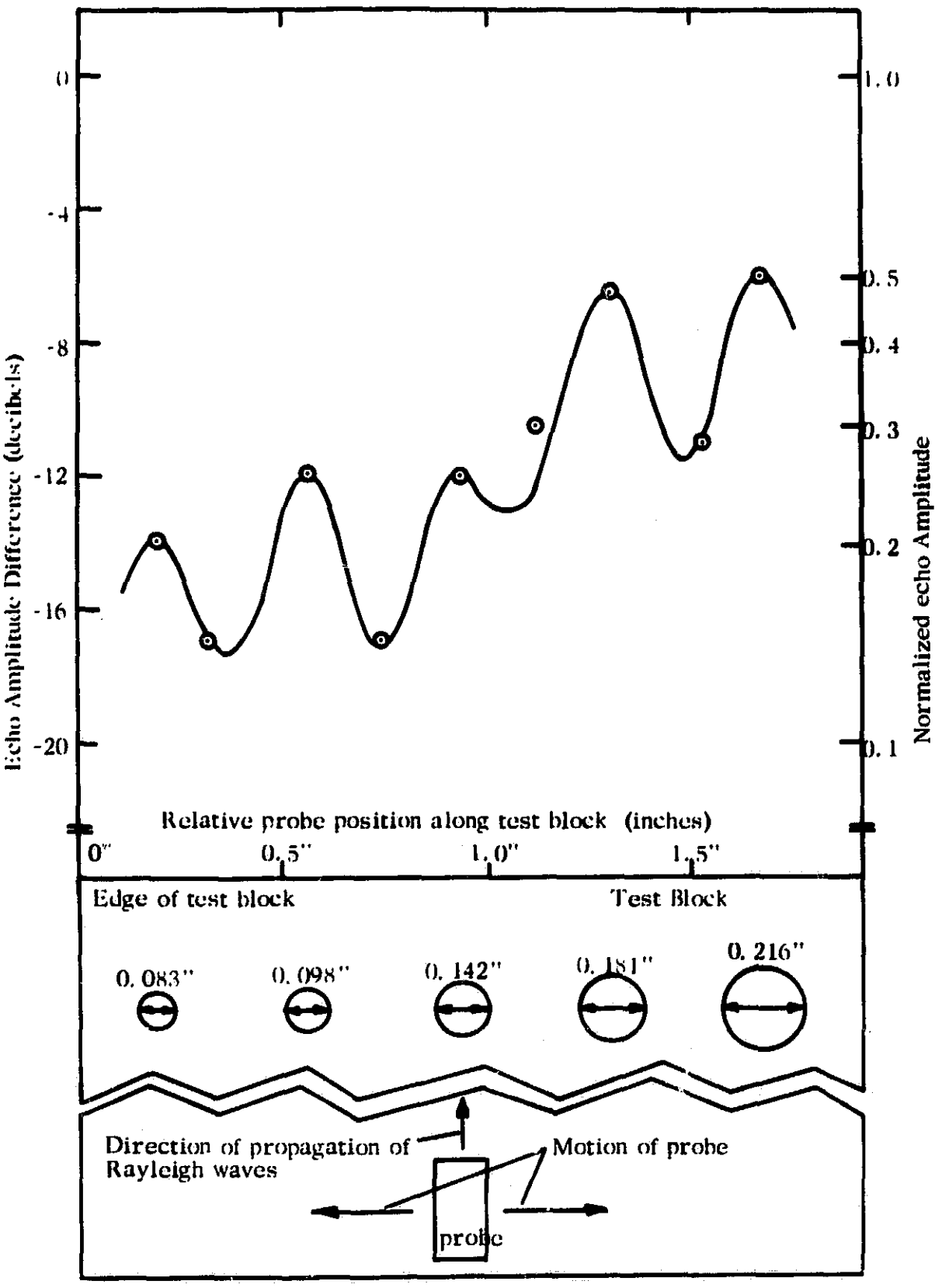

Fig. A-14. Effect of cylindrical holes with axes perpendicular to the surface on Rayleigh waves as a probe moves parallel to straight line joining centers of holes (experimental procedure also illustrated)

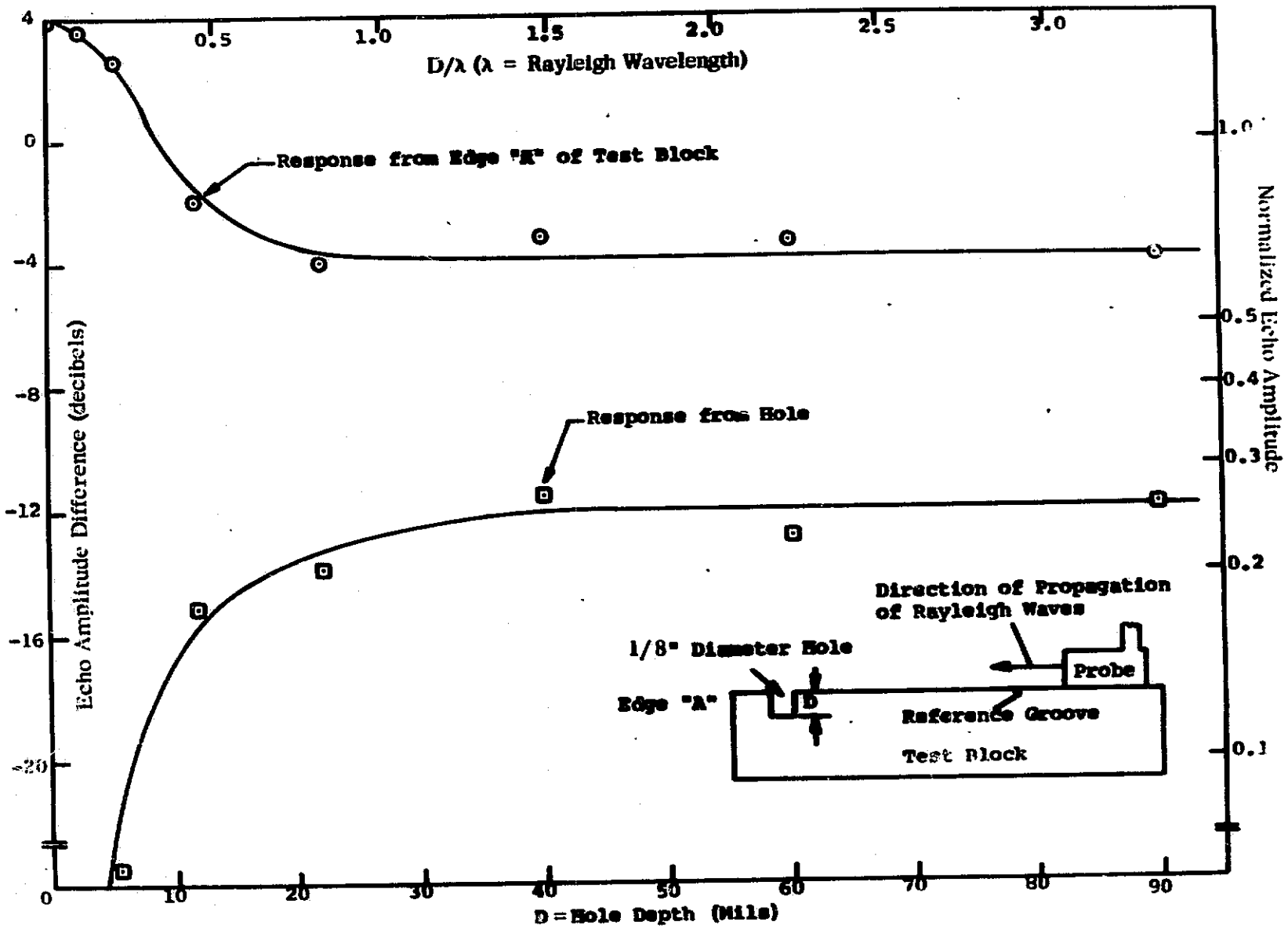

Fig. A-15. Effect of cylindrical holes with axes perpendicular to the surface on Rayleigh waves as a function of hole depth (experimental procedure also illustrated)

when their dimensions became the order of a few tenths of one wavelength. The response saturates when holes with sizes larger then several wavelengths are used.

D. Effect of Edge Angle

When making measurements on fabricated parts, it is important that we know not only from what type of defect reflections are generated, but also what defects or "discontinuties" will have little or no effect. An edge is one such discontinuity that can propagate Rayleigh waves to some extent, especially if it is rounded. In field testing, it would be very useful to be able to propagate around corners. For this reason, various angles of sharp edges were investigated.

One of the characteristic properties of Rayleigh waves is that they can be reflected from sharp edges, but if the edges are rounded they propagate with no reflection. In order to obtain data on this phenomenon, the reflections from various edge angles were obtained. The experimental procedure is illustrated in Fig. A-16 with the results. The ordinate of this plot is the echo amplitude from the edge expressed in db and the abscissa is the angle of the edge in degrees. The data were determined in two stages. The first set was obtained when the probe was placed on side A of the test block (Fig. A-16). The data were plotted as function of angle, Θ_1. The second set was obtained for the probe placed on the opposite side B of the test block, and data were plotted as a function of angle, Θ_2, after compensating for the different attenuations due to different path lengths.

The distance the Rayleigh waves have to travel from the probe to the edge (designated by D in Fig. A-16) on side B of the test block is a variable and decreases with increasing angle. The corresponding distance on side A of the test block, however, was constant and no compensation is necessary. The dashed lines on the test block in Fig. A-16 indicate the successive amount of material removed by machining to create the various test angles. For every cut, two new angles, Θ_1 and Θ_2, were generated and oscillograms were obtained for the two sides of the test bloc

Analysis of the second set of data (angle Θ_2) indicated that the grea the angle between two planes, the smaller the reflection coefficient. Of co

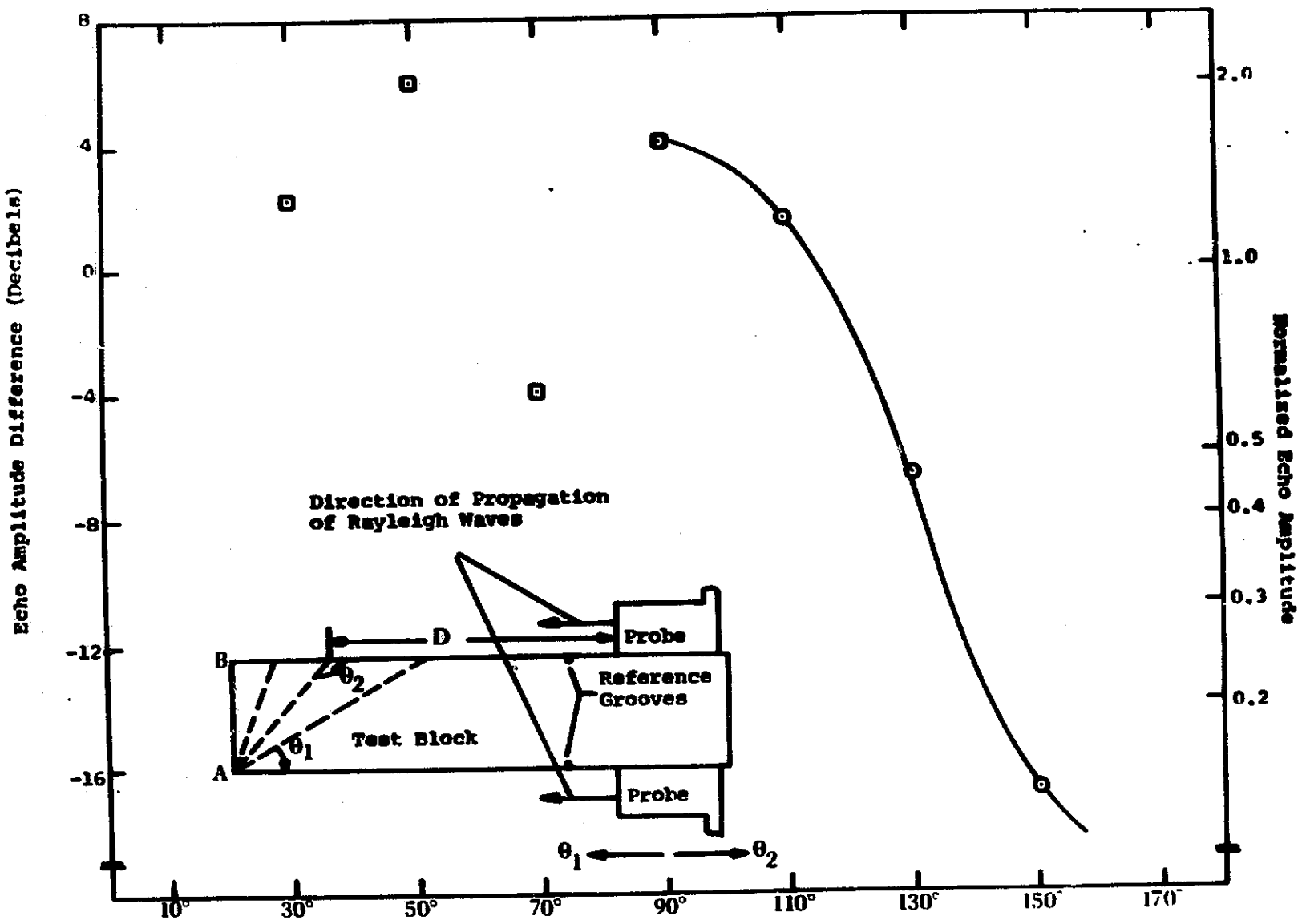

Fig. A-16. Effect of edge angle on Rayleigh waves (experimental procedure also illustrated)

in the limiting case of 180° (i.e., when the two planes become one), there is no reflection at all. Analysis of the first set of data (angle Θ_1), however, showed considerable scatter which would occur if the reflection coefficient oscillates as a function of angle when Θ lies between 0° and 90°. When these results were compared with similar data obtained by others, they agreed very well. This can be seen by examining Figs. D. 5 and D. 14 of our Second Quarterly Report. The data for various vales of Θ_1 is quite consistent with the oscillatory nature of Fig. D. 5 of that quarterly.

These investigations were made on "sharp" edges. Only by using angles near 180° do sharp edges have little effect. Of course, by rounding them the reflection coefficient is drastically reduced.

E. Effect of Reflector Orientation

This investigation was designed to study the change in reflectivity of a Rayleigh wave with reflector orientation. This was determined largely by the beam spreading. For these tests, two kinds of reflecting edges were used: the corner of a test block and a U-shaped groove. The test procedure was as follows. The distance to the reflecting edge was held constant and the probe was rotated. Initially, the probe was adjusted so that the ultrasonic beam was perpendicular to the reflecting edge and this maximum echo amplitude was recorded. Subsequent amplitudes of the echo at different angular positions were normalized with respect to the maximum amplitude.

In this investigation, a constant reflectivity from the edge was assumed along its entire length. It was also assumed that the change in attenuation, when the ultrasonic beam was perpendicular to the edge and when it made a small angle to the rolling direction, could be neglected.

The results are shown in Fig. A-17, along with the experimental arrangement, and indicate a sharp decrease in echo amplitude as expected. This figure is a plot of the decrease of echo amplitude in db and of the normalized echo amplitude versus angle ϕ in degrees, measured from the norma The results are normalized to normal incidence. When the ultrasonic beam makes an angle to the normal, the Rayleigh waves have to travel a slightly longer distance to the reflecting edge. This distance, indicated as d in Fig. A-17, was not compensated for because its contribution was much smaller

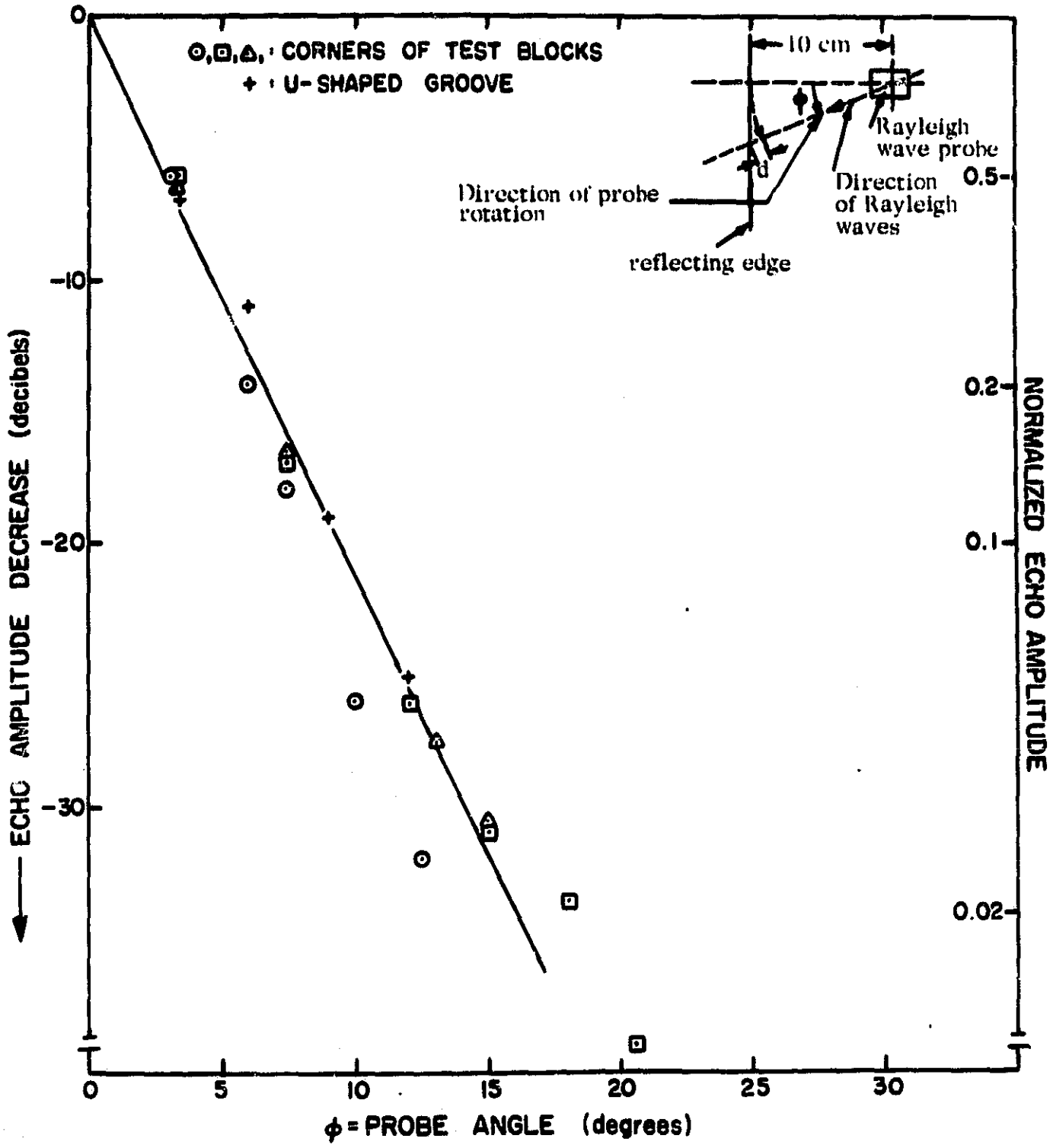

Fig. A-17. Effect of reflector orientation on Rayleigh wave reflection (experimental procedure also shown)

than the angular contribution.

The results also indicate that the behavior of an edge and groove is similar. The sharp decrease in echo amplitudes with probe rotation can be seen in Fig. A-17 by noting that the echo amplitude decreases to half its normal incidence value at an angle of 3°, 0.1 at 9°, and 0.01 at around 20°. The reflected signal decreases about 2.2 db per degree for the particular test conditions and for the angular range studied (0° to 20°).

F. Effect of Parallel Grooves and of Groove Ends

For this experiment, two parallel grooves were cut on a test block, the first half as long as the second. The probe was moved parallel to the grooves and at a constant distance. The results, along with the experimental arrangement, are shown in Fig. A-18. Groove G_1 was 5 μ wide and 40 deep, and its end tapered to 0 depth. Groove G_2 was 100 μ wide and 60 μ deep. The assumption was made that the reflectivity of the grooves was constant along their entire length.

The abscissa of Fig. A-18 is the distance along the entire length of the test block, and the ordinates are expressed in echo amplitude decrease and normalized echo amplitude. Normalization was with respect to the ech from groove G_2 on the side of the test block when groove G_1 was not prese Fig. A-18 is a plot of the Rayleigh wave reflection from each groove and the am plitude along the entire length of the test block. As the probe approaches t end of groove G_1 from the double groove side, the response from G_1 decre rapidly and the G_2 response increases smoothly. This is due to the tapere end of groove G_1. If the depth of G_1 were greater, the two response curve would intersect. The same test block was employed to study the reflection from grooves G_1 and G_2 as a function of probe orientation.

The results are shown in Fig. A-19, along with the experimental pr cedure. Fig. A-19 is plot of echo amplitude versus probe angle. In this graph, the amplitude of reflection of grooves G_1 and G_2 and their differenc are plotted. The responses from G_1 and G_2 are normalized to their values at $\phi = 0°$. The signal amplitudes decrease with increasing angle, as in Fig A-17, with a secondary maximum at 21° in the response curve for groove G This maximum corresponds to the angle where the ultrasonic beam is refle from G_2 only. At th , angle, the end of groove G_1 is sufficiently far from t

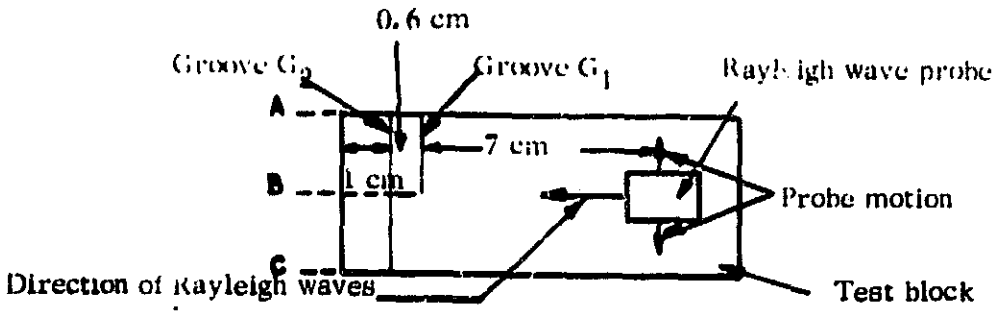

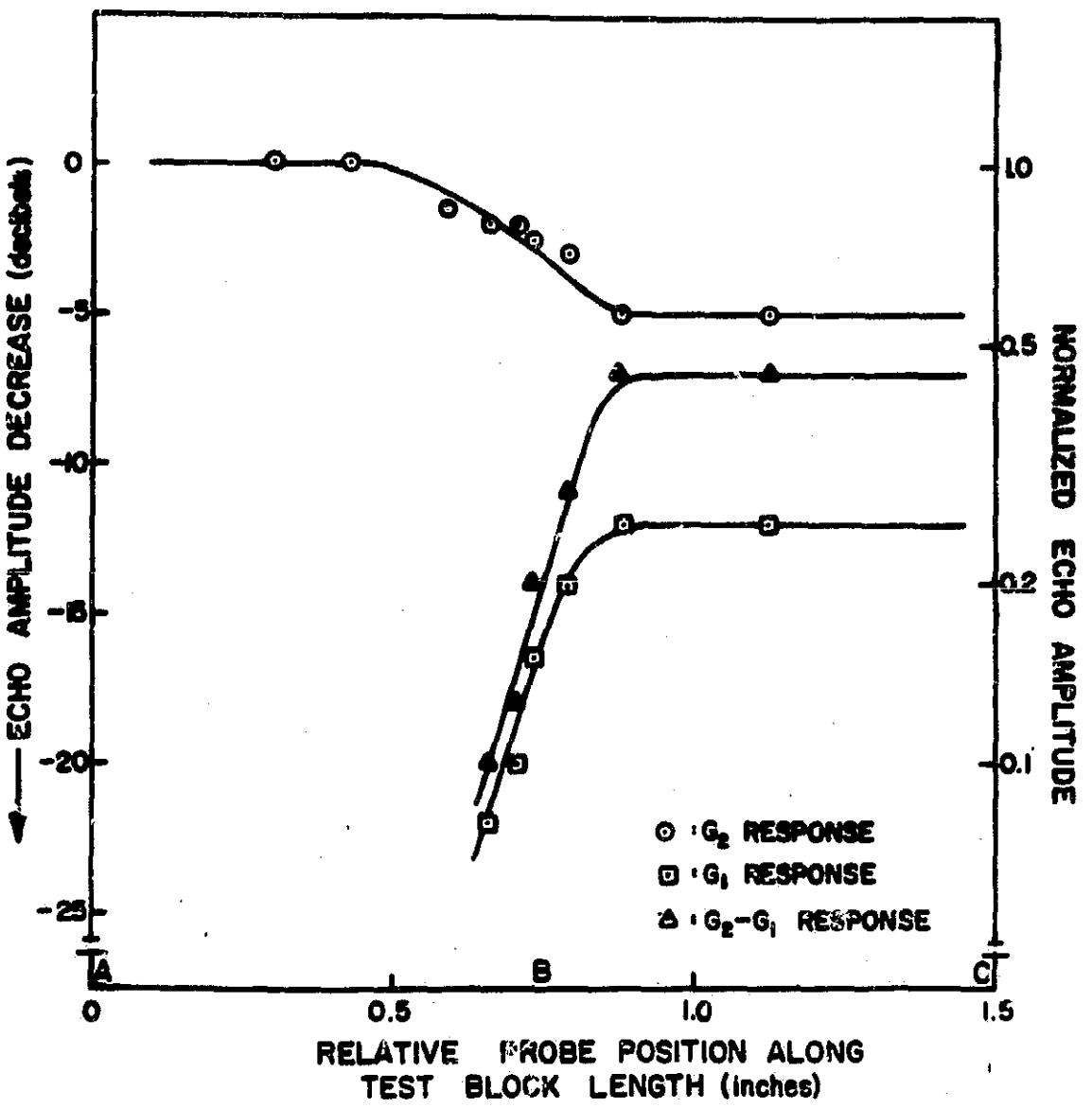

Fig. A-18. Effect of two parallel grooves and groove end on Rayleigh wave reflections for probe movement parallel to grooves (experimental procedure also illustrated)

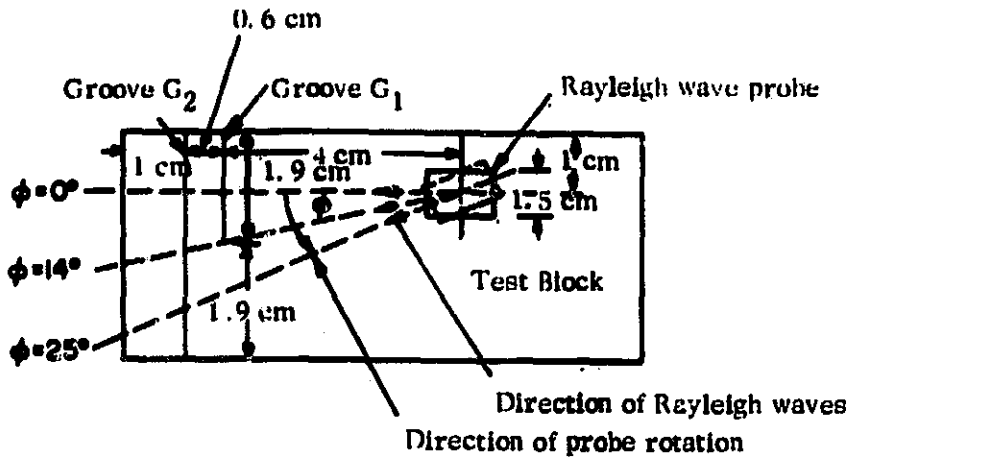

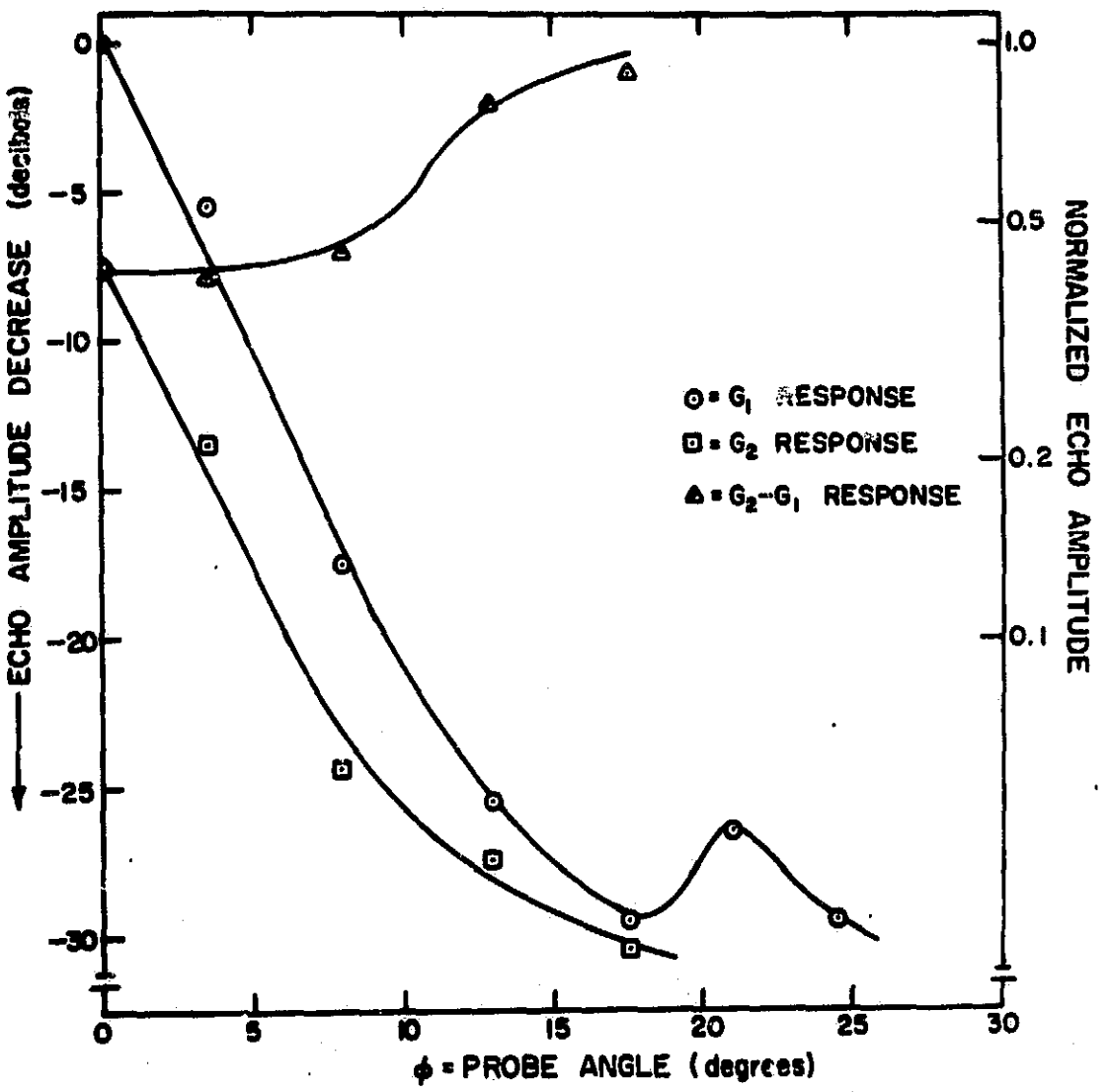

Fig. A-19. Effect of two parallel grooves and groove end on Rayleigh wave reflection as a function of probe angular rotation (experimental procedure also illustrated)

ultrasonic beam to contribute a reflection and thus attenuate the energy reaching G_2. Just before this secondary maximum, the first relative minimum for the response of G_2 occurs at an angle where the reflections from G_1 and G_2 are of approximately equal amplitude. This is shown by the curve indicating the difference in signal amplitude from grooves G_1 and G_2, which approaches 0 db at the angle of the first relative minimum in the response from G_2.

G. Effect of Multiple Parallel Short Grooves

For the SCC study described in Section IV, a rectangular area of the U-bend tensile specimens at the bend was exposed to the corrosive environment, and the cracks that were formed were approximately parallel. Of course, the stress corrosion cracks themselves are not straight and make small angles with the transverse direction, but to simulate the actual case, multiple short parallel grooves of about the same size were cut in a rectangular area on the surface of a test block. These grooves were 0.05 to .1 mm wide, 40 to 100 μ deep, and 2 to 8 mm long. There were two general factors that were different from the actual and simulated cases. In the actual case, the Rayleigh waves have to travel around the convex area of the U-bend specimen to reach the corroded area, whereas in the simulated case the rectangular area containing the grooves and the probe were in the same plane. In the actual case, besides the cracks, there are pits which also act as sources of reflection for the Rayleigh waves, whereas such defects were not included in the simulated area.

In this experiment, the response from the cracks was investigated as a function of the angle of the probe. This measures the sensitivity of the Rayleigh waves to defects on a corroded area not perpendicular to the ultrasonic beam. Fig. A-20 and A-21 show the results and experimental procedures for the actual and simulated cases and are plots of signal amplitude versus probe angle. The amplitude of the highest echo originating from the test and corroded areas was measured and normalized to the echo corresponding to normal incidence from an arbitrarily chosen position at the center of the test block and U-bend specimen. The data were obtained with the probe making angles to the right and left of normal incidence. In the plots of Figs. A-20 and A-21, these angles are indicated as positive and negative, respectively. The data on Fig. A-21 were obtained from four dif-

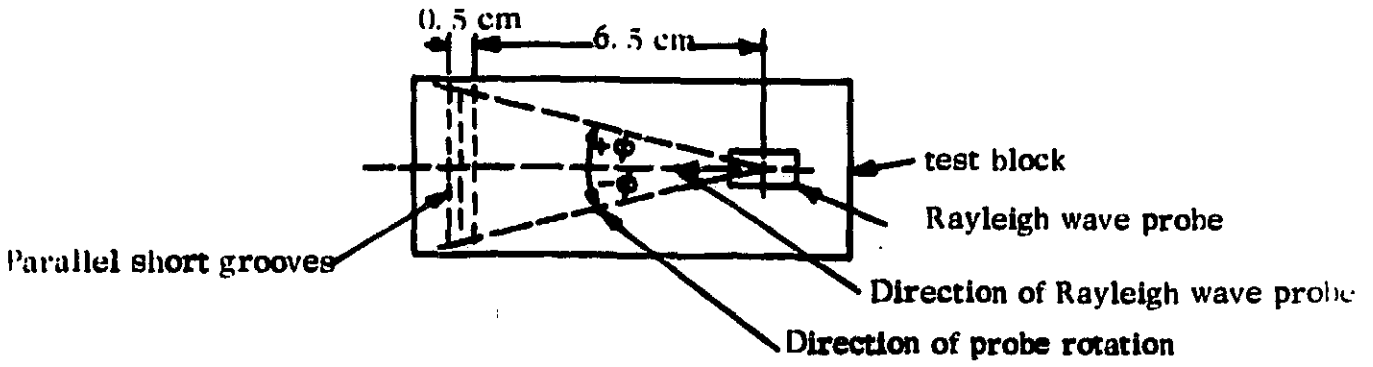

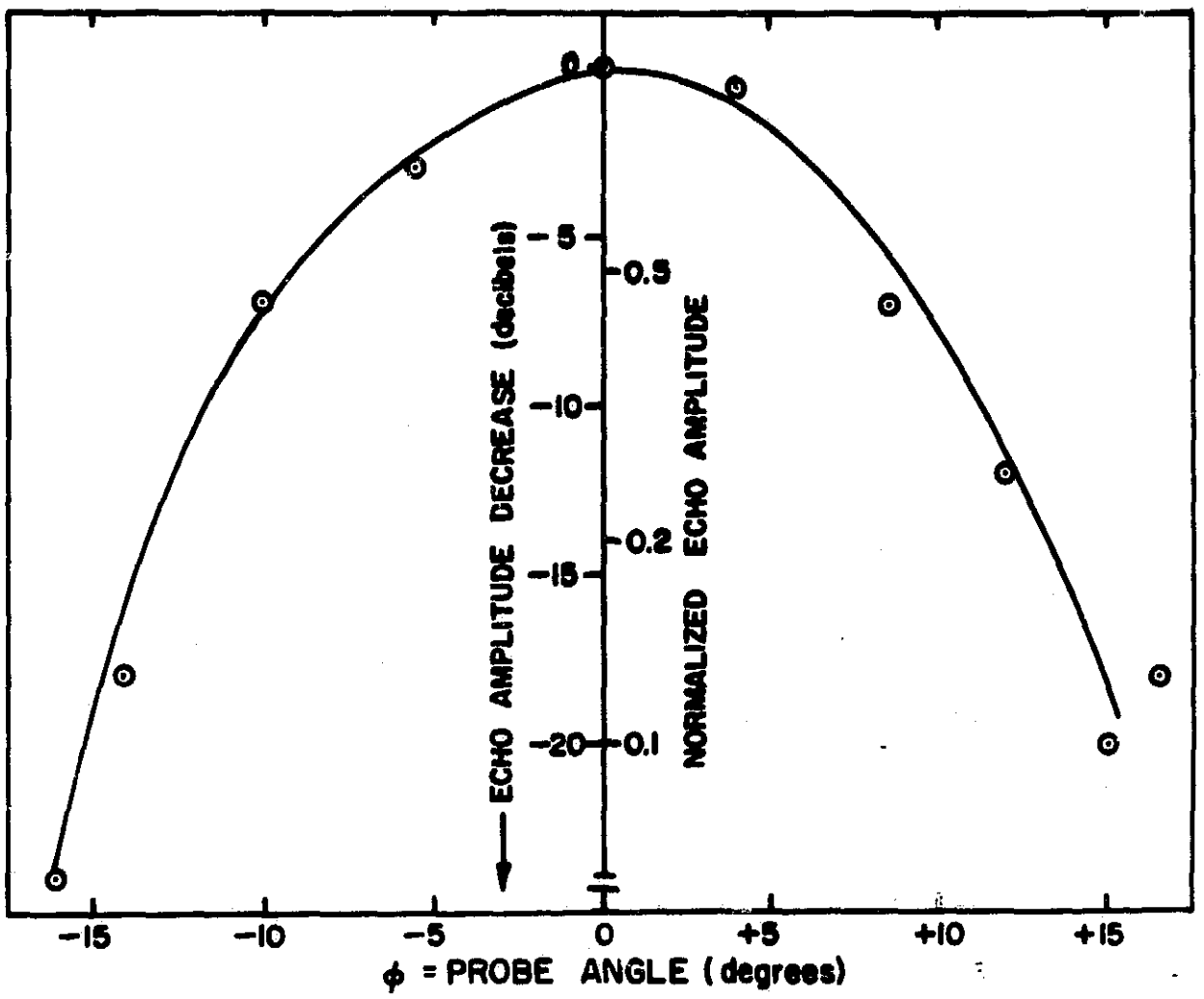

Fig. A-20. Effect of multiple parallel short grooves on Rayleigh wave response as a function of probe angular rotation (experimental procedure also illustrated)

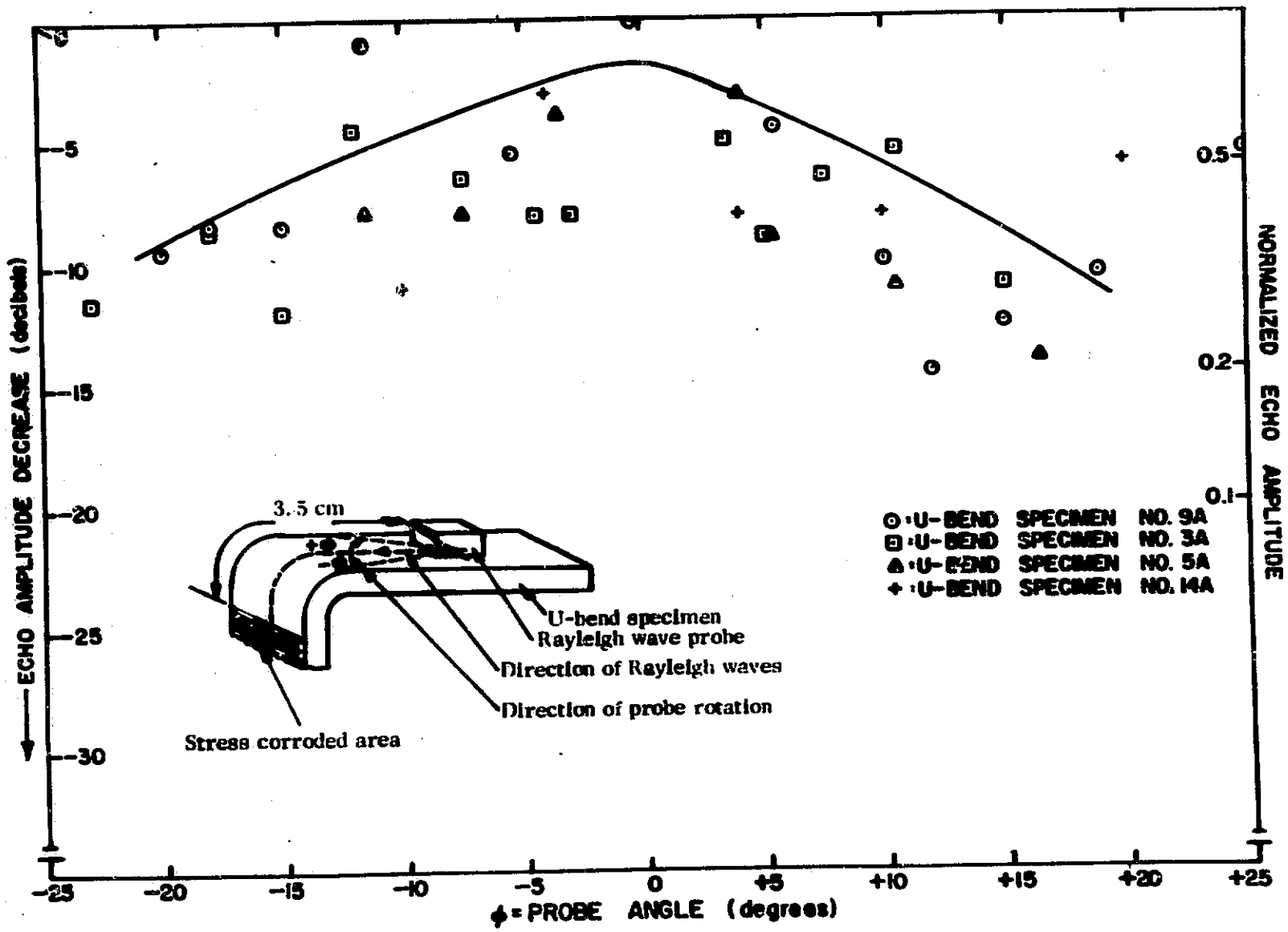

Fig. A-21. Effect of SCC on Rayleigh wave response as a function of probe angular rotation (experimental procedure also illustrated)

ferent U-bend specimens stress corroded under different conditions. The scatter between points of different specimens is of the order of that observed between points of the same sample.

If we compare Fig. A-21 with Fig. A-17, which is a plot of signal amplitude versus probe angle for a single long groove, it is seen that reflections from a broader range of angles are obtained for the case of multiple short parallel grooves. Fig. A-21 shows that for the actual case of SCC, the angular sensitivity is less, making the detection of SCC damage possible from half angles (measured from the normal) as wide as 30°. This means that cracks can be detected, even though the ultrasonic beam makes an angle with the expected direction of the cracks, transverse direction in this case.

A composite plot of the three cases studied is given in Fig. A-22, where curve A corresponds to a single long groove, curve B to multiple short parallel grooves, and curve C to actual SCC conditions. The widening of curve C is possibly due to the fact that some cracks or segments of cracks make an angle with the transverse direction and are thus favorably oriented to the particular probe angle. This increases the angular sensitivity of the probe and makes possible the detection of stress corrosion cracks over wide angular limits.

H. Summary

The results of the investigation with simulated defects, for which the measuring frequency was 4 MHz, are summarized in the following paragraphs:

1. The reflectivity from a single artificial groove increases with increasing depth until it approaches a limiting value at a depth of about 1 wavelength (27 mils or 0.7 mm at 4 MHz). Total reflection was not observed even for grooves which were several wavelengths deep (Fig. A-8).

2. The Rayleigh wave reflection coefficient is proportional to $\exp(-\alpha\ \lambda/D)$, where D is depth of the groove and $\alpha \sim 0.5$ (Fig. A-10). Grooves as shallow as 20 μ can be detected at a probe distance of about 7 cm and on a surface finish as rough as that produced by a 240-grit paper

3. Angular rotation of the probe from normal incidence sharply decreased the echo amplitude from a groove or parallel grooves. For ex

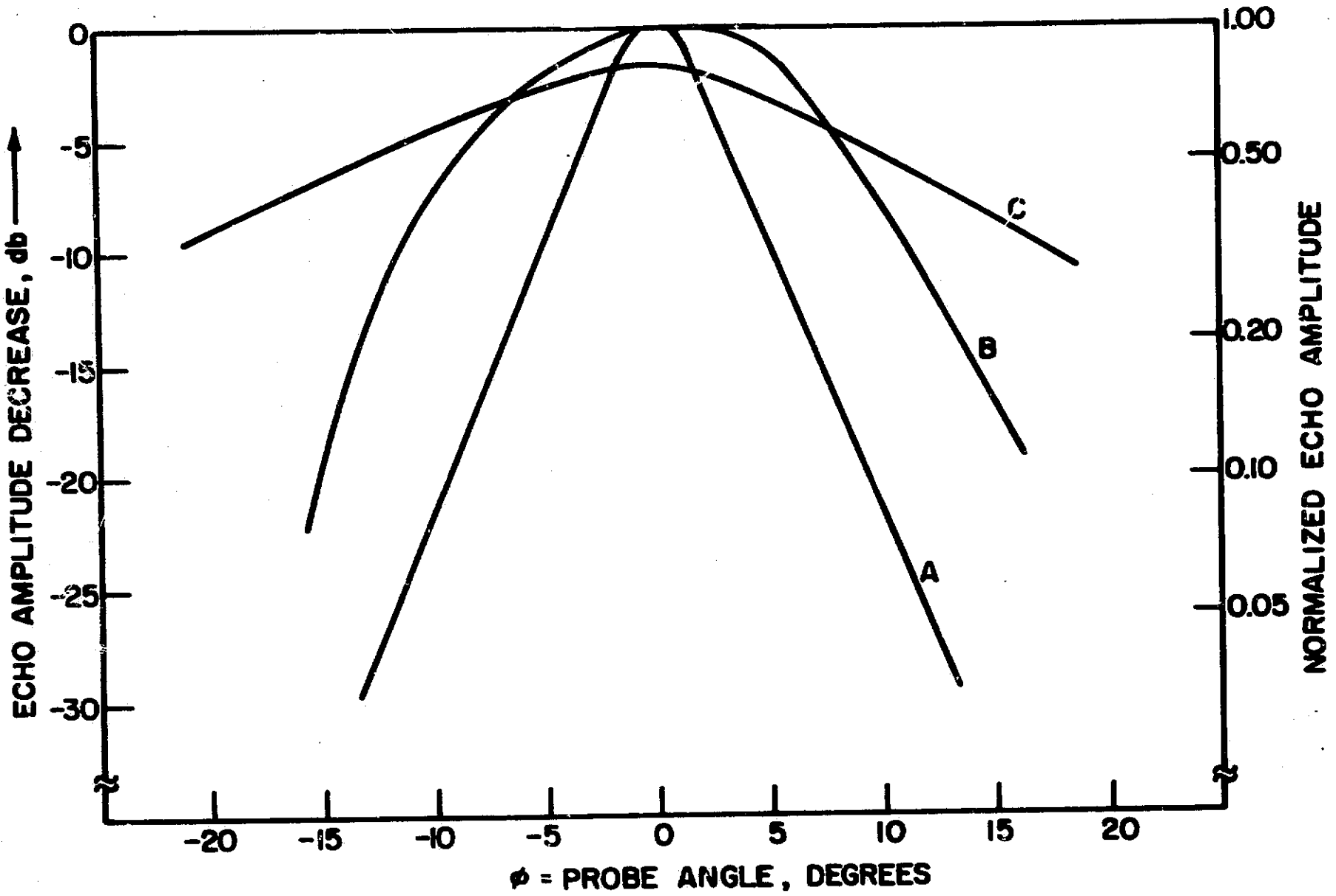

Fig. A-22. Effect of single long groove (A), multiple parallel short grooves (B), and SCC (C) on Rayleigh wave reflection as a function of probe angle (composite plot)

ample, an echo decreases to half its normal incidence value at an angle 3° (Fig. A-22).

4. Multiple parallel, short grooves give an angular distribution in between the SCC case and single groove case (Fig. A-22).

5. A defect that does not intersect the surface is readily detectable at an effective depth below the surface of 1 wavelength or less. Fig. A-11 shows how the tests were performed and gives the results.

6. The reflectivity from cylindrical holes with axes perpendicular to the surface increases with increasing hole diameter to about 4 mm or 7 wavelengths, after which it becomes constant (Fig. A-12). Also, the reflectivity from cylindrical holes increases with increasing hole depth to 1 mm or 1.5 wavelengths. Deeper than 1 mm, the echo remains roughly constant (Fig. A-15).

7. The reflection coefficient of a sharp edge decreases with increasing angle between the two planes from 90 to 180° where there are no reflections at all (Fig. A-16). These investigations were made on "sharp" edges. Of course, by rounding them the reflection coefficient would be drastically reduced.

Summarizing, we can say that if the dimension of a defect is of the order of a few tenths of a wavelength, reflections are readily visible along with an effective increase in attenuation. Defects located deeper below the surface than 1 wavelength are not detectable. The most genera conclusion that can be drawn is that Rayleigh waves are very sensitive to defects, but only in surface layers not more than 1 or 2 wavelengths thick